

Acoustic Sensing Techniques for the Shallow Water Environment

Acoustic Sensing Techniques for the Shallow Water Environment

Inversion Methods and Experiments

Edited by

Andrea Caiti

*University of Pisa,
Italy*

N. Ross Chapman

*University of Victoria, BC,
Canada*

Jean-Pierre Hermand

*Université Libre de Bruxelles,
Belgium*

Sérgio M. Jesus

*University of Algarve,
Faro, Portugal*



A C.I.P. Catalogue record for this book is available from the Library of Congress.

ISBN 978-94-024-0461-6

ISBN 978-1-4020-4386-4 (eBook)

DOI 10.1007/978-1-4020-4386-4

Published by Springer,
P.O. Box 17, 3300 AA Dordrecht, The Netherlands.

www.springer.com

Printed on acid-free paper

Additional material to this book can be downloaded from <http://extras.springer.com>

All rights reserved

All rights reserved for the article of Hines and Coffin and by Osler et al.

© 2006 Springer

Softcover reprint of the hardcover 1st edition 2006

No part of this work may be reproduced, stored in a retrieval system, or transmitted in any form or by any means, electronic, mechanical, photocopying, microfilming, recording or otherwise, without written permission from the Publisher, with the exception of any material supplied specifically for the purpose of being entered and executed on a computer system, for exclusive use by the purchaser of the work.



Acoustic Inversion Methods and Experiments for Assessment of the Shallow Water Environment

2nd Workshop 28-30 June 2004, Ischia, Italy

ADVANCE PROGRAM
30/5/04

	Mon 28 <i>Registration</i>	Tue 29	Wed 30
9.30 – Acoustics <i>Porter, M.; Abawi, A.; Hursky, P.; Siderius, M.</i>	Forward and Inverse Problems in High-Frequency Acoustics	Acoustic scattering from submerged and buried objects <i>Karasalo, I.; Skogqvist, P.</i>	
9.30 – On the assessment of geoaoustic parameters in shallow water environments <i>Le Gac, J.-C.; Stéphan, Y.; Garlan, T.; Weber, N.</i>		Remote sensing of sand ripples using high-frequency backscatter <i>Tang, D.; Williams, K.L.; Thorsos, E.I.</i>	
10.00 – Comparison of geoaoustic inversion approaches <i>Dosso, S.; Detmer, J.; Harrison, C.; Holland, C.; Prior, M.</i>		High-frequency bistatic scattering experiments using proud and buried targets <i>Blondel, Ph.; Jayasundere, N.; Dobbins, P.F.; Cosci, M.</i>	Inversion of propeller harmonics from a light aircraft for the geoaoustic properties of marine sediments <i>Buckingham, M.J.; Giddens, E.M.; Simonet, F.</i>
10.30 – Geoaoustic inversion in shallow water: A review <i>Meyer, M.; Hermand, J.-P.</i>		A sediment probe to measure geotechnical and geoaoustic seabed parameters <i>Osler, J.</i>	Inversion of shallow water ambient noise data by means of differential evolution as a global search method <i>Simons, D.G.; van Moll, C.; Harrison, C.H.</i>
	<i>Coffee break</i>	<i>Coffee break</i>	<i>Coffee break</i>
11.30 – Modal Mapping and Inversion in Range-Dependent, Shallow-Water Environments <i>Frisk, G.V.</i>		In-situ monitoring of photosynthesis by seagrass using sound transmission <i>Hermand, J.-P.</i>	Reflection Loss and Sub-bottom Profiling with Ambient Noise <i>Harrison, C.</i>
12.00 – Acoustic inversion at low kHz frequencies using normal incidence sonar <i>Hines, P.C.</i>		Manifestation of 3D effects in sound propagation in the SWARM'95 experiment and inversion of properties of internal waves in shallow water <i>Katsnelson, B.; Badiéy, M.; Lynch, J.; Pereseltkov, S.</i>	Geoaoustic inversion of high frequency ambient noise data <i>Siderius, M.; Harrison, C.</i>
12.30 – Long-range sediment tomography in the East China Sea <i>Miller, J.H.; Potty, G.R.</i>		Shallow water tomography in a highly variable scenario <i>Soares, C.; Jesus, S.M.; Coelho, E.</i>	Inversion of geoaoustic model parameters using ship noise <i>Chapman, R.; Dizaji, R.; Kirilin, L.</i>

	<i>Lunch break</i>	<i>Lunch break</i>	<i>Lunch break</i>
14.30 – 15.00	The characterization of local seabed properties using synthetic horizontal array data <i>Nielsen, P.L.; Fallat, M.</i>	Determining the forward model for assessing seabed properties by the inversion of reflection data using simulated annealing with rotated coordinates <i>Isakson, M.J.; Neilsen, T.B.; Worley</i>	Matched-field processing and geoaoustic inversion of humpback whale song off eastern Australia <i>Thode, A.M.; Gerstoft, P.; Noad, M.; Stokes, D.; Cato, D.</i>
15.00 – 15.30	The characterization of a range-dependent environment from towed array data from the MAPEX 2000 experiment. <i>Fallat, M.; Nielsen, P.; Dosso, S.; Siderius, M.</i>	Posterior estimation of transmissions loss from ocean acoustic data <i>Gerstoft, P.; Hodgkiss, W.S.</i>	Inversions of horizontal and vertical line array data for the estimation of geoaoustic model parameters <i>Tollefsen, D.; Wilmut, M.J.; Chapman, N.R.</i>
15.30 – 16.00	Accounting for bias in horizontal wavenumber estimates due to source motion <i>Becker, K.M.</i>	A forward model for geoaoustic inversion based on ray tracing and plane-wave reflection coefficients <i>Hovem, J.M.; Dong, H.; Li, X</i>	Geoaoustic inversion in two range-dependent environments with known seabed properties <i>Knobles, D.P.; Gray, M.; Swick, A.; Newman, R.; Stotts, S.A.; Koch, R.A.</i>
	<i>Coffee break</i>	<i>Coffee break</i>	<i>Coffee break</i>
16.30 – 17.00	In-situ observation of gassy sediment properties from acoustic reflection and scattering measurements <i>Holland, C.W.</i>		
– 17.30	Nonlinear acoustical methods in the detection of gassy sediments <i>Tegowski, J.; Klusek, Z.; Jakacki, J.</i>		

Acoustic Inversion Methods and Experiments for Assessment of the Shallow Water Environment

2nd Workshop 28-30 June 2004, Ischia, Italy



Table of Contents

Preface	xi
Acknowledgements	xiii
On the assessment of geoacoustic parameters in shallow water environments <i>Jean-Claude Le Gac, Yann Stéphan, Thierry Garlan and Nicholas Weber</i>	1
Bayesian inversion of seabed reflection data <i>Stan E. Dosso and Charles W. Holland</i>	17
Backpropagation techniques in ocean acoustic inversion: time reversal, retrogradation and adjoint modelling – A review <i>Matthias Meyer and Jean - Pierre Hermand</i>	29
Acoustic inversion at low kHz frequencies using an active, vertical line array <i>Paul C. Hines and Matt Coffin</i>	47
Dispersion of broadband acoustic normal modes in the context of long range sediment tomography <i>Gopu Potty and James Miller</i>	57
Characterization of local seabed properties using synthesized horizontal array data <i>Peter L. Nielsen, Mark Fallat and Christopher Harrison</i>	73
Characterization of a range-dependent environment from towed array data <i>Mark Fallat, Peter Nielsen, Stan E. Dosso and Martin Siderius</i>	87
Accounting for bias in horizontal wavenumber estimates due to source motion <i>Kyle M. Becker</i>	99
Acoustic clutter from buried submarine mud volcanoes <i>Charles W. Holland, Anthony L. Gerig and Piero Boni</i>	109
Nonlinear acoustical methods in the detection of gassy sediments <i>Jarosław Tęgowski, Zygmunt Klusek and Jaromir Jakacki</i>	125
Acoustic scattering from submerged and buried objects <i>Ilkka Karasalo and Patrik Skogqvist</i>	137
High-frequency bistatic scattering experiments using proud and buried targets <i>Philippe Blondel, Peter F. Dobbins, Nic Jayasundere and Mario Cosci</i>	155
A sediment probe for the rapid assessment of seabed characteristics <i>John Osler, Arnold Furlong and Harold Christian</i>	171

Continuous acoustic monitoring of physiological and environmental processes in seagrass prairies with focus on photosynthesis <i>Jean-Pierre Hermand</i>	183
Shallow water tomography in a highly variable scenario <i>Cristiano Soares, Sérgio M. Jesus and Emanuel Coelho</i>	197
Inversions of reflection loss measurements of a smooth water/sand interface <i>Marcia J. Isakson, Tracianne Neilsen and Andrew Worley</i>	213
Estimation of transmission loss and its uncertainty <i>Peter Gerstoft, Chen-Fen Huang and William Hodgkiss</i>	233
A forward model for geoacoustic inversion based on ray tracing and plane-wave reflection coefficients <i>Jens M. Hovem, Hefeng Dong and Xiukun Li</i>	241
Inversion of the propeller harmonics from a light aircraft for the geoacoustic properties of marine sediments <i>Michael J. Buckingham, Eric M. Giddens and Fernando Simonet</i>	257
Inversion of shallow water ambient noise data by means of differential evolution as a global search method <i>Dick G. Simons, Camiel van Moll and Chris H. Harrison</i>	265
Reflection loss and sub-bottom profiling with ambient noise <i>Chris Harrison</i>	281
Inversion of geoacoustic model parameters using ship radiated noise <i>N. Ross Chapman, Reza M. Dizaji and R. Lynn Kirlin</i>	289
Matched-field processing of humpback whale song off eastern Australia <i>Aaron Thode, Peter Gerstoft, Melania Guerra, M. Dale Stokes, Michael Noad and Douglas C. Cato</i>	303
Inversions of horizontal and vertical line array data for the estimation of geoacoustic model parameters <i>Dag Tollefsen, Michael J. Wilmut and Ross Chapman</i>	309
Issues of environmental variability in inverse problems in ocean <i>David P. Knobles, Mason Gray, Robert A. Koch and Adam Cook</i>	321
Author Index	329
Subject Index	331

CD-ROM enclosed, containing full color images which are printed in black-and-white in the book.

Preface

This volume contains the collection of papers from the second workshop on Experimental Acoustic Inversion Techniques for Exploration of the Shallow Water Environment. The workshop theme followed the original concept of the first workshop, held in Carvoeiro, Portugal, in 1999, i.e., to focus on experiments and experimental techniques for acoustic sensing in the shallow ocean. More than forty leading international scientists were invited to meet in the picturesque town of St. Angelo on the island of Ischia, in June 2004, to discuss progress in the application of new experimental techniques for exploration and assessment of shallow water environments.

Acoustic techniques provide the most effective means for remote sensing of ocean and sea floor processes, and for probing the structure beneath the sea floor. No other energy propagates as efficiently in the ocean: radio waves and visible light are severely limited in range because the ocean is a highly conductive medium. However, sound from breaking waves and coastal shipping can be heard throughout the ocean, and marine mammals communicate acoustically over basin scale distances.

The motivation for developing and improving acoustic techniques for shallow water applications remains as strong as ever. Near coast and inshore environments worldwide are critically important habitats for many ecologically, commercially, and socially important species. They are also rich with hydrocarbon and other mineral resources. At the same time, these areas house nearly 60% of the world's population and generate approximately 25% of global primary productivity. Pressure from industrial activity in the coastal cities, development of off shore resources, international and local shipping traffic and even recreation continues to threaten the coastal shallow water environment.

The papers in this book indicate a high level of research interest that has generated significant progress in development and application of experimental acoustic inversion techniques since the last workshop. The applications span a broad scope in geoscience, from geophysical, biological and even geochemical research. The list includes: estimation of geotechnical properties of sea bed materials; navigation and mapping of the sea floor; fisheries, aquaculture and sea bed habitat assessment; monitoring of marine mammals; sediment transport; and investigation of natural geohazards in marine sediments.

Several papers reveal progress in using high frequency acoustic backscatter to image objects on and beneath the sea floor, and generate data bases that combine bathymetry with non-acoustic information to provide comprehensive habitat maps of features such as eel grass. A new nonlinear acoustic technique is reported for detecting and quantifying the amount of gas in shallow marine sediments.

Significant progress is reported in a series of papers related to the development of new techniques for estimating geoacoustic properties of the sea bed by inversion of acoustic field data. Inversion techniques that are described here make use of natural sound sources in the ocean, and also novel experiments that use aircraft and ships as the sound source. The same inversion techniques are also being used for passive detection and tracking of marine mammals, using a new autonomous experimental recording system. A common feature in all the inversion techniques is the inter-relationship of diverse features and processes that

affect sound propagation in the ocean. An inversion for sea bed properties cannot ignore the effect of processes in the water column; uncertainty in one parameter of the environment leads to errors in the estimates of another. Perhaps the best example of this relationship is seen in matched field inversion methods which require explicit understanding of the sound propagation. As was the case in the previous workshop, the second workshop brought together researchers from diverse but fundamentally overlapping interests. The collected papers in this volume provide a comprehensive representation of current research efforts and developments, together with survey papers critically reviewing the progress made in the past years and the most promising trends for future research.

Acknowledgements

Once more, our thanks go to all conference participants for their essential contribution to this volume, and in particular to Orlando C. Rodríguez and Matthias Meyer for their help in the conference organization, maintenance of the conference website* and editing/typesetting of the proceedings.

Andrea Caiti, N. Ross Chapman, Jean-Pierre Hermand and Sérgio M. Jesus

*<http://www.ulb.ac.be/polytech/ehl/eaiw04/>

ON THE ASSESSMENT OF GEOACOUSTIC PARAMETERS IN SHALLOW WATER ENVIRONMENTS

JEAN-CLAUDE LE GAC, YANN STÉPHAN, THIERRY GARLAN
AND NICHOLAS WEBER

*EPSHOM, Centre Militaire d'Océanographie
13, rue Chatellier, BP30316, 29603 Brest Cédex, France
E-mail: {legac,stephan,garlan,weber}@shom.fr*

Seabed characterization nowadays refers to a great variety of tools and techniques related to a huge spectrum of potential needs. This large offer is undoubtedly a richness. However, it is known that each technique leads to bottom modelization that is filtered by the intrinsic characteristics of the techniques. A survey of differentiation criteria among available methodologies is presented in this paper. The complementarity of bottom modelizations they can lead to are argued and illustrated by theoretical and experimental evidence.

1 Introduction

Seabed characterization of shallow water environments is a matter of great interest due to the huge spectrum of potential applications such as hydrography and cartography of littoral regions, military oceanography, marine geosciences, offshore industry, environmental protection,... There are now a great variety of tools and techniques. However, none of these techniques can lead to a unique characterization of the bottom. The purpose of this paper is to show that, despite their diversity, all approaches may be merged in order to lead to a global observation of the bottom and therefore to a univocal geoacoustical model. To do so, we make a rapid survey of most common seabed characterization techniques illustrated by some experimental data sets and show the non-unique representation of the environment they individually lead to. We then focus on some experimental and theoretical evidence showing that coupled measurements involving several techniques can definitely improve the physical representation of the model. We finally point out the need of a global observation of the bottom with several techniques in order to lead to a unique geoacoustic model.

2 A survey of seabed characterization techniques

Seabed characterization is nowadays an expression that has a large number of meanings related to a great variety of requirements such as those listed above. These requirements

are associated with a large number of instrumental devices involving systems like corers, multi-beam echo sounders, sub-bottom profilers, sidescan sonars, seismic systems or sonar-like devices (commonly known as “geoacoustic inversion” that is based on long range acoustical propagation). This large quantity of techniques and systems¹ actually provides a large variety of data that are strongly linked to their intrinsic nature. In order to illustrate the richness of potential bottom representations that can thus be assessed, we propose to focus on the main criteria that differentiate the seabed characterization techniques for geosciences purposes.

2.1 *Geographical covering*

The most obvious difference is the associated geographical covering that can be obtained using one specific technique.

- single point: corings, borings or sediment grabings are the first historical seabed characterization techniques. They lead to what is generally called ground truthing. They provide data that are point measurements by nature even if they can reach a depth penetration of several tens of meters for favourable cases. The estimation of the geoacoustical parameters of the bottom is then a matter of laboratory protocol. They can be directly measured with very high frequency acoustical probes (from a few hundreds of kHz to some MHz) or deduced from geotechnical measurements using phenomenological relations like Hamilton’s ones e.g., [1].
- linear: vertical echo sounders, sub-bottom-profilers, seismic systems and sonar like devices give an information that is located along a transect. Typically, complete geophysical surveys of a particular area are conducted following parallel tracks that can potentially be merged in order to give a surface or even a 3D representation of the bottom (e.g., 3D-seismic).
- surface: today’s techniques of seafloor mapping are dominated by multi-beam echosounders and sidescan sonars. The main interest of these systems is that they can provide a very wide acoustical picture of the bottom with a surface covering and a resolution that depend on the technical characteristics of the systems. Typical sidescan sonar ranges reach a few hundred of meters in shallow and very shallow water environments with a resolution of a few decimeters, while typical ranges for multi-beam echo sounders are around 7 times the local depth with a resolution of a few meters (shallow water equipments) to a few tens of meters (deep water systems).

2.2 *Reflection or backscattering*

Another main difference of seabed characterization techniques is related to the physical phenomena they are based on. Following this distinction, classical techniques can be divided into two main categories: those that exploit the coherent reflection phenomenon, and those that are based on scattering (mostly backscattering).

Coherent reflection: When considering an incident acoustical wave interacting with the seabed interface, coherent reflection (or specular reflection) is related to the reflected wave in a direction symmetrical to that of its direction of arrival. The reflection coefficient depends on the impedance contrast and the grazing angle at the interface. Among the techniques

listed above, reflection seismic systems, sub-bottom profilers and most geoacoustic inversion techniques are based on the coherent reflection phenomenon.

Backscattering: When a sound wave interacts with an irregular interface or penetrates in an inhomogeneous sediment layer, the incident energy is reflected in all angular directions. This is the scattering phenomenon. Backscattering is the physical quantity that is measured by multi-beam echo sounders or vertical echo sounders used for sediment classification.

More interestingly, the consequence of this differentiation criterion is that techniques based on different physical phenomena do not lead to the same geoacoustic representations of the bottom. For example, the use of a calibrated sub-bottom profiler can lead to the evaluation of the reflection coefficient around normal incidence. Assuming a physical model of the reflection coefficient (e.g., visco-elastic, porous or phenomenological), some geoacoustical parameters of the bottom can be inverted. The form of the assumed model obviously defines the parameters that can be estimated (e.g., compressional speeds, attenuations or densities). When using a backscattered oriented device, the physical quantity that can be assessed is the backscattering index. There again, the geoacoustical parameters that can be estimated are also linked to the physical model that is assumed from the simplest (e.g., Lambert law) to the most complex (e.g., models based on the small slope approximation). Moreover, due to the complexity of real sediments (layering, inclusions,...) and in spite of the fact that sediment types have a strong (and visual) influence on measured reflection coefficient and backscattering strength values, no simple mapping can be found between sediment types and geoacoustical parameters. In addition, there is neither an obvious link between coherent reflection coefficient and backscattering strength, nor does there exist any obvious link with the associated models (e.g., some backscattering strength models use some parameters that do not appear in coherent reflection models as for example the Lambert's parameter). Additional differentiation criteria can be further pointed out when considering some specific technical items of the techniques design as described in the following paragraphs.

2.3 *Angular domain*

One main technical difference is that of the grazing angles that are involved: indeed the techniques are generally designed to observe the sea bottom in a limited grazing angle domain. This is for example the case for echo-sounders whose angular aperture is of typical order of around 60-70 degrees from the normal incidence for multi-beam echo-sounders, while it is only a few tens of degrees for sub-bottom profilers. The techniques may also be angular limited by the environment itself: for example, classical geoacoustic inversion techniques based on long range acoustical propagation between a source and a receiver are limited by the multipath structure of horizontal propagation e.g. [2, 19]. The strong attenuation of reflected paths above critical grazing angles results in a measurement that is limited to low grazing angles. Obviously, one particular technique can thus only provide a representation of the bottom that is biased by its intrinsic angular aperture. For example, the bottom reflection coefficient given by a sub-bottom profiler is not the same than that given by a geoacoustic inversion technique: in the first case, the bottom reflection coefficient of the bottom is a local one for grazing angles around normal incidence, while in the second case, it is an integrated one around horizontal grazing angles. Due to the

angular dependance of the reflection coefficient with grazing angle, the measured values are then different.

2.4 *Frequency domain*

Another fundamental difference of seabed characterization techniques is the frequency domains that they involve. The consequences of this differentiation criterion are manifold. Indeed, many different physical processes can be observed. However, their relative importance will depend on the signal frequency.

Scale of the physical processes: Basically, the seafloor may be considered as a rough interface with inhomogeneous underlying layers. The incident sound wave is scattered both by interface roughness and underlying inhomogeneities. The relative effect of every physical process has to be compared to the wavelength of the sound wave in order to estimate the scattering level.

Depth penetration: It is well known that due to an increasing attenuation of the acoustical waves with frequency, the higher the frequency, the less the penetration of the sound into the sediments. The characterization of the bottom provided by sidescan sonars (working at typical frequencies between 100 and 500 kHz) can only be superficial (i.e., it is limited to the sea-bottom interface), while low frequency seismic profiling surveys allow the characterization of the first hundreds of meters of the sediments. Even for similar techniques (e.g., involving the same principles as multi-beam echosounders), the representation can be very different from one system to another one: the reflectivity measurements given by a Kongsberg Maritime EM950 multi-beam echosounder (95 kHz) only involve superficial sediments [4], while those of an EM120 one (12 kHz) can involve a few tens of meters [5].

Resolution: The techniques based on the use of broadband acoustical signals are directly related to the frequency band of the signals themselves (the resolution is inversely proportional to the frequency band). Physical phenomena with spatial and temporal scales below the intrinsic resolution of a particular technique can not simply be assessed by the technique. Once again, techniques based on similar principles can lead to different representations of the bottom (see Figure 1).

2.5 *Signal processing techniques*

More specifically, another differentiation criterion can be pointed out. The signal processing techniques that are involved in the techniques can also directly affect the representation of the bottom that can be assessed. The improvement of signal to noise ratio is the constant aim of signal processing techniques in Underwater Acoustics. However, although the techniques may perform to theoretical limits, one still has to deal with the technical limitations of the acoustical devices, which often results from a compromise between the effective cost of the system, its physical characteristics and the performances that are looked for. Consequently, the quality of the representation that are obtainable can then be very different for systems that are based on the same principle but whose design is different. This is illustrated in the case of a sub-bottom profiler whose signal processing chain is parametrizable (see Figure 2).

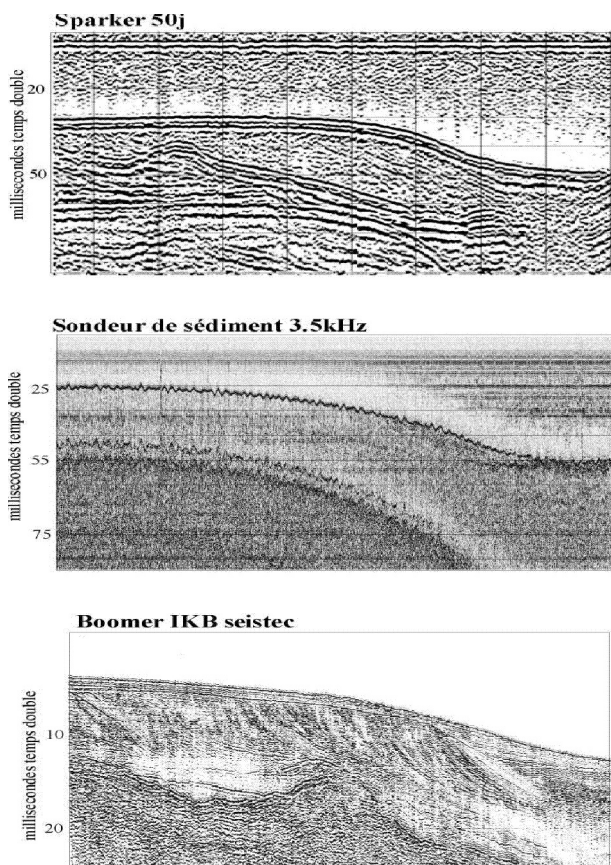


Figure 1. This figure provides a comparison of three different high resolution seismic systems on close transects in the Pertuis-Charentais (France). Top: Image obtained with a mini-sparker SIG (0.2 - 1.2 kHz); Middle: Image obtained with a sub-bottom profiler (2.5 - 4.5 kHz); Bottom: Image obtained with a boomer IKB Seistec (1 - 10 kHz). The intrinsic penetration and resolution are visually linked to the frequency spectrum of the acoustical signals.

2.6 Synthesis

Due to some few fundamental differences listed above, seabed characterization techniques provide a large variety of sediment assessments. The intrinsic limitations of each technique only provide a partial picture of the seafloor. In other words, the seafloor can only be seen through the dioptré of each technique, which more generally implies that the characteristics of the environments are filtered by the techniques themselves (see Figure 3). This is what is commonly known as a “through-the-sensor approach”. The use of an individual technique may of course be well fitted for a particular need. For example, the geometry and the technical characteristics of geoacoustic inversion technique and experimentation are generally very close to those of operational uses of low frequency operational sonars. The geoacoustical parametrization of the bottom that these techniques provide is generally

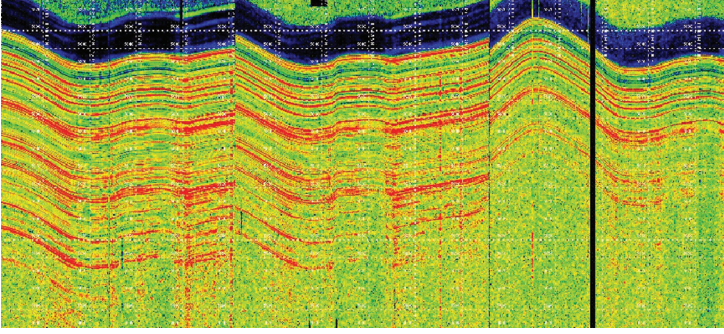


Figure 2. This figure provides a comparison of the new sub-bottom profiler Kongsberg Maritime SBP120 for three different configurations for the same transect over a muddy sediment deep water site in the Bay of Biscay (France). This systems uses a multibeam technology which allows to parametrize both emitting (Tx) and receiving (Rx) apertures. In this case, the best penetration is obtained with a 3 by 3 degrees Tx-Rx configuration (left) (the penetration is around 100 meters depth), while there is a constant degradation of the system performances with the widening of the Tx-Rx apertures (Middle: 6 by 6 degrees - Right: 12 by 12 degrees). The 3 by 3 degrees configuration provides a penetration that is twice that of the 12 by 12 degrees configuration.

good enough to calculate bottom reflection coefficients that can drastically improve sonar performance calculations (see [19]). However, the above differences also imply the following issues:

- When dealing with a particular need, it is not always possible to get access to the technique that can specifically give the necessary and sufficient answers to this need. The question that then arises is then: to what extent can we extrapolate the seabed representation given by one system in order to fulfill this particular need (partially or completely)? (e.g., for operational sonars, how can we extrapolate an adapted characterization of the seabed with standard survey techniques?).
- More generally, the dream of a univocal and global observation of the seabed characteristics that would be sufficient for every need is probably not realizable. However, the fusion of the data that are provided by different systems is undoubtedly a future way of seabed characterization in order to approach more global answers than those given by an individual technique. The issue is then to know how this can be dealt with, and how the potential contradictions can be managed.

3 Some experimental and theoretical evidence of the complementarity of different seabed characterization techniques

With the large diversity of seabed characterization techniques being described, we may wonder whether they can be used in a complementary manner. Several published experiments and studies have already shown that coupling different approaches may drastically improve the understanding of seafloor geoaoustic properties and physical mechanisms. In [6], the author studies the coupling of scattering and reflection measurements. In this paper, Holland's needs are related to the fact that operating active sonar systems in littoral regions requires that seabed reflection and scattering data be provided in order to predict

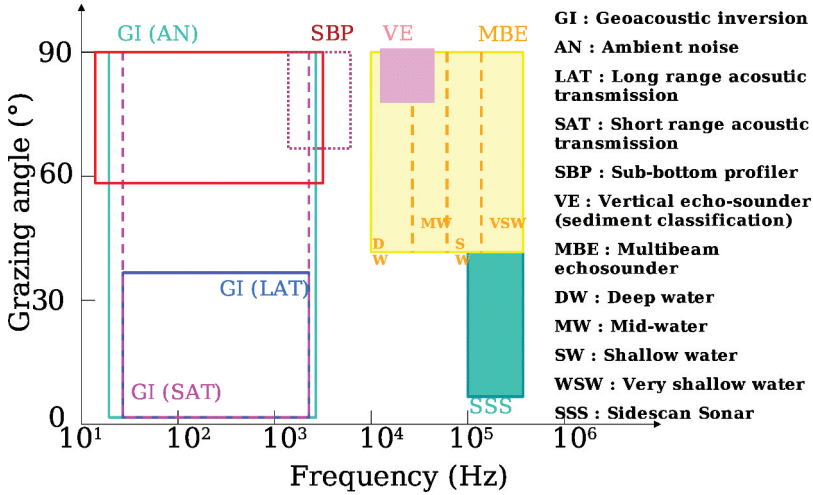


Figure 3. This figure provides a synthesis of the frequency-grazing angle domains that are involved in the available seabed characterization techniques. The techniques based on backscattering measurements are represented by filled areas, while those that are based on coherent reflection are represented by the unfilled areas. Ground truthing techniques (corings) are not represented here: they only involve measurements at very high frequencies (several MHz or hundreds of kHz). This figure obviously shows that each technique provide an image of the sea-bottom that is filtered by the technique itself.

sonar performance. The problem that often arises is that current operational databases are inadequate for supplying this information especially in shallow water. According to the author, this is mainly due to the fact that survey measurements of scattering and reflection are typically conducted, processed and analyzed in a completely separate way. Holland studies scattering and reflection for low to mid-frequencies (1 - 6 kHz) on the Malta Plateau (Mediterranean Sea) and shows that both parameters are not dominated by the water-sediment interface, but by sub-bottom layering. In order to demonstrate the interest of coupled measurements of both parameters, he makes use of two original techniques [7, 8] that allow measurement of both quantities in a coupled manner. The method provides the opportunity to understand the seafloor geoacoustic properties and physical mechanisms. In particular, it is demonstrated that the geoacoustic properties obtained from the reflection data provide insight into the scattering and its site-to-site variability.

The coupling of measurements often becomes a necessity: indeed, the interpretation based on an individual technique can lead to erroneous geoacoustic parameterizations. In [9], the authors study the backscattering strength measured by a 6.5 kHz deep-water sidescan sonar (Gloria) over the Monterey fan. They observe that high backscattering indexes are obtained over silty clay areas with fine sandy sediment layers, while low backscattering indexes are got over sandy areas with a thin surface muddy sediment layer. This result is paradoxical at first glance and shows that backscattering strength model has to include the effects of layering and of inhomogeneities [10]. In this case, the coupling of sidescan sonar imaging and corings is the approach that leads to a better interpretation of the data. The same kind of conclusions have been taken in other regions and with different systems. This is for example the case of the “white stain” that was observed by the French institute IFREMER² with a Kongsberg Maritime EM12 multibeam echo sounder over the Var distal lobe (Mediterranean

Sea) [5]. In this case, low backscattering strength was measured over a sandy bank covered by a thin fine sediments layer. As with the Monterey fan measurements, the result is quite astonishing since the backscattering level is of the same order of magnitude as the one that could have been observed over thick fine sediments. Once again, ground truth measurements with corings provided complementary information to the multibeam echosounders imagery. More generally, it seems that an a priori knowledge of the sedimentological context often avoids erroneous interpretations. This is illustrated by a joint analysis of the sedimentological processes and the EM12 multibeam echosounder imagery on a surveyed area in the Gulf of Oman (Arabic Sea) by the French Hydrographic and Oceanographic Office (SHOM) (see Figure 4). In this case, it is shown that EM12 imagery involves the sediment response of surface and sub-surface sediments, and that including data from cores provides the opportunity to better understand the physical processes that are involved. Another example over a sandy sediment bank near Brest (France) in a coastal area illustrates the interest of the coupling of a higher frequency multibeam echosounder (Kongsberg Maritime EM1002S) and of a sub-bottom profiler (SBP120) (see Figure 5).

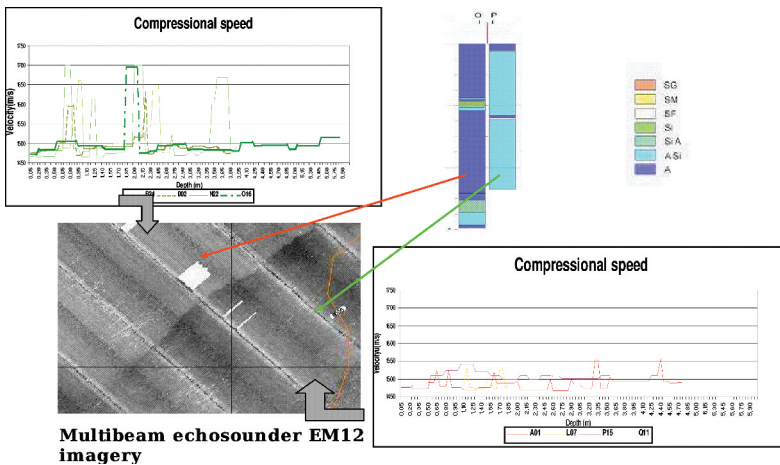


Figure 4. This figure provides a joint analysis of multibeam echosounder EM12 imagery and corings. The picture (c) shows that there are two distinguishable areas: the backscattered level is higher in the dark grey area than in the light grey one. In [11], the author mentions that both areas are governed by two different sedimentological deposit processes that were characterized thanks to several corings (a)-(b)-(d) (4 corings in each area). The superficial sediments are quite the same for both regions (mud). Below the superficial layer, the dark grey area is characterized by several silty thin and hard layers (whose compressional speed are higher than 1700 m/s) surrounded by muddy sediments. The light grey area sub-surface sediments are mixed muddy and silty sediments with very thin hard silty layers. The acoustical energy of the EM12 echosounder is known to reach depth penetrations of a few tens of meters [5]. The seafloor imagery that EM12 give are therefore integrated images of the first superficial layers of the seafloor.

The richness of a multi-frequency approach has already been expressed in section 1. The arguments for a multi-frequency approach have been outlined in terms of the induced variety of depth penetrations and resolutions that can be obtained with some different technical characteristics. Other evidences of the interest of this kind of approach have also been formerly expressed in a workshop dedicated to the benchmark of geoaoustic inversion

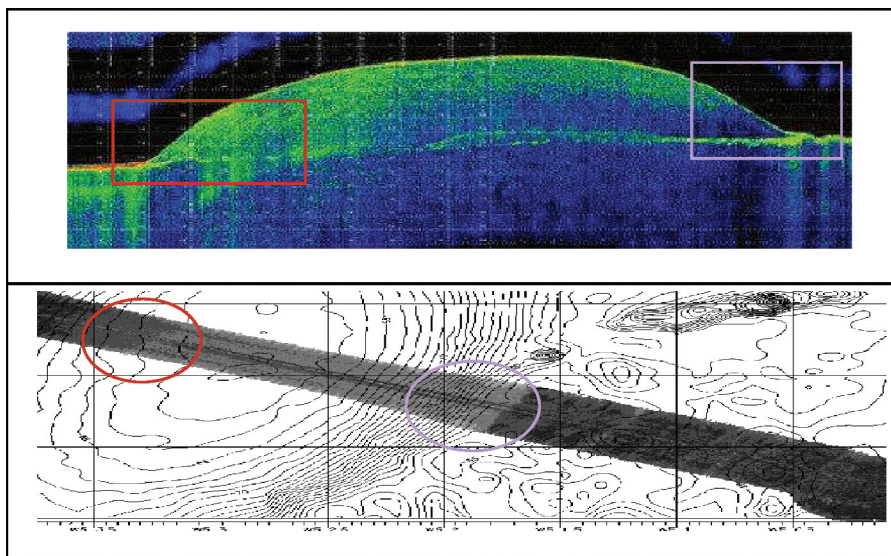


Figure 5. This figure presents a coupled analysis of the imagery provided by an EM1002S (95 kHz) multibeam echosounder and a sub-bottom profiler section on a sandy bank (Armen Bank) in a coastal area in the North-East Atlantic Ocean near Brest (France). The bank is around 30 meters high. On the left side of the bank (dark gray underlined area), a vertical layering can be noticed. The layering is probably due to sedimentological dynamics. In the same area, it can be seen a smooth transition of the multibeam echosounder imagery. On the contrary, on the right side of the bank, there is no layering and the bound of the bank is rather abrupt on the imagery. Though still under investigation, the reasons of these different behaviours of the EM1002S imagery seem to be linked to the sediment processes.

methods that was held in Victoria, Canada in 1997 [12]. In the paper presented in [13], the authors study a matched field inversion process in an iterative manner. The data they use are the simulated complex pressure field measured at a vertical antenna (VLA) location. The distance between the source and the VLA is 5 km. Three individual frequencies (500 Hz, 100 Hz and 25 Hz) are used in the inversion process. Assuming that the lower sediments and the basement have little effects on the 500 Hz propagation, they first use the highest frequency to carry out a two dimensional grid search over the density and the compressional speed at the top of the sediment. The 100 Hz data are then used for investigation of the sediment sound speed. And then a third step is performed to search for every parameter using the most penetrative frequency (i.e., 25 Hz). Indeed, the central idea of this paper is rather intuitive: very different frequencies are sensitive to very different physical processes, which was already mentioned above.

Some more fundamental arguments for a multi-frequency approach can be found in the scientific literature. As underlined in [14] and references herein, “the sediment acoustics literature reveals that, for a wide range of sediment types (fully saturated with seawater), and to first order, attenuation varies according to the first power of measurement frequency and that velocity dispersion is very small, if not negligible, over the frequency range 1 Hz - 1 MHz”. However, it is also noted that “more complex frequency dependencies of

velocity and attenuation are predicted by the Biot model and its derivatives". Moreover there are experimental evidences that support this last assumption [16, 17]. These published results plead for caution in analysis of coupled measurements: the simple extrapolation of a measured geoacoustical parameter from one frequency to one another is not obvious, especially when the frequency difference is very high. That is often the case when one uses data from corings and compares them to low frequency measurements like those provided by seismic systems or geoacoustic inversion techniques. The complementarity of the data is once again demonstrated by the fact that the analysis of an individual technique can lead to misused interpretation.

The reasons for a multi-angular study of the bottom are also rather intuitive. Many arguments can be found in the literature: most of them have to deal with the grazing angle dependency of reflection coefficient and backscattering strength. It is well known that geoacoustical parameters and physical processes effects are different from one grazing angle domain to one another. Sensitivity studies have been extensively made about the impact of geoacoustical parameters on the reflection coefficient. For example, geoacoustic inversion techniques have explicitly exposed the problem of the non-uniqueness of geoacoustical modelization of the bottom: several geoacoustical model can lead to equivalent acoustical responses of the medium. In [18], the authors aim at inverting the geoacoustical properties of the bottom from horizontal acoustical transmissions during the INTIMATE'96 experiment [19]. Broadband signals (chirps between 300 and 800 Hz) are regularly emitted by a source and received on a 5.6 km distant hydrophone. The objective of the study is to determine an acoustical equivalent representation of the bottom given by the reflection coefficient rather than by a set a geoacoustical parameters. It is shown herein that the bottom can equivalently be modeled by a semi-infinite fluid half space, a two layer or a three layer medium: the semi-infinite model provides a reflection coefficient that is a mean approximation of the real reflection coefficient, while the two-layer and the three layers exhibit the same dispersive characteristics for grazing angles below the critical angle. However, when comparing the propagation losses between the source and the receiver, it is also shown that the three models give nearly identical results (see Figure 6). This interesting behaviour of the reflection coefficient is explained thanks to a sensitivity study presented in [19]: among the sets of geoacoustical parameters of the two and the three layers models, some of them have a strong impact on the reflection coefficient (and thus on the measurements) while others are nearly insensitive. Values for these parameters could eventually be chosen randomly within realistic bounds, which finally demonstrates that some angular limited measurements cannot be used in order to estimate them.

The same conclusions can be found in the basic sensitivity study provided in [2] (see Figure 7). The authors study the very simple case of a fluid-fluid and fluid-solid interface. The effects of four geoacoustical parameters are presented. It is shown that compressional speed affects bottom losses for every grazing angle and that it determines the apparent critical angle. The p-wave attenuation has a strong impact only for low grazing angles which obviously shows that it is sensitive for long-range shallow water propagation measurements. On the contrary, density is shown to have only a negligible effect at low grazing angles, while it is seen to be very important near normal incidence, etc. Some similar results can be found about backscattering strength. In [20], an equivalent input backscattering strength model aiming at treating the complex cases of multi-layered bottom is developed. The authors show that physical phenomena effects (e.g., influence of

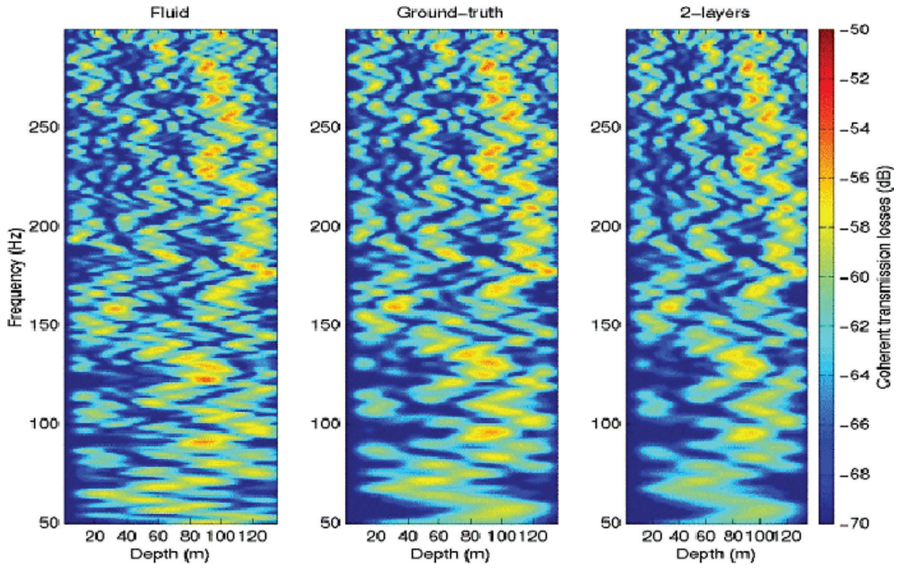


Figure 6. This figure presents the simulated transmission losses on a vertical line array that is 5.6 km distant from the acoustic source in the context of the INTIMATE'96 experiment [18]. The simulation shows that a semi-infinite fluid half space, a two layer bottom or a three layer one provide the same estimates of the propagation losses above 200 Hz. Some differences appear in the range 50 - 200 Hz due to the fact that the measurements were done for frequencies between 300 and 800 Hz.

underlying layers like impedance contrasts, induced refractions and attenuations, volume limitation) are also grazing angle dependent.

As a synthesis, it can be easily understood that the chances of a specific technique to infer some parameters are linked to the measurement sensitivity to these parameters, which can be summarized in the obvious following corollary: the more sensitive the parameter, the higher the chances of success!

A last argument for the observation of the bottom with complementary techniques should finally be mentioned. Multibeam echo sounders and side scan sonars provide data whose horizontal resolution may be quite different. The longitudinal and transversal resolutions of these systems depend either on the angular aperture of the sounders or on the signal characteristics (duration or frequency band for those using coherent processing methods). When possible, the coupling of systems providing different resolutions may be quite meaningful as illustrated in Figure 8.

In order to illustrate the general ideas described in this paper, we finally present a last example (Figure 9) showing the complementarity of some basic and common techniques used for seabed characterization. It is visually shown that a mixed analysis of different techniques can substantially improve the bottom assessment techniques.

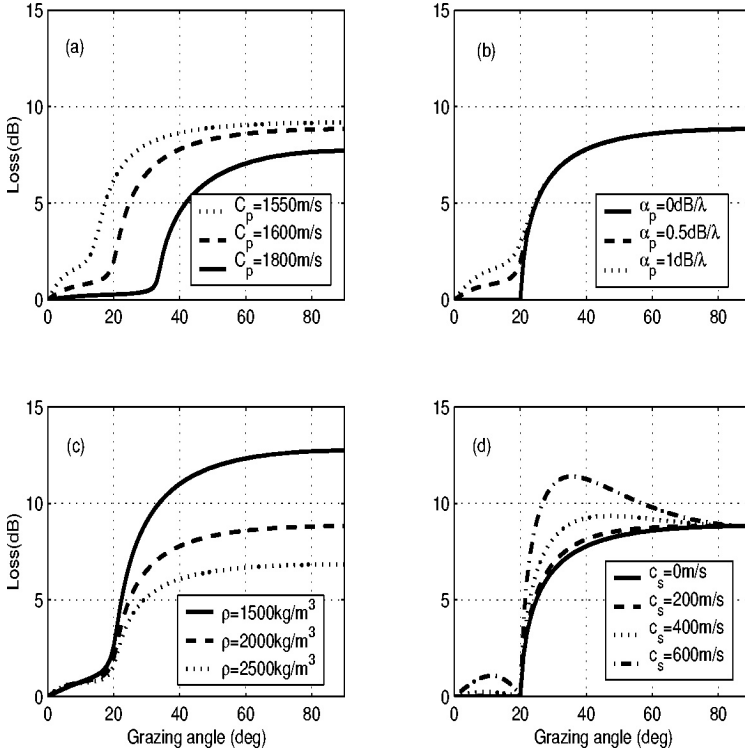


Figure 7. This figure presents a sensitivity study [2] about the effects of geoacoustical parameters for simple fluid-fluid interfaces (a)-(b)-(c) and a fluid-solid interface (d). (a): It is shown that the compressional speed of the bottom has a strong effect on the bottom losses. In particular, it determines the critical angle; (b): Figure (b) displays the effects of p-wave attenuation on bottom losses. This parameter is shown to affect the bottom losses for grazing angles below the critical angle; (c): The effect of density is shown. It has negligible effect below critical angle, while it is seen to have a major influence near normal incidence; (d): Shear speed in the bottom affects bottom losses at both subcritical and intermediate grazing angles.

4 Conclusions and perspectives

The intentions of this paper are rather general. The number of seabed characterization techniques is nowadays very large. Most of them have historically been developed for particular needs. However, the need of a global observation of the seabed characteristics is more and more becoming a new trend in the scientific community [6, 21]. Among the main reasons of this tendency, we have underlined the fact that each technique could only provide a partial picture of the bottom that was biased by the limitations of the technique itself. Moreover, it is theoretically and experimentally proven that complementary results should be assessed using a joint analysis of different techniques. This is particularly true when measurements involve many physical processes and scales. In addition, the need of global databases of geoacoustic parameters remains necessary. However, it is well known that they are often built using data that are acquired, analyzed and processed in an incoherent manner which often results in inadequate databases for some particular needs.

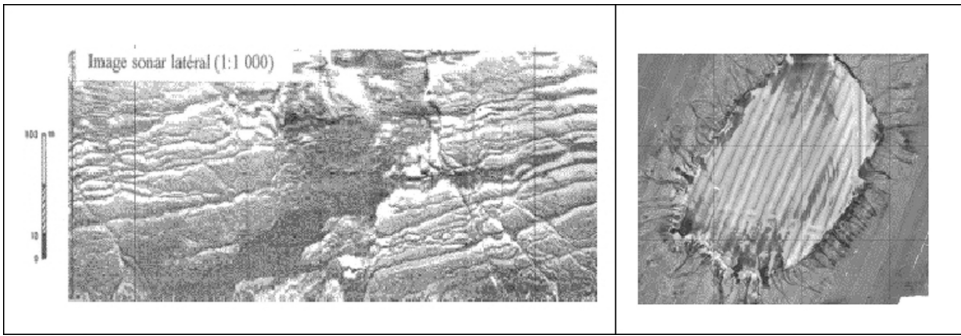


Figure 8. Left: Sidescan sonar Egg 272TD (100 kHz) imagery. The resolution of the system allows to identify sedimentological features at a fine scale. Right: Kongsberg Maritime EM300 (30 kHz) imagery. The covering of this picture is around 0.5 by 0.5 degrees of latitude and longitude. The imagery is more global than those of the sidescan sonar imagery. In the context of shallow and very shallow water environments, both systems can be used, thus providing data that have different resolutions.

This general assumption of a global observation is becoming less and less utopic. The standard equipment of modern scientific ships are at higher and higher levels. This is for example the case of the BHO Beutemps-BeauprL' new scientific ship of the SHOM whose standard equipment for seabed characterization includes a shallow water multibeam echosounder (EM1002S at 95kHz), a deep water one (EM120 at 12 kHz), two sub-bottom profilers (SBP120 and TR109), coring and sidescan sonar capabilities... More specific means can also be managed like low frequency long range propagation measurements, seismic surveys... Moreover, the increasing quantity of available standard equipment is coupled with an overall improvement of the capability of each one. More and more systems now give the opportunity to provide calibrated data which is nowadays an open way toward a generalized quantitative approach for seabed characterization.

Much work needs to be done in order to achieve this goal: general methodologies for the merging and the fusion of data of different types are not yet available. There are only a few of them (e.g. [6]) that are often merged at a basic level at the present time (like the sedimentological interpretation of the multibeam echosounder imagery, the coring and the subbottom profiler data illustrated above). The French institutes SHOM and IFREMER are expected to develop a contribution to the development of methodologies in the near future within the CALIMERO project (CALibration of MEthods for Recognizing the bottom Ocean). The techniques that will be involved include the data acquisition of nearly every category of seabed characterization techniques available at the present time (corings and borings), 3 multibeam echosounder imageries (12, 30 and 95 kHz), imageries of 2 sidescan sonars (100 and 450 kHz), long range low frequency propagations (300 Hz - 1 kHz), surveys with 2 subbottom profilers (3 - 6.5 kHz with multi-beam capabilities, 1.8 - 5 kHz), sediment classification, 2D (and punctually 3D) high (50 - 350 Hz) and very high (650 Hz - 2 kHz) resolution seismic surveys. Further geoacoustical studies by both institutes should involve in the near future the fusion of multi-frequency surface imageries and the characterization of the bottom for low and very low frequencies.

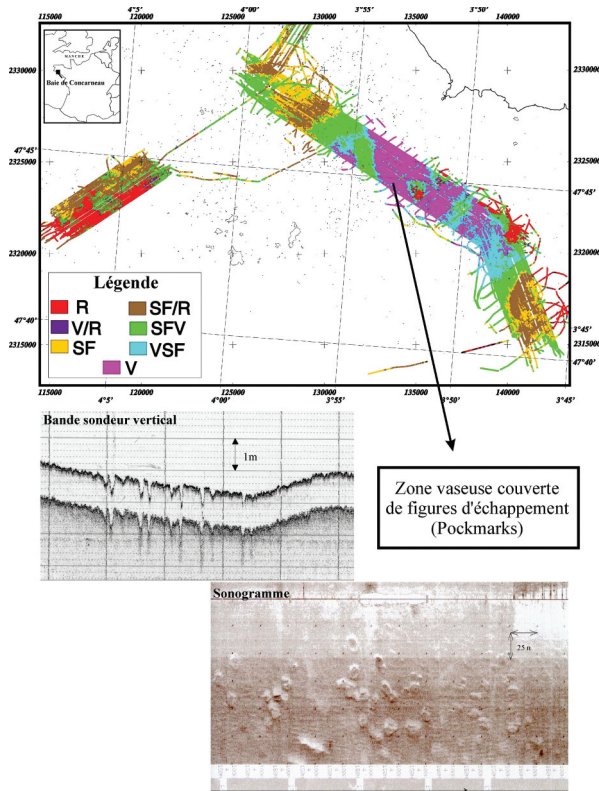


Figure 9. This figure presents the analysis of a sediment classification system (ROXANN) jointly with the data of a vertical echo sounder and those of a Egg 272TD sidescan sonar. The classification system manages to discriminate a muddy sediment area (**V** area) from a surrounding area that is also muddy (**SFV** area). On the vertical echo sounder, the bathymetry is seen to be regularly perturbed. On the sidescan sonar imagery, these perturbations are seen to be correlated with the presence of pockmarks that modify the acoustical response of the seabed. The discrimination provided by the sediment classification system is explained by the presence of the pockmarks field.

Notes

1. In the following text, techniques and systems will not be differentiated any more and will be gathered in the unique word “techniques”.
2. IFREMER: French Research Institute for the Exploitation of the Sea.

References

1. Hamilton E. L. and Bachman R. T., Sound velocity and related properties of marine sediments. *J. Acoust. Soc. Am.* **72**, 1891–1904 (1982).

2. Jensen F. B., Kuperman W. A., Porter M. B. and Schmidt H., *Computational ocean acoustics*, Chapter 1, 46–48, AIP Series in Modern Acoustics and Signal processing, New York (1994).
3. Le Gac J.-C., Asch M., Stéphan Y. and Demoulin X., *Inversion of broadband acoustic data in shallow water on a single hydrophone*. *IEEE Journal of Oceanic Engineering* **28**(3), 479–493 (2003).
4. Hellequin L., *Analyse statistique et spectrale des signaux de sondeurs multi-faisceaux EM950 - Application à l'identification des fonds sous-marins*. PhD manuscript, Université de Rennes 1, France, 180 pages (1998) (In French).
5. Guillon L., *Contribution à l'interprétation géoacoustique de la rétrodiffusion des fonds marins: influence de la stratification, des inclusions et de la porosité*. PhD manuscript, Université du Maine, France, 200 pages (1999) (In French).
6. Holland C. W., *Shallow water coupled scattering and reflection measurements*. Saclantcen report SR-344, 37 pages (2001).
7. Holland C. W., Hollet R. and Troiano L., Measurement technique for bottom scattering in shallow water. *J. Acoust. Soc. Am.* **108**(3), 997–1011 (2000).
8. Holland C. W. and Osler J., High resolution geoacoustic inversion in shallow water: A joint time- and frequency-domain technique. *J. Acoust. Soc. Am.* **107**(3), 1263–1279 (2000).
9. Gardner J. V. et al., Ground truthing 6.5 kHz side scan sonographs: what are we really imaging? *J. Geophys. Res.* **96**(B4), 5955–5974 (1991).
10. Lyons A. P., Anderson A. L. and Dwan F. S., Acoustic scattering from the sea-floor: modeling and data comparison. *J. Acoust. Soc. Am.* **95**(5), 2241–2451 (1994).
11. Garlan T., *Apports de la modélisation dans l'étude de la sédimentation marine récente*. Habilitation for conducting research programs, Université des Sciences et Techniques de Lille, France (To be published) (In French).
12. Special issue on “Benchmarking geoacoustic inversion methods”. *J. Comp. Acous.* **6**(1-2), 290 pages (1998).
13. Hamson R. M. and Ainslie M. A., Broadband geoacoustic deduction. *J. Comp. Acous.* **6**(1-2), 45–59 (1998).
14. Best A. I., Hugget Q. J. and Harris A. J. K., Comparison of in situ and laboratory acoustic measurements on Lough Hyne marine sediments. *J. Acoust. Soc. Am.* **110**(2), 695–709 (2001).
15. Guillon L., La tache blanche: modélisation géoacoustique. Workshop Groupe de Caractérisation des Fonds, Brest, France (2003).
16. Maguer A., Bovio E., Fox W. L. and Schmidt H., In situ estimation of sediment sound speed and critical angle. *J. Acoust. Soc. Am.* **108**(3), 987–996 (2001).
17. Williams K. L., Jackson D. R., Thorsos E. I., Tang D. and Schock S. G., Comparison of sound speed and attenuation measured in a sandy sediment to predictions based on the Biot theory of porous media. *IEEE J. Oceanic Eng.* **27**(3), 413–428 (2002).
18. Le Gac J.-C., *Deux approches de l'inversion géoacoustique: Inversion par signaux large bande et approche variationnelle*. PhD manuscript, Université de Toulon et du Var, France, 196 pages (2003) (In French).
19. Stéphan Y., Demoulin X., Folégot T., Jesus S., Porter M. B. and Coelho E., Acoustical effects of internal tides on shallow water propagation: an overview of the INTIMATE 96 experiment. In *Experimental Acoustic Inversion Methods for exploration of the shallow water environment*. A. Caiti et al., Eds, Kluwer Academic Publishers, 107–124 (2000).
20. Guillon L. and Lurton X., Backscattering from buried sediment layers: The equivalent input backscattering strength model. *J. Acoust. Soc. Am.* **109**(1), 122–132 (2001).
21. Thorsos E. I. et al., An overview of SAX99: Acoustic measurements. *IEEE J. Oceanic Eng.* **26**(1), 4–25 (2001).

BAYESIAN INVERSION OF SEABED REFLECTION DATA

STAN. E. DOSSO

*University of Victoria, School of Earth and Ocean Sciences
Victoria, British Columbia, Canada
E-mail: sdosso@uvic.ca*

CHARLES. W. HOLLAND

*Pennsylvania State University, Applied Research Laboratory
State College, Pennsylvania, U.S.A.
E-mail: cwh10@psu.edu*

This paper applies nonlinear Bayesian inversion to seabed reflection data from two sites in the Strait of Sicily to estimate visco-elastic parameters of the upper-most sediments. At one site the seabed consists of fine-grained, low-velocity sediments, resulting in reflectivity data (bottom loss versus grazing angle) with a well-defined angle of intromission. At the second site the seabed consists of high-velocity sediments, resulting in a critical angle. The Bayesian inversion provides maximum a posteriori parameter estimates with uncertainties quantified in terms of standard deviations and marginal probability distributions. Data uncertainties are quantified using several approaches, including analysis of experimental errors, maximum-likelihood estimation, and treating uncertainties as nuisance parameters in the Bayesian inversion. Statistical tests are applied to the data residuals to validate the assumed uncertainty distributions. Excellent results (i.e., small uncertainties) are obtained for sediment compressional velocity, compressional attenuation, and density; shear parameters are poorly determined although low shear-wave velocities are indicated. The Bayesian analysis provides a quantitative comparison of inversion results for the two sites, and indicates that the geoacoustic information content is significantly higher for angle-of-intromission data.

1 Introduction

Acoustic propagation and reverberation in shallow water is strongly influenced by interaction with the seabed, and knowledge of seabed geoacoustic properties often represents the limiting factor in modeling these phenomena [1]. While matched-field inversion for shallow-water geoacoustic parameters has received wide attention in recent years, e.g., [2]–[7], other approaches such as the inversion of reflection-coefficient (or, equivalently, bottom-loss) data also hold great promise [8]–[11].

This paper presents a general Bayesian approach to reflectivity inversion. The seabed is modeled as a viscoelastic solid with unknown density and compressional- and shear-wave velocities and attenuation coefficients. The inversion is based on estimating properties of the posterior probability density

(PPD) of the model parameters, which combines prior information with observed data expressed in terms of a likelihood function. The multi-dimensional PPD is interpreted in terms of the maximum a posteriori (MAP) estimate, standard deviations of the parameter estimates, and marginal probability distributions, computed using Markov-chain Monte Carlo sampling methods [6, 7, 12, 13].

An important aspect of Bayesian inversion involves specifying the data uncertainty distribution, including measurement and theory errors, which characterizes the likelihood function. Data uncertainties are assumed here to be due to independent, Gaussian-distributed random errors, with several approaches applied to estimate data standard deviations. The assumed form of the uncertainties is validated a posteriori by applying rigorous statistical tests to the distributions of data residuals, an important check that does not appear to have been applied previously in geoacoustic inversion.

The Bayesian inversion is applied to high-resolution reflectivity measurements from two sites in the Straits of Sicily [9, 14]. At one site the seabed consists of fine-grained, water-saturated sediments with a compressional velocity less than that of water, resulting in reflectivity data characterized by a well-defined angle of intromission (near-perfect transmission). The seabed at the second site consists of higher-velocity sediments, resulting in data characterized by a critical angle. The Bayesian analysis provides a quantitative comparison of the inversion results for the two sites in terms of the resolution of specific geoacoustic parameters.

2 Theory

2.1 Seabed reflectivity

The bottom loss BL on reflection is defined in terms of the pressure reflection coefficient R and grazing angle θ at the water-seabed interface as

$$BL(\theta) = -10 \log_{10} |R(\theta)|^2 \quad (\text{dB}). \quad (1)$$

For homogeneous media, boundary conditions of continuity of pressure and particle velocity lead to [15]

$$R = \frac{Z_b - Z_w}{Z_b + Z_w}, \quad (2)$$

$$Z_w = \rho_w v_w / \sin \theta, \quad (3)$$

$$Z_b = \rho v_p \cos^2 2\theta_s / \sin \theta_p + \rho v_s \sin^2 2\theta_s / \sin \theta_s, \quad (4)$$

where v_w and v_p are the compressional-wave velocities in the water and seabed, v_s is the seabed shear-wave velocity, ρ_w and ρ are the densities for the water and seabed, and θ_p and θ_s are the transmission angles for sediment compressional and shear waves given by Snell's law

$$\cos \theta / v_w = \cos \theta_p / v_p = \cos \theta_s / v_s. \quad (5)$$

Attenuation is incorporated by substituting complex wave velocities into Eqs.(2)-(5)

$$v'_p = v_p [1 + i\alpha_p / (40\pi \log_{10} e)]^{-1}, \quad (6)$$

$$v'_s = v_s [1 + i\alpha_s / (40\pi \log_{10} e)]^{-1}, \quad (7)$$

where α_p and α_s are the compressional- and shear-wave attenuation coefficients, respectively, in units of dB/ λ where λ is the wavelength.

2.2 Bayesian inversion

Let \mathbf{m} and \mathbf{d} represent model and data vectors, respectively, considered to be random variables. Bayesian inversion is based on Bayes' rule, which may be expressed

$$P(\mathbf{m}|\mathbf{d}) \propto P(\mathbf{d}|\mathbf{m})P(\mathbf{m}), \quad (8)$$

where $P(\mathbf{d}|\mathbf{m})$ represents the data information, $P(\mathbf{m})$ is the prior information, and $P(\mathbf{m}|\mathbf{d})$ is the PPD. Interpreting $P(\mathbf{d}|\mathbf{m})$ as a function of \mathbf{m} for the (fixed) measured data defines the likelihood function $L(\mathbf{m}, \mathbf{d})$, which can generally be expressed $L(\mathbf{m}, \mathbf{d}) \propto \exp[-E(\mathbf{m}, \mathbf{d})]$, where E is a measure of data misfit (defined in the following section). The PPD can then be written

$$P(\mathbf{m}|\mathbf{d}) = \frac{\exp[-\phi(\mathbf{m}, \mathbf{d})]}{\int \exp[-\phi(\mathbf{m}', \mathbf{d})] d\mathbf{m}'}, \quad (9)$$

where a generalized misfit function (combining data and prior) is defined

$$\phi(\mathbf{m}, \mathbf{d}) = E(\mathbf{m}, \mathbf{d}) - \log_e P(\mathbf{m}), \quad (10)$$

and the domain of integration spans the parameter space. The multi-dimensional PPD is interpreted in terms of properties defining parameter estimates and uncertainties, such as the maximum *a posteriori* (MAP) estimate, the covariance of this estimate, and marginal probability distributions, defined

$$\hat{\mathbf{m}} = \text{Arg}_{\max}\{P(\mathbf{m}|\mathbf{d})\}, \quad (11)$$

$$\mathbf{C} = \int (\mathbf{m}' - \hat{\mathbf{m}})(\mathbf{m}' - \hat{\mathbf{m}})^T P(\mathbf{m}'|\mathbf{d}) d(\mathbf{m}') \quad (12)$$

$$P(m_i|\mathbf{d}) = \int \delta(m'_i - m_i) P(\mathbf{m}'|\mathbf{d}) d\mathbf{m}', \quad (13)$$

where δ is the Dirac delta function. The diagonal terms of \mathbf{C} provide variance estimates for the MAP parameters. For nonlinear problems, analytic solutions to these equations do not exist, and numerical approaches must be applied. Here, MAP estimates $\hat{\mathbf{m}}$ are determined by minimizing $\phi(\mathbf{m}, \mathbf{d})$ using adaptive simplex simulated annealing (ASSA), a hybrid optimization algorithm that combines the downhill simplex method with fast simulated annealing and has proved to be highly effective for geoacoustic inversion [5]. The integrations required for Eqs. (12) and (13) are computed using fast Gibbs sampling (FGS), an efficient Markov-chain Monte Carlo method originally developed for matched-field inversion [6, 7].

2.3 Likelihood function and prior distribution

An important aspect of Bayesian inversion involves specifying the uncertainty distribution of the measured data, which in turn characterizes the likelihood function. Data uncertainties must include both measurement error (e.g., errors due to instrument uncertainties or experiment procedure) and theory error (due to the simplified model parameterization and idealized treatment of the forward problem), which are often not well known. However, given reasonable assumptions, uncertainties can often be estimated from the data themselves. For Bayesian geoacoustic inversion to date, this has been done using a fixed maximum likelihood (ML) estimate [4, 7]. An alternative approach is to include the data error as an unknown random parameter (nuisance parameter) within the inversion process [16], thereby including the effects of uncertainty in the error and of any inter-relationships between error and model parameters.

Consider a vector of N data \mathbf{d} related to an M -parameter model \mathbf{m} by $\mathbf{d} = \mathbf{d}(\mathbf{m})$ plus errors. Under the assumption of independent, Gaussian-distributed random errors, the likelihood function is given by

$$L(\mathbf{m}, \mathbf{d}) = \frac{1}{(2\pi)^{N/2} \prod_{i=1}^N \sigma_i} \exp \left\{ -\frac{1}{2} \sum_{i=1}^N [d_i - d_i(\mathbf{m})]^2 / \sigma_i^2 \right\}, \quad (14)$$

where σ_i represents the standard deviation for datum d_i . If the standard deviations σ_i are known, the data misfit employed in Eq. (10) is given by

$$E(\mathbf{m}) = \frac{1}{2} \sum_{i=1}^N [d_i - d_i(\mathbf{m})]^2 / \sigma_i^2. \quad (15)$$

If the errors are not known, they can be estimated from the data as follows. For identically-distributed errors ($\sigma_i = \sigma$), the ML estimate is obtained by maximizing the likelihood, Eq. (14), over σ and \mathbf{m} leading to

$$\hat{\sigma} = \left| \frac{1}{N - M} \sum_{i=1}^N [d_i - d_i(\hat{\mathbf{m}})]^2 \right|^{1/2}, \quad (16)$$

where $\hat{\mathbf{m}}$ is the ML model estimate determined by minimizing $\sum_i [d_i - d_i(\mathbf{m})]^2$. The data misfit function for FGS then becomes

$$E(\mathbf{m}) = \frac{1}{2} \sum_{i=1}^N [d_i - d_i(\mathbf{m})]^2 / \hat{\sigma}^2. \quad (17)$$

An alternative to ML error estimation is to treat the error as a nuisance parameter within the inversion. For identically-distributed errors this involves including σ as an unknown parameter in FGS and employing the data misfit function

$$E(\mathbf{m}) = \frac{1}{2} \sum_{i=1}^N [d_i - d_i(\mathbf{m})]^2 / \sigma^2 + N \log_e \sigma. \quad (18)$$

The assumptions regarding the data uncertainty distribution should be validated *a posteriori* by applying appropriate statistical tests to the standardized data residuals (difference between the measured data and data predicted for the MAP estimate $\hat{\mathbf{m}}$, divided by the estimated standard deviation). In particular, for Gaussian-distributed errors, the residuals should be approximately Gaussian distributed with zero mean and unit standard deviation. The Kolmogorov-Smirnov (KS) test [17] can be applied to test the null hypothesis H_0 that the data residuals are from the Gaussian distribution against the alternate hypothesis H_1 that the residuals are not from this distribution, based on the maximum difference between the respective cumulative marginal distributions. The corresponding p value represents the probability of obtaining a test statistic at least as extreme as that observed assuming the null hypothesis is true, quantifying the strength of the evidence against H_0 . Commonly, $p > 0.1$ is considered to provide little or no evidence, $0.05 < p \leq 0.1$ provides moderate evidence, $0.01 < p \leq 0.05$ provides strong evidence, and $p \leq 0.01$ provides very strong evidence.

The randomness (independence) of the data errors can be examined qualitatively by plotting the autocorrelation function for the residuals. For random errors, the autocorrelation should exhibit a narrow peak at zero lag; a wide peak indicates that successive residuals tend to have the same sign and may be correlated. The (one-tailed) median-delta test for randomness [18] tests the null hypothesis of random residuals versus the alternative hypothesis of (positively) correlated residuals. The test statistic consists of the number of runs of residuals on either side of the observed median value; the value provided by the median-delta test is interpreted as above.

In addition to specifying the likelihood function, Bayesian inversion requires the prior distribution be defined. The prior employed here consists of a uniform distribution for each parameter on a bounded interval $m_i^- \leq m_i \leq m_i^+$, with limits designed to impose physical reality (e.g., non-negative shear velocities), but wide enough so that the data, rather than the prior, primarily determine the inversion results. Parameter limits used here are given in Table 1.

Table 1. Lower and upper bounds defining uniform prior distributions for model parameters.

	v_p (m/s)	ρ (g/cm ³)	α_p (dB/ λ)	v_s (m/s)	α_s (dB/ λ)	σ (dB)
Lower bound	1450	1.2	0	0	0	0.1
Upper bound	1800	2.2	1	500	5	10

3 Reflectivity Data and Errors

Seabed reflection data were collected at two sites over the Malta Plateau in the Strait of Sicily, as shown in Fig.1. The first site was characterized by low-velocity, water-saturated, silty-clay sediments, and is referred to here as the clay site. Data were collected at this site as part of the SCARAB (SCattering And ReverberAtion from the sea Bottom) experiment series [8, 10]. The second site was characterized by high-velocity, clayey-sand sediments, and is referred to as the sand site; data were collected here as part of the Boundary 2000 experiment [14]. The experiment geometry involved a moored omni-directional receiver and a broadband source (seismic Boomer) towed near the surface (0.35-m depth). The magnitude of the reflection coefficient was computed as the ratio of the bottom-reflected to direct arrival energy, corrected for source directivity and geometric spreading. To restrict data sensitivity to surficial sediments near the water-sediment interface, the recorded acoustic time series were windowed to extract energy from the initial bottom reflection, and frequency averaged. Figure 2 shows the measured data with experimental error bars (described below). The data clearly illustrate angle-of-intromission and critical-angle behaviour at the clay and sand sites, respectively.

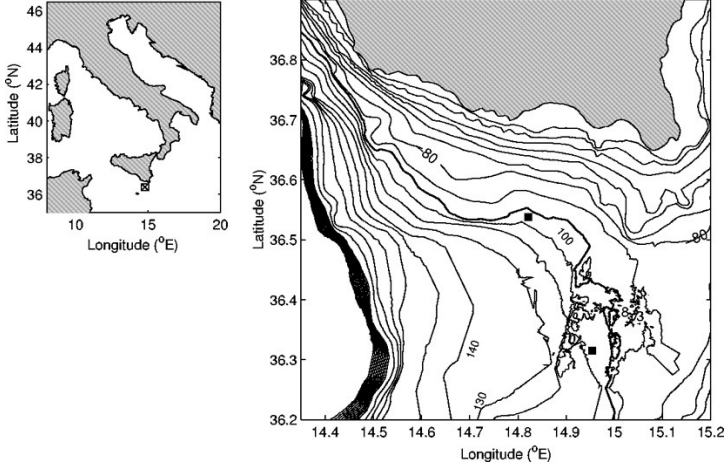


Figure 1. Location of the seabed reflection measurements in the Strait of Sicily: clay site (north), sand site (south).

A thorough analysis of the experimental uncertainties in processing the reflection data is presented in [11] which shows that the dominant error is due to the uncertainty of the source directivity

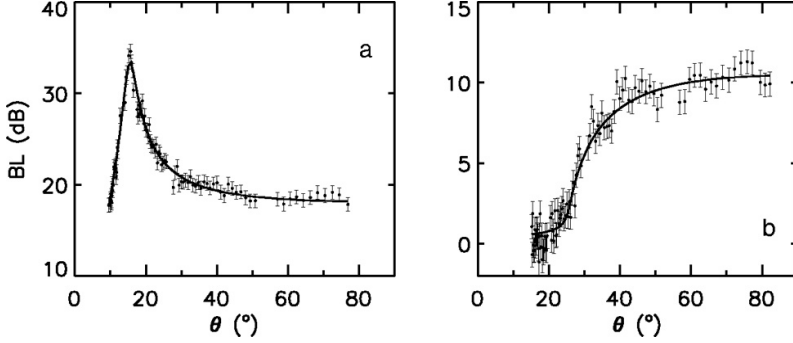


Figure 2. Measured BL data for (a) the clay site, and (b) the sand site, with one standard-deviation error bars estimated from the experimental uncertainties. Each panel also shows the fit to the data computed for the MAP parameter estimates (solid lines).

($\sigma_\theta \sim 75$ dB). Errors in the measured grazing angles were also estimated and converted to an equivalent uncertainty in BL according to

$$\sigma_{BL}(\theta) = |BL(\theta + \sigma_\theta) - BL(\theta - \sigma_\theta)|/2, \quad (19)$$

where BL was evaluated for a representative geoacoustic model. These two uncertainties are combined assuming independent errors; the resulting measurement error estimates for each site are shown in Fig. 3 and included as error bars in Fig. 2.

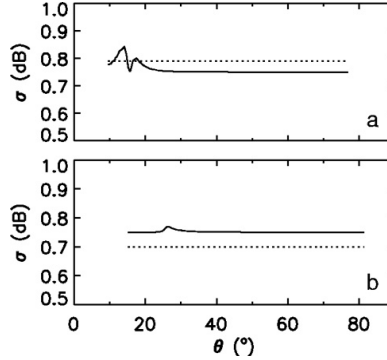


Figure 3. Data standard deviations estimated for (a) clay-site data, and (b) sand-site data. Solid lines indicate angle-dependent errors estimated from experimental procedure; dashed lines indicate ML estimate of uniform error.

4 Inversion Results

4.1 Clay-site (intromission) inversion

The section presents the results of Bayesian inversion of the clay-site reflectivity data, employing several approaches to quantify the data uncertainty distribution. The first case considered assumes independent, identically-distributed (i.e., angle-independent) Gaussian errors. The ML estimate of

the data standard deviation is $\hat{\sigma} = 0.79$ dB, computed using Eq. (16) and ASSA optimization. Figure 3(a) shows that the ML estimate for the total error is similar to the measurement errors, indicating theory errors are relatively small in this case. Figure 2(a) shows a good fit for all grazing angles between the measured BL data (with one $\hat{\sigma}$ error bars) and data predicted for $\hat{\mathbf{m}}$.

The validity of the assumed data uncertainty distribution is investigated by considering the data residuals in Fig. 4. Figure 4(a) shows good agreement between the distribution of residuals plotted in histogram form and the theoretical Gaussian curve. The KS test yields $p > 0.2$, indicating no evidence against the hypothesis of Gaussian-distributed errors. The independence of the data errors is considered in Fig. 4(b), which shows the autocorrelation function for the residuals. The central peak in Fig. 4(b) has a half-width of 1–2 lag points before decreasing to the noise level. The median-delta test for randomness yields $p = 0.14$, indicating acceptance of the hypothesis of random errors.

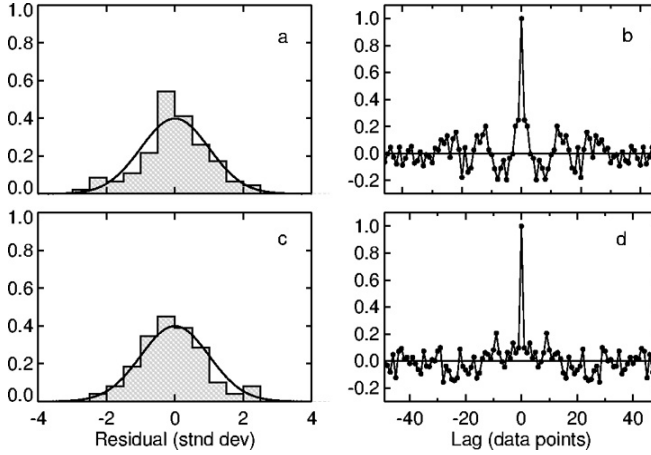


Figure 4. Analysis of data residuals from MAP inversion with ML standard-deviation estimates. Left column compares histograms of residuals (in units of data standard deviation) to theoretical Gaussian distributions (smooth curve). Right column shows residual autocorrelation functions. Panels (a) and (b) show results for clay-site data, and (c) and (d) for sand-site data.

Marginal probability distributions for the geoacoustic parameters are shown in Fig. 5 applying various approaches to quantifying data errors: the fixed ML estimate $\hat{\sigma}$ described above (histogram set labeled 1), including σ as a nuisance parameter in the FGS inversion according to Eq. 18 (histograms labeled 2); and applying angle-dependent errors estimated for the experimental procedure with theory errors assumed negligible (histograms labeled 3). The marginal PPDs are represented as histograms normalized so that the integral over the plot bounds, scaled to $[0, 1]$, is unity (note that the plot bounds are narrower than the prior bounds for all parameters except α_s).

Comparison of the marginal distributions obtained for all approaches in Figs. 5 show no significant differences in inversion results, from which a number of conclusions can be drawn. First, the effect of uncertainty in σ and of possible inter-relationships between σ and the geoacoustic parameters appears negligible, as virtually identical results are obtained using a fixed estimate $\hat{\sigma}$ or including σ as a nuisance parameter in the inversion. Second, measurement errors appear sufficient to represent the total data uncertainty in this case. Finally, the consistency in results suggest that the inversion is not overly sensitive to the exact form of the data uncertainties, and provides overall confidence in the results.

The results of Fig. 5 show that compressional-wave velocity, density, and compressional attenuation are determined to high precision, with MAP estimates and two-standard deviation uncertainties

of $v_p = 1474 \pm 3$ m/s, $\rho = 1.36 \pm 0.02$ g/cm³, and $\alpha_p = 0.28 \pm 0.03$ dB/ λ . The shear-wave velocity is $v_s = 10 \pm 100$ m/s, and the shear attenuation α_s is undetermined from the reflectivity data (flat marginal distributions over the prior bounds).

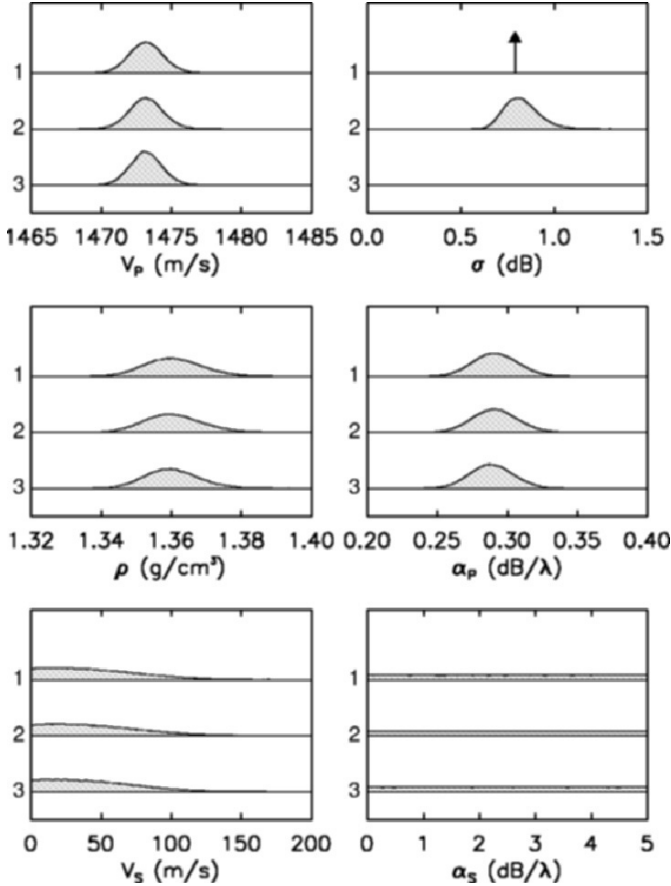


Figure 5. Marginal probability distributions from clay-site data. Histograms labeled 1 computed using ML estimate for σ ($\hat{\sigma}$ indicated by arrow); histograms labeled 2 computed with σ included in Bayesian inversion; histograms labeled 3 used standard deviations derived from experimental uncertainties.

4.2 Sand site (critical-angle) inversion

This section presents the results of Bayesian inversion of the sand-site data, again employing several approaches to quantify the data uncertainties. Figure 3(b) shows that similar data standard deviations are obtained from ML estimation ($\sigma = 0.71$ dB, angle independent) and from consideration of measurement errors ($\hat{\sigma} \approx 0.75$ dB, weakly angle dependent). The measured data are shown in Fig. 2(b) with one $\hat{\sigma}$ error bars, and are well fit by *BL* data predicted for the MAP model estimates. The data residuals computed for the MAP parameters (angle-independent errors) are shown in histogram form in Fig. 4(c), and compare well with the theoretical Gaussian distribution (KS test $p > 0.2$).

The autocorrelation for the residuals, shown in Fig. 4(d), has a central peak less than one lag point wide, indicating uncorrelated errors (median-delta test $p = 0.15$).

Geoacoustic marginal probability distributions for the sand-site data are shown in Fig. 6 for three approaches to quantifying data uncertainties: ML estimation, including σ in the inversion, and estimating σ from measurement errors. The results are essentially identical (within uncertainties) in each case: $v_p = 1676 \pm 10$ m/s, $\rho = 1.73 \pm 0.05$ g/cm³, $\alpha_p = 0.55 \pm 0.16$ dB/ λ , and $v_s = 120 \pm 150$ m/s (shear attenuation is undetermined).

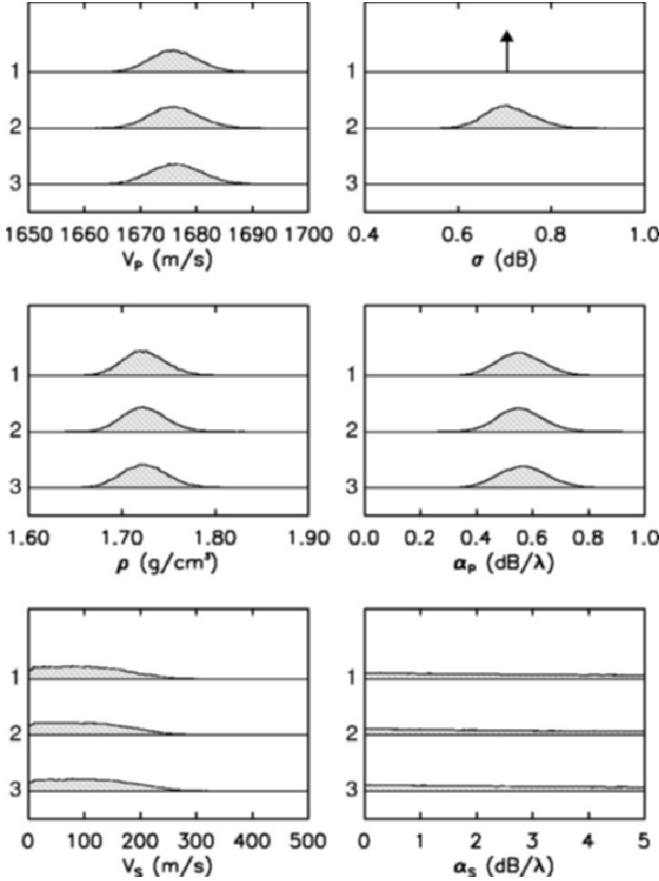


Figure 6. Marginal probability distributions from sand-site data: 1–ML standard deviation estimate, 2–standard deviation included in Bayesian inversion, and 3–angle-dependent standard deviations from experimental errors.

5 Summary and Conclusions

This paper applied Bayesian reflectivity inversion to estimate sediment viscoelastic parameters at sites with low- and high-velocity sediments resulting in data characterized by intromission and critical angles, respectively. Data uncertainties were assumed to be due to independent, Gaussian-distributed errors with several approaches applied to estimate the standard deviation. All methods

led to similar inversion results, suggesting the approach is not overly sensitive to the exact form of the data uncertainties and providing confidence in the results. In particular, measurement errors appear sufficient to represent the total data uncertainty in this case, in marked contrast to other approaches to geoaoustic inversion, such as matched-field inversion, where theory errors typically dominate [4, 7]. The assumed form of the data errors was validated by applying rigorous statistical tests to the data residuals.

The inversion results indicate well-defined estimates for compressional-wave velocity, density, and compressional attenuation at both sites. In addition, low shear-wave velocities were indicated; however, shear attenuation was unconstrained by the reflection data. Variations in v_p , ρ , and α_p are clearly resolved between the two sites, with differences between parameter estimates that are substantially larger than the estimate uncertainties (more than an order of magnitude for v_p). Smaller geoaoustic uncertainties are obtained for the clay-site data than for the sand site by a factor of 2–3 for v_p and ρ , and more than a factor of 5 for α_p . Since the two data sets consist of a similar number of measurements with similar errors, it appears that the geoaoustic information content for data characterized by an angle of intromission is significantly higher than that for critical-angle data.

Acknowledgments

The authors gratefully acknowledge the NATO SACLANT Undersea Research Centre and the Office of Naval Research who supported this work. The second author also thanks the captain, officers, crew, and scientific crew aboard the NRV Alliance who contributed to the success of these measurements.

References

1. Ferla C. M. and Jensen. F. B., Are current environmental databases adequate for sonar predictions in shallow water? In *Impact of littoral environmental variability on acoustic predictions and sonar performance*. Edited by N. G. Pace and F. B. Jensen (Kluwer Academic, Dordrecht, 2002), pp. 555–562.
2. Collins M. D., Kuperman W. A. and Schmidt H., Nonlinear inversion for ocean-bottom properties. *J. Acoust. Soc. Am.* **92**, 2770–2783 (1992).
3. Dosso S. E., Jeremy M. L., Ozard J. M. and Chapman N. R., Estimation of ocean-bottom properties by matched-field inversion of acoustic field data. *IEEE J. Oceanic Eng.* **18**, 232–239 (1993).
4. Gerstoft P. and Mecklenbrauker C. F., Ocean acoustic inversion with estimation of a posteriori probability distributions. *J. Acoust. Soc. Am.* **104**, 808–819 (1998).
5. Dosso S. E., Wilmut M. J. and Lapinski A. L., An adaptive hybrid algorithm for geoaoustic inversion. *IEEE J. Oceanic Eng.* **26**, 324–336 (2001).
6. Dosso S. E. Quantifying uncertainties in geoaoustic Inversion I: A fast Gibbs sampler approach. *J. Acoust. Soc. Am.* **111**, 129–142 (2002).
7. Dosso S. E. and Nielsen. P. L., Quantifying uncertainties in geoaoustic inversion II: Application to a broadband shallow-water experiment. *J. Acoust. Soc. Am.* **111**, 143–159 (2002).
8. Holland C. W. and J. Osler., High-resolution geoaoustic inversion in shallow water: A joint time- and frequency-domain approach. *J. Acoust. Soc. Am.* **107**, 1263–1279 (2000).
9. Holland C. W., Geoaoustic inversion for fine-grained sediments. *J. Acoust. Soc. Am.* **111**, 1560–1564 (2002).
10. Holland C. W., Shallow water coupled scattering and reflection measurements. *IEEE J. Oceanic Eng.* **27**, 454–470 (2002).
11. Holland. C. W., Seabed reflection measurement uncertainty. *J. Acoust. Soc. Am.* **114**, 1861–1873 (2003).

12. Tarantola A., Inverse Problem Theory: Methods for Data Fitting and Model Parameter Estimation. Elsevier, Amsterdam (1987).
13. Sen M. K. and Stoffa P. L., Global Optimization Methods in Geophysical Inversion. Elsevier, Amsterdam, 1995.
14. Holland C. W. et al., Bayesian inversion of Seabed Reflection Data Boundary characterization experiment series overview. *IEEE J. Ocean. Eng.*, in review (2004).
15. Jensen F. B., Kuperman W. A., Porter M. B. and Schmidt H., Computational Ocean Acoustics, American Institute of Physics, New York (1994).
16. Michalopoulou Z.-H., Gibbs sampling estimation in underwater sound problems. *Proc. Oceans* 2, 782–785 (2001).
17. Press W. H., Teukolsky S. A., Vetterling W. T. and Flannery B. P., Numerical Recipes in FORTRAN. Cambridge U.P., Cambridge, (1992).
18. Freund J. E., Modern Elementary Statistics, Third Ed. Prentice Hall, New Jersey (1967).

BACKPROPAGATION TECHNIQUES IN OCEAN ACOUSTIC INVERSION: TIME REVERSAL, RETROGATION AND ADJOINT MODELLING – A REVIEW

MATTHIAS MEYER¹ AND JEAN-PIERRE HERMAND^{1,2}

¹*Université libre de Bruxelles,
Environmental Hydroacoustics Laboratory
Department of Optics and Acoustics,
Avenue F. D. Roosevelt, 50 - CP 194/05,
B-1050 Brussels, Belgium
E-mail: mmeyer@ulb.ac.be*

²*Royal Netherlands Naval College,
P.O. Box 10000, 1780 CA Den Helder,
The Netherlands
E-mail: jhermand@ulb.ac.be*

In light of recent interest in adjoint modelling in underwater acoustics, we present a selective review which is mainly focused on the underlying concept of backpropagation. The different implementations of that concept to date are compared and discussed in the framework of experimental acoustic inversion in shallow water with application to source localisation, ocean acoustic tomography, geoacoustic inversion and underwater communications. Well established inversion or focalisation methods based on matched field processing, model-based matched filter and time reversal mirror are related to less popular ones such as acoustic retrogradation and other variants of backpropagation. In contrast to the latter, adjoint-based, variational inversion approaches make use of the adjoint of a forward model to backpropagate the model-data mismatch at the receiver toward the source. The paper describes in greater detail adjoint methods and applications in underwater acoustics. We also present results using environmental data obtained during a geoacoustic inversion experiment in the Mediterranean.

1 Introduction

Comprehensive monographs on inversion techniques in underwater acoustics are still lacking. A few review articles exist that mostly deal with specialized topics, e.g., modal inverse and linear perturbative methods, matched field processing, global optimisation, etc. Although not intended as an exhaustive review either, the present paper focuses on the general concept of *backpropagation* and reviews the techniques that implement that concept in different ways for solving inverse problems: source localisation, geoacoustic inversion, ocean tomography and underwater communications.

The review covers a number of approaches ranging from Tappert's original acoustic retrogradation to Parvulescu's time reversal and adjoint modelling. Even though they are not implementing back-propagation as a mechanism of optimisation (they rely on global optimisation), the classical matched-field processing (MFP) and the model-based matched filter (MBMF) approaches are discussed in this review since they can be viewed as a model-based version of the phase-conjugation and time-reversal concepts, respectively. The basic ideas behind the different approaches are surveyed using a selection of key references and—whenever possible—trying to maintain a chronological order.

Starting with Parvulescu's pioneering work on matched equivalent-space signal (MESS) processing in Sec. 2 we subsequently outline the development of classical matched filter processing, beginning with Bucker's original work and focusing on some of the most relevant processors in Sec. 3.

Tappert's work on acoustic retrogradation in the 80s, which actually coincides with the early work on matched field processing, can be considered as "unconventional" matched field processing. Together with the ray based backpropagation (Voltz) and the later retrogradation variant by Thomson *et al.*, it is dealt with in Sec. 4. Since focalisation (Collins), by itself a generalised matched field approach, contains a backpropagation part, it is included here in Sec. 4.2. The most recent application of backpropagation in geoacoustic inversion to date is the phase regulated approach by Dizaji *et al.*, presented in Sec. 4.3.

Section 5 is devoted to time reversal (TR) in its mutual implementations—active or passive vs. blind or model-based—from the early work by Jackson at the end of the 80s to the latest TR applications. The model-based matched filter receiver which "unifies" matched field processing and time reversal is described in Sec. 5.3.

Section 6 introduces adjoint modelling as a complement or alternative to the global optimisation approaches typically used for solving inverse problems in ocean acoustic tomography and geoacoustic inversion. At the end of the paper example inversion results are given for an adjoint-based inversion of the complex acoustic field synthesised from the ocean sound speed profile and sub-bottom acoustic properties collected during the YELLOW SHARK '94 experiments, south of the Island of Elba, Italy.

2 Matched signal processing and time reversal

The concept of matched equivalent-space signal (MESS) processing was introduced by Parvulescu [1] in 1961 for signal detection in a multipath medium with application in geophysics and architectural acoustics. The impulse response of an ideal detector was known to be equal to the "inverse" of the impulse response of the multipath channel and as such difficult to obtain (to model). Instead of designing an optimal receiver Parvulescu sought to construct an "inverse signal" which would be recombined by the medium *itself* into a single impulse at the receiver. By means of the MESS, i.e., the time-reversed impulse response of the medium, a considerable gain in detectability, directivity and noise rejection was experimentally verified. Parvulescu had the MESS technique patented in 1962 ("Correlation system using matched signals", 1962–1976) and subsequently conducted extensive environmental measurements to demonstrate time reversal in the ocean [2, 3]. The experiments included deep ocean tests as well as shallow water studies regarding also temporal and spatial stability.

In the late eighties, long after the expiration of Parvulescu's patent, the underwater acoustics community rediscovered the potential of time reversal as will be discussed in Sec. 5. Especially, the original concept of an optimum receiver was realised later on in the MBMF work presented in Sec. 5.3. The following section gives a brief survey of the matched field processing approach, beginning with Bucker's ground-breaking work on integrating signal processing and acoustic modelling in 1976.

3 Matched Field Processing

The classical “matched field” processing is probably the inversion approach most widely used in underwater acoustics so far. It was introduced by Bucker [4] in 1976 as a generalised beamforming method for source localisation with a vertical receiver array (VRA). Later, it was extended to the estimation of environmental parameters for known or partially known source-receiver geometry assuming a specific parametrisation of the environment (water column or bottom models). The approach in the above cases is to minimise an objective function that compares the measured acoustic pressure field with a modelled field (replica) that is calculated for a specific parametrisation. This minimisation problem is not solved by direct inversion, e.g., through linearisation, but by “exhaustively” solving the forward problem (global search) and finding the best “match” to the measured data, i.e., the parameter set in the model space that gives the highest correlation between the replica of the field and the measured data is taken as the solution.

Tolstoy [5] gives an overview of the early work on standard MFP and its use in underwater acoustics. In addition, the paper by Baggeroer *et al.* [6] reviews several experiments using MFP. Also the special issues of the *IEEE Journal of Oceanic Engineering* [7, 8, 9] and a number of conference proceedings [10, 11, 12] provide a good overview of the applications of both, matched field processing and linear inverse methods with experimental data in shallow water, especially for characterising the ocean bottom.

Over the years a number of different processors have been used; Bartlett, matched mode, minimum variance and multiple constraints processors are the most common. Conventional narrow-band MFP was extended to match the spatial structure of continuous-wave (CW) pressure fields at several frequencies. Moreover it was shown by the experimental results (YELLOW SHARK’94) in [13] that *joint* optimisation across a broad range of discrete frequencies was necessary to obtain correct inversion results. Some of the different variants of the Bartlett processor that have been introduced are, e.g., the incoherent processor by Baggeroer [14], and proceeding in chronological sequence, Richardson and Nolte’s “Optimum uncertainty field processor” (OUFP) [15], Krolik’s multiple-linear-constraint variant of the minimum variance processor [16] for random inhomogeneities in the sound-speed profile. Further important processors were the multiple-point constraint version of the minimum variance distortionless response (MVDR) processor [6], the coherent normalised processor [17] or the matched-phase processor [18] and the incoherent cross-frequency processor [19]. The latter contains a comparison of the performance of different processors on experimental data. In this respect Ref. [13] contains an extensive review section covering the various broadband matched field techniques. The closely related concept of the MBMF receiver, which was first applied in the WEST SARDINIA ’89 experiments by Hermand and Roderick [20], will be addressed later in Sec. 5.3.

Already at the time of the early matched field work in the 80s, extensions of the classical MFP were introduced that proposed backpropagation as a means to facilitate the problem of source localisation. Using the backpropagated field turned out to be a way to reduce the computational load of “exhaustively” solving the forward problem in search of the best data-model fit. In the next section, a short historical overview of backpropagation techniques for source localisation is followed by a description of the backpropagation included in Collin’s focalisation method and an example of backpropagation for geoaoustic inversion.

4 Backpropagation Methods

The concept of backpropagation, at its heart, can still be considered as an alternative representation of the classical MFP. Backpropagation is based on the same concept of reciprocity and superposition of the ocean waveguide that was verified by Parvulescu’s early TR experiments (Sec. 2).

This section reviews the following different backpropagation approaches: Tappert’s original method of acoustic retrogradation for source localisation which is based on backpropagation of acoustic

fields calculated by a PE model and which was later refined by Thomson *et al.*, the time-domain backpropagating ray technique by Voltz *et al.*, the so-called focalisation approach by Collins and finally the phase-regulated backpropagation method for geoacoustic inversion by Dizaji.

It is important to note that the use of backpropagation differs significantly in the above applications. While Tappert, Thomson and Voltz (Sec. 4.1) apply backpropagation directly as a mechanism of optimisation in order to obtain an estimate of the source position without the burden of exhaustively solving the forward problem, the use of backpropagation by Collins (Sec. 4.2) and Dizaji (Sec. 4.3) is somewhat different. Although they apply backpropagation for different purposes, i.e., environmental focusing for source localisation and geoacoustic inversion, respectively, both use the spatial convergence of the backpropagated field at the source position as a criterion to determine the best set of (environmental) parameters by means of global search.

4.1 Acoustic retrogradation for source localisation

The concept of *acoustic retrogradation* was originally introduced in 1985 by Tappert *et al.* [21] as an alternative to conventional MFP. The one-way PE method using the split-step Fourier (SSF) algorithm was first shown to preserve the acoustic properties of reciprocity and superposition in fully range-dependent and lossy oceanic environments in the absence of currents and other reciprocity breaking effects [22]. The effect of ocean currents on PE sound transmission and the reciprocity in the time domain was then treated in [23].

In a generic matched-field processor the CW pressure fields measured on a hydrophone array are compared to replica fields that are synthesised by a full-field acoustic model for a given target position. This matching is carried out for many potential target locations within a search region (range, depth and bearing) to form an ambiguity surface whose peak values provide the greatest likelihood that targets are present at the corresponding points.

Acoustic retrogradation involves combining the acoustic field measured on a VRA with PE starting fields for each array element to form a correlation function. The PE algorithm requires such a starting field at the range of the source in order to propagate the solution of the one-way equation outward in range. For an N-element array, reciprocity is invoked and by allowing the interchange of source and receiver positions the computational effort is limited to the generation of N replica surfaces corresponding to a point source located at each of the N hydrophones of the VRA. The linear property of superposition allows all N replicas to be propagated at the same time, thus reducing the computational load to computing N replica fields at each point of the search grid. The normalised correlation surface is then marched outward from the VRA toward the potential target location using the SSF algorithm. Thomson *et al.* [24, 25] have refined Tappert's matched-field processor with an unnormalised ambiguity surface which is backpropagated using a higher-order Padé PE algorithm. Importantly, the computational effort needed to form the modified ambiguity surface is independent of the number of elements in the VRA. In [26] the authors also indicate how the backpropagated PE method can be used for spectral decomposition and matched-mode processing applications.

In contrast to the two PE-based methods dealt with so far, Voltz and Lu [27, 28] apply a backpropagating ray technique for source localisation that exploits both the temporal and the spatial characteristics of the multipath arrival structure at a VRA.

In a first step the angles and relative arrival times are estimated for the various multipath trajectories that join the unknown source and the VRA elements (eigenrays). The second step utilises a ray tracing technique to backpropagate the rays and produces an estimate of the source position by making full use of all the spatial and temporal information extracted by the array. Phase ambiguity is eliminated by employing the group delay of arriving wave packets and the localisation ambiguity is minimised by utilising ray travel times as well as path convergence. The actual ray tracing for the backpropagation is numerically very efficient and the approach does not require full-wave matched-field processing.

Exploiting both the arrival time structure of the multipath rays and the spatial information provided by the ray trajectories results in an ambiguity surface which is well behaved in that it is slowly varying and has a well defined optimal point, in contrast to typical MFP ambiguity surfaces.

Due to the numerical efficiency of this ray backpropagation method it is further proposed as a means to obtain an initial coarse estimate of the source position which then could be used as input to a local matched-field type method with significantly less processing required for the global optimisation.

4.2 *Focalisation: Environmental focusing and source localisation*

Preceding Voltz and Lu's time-domain backpropagating ray technique by about a year, Collins and Kuperman [29] had introduced a medium-focusing source localisation method that they termed *focalisation*.

Ray backpropagation is used to determine the source location by searching for spatial convergence of the rays, and environmental focusing by simulated annealing is employed to adjust for an uncertain sound speed profile in the water column. While conventional MFP source localisation required accurate knowledge of the ocean acoustic environment, focalisation, which simultaneously focuses the environment and localises the source, eliminates this requirement by including the environment in the parameter search space. However, focalisation does not retrieve a complete description of the environment but instead resolves the environment to the minimum required for a correct localisation of the source. Since focalisation involves more unknown parameters than conventional MFP it requires a high-resolution cost function and an implementation based on efficient optimisation algorithms to search over the large focalisation parameter space. For ray-based focalisation the acoustic field is represented by the Lloyd's mirror beams propagating from the point on the surface directly above the source. In case of a known sound speed distribution in the water column the backpropagated rays focus at the ocean surface at the source range so that the depth of the source can be determined by the Lloyd's mirror beam pattern. In the presence of significant uncertainties in the sound speed distribution the partially known profile is gradually adjusted using simulated annealing until the rays focus at a point near the ocean surface.

In analogy to the ray-based focalisation method Collins and Kuperman also implemented focalisation by backpropagating the phases of the normal modes using the adiabatic normal mode approximation. Recently the approach of focalisation has been proven to be effective for problems involving deterministic environmental parameters but has also been adapted for problems involving stochastic parameters in the presence of reciprocity breaking effects such as internal waves and currents [30].

4.3 *Back wave propagation for geoacoustic inversion*

As mentioned in the introduction of this section the back wave propagation technique can also be applied to invert for geoacoustic parameters. A so-called *phase regulated back wave propagation technique* for geoacoustic parameter estimation has been presented by Dizaji [31, 32]. Similar to the backpropagation methods in the previous section, back wave propagation for geoacoustic inversion is also based on the reciprocity and superposition properties of the ocean acoustic waveguide. In this approach the conjugate of the measured pressure field at a VRA is weighted by the square root of the range and then backpropagated from the array using a normal mode code. The real data were taken from the Pacific Shelf experiment carried out off the West coast of Vancouver Island [33]. Since the backpropagated wave field converges at the location of the source only for the true ocean environmental parameters this technique can be used for obtaining the best match between the measured field and a replica that is generated using the geoacoustic model parameters. The criterion to be minimised by an efficient multistep search procedure is the spatial variance of the backpropagated signal energy in the vicinity of the true source location.

Dizaji further introduces a post processing, phase regulation technique to improve the method for estimating parameters with low sensitivity by means of a weighting factor. A recent application of this approach can also be found in [34].

Except for the considerable improvement achieved by environmental focusing (Sec. 4.2), the traditional backpropagation methods for source localisation by Tappert, Thomson and Voltz (Sec. 4.1) are strongly dependent on accurate and detailed *a priori* knowledge of the ocean acoustic environment along the propagation path. Since the necessary measurements of environmental parameters which are required for adequate simulation of the wave fields are often not practical, this poses an essential limitation on the classical backpropagation.

For applications where it is not the primary goal to invert for the ocean acoustic environment or the source position, it is sufficient to substitute the numerical backpropagation in the previous approaches with a physical backpropagation. In contrast to numerical backpropagation, the phase conjugation or time reversal operators in the following Sec. 5.1 and 5.1 do not require any *a priori* knowledge of the propagation medium. It is because of their inherent ability to operate in unknown complex acoustic environments, that active and passive phase conjugation methods find application, e.g., in underwater communications, active sonar systems or acoustic surveillance systems.

However, with regard to inversion purposes such as source localisation or geoacoustic inversion, phase conjugation by itself is not an alternative to MFP. In this respect, the model based matched filter approach presented in the next section exploits both the temporal and the spatial characteristics of the multipath arrival structure at the receiver array and can thus be seen as a combination of MFP and time reversal.

5 Time reversal

More than 20 years after the prosecutor work of Parvulescu, and strongly motivated by the application of phase-conjugate mirrors in optics, where they were used to compensate for aberrations caused by inhomogeneities in the propagation medium and by imperfections in optical components, the underwater acoustics community rediscovered the potential of time reversal.

5.1 Active time reversal

Most importantly, “active” phase conjugation (APC), e.g., Jackson and Dowling [35], did not require knowledge of the medium properties or experimental geometry, whereas standard MFP source localisation methods suffered from the need for a nearly perfect and often unobtainable description of the medium. Compensation for multipath propagation and array imperfections was automatically achieved by a time-reversed retransmission of signals received by an array.

Proceeding in chronological order, a number of experimental demonstrations of the TR mirror/phase conjugate array followed in the second half of the 90s. The first of a series of focused acoustic field (FAF) experiments was the active TR demonstration FAF ’96 in the Mediterranean Sea [36]. The tests were carried out in the same vertical section off the Formiche di Grosetto islands as the earlier YELLOW SHARK ’94 experiment.

More recently the robustness of TR focusing in the ocean has been investigated [37, 38, 39] especially under the effects of ocean currents, TR array deformation and broadband performance with a moving source [40, 41] or for environmentally adaptive reverberation nulling [42]. In addition, Sabra *et al.*, experimentally demonstrated time-reversed reverberation focusing in an oceanic waveguide [43].

Moreover, the method of an iterative time reversal mirror [44], a technique originally derived in ultrasonics for focusing selectively on the strongest target in a multitarget medium was extended to waveguide propagation in the ocean [45, 46].

5.2 *Passive TR*

Following his earlier work together with Jackson on active time reversal, Dowling [47] generalised the concept of phase conjugation in the mid 90s to a passive implementation. While active time reversal required an array capable of both receiving and transmitting in order to refocus a field incident on the array both in time and space back at the location of the original source, passive phase conjugation (PPC) just needed a receive-only array. The PPC processing consists of using a probe pulse preceding the original signal pulses that have traversed a complex refractive medium, as an inverse filter for the deconvolution of the medium effects. The PPC processor creates an unambiguous temporal peak even when a complex multipath environment separates the acoustic source and receiver; temporal sidelobes in the PPC processor output can be suppressed by increasing the number of receivers and coherently summing their output.

Dowling's concept of PPC, which was of fundamental importance for pulse compression, set the stage for all later applications of the time-reversal based acoustic communications [48, 49]. It is also referred to as artificial time reversal, e.g., for blind deconvolution in ocean waveguides in [50]. The performance of PPC has been compared to decision feedback equaliser [51] and it is been used extensively to reduce intersymbol interferences for underwater acoustic communications in a multipath environment. [52]. For this purpose a number of passive phase conjugation tests were carried out, e.g., in Puget Sound near Seattle (Jackson, Rouseff *et al.*) in 2000. Very recently, so-called round robin realisations with multiple input multiple output (MIMO) have been applied in ocean acoustics [53]. In fact, the MIMO configuration is the extension of Dowling's concept of PPC to more than one source.

A *model-based* extension of the acoustic TR mirror, which is closely related to the model-based matched filter approach described in the next section, was investigated by Hermand [54, 55]. Instead of only measuring the medium impulse response and then using it as such to deconvolve the propagation effects, the measurement is used to obtain a geoacoustic model of the environment. This allows to *predict* the medium impulse response for any desired range and depth of a virtual source and to synthesise and backpropagate array signals that focus their energy to an arbitrary position, computationally or physically. Since the constructed signal which is backpropagated in model-based TR is both noise and reverberation free, this procedure overcomes the noise and reverberation limitations inherent to the "blind" TRM operation.

A good overview of the different TR implementations in underwater acoustics—active or passive vs. blind or model-based—seen from a signal processing prospective is contained in [56]. Especially the close relation between TR and spatio-temporal matched filter is addressed by Chambers *et al.* [57]. With respect to reciprocity and time invariance, a more general constraint for the medium Green's function is derived that allows a TR mirror to implement the spatio-temporal matched filter even when conditions are time varying.

5.3 *Model-based matched filter receiver*

Independently of the time reversal work in the previous section, mostly inspired by Parvulescu's early experiments and Clay's work on optimum time domain signal transmission [58], Hermand and Roderick [20] proposed a *model-based matched filter* (MBMF) processing which exploits detailed temporal and spatial characteristics of the arrival structure at a receiver array. It was originally applied for source localisation in range, depth and Doppler (WEST SARDINIA '89).

In contrast to the passive TR discussed in the previous section it uses a *predicted* TR operator to numerically refocus the energy at the receiver (optimum receiver concept). The environment is probed with broadband, large time-bandwidth product waveforms such as "chirp", instead of the multi-frequency continuous waves (CW) used by conventional MFP. The received signal is matched-filtered with a set of reference signals synthesised from frequency-dependent, medium Green's functions predicted for trial source positions or trial environmental properties, i.e., a reference channel

contains the emitted signal convolved with the time-reverse of a predicted medium impulse response. MBMF is a TR processor that fully exploits for inversion purposes the (frequency-dependent) sound propagation characteristics of multipath, time dispersion and attenuation due to refraction in the medium and reflection from the sea surface and bottom sediment layers. The time reversal of the (noise-free) transmitted signal between a source and a receiver in a waveguide gives an optimum filter for the reduction of transmission distortion increasing the peak signal-to-noise ratio at the receiver output (processing gain). Since the impulse response is a function of waveguide structure and their respective depths and range, one can use the fine structure of the impulse response to determine a source location or to obtain an environmental characterisation of the waveguide.

While [13] extended conventional MFP to match the spatial structure of CW pressure fields by means of joint optimisation across a wide range of discrete frequencies, the MBMF approach [59] allows focusing not only in space but also in time by exploiting waveguide modal dispersion (pulse spreading) and therefore the phase relationship between a broad *continuum* of frequencies. Substantial processing gains were obtained in most of the experimental situations investigated, depending on the time dispersion, spatial diversity, predictability and coherence of the specific acoustic channel. Correct and stable inversion results were possible even from a sparse but representative set of hydrological data. In contrast to MFP large and densely-populated receiver arrays are not necessary. In [59] geoacoustic inversion results were obtained with a fixed source and a single hydrophone or very few elements of a VRA.

The concept of MBMF does not necessarily impose to include all propagation paths or modes in the reference signal. For example, in a source localisation experiment [20] eigenray filtering was used to include only the ducted part of the propagation. In [61] a partially coherent version of the MBMF was applied whereby only the deterministic, most stable part of the (envelope) channel impulse response was included. This leads to a computationally effective inversion scheme when allowed by the encountered propagation conditions such as in the INTIMATE '96 experiment on the Portuguese shelf break [62]. The latter approach is not suitable in the case of non-resolved, time-dispersed arrivals, which occurs, e.g., with soft bottom types [59]. Other applications for geoacoustic inversion purposes exploited the whole acoustic-channel response [59, 60] (YELLOW SHARK '94/95 and SWELLEX '96 experiments, respectively).

6 Adjoint modelling

The inversion techniques presented in the previous sections actually use the concept of backpropagation as a variant of matched field processing in order to obtain estimates of source location or geoacoustic parameters. The adjoint models described in this section backpropagate (time reverse) the *mismatch* between the model predictions and the measured observations outward from the receiver array to the unknown medium perturbations. The residual field, i.e., the measured *minus* the modelled field, is due to perturbations in the propagation medium that were not taken into account in the modelling. By means of the adjoint model this residual field is backpropagated in order to locate where the medium properties need to be adjusted so that the model reproduces the measured field. In mathematical terms, the adjoint model provides the necessary gradient information, i.e., the corrections to the respective model inputs that caused the mismatches between the observations and model predictions.

It was nearly at the same time of Parvulescu's early time reversal experiments that Kalman and Bucy [63] published the original paper on linear filtering and prediction theory and Bellman's work [64] on adaptive control came out. Other seminal publications on optimal control systems followed [65, 66, 67, 68, 69, 70] until Lions [71] provided an exact mathematical formulation of optimal control of systems governed by partial differential equations in 1971. Lion's original work and the later sequel [72] can be considered as the main basis of the adjoint modelling approaches presented in this section.

Closely related to the adjoint state method is also the *state-space model-based* processor introduced by Candy and Sullivan [73, 74]. The state-space formulation [75] allows the unknown parameters of the propagation model to be estimated by an extended Kalman filter.

Adjoint models nowadays are being used for data assimilation, model tuning and sensitivity analysis in several fields, among which meteorology, oceanography and seismics are the most common [76, 77, 78, 79, 80, 81, 82]. The adjoint approach is also being applied as optimal design method in computational fluid dynamics, particularly for aeronautical applications, e.g., [83]. Other applications are inverse problems in the field of electromagnetic induction and resistivity, particle transport and thermal diffusion. Good comparative studies of the different adjoint approaches can be found in [84] and [85, 86] dealing respectively with 1D and 2D resistivity problems and inverse scattering, shape reconstruction.

In the following subsections we will first give an intuitive example of a simple operator and its adjoint and explain the general conceptual flow of an adjoint-based inversion. Subsequently in subsection 6.2 we present a brief survey of the different adjoint approaches which are currently in use in underwater acoustics and highlight some of the differences in their implementation (continuous vs. discrete) in subsection 6.3.

Subsection 6.4 concludes with an example of the adjoint method applied to a complex acoustic field synthesised from oceanographic and acoustic data of the South Elba environment; the data were obtained during the YELLOW SHARK '94 geoacoustic inversion experiments in the Mediterranean.

6.1 A simple example of an adjoint operator and the adjoint-based inversion scheme

Given an integral inner product over some domain Ω

$$\langle u, v \rangle = \int_{\Omega} uv \, dx \quad (1)$$

the adjoint operator L^* is defined by the identity

$$\langle Lu, v \rangle = \langle u, L^*v \rangle. \quad (2)$$

For the simple case of a linear differential operator $L = \frac{d}{dx}(\cdot)$ we obtain by means of partial integration

$$\langle Lu, v \rangle = \int_{\Omega} \frac{du}{dx} v \, dx \quad (3)$$

$$\Leftrightarrow \langle u, L^*v \rangle = [uv]_{\Omega} - \int_{\Omega} u \frac{dv}{dx} \, dx. \quad (4)$$

Defining the corresponding adjoint boundary conditions such that the boundary term in Eq. 4 vanishes, we can identify the adjoint operator $L^* = -\frac{d}{dx}(\cdot)$.

This reversal in sign of the first derivative in the adjoint operator, which also occurs, e.g., in the parabolic operator produces a reversal in the propagation direction (the sign of the second derivative remains unchanged). Therefore, the initial conditions for the adjoint operator have to be provided at the final range, and the adjoint field propagates backward in range toward the initial range.

As an example, Fig. 1 displays the typical flow of an adjoint approach embedded within an iterative descent algorithm such as steepest descent, conjugate gradient, etc. as described in [87]. Starting with an initial guess for the unknown control γ_{init} one forward run of the direct model is required to calculate the resulting mismatch between the model results and the observations. This mismatch is used to initiate the adjoint model run, which backpropagates the mismatch in range toward the source. With the information thus obtained, the overall gradient of the cost function can be determined and, if necessary, the current γ is updated accordingly.

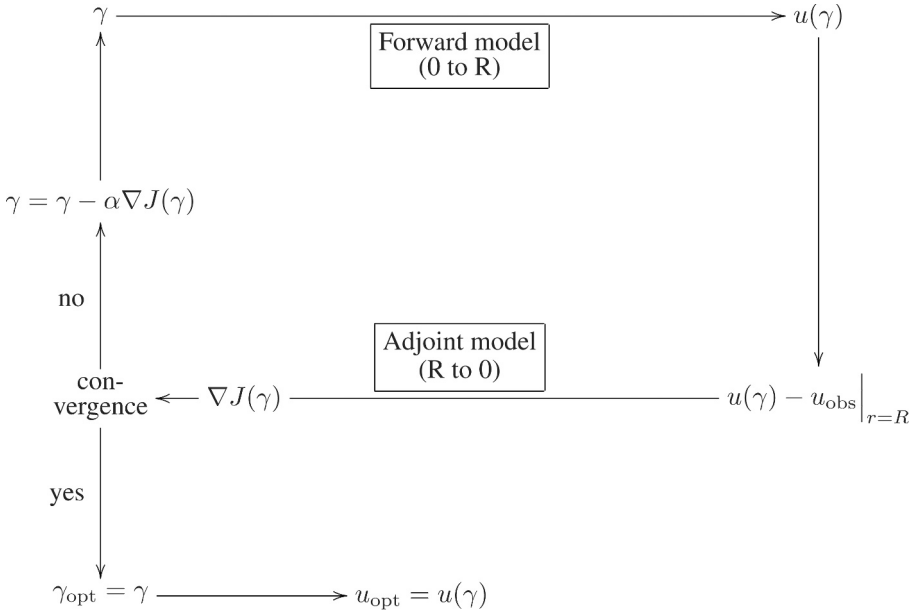


Figure 1. Conceptual flow of an adjoint-based iterative inversion scheme.

In terms of the optimisation scheme, the adjoint approach as a gradient-based optimisation therefore inherits the limitations of this local optimisation method. If the objective function contains multiple minima, then using the method of steepest descent or conjugate gradient methods with the calculated gradient of the cost function ensures moving downhill efficiently, but it bears at the same time the risk of potentially being trapped in a local minimum. Initialising the iterative inversion with many different starting models, applying regularisation methods or using multiple-source or multiple-frequency cost functions can overcome the problem. Otherwise, for an objective function which is known to have multiple local minima, and possibly discontinuities, a hybrid approach in combination with global search algorithms might be the solution.

6.2 Application of the adjoint approach in underwater acoustics

Currently there are three different approaches applied for both ocean acoustic tomography (OAT) and geoacoustic inversion (GI) with equivalent adjoint formalisms: Lagrange multiplier method, variational approach and perturbative approach (adjoint Green's function method). These are implemented with different propagation models: the standard PE, the wide-angle PE and normal modes both as discrete and as continuous adjoints.

In ocean acoustic tomography two different approaches have been recently published: the discrete PE adjoint modelling method presented in [88] and the analytic adjoint normal mode approach in [89]. The latter has been further extended in [90]. For geoacoustic inversion an analytic adjoint PE approach based on optimal control theory was first presented in [91] and subsequently refined in [87, 92, 93]. Basically the idea is the same as for OAT, the adjoint method produces the necessary corrections to the respective model inputs that caused mismatches between the observations and model predictions either by using the adjoint of a parabolic approximation of the Helmholtz equation forward model or by applying the adjoint of a normal mode model. Thus the number of modelling

runs required for the inversion of an acoustic field can be significantly decreased. Especially when the number of unknown parameters is much greater than the number of observations, the adjoint approach can be a less costly method of calculating gradient information than simply running the forward model for each variation of the unknown parameters [88]. In [91, 87, 92, 93] the main goal of the adjoint approach is to obtain an equivalent geoacoustic model which reproduces the acoustic transmission losses. The adjoint-based control approach is applied to the impedance boundary condition and the gradient of the obtained cost function is computed according to the flow diagram in Fig. 1. The adjoint model is derived in the continuous domain using Fréchet derivatives and subsequently both the adjoint and the direct models are discretised (“continuous approach”). In [88] the adjoint assisted inversion technique is used to invert errors in pressure predictions at a VRA for sound speed perturbations due to internal tides using simulated data based on the INTIMATE ’96 experiment [62]. In this approach a tangent linear model for the parabolic equation is first derived and subsequently the adjoint of this model is used with synthetic acoustic data to demonstrate the feasibility of inverting for a sequence of internal tides. Like many other approaches in geophysics it implies first the discretisation of the parabolic equation, its tangent linear model and the subsequent formulation of the adjoint model by means of the standard technique of Lagrange multipliers (“discrete approach”). This distinguishes it from the continuous approach where the adjoint is computed in the continuous domain and ultimately both the model and its adjoint are discretised (see also Fig. 2 in Sec. 6.3).

As for the adjoint approach in [89] and [90] the work concentrates on the inversion of waveguide environmental parameters by means of adjoint normal modes. The authors describe how an analytic adjoint approach is applied to a normal-mode waveguide Green’s function in order to derive multiple order environmental pressure derivatives by applying the Born approximation. This is illustrated with experimental data from SWELLEX-3 experiments.

6.3 Continuous vs. discrete approach

Many approaches particularly those influenced by the geophysical literature apply the discrete adjoint, i.e., discretise first, after which manipulations are applied to matrices, rather than to the governing partial differential or integral equations. However, the continuous-space results are also applicable when the problem is ultimately discretised, or when the continuous control is characterised *a priori* by a finite number of undetermined parameters, the finitedimensional problem [85]. The same problem is also addressed in [81] whether to use finite difference of adjoints or adjoints of finite differences. The difference between the discrete and the continuous adjoint approaches to forming discrete adjoint equations is illustrated schematically in Fig. 2.

Next to the fully discrete and the fully continuous approaches, the dashed arrow represents an intermediate path, linearising the original partial differential equations (p.d.e.), discretising them and then taking the transpose. “In principle, if each of the steps is performed correctly, and all of the solutions are sufficiently smooth then in the limit of infinite grid resolution all three approaches should be consistent and converge to the correct analytic value for the gradient of the objective function. However, there are important conceptual differences between the different approaches, and for finite resolution grids there will be differences in the computed results.” [83] So far, both the discrete and the continuous method have performed well in practice. For sophisticated state-of-the-art forward models though, an analytical adjoint derivation for obtaining a closed form gradient is often out of reach. As for the cases presented here, the final choice may always remain, to some extent, a matter of personal taste.

6.4 Inversion results for the South Elba environment

In order to retrieve the corresponding geoacoustic model and correctly reproduce acoustic transmission losses, the adjoint-based inversion proposed in [87, 92, 93] was assessed on complex acoustic

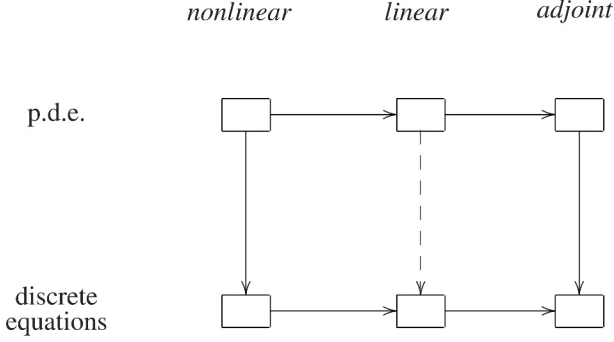


Figure 2. Alternative approaches to forming discrete adjoint equations. Adapted from [83].

fields synthesised from ocean sound speed profiles and subbottom acoustic properties collected in real environments. The example we present here is displayed in more detail in [94] and is based on simulations of the YELLOW SHARK'94 experiments, south of the Island of Elba, Italy, using environmental parameters available from full-field inversions of acoustic data, and from an oceanographic survey with a towed-oscillating CTD profiler [13, 59].

The site is modeled as in [95], and consists of: a water column with an average depth of 113.1 m on top of a 7.5-m thick clay sediment layer with a compression-speed gradient ($\rho = 1.5 \text{ g cm}^{-3}$, $c = 1470 \text{ m s}^{-1}$, $g = 2 \text{ s}^{-1}$, $\alpha = 0.03 \text{ dB } \lambda^{-1}$), and a homogeneous fluid halfspace model of a silty-clay sediment ($\rho = 1.8 \text{ g cm}^{-3}$, $c = 1530 \text{ m s}^{-1}$, $\alpha = 0.15 \text{ dB } \lambda^{-1}$). The source depth is set to 69.2 m as in one of the experimental runs [13] and the source frequency is set to 500 Hz. The range average of the sound speed profiles measured during one of the runs is used for the modelling; it is strongly downward refracting as seen in Fig. 3b.

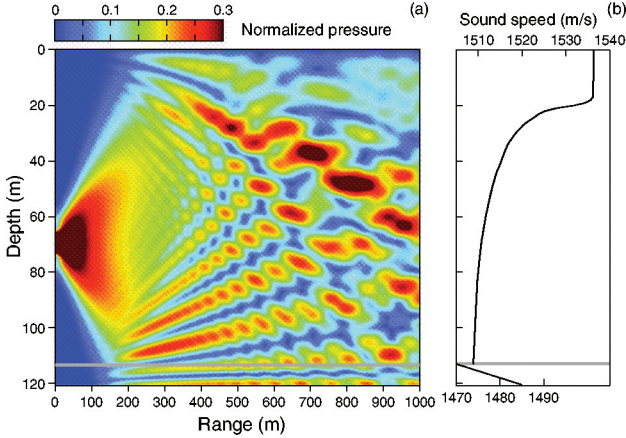


Figure 3. South Elba environment. (a) Acoustic pressure field generated with the wide-angle PE using NLBC calculated from measurement of the subbottom properties. The color scale represents the modulus of the complex-valued ψ , normalised to unity. (b) Range-average sound speed profile of the water column and sediment layer used for the modeling. The upper and lower scales refer to water and sediment, respectively.

The acoustic field has been generated accordingly on a sampling grid of 512 points in both range and depth using Claerbout's wide-angle PE in combination with Yevick and Thomson's [96] non-local impedance boundary condition (NLBC) at the water-bottom interface (Fig. 3a). The analytic adjoint of the Claerbout wide-angle parabolic equation model is used in an iterative inversion scheme as shown in Fig. 1 to retrieve the unknown non-local impedance boundary condition, which in the following shall be represented formally by the control parameter $F(r)$. For the inversion the low-absorbing sediment layer was assumed to be known while the NLBC associated with the layer-subbottom interface were inverted for. For the initial conditions a sand bottom was assumed with a much higher compression speed and sound attenuation ($c = 1575 \text{ m s}^{-1}$, $\alpha = 1 \text{ dB } \lambda^{-1}$).

The performance of the adjoint-based optimisation is displayed in Fig. 4. The convergence of the matched-field cost function in Fig. 4a indicates that already after a couple of iterations the reconstructed field at range $R = 1 \text{ km}$ agrees very well with the true one, even though in Fig. 4d the initial field is seen to be quite different from the true field. Adjoint-based inversion of the field observed at the single range $R = 1 \text{ km}$ (Fig. 4d) produces a reconstructed field that is nearly identical to the true one not only at that range but at all range and depth (Fig. 4c). The overall error across range and depth is reduced from initially $>50\%$ to $<3\%$ upon completion of the process (Fig. 4b). Likewise, the control parameter F in Fig. 4c is well retrieved at all range (Fig. 4c). Upon completion of the process the field obtained at range $R = 1 \text{ km}$ (Fig. 4d), as well as in the whole section (Fig. 4b), and the control parameter F vs. range (Fig. 4c) correspond to their true counterparts.

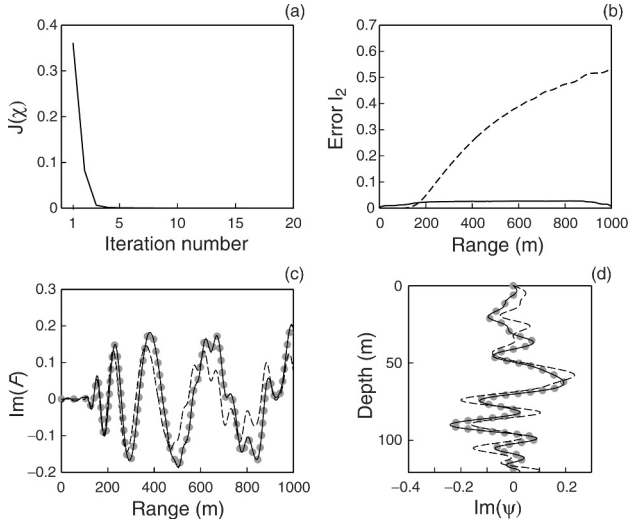


Figure 4. Inversion results for the South Elba environment. Optimal control of the subbottom NLBC for the WAPE. (a) Convergence of the algorithm vs. iteration number; (b) Relative error between the initial and the true fields (dashed), and between the calculated and the true fields (solid); (c)–(d) Comparison of the initial (dashed, black), the true (dots, gray) and the inverted (solid, black) imaginary parts of the control parameter F vs. range and the pressure field vs. depth at 1-km range.

The results show that adjoint-based optimal control of the wide-angle PE in combination with conjugate gradient optimisation accelerates drastically the convergence of matched-field inversion when compared to the conventional. Based on tests made for other constellations the above results can be considered as representative of the performance of this approach provided that the environment is supported by the underlying bottom model.

Acknowledgements

The preparation of this review paper was supported by the AquaTerra Project “Integrated modelling of the river-sediment-soil-groundwater system” funded by the European 6th Framework Programme, research priority 1.1.6.3 Global change and ecosystems (European Commission, Contract No. 505428-GOCE). It is part of Flux3 “Input/output mass balances in river basin: dissolved and solid matter load”, a sub-component of the AquaTerra Integrated Project. The adjoint work itself was supported by the Royal Netherlands Navy and the Service Hydrographique et Océanographique de la Marine Française under the projects REA and SIGMAA (Contract Nos. 631.380026.01 and CA-2004/03/CMO).

References

1. Parvulescu A., Signal detection in a multipath medium by M.E.S.S. processing. *J. Acoust. Soc. Am.*, **33**(11):1674, November (1961).
2. Parvulescu A. and Clay C.S., Reproducibility of signal transmissions in the ocean. *Radio Elec. Eng.*, **29**:223–28 (1965).
3. Parvulescu A., Matched signal “MESS” processing by the ocean. *J. Acoust. Soc. Am.*, **98**(2):943–60, November (1995).
4. Bucker H.P., Use of calculated sound fields and matched-field detection to locate sound sources in shallow water. *J. Acoust. Soc. Am.*, **59**(2):368–373 (1976).
5. Tolstoy A., *Matched Field Processing for Underwater Acoustics*. World Scientific, Singapore (1993).
6. Baggeroer A.B., Kuperman W.A. and Mikhalevsky P.N., An overview of matched field processing in ocean acoustics. *IEEE J. Oceanic Eng.*, **18**(4):401–24, October (1993).
7. Wilson J.H., Rajan S.D. and Null J.M., editors. Inverse techniques and the variability of sound propagation in shallow water. *IEEE J. Oceanic Eng., Special issue*, **21**(4), October (1996).
8. Chapman R., Chin-Bin S., D. King and Evans R., editors. Geoacoustic inversion in range-dependent shallow water environments. *IEEE J. Oceanic Eng., Special issue (Pt.1)*, **28**(3), July (2003).
9. Chapman R., Chin-Bin S., King D. and Evans R., editors. Geoacoustic inversion in range-dependent shallow water environments. *IEEE J. Oceanic Eng., Special issue (Pt.2)*, **29**(1), January (2004).
10. Diachok O., Caiti A., Gerstoft P. and Schmidt H., editors. *Full field inversion methods in ocean and seismo acoustics*, Norwell, MA, USA, and Dordrecht, The Netherlands, 1995. Kluwer Academic Publisher.
11. Caiti A., Hermand J.-P., Porter M.B. and Jesus S., editors. *Experimental Acoustic Inversion Methods for Exploration of the Shallow Water Environment*. Kluwer Academic (2000).
12. Taroudakis M.I. and Markaki M.G., editors. *Inverse Problems in Underwater Acoustics*. Springer (2001).
13. Hermand J.-P. and Gerstoft P., Inversion of broad-band multitone acoustic data from the YEL-LOW SHARK summer experiments. *IEEE J. Oceanic Eng.*, **21**(4):324–46, October (1996).
14. Baggeroer A.B., Kuperman W.A. and Schmidt H., Matched field processing: Source localization in correlated noise as an optimum parameter estimation problem. *J. Acoust. Soc. Am.*, **83**(2):571–87 (1988).
15. Richardson A.M. and Nolte L.W., A posteriori probability source localization in an uncertain sound speed, deep ocean environment. *J. Acoust. Soc. Am.*, **89**(5):2280–2284 (1991).
16. Krolik J.L., Matched-field minimum variance beamforming in a random ocean channel. *J. Acoust. Soc. Am.*, **92**(3):1408–1419 (1992).
17. Michalopoulou Z.-H. and Porter M.B., Matched-field processing for broad-band source localization. *IEEE J. Oceanic Eng.*, **21**(4):384–92, October (1996).

18. Orris G.J., Nicholas M. and Perkins J.S., The matched-phase coherent multi-frequency matched-field processor. *J. Acoust. Soc. Am.*, **107**(5):2563–75 (2000).
19. Soares C. and Jesus S.M., Broadband matched field processing: Coherent and incoherent approaches. *J. Acoust. Soc. Am.*, **113**(5):2587–98, May (2003).
20. Hermend J.-P. and Roderick W.I., Acoustic model-based matched filter processing for fading time-dispersive ocean channels: Theory and experiment. *IEEE J. Oceanic Eng.*, **18**(4):447–465, October (1993).
21. Tappert F.D., Nghiem-Phu L. and Daubin S.C., Source localization using the PE method. *J. Acoust. Soc. Am.*, **78**(S1):S30 (1985).
22. Nghiem-Phu L. and F.D. Tappert, Modeling of reciprocity in the time domain using the parabolic equation method. *J. Acoust. Soc. Am.*, **78**(1):164–71, July (1985).
23. Nghiem-Phu L. and F.D. Tappert, Parabolic equation modeling of the effects of ocean currents on sound transmission and reciprocity in the time domain. *J. Acoust. Soc. Am.*, **78**(2):642–48, August (1985).
24. Thomson D.J., Ebbeson G.R. and Maranda B.H., A matched field backpropagation algorithm for source localization. In *Proceedings of MTS/IEEE Oceans 1997*, volume 1, pages 602–607, Washington, DC, (1997). Marine Technol. Soc.
25. Thomson D.J., Ebbeson G.R. and Maranda B.H., A parabolic equation based backpropagation algorithm for matched field processing. *J. Acoust. Soc. Am.*, **103**(5):2821, May (1998).
26. Thomson D.J. and Ebbeson G.R., A backpropagated PE method for matched field and matched mode localization. In *Proceedings of the 6th International Conference on Theoretical and Computational Acoustics*. Hawaii, USA (2003).
27. I-Tai Lu and Voltz P., A back-propagating ray technique for source localization. *J. Acoust. Soc. Am.*, **91**(4):2366–2366 (1992).
28. Voltz P. and I-Tai Lu., A time-domain backpropagating ray technique for source localization. *J. Acoust. Soc. Am.*, **95**(2):805–812 (1994).
29. Collins M.D. and Kuperman W.A., Focalization: Environmental focusing and source localization. *J. Acoust. Soc. Am.*, **90**(3):1410–1422, September (1991).
30. Collins M.D. and Baer R.N., Focalization in the presence of internal waves. *J. Acoust. Soc. Am.*, **114**(4):2401, October (2003).
31. Dizaji R.M., Chapman N.R. and Kirlin R.L., Geoacoustic parameter estimation using back wave propagation technique. In M. Meng, editor, *Proceedings of the IEEE Canadian Conference on Electrical and Computer Engineering*, volume 3, pages 1547–52. IEEE, Piscataway, NJ (1999).
32. Dizaji R.M., Chapman N.R. and Kirlin R.L., A phase regulated back wave propagation technique for geoacoustic inversion. *J. Acoust. Soc. Am.*, **111**(2):800–8, February (2002).
33. Ozard J.M., Jeremy M.L., Chapman N.R. and Wilmut M.J., Matched-field processing in a range-dependent shallow water environment in the northeast pacific ocean. *IEEE J. Oceanic Eng.*, **21**(4):377–83, October (1996).
34. Gerstoft P., Hodgkiss W.S., Kuperman W.A., and Song H., Phenomenological and global optimization inversion. *IEEE J. Oceanic Eng.*, April (2003).
35. Jackson D.R. and Dowling D.R., Phase conjugation in underwater acoustics. *J. Acoust. Soc. Am.*, **89**(1):171–181 (1991).
36. Kuperman W.A., Hodgkiss W.S., Song H.C., Akal T., Ferla C. and Jackson D.R., Phase conjugation in the ocean: Experimental demonstration of an acoustic time-reversal mirror. *J. Acoust. Soc. Am.*, **103**(1):25–40 (1998).
37. Hodgkiss W.S., Song H.C., Kuperman W.A., Akal T., Ferla C. and Jackson D.R., A long-range and variable focus phase conjugation experiment in shallow water. *J. Acoust. Soc. Am.*, **105**:1597–1604 (1999).

38. Edelman G., Akal T., Hodgkiss W.S., Kim S., Kuperman W.A. and Song H.C., An initial demonstration of underwater acoustic communication using time reversal. *IEEE J. Oceanic Eng.*, **27**:602–609 (2002).
39. Kim S., Kuperman W.A., Hodgkiss W.S., Song H.C., Edelmann G.F. and Akal T., Robust time reversal focusing in the ocean. *J. Acoust. Soc. Am.*, **114**(1):145–157 (2003).
40. Sabra K.G. and Dowling D.R., Effects of time-reversing array deformation in an ocean wave guide. *J. Acoust. Soc. Am.*, **115**(6):2844–2847 (2004).
41. Sabra K.G. and Dowling D.R., Broadband performance of a time reversing array with a moving source. *J. Acoust. Soc. Am.*, **115**(6):2807–2817 (2004).
42. Song H.C., Kim S., Hodgkiss W.S. and Kuperman W.A., Environmentally adaptive reverberation nulling using a time reversal mirror. *J. Acoust. Soc. Am.*, **116**(2):762–768 (2004).
43. Sabra K., Roux P., Song H.-C., Hodgkiss W., Kuperman W., Akal T. and Stevenson M., Experimental demonstration of time reversed reverberation focusing in an oceanic waveguide. *J. Acoust. Soc. Am.*, **116**(4):2526–2526 (2004).
44. Prada C., Wu F. and Fink M., The iterative time reversal mirror: A solution to self-focusing in the pulse echo mode. *J. Acoust. Soc. Am.*, **90**(2):1119–1129 (1991).
45. Prada C., Manneville S., Spoliansky D. and Fink M., Decomposition of the time reversal operator: Detection and selective focusing on two scatterers. *J. Acoust. Soc. Am.*, **99**(4):2067–2076 (1996).
46. Song H.C., Kuperman W.A., Hodgkiss W.S., Akal T. and Ferla C., Iterative time reversal in the ocean. *J. Acoust. Soc. Am.*, **105**(6):3176–3184 (1999).
47. Dowling D.R., Acoustic pulse compression using passive phase-conjugate processing. *J. Acoust. Soc. Am.*, **95**(3):1450–1458 (1994).
48. Rouseff D., Jackson D.R., Fox W.L.J., Jones C.D., Ritcey J.A. and Dowling D.R., Underwater acoustic communication by passive-phase conjugation: theory and experimental results. *IEEE J. Oceanic Eng.*, **26**(4):821–831 (2003).
49. Svensson E., Karasalo I. and Hermand J.-P., Time variability of an underwater acoustic channel. In *Proceedings of the 10th International Congress on Sound and Vibration*, pages 2633–2642. International Institute of Acoustics and Vibration, July (2003).
50. Sabra K.G. and Dowling D.R., Blind deconvolution in ocean waveguides using artificial time reversal. *J. Acoust. Soc. Am.*, **116**(1):262–271 (2004).
51. Yang T.C., Performance comparisons between passive-phase conjugation and decision-feedback equalizer for underwater acoustic communications. *J. Acoust. Soc. Am.*, **115**(5):2505–2506 (2004).
52. Rouseff D., Intersymbol interference in underwater acoustic communications using time-reversal signal processing. *J. Acoust. Soc. Am.*, **117**(2):780–788 (2005).
53. Roux P., Kuperman W.A., Hodgkiss W.S., Song H.C., Akal T. and Stevenson M., A nonreciprocal implementation of time reversal in the ocean. *J. Acoust. Soc. Am.*, **116**(2):1009–1015 (2004).
54. Hermand J.-P., A model-based acoustic time-reversal mirror for robust variable focusing. *J. Acoust. Soc. Am.*, **110**(5):2708: 3aSP8 (2001).
55. Hermand J.-P., Model-based spatial diversity processing with sparse receive arrays: Application to coherent acoustic communication in shallow water. In *Proceedings of the 6th European Conference on Underwater Acoustics, ECUA 2002*, pages 289–294. Gdansk, Poland, September (2002).
56. Candy J.V., Meyer A.W., Poggio A.J., and Guidry B.L., Time-reversal processing for an acoustic communications experiment in a highly reverberant environment. *J. Acoust. Soc. Am.*, **115**(4):1621–31, April (2004).
57. Chambers D.H., Candy J.V., Lehmann S.K., Kallman J.S., Poggio A.J. and Meyer A.W., Time-reversal and the spatio-temporal matched filter (L). *J. Acoust. Soc. Am.*, **116**(3):1348–50, September (2004).

58. Clay C.S., Optimum time domain signal transmission and source localization in a waveguide. *J. Acoust. Soc. Am.*, **81**(3):660–64 (1987).
59. Hermand J.-P., Broad-band geoacoustic inversion in shallow water from waveguide impulse response measurements on a single hydrophone: Theory and experimental results. *IEEE J. Oceanic Eng.*, **24**(1):41–66, January (1999).
60. Michalopoulou Z.-H., Matched-impulse-response processing for shallow-water localization and geoacoustic inversion. *J. Acoust. Soc. Am.*, **108**(5):2082–90, November (2000).
61. Le Gac J.-C., Asch M., Stéphan Y. and Demoulin X., Geoacoustic inversion of broadband acoustic data in shallow water on a single hydrophone. *IEEE J. Oceanic Eng.*, April (2003).
62. Stéphan Y., Demoulin X., Folegot T., Jesus S.M., Porter M.B. and Coelho E., Acoustical effects of internal tides on shallow water propagation: an overview of the INTIMATE 96 experiment. In A. Caiti, J.P. Hermand, S.M. Jesus, and M.B. Porter, editors, *Experimental Acoustic inversion methods for exploration of the shallow water environment*, pages 19–38. Kluwer Academic, Dordrecht, The Netherlands (2003).
63. Kalman R.E. and Bucy R.S., New results in linear filtering and prediction theory. *Trans. Amer. Soc. Mech. Eng. J. Basic Engineering*, **83**:95–108 (1961).
64. Bellman R., *Adaptive Control Process*. Princeton University Press (1961).
65. Gelfand I.M. and Fomin S.V., *Calculus of Variations*. Prentice-Hall, Englewood Cliffs, NJ (1963).
66. Feldbaum A.A., *Optimal Control Systems*. Academic Press, New York (1965).
67. Luenberger D.G., *Optimization by Vector Space Methods*. Wiley, New York (1969).
68. Kirk D.E., *Optimal Control Theory*. Prentice-Hall, Englewood Cliffs, NJ (1970).
69. Jazwinski A.H., *Stochastic Processes and Filtering Theory*. Academic Press, New York (1970).
70. Sage A.P. and Melsa J.L., *Estimation Theory with Application to Communication and Control*. McGraw-Hill, New York (1971).
71. Lions J.L., *Optimal Control of Systems Governed by Partial Differential Equations*, volume 170 of *A series of comprehensive studies in mathematics*. Springer Verlag, New York (1971).
72. Lions J.L., Exact controllability, stabilization and perturbations for distributed systems. *SIAM Review*, **30**:71–86, March (1988).
73. Candy J.V. and Sullivan E.J., Ocean acoustic signal processing: A model-based approach. *J. Acoust. Soc. Am.*, **92**(6):3185–3201, December (1992).
74. Sullivan E.J. and Candy J.V., Space-time array processing: The model-based approach. *J. Acoust. Soc. Am.*, **102**(5):2809–20, November (1997).
75. Candy J.V., *Signal Processing: The Model-Based Approach*. McGraw-Hill, New York (1986).
76. Tarantola A., Inversion of seismic reflection data in the acoustic approximation. *Geophysics*, **49**:1259–1266 (1984).
77. Tarantola A., *Inverse Problem Theory: Methods for data fitting and model parameter estimation*. Elsevier, New York (1987).
78. Talagrand O. and Courtier P., Les équations adjointes - Application à la modélisation numérique. Atelier modélisation de l'atmosphère, Direction de la météorologie, Toulouse, France (1986).
79. Carthel C., Glowinski R. and Lions J.L., On exact and approximate boundary controllabilities for the heat equation: A numerical approach. *Journal of Optimization Theory and Applications*, **82**(3):429–84 (1994).
80. Leredde Y., Lellouche J.-M., Devenon J.-L. and Dekeyser I., On initial, boundary conditions and viscosity coefficient control for Burgers' equation. *Int. J. Num. Meth. Fluids*, **28** (1998).
81. Sirkes Z. and Tziperman E., Finite difference of adjoint or adjoint of finite difference. *Monthly Weather Rev.*, **125**:3373–3378 (1997).

82. Errico R.M., What is an adjoint model? *Bulletin of the American Meteorological Society*, **78**:2577–91 (1997).
83. Giles M.B. and Pierce N.A., An introduction to the adjoint approach to design. *Flow, Turbulence and Combustion*, **65**:393–415 (2000).
84. Gillivray P.R. and Oldenburg D.W., Methods for calculating Fréchet derivatives and sensitivities for the non-linear inverse problem: A comparative study. *Geophysical Prospecting*, **38**:499–524 (1990).
85. Norton S.J. Iterative inverse scattering algorithms: Methods of computing Fréchet derivatives. *J. Acoust. Soc. Am.*, **106**(5):2653–60, November (1999).
86. Norton S.J., Iterative algorithms for computing the shape of a hard scattering object: Computing the shape derivative. *J. Acoust. Soc. Am.*, **116**(2):1002–08, August (2004).
87. Le Gac J.-C., Stéphan Y., Asch M., Helluy P. and Hermand J.-P., A variational approach for geoacoustic inversion using adjoint modeling of a PE approximation model with non local impedance boundary conditions. In A. Tolstoy, Y.C. Teng, and E.C. Shang, editors, *Theoretical and Computational Acoustics 2003*, pages 254–263. World Scientific Publishing (2004).
88. Hursky P., Porter M.B., Hodgkiss W.S. and Kuperman W.A., Adjoint modeling for acoustic inversion. *J. Acoust. Soc. Am.*, **115**(2):607–19 (2004).
89. Thode A., The derivative of a waveguide acoustic field with respect to a three-dimensional sound speed perturbation. *J. Acoust. Soc. Am.*, **115**(6):2824–33 (2004).
90. Thode A. and Kim K., Multiple-order derivatives of a waveguide acoustic field with respect to sound speed, density, and frequency. *J. Acoust. Soc. Am.*, **116**(6):3370–83 (2004).
91. Asch M., Le Gac J.-C. and Helluy P., An adjoint method for geoacoustic inversions. In *Proceedings of the 2nd Conference on Inverse Problems, Control and Shape Optimization*. Carthage, Tunisia (2002).
92. Meyer M., Hermand J.-P. and Asch M., Derivation of the adjoint of a wide angle parabolic equation for acoustic inversion. In *Proceedings of the 7th European Conference on Underwater Acoustics, ECUA 2004*, pages 727–32. Delft, The Netherlands, July (2004).
93. Meyer M., Hermand J.-P., Le Gac J.-C. and Asch M., Penalization method for WAPE adjoint-based inversion of an acoustic field. In *Proceedings of the 7th European Conference on Underwater Acoustics, ECUA 2004*, pages 243–48. Delft, The Netherlands, July (2004).
94. Meyer M. and Hermand J.-P., Optimal nonlocal boundary control of the wide-angle parabolic equation for inversion of a waveguide acoustic field. *J. Acoust. Soc. Am.*, **117**(5):2937–48, May (2005).
95. Holland C.W., Hermand J.-P. and Dosso S., Fine-grained sediment geoacoustic properties from remote acoustic measurements. In *Proceedings of the 7th European Conference on Underwater Acoustics, ECUA 2004*, pages 677–84. Delft, The Netherlands, July (2004).
96. Yevick D. and Thomson D.J., Nonlocal boundary conditions for finite-difference parabolic equation solvers. *J. Acoust. Soc. Am.*, **106**(1):143–50, July (1999).

ACOUSTIC INVERSION AT LOW KHZ FREQUENCIES USING AN ACTIVE, VERTICAL LINE ARRAY

PAUL C. HINES AND MATT COFFIN

*Defence R&D Canada Atlantic,
P.O. Box 1012, Dartmouth, NS, Canada, B2Y 3Z7
E-mail: paul.hines@drdc-rddc.gc.ca*

Techniques to characterize the seabed are particularly important in littoral environments, because of the extensive acoustic interaction with the seabed and the spatial variability of seabed properties. It has been established that normal incidence acoustic returns from the seabed can be used as a classification tool to discriminate between, for example, sand, mud, or rock bottoms; however, this has typically been accomplished using systems that operate in the range of several 10s of kHz. This implies that bottom roughness at the seabed interface is the dominant scattering mechanism and no information is provided about seabed composition beneath the interface. Theoretical and experimental results indicate that at lower frequencies (1-10 kHz), returns from the sub-bottom provide an additional discrimination tool without significantly corrupting the information contained in the scatter returns from the seabed interface. This paper describes an experimental methodology and presents preliminary results using a broadband acoustic source and a vertical line array of receivers. Information about the seabed is provided down to several meters which should enhance sonar performance predictions.

1 Introduction

Acoustic inversion can be loosely defined as the utilization of acoustic techniques to measure non-invasively, the geophysical properties of the seabed. This research area spans an enormous frequency band: from seismic frequencies of a few Hz, through what one might refer to as mid-frequencies using Matched Field Processing (MFP), up to 10 s of kHz using seabed classification systems frequently employed in mine detection. It is interesting to note that the work at low and mid-frequencies concentrates on acoustic inversion for geotechnical and geophysical properties. In contrast, research at the upper end of the frequency band tends toward classification of sediment type and/or texture analysis (e.g., Is it silt, sand, or gravel?). In the present paper we adopt the high-frequency approach of sediment classification but attempt to apply it at low kilohertz frequencies of interest to ASW sonar operations. By interrogating the seabed with a wide-bandwidth and a variety of pulse lengths one can obtain information not only about the seabed composition at the interface but the seabed several meters below the interface. This region has a significant impact on ASW performance in littoral waters.

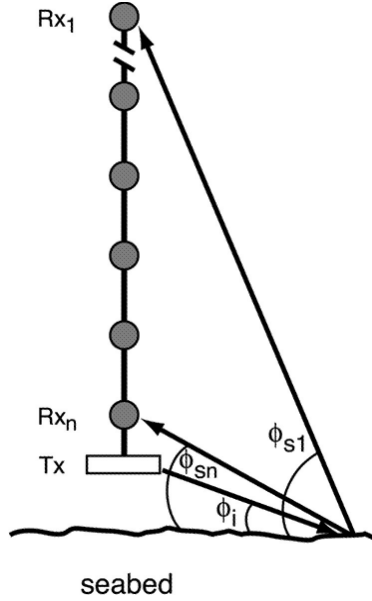


Figure 2. Schematic of a vertical line array for seabed classification using monostatic and bistatic returns. The transmitter (**Tx**) and an array of hydrophone receivers (**Rx**) are depicted along with the bistatic angle paths ϕ_i , the incident grazing angle; ϕ_{s1} , the scattered grazing angle to the first hydrophone; and ϕ_{sn} , the scattered grazing angle to the n th hydrophone.

The vertical array of receivers also allows one to discriminate between a signal scattered from within the seabed at normal incidence, and one scattered from a surface feature located at an equivalent slant range. This is because the surface of time-coincident arrivals for the bistatic returns results in a set of ellipsoids rather than a sphere. This allows one to distinguish a surface feature from a sub-bottom layer (See Figure 3 of [4]). Finally, the vertical array would eliminate the requirement for the second fathometer return to obtain the bistatic arrival (Recall Figure 1.); this removes the effect of the air-sea interface which will vary with sea-state.

An initial set of experiments to test the technique at low-kiloHertz frequencies was conducted in the vicinity of AMCOR 6010 [5] on the ONR Strataform East experimental area of the New Jersey continental shelf. The system consisted of a vertical line array of 8 hydrophones and a pair of projectors. These results were reported by Osler et alia [6]. The data were obtained using several frequencies and pulse types but experimental constraints required that the system be moored — this limited the measurements to a single location. Nonetheless, the results were promising and compared favourably to model estimates for a sandy seabed, which was consistent with the ground truth measurements made in the area. In the spring of 2004, a seabed classification experiment was performed on the Malta Plateau off the southern coast of Sicily using a drifting version of this system. In this paper, this experiment is described, some preliminary experimental results are presented, and these results are compared qualitatively to model estimates.

2 The Underwater Acoustic Target (UAT)

The experiments were conducted using the DRDC Atlantic Underwater Acoustic Target (UAT). The UAT is a ship-launched system which can be used either as an echo-repeater or as a stand-alone research array. A photograph of the system is provided in Figure 3. The photograph shows the sys-

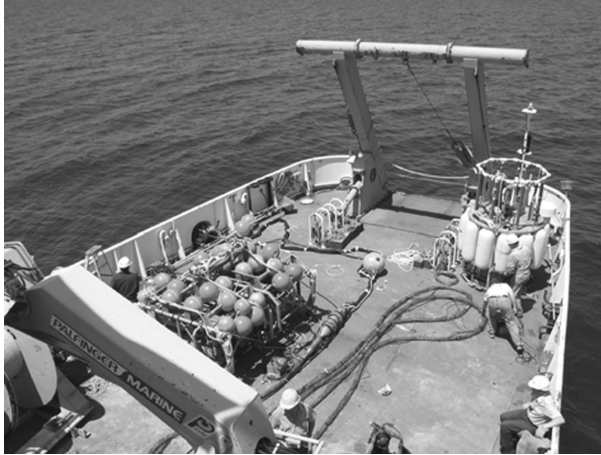


Figure 3. Photograph of UAT laid out on the Quarterdeck of the research vessel CFAV QUEST prior to launch. The vertical line array (VLA) is shown flaked out on the deck, the electronics package is to the left of the VLA and the surface float is at the right-aft of the deck.

tem laid out on the Quarterdeck of the research vessel CFAV QUEST prior to launch. An artist's rendering of the system including the key dimensions is shown in Figure 4. In the present configuration, the system consists of a 15 hydrophone vertical line array (VLA) with 2.1 m spacing between hydrophones and a pair of transmitters located 2-3 m below the array. The power and electronics modules for the UAT are housed in a space frame, the top of which floats approximately flush with the water surface. Mechanical isolation of the VLA from sea-surface induced motion is achieved using a compliant suspension. Communication and system control is done from QUEST via a 900 MHz command link. Data can be transmitted directly back to the ship for immediate analysis using a 2.37 GHz data telemetry link, or the data can be stored in the UAT so that QUEST is free to maneuver and/or leave the vicinity of the UAT. Any 8 of the 15 hydrophones can be used, but the 8 hydrophones (denoted channels 1-8) must be selected prior to deployment. For the seabed classification experiments, the hydrophones were selected to include the one closest to the projectors to provide a near-monostatic return (channel 8), the one furthest from the projectors to provide the maximum range of bistatic angles (channel 1) and where possible to maintain an equal spacing between hydrophones. This resulted in channels 1-4 and channels 5-8 being equally spaced at 4.2 m with channels 4 and 5 separated by 8.4 m. Approximately 2 m below the VLA, was a pair of ITC free-flooding ring (FFR) projectors mounted side by side and enclosed in a protective shroud [7]. The FFRs were oriented such that the projector null pointed horizontally. This was done to maximize the acoustic signal directed at the seabed. The smaller of the FFRs covered the frequency band 1-4 kHz and the larger covered the band 3-10 kHz.

3 Seabed Classification Experiment

The seabed classification experiments were conducted along two separate drift tracks in the waters separating the Mediterranean islands of Malta and Sicily at the locations depicted in Figure 5. Initially, the UAT was deployed at the south-eastern (SE) location so that as it drifted westward, it would traverse alternating areas of rock, sand, and silt, with a variety of layer thicknesses. However, as often happens during sea experiments, Mother Nature did not choose to comply with the scientific cruise plan and the drift direction changed by 180° resulting in the "C" shaped drift seen in the figure. As a result, the UAT was recovered and re-deployed to the north west (NW) and allowed to drift

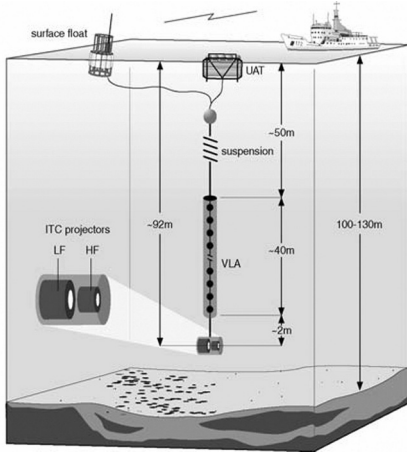


Figure 4. Illustration of the UAT in a typical experiment. The system is deployed so that it drifts over a variety of sediment types.

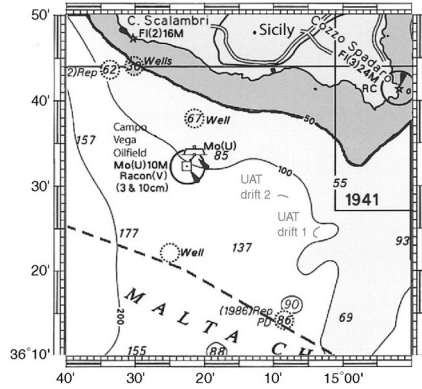


Figure 5. Map showing the experiment location on the Malta Plateau. The UAT drift tracks are labeled.

eastward. During the first (that is, the SE) deployment, the UAT traversed a portion of the Ragusa Ridge which alternated between rocky outcrops and areas which had sandy sediment deposits up to 4 m deep overlaying the rock. During the second deployment, it traversed an area with silty-clay sediments 10s of meters deep. The combined data set provides a substantial variety of bottom types with which to examine the classification technique.

As the UAT drifted, a series of 20 pulses per frequency, at a pulse repetition rate of 2 per second were transmitted at frequencies of 1, 2, and 3 kHz on the low-frequency projector. This was followed immediately by the same pulse sequence at 3, 5, and 8 kHz on the high-frequency projector. The 3 kHz pulses were sent from both projectors to help identify artifacts in the data that might be caused by differences in the projectors rather than frequency dependences of the seabed scatter that would aid classification. Alternating frequencies every 10 seconds (20 pulses at 2 per s) ensured that approximately the same area was being ensounded at each frequency. This series of pulses was transmitted at 1, 2, and 5 ms and the sequence was repeated continuously during the deployments.

4 Preliminary Results from the Seabed Classification Experiment

In this section some preliminary results of the analysis are presented. The analysis can be separated into the bistatic and monostatic results which complement the modeling components discussed in the introduction. First we look briefly at the bistatic nature of the data, examining some of the visualization schemes and highlighting some of the issues under consideration. Then we focus on the frequency dependence of the monostatic backscatter data to see if there are classification clues contained therein.

Figure 6 shows the bistatic nature of the returns for each of the 8 hydrophone channels for a typical return. At normal incidence, the incident and scattered angle are both 90° . Since the transmitter is located at the bottom of the array, the incident angle is shallower than the scattered angle as the wave propagates outward along the bottom. The difference between the scattered and incident angle is plotted along the vertical axis and is greatest for channel 1 and smallest for channel 8. The peak in each curve corresponds to the incident angle at which the maximum difference between incident and scattered angles is encountered for that hydrophone. For channel 1 for example, this would be $(\phi_i, \phi_{s1}) = (30.6^\circ, 26.6^\circ)$. Of course, these values are functions of water depth.

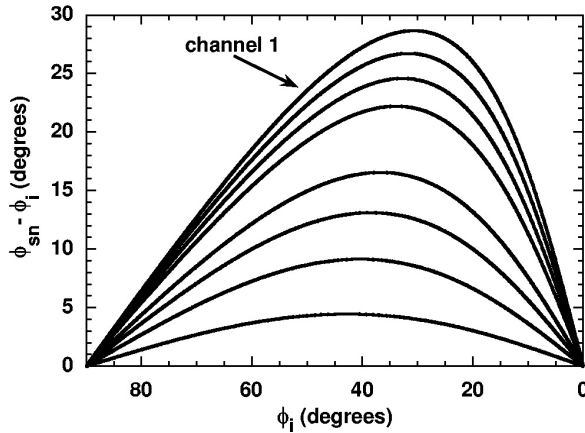


Figure 6. Plot of the bistatic angle as a function of incident grazing angle for each of the 8 channels in the array. The curves are for channel 1 (top curve) which corresponds to the hydrophone nearest the surface consecutively through channel 8 (bottom curve) which corresponds to the hydrophone nearest the seabed.

Figure 7 shows a typical energy time series for each of the two deployments for a frequency of 3 kHz and a pulse length of 2 ms. To avoid crowding in the figure, only the data for hydrophones 1, 3, 5, and 7 are shown. Pulse transmission is denoted by the vertical dashed line. Each trace represents the power average of a series of 20 pulses. The direct, first bottom reflection, and first surface reflection are labeled in the figure. Note that the seabed reflection is substantially lower from the silty seabed present at the NW deployment than at the sandy area of the SE location. Additionally, the split peak of the first bottom return at the NW location indicates the present of a near-surface layer.

It is the frequency dependence of the monostatic backscatter data (hydrophone 8) and slope change that results from the transition from roughness scatter to volume scatter that is employed for classification of the volume beneath the interface. Sample plots of that data are shown for the silty seabed in Figure 10 and the sandy seabed in Figure 11. As the pulse reaches the seabed, the energy scattered from the interface increases as the surface contacted by the pulse grows. This time corresponds to the initial steep rise in the scattered intensity which in Figure 10 commences at about 44 ms. As the pulse propagates outward, the ensonified spot transitions to an annulus as the back of the pulse propagates into the bottom. This corresponds to the maximum in the seabed reflection that occurs at about 46 ms. It is the decay of the reflection at steep angles (approximately 46-52 ms) that is used in high-frequency seabed classification systems. At later times volume scatter from the seabed typically dominates the returns and therefore this region of the curve can provide information about the volume. The decay of the experimental data at these later times has a considerable amount of structure, in part due to layering and in part due to the stochastic nature of the scattering process. However, the slopes of the least squares fits to the data shown by the straight lines plotted in Figures 10 and 11 shows a monotonic increase in decay rate with increasing frequency. For comparison, model estimates for generic silt and sand seabeds are overplotted on the data in Figures 12 and 13, respectively. There was insufficient time between the data collection and the writing of this paper — the experiment was performed 1 month ago — to provide model comparisons tailored to the geotechnical properties measured at the sites. Instead, the volume scatter intensity calculated at 1, 5, and 10 kHz for generic silt and sand seabeds have been reproduced from [4]. Note that the model levels have been adjusted to correspond to the data and it is only the slope of the decay that is being compared. That said, the model outputs for the silt seabed show a remarkable similarity to the data. The model-data agreement for the sand bottom is less impressive but agreement at 2 kHz

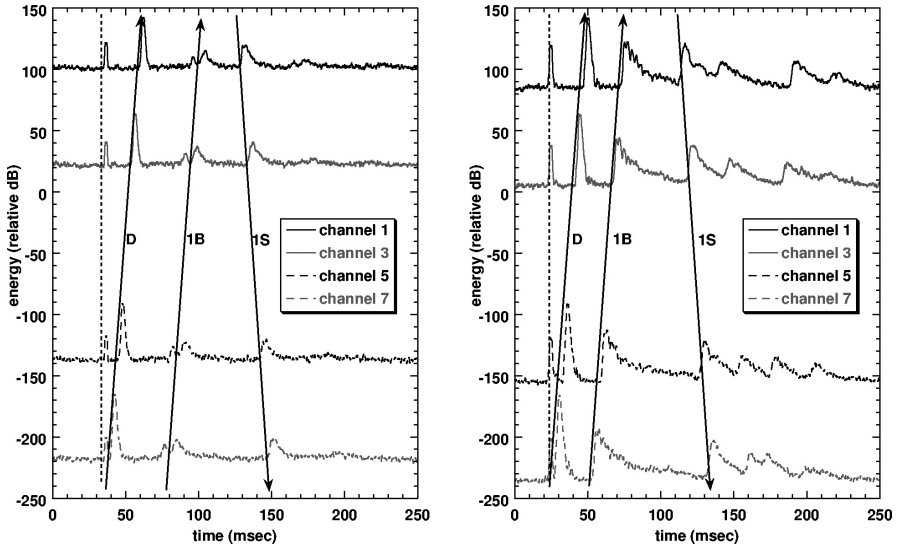


Figure 7. Sample of energy time series for channels 1, 3, 7 for a frequency of 3 kHz and a pulse length of 2 ms. The lhs is data taken during the north-western deployment and the rhs is data from the south-eastern deployment. Electronic cross-talk during transmit (highlighted by the vertical dash line) was used to synchronize the receive time series on each channel. The upward-going direct signal (D), the first bottom reflection (1B), and the first surface reflection (1S) are denoted by the arrowed lines. The arrow heads on the lines show the direction of propagation. The offsets for the waterfall were selected so that the vertical axis is proportional to hydrophone spacing.

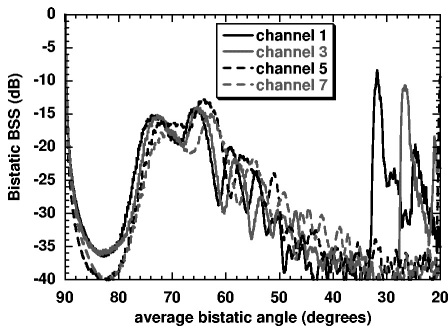


Figure 8. Bistatic scattering strength for 4 of the hydrophones at a frequency of 3 kHz and a pulse length of 2 ms, plotted against the average bistatic angle corresponding to each hydrophone. Below about 35° , interference from the surface returns contaminates the data.

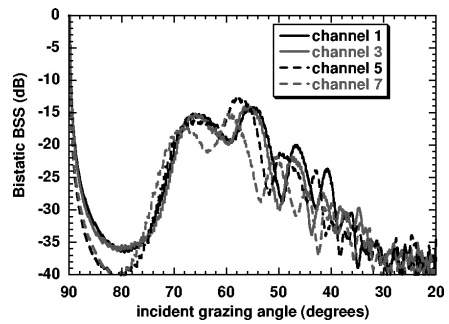


Figure 9. Bistatic scattering strength at a frequency of 3 kHz and a pulse length of 2 ms as a function of incident grazing angle. By plotting the data vs. incident grazing angle, any vertical slice through the curves corresponds to the same patch on the seabed for all the hydrophones.

is reasonable. The poor match at higher frequencies is likely due to the difference between the beam characteristics of the FFR projectors and those employed in the model. A narrow beam, normal incidence source was employed in the model and the steep decay predicted at higher frequencies (for sand), results from the high rate of absorption as the wave propagates vertically down into the

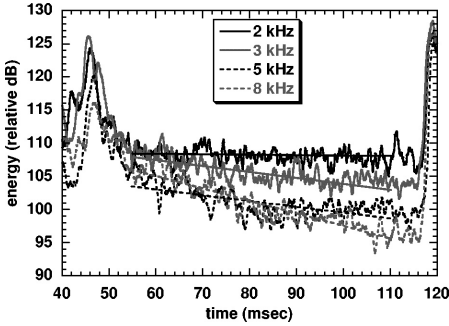


Figure 10. Energy decay with time for 4 frequencies for a silty seabed (north-western deployment). Least squares fit for the portion of the return thought to be dominated by volume scatter is also plotted for each of the curves.

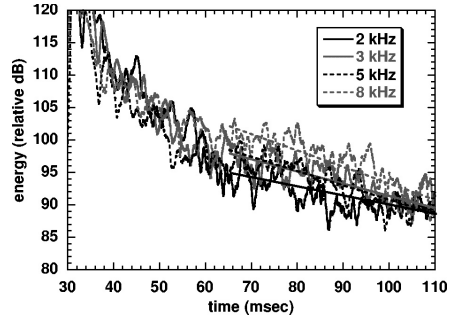


Figure 11. Energy decay with time for 4 frequencies for a sandy seabed (south-eastern deployment). Least squares fit for the portion of the return thought to be dominated by volume scatter is also plotted for each of the curves.

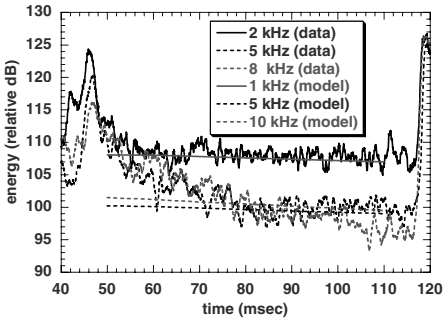


Figure 12. Comparison of modeled results (straight lines) for a generic silt seabed with the energy time series data from Figure 10.

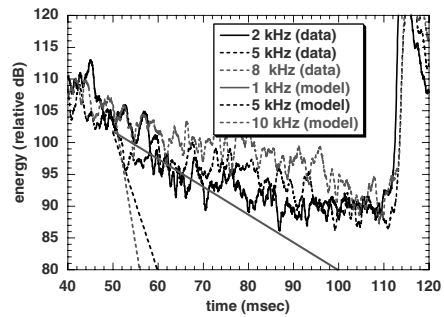


Figure 13. Comparison of modeled results (straight lines) for a generic sand seabed with the energy time series data from Figure 11.

sediment. The wide beamwidth of the FFR projectors means that the later returns (after say 60-70 ms) are still dominated by the volume but it is the volume a few meters below the interface at shallower grazing angles. Correcting the source beamwidth in the model with the characteristics of the FFR projector would substantially reduce the decay rate of the model results and bring them more in line with the data. This inaccuracy with the source model is not noticeable at the silt location because absorption is so low.

5 Concluding Remarks and Future Direction

In this paper an experiment was described and preliminary results were presented to assess the usefulness of a sediment classification scheme developed for low-kiloHertz frequencies. Although data analysis is still in the early stages (the experiment was completed only 1 month prior to the time of writing), it appears promising that it should be possible to discriminate between different sediment types using the simple yet effective seabed model employed in the classification scheme. The next phases of this work are to perform a more comprehensive examination of the data, to compare the

results to complementary ground truth measurements taken at the experiment locations, and to modify the model inputs to more closely match the experimental conditions. These additions will allow one to more accurately assess the potential of the classification method.

Acknowledgements

The authors wish to acknowledge the exceptional experimental support of Mr. Roger Arsenault, Mr. Trevor Ponee, Mr. Doug Caldwell, and Mr. Dave Wheaton of DRDC Atlantic, Mr. Ron Cunningham of Pernix Technologies, Dartmouth NS, and the officers and crew of CFAV QUEST.

References

1. Heald G. J., High frequency seabed scattering and sediment discrimination. *Proc. Inst. of Acoustics* **23**, 258–267 (2001).
2. Pace N. G., Al-Hamdani Z. and Thorne P. D., The range dependence of normal incidence acoustic backscatter from a rough surface. *J. Acoust. Soc. Am.* **77**, 101–112 (1985).
3. Briggs K. B., Tang D. and Williams K. L., Characterization of Interface Roughness of Rippled Sand Off Fort Walton Beach, Florida. *IEEE J. of Ocean. Eng.* **27**, 505–514 (2002).
4. Hines P. C. and Heald G. J., Seabed classification using normal incidence backscatter measurements in the 1-10 kHz frequency band. *Proc. Inst. of Acoustics* **23**, 42–50 (2001).
5. Carey W. M., Doult J., Evans R. B. and Dillman L. M., Shallow-water sound transmission measurements on the New Jersey Continental Shelf. *IEEE J. of Ocean. Eng.* **20**, 321–336 (1995).
6. Osler J. C., Hines P. C. and Trevorrow M. V., Acoustic and In-Situ Techniques for Measuring the Spatial Variability of Seabed Geoacoustic Parameters in Littoral Environments. In *Proc. Impact of Littoral Environmental Variability on Acoustic Predictions and Sonar Performance*, Ed. N.G. Pace and F.B. Jensen (Kluwer Academic Publishers, 2002) pp. 83–90.
7. In the previous seabed classification experiments using the UAT (See [6]) a pair of vertically separated spherical projectors were used so that cardioid pulses could be formed to direct a null at the sea surface. However, this limited the lowest frequency to 3 kHz so the decision was made to use FFR's to extend the frequency band down to 1 kHz.

DISPERSION OF BROADBAND ACOUSTIC NORMAL MODES IN THE CONTEXT OF LONG RANGE SEDIMENT TOMOGRAPHY

GOPU POTTY AND JAMES MILLER

*Department of Ocean Engineering
University of Rhode Island
Narragansett, RI-02882
E-mail: potty@oce.uri.edu*

The long range sediment tomography technique exploits acoustic normal mode dispersion in shallow water. This paper discusses the effect of variations in sediment distribution – both spatial and depth-wise – on the resulting dispersion characteristics. Dispersion data from two locations collected as part of different field experiments are presented and compared. The modal dispersion at these locations – Middle Atlantic Bight and East China Sea – appears to be very different. Possible factors resulting in differences in dispersion behavior at these two locations are discussed based on the sediment information from historic data, core data, geophysical surveys and inversions. In the East China Sea the dispersion from two sides of a sediment boundary between two different types of sediments show different characteristics. Some factors which need to be considered in experimental design are also discussed.

1 Introduction

Long range sediment tomography is a technique developed by Potty *et al.* [1] for the estimation of sediment parameters using non-linear inversion techniques. The development of this technique was inspired by previous research by a number of researchers. Some of the most relevant earlier research works are cited here. The concept of inversion of sound speed structure by comparing the measured and predicted times of arrivals of rays or multipaths to a receiver from a pulsed source was introduced to the acoustic community by Munk and Wunch [2]. The sediment tomography technique is based on the dispersion characteristics of acoustic signals from an explosive source. In a shallow water waveguide, which supports modal propagation, the mode arrivals exhibit dispersion when received at a hydrophone at sufficient ranges. Observations and theory for dispersion in shallow water waveguide have been reported in the 1940's by Pekeris, Ewing, Worzel, and Hersey [3]. Mesoscale ocean acoustic tomography using explosives was later proposed by Tolstoy, Diachok, and Frazer [4]. Group speed dispersion based inversion for compressional wave speeds was attempted by Rajan *et al.* [5] using a linear perturbation approach. This approach will yield accurate solutions provided the starting model is close enough to the final solution.

1.1 Overview of the long range sediment tomography technique

The long range sediment tomography technique, as in the perturbation approach of Rajan *et al.*, also uses the dispersion characteristics of the broadband acoustic signal to estimate the sediment properties. The experimental setup typically adopted for the technique is illustrated in Figure 1. An explosive charge set to explode at some depth provides the broad band acoustic energy for the technique. The technique has been found successful in shallow waters with water depths approximately 100 m.

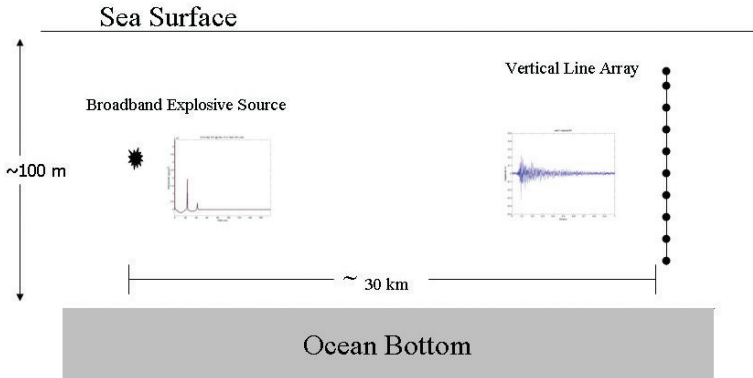


Figure 1. Experimental scenario for long range sediment tomography. The dispersed modal arrivals at the receiver array are used to infer the properties of the sediments.

The acoustic signal is received at ranges of the order of 30 to 40 km on an array of hydrophones. Even though an array of hydrophones is typically used the technique works well with a single hydrophone. The arrival times corresponding to various modes can be identified from signals received at a single hydrophone. The acoustic signal received at a hydrophone is analyzed by a wavelet based approach (time-frequency analysis) to identify the individual mode arrivals. Depending on the signal to noise ratio we have been able to identify modes one to nine. The mode arrival times as a function of frequency forms the input data for the inversion scheme.

The quality of the data (input to the inversion) depends on the signal to noise ratio, quality of the time-frequency processing (time-frequency resolution) and the separation between the individual arrivals. The factors affecting these include the weight and depth of explosion of an individual charge, the source-receiver separation, properties of the sediment (compressional wave speed and attenuation) in addition to bathymetry, properties of the water column and other small scale effects. The ideal situation is in which we can observe many modes (especially higher order modes), the arrivals are well separated from one another and the peaks corresponding to each arrival are sharp and easily identifiable. Higher charge weights provide better signal to noise ratios but the charge weight is often restricted due to availability and concern of potential environmental impacts. The range should be such that there is enough signal strength at the receiver and at the same time the modes have traveled enough distance providing adequate separation. Time-frequency analysis is often an iterative process, adjusting the wavelet parameters to achieve the best time-frequency resolution.

The factors mentioned above can be easily incorporated in our experimental planning as they are known *a priori* most of the times. The unknown factor in the experimental design is the properties of the sediment itself (which we are inverting for). The compressional and shear wave speeds and attenuation of the sediment, its spatial (horizontal and vertical) variability have significant impact

Table 1. Sediment types and compressional wave speeds (from Hamilton [6]).

Sediment Type	Compressional wave speed (m/s)
Fine sand	1750
Silty sand	1645
Sand-silt-clay	1579

on the quality of the data and hence in the success of the technique. The remainder of this paper will explore this in light our experience in two experiments conducted in two regions with drastically different sediment characteristics. Modeled dispersion in different sediment types is described in Section 2. Section 3 compares the two experimental locations and the dispersion characteristics. Section 4 summarizes the sediment data at these locations and Section 5 discusses the effects of the sediment properties on the dispersion behavior. Section 7 concludes the discussion.

2 Dispersion characteristics for various sediment types

To investigate the effect of sediment compressional wave speed on the dispersion characteristics several scenarios with different sediment types were considered. Two types of layering (sediment over basement and two layers of sediment over a basement) and three sediment types (fine sand, silty sand and sand-silt-clay) were considered as described in Figure 2 and Table 1. The compressional wave speeds for these sediment types (Table 1) were approximated using Hamilton's values for continental terrace sediments [6]. The sediment layering models (Figure 2) represent two of the most appropriate sediment representations for the field experiment locations considered (PRIMER and East China Sea).

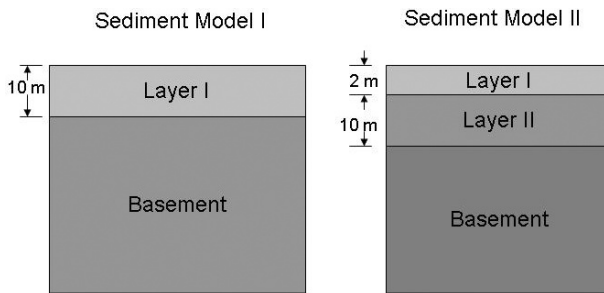


Figure 2. Sediment description for the sensitivity study. Two types of sediment descriptions are shown in the left and right panels. The right panel has a thin (2 m) sediment layer over Model I.

Figure 3 compares the arrival time pattern for two different types of sediment layers over a basement layer of coarse sand. The two sediment types produce different arrival time patterns which have strong implications in the quality of the resulting data. The fine sand sediment layer produces a well spread out arrival structure (left panel in Figure 3) compared to a compressed arrival structure produced by silty sand (right panel in Figure 3). Low frequency energy corresponding to mode 7 arrives at 2.5 s for fine sand whereas it arrives at 2.0 s in the case of silty sand. From a signal processing point of view an arrival structure shown in the left panel of Figure 3 is more desirable compared to the one in the right panel where the arrivals are closer and hence difficult to separate

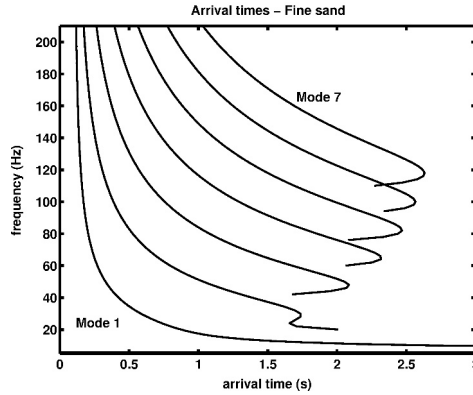


Figure 3. Arrival time dispersion at 30 km for two different sediment types (Sediment Model I). The left panel shows the arrival times corresponding to a 10 m thick layer of fine sand over coarse sand. The right panel shows the arrival times when the surface layer is changed to silty sand. Arrival times corresponding to modes 1 to 7 are shown in both the figures.

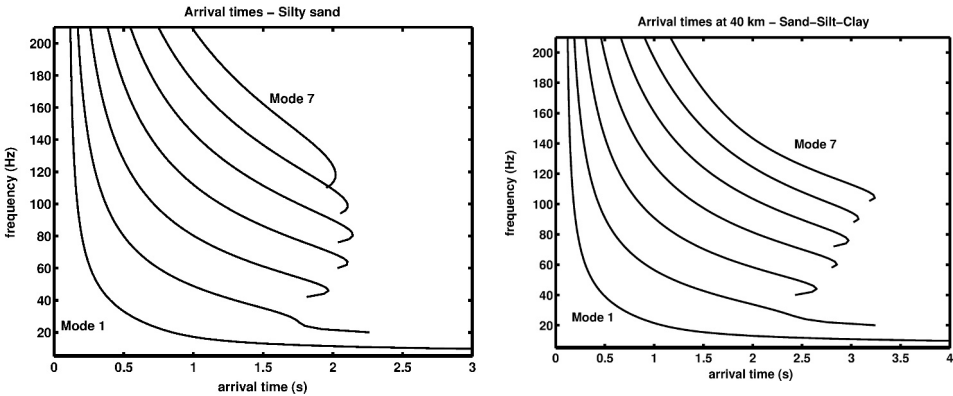


Figure 4. Arrival times corresponding to a 10 m layer of sand-silt-clay over coarse sand. Modes 1 to 7 arrivals are shown. Effect of reducing the range from 40 km (left panel) to 30 km (right panel) is also highlighted in the figure (layer I in the left panel of Figure 2).

out and pick. This is especially significant considering the variable time-frequency resolution of a wavelet time-frequency analysis. A low speed sediment layer such as sand-silt-clay results in a desirable spread out arrival structure as in the case of the high speed fine sand layer (Figure 4). Figure 4 also shows the effect of range on the arrival time pattern. A larger range is desirable if adequate signal to noise ratio can be achieved.

The sediment distribution (depth-wise) modeled by Sediment Model II generates some interesting scenarios. Now there are two different sediment layers over a coarse sand basement layer (Sediment Model II). Two cases are considered for the two layer sediment over basement model: a high speed sediment in layer I and a low speed sediment in layer II (left panel in Figure 5) and vice versa (right panel in Figure 5). The arrival structure shown in the left panel corresponding to a thin layer (2 m) of fine sand over sand-silt-clay represents a very difficult scenario for time-frequency processing. The arrivals are very close together and hence very difficult to separate. On the other hand the reverse scenario (sand-silt-clay over fine sand) is not very much different from the case where only the fine sand layer was present over the basement. Even though it is hard to generalize the arrival structure based on sediment types based on the few examples studied here, it can be stated

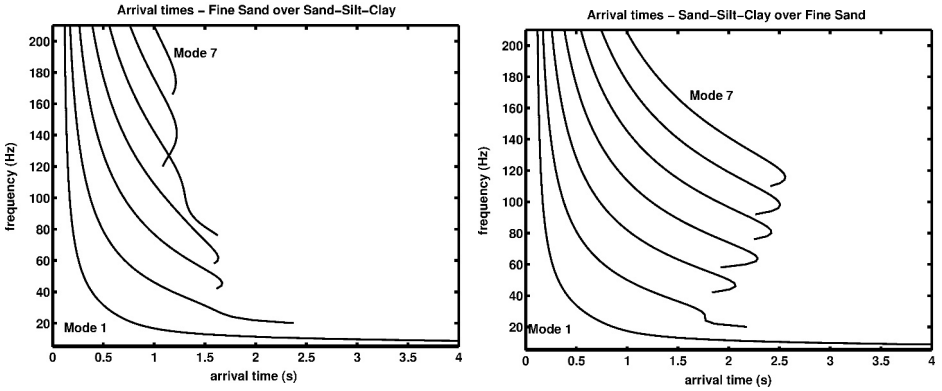


Figure 5. Modal arrivals corresponding to sediment model II (Figure 2). The sediment types in layer I and II are fine sand over sand-silt-clay (left panel) and sand-silt-clay over fine sand (right panel).

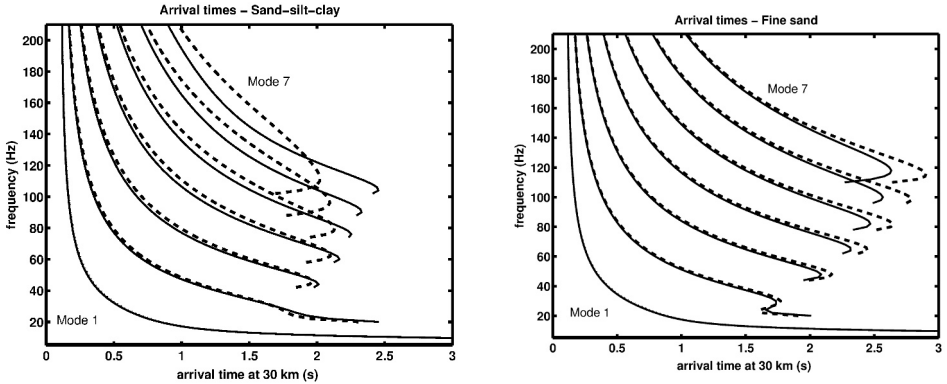


Figure 6. Modal arrival perturbations due to changes in surface sediment compressional wave speeds. The left panel shows the changes in arrival times due to a 50 m/s increase in compressional wave speed in the sand-silt-clay layer whereas the right panel shows the changes when the top layer is fine sand.

that the sediment layering and types plays an important role in the quality of the data and hence the success of the inversion scheme.

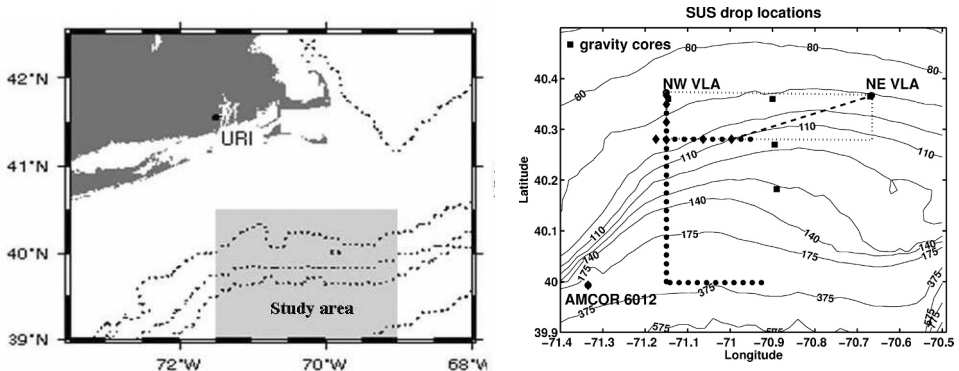
Finally sensitivity of arrival times (for Sediment Model II) to changes in compressional wave speeds is considered in Figure 6. As can be seen in the left panel of Figure 6, the low speed sediment (sand-silt-clay) seems to be more sensitive to an increase of 50 m/s from a baseline value, compared to a high speed sediment (fine sand) shown in the right panel. Since the changes were confined to the top layer (layer I in Figure 2) only higher modes seem to be affected. Overall, we see that the sediment types and their distribution in depth seem to have profound impact on the arrival time pattern and sensitivity of different modes. It can also be seen that the higher order modes are more sensitive to the subtle changes in sediment model structure compared to lower modes. Two different regions where we conducted sediment tomography will now be discussed in the next section.

3 Sediment tomography in New England Bight and East China Sea

The sediment tomography experiments conducted in New England Bight as part of the PRIMER field study in 1996 and in the East China Sea as part of the Asian Seas International Acoustic Experiment (ASIAEX) will be briefly outlined first. The key dispersion characteristics observed in these two experimental data will also be discussed based on the available sediment descriptions at these sites in the form of core data, geophysical surveys, historic data and inversions. The two experimental locations offers two different sediment distributions in approximately similar water depths. The dispersion patterns discussed here were taken from the two sites approximately equal (30 km) source-receiver range. The selected signals were from regions with mildly varying bathymetry.

3.1 Shelf Break PRIMER Experiment in the New England Bight

The long range sediment tomography technique was first applied to data collected during the Shelf Break Primer Experiment (PRIMER). The location of this experiment is shown in Figure 7. The right panel in Figure 7 shows the locations where SUS charges weighing 0.8 kg were dropped. These charges were dropped from an airplane and were set to explode at 18 m depth of water. Data were collected at two Vertical Line Arrays (VLA) in the North-East and North-West corners of the experimental area (Figure 7). The locations of the five gravity cores taken as part of the experimental program (3 cores in line with the VLAs and two others at water depths 120 m and 130 m respectively) and an Atlantic Margin Coring Project deep core (AMOCR-6012) are also shown in the right panel of Figure 7. The compressional wave speeds from these cores will be later used to characterize the sediments in Section 4.1.



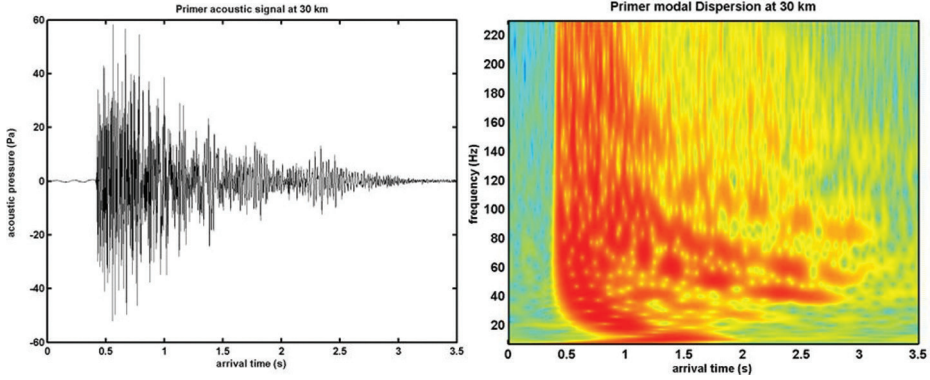


Figure 8. Acoustic signal received at 30 km during the PRIMER experiment and its time-frequency display.

3.2 Asian Seas International Acoustic Experiment (ASIAEX) in the East China Sea (ECS)

The second location where we applied the long range sediment tomography technique was the East China Sea as part of the ASIAEX experiment. The location of the experiment is shown in Figure 9.

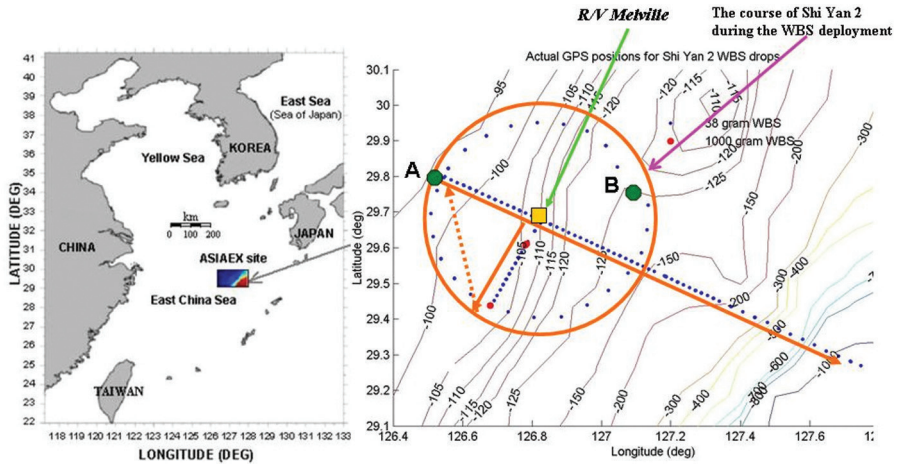


Figure 9. The location of the ASIAEX experiment in the East China Sea (Left panel). The right panel shows the bathymetry and locations of the Wide Band Source deployments.

The right panel in Figure 9 shows the locations where the Wide Band Sources (WBS) were deployed. The WBS were 0.36 g in weight and were set to explode at 50 m of depth in water.

Over 200 Wide Band Sources (WBS) were deployed from the Chinese R/V Shiyan-2 during the experiment. The geometry of the explosive source deployment is shown in the right panel of Figure 9. The acoustic signals from the shots were collected on a Vertical Line Array which was deployed from a US R/V Melville near the center of the circle shown in Figure 9.

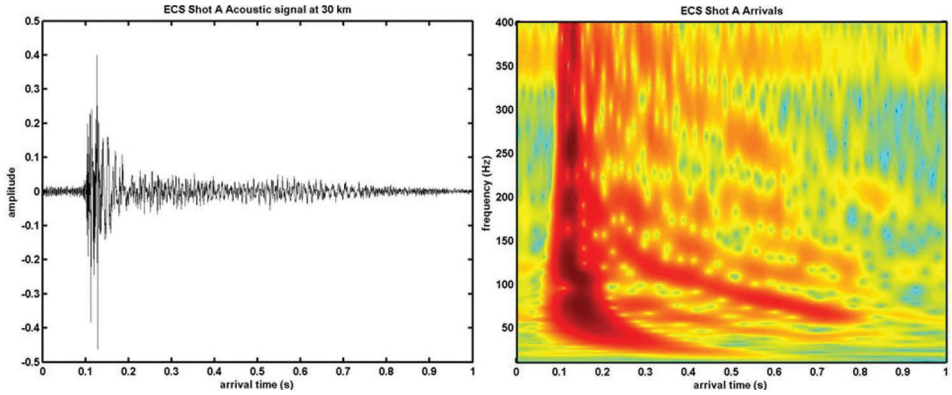


Figure 10. Acoustic signal and its time-frequency representation for one of the WBS deployed during the ASIAEX experiment. The signal shown here corresponds to shot A (Figure 9) on the North-West side of the circle of shot deployments received at 30 km.

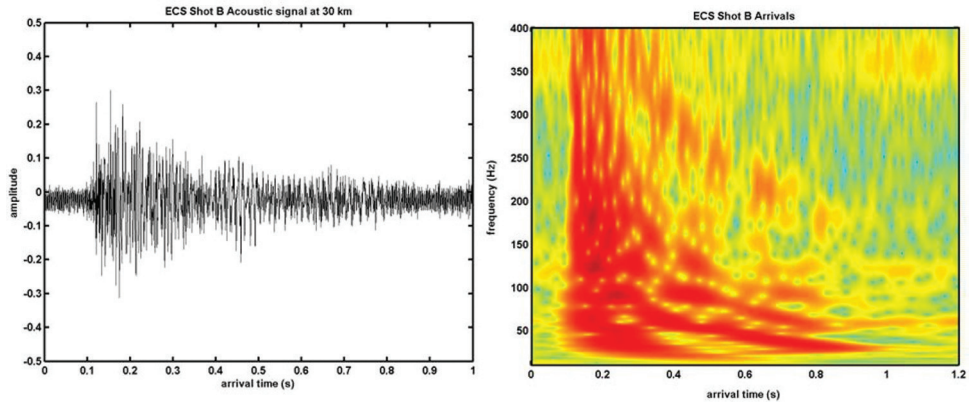


Figure 11. Acoustic signal and its time-frequency representation for one of the WBS deployed during the ASIAEX experiment. The signal shown here corresponds to shot B (Figure 9) on the North-East side of the circle of shot deployments received at 30 km.

4 Sediment description at the experimental locations

The sediments at the two experimental locations now will be characterized based on available core data, geophysical surveys, historic data and inversions. The inversions were carried out based on the sediment tomography technique. The sediment tomography technique estimates compressional wave speeds at different depths in the sediment by matching the dispersion produced by the environment with the dispersion data. The modal arrival time predictions calculated using a normal modal model is matched to the measured dispersion data in an iterative scheme. The iterative procedure is carried out efficiently using a hybrid scheme which is a combination of a Genetic Algorithm and Levenberg-Marquardt approach. Potty *et al.* [1] provides a detailed description of the sediment tomography approach.

4.1 Sediment Description at Primer Location

The dispersion data shown in Figure 8 is from the continental shelf part of the Primer experimental site. Various types of sediment descriptions are available in the form of inversions using these shot data, cores and sediment texture data from USGS database. The tomography inversions for the surface sediments estimate the compressional speeds values in range 1550-1650 m/s (left panel in Figure 12).

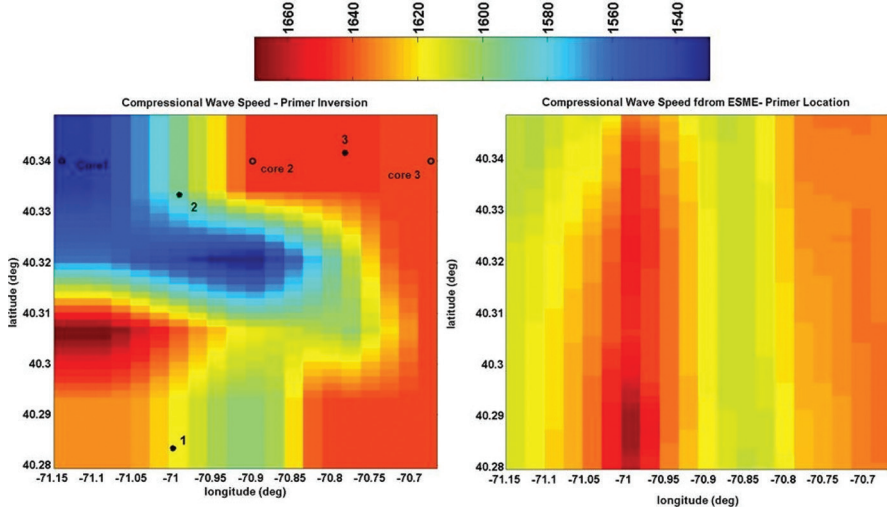


Figure 12. Surface sediment description at Primer location. Left panel shows the sediment tomography inversions [7]. The location of gravity cores (core 1, core 2 and core 3) and the USGS data (1, 2 and 3) are also shown. The right panel shows the predictions from the ESME sediment model [8].

The three data points from the USGS sediment texture database [9], which lie in the Primer experimental area, are shown in Figure 12 (left panel). The grain size provided in the database (Table 2) corresponds to silt or sandy silt at the three locations. The compressional sound speed, based on Hamilton's values, will then be in the range 1615-1652 m/s. Potty and Miller [8] have used the USGS sediment texture values and Buckingham's model [10] along with other historic data to provide a sediment model for the US East Coast as part of the Effect of Sound on Marine Environment (ESME).

The compressional speed values predicted by this ESME sediment model fall within the range of values 1600-1650 m/s. The gravity cores also show compressional wave speed values in the range 1570 m/s to 1625 m/s down to a depth of 1.25 m (left panel in Figure 13). At deeper depths the compressional speed values increase to 1700 to 1750 m/s (right panel in Figure 13). In general the surface sediment in the Primer location is sandy silt or silt with compressional wave speed in the range 1600 to 1650 m/s. At the deeper depths (greater than 5 m) the compressional wave speed increases to 1700 to 1750 m/s.

Table 2. Sediment parameters at Primer location (from USGS Sediment Texture Database [9])

Sample Number	Water Depth	Sediment Type	Grain Size ϕ	Compressional wave speed (Hamilton [6])
1	120.00	silt	5.42	1615
2	93.00	sandy silt	5.11	1652
3	97.00	silt	5.56	1615

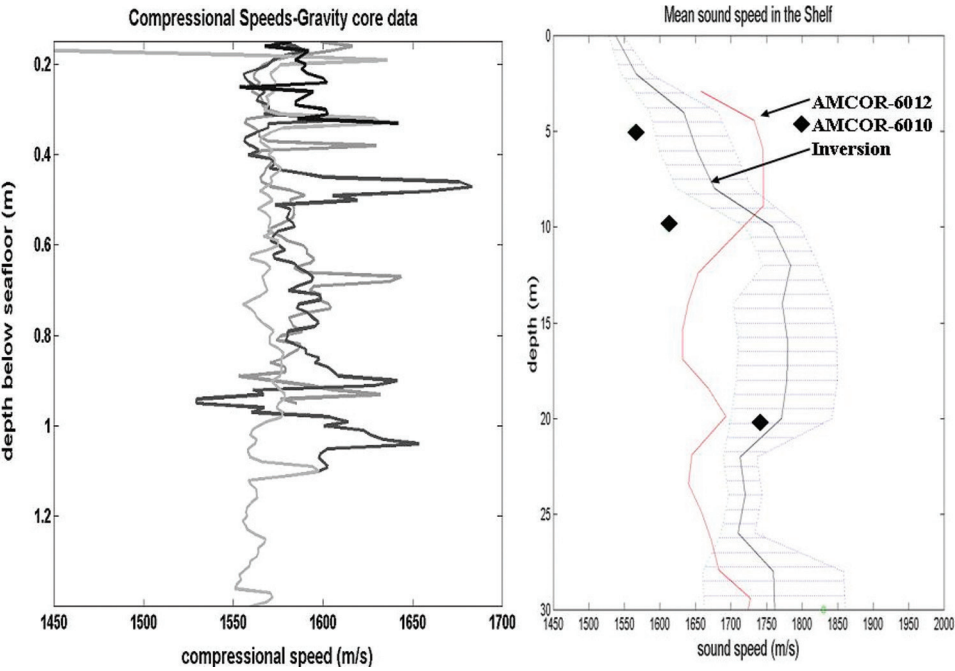


Figure 13. Surface sediment description at Primer location. Left panels show the gravity core data at 3 locations (core 1, core 2 and core 3). Right panel shows the mean sediment compressional speed from inversions and the AMCOR (6010 and 6012). The location of the AMCOR site is shown in Figure 7.

4.2 Sediment description at the East China Sea

The sediment descriptions at the East China Sea were in the form of historic data, gravity and piston cores, geophysical surveys and tomography inversions. A detailed description of the sediments at East China Sea is available in Miller *et al.* [11]. Only a brief description of the sediments is provided here. A historical data set on the sediments of the East China is given by Niino and Emery [11]. They used 45,000 echo sounder reflection amplitude notations on nautical charts to map the surficial sediments in the East China Sea and South China Sea. The ASIAEX experiment area straddles a border between mud-and-sand and sand as shown in Figure 14 with softer sediments to the west of the boundary. Gravity core analysis shows that the surface sediment layer varies in compressional wave speed from a minimum near 1600 m/s in the northwest corner of the experiment area to a maximum of 1660 m/s in the southeast corner of the experimental area. Mean grain size values from the piston cores vary from 3.7 to 5.8 ϕ , corresponding to very fine sand or clayey sand to medium silt or sand-silt-clay or sandy mud. In between these endpoints, the sediments may be coarse silt, sandy silt, or gravelly mud. This spatial distribution of sediments is consistent with the sediment

description showing two types of sediments in the area (Figure 14). The softer sediments are in the west side of the experimental area whereas the sandy sediments are in the east side of the area.

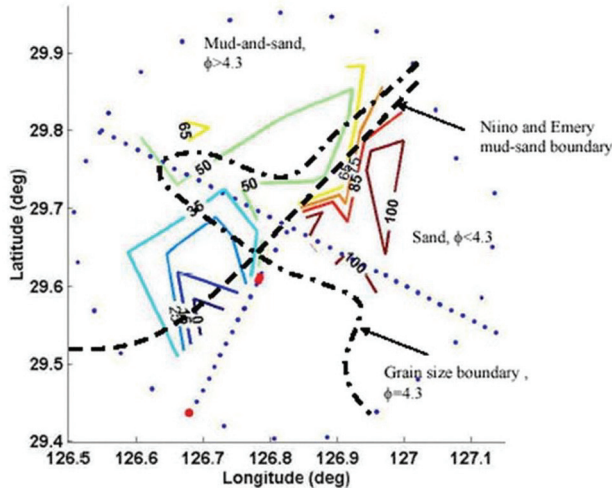


Figure 14. Summary of the East China Sea sediment information. The contour lines are the sediment compressional speeds in excess of 1600 m/s obtained from tomography inversions. The two dashed lines indicate the grain size boundary (separating ϕ less than and greater than 4.3) and the Niino and Emery boundary separating sand and mud and sand (Miller *et al.* [11]).

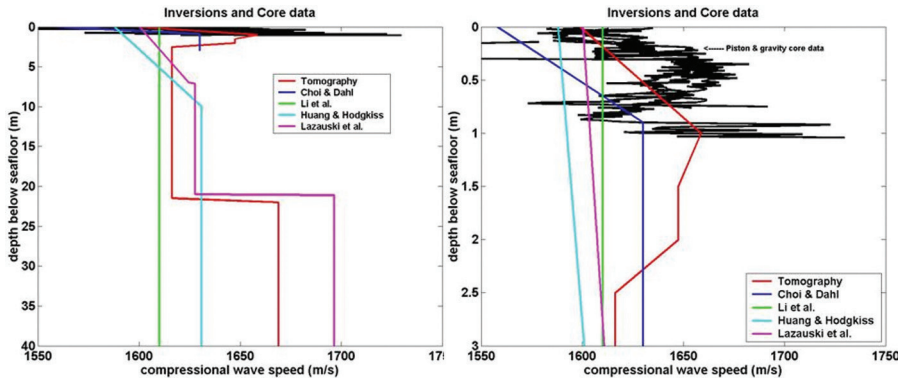


Figure 15. Sediment tomography inversions for the top 40 m (left panel) and top 3 m (right panel) of the East China Sea. Comparisons with other inversions are also provided (Miller *et al.* [11]).

A range-independent compressional-wave-speed-depth profile (marked ‘Tomography’) estimated for the top 40 meters of sediment is shown in Figure 15. We have compared data from Lazauski *et al.* [12], Li *et al.* [13], Huang and Hodgkiss [14], and Choi and Dahl [15] to the tomographic inversions (Figure 15). In addition to these data, the layering of the sediments is available from geophysical surveys (Figure 16)). The thickness of the surface layer (0-3 m) and the sub-bottom layer (3 to 10 m) is shown in Figure 16. The linear feature in the southwest portion of the circle in Figure 16 is an ancient river channel. In general the sediments in East China Sea exhibits large spatial

Table 3. Primer and East China Sea experimental parameters.

	Primer	East China Sea
Charge weight	0.82 kg	0.38 kg
Charge depth	18 m	50 m
Range	30 km	30 km
Water depth	~100 m	~100 m
Sampling frequency	1395 m/s	2048 Hz

and depth variations as shown in Figures 14 and 16. But compared to the Primer experimental location more independent direct and indirect measurements are available in the East China Sea to better characterize the sediments. The dispersion characteristics displayed by the explosive data at these two different sites will now be discussed in the context of these differences in sediment properties.

5 Dispersion and sediment characteristics at New England Bight and East China Sea

We will now attempt to explore the differences in the dispersion behaviors exhibited by the explosive sources in the Middle Atlantic Bight (Figure 8) and in the East China Sea (Figures 10 and 11). Some of the key experimental parameters between the two locations (other than the sediment types and ocean sound speed) are summarized in Table 3.

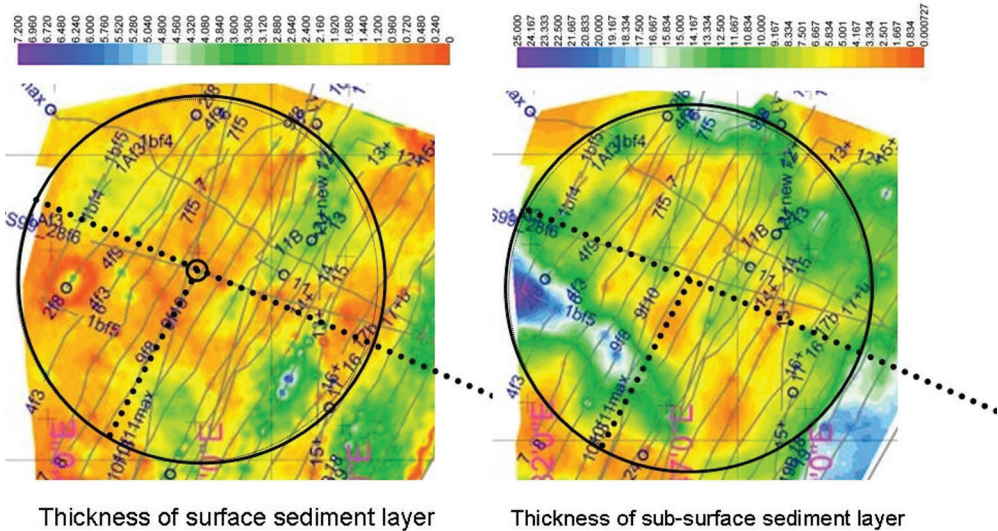


Figure 16. Sediment layer thicknesses estimated by water gun surveys. The surface layer thickness in meters is shown in the left panel whereas the sub-surface layer thickness in meters is shown in the right panel (Miller *et al.* [11]).

As seen from the table the bathymetry at both the locations are identical (nearly equal to 100 m). Variation in bathymetry was kept to a minimum in selecting the shots for the study. The source-receiver ranges at the Primer site (for the dispersion diagram in Figure 8) and at the East China Sea (Figures 9 and 10) were 30 km. This enables us to make some comparisons between the dispersion at the two sites. It should be noted here that the variability in the sound speed profile in the water column can cause changes in dispersion diagram and this is not addressed in the discussion in this

Section. The major difference in the dispersion at the two locations seems to be the arrival time spread. Arrival time spread is the difference in time between the last observable arrival and the initial water borne arrival. The spread of arrivals depends on the group speed minimum (Airy phase) and also on the attenuation of the sediments. Usually attenuation plays a major role at higher frequencies and higher modes.

A larger spread of arrivals will help the sediment tomography technique in identification of individual mode arrivals. The time-frequency resolution limitations associated with wavelet processing introduce errors in picking the peak corresponding to individual mode arrival peaks (sharp vs flat peaks). A well dispersed arrival helps to identify and pick the modes in the presence of these difficulties. On the other hand, sometimes the sediment type which produces a lower time spread is more sensitive to changes in compressional wave perturbations compared to a sediment type which produces a larger time spread. Of the two sites considered in this study the Primer data (Figure 8) shows a larger arrival time spread (2.5 s) when compared to the ECS shots shown in Figure 10 and Figure 11 (0.7s and 0.9 s). Based on the modeled dispersion shown in Figure 3 and Figure 5 this suggests that the sediment types at the Primer location may be silty sand over coarse sand (model I) or a thin layer of sand-silt-clay over fine sand (model II). A plausible approximation can also be a low speed surface layer over a high speed sub-surface layer which is supported by the sediment profiles shown in Figure 13 (right panel). This will be similar to the scenario presented in the right panel in Figure 5. Unfortunately we do not have geophysical layering information to support this argument at the Primer site.

A two layer sediment model over a basement (Sediment Model II) seems to be a reasonable approximation for ECS sediments based on the sediment layering observed by the geophysical surveys. The low values of arrival time spread at ECS indicates that the sediment to be similar to a pattern shown in the left panel of Figure 5 (fine sand over sand-silt-clay). Based on the available sediment information (Figures 14 and 15), the surface layer seems to be silty sand (compressional wave speed ~ 1650 m/s) and sub-surface layer to be sand-silt-clay (1600 m/s). At ECS the surface layer (0-3 m) consists of modern silty sediments [11]. Below this layer there is a sandy layer over silty marine sediments (3–10 m). It is possible that the subsurface layer which produces dispersion as shown in the left panel in Figure 5 is a mixture of sand, silt and possibly some clay. We do not have deep core measurements which reach the subsurface layer to verify this hypothesis about the sub-surface sediments.

The two shots on either side of the circle (A and B) also show different dispersion behavior. The major difference is in the relative strengths of mode arrivals in the two dispersion diagrams (Figure 10 and Figure 11). This may be due to the presence of sediments with higher attenuation on side A compared to the sediments in side B. Another possible reason can be changes in the source depth which then can cause different modes to be excited to different extents. We have observed this difference between the shots on two sides (near A and B) on many shots. Hence we believe that the difference can be attributed to the changes in sediment types on two sides of the circle. The sediment data (historic, cores and tomography) also indicate two different types of sediments in the region, a silty area to the west and a sandy area to the east, with the approximate location of the boundary indicated in Figure 14. The shot A lies in the western side of this boundary and hence in the silty (softer) region. Shot B, on the other hand, lies in the Eastern side in harder (sandy) type sediments. It should be noted that this spatial variation is applicable to surface sediment only as not enough information is available to extend this to sub-surface sediments.

There is also a difference in arrival time spread of the order of 0.2 s between the two shots. We also see that the dispersion corresponding to the hard sediment (Shot B) has this increased time spread of 0.2 s. This is significant as Shot B has a reduced range (28.875 km) compared to the range for Shot A (30 km). Since Shot B has a shorter range we expect the modes to arrive earlier compared to Shot B. Instead we see that the changes in the sediments cause the modes to arrive later than those for Shot A. In order to explore this effect we introduced changes in the compressional wave speed

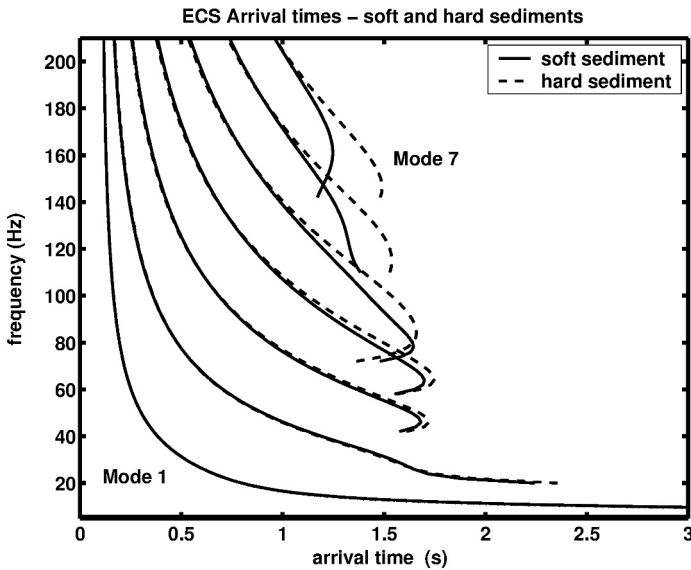


Figure 17. Two layer sediment model and the effect of variation in the surface sediment. The continuous curves show the dispersion when the surface layer is silty sand. The dashed curves show the dispersion when the compressional wave speed in the surface layer and sub-surface layer is increased by 30 m/s. The basement is coarse sand.

in the surface as well as sub-surface layer and observed the dispersion (Figure 17). Here a surface layer of fine sand over a sub-surface layer of sand-silt-clay (sediment model II) is considered. The continuous lines show the dispersion for this scenario. Since ECS data show changes in the lower modes also (mode 1 and 2) the spatial variation is not limited to the surface sediments alone. When the changes are made in the thin surface layer the higher modes are affected the most. In order to introduce changes corresponding to lower modes the sub-surface layer was also modified. The dashed lines in Figure 17 show the dispersion when the compressional wave speed of the surface and sub-surface layer is increased by 30 m/s (harder sediment). The combined (surface and sub-surface layers) change in compressional wave speed by +30 m/s introduces changes in arrival times of modes 3, 4 and 5 by 0.1 s with the arrivals corresponding to the harder sediment coming in later than softer sediments. Still mode 1 and mode 2 are not affected much and they be affected mostly by the changes in compressional wave speed in the basement.

6 Sediment type considerations in experimental design

Some sediment profiles can produce closer modal arrivals (left panel in Figure 5) which are less desirable from the time-frequency analysis point of view. Adequate modal separation in this case can be achieved at longer ranges which often require a bigger charge in order to maintain good signal to noise ratio. But the use of bigger charges is often restricted in a field experiment. Based on the limited cases considered in this study some of these factors can be taken into consideration while designing the sediment tomography experiment. It should be noted that the effect of sediment can be taken into account only if some of the sediment properties are known a priori (which is not always true).

Sediment properties corresponding to various sediment types and their spatial and depth-wise distribution are important. Surface sediment is important as it affects the higher order modes which

attenuate fast. This will then have an effect in the charge weight-range trade off. For example in Primer like sediments we can get good dispersion at longer ranges even with a smaller charge weight. But for a sediment model which produces dispersion behavior as shown in Figure 5 a smaller charge weight will significantly erode the signal to noise ratio at longer ranges.

The depth of the explosion also can play a key role in exciting some modes while suppressing others. In a region consisting of sediments which present unfavorable propagation conditions for higher order modes care should be taken to place the source at depth which will excite the higher order modes. If a vertical line array is not available then this argument holds for the receiver also. Also some amount of a priori information will help to deploy the sources spatially in an efficient manner to capture this variation in the sediment tomography.

7 Conclusion

The spatial and depth variability in sediments at two regions Middle Atlantic Bight and East China Sea- are explored. The effects of this variability on the dispersion behavior of broad band acoustic signals are also explained with the help of theoretical predictions. The effect of these variations in sediment types on the design of the long range tomography technique is summarized. The amount of information that can be extracted from the dispersion diagrams even without sophisticated inversions can be significant. The type and distribution of sediments in a region have considerable influence on the success of sediment tomography.

Acknowledgements

This work was supported by the United States Office of Naval Research (ONR), Code 321 OA. Authors would like to thank the participants of the Primer and ASIAEX field experiments.

References

1. Potty G., Miller J., Lynch J. and Smith K., Tomographic Inversion for sediment parameters in shallow water. *J. Acoust. Soc. Am.* **108**(3), 973–986 (2000).
2. Munk W. H. and Wunsch C., Ocean acoustic tomography: a scheme for large scale monitoring. *Deep Sea Res.* **26**(A), 123–161 (1979).
3. Pekeris C. L., Theory of propagation of explosive sound in shallow water. *Geol. Soc. Am. Mem.* 27 (1948).
4. Tolstoy A., Diachok O. and Frazer L. N., Acoustic tomography via matched field processing. *J. Acoust. Soc. Am.* **89**, 1119–1127 (1991).
5. Rajan S. D., Lynch J. F. and Frisk G. V., Perturbative inversion methods for obtaining bottom geoacoustic parameters in shallow water. *J. Acoust. Soc. Am.* **82**(3), 998–1017 (1987).
6. Hamilton E. L., Geoacoustic modeling of seafloor. *J. Acoust. Soc. Am.* **68**(5), 1119 (1980).
7. Potty G. and James Miller J., Tomographic Mapping of Sediments in Shallow Water. *IEEE J. Oceanic. Eng.* **28**(2), 186–191 (2003).
8. Potty G. and Miller J., Sediment specification in ESME. *IEEE J. Oceanic. Eng.* (submitted).
9. Paskevich V. and Poppe L. J., USGSECSTDB: USGS East Coast Sediment Texture Database: U. S. Geological Survey, Coastal and Marine Geology Program, Woods Hole Field Center, Woods Hole, MA. <http://pubs.usgs.gov/of/2003/of03-001/data/seddata/usgsecstdb/usgsecstdb.htm> (2003).
10. Buckingham. M. J., Theory of compressional and shear waves in fluid like marine sediments. *J. Acoust. Soc. Am.* **103**(1), (1998).
11. Miller J. H., Bartek L., Potty G. R., Tang D. J., Na J. and Qi Y., Sediments in the East China Sea. *IEEE J. Oceanic. Eng.* **29**(4), 940–951 (2004).

12. Lazauski C. J., Miller J. H. and Potty G., The use of Airy phase measurements for geoacoustic inversion: ASIAEX East China Sea Experiment. *IEEE J. Oceanic. Eng.* (under revision).
13. Li Z., Zhang R., Yan J., Li F. and Liu J., Geoacoustic inversion by match field processing combined with the vertical reflection coefficients and transmission loss. *IEEE J. Oceanic Eng.* **29**(4), 973–979 (2004).
14. Huang C.-F. and Hodgkiss W., Matched field geoacoustic inversion of low frequency source tow data from the ASIAEX East China Sea Experiment. *IEEE J. Oceanic Eng.* **29**(4), 952–963 (2004).
15. Choi J. and Dahl P., Mid to high frequency bottom loss in the East China Sea. *IEEE J. Oceanic. Eng.* **29**(4), 980–987 (2004).

CHARACTERIZATION OF LOCAL SEABED PROPERTIES USING SYNTHESIZED HORIZONTAL ARRAY DATA

PETER L. NIELSEN, MARK FALLAT AND CHRISTOPHER HARRISON

*NATO Undersea Research Centre,
Viale S. Bartolomeo 400, 19138
La Spezia, Italy*

In April 2002 NATO Undersea Research Centre conducted the BOUNDARY 2002 experiment on the Malta Plateau, Mediterranean Sea, with the aim of collecting high-quality environmental and acoustic data. A part of these data were directly intended for geoacoustic inversion characterizing the bottom properties by acoustic measurements. The acoustic data were collected by using towed sources covering a frequency band 180–7000 Hz and received on a bottom-moored vertical array. The sources were towed about 1 km on both sides of the array and passing the shallowest hydrophone at a range of 21 m. The transmission rate was every 3 s resulting in high spatial sampling of the acoustic field. The high repetition rate of the transmissions provides the possibility of building a 1-km synthetic horizontal array with a virtual hydrophone spacing of around 5.9 m. The principle of reciprocity, i.e., interchanging the source and receiver positions, is applied to build the synthetic horizontal array. The acoustic data collected from this synthetic horizontal array are used to characterize the bottom properties locally by matched-field geoacoustic inversion. The results from the inversion are compared with independent “ground truth” data collected at the experimental site.

1 Introduction

Sound propagation in shallow-water regions is often strongly dependent on the seabed properties. Prediction of sound propagation in these shallow-water areas requires a detailed description of the bottom used as input to numerical models. However, the bottom properties (sound speed, density, attenuation, layering structure) are probably the most difficult to obtain compared to other environmental parameters (water depth, water-column sound speed) considering wide-area and depth coverage. Although bottom databases are available it has been shown that the database information can produce wrong prediction performance, where 10s of dB difference in predicted and measured transmission loss (TL) can appear for source-receiver separations out to 50 km [1].

Model-based matched-field processing geoacoustic inversion (MFP) has been demonstrated successfully on acoustic data during the past decade [2]–[8]. In MFP inversion computer simulations of the acoustic propagation are compared to the measured data, and the geometry (source-receiver depth and range, water depth) and bottom properties are continuously altered until the best match between model output and data is obtained. The environment that results in the best match between

model and data is denoted as the “true” environment. Often the propagation modeling during the inversion is obtained by assuming range-independent environments although the real environment is range dependent. However, range-dependent modeling is far too computational intensive when thousands of forward model runs are required in the search for the “true” environment. The search for the bottom parameters is normally performed by applying a global search algorithm. The MFP appears to be an attractive approach as acoustic propagation measurements are used for extracting bottom properties to be used for acoustic propagation predictions.

The majority of the MFP inversion research has been focused on using moored vertical line arrays (VLA) with several hydrophones to measure the acoustic field across the water column [2]–[4]. Signals are typically transmitted from a moored or towed source and the acoustic field is measured several kilometers down-range. Geoacoustic inversion of this type of relatively long-range propagating acoustic fields results in range-averaged bottom properties between source and receiver. In cases of range-dependent environments the geometric and bottom properties found by the inversion are effective parameters. These effective parameters do not necessarily represent the optimum bottom properties if the source and receiver are relocated slightly from the position used for the inversion. This will degrade the prediction and a new inversion of the long-range acoustic data is required to find a new set of optimum effective parameters corresponding to the relocated source and receiver.

Towed source and horizontal line arrays (HLA) have been shown feasible to use in MFP [5]–[8]. In this configuration the distance between source and receiver is typically a few 100 m. Geoacoustic inversion of the field received directly on the HLA at this short range provides local bottom properties. The advantage of the short source-receiver separation is a minimized impact of range-dependent environmental properties on acoustic propagation and, therefore, eliminating the requirement of range-dependent modeling in the inversion for the bottom properties. Further, a towed system that transmits signals regularly provides data for geoacoustic inversion in range-dependent environments. Each range-independent geoacoustic inversion of a single transmission represents an environmental sector in a range-dependent environment. As the towed acoustic system is moving along a predefined track a range-dependent environmental description can be achieved by merging multiple range-independent sectors. A similar local technique has been demonstrated by measuring the wide-angle reflection coefficient [9]. Here a bottom moored VLA is used to receive acoustic signals from a towed source passing close to the VLA. The wide-angle reflection coefficient ($\sim 10^\circ$ – 90° grazing angle) is derived by a time-frequency analysis of the reflected arrivals from the bottom layering structure. These arrivals contain information about the geoacoustic properties of the layering structure described through the frequency and grazing angle dependent reflection coefficient. A unique descriptor of the bottom properties is achievable by calculating the plane wave reflection coefficient [10]. The wide-angle reflection technique is also applicable for range-dependent environments if the position of the VLA is changed or by using launched sono-buoys. The 2 measuring techniques mentioned above are applicable for large-area coverage of geoacoustic characterization.

In April 2002 NATO Undersea Research Centre conducted the BOUNDARY 2002 experiment on the Malta Plateau in the Strait of Sicily, Mediterranean Sea [11]. The main objective of this experiment was to assess different acoustic measuring techniques for characterizing the shallow-water environment, with emphasis on geoacoustic and scattering/reverberation properties of the seabed. This paper describes one of the experimental set-ups where a 4-element bottom moored VLA was used to acquire acoustic signals transmitted from a towed source. The experimental geometry was similar to the wide-angle reflection measurements [9] with R/V *Alliance* towing a broadband source along a straight track passing closely to the VLA. The transmission rate of the signals was high enough to simulate a long horizontal array and a fixed sound source by applying the principle of reciprocity [12]. MFP is applied to these synthetic horizontal array data to characterize the local bottom properties.

2 The BOUNDARY 2002 experiment

The experimental area for the BOUNDARY 2002 (Fig. 1) is well-known from independent sea trials conducted in the same area. Extensive environmental (water sound speed profiles, seismic surveys, cores etc.), and acoustic data have been collected in the Strait of Sicily in different times of year. These data offer significant pre-knowledge of the environment. Various acoustic measurements were performed on the sites to extract geoacoustic properties at these locations. One of the sites (Site 13 in Fig. 1) is considered here for geoacoustic characterization of the bottom.

On April 6, 2002, a 4-element VLA was bottom moored at Site 13 with a hydrophone spacing of 10 m and the deepest hydrophone 10 m above the seabed. The water depth at the mooring position was ~ 145 m. An acoustic track was defined parallel to the bathymetry contour in direction North-South, and the total track length was approximately 2 km with R/V *Alliance* passing the VLA as close as possible. R/V *Alliance* deployed a seismic source and towed the source along the acoustic track providing seismic profiles (Fig. 2) and data for wide-angle reflection loss measurements [9].

The seismic profile acquired along the acoustic track is shown in Fig. 2. The profiles indicates at least 2 strong reflecting interfaces at a depth of ~ 15 m and ~ 30 m from the water-sediment interface. This stratification persists along the acoustic track and only very weak range-dependence is observed. The reflection of the 3 identified interfaces is rather diffuse and extends about 5 m in depth. It is unknown at present if thin reflecting layers exist within this diffuse reflection.

After the seismic and bottom loss measurements R/V *Alliance* deployed a tow-body with 3 acoustic transducers: 2 flextensional and a free-flooded ring transducer. The 2 flextensional transducers covered a frequency band from 180-850 Hz and 800-1500 Hz, respectively. The free-flooded ring was used in the band 2600-7000 Hz. The transducers were driven sequentially by transmitting 100-ms Linear-Frequency-Modulated (LFM) signals from each transducer. The separation between the signals was 500 ms, and the transmission sequence was repeated every 3 s. The received signals on the VLA were continuously transferred via telemetry to R/V *Alliance* for 54 s. The acquisition system was reset for 6 s and a new 54-s data stream from the VLA was initiated.

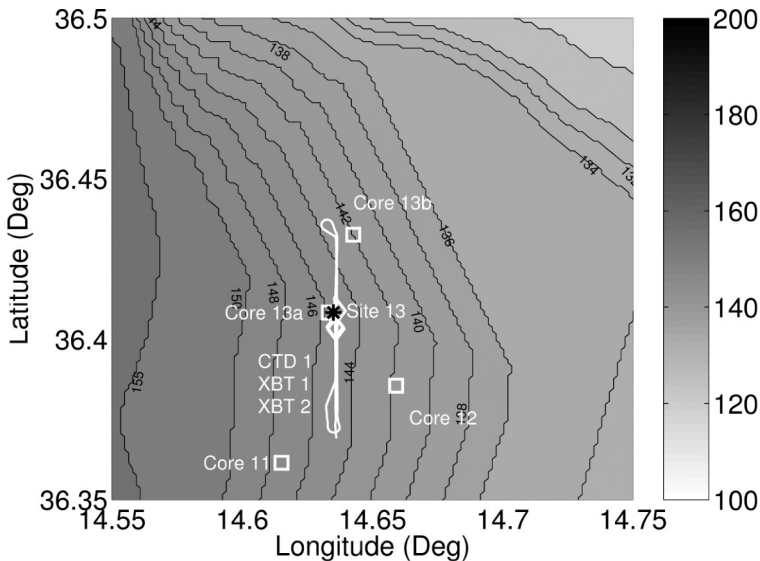


Figure 1. Experimental area and specific track visited during the BOUNDARY 2002 experiments.

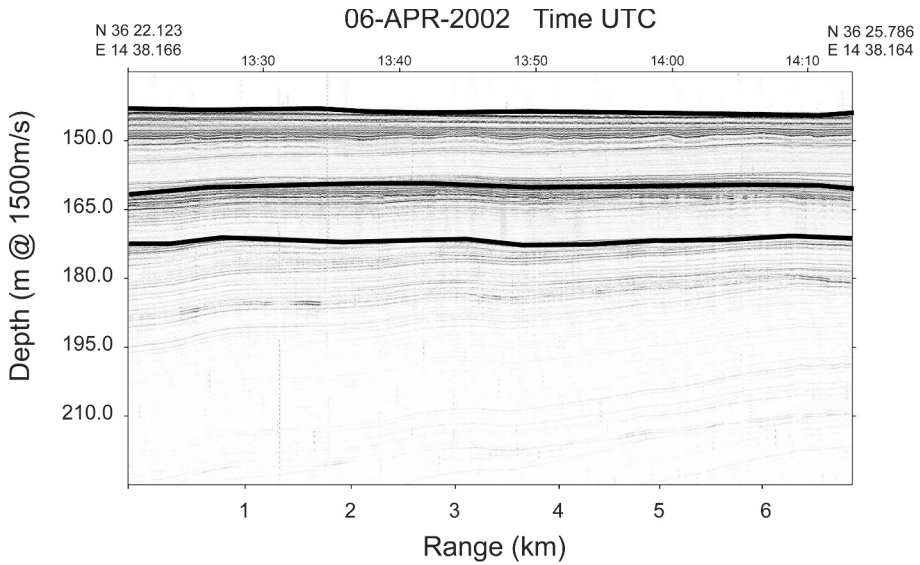


Figure 2. Seismic profile along the acoustic propagation track indicating the stratification of the bottom. The 3 main reflectors are highlighted by the solid black lines.

The acquisition sequence provided 18 signals from each frequency band every minute separated equidistantly in time and space assuming a constant ship speed. The ship speed was around 1.95 m/s in average along the acoustic track leaving 5.9 m change in range to the VLA between the transmissions of the same type of LFM sweep. The depth of the tow-body was nominally 60 m and is expected to vary only within a couple of meters based on observations from previous experiments using the same tow-body with a depth sensor. Therefore, the synthetic horizontal array is not completely straight which may affect the characterization of the bottom properties slightly as the inversion method applied does not allow for source-depth variations along the acoustic track.

The measured environmental properties for these sites were characterized by sound-speed in the water column and cores of the seabed analyzed for sound speed and density as a function of depth. The water column sound speed, sediment sound speed and density for Site 13 are shown in Fig. 3. The 3 sound-speed profiles in the water column were measured during the 3-h acoustic experiment and only weak variations in the sound speed are observed [Fig. 3(a)]. The variation in depth is also weak with only 2 m/s change in the sound speed from the sea surface to the bottom. However, the water column is clearly divided into a low-speed region in the upper 60 m and a high-speed region at deeper depths. The sound source was towed at a depth close to the transition between these regions.

The cores provide sound speed and density measurements to a maximum depth of 1 m [Fig. 3(b) and (c)] in the region around the experimental site (Fig. 1). These core measurements are only considered as an indication of the bottom type rather than ground truth information. Core 13a was acquired during the BOUNDARY 2002 experiment [11] while cores 11, 12 and 13b were collected during an independent experiment [13]. The sediment sound speed is close to the water sound speed at the water-sediment interface. The sound speed increases down to a depth of 0.5 m from the water-sediment interface and is hereafter almost constant. The density follows the same trend although the density of the sediment at the water-sediment interface is higher than in water. The variability in sound speed and density measurements is around 100 m/s and 0.4 g/cm^3 which defines the expected range of variability and accuracy of the bottom properties that can be determined by geoacoustic inversion of the acoustic data. The core data indicate that the upper bottom layer in this region can be classified as a silt-like sediment [12].

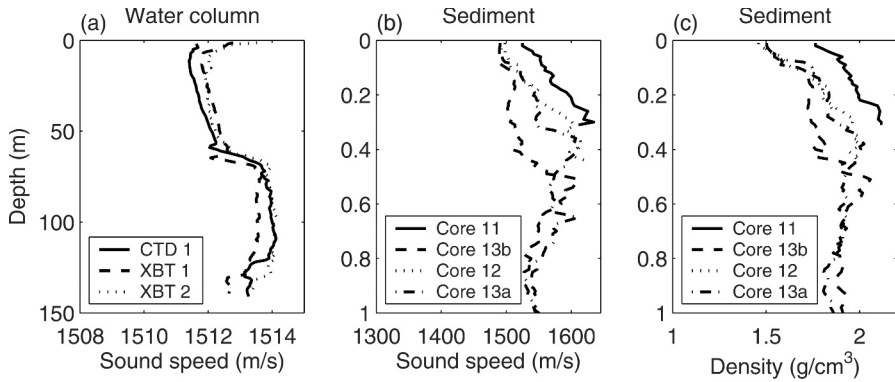


Figure 3. Acquired environmental data (a) water sound-speed profiles from CTD and XBT, (b) sediment sound speed from cores and (c) density profiles from cores.

The acoustic data used for geoacoustic inversion are limited here to the low-frequency sweep between 180–850 Hz. These acoustic data were deconvolved with an estimate of the source signature to obtain the band-limited impulse response of the shallow-water environment. This calibration provides: (1) the necessary phase information across frequency to be used in the geoacoustic inversion, and (2) acoustic pressure received at the array in μPa re $1\mu\text{Pa}$ @ 1 m from the source for model-data comparisons. The estimate of the source signature is achieved by using the received signal at the closest position between source and upper receiver of the array. The minimum range between source and receiver is determined to be 21 m by the arrival time of the signal.

The sea-surface reflected arrival at this position appears 113 ms after the direct arrival. The source signature with sea-surface reflection can introduce false precursors in matched-filtering or in estimating the transfer function of the underwater environment. The influence of the sea-surface reflected arrival on the source signature is eliminated by deconvolving the measured source signature with a synthetically generated LFM to obtain an estimated band-limited impulse. This impulse is time gated to exclude the sea surface arrival and then the remaining signal is convolved with the synthetic LFM. The source signature and spectrum with and without the sea surface reflected path is shown in Fig. 4. Ideally, the source spectrum should be constant *versus* frequency as the signal does not interact with any boundaries prior to the arrival at the closest hydrophone. Boundary interaction would introduce constructive and destructive interference in the received signal similar to that shown in Fig. 4. However, the interference-like behavior of the measured spectrum is expressed by nulls at 300, 350 and 400 Hz, and these nulls may be due to the mechanical structure of the tow-body and the 3 sources.

The received acoustic signals on the VLA were deconvolved with the measured source spectrum to obtain calibrated data consistent with numerical prediction models. The envelope of the matched-filtered signal in the band 180–850 Hz is shown in Fig. 5 as the source is moving toward (negative range), passing and moving away from the VLA (positive range). The first arrival is from the direct path followed by a bottom and the sea-surface path. The later arrivals have multiple sea-surface and bottom interactions. The vertical white lines indicate the positions along the track where the acquisition system was reset and, therefore, no acoustic data was recorded at these ranges.

The calibrated acoustic data are shown in Fig. 6 as a function of range and frequency using the measured source spectrum shown in Fig. 4. A striation pattern is observed in the data similar to the interference pattern seen on towed source-array data. Note also the excellent symmetry in amplitude of the acoustic field as R/V *Alliance* passes the VLA. The horizontal white lines indicate the ranges

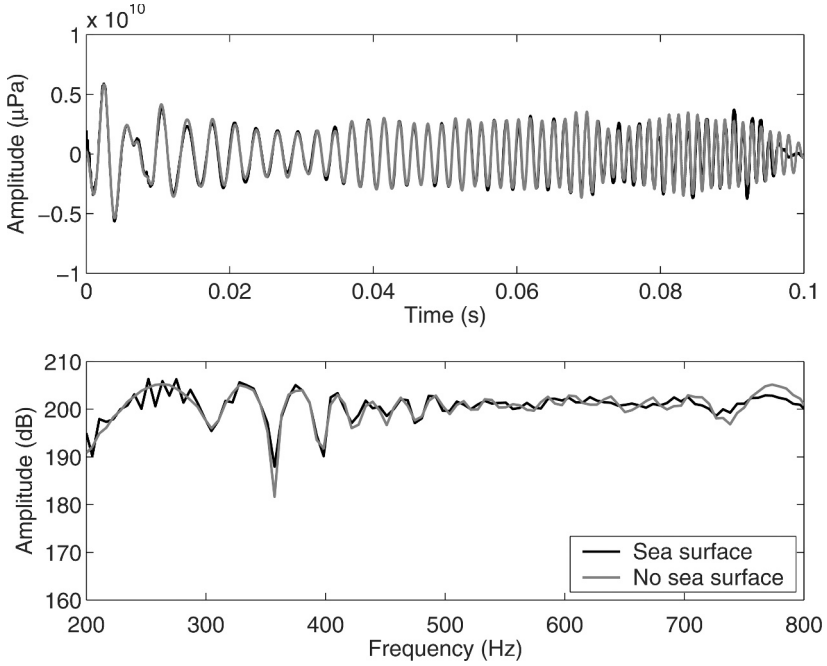


Figure 4. Source signature and spectrum with and without the sea-surface reflected path. The source signature without the sea-surface reflected path is used to calibrate the received signals on the moored VLA.

where the acquisition system was reset. The data shown in Fig. 6 are used in MFP to determine the bottom properties assuming a fixed source and a horizontal array. This is obtained in the inversion by applying reciprocity where source and receiver locations are interchanged.

3 Geoacoustic inversion results

The MFP inversion of the acoustic data is performed by a simultaneous global search over geometry and bottom properties for the best match between modeled and measured acoustic complex fields. The global search algorithm is the Adaptive Simplex simulated annealing (ASSA) [14], [15] which is an efficient version of the traditional simulated annealing. The ASSA is one of several global search methods that is applicable for solving the inversion problem defined here.

The ray-trace propagation model GAMARAY [16], [17] has been linked to the ASSA to calculate the complex acoustic field for each combination of the search parameters. GAMARAY accepts a geoacoustic description of the bottom properties as input, and the model has shown excellent agreement with wave-based models at frequencies down to 100 Hz. The ray-trace model is also very efficient computationally compared to wave-based models. This efficiency increases as the acoustic frequency increases and allows for several hundred thousands forward-model runs in the search of the optimum environment within a reasonable time.

The objective function (E) minimized during the inversion is based on the Bartlett processor where the measured and modeled acoustic fields are summed coherently in frequency and incoherently in range as follows:

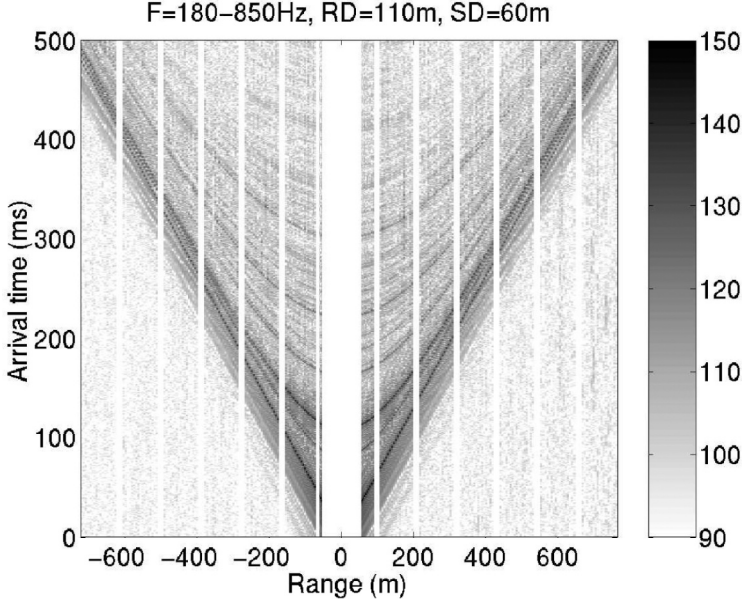


Figure 5. Stacked matched-filtered signal as the source is towed toward (negative range), passing and towed away (positive range) from the VLA.

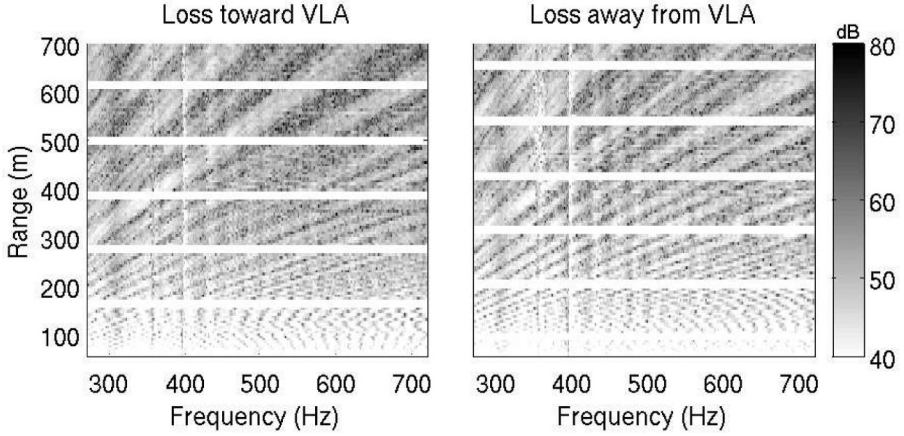


Figure 6. Transmission loss of the acoustic field at the shallowest hydrophone when the source is towed toward, passing and towed away from the moored vertical array.

$$E = 1 - \frac{1}{N_R} \sum_{j=1}^{N_R} \frac{\left| \sum_{i=1}^{N_F} p_{ij}^* q_{ij} \right|^2}{\sum_{i=1}^{N_F} |p_{ij}^* p_{ij}| \sum_{i=1}^{N_F} |q_{ij}^* q_{ij}|} \quad (1)$$

where N_R is the number of hydrophones and N_F is the number of frequencies. The complex pressure vectors from observations and modeling are given by p_{ij} and q_{ij} , and $(*)$ denotes complex conjugate. The objective function is normalized to values between 0 and 1, where the value 0 in-

indicates a perfect match between model and data and a value of 1 totally uncorrelated fields. This objective function has been applied successfully to towed horizontal array data acquired during other experiments [7], [8] and is equivalent to matching the band-limited impulse response at several hydrophones [18].

Only the low-frequency transmissions in the band 250-750 Hz are considered in the inversion, 11 frequencies at 50-Hz increments within the band are used to match the modeling results to the data. The acoustic data were received on the shallowest hydrophone at a depth of ~ 105 m. Two approaches are used to match the acoustic field in range: (1) Each of the 6 range segments consisting of 18 acoustic fields measurements equidistantly spaced in range as the source is towed toward the VLA are inverted independently. Segment 1 is the section of the track farthest from the VLA and segment 6 is the closest section to the VLA. (2) The full aperture is used in the inversion corresponding to 108 field measurements as the source is towed toward the VLA. The field measurements for the full aperture are not separated equidistantly in space (or time) as mentioned in Section 2. Two field measurements are missing in the acquisition sequence for each of the 6 segments in order to obtain a long array with equidistant spacing of transmissions. These missing measurements are included in the modeling for compatibility reasons but excluded in the calculations of the objective function.

The environment along the propagation track is assumed range-independent during the inversion, and the bottom is described by a single sediment layer overlying an infinite half-space. The sound speed, density and attenuation are assumed constant in depth within the sediment (c_s , ρ_s and α_s) layer and halfspace (c_b , ρ_b and α_b). Trial inversion runs showed that with an additional sediment layer did not improve the inversion results. Therefore, the acoustic data considered here do not contain more information about the bottom properties than a single sediment layer over a halfspace although the seismic profile (Fig. 2) indicates multiple layering structure in the bottom.

The geometric search parameters are source depth (zs), receiver depth (zr), source-receiver range (r), water depth (wd), hydrophone spacing (Δr) and sediment thickness (h). The source depth and receiver depth in the inversion correspond to the receiver depth and source depth, respectively, in the experimental set-up. The search bounds for the geometric and bottom properties used in the inversions are given in Table 1. The initial range between source and the first hydrophone, r_0 , for each segment is determined by time of arrival from the data.

Table 1. Search bounds for the geometric and bottom parameters used in the inversions.

Parameter	Search bounds
zs (m)	95–115
zr (m)	50–70
r (m)	$(r_0 - 50) - (r_0 + 150)$
wd (m)	138–148
Δr (m)	4.5–6.5
h (m)	1–30
c_s (m/s)	1460–1650
α_s (dB/m/kHz)	0.0–1.5
ρ_s (g/cm ³)	1.2–2.15
c_b (m/s)	1550–1900
α_b (dB/m/kHz)	0.0–1.5
ρ_b (g/cm ³)	1.2–2.15

The objective function value distribution obtained by inversion of the acoustic data collected in the 1st segment of the acoustic track is shown in Fig. 7 for the geometric parameters and in Fig. 8 for the bottom parameters. The source-receiver geometry and water depth are well determined with a

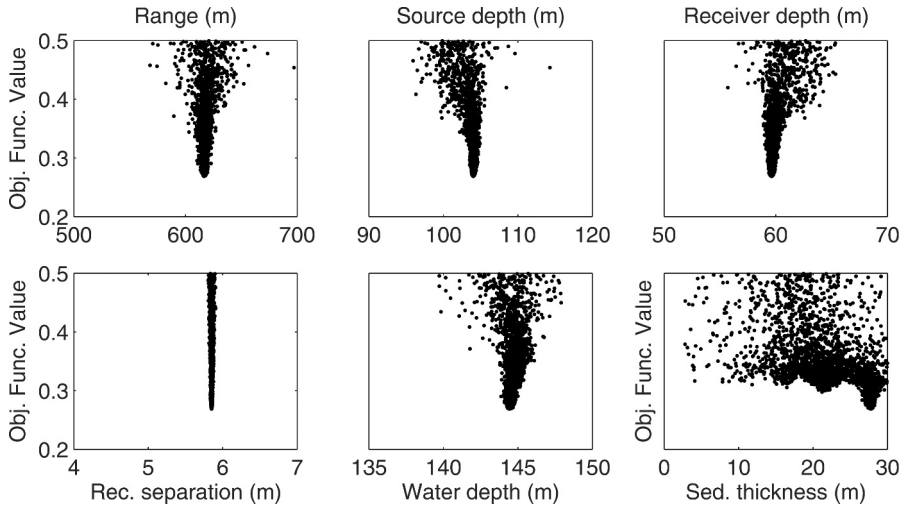


Figure 7. Objective function value distributions for all accepted combinations of geometric search parameters during the inversion of the acoustic data acquired in the 1st segment of the propagation track.

narrow objective function value distribution over the search bounds. The distribution for the sediment thickness is not as narrow although there is a clear minimum in the objective function. There is a tendency of multiple local minima for the sediment thickness over the search bound. The objective function value distribution for the bottom properties (Fig. 8) does not appear as sensitive as for the geometric parameters. However, there is clearly a minimum in the objective function for all the bottom parameters, in particular for the sediment sound speed and attenuation, and the sound speed in the sub-bottom.

The distribution of the objective function values for the remaining 5 segments is similar to the distribution for segment 1. However, the minimum value of the objective function varies from segment to segment in the range from 0.18 in segment 6 (closest range) to 0.44 in segment 3 (around mid-track). This variation in the minimum value of the objective function also alters the optimum values of the search parameters slightly from segment to segment. The distributions of the objective function value become narrower at closer source-receiver separation (segment 1 toward segment 6) for the geometric search parameters while very weak sensitivity is seen for the bottom parameters at these close ranges. The inversion of all segments simultaneously shows similar behavior: the objective function is strongly sensitive to geometric parameters and weakly dependent on the bottom search parameters. The minimum value of the objective function is 0.44 which is similar to the value of the objective function from the worst inversion in segment 3.

The geometric and bottom properties resulting in lowest objective function value from the individual and simultaneous inversions of the acoustic data collected in segments 1-6 are shown in Fig. 9 and 10, respectively. The inversion results are obtained by ~ 25000 forward model calls to **GAMARAY**, and the optimum solution is determined within ~ 6600 accepted search parameter combinations. The first 6 data points for each inversion parameter in Fig. 9 and 10 represent the results from the individual inversions of the 6 segments. The last data point is the inversion result considering the 6 segments simultaneously. There is noticeable variability in the geometric parameters during the individual inversions. In particular significant variations in source-receiver depths and the water depth are observed, which may be due to coupling of these parameters. For instance, when the water depth is shallow as for the inversion result from segment 3 then the receiver depth is also shallow.

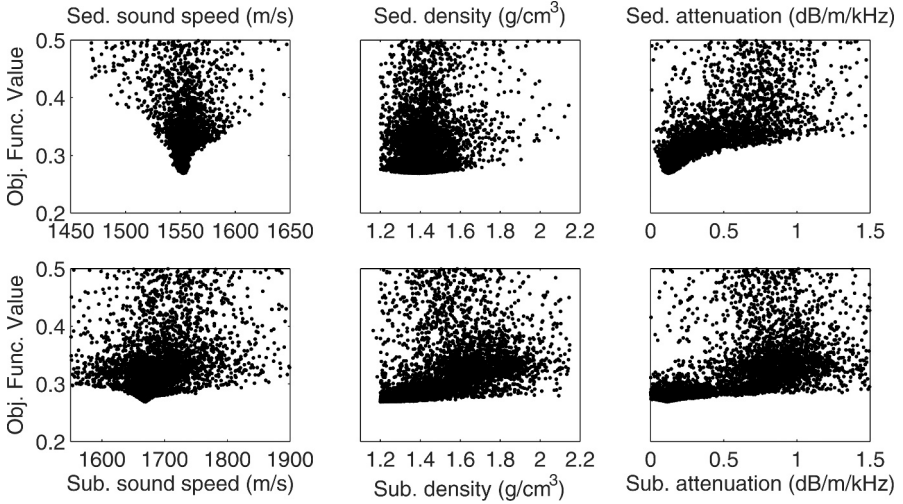


Figure 8. Objective function value distributions for all accepted combinations of bottom search parameters during the inversion of the acoustic data acquired in the 1st segment of the propagation track.

As the water depth increases in the following segments the receiver depth also increases. This is less pronounced for the source depth. Note the inversion for the range between the source and the first receiver in segment 6 and the full array is the same as required. The remaining geometric values obtained from the inversion of segment 6 and the full array are very similar. This may be caused by the same source-first receiver range from these 2 inversions, which can constrain values of the remaining geometric parameters. Therefore, the values of the geometric parameters are almost the same using a synthetic horizontal array with 18 hydrophones in segment 6 or the full array with 108 hydrophones.

The sediment thickness varies from ~ 5 -30 m between the inversion of each segment. This range of layer thicknesses is not clearly seen in the seismic profile (Fig. 2), although the seismic data show diffuse reflections from 3 main reflectors that could contain thin stratifications as discussed in Section 2.

Variability in bottom properties between segments is also observed with sound speed in sediment and sub-bottom varying ± 70 m/s along the track. In general, the density and attenuation show stronger variability in the sub-bottom than in the sediment between segments. This may be caused by higher attenuation of the acoustic field interacting with the sub-bottom than the sediment resulting in weak (or no) reflections from the sub-bottom. The density and attenuation in sediment and sub-bottom are included in the inversion because the acoustic field is sensitive to the bottom attenuation at long ranges (segment 1) and less sensitive to the density at these ranges. For short propagation ranges (segment 6) the acoustic field is affected by the bottom density and less influenced by the attenuation [12].

In general, the geometric parameters are determined within ± 10 m of the values known from the experimental set-up except for the sediment layering. The determined sound speed in the sediment agrees very well the measured sound speed from the cores, but the inversion for density shows, in general, slightly lower values than the measured densities (Fig. 3).

The propagation modeling result using the average properties from the individual inversions of segments 1-6 is compared to the data (ship towing the source toward the VLA) in Fig. 11. Qualitatively the agreement between the model and data using the determined geometric and geoacoustic

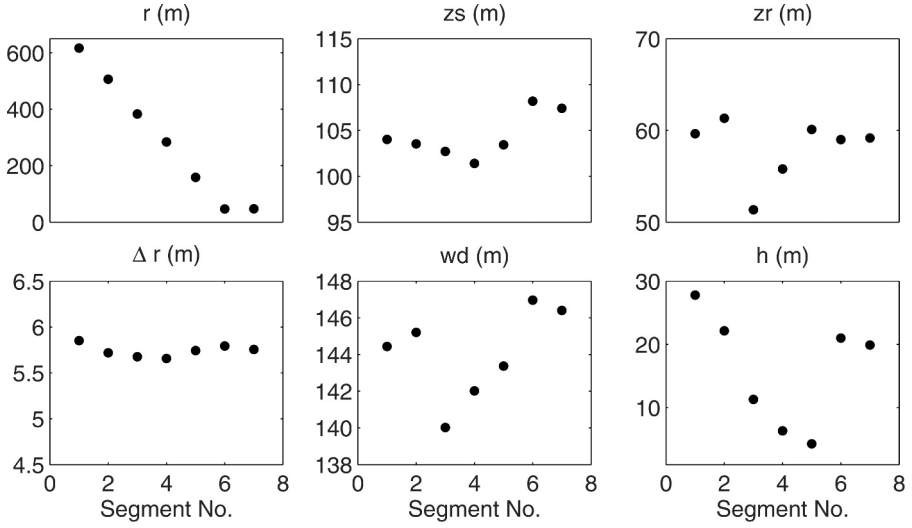


Figure 9. Optimum values of the geometric search parameters obtained by inversion of the acoustic data acquired in the 6 independent segments along the propagation track and the 6 segments simultaneously.

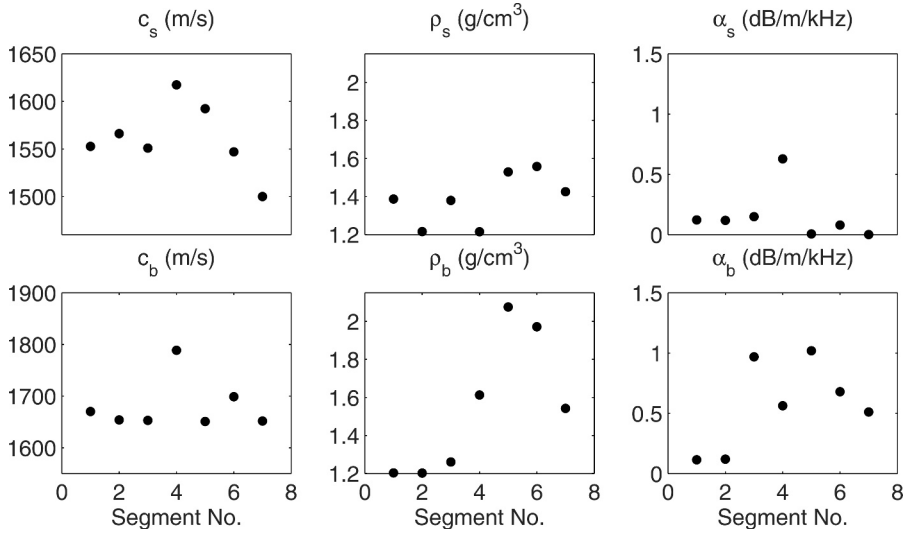


Figure 10. Optimum values of the bottom search parameters obtained by inversion of the acoustic data acquired in the 6 independent segments along the propagation track and the 6 segments simultaneously.

properties from the inversion as input to **GAMARAY** is good. The main interference structure (striation pattern) and level of the measured acoustic data are correctly modeled by **GAMARAY**. The model also predicts the arrival time and amplitude of the time series as shown in Fig. 12 for the closest, mid and longest propagation ranges. However, some of the arrivals observed in the data are

not appearing in the model results, which could be caused by environmental factors not included in the modeling.

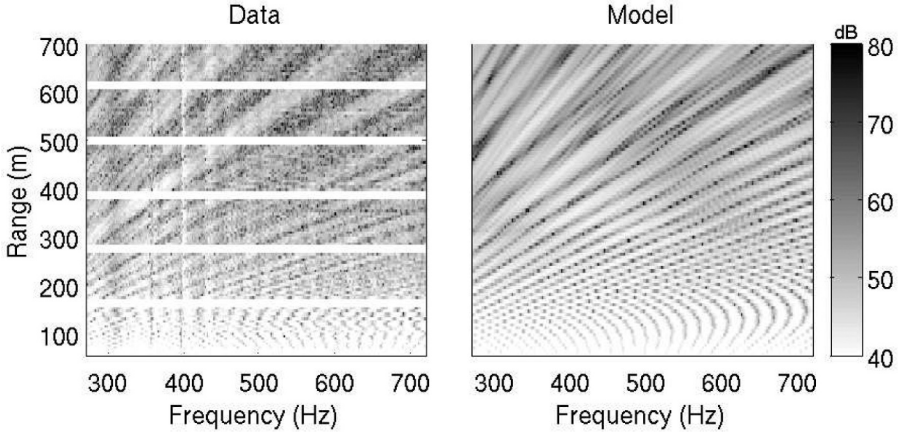


Figure 11. Comparison of modeled and measured pressure fields using the average geometric and bottom properties found by the independent inversion of the acoustic data collected in segment 1-6.

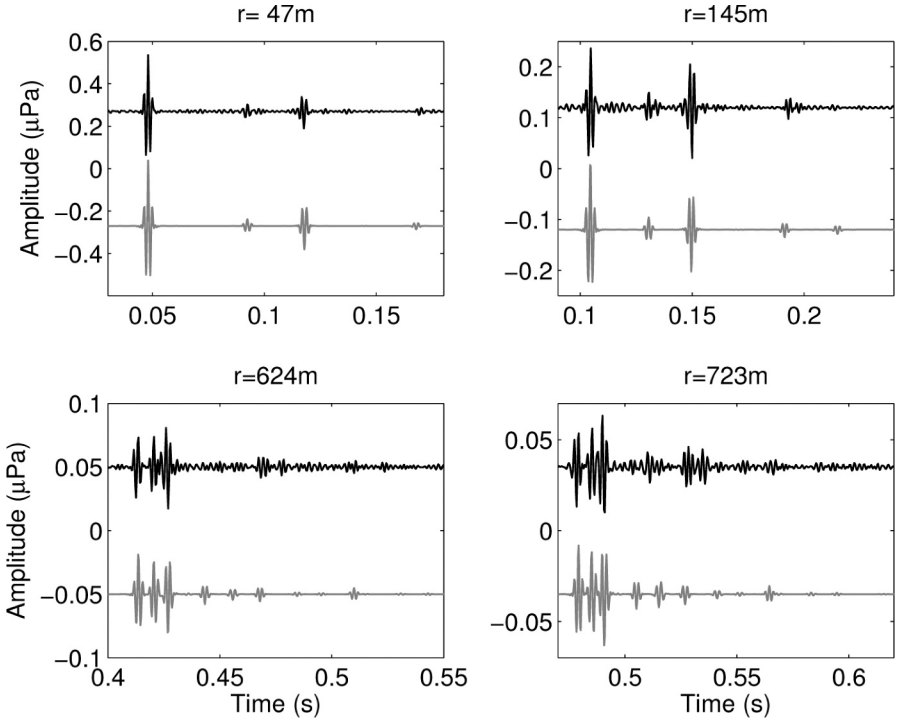


Figure 12. Comparison of modeled and measured time series using the average geometric and bottom properties found by the independent inversions of the acoustic data collected in segment 1-6.

4 Conclusions

Knowledge of the bottom properties in shallow-water regions is critical for accurate acoustic propagation modeling. Matched-Field Processing (MFP) geoacoustic inversion has been shown as a promising technique to extract these bottom properties. The majority of the research in MFP inversion has focused on acoustic data received on vertical line arrays (VLA). However, recently developed inversion techniques using data from towed horizontal arrays (HLA) have shown similar performance with several advantages compared to VLA geoacoustic inversion.

The concept of MFP geoacoustic inversion of HLA data is adopted in this paper to characterize the bottom properties at a particular site visited during the BOUNDARY 2002 experiment. In this experiment the HLA was formed synthetically by towing a sound source along a 1-km propagation track passing a 4-element bottom-moored VLA. Acoustic data in the frequency band 250-750 Hz received on the shallowest hydrophone of the VLA were used in the MFP geoacoustic inversion. The principle of reciprocity was applied in the modeling environment during the inversion of the data to simulate the received acoustic signals on the synthetic HLA. The inversion was performed by using 6 individual horizontal array segments with 18 hydrophones and by combining these segments into a full array with 108 hydrophones. The objective function minimized during the inversion has a higher value for the full array inversion than for the individual segment inversion. This high objective function value for the full array inversion is most likely caused by the attempt to match more hydrophone data and variability in source range and depth as towed along the track. In general, the inversion showed higher sensitivity to the geometric parameters than to any of the bottom properties. However, the inversion results for each parameter from the individual segments and the full array show moderate variability, and the determined geometric and bottom properties are in good agreement with the *a priori* knowledge of the experimental configuration, seismic profile and core data acquired in the same region. Modeling results based on the inverted environmental properties reconstruct the main features in the transmission loss acquired along the track in the frequency band transmitted (striation pattern and level). Further, modeling of the band-limited impulse response shows good agreement with the data both in amplitude and arrival structure in this multi-path environment. The results presented here demonstrate the potential of using synthesized horizontal array data for MFP geoacoustic inversion.

Acknowledgements

The authors wish to acknowledge all the members who participated in the BOUNDARY 2002. Special thanks to E. Michelozzi as engineering coordinator and P. Boni for managing the data acquisition. The author would also like to gratefully acknowledge the crews of R/V *Alliance* and ITNS *Vega*. This work was sponsored by NATO.

References

1. Ferla C. M. and Jensen F. B., Are current environmental databases adequate for sonar predictions in shallow water?. In *Impact of Littoral Environmental Variability on Acoustic Predictions and Sonar Performance*, N. G. Pace, F. B. Jensen, Editors, Kluwer Academic Publishers, 555–562 (2002).
2. Gingras D. F. and Gerstoft P., Inversion for geometric and geoacoustic parameters in shallow water: Experimental results. *J. Acoust. Soc. Am.* **97**, 3589–3598 (1995).
3. Hermard J.-P. and Gerstoft P., Inversion of broad-band multitone acoustic data from the YEL-LOW SHARK summer experiments. *IEEE J. Ocean. Eng.* **21**, 324–346 (1996).
4. Siderius M. T., Nielsen P. L. and Sellschopp J., Experimental study of geoacoustic inversion uncertainty due to ocean sound-speed fluctuations. *J. Acoust. Soc. Am.* **110**, 769–781 (2001).

5. Jesus S. M. and Caiti A., Estimating geoacoustic bottom properties from towed array data. *J. Comput. Acoust.* **4**, 273–290 (1996).
6. Caiti A., Jesus S. M. and Kristensen A., Geoacoustic seafloor exploration with a towed array in a shallow water area of the Strait of Sicily. *IEEE J. Ocean. Eng.* **21**, 355–366 (1996).
7. Siderius M. T., Nielsen P. L. and Gerstoft P., Range-dependent seabed characterization by inversion of acoustic data from a towed receiver array. *J. Acoust. Soc. Am.* **112**, 1523–1535 (2002).
8. Fallat M., Nielsen P. L. and Siderius M. T., Geoacoustic characterization of a range-dependent ocean environment using towed array data. Accepted for publication in *IEEE J. Ocean. Eng.* (2004).
9. Holland C., Coupled scattering and reflection measurements in shallow water. *IEEE J. Ocean. Eng.* **27**, 454–470 (2002).
10. Harrison C. H. and Nielsen P. L., Plane wave reflection coefficient from near field measurements. *J. Acoust. Soc. Am.* **116**, 1355–1361 (2004).
11. Nielsen P. L. *et al.*, BOUNDARY 2002 April 4–23 Malta Plateau. SACLANTCEN CD-57 (2002).
12. Jensen F. B., Kuperman W. A., Porter M. B. and Schmidt H., *Computational Ocean Acoustics*, New York, AIP Press (1994).
13. Nielsen P. L. *et al.*, BOUNDARY 2003 July 5–24 Malta Plateau. SACLANTCEN CD-69 (2003).
14. Fallat M. R. and Dosso S. E., Geoacoustic inversion via local, global and hybrid algorithms. *J. Acoust. Soc. Am.* **105**, 3219–3230 (1999).
15. Dosso S. E., Wilmut M. J. and Lapinski A.-L. S., An adaptive hybrid algorithm for geoacoustic inversion. *IEEE J. Ocean. Eng.* **21**, 324–336 (2001).
16. Westwood E. K. and Vidmar P. J., Eigenray finding and time series simulation in a layered-bottom ocean. *J. Acoust. Soc. Am.* **81**, 912–924 (1987).
17. Westwood E. K. and Tindle C. T., Shallow-water time series simulation using ray theory. *J. Acoust. Soc. Am.* **81**, 1752–1761 (1987).
18. Siderius M. T., Gerstoft P. and Nielsen P. L., Broadband geoacoustic inversion from sparse data using genetic algorithms. *J. Comput. Acoust.* **6**, 117–134 (1998).

CHARACTERIZATION OF A RANGE-DEPENDENT ENVIRONMENT FROM TOWED ARRAY DATA

MARK FALLAT AND PETER NIELSEN

*NATO Undersea Research Centre,
Viale San Bartolomeo 400, La Spezia, 19138, Italy.*

STAN E. DOSSO

*University of Victoria, School of Earth and Ocean Sciences
Victoria, British Columbia, Canada
E-mail: sdozzo@uvic.ca*

MARTIN SIDERIUS

*Science Application International Corporation,
1299 Prospect St., La Jolla, CA 92037, USA.*

This paper examines the inversion of data from a towed acoustic source and towed horizontal array collected over a region with range-dependent geoacoustic properties. The inversion technique combines the results from a series of short-range, range-independent inversions to form a range-dependent representation of the environment. The acoustic data are taken from the MAPEX 2000 experiment conducted in the Malta Channel, Mediterranean Sea. Two inversion algorithms are used, adaptive simplex simulated annealing (ASSA) and Fast Gibbs Sampling (FGS). The results of the ASSA inversions are combined to characterize the range-dependent environment. The FGS results provide estimates of the uncertainties associated with the various geoacoustic parameters. The results agree favourably with a high-resolution seismic profile and measurements from several core samples.

1 Introduction

This paper describes an inversion technique for characterizing an environment with range-dependent geoacoustic properties. The technique uses acoustic data from a towed swept-frequency source recorded at a towed horizontal array (HA). The goal is to produce a representation of a range-dependent environment by combining the results from a series of short-range, range-independent inversions. Two inversion algorithms are used in this study: the hybrid inversion algorithm, adaptive simplex simulated annealing (ASSA) [1, 2], and the uncertainty analysis algorithm, Fast Gibbs Sampling (FGS) [3, 4]. ASSA provides an optimal estimate of the geoacoustic parameters while FGS gives a description of the uncertainties associated with these parameters. The modelled acoustic data were computed using the ray theory based forward model GAMARAY [5, 6]. Some of the first

geoacoustic inversion work on HA data was carried out on by [7, 8]. The HA data analyzed in this study are from the MAPEX 2000 experiment [9]. Previous studies have been carried out on these data focusing on a very limited set of data [9, 10]. The first study [9] examined the feasibility of inverting HA data, with an emphasis on comparing the inversion results with results from vertical array data inversion. In addition, nine sets of HA data from along a 10 km track were inverted in an attempt to estimate the range-dependent features of the environment, but with no comparison to ground truth. The second study [10] utilized the data to investigate algorithm-induced variability in geoacoustic inversion. In this work, a large number (37) of independent acoustic data sets from the MAPEX 2000 are analyzed. For each of these data an ASSA inversion is carried out to obtain estimates of the geoacoustic parameters. The FGS analysis is carried out on two data sets, one at either end of the experimental track. The results from both inversions are compared to independent seabed information from a high-resolution seismic profile and shallow core samples.

2 MAPEX 2000 Experiment

In the spring of 2000, the NATO Undersea Research Centre conducted the MAPEX 2000 experiment in the Malta Channel, Mediterranean Sea [9]. Figure 1 shows the ship track for the portion of MAPEX 2000 considered here. Two course deviations were required which, because of the resulting deformation of the towed array, meant that fewer or no inversions could be carried out in these regions. This site was chosen, in part, because previous experiments had provided ground truth for range-dependent geoacoustic properties in the form of a high-resolution seismic profile and sediment core samples (see Fig. 1).

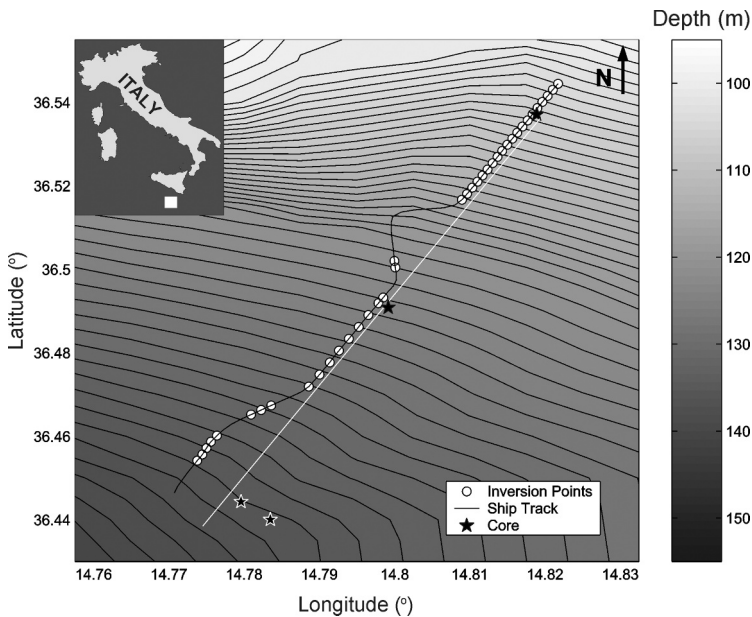


Figure 1. Ship track (solid line), including the points where inversions were performed (circles), core locations (stars), and a high-resolution seismic profile (white line).

The high-resolution seismic profile is shown in Fig. 2 [11], and indicates three well defined reflectors out to a range of approximately 8 km. The first reflector is the water-sediment interface. The second reflector represents the bottom of a low-speed inclusion [9, 11] that gets thinner with

range and pinches out at 8–9 km. The third reflector has a relatively constant separation of ~ 20 m from the water-sediment interface, and is taken to represent the acoustic basement.

Figure 2 also shows the sound speeds measured from four core samples of surficial sediments to approximately 1-m depth. The cores at the northern end and the middle of the track, referred to here as the northern (N) cores, indicate a uniform sound speed of approximately 1460 m/s to a maximum penetration depth of 1.2 m. This speed is lower than what was measured in the water column (1512 m/s). These core locations correspond to the inclusion shown in the seismic profile. The two cores at the southern (S) end of the track only penetrated 0.3 and 0.6 m due to the more consolidated nature of the sediments. For these cores, which correspond to locations where the inclusion is very thin or absent, the measured sound speed increases with depth from about 1480 m/s (which is likely from the inclusion) at the sea floor to ~ 1550 m/s. Since the sound speed at greater depths is likely to be at least this high, a sound speed of 1550 m/s is adopted for comparison with the inversion results. The acoustic signals were generated using an extensional source, towed at a nominal depth of 60 m, and consisted of 1-s linear frequency modulated sweeps from 250–750 Hz. To produce an equalized signal, the acoustic data were calibrated by deconvolving with a measured source spectrum. The source spectrum was recorded prior to the experiment using a reference hydrophone located 2 m from the (stationary) source.

The acoustic data were recorded at a HA towed at a nominal depth of 60 m. The array depth was measured by pressure sensors at the head and tail of the array, which showed an average tilt of $\sim 1^\circ$. The array contained 64 sensors spaced 4 m apart for a total acoustic aperture of 252 m. The source and array were separated by ~ 300 m.

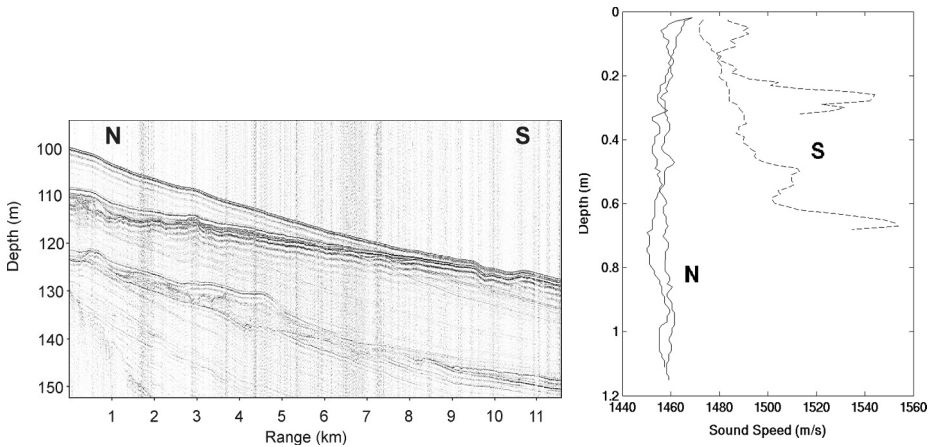


Figure 2. High resolution seismic profile and sound speed profiles from the core samples from the MAPEX 2000 site.

3 Inversion Algorithms

This section provides a brief overview of the inversion algorithms used in this work. The goal of these algorithms is to find an optimal set of model parameters that will minimize some measure of mismatch between measured and modelled acoustic data. For this work, the mismatch was based on the Bartlett processor coherent in frequency and summed incoherently over the receivers.

3.1 Adaptive simplex simulated annealing

Adaptive simplex simulated annealing (ASSA) [1, 2] is a hybrid optimization algorithm that combines the downhill simplex (DHS) method with a variant of fast simulated annealing (FSA). The resulting algorithm has proved more efficient and effective than either of the individual algorithms [2].

The DHS algorithm is based on an intuitive geometric scheme for moving downhill in the parameter space [12, 13]. Although DHS is not the most efficient algorithm for local downhill moves, it has the advantages of not computing partial derivatives or solving systems of equations. The algorithm operates on a simplex of $M + 1$ models in a M dimensional parameter space. The initial simplex is chosen at random and subsequently undergoes a series of transformations to move downhill. First, each model is ranked according to its mismatch, E , from highest to lowest. The algorithm initially attempts to improve the model with the highest E value by reflecting it through the face of the simplex containing the model with the lowest E . If this new model has the lowest E , an extension by a factor of two in the same direction is attempted. If the reflection results in a model that still has the highest E , the move is rejected and a contraction by a factor of two is attempted. If none of the steps decrease the mismatch, then a contraction by a factor of two in all dimensions toward the model with the lowest E is performed. This process is repeated until the E values for all models converge to within a user defined tolerance.

FSA [14, 15] consists of a series of iterations involving random perturbations to model parameters. The parameter perturbations are generated using a Cauchy distribution, which has the desirable properties of a Gaussian-like peak and Lorentzian tails. This distribution provides concentrated local sampling of the parameter space while attempting occasional large perturbations. Perturbations that result in a decrease in E will always be accepted. Perturbations that produce an increase in E are accepted conditionally with a probability given by the Gibbs or Boltzmann distribution:

$$P(\Delta E) = \exp\left(\frac{-\Delta E}{T}\right). \quad (1)$$

The quantity T is a control parameter, often referred to as temperature, that is decreased slightly after each perturbation. Accepting some increases in E allows the algorithm to escape local minima in search of a better solution. When T is high (at the early stages of the optimization) the algorithm will essentially search the parameter space in a random manner. As T decreases, accepting increases in E becomes less probable and the algorithm spends more time searching regions with lower E values. Eventually the algorithm will converge to a solution that should approximate the global minimum.

ASSA combines the DHS method and FSA in an adaptive optimization scheme. Unlike standard FSA, it operates on a simplex of models rather than a single model, and instead of employing purely random perturbations to the model, a DHS step followed by a random perturbation is used to compute the new model parameters. The new model is then evaluated for acceptance using Eqn. (1). The size of the random perturbations, for individual parameters, is determined adaptively based on a running average of recently accepted perturbations.

3.2 Fast Gibbs Sampling

The FGS algorithm [3, 4] is based on a Bayesian formulation of the inverse problem. Bayesian inversion focuses on evaluating the *posterior probability density* (PPD). Of particular interest in this paper are the marginal probability distributions given by the following expression

$$P(m_i | \mathbf{d}^{obs}) = \int \delta(m'_i - m_i) P(\mathbf{m}' | \mathbf{d}^{obs}) d\mathbf{m}', \quad (2)$$

where m_i is the model parameter of interest, δ is the Dirac delta function and $P(\mathbf{m}' | \mathbf{d}^{obs})$ is the PPD (i.e., the conditional probability of the model \mathbf{m} given an observed data set \mathbf{d}^{obs}). For matched

field inversion of acoustic data with Gaussian errors and uniform prior information when receiver amplitude and phase are not well known, it can be shown that the PPD is given by

$$P(\mathbf{m}|\mathbf{d}) = \frac{\exp[-E(\mathbf{m})]}{\int \exp[-E(\mathbf{m}')] d\mathbf{m}'} \quad (3)$$

where $E(\mathbf{m})$ is the normalized Bartlett mismatch coherent over frequency and summed incoherently over receivers. The integral in Eqn. (3) can be evaluated by sampling from the PPD using Metropolis Gibbs sampling, i.e., applying random model perturbations according to Eqn. (1) at $T = 1$.

The FGS algorithm is an efficient implementation of Gibbs sampling based on several straightforward modifications. First, an adaptive scheme for scaling the perturbation sizes is applied. Second, the influence of inter-parameter correlations is minimized by carrying out a parameter space rotation. The rotation is done using principal-component analysis to determine the dominant correlation directions using the eigenvectors of the covariance matrix. Finally, convergence of the integral estimates is monitored by comparing the cumulative probability density functions of two independent samples run in parallel. At convergence, the two samples are combined to evaluate the integral.

4 ASSA Results

Acoustic data from 37 positions along the experimental track were processed and inverted using ASSA. An important aspect of inverting experimental data is determining a suitable environmental parameterization (e.g., how many layers to include in the sub-bottom) given the resolving power of the data. In this case, the seismic profile provided some insight about the layering structure of the environment by indicating three layers at the northern end of the track transitioning to two layers at the southern end. However, the acoustic data may or may not be able to resolve this layering structure. Therefore, two environmental parameterizations were employed for the inversions, the first was comprised of two layers (one sediment layer over a basement) and the second included three layers (two sediment layers over a basement). Included in the inversions were water depth, sediment depth, sediment and basement sound speeds, depth-dependent density and attenuation and small corrections to the geometric parameters (source and receiver depths and range). The density and attenuation were poorly determined and therefore not discussed here. Also, since we are investigating geoaoustic properties the results for the geometric parameters are not described.

Figure 3 shows the inversion results for the two-layer environment. The top panel shows the results for the water and sediment depths. In this paper, the sediment depth refers to the depth measured from the sea surface while sediment thickness refers to the depth measured from the water-sediment interface. The results have been superimposed onto the seismic profile for comparison. Also included are three lines which are interpretations of the major reflectors. The results for the water depth agree well with the water-sediment interface. The exceptions are several points between 6–9 km where the water depth appears to be varying between the water-sediment interface and the bottom of the inclusion. This variation is due to the fact that the low-speed inclusion appears acoustically similar to the water column, making it difficult to determine the water-sediment interface accurately [16].

The results for the sediment depth are also in good agreement with the layering structure shown in the seismic profile, although there is a significant change at 2 km. Before 2 km the sediment depth follows the bottom of the inclusion while beyond 2 km it follows the interface of the basement.

The lower panel shows the results for the sediment (topmost results) and basement sound speeds. The results for the sediment sound speed out to 2 km are in good agreement with the estimate from the northern core samples and are all lower than the speed in the water column (1512 m/s). Beyond 2 km the sound speed in the sediment agrees well with the southern core samples. In the region from 2–6 km, the sound speeds are lower than from 7–10 km. This is consistent with a sediment layer that represents a depth average over the lower-speed inclusion and the higher-speed deeper layer.

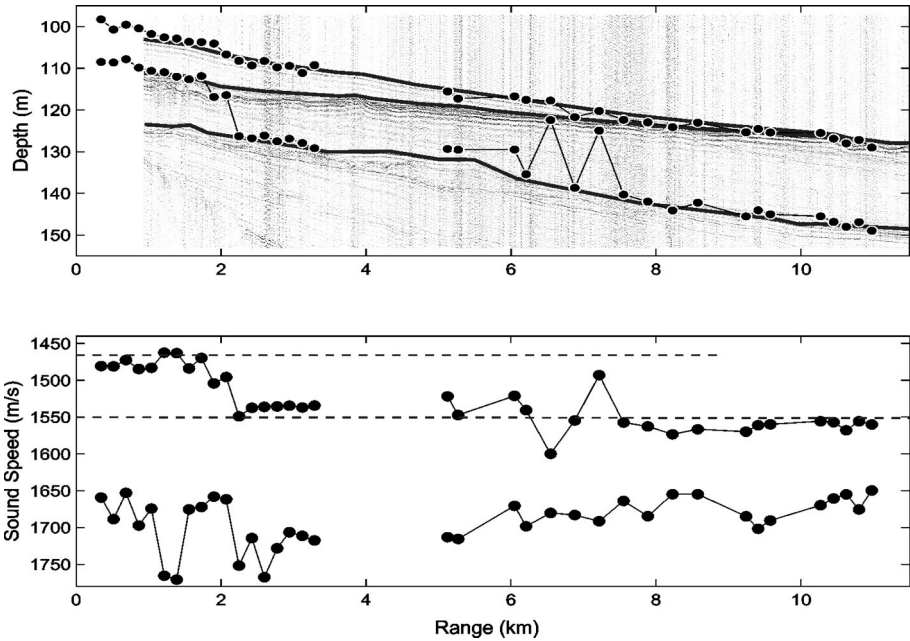


Figure 3. Inversion results for the two-layer parameterization. The \bullet represent the results from the inversions. Solid lines have been added to help discriminate the significant reflectors. The dashed lines are sound speed estimates from the cores samples.

Unfortunately, the core data do not extend deep enough into the sediment for comparison with the basement sound speed obtained by the inversions. However, the variation in inversion results provides an indication of the stability of the estimates. Since this deeper layer is expected to be range-independent over this scale, the inversion results should show little variation. In the region from 0-4 km there is more variation in the results compared to the rest of the track. This is likely due to the fact that in this region there are three layers yet the inversion is restricted to two layers. Therefore, the speeds in the layers are being depth-averaged. In the region between 5-10 km the results are quite stable with a maximum variation of 50 m/s.

The inversion results for the three-layer environment are shown in Figure 4. Again the water depth is in good agreement with the water-sediment interface. The results for the depth of the first sediment layer are quite similar to the two-layer case; that is, they follow the bottom of the inclusion until around 2 km and then follow the basement interface. Finally, the depth for the second sediment layer shows considerable variation between inversion results and does not seem to follow any structure in the seismic profile.

The inversion results for the sound speeds are shown in the lower panel of Fig. 4. The sound speed in the first sediment layer is similar to the two-layer case with slightly more variation between points. The results for the sound speeds in the second sediment layer and the basement show considerable variation and do not appear to be well determined.

The final mismatch values of the inversions are shown in Figure 5. There is no significant difference between the mismatches obtained for the two environmental parameterizations. This indicates that using the more complicated three-layer environment does not improve the mismatch and therefore is not warranted for these data.

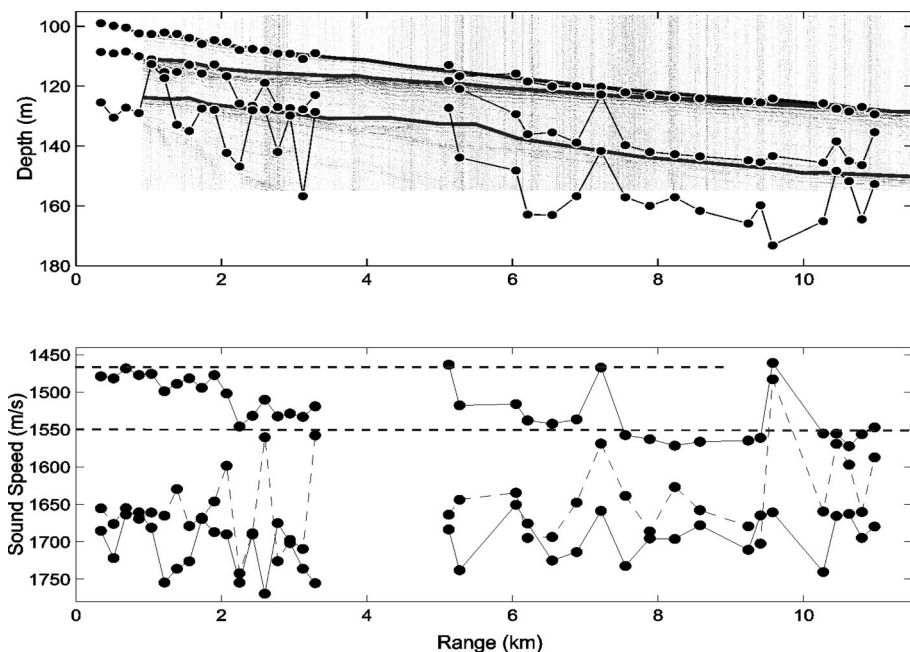


Figure 4. Inversion results for the three-layer parameterization. The dashed \bullet line represents the sound speed in the second sediment layer.

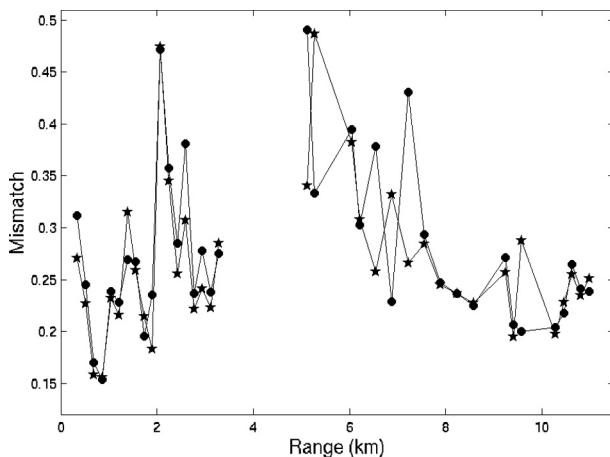


Figure 5. The final mismatch values for the inversions of the MAPEX 2000 experimental data. Included are both the two- and three-layer parameterizations (\bullet and \star respectively).

5 FGS Results

For the FGS analysis, data from two positions along the track were analyzed because these uncertainty estimates are expected to be representative of the extremes of the environment and the algorithm is numerically intensive. The first data set analyzed was the fifth point from the northern

end of the track at approximately 1-km range (see Fig. 3). The second data set was from 9.5 km. These two data sets were chosen because they represent points where there are significantly different geoacoustic properties. In both cases a two-layer environmental parameterization was used because the ASSA analysis indicated that the data cannot resolve a three-layer environment (see Sec. 4).

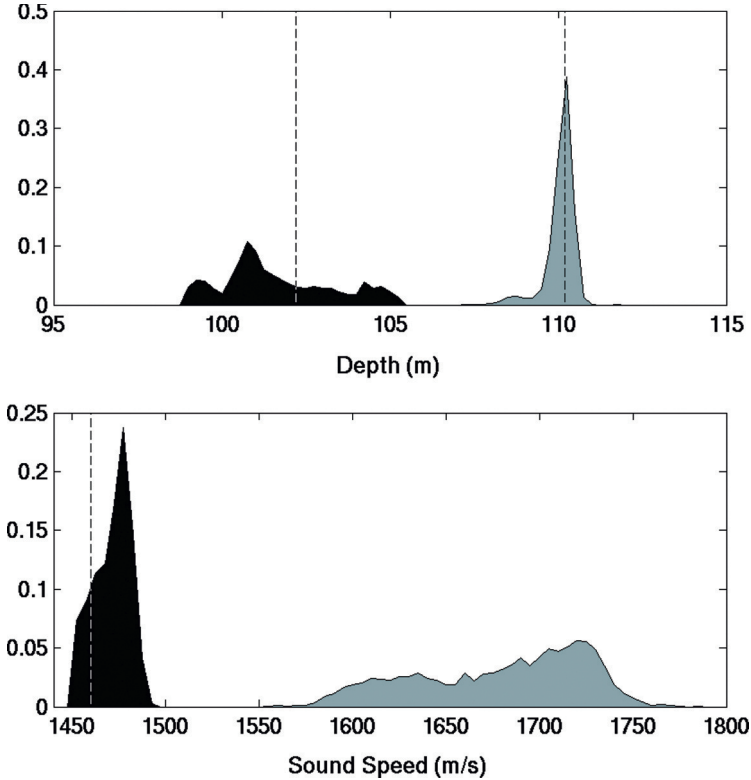


Figure 6. Marginal probability distributions for the northern set of data. The dashed lines represent ground truth values.

Figure 6 shows the 1-D marginal probability distributions for the northern data. In each case, the marginal probability distributions are represented by histograms of the sampled models. Within a panel, the distributions have the same bin size and have been normalized to unit area so that they can be directly compared. The top panel shows the distributions for the water depth (black) and the sediment depth (gray). The dashed lines represent the measured bathymetry and estimates of the sediment depth, from the seismic data. The marginal distribution for the water depth is quite at compared to that for the sediment depth. This is a result of the low-speed sediment layer that makes it difficult to determine the water-sediment interface accurately. The distribution for the sediment depth has a significant peak centered near the sediment depth estimate from the seismic profile.

The lower panel shows the distributions for the sound speed in the sediment (black) and the basement (gray). The dashed line represents the estimate of the sediment sound speed from the core data. The distribution for the sediment sound speed has a broad base extending over approximately 50 m/s and a peak at 1480 m/s. It is interesting to note that even though the base of the distribution is

somewhat broad all values are below 1500 m/s (i.e., lower than in the water column). This shows that even though the data may not be able to obtain an accurate estimate of the sound speed it can resolve the fact that the layer is low-speed. Also, the sound speed indicated by the peak is higher than the core sample, likely because the core only sampled the top meter of sediment while the acoustic data sample the entire 8-m layer. The distribution for the basement sound speed is very at which shows that the data are not sensitive to this parameter.

Figure 7 shows 2-D marginal probability distributions for combinations of the water depth, sediment thickness and the sediment sound speed. In this case, the distributions have the same number of bins for each parameter. The 2-D marginals are useful for investigating correlations between the geoaoustic parameters. It should be noted that the small scale structure in these plots is a result of undersampling and does not represent local structure of the PPD. The top panel shows a negative correlation between the water depth and sediment thickness. That is, high marginal probabilities are obtained for a range of property values provided the sediment thickness decreases as the water depth increases. This correlation is commonly observed in areas with a low-speed sediment layer [4, 16]. The 2-D marginal for the sediment thickness and sound speed given in the bottom panel, shows a significant positive correlation, representing conservation of travel time through the layer.

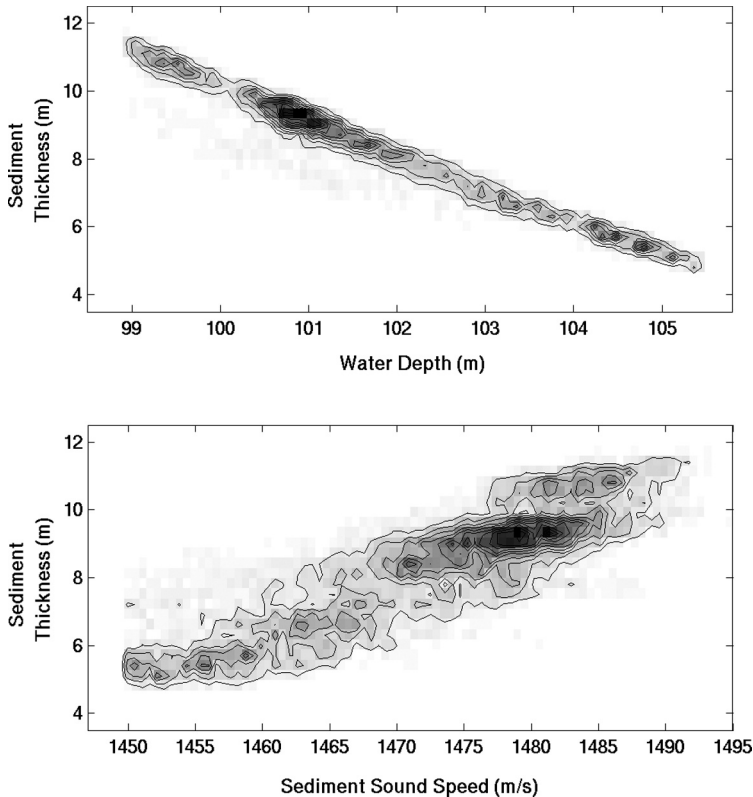


Figure 7. 2-D marginal probability distributions for the northern data set.

The 1-D marginal probability distributions for the southern data are shown in Figure 8. In this case, the low-speed sediment layer is absent resulting in a noticeable difference, with respect to Fig. 6, in the distribution for the water depth. There is a peak located quite close to the value of the measured bathymetry. The distribution for the sediment depth has a peak which coincides with the estimate from the seismic profile. The distribution for the sediment sound speed is peaked at a value that is slightly higher than the sound speed estimate from the southern core. The distribution for the basement speed is quite at, similar to that for the northern data. For this data set 2-D marginals were not plotted because they showed no significant correlations between parameters.

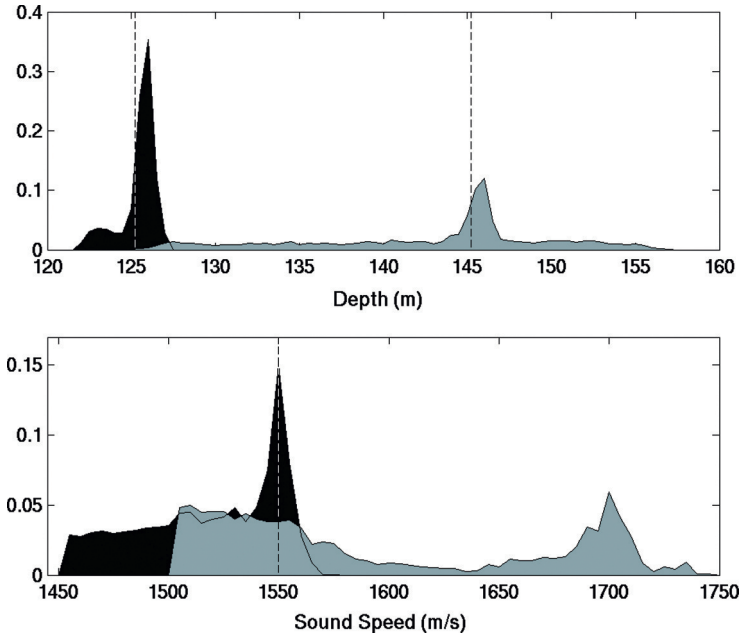


Figure 8. Marginal probability distributions for the southern set of data. The dashed lines represent ground truth values.

6 Summary

This paper described a technique for characterizing a range-dependent environment using information obtained from a series of short-range, range-independent inversions. First, inversions were carried out using adaptive simplex simulated annealing to obtain an optimal estimate of the geoacoustic parameters. This was followed by a more detailed analysis of the parameters uncertainties using the Bayesian inversion algorithm, fast Gibbs sampling.

The results of the ASSA inversions showed that it was possible to produce a range-dependent representation of the environment from a series of short-range, range-independent inversions. In particular, these data were able to resolve a two-layer environment that agreed with layering structure from a high-resolution seismic profile and sound speed estimates from core samples. The more complicated three-layer environment proved to be beyond the resolving power of the data. Also, it appeared that for this particular inversion technique, there was a minimum sediment thickness that was resolvable by the data regardless of the environmental parameterization that was used.

The FGS results showed that, for a portion of the track with a low-speed sediment layer, it was difficult to determine accurately the water depth but the sediment depth and the sediment sound speed were resolvable. For the rest of the track the water depth and sediment properties were well determined. In both cases the basement sound speed could not be determined accurately.

References

1. Fallat M. R. and Dosso S. E., Geoacoustic inversion via local, global and hybrid algorithms. *J. Acoust. Soc. Am.* **105**(3), 219–230 (1999).
2. Dosso S. E., Wilmut M. J. and Lapinski A-L. S., An adaptive hybrid algorithm for geoacoustic inversion. *IEEE J. Ocean. Eng.* **21**(3), 324–336 (2001).
3. Dosso, S. E., Quantifying uncertainty in geoacoustic inversion I. A fast Gibbs sampler approach. *J. Acoust. Soc. Am.* **111**, 129–142 (2002).
4. Dosso S. E. and Nielsen P. L., Quantifying uncertainty in geoacoustic inversion II. Application to broadband, shallow-water data. *J. Acoust. Soc. Am.* **111**, 143–159 (2002).
5. Westwood E. K. and Vidmar P. J., Eigenray finding and time series simulation in a layered-bottom ocean. *J. Acoust. Soc. Am.* **81**, 912–924 (1987).
6. Westwood E. K. and Tindle. C. T., Shallow water time series simulation using ray theory. *J. Acoust. Soc. Am.* **81**, 1752–1761 (1987).
7. Jesus S. M. and Caiti. A., Estimating geoacoustic bottom properties from a towed array data. *J. Comp. Acoust.* **4**, 273–290 (1996).
8. Caiti A., Jesus S. M., and Kristensen A., Geoacoustic sea floor exploration with a towed array in a shallow water area of the Strait of Sicily. *IEEE J. Ocean. Eng.* **21**, 355–366 (1996).
9. Siderius M., Nielsen P. L. and Gerstoft P., Range-dependent seabed characterization by inversion of acoustic data from a towed receiver array. *J. Acoust. Soc. Am.* **112**, 1523–1535 (2002).
10. Fallat M. R., Dosso, S. E and Nielsen P. L., An investigation of algorithm-induced variability in geoacoustic inversion. *IEEE J. Ocean. Eng.* **29**, 78–87 (2004).
11. Osler J. and Algan O., A high resolution seismic sequence analysis of the Malta Plateau. Tech. Rep. SR 311, SACLANT Undersea Research Centre, La Spezia, Italy (1999).
12. Nelder J. A. and Mead R., A simplex method for function minimization. *Computer Journal* **7**, 308–311 (1965).
13. Press W. H., Teukolsky S. A., Vetterling W. T. and Flannery B. P., *Numerical Recipes*, Cambridge University Press, Cambridge, England (1992).
14. Szu H. and Hartley R., Fast simulated annealing. *Phys. Lett.* **A122**, 157–162 (1987).
15. Liu P., Hartzell S. and Stephenson W., Non-linear Multiparameter Inversion Using a Hybrid Global Search Algorithm: Applications in Reflection Seismology. *Geophys. J. Int.* **122**, 991–1000 (1995).
16. Fallat M. R., Nielsen, P. L. and Dosso S. E., Hybrid geoacoustic inversion of broadband Mediterranean Sea Data. *J. Acoust. Soc. Am.* **107**, 1967–1977 (2000).

ACCOUNTING FOR BIAS IN HORIZONTAL WAVENUMBER ESTIMATES DUE TO SOURCE MOTION

KYLE M. BECKER

The Pennsylvania State University Applied Research Laboratory

P. O. Box 30, State College, PA 16803, USA

E-mail: kmbecker@psu.edu

Modal-based techniques for geoacoustic inversion require estimates of discrete horizontal wavenumbers corresponding to the propagating modes in a shallow-water waveguide. Horizontal wavenumber estimates can be obtained from the pressure field of a monochromatic point source measured as a function of range at a fixed depth. Previous experimental efforts have employed either fixed source/moving receiver or fixed receiver/moving source geometries to measure the field with range. Often, due to the slowly moving source/receiver, the problem is assumed to be static and that reciprocity holds. However, source motion and receiver motion impact the time-domain solution to the depth-dependent acoustic wave equation in different ways. One particular effect of source motion is a Doppler frequency shift in the depth-dependent Green's function, or integration kernel, used in the inverse Fourier transform to get the time-domain solution for the field. The Doppler shift in the Green's function equates to a Doppler shift in the horizontal wavenumbers corresponding to the individual propagating modes. Therefore, modal wavenumber estimates made for a source moving at constant velocity will be biased due to the Doppler shifts. In order for the estimates to properly represent modes consistent with the waveguide boundary conditions as required for modal inverse techniques, the bias should be removed. In this paper, a simple method is presented for effectively removing the bias in wavenumber estimates due to the Doppler effects induced by a moving source. An example is provided showing the Doppler shift measured from real experimental data. The impact on inversion results due to not accounting for moving source effects is also presented. Finally, a method for directly measuring modal group velocity from Doppler shifted wavenumber estimates is proposed.

1 Introduction

In this paper are presented results and observations from a geoacoustic inversion experiment conducted in shallow water on the New Jersey shelf in October 2000. The intent of the work was to estimate range-dependent geoacoustic properties of the seabed using estimates of local wavenumber spectra for a point-source acoustic field. The field was measured on a synthetic aperture horizontal array created by the relative motion between a single source and three independent receiving plat-

forms. Each platform was comprised of a single hydrophone suspended at a fixed depth from a freely drifting buoy equipped with a GPS receiver and a VHF transmitter. The analysis presented is focused on a single data set acquired while the source was being towed and while the receiver remained approximately stationary. The geometry of the experiment was primarily determined by the track of the towed source. For the data of interest, the source was towed along a radial away from the receiver and then turned around and towed toward the receiver along approximately the same radial. A shift in the peak locations of the wavenumber spectra was observed for wavenumber content estimated independently along the outbound and inbound tracks. Peaks were shifted to higher wavenumber values for the source closing on the receiver compared to those estimated when the source was moving away from the receiver. The observed shift was attributed to a Doppler shift in the modal eigenvalues owing to the source motion. Based on this understanding, and the simple geometry of the experiment, the wavenumber bias could be corrected. In addition, the simple approach suggested a technique which would allow for the estimation of modal group velocity directly from the shifted wavenumber estimates.

The remainder of the paper is organized as follows. In the following section, a brief overview of the modal inverse technique is presented. Assuming a horizontally stratified medium and fixed source/receiver geometry, the pressure field is approximated by a sum of normal modes. Next, the inverse problem is presented as a perturbation to a background modal sum. The problem is then considered including the effects of source motion. Section 3 describes the experimental data and analysis illustrating the bias in the wavenumber estimates. A method is presented for correcting the wavenumber bias along with determining modal group velocity. A summary of the results is presented in the final section along with suggestions for future work.

2 Overview of Modal Inversion Technique

A detailed description of the modal inverse technique for shallow water is presented in [1]. Modal based inversion methods use estimates of modal wavenumbers as input data to the inversion algorithms. For this work, wavenumber content is estimated from horizontal array measurements of the complex acoustic pressure field. The method is based on the Hankel transform relationship between a point-source acoustic field, measured on a sufficiently sampled range grid, and the depth-dependent Green's function for a horizontally stratified waveguide [2]. For a point source, located at fixed depth, in a waveguide environment having a constant density water column with depth-dependent sound-speed profile overlying a horizontally stratified medium, the depth-dependent Green's function, $g(k_r)$, satisfies the inhomogeneous Helmholtz equation

$$\left(\frac{d^2}{dz^2} + \rho(z) \frac{d}{dz} \left[\frac{1}{\rho(z)} \frac{d}{dz} \right] + k^2(z) - k_r^2 \right) g(k_r; z, z_0) = -2\delta(z - z_0), \quad (1)$$

along with impedance boundary conditions at the surface and bottom [3]. Assuming a pressure-release condition at the surface, and a bottom boundary characterized by the plane-wave reflection coefficient $\mathcal{R}(k_r)$, the depth-dependent Green's function has the form [3]

$$g(k_r; z, z_0) = \frac{i \left\{ e^{ik_z|z-z_0|} - e^{ik_z(z+z_0)} + \mathcal{R}(k_r) e^{i2k_z H} [e^{-ik_z(z+z_0)} - e^{-ik_z|z-z_0|}] \right\}}{k_z [1 + \mathcal{R}(k_r) e^{i2k_z H}]}. \quad (2)$$

In the above equations, the source and receiver depths, z_0 and z respectively, are treated as parameters in the problem and $k = \omega/c(z)$ is the total acoustic wavenumber. The complex-pressure field is related to the depth-dependent Green's function through a conjugate Hankel transform pair relationship

$$p(r; z, z_0) = \int_0^\infty g(k_r; z, z_0) J_0(k_r r) k_r dk_r, \quad (3)$$

$$g(k_r; z, z_0) = \int_0^\infty p(r; z, z_0) J_0(k_r r) r dr, \quad (4)$$

where the conjugate transform variables are range r and horizontal wavenumber k_r . J_0 is the Bessel function of order zero. Taken together, these equations illustrate the intimate relationship between the Green's function and properties of the seabed through the plane-wave reflection coefficient. Referring to (2), the modal eigenvalues are determined by the simple poles of the integral (3). Evaluating the integral at the pole locations using calculus of residues results in a modal representation of the pressure field in terms of the modal eigenvalues k_n [3]

$$p(r, z) \sim \frac{\sqrt{2\pi} e^{i\pi/4}}{\rho(z_0)} \sum_{n=1}^{n_{max}} \phi_n(z_0) \phi_n(z) \frac{e^{ik_n r}}{\sqrt{k_n r}}, \quad (5)$$

where ϕ_n are mode functions evaluated at the source and receiver depths and the large-argument approximation $k_r r \gg 1$ has been used.

The modal inversion technique is based on making a small perturbation to the sound speed in the depth-dependent wave equation. The result is an integral equation over depth of the mode functions that relates a small change made to a background sound-speed profile with a change in modal eigenvalues [1].

$$\tilde{k}_n - k_n = \Delta k_n = \frac{1}{k_n} \int_0^\infty \rho^{-1}(z) \phi_n^2(z) k^2(z) \frac{\Delta c(z)}{c(z)} dz, \quad (6)$$

where \tilde{k}_n are modal eigenvalues estimated from data, k_n and $\phi(n)$ are modal eigenvalues and mode functions that satisfy an assumed background model, and $c(z)$ and $\rho(z)$ are the sound speed and density of the assumed background model. The inversion algorithm is initialized by discretizing the integral equation in depth and assuming a background environmental model for the waveguide. For a fluid model, the background model is constructed by prescribing initial values for sound speed, density, and attenuation in both the water column and the seabed. The inversion method proceeds by making small perturbations to the background sound-speed profile and comparing the resulting eigenvalues with the estimated input values. The background profile is iteratively updated until the eigenvalues of the updated profile agree with the measured input data.

As described, the input data to the inverse algorithm are estimates of modal eigenvalues from the measured complex-pressure field. This is most easily accomplished by considering the far-field approximation to the Hankel transform pair relationship between pressure and the depth-dependent Green's function. Replacing the Bessel function $J_0(k_r r)$ in (4) with its large argument asymptotic form, the Green's function can be approximated by a Fourier transform of the measurement data [3]

$$g(k_r; z, z_0) \sim \frac{e^{i\pi/4}}{\sqrt{2\pi k_r}} \int_{-\infty}^\infty p(r; z, z_0) \sqrt{r} e^{-ik_r r} dr, \quad k_r r \gg 1, \quad k_r > 0. \quad (7)$$

This form is an expression of the Green's function as a horizontal wavenumber spectrum of the product $p(r) \sqrt{r}$. Modal eigenvalues for use as input data to the inverse algorithm are determined by the peak locations in the wavenumber spectrum.

The above discussion was presented assuming a fixed source. However, when the field is excited by a moving source, the potential impact of a Doppler frequency shift must be taken into consideration when interpreting modal wavenumber estimates. The modal solution for propagation in a waveguide for a moving source was considered by Hawker. For a source moving along a horizontal

plane at a constant velocity v_s past a stationary receiver, the modal solution can be approximated by [4]

$$p(r; z, z_0) \sim \frac{\sqrt{2\pi} e^{i\pi/4}}{\rho(z_0)} \sum_{n=1}^{n_{max}} \frac{\phi_n(z_0)\phi_n(z)}{\sqrt{k_n R}} \exp \left[i k_n R \left(1 - \frac{v_s}{v_n^g} \sin \theta \right) \right], \quad (8)$$

where R and θ are the slant range and angle between the source and receiver and v_n^g is the modal group velocity. Compared to the modal summation for a fixed source (5), there is an additional phase term proportional to the ratio of source speed to modal group velocity. The additional term amounts to a Doppler shift in modal eigenvalues that is related to the unshifted wavenumbers by

$$k_n^* \approx k_n \left(1 - \frac{v_s}{v_n^g} \sin \theta \right). \quad (9)$$

This result was verified in [5] where the full time and spatial domain solutions were derived for the problem. It was shown that source and receiver motion contribute in different ways to the time domain and spatial domain solutions. Although, in the time domain solution both source and receiver motion contribute to a Doppler frequency shift, only source motion contributes to a Doppler shift in the wavenumber domain. The asymmetric contribution makes the problem inherently non-reciprocal. In this work, using a towed source, the Doppler shifted modal eigenvalues are the measurement data. In order to use the estimated wavenumber values as input data for inversion, the Doppler shift should be accounted for.

3 Experimental Measurements and Analysis

A detailed overview of the experimental setup is given in [6]. The acoustic field was generated using an omni-directional low-frequency source suspended at a fixed depth and towed at a constant speed. The relative source/receiver geometry shown in Fig. 1 was dominated by the source motion, as the receiver remained nearly stationary over the duration of the measurement.

The acoustic field was measured on a single hydrophone suspended from a drifting buoy while the source was towed at about 2 m/s. The particular data of interest was collected along NW and SE tracks corresponding to segments 2 and 3, respectively. The spatial field at 50 Hz for the entire run, plotted relative to the source positioned at the origin, is shown in Fig. 2. The complex pressure fields (magnitudes and phases) measured over 4 km for the out and back segments of the track near the turnaround point are shown in Fig. 3. Segment 2 refers to data taken along the NW leg where the source/receiver were opening in range, and segment 3 refers to the return leg where source/receiver were closing in range. The modal interference patterns for the two segments, shown in the top of Fig. 3, appeared very similar with only a slight shift in the null locations observable. Other observable differences appeared to be due to noise. The phase shown in the bottom plot is a residual phase obtained by multiplying the original pressure signal by $\exp(-ik_0 r)$ where $k_0 = \omega/c_0$ is a reference wavenumber. The residual phase, or slowed down phase, was used to highlight differences in the phase behavior for the two segments as shown in the figure, where $c_0 = 1500 \text{ m/s}$ and $\omega = 100\pi$ were used. Estimates of wavenumber content with range were determined by employing a high-resolution sliding window-spectral estimation technique using an aperture of 1000 m and 900 m overlap. Details of the estimator and its performance characteristics are given in [7]. Figures 4–5 show wavenumber estimation results for segments 2 and 3 as a function of range. These figures show two dominant modes propagating in range through the waveguide. Determining the peak locations with range from the wavenumber estimates, the evolution of modes 1 and 2 for the out and back track segments are shown in Fig. 6. The data used to estimate wavenumber content for these two segments were collected in roughly the same region of the waveguide. As such, the depth-dependent Green's functions estimated to characterize the bottom should have the same spectral content. However, a clear bias in the wavenumber estimates between segments 2 and 3 was observed over all ranges. The

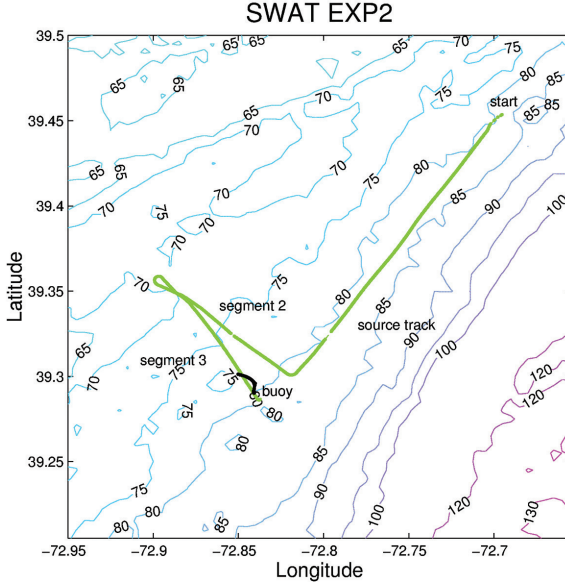


Figure 1. Source/Receiver geometry for entire 50 Hz track. The data of interest was taken along Segment 2 (opening in range) and segment 3 (closing in range). Bathymetric contours are in meters.

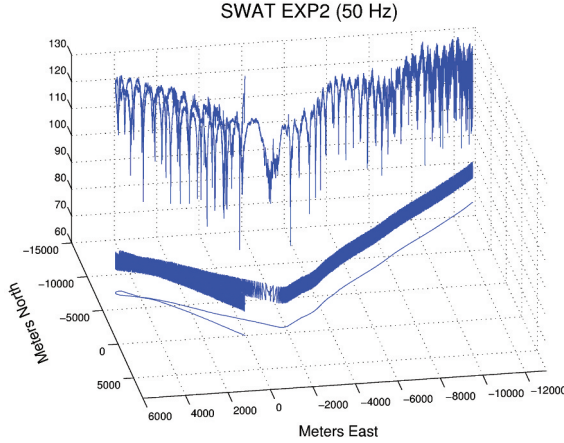


Figure 2. Spatial pressure field relative to source at 50 Hz. Upper is pressure magnitude, middle is phase, and lower is relative receiver position.

bias was consistent with the wavenumber shift for a moving source given by Hawker [4] and also observed by Rajan *et al.* [8].

In order to infer accurate values of bottom geoacoustic properties, the bias in the wavenumber estimates should be accounted for. Returning to Eq. (9), and assuming that the source traveled along a line that extends through the receiver, the measured wavenumbers can be approximated by

$$k_n^* \approx k_n \left(1 \pm \frac{v_s}{v_n^g} \right), \quad (10)$$

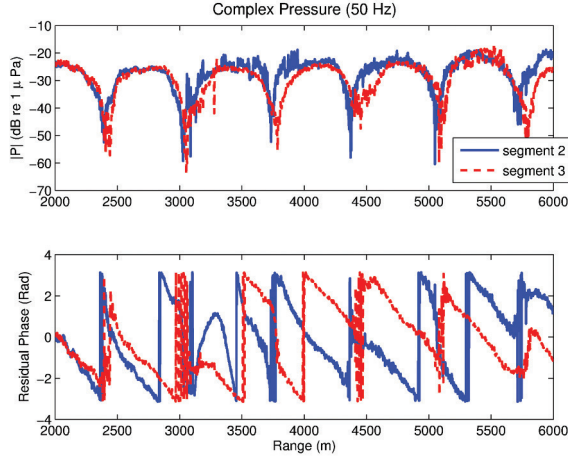


Figure 3. Pressure magnitude and phase at 50 Hz for opening and closing segments of track near turnaround.

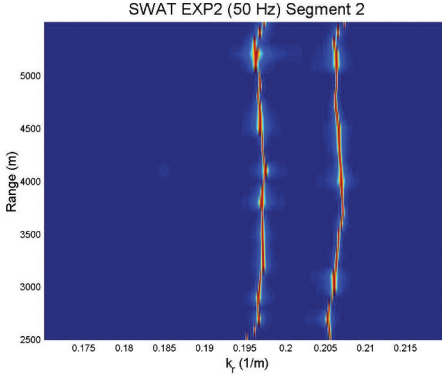


Figure 4. Wavenumber estimation with range along segment 2 for 50 Hz data.

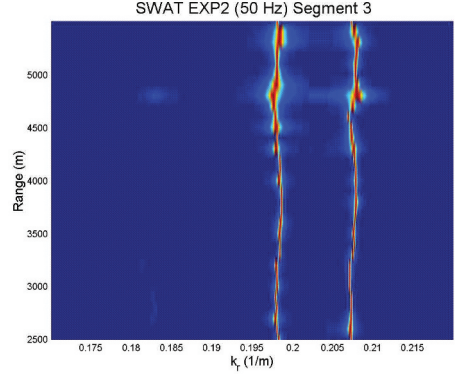


Figure 5. Wavenumber estimation with range along segment 3 for 50 Hz data.

where v_s is the source speed, positive when moving toward the receiver. Using the above and taking advantage of the simple geometry of the experiment, the expected values for the unbiased wavenumbers can be obtained by taking the mean of the biased estimates. Simply stated, for a source moving out and back along the same path at a constant speed, the unbiased wavenumber estimate is obtained by

$$k_n = \left(k_n^{*(v+)} + k_n^{*(v-)} \right) / 2, \quad (11)$$

where

$$k_n^{*(v+)} = k_n \left(1 + \frac{v_s}{v_n^g} \right) \quad (12)$$

$$k_n^{*(v-)} = k_n \left(1 - \frac{v_s}{v_n^g} \right) \quad (13)$$

and v_{\pm} correspond with the relative speeds for the tracks closing and opening in range.

To demonstrate the potential impact of source motion on inversion, both corrected and uncorrected wavenumber estimates were used as input data to the inversion algorithm. To simplify inter-

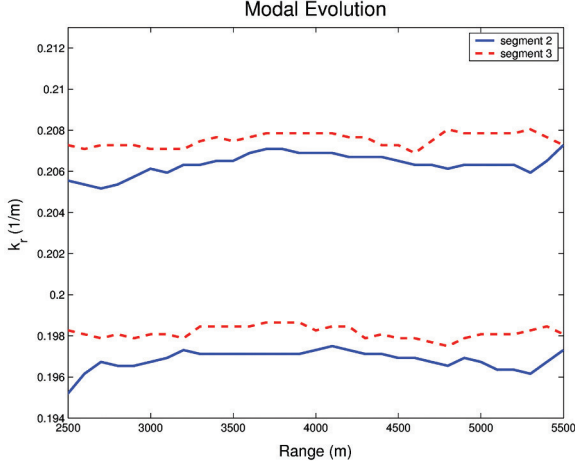


Figure 6. Evolution of modes 1 and 2 with range illustrating bias in wavenumber estimates due to source motion along segments 2 and 3.

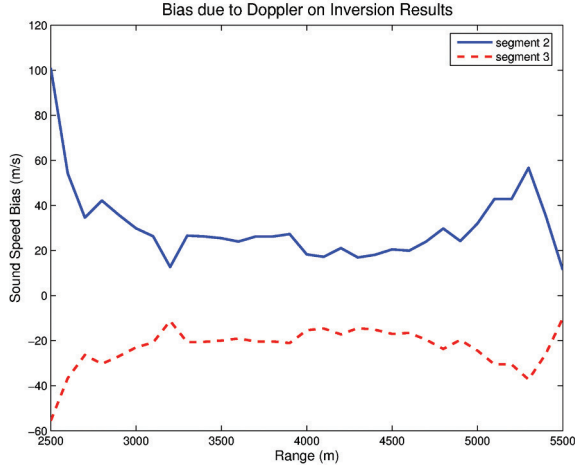


Figure 7. Bias in inferred sound speed for the halfspace with range using uncorrected modal eigenvalue estimates for segments 2 and 3.

pretation of the results, the bottom was modeled as a halfspace. Sound speed in the halfspace was then inferred using the estimated mode values. At each range, the sound speed in the halfspace for the background model was set proportional to the phase speed associated with the highest order mode measured in the experiment at that range. Specifically, the background sound speed in the bottom at each range was equal to $1.01c_{max}$, where $c_{max} = \omega/k_{max}$, and k_{max} was the highest order modal eigenvalue observed at the frequency ω . The inversion process was carried out using both corrected and uncorrected wavenumber estimates. The results obtained using the corrected wavenumber values were subtracted from the uncorrected results obtained at each range. Figure 7 illustrates that for a source towed at the relatively slow speed of 2 m/s the inferred sound speed in the bottom was biased on the order of 20 m/s over most ranges.

The analysis of the Doppler shifted wavenumber data for the simple experimental geometry suggested the possibility of directly computing modal group velocity from measurements made on a single hydrophone. Considering Eq. (10), for a source moving at a constant speed back and forth along the same line, the difference in wavenumbers for the out and back segments is

$$\Delta k_n^* = k_n^{*(v_+)} - k_n^{*(v_-)} = k_n \left(\frac{v_+}{v_n^g} - \frac{v_-}{v_n^g} \right). \quad (14)$$

For the source moving at the same speed along the out and back segments $v_+ = -v_-$ and the above expression can be simplified and solved for the group velocity

$$v_n^g = \frac{2k_n v_s}{\Delta k_n^*}. \quad (15)$$

Combined with the result for correcting wavenumber bias, modal group velocity can be expressed as the ratio of sums and differences of Doppler shifted modal eigenvalues for a towed source

$$v_n^g = \frac{k_n^{*(v_+)} + k_n^{*(v_-)}}{k_n^{*(v_+)} - k_n^{*(v_-)}} v_s. \quad (16)$$

This approach was first applied to the data in the range/wavenumber plot shown in Fig. 6 to extract modal group velocities as a function of range. However, individual results were inconsistent between range steps and highly variable. Taking the range average of the individual results yielded estimates of modal group velocities of 784.4 m/s and 668.9 m/s for mode 1 and mode 2 respectively. Relative to the minimum sound speed in the water column of 1496 m/s, these values were low by a factor of 2 or 3. There were a number of factors that may have contributed to the poor results. A closer look at the track data showed that the source speed was not constant between kilometers 2 and 4 of segment 2. Also, the source tracks did not precisely go over the same section of the seabed. In addition, the receiver was not absolutely stationary over the course of the measurements. Finally, although the acoustic SNR was estimated to be about 20 dB, the data appeared to be contaminated by some other, as yet undetermined, source of interference. The contamination is particularly evident around km 4 in the pressure magnitude data for segment 2 where there is step-function like change in amplitude. Other data sets, taken during the same experiment indicate ship board communications with a shore station may have contaminated the data being transmitted back to the ship over VHF [9]. These factors, along with possible range-dependence in the waveguide environment, combined to produce the variations in modal wavenumber estimates with range shown in Fig. 6. Consequently, the variations in group velocity estimates could be expected as the individual modal wavenumber differences were not constant, or even smoothly varying, as a function of range. The effect is particularly pronounced at the beginning and end of the full data apertures.

Given the unacceptable amount of variation over range, the approach was applied to a single aperture of the measured data between 3500 m and 5000 m. Over this range interval the inferred sound speed biases were near constant and the phase of the acoustic fields appeared well behaved. The estimated (normalized) horizontal wavenumber spectra for the 1500 m apertures of segments 1 and 2 are shown in Fig. 8. From wavenumber estimates for modes 1 and 2 of the two segments, obtained from the peak position locations, modal group velocities were estimated using Eq. (16). The resulting modal group velocities were $v_g^1 = 1440.8$ m/s and $v_g^2 = 1015.0$ m/s. These results were an improvement over the initial results, yet they still appear slow for a waveguide bounded by a halfspace with a velocity ratio near 1.05, as was determined for this data. Pekeris predicts a group velocity for the first mode between 0.98 and 0.99 of the water wavenumber in this case [10].

4 Summary and Conclusions

A Doppler shift in modal eigenvalues was observed for data acquired from a moving source towed out and back along the same track at a slow speed. Using the Doppler shifted values as input data to

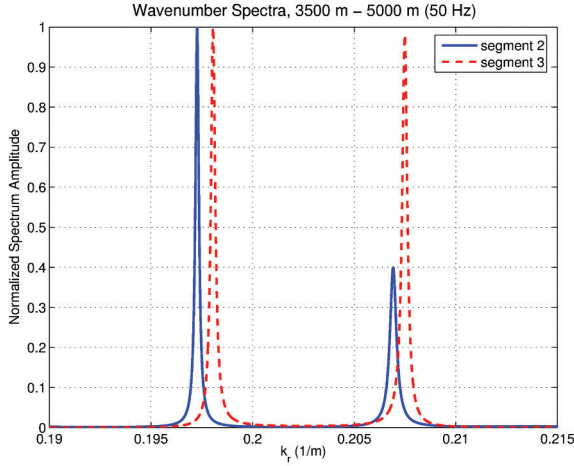


Figure 8. Spectral estimates for single aperture of moving source data. Source speed was 2 m/s.

the inversion algorithm resulted in biased sound speed estimates. This result suggests that inversions based on field data obtained using a moving source are subject to bias in the sound speed estimates of the seabed. Although the seabed properties obtained may be used to model the field data, they may not truly represent properties of the bottom.

For the simple geometry of the experiment, a technique was devised for estimating the unbiased values of the discrete wavenumbers that are used to characterize the waveguide. The wavenumber estimates obtained at each range for the outgoing and incoming source tracks were averaged to obtain unbiased estimates. The approach suggested a wavenumber differencing technique that allows for the modal group velocity to be obtained directly from a measure of the Doppler shifted eigenvalues. This approach, using a single hydrophone, is much simpler than the traditional approach where modal group velocity is determined by integrating the mode functions over the depth of the waveguide [11]. The latter approach, that relies on estimates of both mode shapes and eigenvalues, requires measuring the field on a vertical array of hydrophones that spans the water column and that would ideally extend into the bottom.

Estimating modal group velocities from the experimental data was not entirely successful. The lack of success was attributed to deficiencies in the data, including noise, non-constant source speeds, and non-overlapping source tracks. However, the results of a numerical study for a similar waveguide environment and source speeds were more promising. Acoustic field data synthesized for source speeds of ± 2 m/s and contaminated by random Gaussian white noise with a SNR of 20 dB yielded modal group velocities within 1.3% of expected values. These results suggest future work that would seek to validate these studies by a carefully designed experiment. The field would be created by towing a source out and back along radials from a fixed receiver, or vertical line array (VLA), at constant speed. Care would be taken to ensure that the source was constrained to move out and back exactly over the same section of the seabed. Ideally, the environment would be range-independent or piecewise range-independent over apertures of 1-1.5 km. Accurate phase measurement of the acoustic field would be obtained by tracking the source location using precision GPS and time synchronization of the source signal and data acquisition system. Finally, for measurements made on a VLA, results from individual elements could be compared with group velocities determined using the full array data.

Acknowledgements

This work sponsored by ONR Ocean Acoustics. Data was acquired while doing graduate work at MIT/WHOI under the supervision of Dr. G. V. Frisk.

References

1. Rajan S. D., Lynch J. F., and Frisk G. V., "Perturbative inversion methods for obtaining bottom geoacoustic parameters in shallow water", *J. Acoust. Soc. Amer.*, **82**(3):289-300, 1987.
2. Frisk G. V. and Lynch J. F., "Shallow water waveguide characterization using the Hankel transform", *J. Acoust. Soc. Amer.*, **76**(1):205-216, 1984.
3. Frisk G. V., *Ocean and Seabed Acoustics: A Theory of Wave Propagation*, PTR Prentice Hall, Englewood Cliffs, NJ, 1994.
4. Hawker K. E., A normal mode theory of acoustic Doppler effects in the oceanic waveguide, *J. Acoust. Soc. Amer.*, **65**(3):1979.
5. Schmidt H. and Kuperman W. A., "Spectral and modal representations of the Doppler-shifted field in ocean waveguide", *J. Acoust. Soc. Amer.*, **96**(1):386-395, 1994.
6. Frisk G. V., Becker K. M., and Douth J. A., Modal Mapping in Shallow Water Using Synthetic Aperture Horizontal Arrays, *Proceedings Oceans 2000 MTS/IEEE Conference and Exhibition*, Providence, RI, pp. 185-188 (September 2000).
7. Becker K. M., Geoacoustic Inversion in Laterally Varying Shallow-Water Environments Using High-Resolution Wavenumber Estimation, Ph.D. Thesis, MIT/WHOI, 2002-03 (2001).
8. Rajan S. D., Douth J. A., and Carey W. M., Inversion for the compressional wave speed profile of the bottom from synthetic aperture experiments conducted in the Hudson Canyon area, *IEEE J. Oceanic Eng.*, **23**(3):174-187, 1998.
9. Sellers C. J., *personal communication* (February 2005).
10. Pekeris C. L., Theory of Propagation of Explosive Sound in Shallow Water. In *Propagation of Sound in the Ocean*, Geol. Soc. Am. Mem. **27**(1948).
11. Tolstoy I. and Clay C. S., *Ocean Acoustics: Theory and Experiment in Underwater Sound*, AIP Press, New York (1987).

ACOUSTIC CLUTTER FROM BURIED SUBMARINE MUD VOLCANOES

CHARLES W. HOLLAND, ANTHONY L. GERIG

*The Pennsylvania State University, Applied Research Laboratory,
State College, PA, 16804
E-mail: cwh10@psu.edu*

PIERO BONI

NATO Undersea Research Centre, La Spezia, Italy

Submarine mud volcanoes occur in many parts of the world's oceans and form an aperture for gas (mostly methane) and fluidized mud emission from the earth's interior. Their characteristics are of considerable interest to the geology, geophysics, geochemistry and underwater acoustics communities. The presence of mud volcanoes (and other related gassy sediment structures) has a profound effect on low frequency acoustic reverberation. Reverberation data from the Strait of Sicily indicate high scattering from buried mud volcanoes from 150-800 Hz at ranges of 10 km. The scattering decreases sharply above 800 Hz. Two hypotheses are explored regarding the scattering mechanism, scattering by sediment entrained gas, and scattering from the mud volcano structure itself. Modeling indicates that large bubble sizes (mean radius greater than 1 cm) are required to fit the scattering data, suggesting that this hypothesis may be unreasonable. The scattering from the structure itself appears to be the most reasonable scattering mechanism. The cause of the observed sharp decrease with frequency above 800 Hz in the backscattered response is not presently understood.

1 Background and Objectives

One of the important problems limiting active sonar system performance is the large number of false targets. Frequently, the false targets are due to scattering from discrete features on or in the seabed. Scattering that produces "target-like" returns is called clutter, and geoclutter refers to target-like returns from features of geologic origin. Geoclutter may be classified in two broad categories, 1) clutter produced from bathymetric features, e.g., outcropping rock or ridge structures and 2) clutter produced from features that are at or below the seabed interface. The latter category is the focus of this paper, as they may occur in areas where the seabed is otherwise relatively flat and featureless.

One of the seabed features leading to sonar clutter on the Malta Plateau appears to be submarine mud volcanoes. These and related carbonate mound structures [1] may be completely below, near, or several meters above the surrounding seabed. For active mud volcanoes, (at or above the seafloor) gas is expelled into the water column, and the presence of the gas plume is a potential mechanism

for clutter (only “geoclutter” in the sense that its origins are geologic). Some of the mud volcanoes are buried a several meters under a fine-grained silty-clay that has a lower sound speed than that in the water column (i.e., there is no critical angle, and very low compressional wave attenuation).

Since the sediment above the mud volcanoes is nearly acoustically transparent, these sub-bottom features are a potential source of geoclutter. It is this kind of feature that is the focus of the analysis here.

Mud volcanoes form due to the rise of fluidized sediments along a fault or on top of a seafloor-piercing shale diapir. They may occur in areas of earthquake activity, originate from thick clay beds, usually erupt along fault lines, and often bubble methane gas, and sometimes oil. Although there is a considerable body of literature pertaining to sub-aerial (on-land) mud volcanoes, submarine mud volcanoes are a relatively new research field. They are known to occur both in deep and shallow water and in a variety of geologic settings, including the abyssal parts of inland seas, active margins, continental slopes of passive margins and continental shelves. A recent review article estimates the number of deep-water submarine mud volcanoes at 103-105 [2]. Mud volcanoes studied along the Mediterranean Ridge at water depths ~ 2000 m are of order several 103m in diameter and 102m in height [3]. Deep-water mud volcanoes often are associated with gas hydrates.

Much less is known about shallow water mud volcanoes, and it is anticipated that continued advances in ocean exploration will bring new discoveries of mud volcanoes in areas presently not associated with mud volcanism. The recently discovered mud volcanoes in the Straits of Sicily [1] are much smaller than their deep-water counterparts, of order 10m in diameter and several meters in height. They occur in water depths of 70-170m along the Scicli fault zone, shallow enough so that gas hydrates do not form. The source of the gas is likely to be of order 1000 m below the water sediment interface.

The long-term objective motivating this research is to understand and model the seabed mechanisms that lead to sonar clutter. The main focus of this paper is to demonstrate a correlation between high scattering strength and buried MVs, and to try to determine the dominant scattering mechanism.

The paper is organized in the following manner. Geophysical observations of seabed features on the Malta Plateau are provided in Section 2. In Section 3, acoustic observations of the clutter from long-range reverberation are presented and the sediment features corresponding to the clutter events are described. Sections 4 and 5 respectively explore two hypotheses about the scattering mechanism: sediment-entrained gas bubbles and the structure itself. Conclusions are presented in the final section. Here goes the introduction.

2 Malta Plateau description

The Malta Plateau occupies the northern edge of the North African passive continental margin and is a submerged section of the Hyblean Plateau of mainland Sicily. A discussion of the geology of this area, along with seismic reflection data can be found in [4, 5]. The region (see Figure 1) is divided by the Ragusa Ridge, roughly defined by depths shallower than 110 m, which forms a spine ~ 20 km wide between Sicily and Malta. The area west of the ridge is blanketed with a silty-clay sediment, which thickens from about 1m at 150 m water depth to about 8m at the 100m contour.

While clutter and masking is observed from the Ragusa ridge, reverberation measurements show numerous clutter events, which appear west of the ridge, where the seabed is flat and thickly sedimented. High-resolution sub-bottom profiler and sidescan surveys in this area (west of the ridge) have shown the presence of numerous structures associated with gas. An example of such features as detected on seismic reflection and co-located sidescan data are shown in Figs. 2-3. In Fig. 2, the three conical structures at the water-sediment interface between 4-6 km range are believed to be mud volcanoes. The raw seismic reflection data (Fig. 2 inset) show reflection and/or scattering in the water above one of the cones, which may be gas escaping from the sediment into the water.

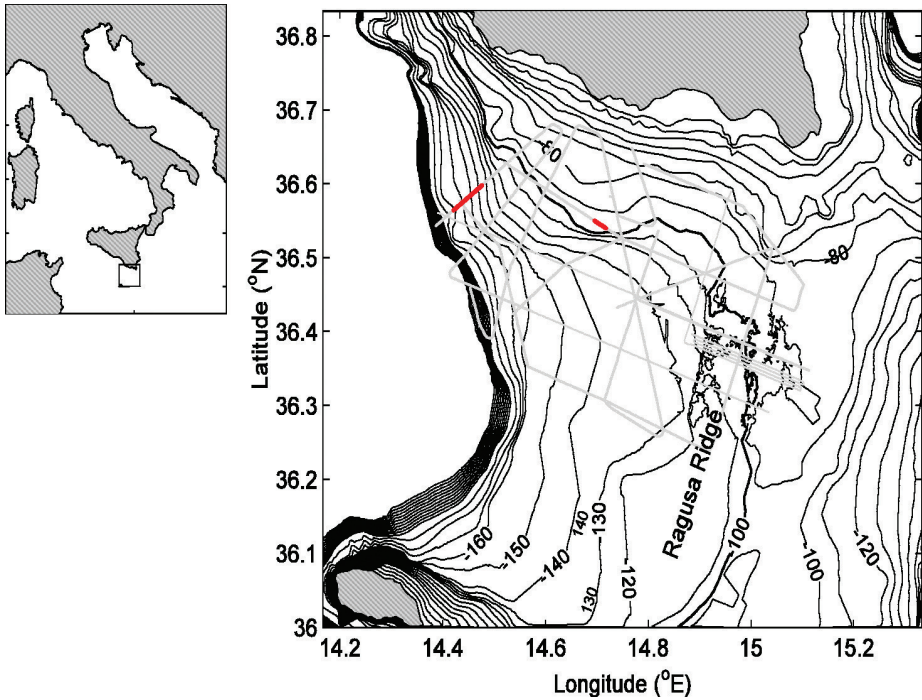


Figure 1. Malta Plateau study area between Sicily (to the north) and Maltese island of Gozo (to the south). Seismic reflection survey, tracks are indicated by grey lines, depths are in meters. Seismic reflection survey lines of interest for this paper are indicated by the solid red line with a NE bearing (Figure 2) and the red line with a NW bearing (Figure 7).

Co-located sidescan data (Fig. 3) show regions of high scattering at the three main locations, corresponding to the locations of the cone-like structures of Figure 2. The sidescan data reveals two scales of features: clusters of truncated cylinders roughly 10 m in diameter rising as high as 4 meters above the seafloor, and surrounding these, high scattering strength patches of order 50 m in diameter. While in the seismic reflection data (Fig. 2 inset) venting gas is visible out of only the southern-most cone, the raw side-scan data (e.g., Figure 4) indicate that gas is venting from all three. The reason that the seismic reflection data (Figure 2) show the features as cones instead of truncated cylinders as apparent from the shadows of Figure 5, is that the source has a wide beamwidth and tends to integrate or “smear out” any large local slopes and “smear in” out-of plane scatterers. The truncated cylinders observed at this location appear to be mud volcanoes [1].

Figure 2 not only clearly shows the surficial mud volcanoes, but also several that are buried below the water-sediment interface. There are two buried mud volcanoes at 4 km range, one ~ 2 meters sub-bottom and the second ~ 20 meters sub-bottom; there are several small mud volcanoes at 20m sub-bottom between 5 and 6.5 km and several near the acoustic basement interface. These mud volcanoes were imaged “by chance” in the sense that the survey line spacing (of order 1-10km) is much greater than the scale of the features. Thus, it is believed that there are likely to be many more submarine mud volcanoes on the Malta Plateau in addition to those already reported.

3 Clutter Observations

Long-range reverberation data were acquired in April 1998 using impulsive (Sound Undersea Signal, SUS) sources at 91 m depth. The primary advantage of the impulsive sources is the broad frequency

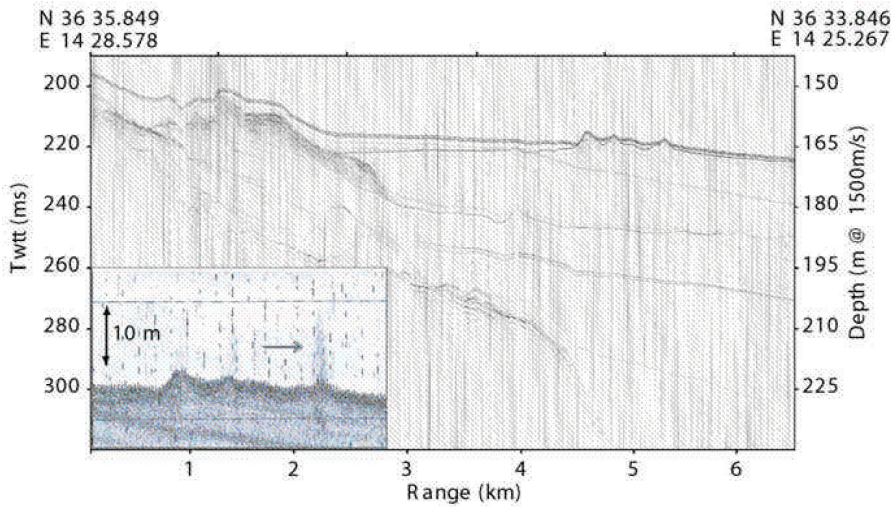


Figure 2. Swell-filtered seismic reflection data (track is along solid line in Figure 1) showing cone-like features (between 4–6 km) on the seabed. Vertical exaggeration is $\sim 40:1$. Raw seismic reflection data (inset) show evidence of venting gas from at least one of features.

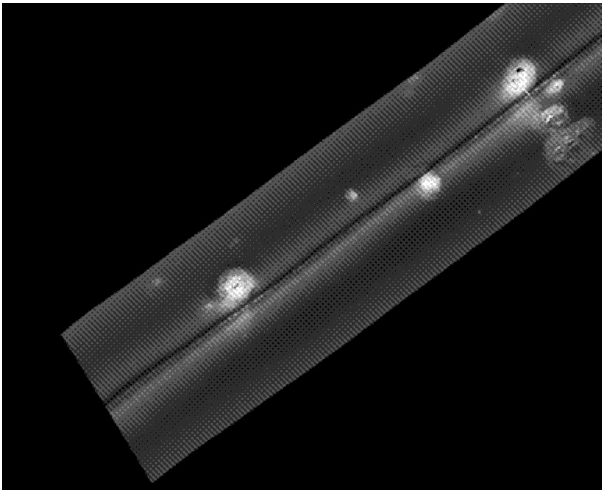


Figure 3. Geo-referenced (north is up) 100 kHz side scan image over the same track as Fig 2a. White indicates high scattering, and the main three scattering regions closest to the tow track center-line correspond to the three features of Fig 2. The track length is ~ 1 km, and the cross-range dimension is ~ 320 m.

coverage. That is, the frequency dependence of the observed clutter contain clues that may reject or support potential scattering mechanisms. The receiver was a 3-aperture nested array of 256 elements with element spacings of 0.5, 1 and 2 m towed at a depth of ~ 50 m.

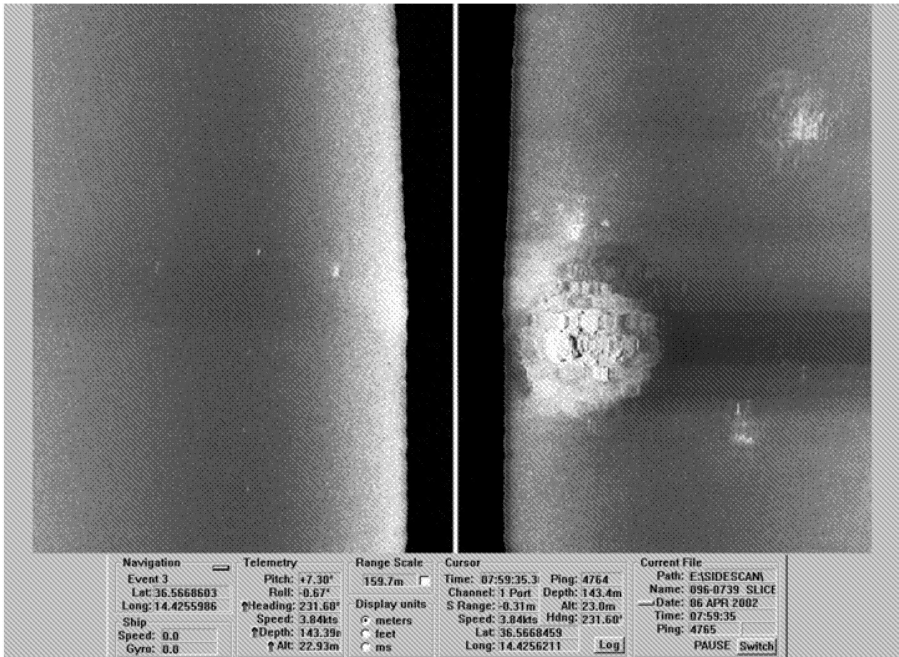


Figure 4. Raw 100 kHz sidescan data at the southern cone-like feature of Figure 3. The scale is 320 m in cross-range with approximately square pixel size; white indicates high scattering. The dark shadow behind the mud volcano is interpreted to be caused by attenuation due to venting gas.

The reverberation data were collected near the center of the study area (see Figure 8) at 5 minute intervals. The study area (Straits of Sicily) is subject to heavy merchant ship traffic. Noise generated from nearby vessels sometimes precluded observation of clutter events of interest. During the reverberation measurements, transmission loss, XBT, seismic reflection and wind speed data were collected. The low wind speeds during the measurement period (1-6 m/s) suggest that the reverberation was not dominated by sea surface scattering.

Broadband reverberation (100-1800 Hz) from SUS charges and a 128 element (0.5 m) aperture with Hanning shaded beams is shown in Figure 6. The data have a time varying gain correction to aid in visualization of clutter events far from the source; the units are relative decibels. The left-right ambiguity from the array is clearly seen; the array heading is roughly west northwest. Resolving the ambiguity was performed by measuring reverberation at a variety of positions and array headings. The highest return in Figure 6 is from a nearby tanker (the noise from the tanker is visible along the entire radial). Also visible are returns that correspond to the position of 2 mud volcanoes. The southernmost mud volcano cluster is actually buried approximately 3m sub-bottom (see Figure 7, feature at a ~1 km). A sidescan survey indicated that actively venting mud volcanoes are not part of the cluster. It is reasonable, however, to expect that sub-bottom features may produce clutter since the sediments above the mud volcanoes are nearly acoustically transparent (0.98 sound speed ratio, 1.3 density ratio, see [6]).

Multiple reverberation measurements were conducted along a track (see Figure 8) 8-10 km away from the sub-bottom features. The spectral characteristics of the clutter events were obtained by a simple sonar equation approach in order to factor out the frequency dependence of the source and the two-way propagation. The target strength (TS) of the clutter was computed as

$$TS = RLSL + TL_1 + TL_2 \quad (1)$$

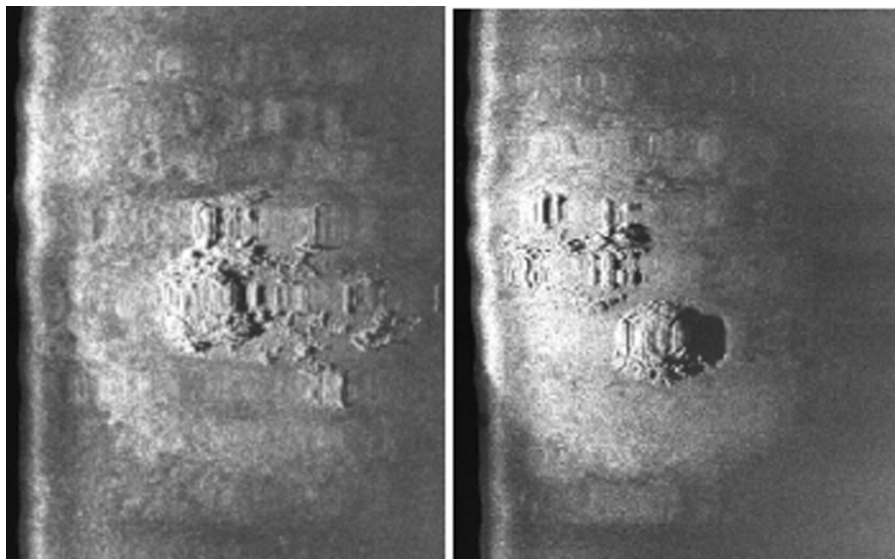


Figure 5. Raw 384 kHz sidescan data at the southern cone-like feature (left) and northern feature (right) of Figs. 2, 3. The scale is 50 m in cross-range with approximately square pixel size; white indicates high scattering. The mud volcanoes are approximately 10m in diameter.

where RL is the received level, SL the source level and $TL_{1,2}$ are the propagation losses to and from the scatterer. Although no propagation data were available along this bearing, there were upslope and downslope measurements nearby (see Figure 9).

In addition to the spectral characteristics of the clutter event, the spectral characteristics of the background reverberation (immediately before the clutter event) were also processed. A comparison between the two spectra provides an indication of the relative strength of the clutter event. The actual process responsible for the “background reverberation” (dashed line in Figure 9) is scattering, thus it would normally be referenced to as scattering strength. However, the data were left as “nominal target strength” so they could be used to determine when the clutter event was significant relative to the background reverberation. Below about 750 Hz, the clutter mechanism (solid line) dominates above the local scattering phenomenon. The target strength data were averaged over a 60 Hz sliding window.

There are at least four possible mechanisms that could give rise to the observed scattering. The first is scattering from bubbles entrained in the sediment around the mud volcano. Second is scattering from the mud volcano structure itself. Third is scattering from bubbles in the water column. However, given that a sidescan survey showed that there are no active MVs or pockmarks within the clutter area, the latter mechanism seems unlikely. The fourth mechanism is scattering from fish. This mechanism also seems unlikely, due to data from extensive surveys during this and later experiments. In the following two sections, the first two hypotheses are explored.

4 Acoustic estimation of bubble size distribution

One of the potential mechanisms for the observed clutter from the buried mud volcano (Figure 6) is scattering from sediment-entrained bubbles in the vicinity of the buried mud volcano. If bubbles are the dominant mechanism, their size distribution can be estimated by fitting the observed target

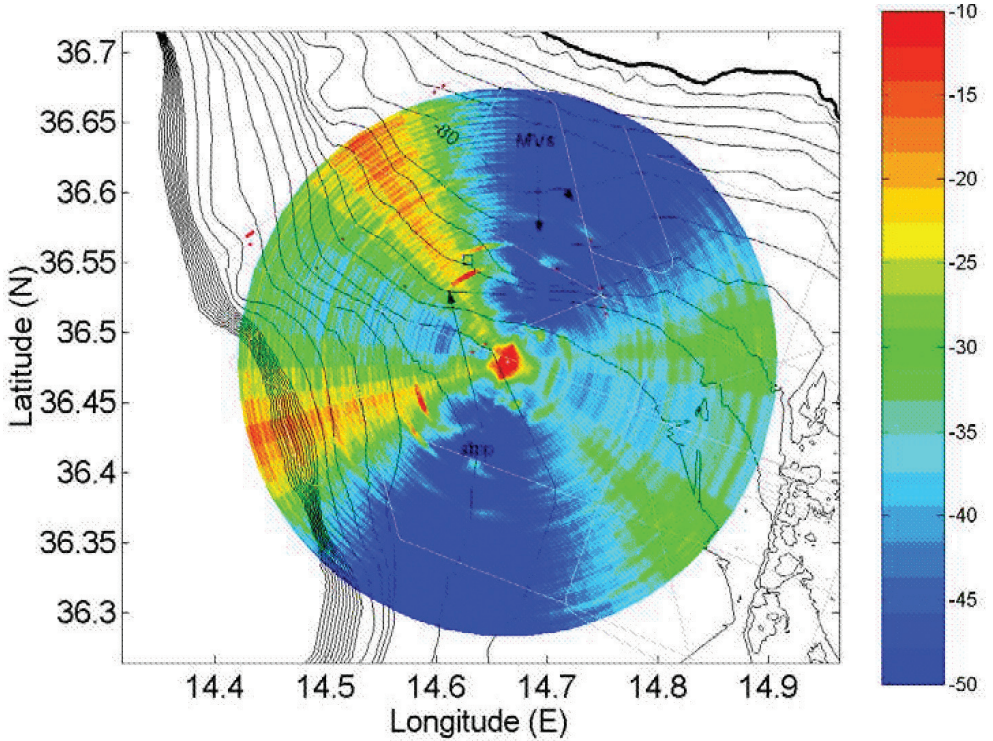


Figure 6. Broadband reverberation (relative dB) from SUS in the Straits of Sicily. The island of Sicily is in the upper right hand corner. The data have a time varying gain. There is a left-right ambiguity in the figure around the axis of the towed array. The strong radial line to the northwest is from a ship (tanker) tending the Campo Vega oil rig (box). The reverberation return from two mud volcanoes (MV's) are indicated by the arrows. MV's are indicated by dots.

strength with a model. We first describe the geoaoustic properties of the host sediment and then the target strength model.

4.1 Sediment Geoaoustic Properties

In order to model the scattering from sediment-entrained gas, estimates of the sediment geoaoustic properties are required. Analysis of seabed reflection data at a nearby site [6] yielded the following sediment densities, velocities and attenuations, $\rho_1 = 1.32 \text{ g/cm}^3$, $c_1 = 1480 \text{ m/s}$, and $\alpha_{dB} = 0.01 \text{ dB/m/kHz}$ at the water-sediment interface. Further analyses has shown that the velocity has a weak gradient $O(10^0) \text{ s}^{-1}$ over the upper few meters and can be neglected. The density has a much larger gradient and is $\sim 1.5 \text{ g/cm}^3$ at 1.5 m depth.

Analyses of reflection data show that the shear speed near this site is low, between 0-60 m/s [7]. In-situ surficial measurements in the Italian littoral with similar compressional velocity and density ratios yield shear speeds of $\sim 25 \text{ m/s}$ [8].

The shear modulus is also required at the depth of the bubble layer, which can be obtained from the density and estimates of the shear velocity. The bubble layer depth is estimated from seismic reflection data to be at approximately 3 m sub-bottom. Since the real part of the shear modulus has a significant impact on the bubble scattering cross-section, two extreme values: 1e6 Pa (corresponding

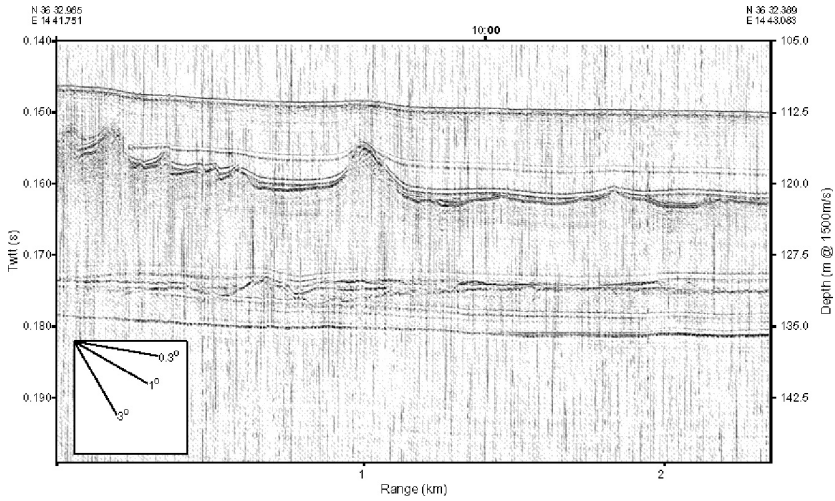


Figure 7. Seismic reflection data along a WNW track showing the mud volcanoes at 4 km corresponding to the southernmost MVs shown in Figure 6. The track location is shown in Fig. 1.

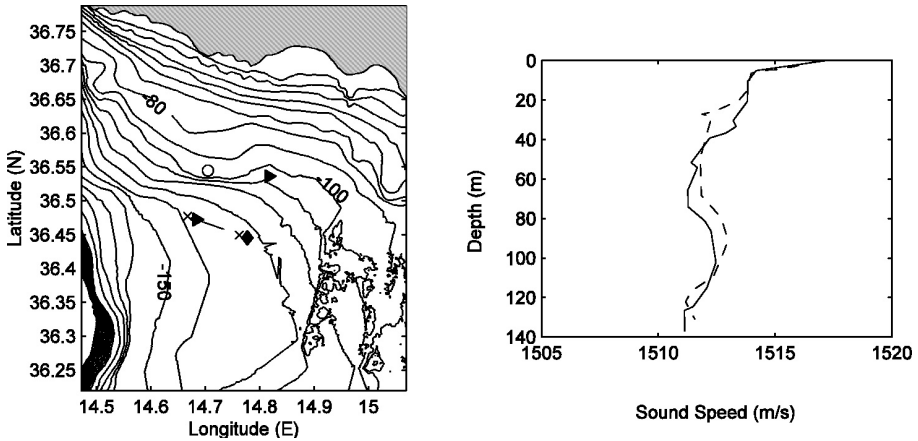


Figure 8. (left) location of source/receiver for reverberation measurements (along solid line), position of receiver for propagation (\blacklozenge), SUS position for downslope and upslope propagation (\blacktriangleright), mud volcanoes (\circ), XBT casts (\times); (right) sound speed profiles along reverberation track near the start of track (solid), near end of track (dashed). Track goes from east to west.

to $v_s = 25$ m/s) and $2e7$ Pa ($v_s = 110$ m/s) were selected to bound the problem. The lower bound assumes no shear gradient in the upper 3 meters, the upper bound was obtained from an empirical equation ($v_s = 78.99z^{0.312}$, where z is depth [9]). The imaginary part of the shear modulus is also required in the model but has a negligible impact on the predictions for reasonable values; values of one-tenth the real part were chosen in the simulations.

While the finite sediment rigidity has a profound effect on the bubble scattering cross-section, it has a nearly negligible effect on acoustic propagation into, and through the sediment (see next section).

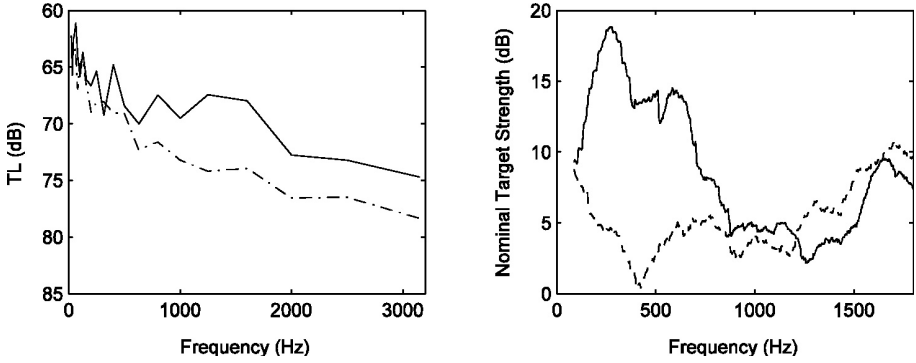


Figure 9. (left) upslope (solid) and downslope (dash dot) propagation loss at 9.2 km for both directions (see Figure 8 (left) for location); (right) nominal target strength for clutter event (solid) and reverberation just before clutter event (dashed).

4.2 Target Strength Model

The target strength, $10 \log(\zeta)$, from a thin layer of sediment-entrained bubbles in the Born approximation is:

$$\zeta = e^{-4\alpha f d} T_{\pi}^2 \int_0^{\infty} a^2 \left(\left[(f_R(a)/f)^2 - 1 \right]^2 + \delta^2 \right)^{-1} n(a) da \quad (2)$$

where the first factor accounts for attenuation α at frequency f along path length d in the sediment. Attenuation is assumed to vary linearly with frequency, which is reasonable for a silty-clay fabric [9]. The factor T_{π}^2 is the two-way power transmission coefficient across the water-sediment interface:

$$T_{\pi} = 4 \frac{\beta \cos \theta_1 / \cos \theta_0}{(\beta + \cos \theta_1 / \cos \theta_0)^2} ; \beta = \rho_1 c_1 / \rho_0 c_0 \quad (3)$$

where the subscripts 0,1 refer to the water-column and sediment respectively. Transmission coefficient calculations show that the fluid-fluid model and fluid-solid models are nearly identical for the low shear speeds at this site. The integrand in Eq (2) is the scattering cross-section [10, 11], scaled by the bubble size distribution $n(a)$ of units $1/m$ where a is the bubble radius, f_R is the resonance frequency of the bubble, and δ accounts for the bubble damping due to radiation, thermal and viscous losses. This expression for target strength has several differences¹ with the gassy sediment scattering models in [12] and [13].

Methane was assumed to be dominant gas inside the bubble and the bubble size distribution was assumed to follow a gamma distribution, i.e.,

$$n(a) = \frac{a^p e^{-a/g}}{g^{p+1} p!} \quad \mu = g(p+1), \sigma = \mu/(p+1)^{1/2} \quad (4)$$

where μ and σ are the mean and standard deviation. This distribution is convenient because it allows for a variety of distributions from exponential (at $p=0$) to Gaussian at large p values.

In order to estimate the attenuation and the transmissivity factors in Eq(2), five degrees was chosen as reasonably representative of the grazing angles in the reverberation data. While obviously simplistic, a single angle is probably adequate because 1) the attenuation term is expected to be small (~ 0.25 dB at 1 kHz at 5°) and 2) the transmissivity (assuming a single interface between the seafloor and the bubbles) is small and frequency independent, ~ 1 dB at 5° . Thus, the estimate of the bubble size distribution may be biased based on a poor choice for average angle, but the shape of the distribution should be roughly correct.

There is evidence that sediment entrained bubbles larger than a few millimetres are often coin-shaped rather than spherical [13, 14]. The large aspect ratio bubbles can be incorporated into the above model by defining an effective radius, which is proportional to the square root of the surface area ratio, γ , between the non-spherical bubble and a sphere of equal volume [13]. The effective pressure at the bubble layer is scaled by the same ratio cubed. The effect of non-spherical bubbles is that they reduce the resonant frequency and increase the target strength relative to a spherical bubble. The magnitude of the effect depends upon several parameters, but most importantly in this case, the shear modulus. In order to show the interconnected effects of the sediment shear modulus and the bubble sphericity, model simulations were compared to the measured target strength varying both the shear modulus and the sphericity. In [13] it is shown that γ is proportional to bubble size. Using CT image data from a core yielded $\gamma \sim 5$ for the equivalent radii of 0.7 cm, and this value was employed as a lower bound in non-spherical simulation. $\gamma = 5$ corresponds to an oblate spheroid with a ratio of major/minor axes of $100/\pi$.

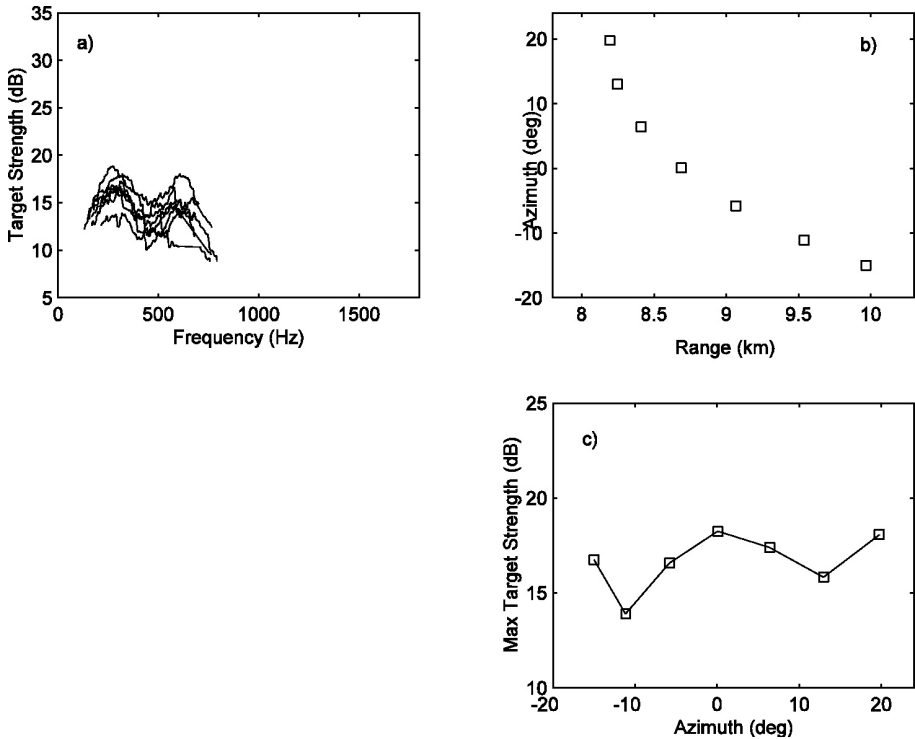


Figure 10. Comparison of multiple observations of clutter from mud volcano: top left, target strength data; top right, the dependence on range and azimuth from source/receiver to the mud volcano, bottom right, azimuthal dependence of maximum target strength.

For the non-spherical bubble, reasonable fits to the mean TS data were made for the upper and lower bounds of the shear moduli (see Figure 11, top left). Fitting parameters are given in Table 1. Though the fits are reasonable for both simulations, the underlying distributions for each assumed shear modulus are clearly different, reflecting the sensitivity to shear modulus. The number of bubbles (per cm bin) is shown in Figure 11, top right. Reasonable fits were also made assuming spherical bubbles (see Figure 11, bottom left-right). The model results show the dependence of bubble sphericity on shear modulus; sphericity has a small effect for low shear modulus, but a

rather significant effect when the shear modulus is large. The large bubbles near the mud volcano are believed to be non-spherical, so that Figure 11, top is probably more representative than Figure 11, bottom.

The reverberation data (Figure 6) indicate that the scattering is occurring over a broad area, roughly 1 km². Target strength is computed using the pixel with the maximum response. Since beamwidth is a function of frequency, theinsonified area is also a function of frequency. At 325 Hz, the cross-range pixel width is ~ 1 km, which decreases to ~ 500 m at 650 Hz. If the bubble distribution was spatially uniform, there would be a 3 dB decrease in TS over that octave due to beampattern effects. This possible frequency dependence has not been accounted for in the processing. The evidence indicates that the distribution of gas is patchy, and centered around the mud volcano clusters (see Figure 7 and Figure 3, though the latter is from a different location). As a rough estimate the, the modeled bubble size distribution pertaining to a single pixel might contain ~ 1 -3 clusters.

Although the actual sphericity is unknown, the modelling indicates that the mean bubble radius is 2.6-4 cm. For larger , the mean radius for the upper bound shear modulus continues to decrease toward 2.6 cm and the lower bound shear modulus is insensitive to changes in . Thus, if the lower bound for is correct, the range of possible bubble size distributions is reasonably well-constrained. In addition to uncertainties about bubble sphericity and sediment shear modulus, the TS data themselves have some uncertainty associated with them. As a rough estimate, the TS data has an uncertainty of ± 5 dB, assuming an uncertainty in the source level of 2 dB and 3 dB for each TL term. It is believed that this uncertainty is largely a bias and mainly affects the total number of bubbles (by factor of ± 3) rather than the distribution itself, although there is some uncertainty in the distribution induced by uncertainty in the beam pattern effects. The estimated total number of bubbles and the associated volume of sediment-entrained gas are given in Table 1.

Table 1. Fitting parameters (μ, σ) used to fit the sediment-entrained gas model with target strength data in Figure 11. Resulting bubble size distribution statistics are also provided.

γ	Shear Mod (Pa)	mean radius μ (cm)	std dev (cm)	# bubbles	total volume (m ³)
5	$2 \cdot 10^7$	4	2.8	720 0.55	
5	10^6	2.6	1.8	1150 0.24	
1	$2 \cdot 10^7$	7	4.9	830 3.5	
1	10^6	2.6	1.8	2000 0.45	

Table 2. Sediment properties for scattering calculations.

	Compressional Speed (m/s)	Comp. Attenuation (dB/m/kHz)	Shear Speed (m/s)	Shear Attenuation (dB/m/kHz)	Density (g/cm ³)
Sediment	1480	0.01	-	-	1.32
Sphere 1	2200	0.1	1000	20	2.2
Sphere 2	4000	0.02	1800	3	2.2

5 Scattering from the mud volcano structure

In this section, we examine the hypothesis that the scattering mechanism was the mud volcano structure itself. The carbonate mounds associated with the mud volcano have been observed visually as well as acoustically and very approximately resemble truncated cylinders, at least the features above

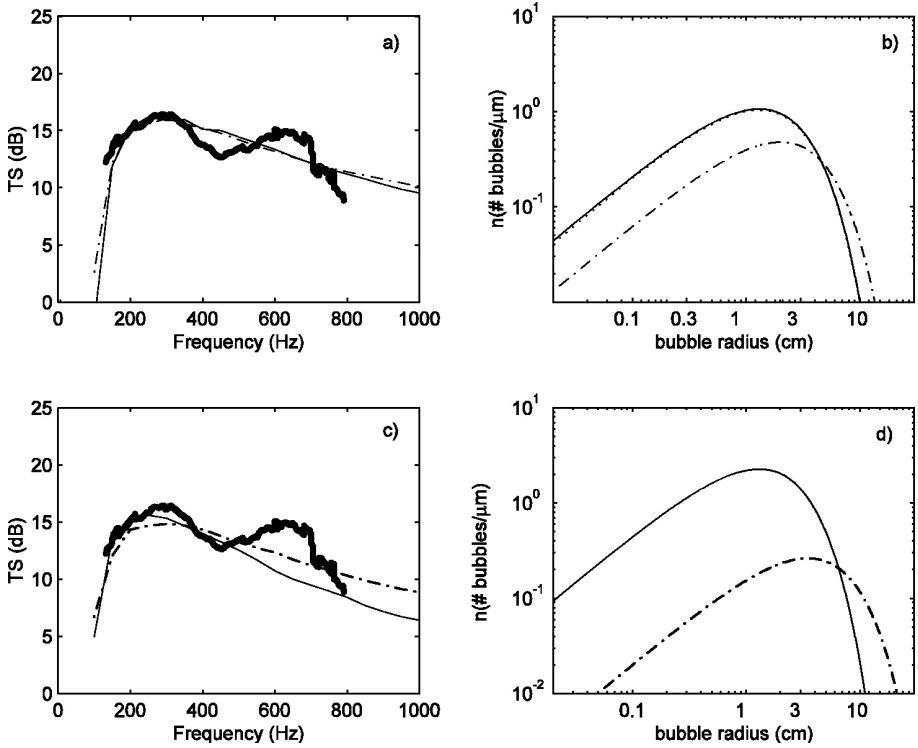


Figure 11. Relationship between sediment bubble size distribution and target strength assuming sediment shear modulus of $1e6$ Pa (black solid) and $2e7$ Pa (chain dash); (top left) modeled TS ($\gamma = 5$) and measurements at the buried mud volcano site (grey solid line); (top right) modeled bubble number density, $\gamma = 5$; Bottom left-right same as Top, except for spherical bubbles, $\gamma = 1$.

the water sediment interface. The mounds are of consolidated material and appear to be massive outcrops in some cases (reef-like) and in other cases mounds of sub-meter scale consolidated slabs. The carbonate mounds may be also connected to a carbonate pavement (the high scattering from a ~ 30 m diameter region in Figure 5, right, may be from such a pavement), but this is uncertain, especially for the buried features. In order to make a first order estimate of the scattering, we employed a first-order model for the mounds treating them as solid spheres in a host fluid sediment material.

A very simple model is used to treat the effects of the sediment layers. The feature is assumed to be in an infinite halfspace of sediment so that the modeled target strength from the sphere s can be approximated by

$$\zeta_S = e^{-4\alpha f d} T_\pi^2 \sigma_d \quad (5)$$

where σ_d is the differential backscattering cross section of the sphere. The formalism of [15] was employed for the scattering calculation. His closed-form solution requires summation of spherical Hankel function-Legendre polynomial products from order zero to infinity. Convergence was obtained when terminating the sum at order fifty for the frequency range and physical size of the scatterer under consideration. The fact that the calculations were done in the far field permitted the use of asymptotic expressions for the spherical Hankel functions.

Target strength observations from this feature generally show a rapid increase in the measured target strength to a peak at about 250 Hz (see Figure 9, right, and Figure 10). At frequencies above this peak, the target strength generally decreases slowly or is roughly constant until about 750 Hz.

This kind of behavior is similar to scattering from a sphere, where at low frequencies (below $ka \sim 1$ where k is the wavenumber and a the radius) the scattering strength drops off rapidly (as $(ka)^4$).

For a lossless fluid sphere of radius 2.5 m, the free-field differential scattering cross-section above a few hundred Hz is near 0 dB. For penetrable, solid, lossless, spheres of material properties bounding reasonable values for the carbonate material (see Table 2), the free-field d is ~ 10 dB larger (see solid lines in Figure 12). The large increase in DSC is due to the presence of shear resonances. The results in Figure 12 show that the loss-less d values are similar, despite the wide difference in carbonate properties. For the lossy case, compressional attenuation in the host material and scatterer have only a modest effect on the predicted scattering (smoothing out the resonances somewhat and lowering the overall levels by a few dB at the highest frequencies). Shear attenuation, however, has a significant effect and is shown in Figure 12 in the dashed lines. As shear attenuation increases, the scattering approaches the fluid sphere (shown in the dotted line).

The 2.5 m radius was chosen based on the rapid rise in the measured TS data, peaking at about 250 Hz (see Figure 9, right, and Figure 10). Smaller spheres of the same composition would peak at higher frequencies and lower levels. Since the seismic data indicate that besides the largest mud volcano, there are several other smaller features, we summed together several spheres incoherently to mimic the presence of multiple features. A flat distribution was assumed between 1 and 2.5 m and the results for multiple volcanoes (spheres) are shown in Figure 13. The predictions for the cases 1 and 2 of Table 2 were averaged over a 60 Hz band, like the measurements. The effects of attenuation and the transmission coefficient are expected to be small, ~ 1 dB, and were not included in the comparison. For the material parameters of case 1 and case 2, about 90 spheres and 20 spheres respectively were required to fit the data (see Figure 13, left). For the same cases, if the shear attenuation is set to a smaller value (0.5 dB/m/kHz), the number of volcanoes required to fit the data is smaller, ~ 10 (see Figure 13, right). This number seems much more reasonable, based on the relatively few numbers of features observed in the sub-bottom profiler data, however, we have no independent estimate of the shear attenuation in the carbonate mounds.

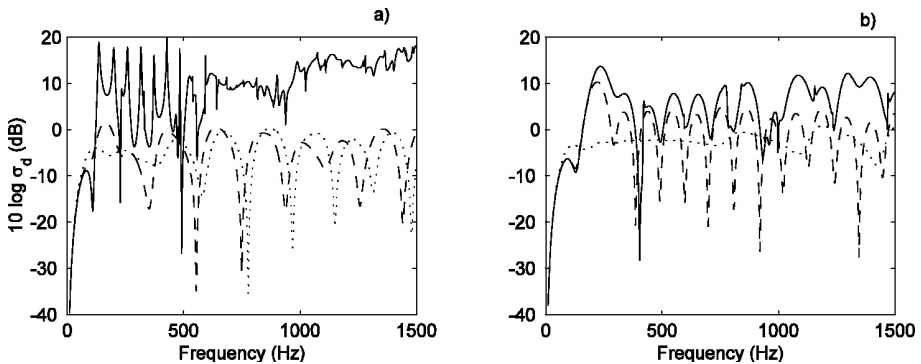


Figure 12. Free-field target strength for a sphere in a host fluid medium. The host fluid and scatterer properties for case 1 and case 2 are given in Table 2. Left: case 1 no attenuation (solid), attenuation (dashed) and fluid sphere (dotted); Right: case 2 no attenuation (solid), attenuation (dashed) and fluid sphere (dotted). Model results have not been averaged over frequency.

Below 750 Hz, there is reasonable agreement between the scattering model and the data (see Figure 13). However, above 750 Hz, the measured TS drops off very rapidly. Scattering from a sphere can not explain this behavior since the scattering increases rapidly up to about $ka \sim 1$, and then oscillates about a more or less fixed value. The sediment appears to be homogeneous near the feature and so the two-way transmission coefficient should be independent of frequency; moreover from the previous section T^2 is expected to be small, of order 1 dB. The most obvious reason for a

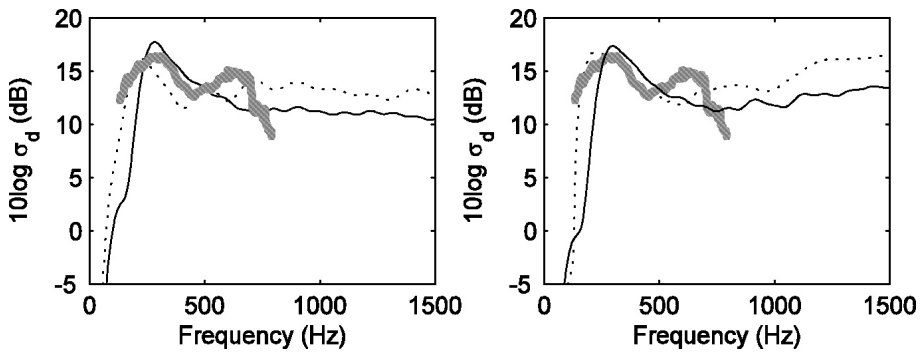


Figure 13. Comparison of measured target strength (grey solid) with model results assuming a distribution of (left): 90 and 20 spherical scatterers for case 1 (dashed) where $N = 90$ and case 2 (solid) respectively; and (right): 10 spherical scatterers for both case 1 (dashed) and case (2) but with the shear attenuation set to 0.5 dB/m/kHz.

strong decrease in frequency is due to attenuation in the sediment. However, to match the fall-off of the data, attenuation values of 1-10 dB/m/kHz are required. There is evidence (at least at a nearby site) that the attenuation is 2-3 orders of magnitude smaller than that. Thus, attenuation seems like an unlikely possibility, unless the sediment surrounding the feature has been greatly altered and is materially different from the sediment at nearby sites. If this were the case, (i.e., that the attenuation was large) then many more spheres would be required for reasonable fits to the data based on the shear attenuation in Table 2. In summary, model predictions fit the data with a reasonable number (~ 10) of spheres if there is a small silty-clay compressional attenuation (0.01 dB/m/kHz) and a carbonate shear attenuation less than ~ 1 dB/m/kHz.

6 Discussion and Conclusions

While there are no independent estimates of the bubble size distribution, the large bubble sizes (> 1 cm) required to fit the data suggest that the inversion results are probably unreasonable. While bubbles may exist in the sediment, such large dimensions seem unlikely. Scattering calculations from the carbonate mound itself, seem to provide a more reasonable explanation of the scattering mechanism. In the scattering calculations, the carbonate mound was treated as a solid sphere ranging in radius from 1-2.5 m. These radii seem consistent with the observations² since the target strength should be proportional to the cross-sectional area of the scatterer, and nearby mud volcanoes have cross sectional areas ranging from $\sim 110 \text{ m}^2$. Measurements of compressional attenuation in the host material and shear attenuation in the carbonate could help validate the scattering hypothesis.

An important clutter mechanism in the Malta Plateau appears to be associated with mud volcanoes, i.e., conical structures whose peak may be completely below or near or even slightly above the surrounding seabed. Scattering from these features is observable even when they are buried several meters below the water-sediment interface. The most likely scattering mechanism appears to be from the carbonate mound itself. Another possible scattering mechanism is scattering from gas released into the water column. However, given that a sidescan survey showed that there are no active MVs or pockmarks within the clutter area, the latter mechanism seems unlikely.

Acknowledgements

The authors thank the Office of Naval Research and the NATO Undersea Research Centre who supported this research as well as the captain and entire crew of the R/V Alliance for their skill and

dedication during the data collection efforts. Peter Nielsen is gratefully acknowledged for his role as Chief Scientist during two of the experimental campaigns (Boundary2002 and Boundary2004). We also thank Tony Lyons for helpful discussions on bubbles in marine sediments.

Notes

1. Eq.(2) is similar to that used in [12] except that it treats a thin scattering layer rather than a distribution in depth and Eq.(2) is solved numerically eliminating the a priori assumption that only bubbles close to resonance contribute to the scattering. [12] uses a factor of 2 in the exponent of the attenuation term (see their Eq.(12)), however, since scattering cross section is an intensity quantity and the units of the attenuation are for a pressure quantity, their Eq.(12) is missing a factor of 2. Another potential difference is their treatment of the transmission losses across the interface which they treat as a reflection loss (in the commonly used definition of reflection loss their term is incorrect and should be two-way transmission loss). Eq.(2) is also similar to [13] except that
 - they treat a bubble size distribution with depth,
 - their solution (see their Eq(8)) also has a factor of 2 error in the exponent associated with the attenuation, and
 - they neglect the transmission coefficient across the boundary.
2. The sidescan data provides the most accurate measure of size. Because of the wide beamwidth of the seismic reflection source, the seismic reflection data “smear out” the true scales of the features.

References

1. Holland C. W., Etiope G., Milkov A. V., Michelozzi E. and Favali P., Mud P.,volcanoes discovered offshore Sicily. *Marine Geology* **199**, 1–6 (2003).
2. Milkov A.V., Worldwide distribution of submarine mud volcanoes and associated gas hydrates. *Marine Geology* **167**, 29–42 (2000).
3. Cifci G., Limonov A., Dimitrov L. and Gainanov V., Mud volcanoes and dome-like structures an the Eastern Mediterranean Ridge. *Marine Geophysical Res.* **19**, 421–438 (1997).
4. Osler J. and Algan O., A high resolution seismic sequence analysis of the Malta Plateau, SACLANT Centre Report SR-311 (1999).
5. Max M. D., Kristensen A. and Michelozzi E., Small scale Plio-Quaternary sequence stratigraphy and shallow geology of the west-central Malta Plateau, SACLANT Centre Report SR-209 (1993).
6. Holland C. W., Shallow water coupled scattering and reflection measurements. *IEEE J. of Ocean Eng.* **27**, 454–470 (2002).
7. Dosso S. E. and Holland C.W., Bayesian geoacoustic inversion of seabed reflection data. *J. Acoust. Soc. Am.*, in review.
8. Richardson M. D., In-situ shallow-water sediment geoacoustic properties. *In Shallow Water Acoustics*, ed. R. Zhang and J. Zhou, China Ocean Press, 163–170 (1997).
9. Bowles F. A., Observations on attenuation and shear wave velocity in fine-grained marine sediments. *J. Acoust. Soc.* **101**, 3385–3397 (1997).
10. Anderson A. L. and Hampton L. D., Acoustics of gas-bearing sediments. II Measurements and models. *J. Acoust. Soc. Am.* **67**, 1891–1903 (1980).
11. Clay C. and Medwin H.: *Acoustical Oceanography*. John Wiley and Sons (1977).
12. Boyle F. A. and Chotiros N., A model for acoustic backscatter from muddy sediments. *J. Acoust. Soc. Am.* **98**, 525–530 (1995).

13. Lyons A. P., Duncan M. E. and Anderson A. L., Predictions of the acoustic scattering response of free-methane bubbles in muddy sediments. *J. Acoust. Soc. Am.* **99**, 163–172 (1996).
14. Gardiner B. S., Boudreau B. P. and Johnson B. D., Growth of disk-shaped bubbles. *In sediments, Geochimica et Cosmochemica Acta* **67**, 1485–1494 (2003).
15. Faran J. J., Sound Scattering by Solid Cylinders and Spheres. *J. Acoust. Soc. Am.* **23**, 405–418 (1951).

NONLINEAR ACOUSTICAL METHODS IN THE DETECTION OF GASSY SEDIMENTS

JAROSŁAW TĘGOWSKI, ZYGMUNT KLUSEK AND JAROMIR JAKACKI

*Institute of Oceanology,
Polish Academy of Sciences,
Powstancow Warszawy 55,
81712 Sopot, Poland*

The methods of detection of gas bearing deposits are based on the fact that gas strongly changes physical properties of sediments. The presence of gas concentrations is easily recognised by conventional acoustic remote sensing methods due to changed acoustic properties of gassaturated sediments. However, for low gas concentrations, conventional acoustics fails to distinguish gas bubbles from other volume scatterers. A nonlinear acoustic method was applied to estimate gas bubbles concentration in the subsurface layers of sediments. The method is based on the theory of nonlinear response of a damped single gas bubble in a fluidlike medium at resonance frequency to a highintensity sound. The observations were performed using two signals with different frequencies and nonlinear components of scattering signals were observed. The gas bubble concentration was estimated using sum harmonics, generated by gas bubbles only. The appearance of the nonlinear components in the echo signal makes it possible to distinguish between bubble and nobubble scattering. The method seems to be a promising tool in a remote sensing of free gas presence, control of gas emanation during drilling, ecological monitoring of methane or sulphuretted hydrogen presence in the top sediment layers. Results, which were collected for different types of bottom sediments in the Gulf of Gdansk of the Baltic Sea, are presented.

1 Introduction

Gas bubbles in sediments have been detected in many places of continental shelves, inner seas and lakes. There are several known sources of gas bubbles in the top layer of sediments: (i) bacterial decomposition of organic matter; (ii) gas hydrates, (iii) natural cracking of organic material buried at great depths; (iv) submarine volcanic and geothermal processes; (v) penetration into sediment of gases originally dissolved in sea water due to the turbulent processes.

The Baltic Sea deposits are a good example of this phenomenon, since sediments saturated by methane, hydrogen sulfide or carbon dioxide were found in various areas [1, 2]. Recently human agricultural activity caused formation of “dead” shallow water areas with methane presence in the surface layer of sediments. This phenomenon is usually investigated by geochemical methods of gas detection and its concentration estimation. Geochemical experimental procedures employ time-

and cost consuming sample collection techniques. There is a need of finding noninvasive and more effective methods, which would facilitate the measurements of gas bubble concentration in the top layer of deposits.

Presence of gas in sediments results in changes of their physical properties as acoustic attenuation, reflective characteristics, turbidity and the wave propagation speed comparing to gas-free deposits [3, 4, 5] which could be easily recognised by conventional remote sensing acoustic methods. The results of seabed acoustic properties investigation performed in the Gulf of Gdańsk area are demonstrated in Figures 1 and 2. Figure 1 shows an example of gas seepage from the sandy bottom in a location close to the end of the Hel Peninsula, recorded with a 30 kHz single beam echosounder. This area is known for methane emissions and therefore we can assume that the detected gas rising to the sea surface from the deeper bottom layers is certainly methane. Another typical record of gassy sediments using a 3.5 kHz subbottom profiler is shown in Fig. 2. This measurement was made in the central part of the Gulf of Gdańsk in an area covered by muddy sediment (dashed line in the map Fig. 7.a shows 3.5 kHz acoustic transect). Gas bubbles trapped in the top layer of the sea floor block the deep penetration of acoustic pulse, which is reflected in the vanishing of observed layered structure of sediments in the echo signal.

The method presented in this paper is based on nonlinear properties of a gas bubble mechanically stimulated at resonant frequency, where the oscillating bubble is a strong nonlinear source of acoustical waves [6]. However, using one forcing frequency, we can expect generation of harmonics not only in the bottom volume but also in the measurement setup itself. This disadvantage can be partially omitted by emission of a twofrequency signal. The harmonic frequencies generated by gas bubbles are formed in the volume of sediment where both beams are crossed.

2 Theory

The measurements of gas bubbles in sediments using X-ray and optical microscopy methods [1, 7, 8] show that the bubble shape is generally different from spherical. Only small bubbles with radii of a few micrometers have spherical surfaces. Increasing the bubble size results in shape changing from ellipsoidal to irregular elongated cylinder for the biggest bubbles.

Resonant properties of gas bubbles in sediments are different from properties of bubbles drifting in the water body. Anderson and Hampton [9, 10], in a pioneering work, measured resonant frequency of gas bubbles trapped in different media such as water, agar and silt. They demonstrated that due to the viscoelastic properties of the bubble surface and oscillating mass of a surrounding medium, the resonant frequency is higher for a sediment bubble than for a water bubble having the same diameter.

The resonant frequency of bubble in sediment is described by following equation [7]

$$f_0 = \frac{1}{2\pi a} \sqrt{\frac{3\gamma p_H}{A\rho_s} + \frac{4G}{\rho_s}} \quad (1)$$

where: p_H – ambient pressure close to the bubble, a – bubble radius, γ – ratio of specific heats in gas, G – real part of the dynamic shear modulus, ρ_s – density of the sediment, A – polytrophic coefficient, $A \approx 1$.

The shear modulus depends strongly on the class of sediments. In muddy sediments shear modulus is of an order of 10^2 kPa. In the case of very liquid sediments, G is near zero or in deeper area, the resonant frequency of pulsating bubble can be expressed by more simple Minneart formula [11]:

$$f_0 = \frac{1}{2\pi a} \sqrt{\frac{3\gamma p_H}{\rho_s}} \quad (2)$$

where one should take into account only changes of the resonant frequency with depth.

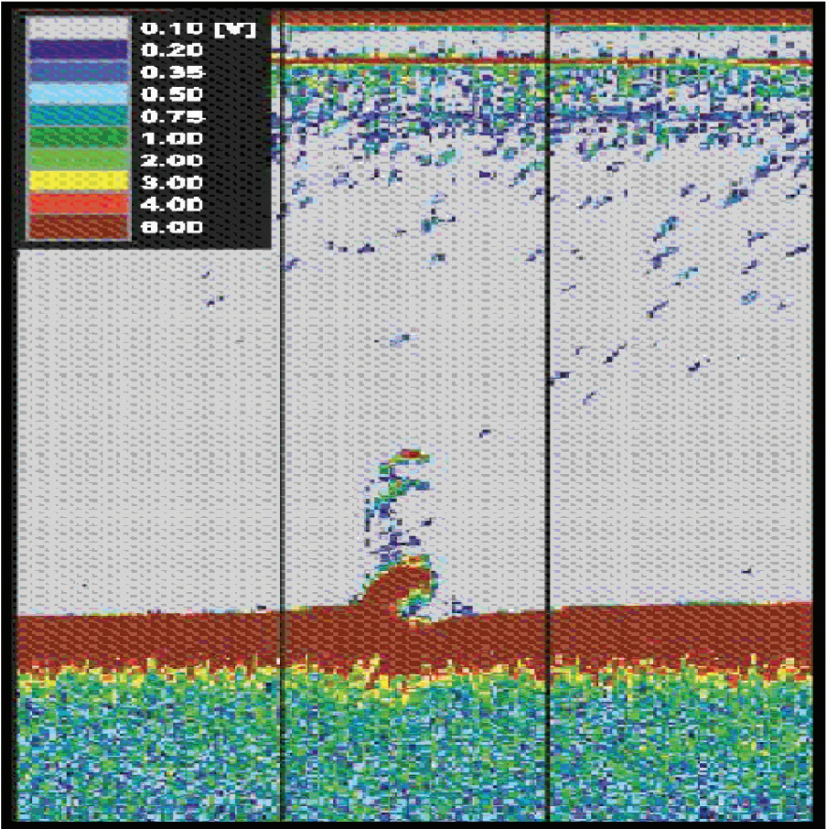


Figure 1. Gas seepage in the Gulf of Gdańsk, Baltic Sea.

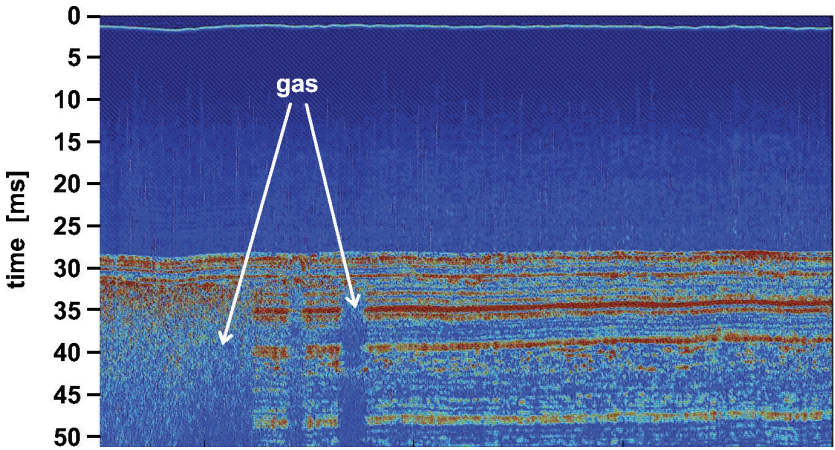


Figure 2. The 3.5 kHz subbottom profile indicating gas in deep bottom layers – Gulf of Gdańsk, Baltic Sea.

Karl *et al.* [12] showed that small spherical gas bubbles in porous medium have two resonant frequencies. This result introduces ambiguousness in acoustical methods utilizing resonant properties of mechanically excited bubble. As the consequence of this discovery we should limit our nonlinear acoustic method of bubble density estimation to a restricted class of sediments. We should make an assumption that pulsating gas bubble is immersed in the semifluid poreelastic medium such as waterfilled muds or silts. Our investigation of gassy sediments were conducted in the central part of the Gulf of Gdańsk (see Fig. 7.a) where the bottom is covered by thick layer (up to 10 meters) of muddy sediments containing a large amount of the organic matter [13].

For acoustically hard sandy sediments, the two-frequency–signal (non-linear) method should be limited to qualitative measurement of gassy deposits. The forced gas bubble oscillates changing its volume or shape. For large amplitudes of incident wave, nonlinear effects play a dominant role. In the spectrum of scattered field, the primary frequencies (the same as in the incident wave), as well as harmonic frequencies being the multiply or fraction of primary frequency are observed.

The first theoretical description of the gas bubble oscillations forced by the acoustical wave was made by Rayleigh in 1917 for the non-compressible fluid and no surface tension. Later it was substituted by a more realistic models including vapour pressure inside the bubble, surface tension and viscous loss (RPNNP model for example). The non-linear equation of bubble oscillations is expressed by:

$$\rho R \ddot{R} + \frac{3}{2} \rho \dot{R}^2 = p_g \left(\frac{a_0}{R} \right)^{3\kappa} + p_v - p_{stat} - \frac{2\sigma}{R} - 4\mu \frac{\dot{R}}{R} - p(t), \quad (3)$$

where: R – bubble radius, ρ – fluid density, p_{stat} – static pressure in environment (the sum of hydrostatic and atmospheric pressures), κ – exponent of adiabat (ratio of heat capacity for constant pressure to the capacity in constant volume), σ – surface tension coefficient, μ – dynamic viscosity coefficient, p_v – steam pressure inside bubble, $p_g = 2\sigma/R_n + p_{stat} - p_v$, $p(t)$ – ambient pressure forced of bubble oscillations, a_0 equilibrium bubble radius.

There are no exact analytical solutions of this equation. An approximate solution can be obtained assuming a small variation of bubble radius [14].

The other approach to the solution of equation 3 was made by Zabolotskaya and Soluyan [6]. They transformed the Rayleigh equation for radius changes in time applying bubble volume for the case of small rates of oscillating bubble volume V in relation to the equilibrium bubble volume V' ($V'/V_0 \ll 1$). In this method, pressure P of incident wave should be much smaller than equilibrium pressure p_0 ($P/p_0 \ll 1$). Therefore, equation expressing the changes of bubble volume can be written as follows:

$$\ddot{V} + \omega \delta \dot{V} + \omega_0^2 V + \epsilon P = \alpha V^2 + \mu(2\ddot{V}V + \dot{V}^2), \quad (4)$$

where ω is frequency of volume oscillation, δ is resonant attenuation constant, bubble resonant frequency is ω_0 and α, μ, ϵ are coefficients defined as follows:

$$\omega_0^2 = \frac{3\kappa p_0}{\rho_0 a_0^2}, \quad (5)$$

$$\mu = \frac{1}{8\pi a_0^3}, \quad (6)$$

$$\alpha = 3\mu(\kappa + 1)\omega_0^2, \quad (7)$$

$$\epsilon = 4\pi a_0 / \rho_0. \quad (8)$$

We assume that two sinusoidal waves of amplitudes P_1 and P_2 with angular frequencies ω_1 and ω_2 and phases ϕ_1 and ϕ_2 , $P = P_1 \cos(\omega_1 t + \phi_1) + P_2 \cos(\omega_2 t + \phi_2)$ force the oscillation of the bubble. The insertion of such defined pressure P to equation 4 gives:

$$\ddot{V} + \omega \delta \dot{V} + \omega_0^2 V = -\epsilon[P_1 \cos(\omega_1 t + \phi_1) + P_2 \cos(\omega_2 t + \phi_2)] + \alpha V^2 + \mu(2\ddot{V}V + \dot{V}^2). \quad (9)$$

Among many theoretical approaches to the behavior of a single bubble driven by high intensity biharmonic source here for approximate solving equation 9 we follow the procedure presented by Boyle and Chotiros [15] and Jakacki [16]. In this case the expressions for primary, double, difference and sum scattering cross-sections are as follows:

$$\sigma_{\omega_{1,2}} = \frac{4\pi a_0^2 \omega_{1,2}^4}{[(\omega_0^2 - \omega_{1,2}^2) + \delta^2 \omega_{1,2}^4]}, \quad (10)$$

$$\sigma_{2\omega_{1,2}} = \frac{36\pi \omega_{1,2}^4 [(\kappa + 1)\omega_0^2 - \omega_{1,2}^2]^2 P_{1,2}^2}{\rho_0 a_0^2 [(\omega_0^2 - \omega_{1,2}^2) + \delta^2 \omega_{1,2}^4] [(\omega_0^2 - 4\omega_{1,2}^2) + 4\delta^2 \omega_{1,2}^4]}, \quad (11)$$

$$\sigma_{\Omega_{\pm}} = \frac{\pi \Omega_{\pm}^4 [3(\kappa + 1)\omega_0^2 - (\omega_1^2 + \omega_2^2 \pm \omega_1 \omega_2)]^2 P_1^2 P_2^2}{\rho_0^2 a_0^2 [(\omega_0^2 - \omega_1^2) + \delta^2 \omega_1^4] [(\omega_0^2 - \omega_2^2) + \delta^2 \omega_2^4] [(\omega_0^2 - \Omega_{\pm}^2) + \delta^2 \Omega_{\pm}^4] [P_1^2 + P_2^2]}, \quad (12)$$

where: $\Omega_{\pm} = \omega_1 \pm \omega_2$, $\gamma = c_p/c_v$ and scattering cross section for each of the scattered components is defined as the ratio of the power radiated by a bubble in the given frequency band to the intensity of incidence wave P . For example the sum frequency scattering cross section can be written as follows:

$$\sigma_{\Omega_+} = 4\pi a_0^2 \left| \frac{P_{sc, \Omega_+}}{P} \right|^2, \quad (13)$$

In our estimations of bubble population in sediments, we chose the sum frequency component of scattering signal because its scattering cross section for non-linear interaction has the greatest value. The confirmation of this choice is shown in Fig. 3 which displays the comparison of scattering cross sections computed for the different linear and non-linear components. The resonant frequency of gas bubble is 30 kHz. We linearly change the frequencies f_1 and f_2 and calculate the normalised scattering cross sections as a function of normalised frequency.

An example of the spectral density function level of a signal scattered at the bubble layer in sediment is shown in Fig. 4. The linear frequencies f_1 and f_2 are the consequence of scattering by the diverse volume scatterers in sediment whereas harmonic frequencies $2f_1$ and $2f_2$ and $f_1 + f_2$ are the result of non-linear oscillations of gas bubbles only. The noise generated by research vessel masked the difference frequency. To avoid this disturbance, difference frequency signal was filtered out using an analogue filter at the input of preamplifier.

In computations of gas bubble density we chose the sum frequency of non-linear response of gassy sediment. For small densities of gas bubbles in sediments the scattering process is incoherent. The intensity of backscattered signal is defined as:

$$dI_{sc} = \frac{I_0 S_{v\Omega_+}}{4\pi r^2} dV(r, \Omega_+) \quad (14)$$

where $S_{v\Omega_+}$ is the volume backscattering coefficient of the wave at the sum frequency Ω_+ , dV – the scattering volume for the sum frequency calculated numerically on the basis of geometry of the transmitters, r – distance between centre of transducers system and scattering volume.

For given bubble sizes distribution coefficient $S_{v\Omega_+}$ is the sum of scattering cross sections $\sigma_{\Omega_+}(a_0)$ over all size ranges of radiating bubbles:

$$S_{v\Omega_+} = \int_0^{\infty} n(a_0) \sigma_{\Omega_+}(a_0) da_0, \quad (15)$$

where $n(a_0)da_0$ – bubble density in the unit volume (1 m^3) and radius range of $[a, a + da]$ (usually $da = 1 \mu\text{m}$). The volume scattering coefficient of the insonified volume for the sum frequency in the

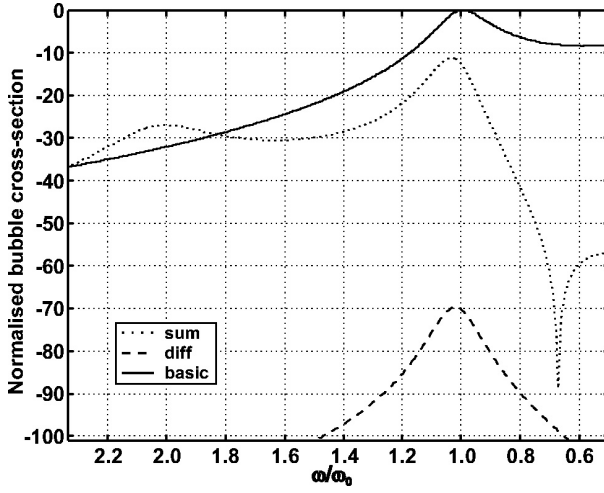


Figure 3. Scattering cross-sections of a bubble for different components as a function of driven frequency normalized to maximum linear cross-section value at natural resonance frequency. Parameters used in calculations were as follows: medium density $\rho_0 = 1200 \text{ kg/m}^3$, ambient pressure $p_0 = 2000 \text{ hPa}$, incident wave amplitudes $P_1 = P_2 = 5 \text{ kPa}$, bubble attenuation constant as in water, $\delta = 0.1$.

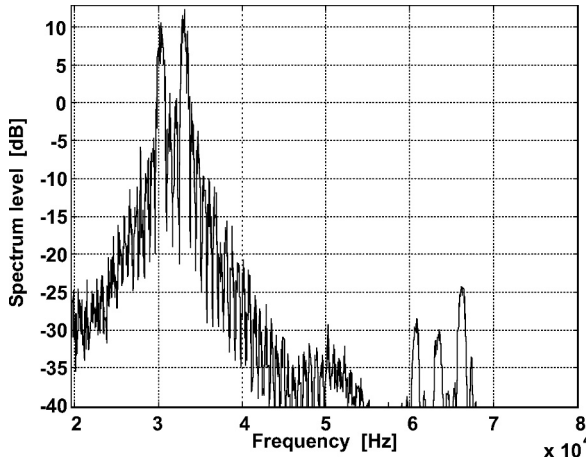


Figure 4. Example of a spectrum of returned signal from a bottom, where fundamental frequencies were $f_1 = 30.4 \text{ kHz}$ and $f_2 = 33.6 \text{ kHz}$. Harmonics are: $2f_1 = 60.8 \text{ kHz}$, $2f_2 = 67.2 \text{ kHz}$, and sum frequency $f_1 + f_2 = 64 \text{ kHz}$. The smaller scattering volume at sum frequency (the crossed two beams) resulted in lower level of sum frequency component comparing to the two harmonics.

case of very close primary frequencies, in approximation that only bubbles near resonance contribute to the generation of the sum frequency component take the form [17]:

$$S_{v\Omega_+} = \frac{\pi\Omega_+^4 \left[3(\kappa+1)\omega_0^2 - (\omega_1^2 + \omega_2^2 + \omega_1\omega_2) \right]^2 P_1^2 P_2^2}{\rho_0^2 \left[(\omega_0^2 - \Omega_+^2)^2 + \delta^2 \Omega_+^4 \right] (P_1^2 + P_2^2)} \times n(a_r) \times \frac{\pi}{4\delta^3 a_r}, \quad (16)$$

where $a_r = \sqrt{a_0(\omega_1)a_0(\omega_2)}$ – geometrical mean of bubble radii in resonance at both driven frequencies. Using volume scattering coefficients for sum frequency $S_{v\Omega_+}$ one may derive a formula for the bubble density.

In order to obtain the amplitudes of acoustic waves, incident on a bubble we should measure the local reflection or transmission coefficients for the waterbottom interface, acoustical wave attenuation in sediments and on bubbles for the fundamental and sum frequencies. The reflection coefficient at the sea floor was computed using the sonar equation for a calibrated system. The more complicated problem is with the estimation of the attenuation of both forward or backward propagated acoustical waves in the sediments. No straight measurements were performed in situ, so the attenuation coefficients were taken from literature data for standard types of sediments.

3 Experimental configuration

The configuration of the experimental setup is shown in Fig. 5. The frame containing pairs of transmitters and a hydrophone is placed at the distance from 10 to 20 m above the seabottom. The suitable distance for bubbles harmonic generation is limited by transmitter beam widths, their configuration and emitted sound pressure, which in our experiments did not exceed a value of 57 kPa at the distance of 1 m from each transducer.

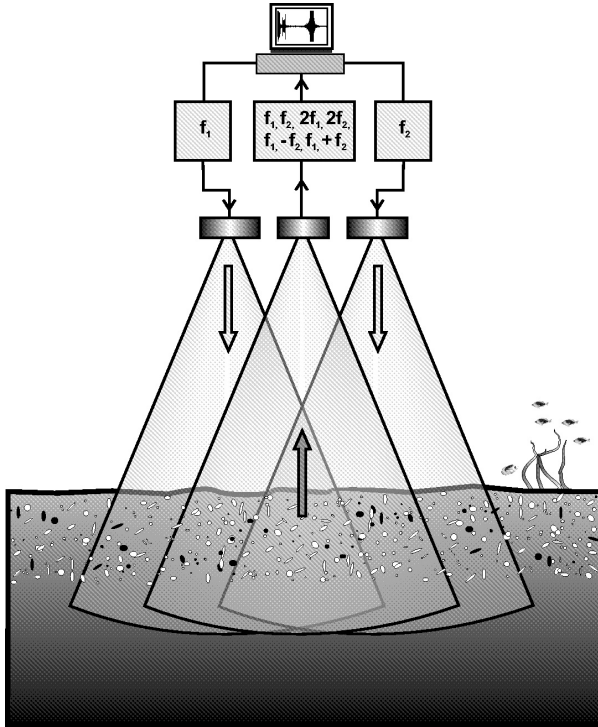


Figure 5. Configuration of measuring instruments.

The scattering volume for difference and sum frequencies is limited to intercrossed cones of the emitter beams. The signal backscattered at the sediment inhomogeneities is received by the hydrophone located in the centre of the measuring system and after amplification it is converted into digital form (Fig. 6).

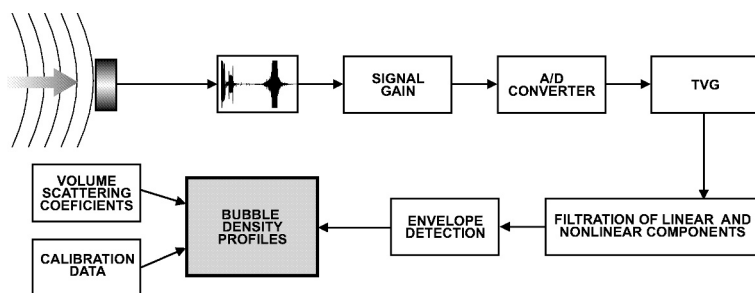


Figure 6. Scheme of data processing procedure.

Compensation of the acoustic energy loss due to spreading and absorption is realised by the numerical timevaried gain (TVG) procedure. Subsequently, transformed signal is bandpass filtered for separation of linear and non-linear components. Envelopes of signal are estimated with the Hilbert transform method. Calibration data, volume scattering coefficients and signal envelopes are the inputs to the sonar equation (see equations 12–16). As the result of the above presented signal processing procedure, estimation of bubble density profiles are obtained.

It should be stated that in the all phases of signal registration and amplification, measurement systems could have generated some level of non-linear components. It was the reason for keeping the especially high accuracy in all stages of measurements to avoid of signal saturation in electronic systems.

4 Results

The acoustic data were collected during the experiment performed in the Gulf of Gdańsk area (Baltic Sea) where the geophysical, sedimentological and acoustical properties of bottom were known from earlier investigations (e.g. [13, 18]). The experiments were carried on board the r/v OCEANIA drifting above the measurement points, whose locations are shown in the map Fig. 7.a. About 500 echo pulses were recorded at each station. White circles and black crosses mark the survey stations for frequencies 30.4/33.6 kHz and 105.5/115 kHz adequately and dashed line mark the transects of 3.5 kHz subbottom profiling. Measurements were conducted in two regions of the Gulf of Gdańsk in the central part of the gulf and in the area located north of the Vistula River estuary. Additionally, one survey station was positioned east of the Gdynia harbor in the place of anthropogenic deposit location.

The Gulf of Gdańsk seabed contains very diverse sediments (Fig. 7.b) from acoustically hard marine sands and gravels, mixtures of sand with till and silt to marine silts, muds and semi liquid organic origin fluffy sediments. Shallow water areas are covered by gravels and marine sands of different grain while deeper regions have muddy sediments. Water depths at the sampling sites varied from 10 m to 65 m. In the central part of the Gulf of Gdańsk, dominant sediments are marine muds and silts containing gas bubbles originate from the bacterial decomposition of organic matter.

The thickness of muddy sediments in most areas is between 3 m and 6 m, locally reaching up to 10 m. Moreover, in this area, acoustical anomalies have been observed (Fig. 1) gas seepages and rapid decay of acoustical signal in muddy sediments (Fig. 2). The most probable reason of this phenomenon involves the migration of methane from the deep bottom gassy layers.

The quality of measurement channel is confirmed by two examples of gas bubbles occurrence in sediments, made in the preliminary survey. The first measurement (Fig. 8) was made at the point ZG4 [13] at the position 18°52.6'N and 54°27.7'E, where top layer of sediment is marine silty sand lying on deltaic silts.

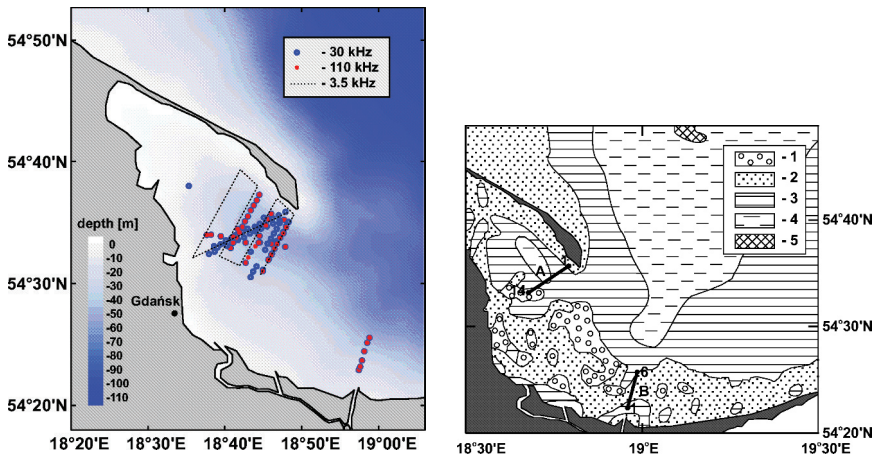


Figure 7. a) Area of gas detection in sediments in the Gulf of Gdańsk. White circles indicate non-linear acoustic measurement at frequency 30.4/33.6 kHz, black crosses 105.5/115 kHz, dashed line the transect of 3.5 kHz subbottom profiling; b) types of sediments: 1 – gravel, stones, 2 – sands, 3 – marine silty clay, 4 – marine clayey silt, glacial marine clay, 5 – till (from Pieczka, 1980).

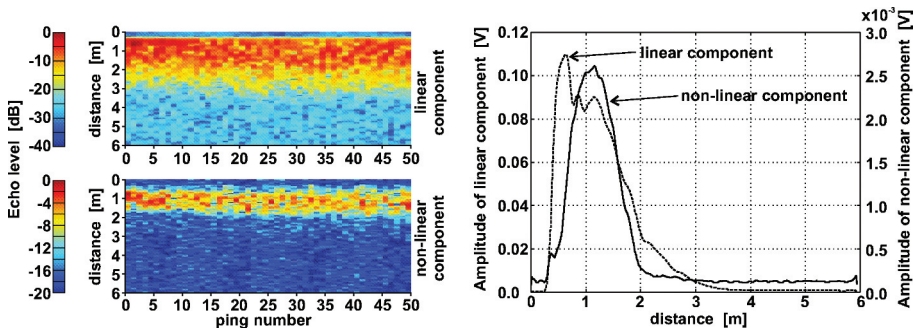


Figure 8. The echograms and amplitudes of linear and non-linear components of echo signals measured at the station where the top layer of sediment is marine silty sand laying on the deltaic silts. Frequency 30.4/33.6 kHz.

The right figure shows two envelopes of the scattered signal: dashed one is the linear component, solid one is the non-linear component. The linear echo component comes from the volume and surficial scattering at the top sandy sediment. The non-linear component echo comes from the muddy layer placed below sandy layer which is the barrier for the gas bubbles.

The opposite result was obtained for the station EL1 [13] at the position of $19^{\circ}19.5'N$ and $54^{\circ}26.0'E$, where the non-linear component envelopes are the effect of scattering at the thin layer of top muddy sediment (Fig. 9). Both examples prove that the non-linear component appearing in the echo signals is not an artifact generated in the measurement system. The computations were made for the raw signals which did not include any correction coefficients.

The gas bubbles density estimation was done for the above 150 points located in the Gulf of Gdańsk area [20]. The first analyzed registration was conducted for the Hel Gdynia direction transect marked by the letter A in the map of sediment locations (Fig. 7.b). Figure 10 shows echograms of gas bubble concentration measured at fourteen stations A distanced from each other by 0.5 nm. Each echogram consists of about 500 depth profiles of concentration recorded during the slow movement

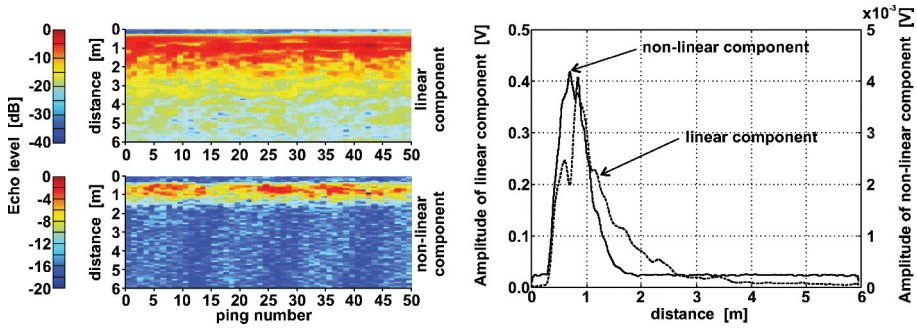


Figure 9. The echograms and amplitudes of linear and non-linear components of echo signals measured at the station where the top layer of sediment is the thin layer of mud laying on the sand. Frequency 30.4/33.6 kHz.

of drifting ship. The results of measurements show resonant gas bubble concentrations varying from about 0 (station 6, 7, 8) to 350 m3m1 (stations 3, 9, 10). Measured quantity of concentration varies strongly between the stations and does not depend on the sea depth. Biggest values of concentration were registered at stations 3 and 10 where depths were comparable and the sediment is marine silty clay, in opposite to stations 6, 7, 8 the smallest concentrations, where sediment is marine clayey silt and glacial marine clay (Fig. 7.b). However, despite the considerable difference of depth, the bubble concentrations at stations 4 and 11 are comparable too. We should point out that for varied depth at consecutive stations the bubble resonant radius depends on hydrostatic pressure (depth).

Figure 11 shows the results of bubble density estimation in the Vistula estuary survey marked by transect B in Fig. 7.b. For six consecutive stations we show results for the sum frequency component for incident waves at primary frequencies of 30.4/33.6 kHz in the top row of pictures and 105.5/115 kHz in the bottom. In the investigated area, the sediment consists of marine sand covered by the thin layer of fluffy mud containing gas bubbles of bacterial decomposition origin.

5 Conclusion

The presented method of non-linear acoustics can be helpful for gas bubble detection and their density estimation in the upper layer of sediments. The theoretical assumptions of spherical bubble oscillations in semiliquid media impose limitations for the sort of sediments for which the method is valid. These are for example the unconsolidated deposits as marine muds and silts like the ones covering large areas of the top layer of the Gulf of Gdańsk bottom. The appearance of the non-linear components (sum and double frequencies) in the echo signal makes it possible to distinguish between bubble and nobubble scattering. The method seems to be a promising tool in a remote sensing of free gas presence, control of gas emanation during drilling, ecological monitoring of methane or sulphuretted hydrogen presence in the top sediment layers. Other application of the presented method involves the information on non-linear bottom sediment properties which is useful for acoustical bottom classification.

Acknowledgements

This work was supported by a grant from the State Committee for Scientific Research of Poland, grant No. 8 T12B 006 20.

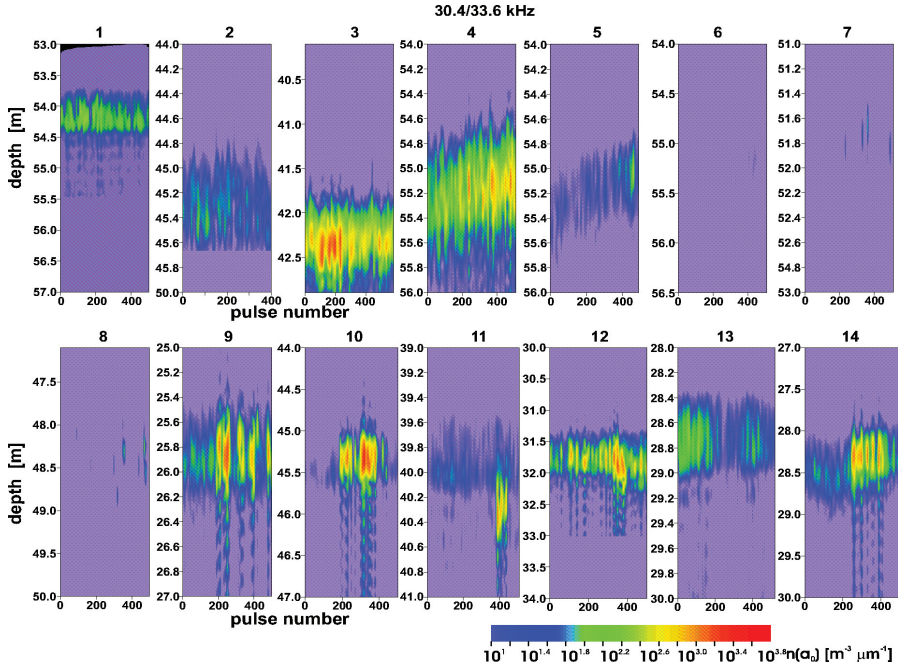


Figure 10. The spatial distribution of gas bubbles density along the transect A (see Fig. 7.b) for consecutive stations. At each station the vessel was drifting during the measurements. Results were estimated for sum frequency component of the pair of incident waves at 30.4/33.6 kHz.

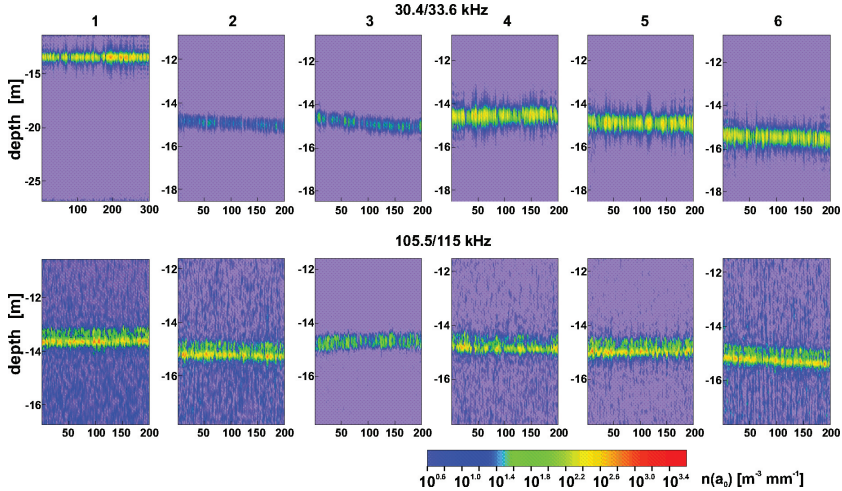


Figure 11. The comparisons of spatial distributions of gas bubbles densities in transect B (see Fig. 7.b) for consecutive stations. The top figures show results for sum frequency component of incident waves of 30.4/33.6 kHz, while the bottom figures for 105.5/115 kHz.

References

1. Abegg F. and Anderson A. L., The acoustic turbid layer in muddy sediments of Eckernförde Bay, Western Baltic: methane concentration, saturation and bubble characteristics. *Mar. Geol.* **137**, 137–147 (1997).
2. Anderson A. L., Abegg F., Hawkins J. A., Duncan M. E. and Lyons A. P., Bubble populations and acoustic interaction with the gassy floor of Eckernförde Bay. *Continental Shelf Research* **18**, 1807–1838 (1998).
3. Hovem J. M., The nonlinearity parameter of saturated marine sediments. *J. Acoust. Soc. Am.* **66**, 1463–1467 (1979).
4. Stefanon A., Marine sedimentology through modern acoustical methods: UNIBOOM. *Boll. Oceanol. Teor. Appl.* **II**(6), 113–144 (1985).
5. Turgut A. and Yamamoto T., Measurements of acoustic wave velocities and attenuation in marine sediments. *J. Acoust. Soc. Am.* **87**, 2376–2383 (1990).
6. Zabolotskaya E. A. and Soluyan S. I., Emission of harmonic and combination–frequency waves by air bubbles. *Sov. Phys. Acoust.* **18**, 396–398 (1972).
7. Lyons A. P., Duncan M. E., Anderson A. L. and Hawkins J. A., Predictions of the acoustic scattering response of free methane bubbles in muddy sediments. *J. Acoust. Soc. Am.* **99**, 163–172 (1996).
8. Boudreau B. P., Gardiner B. S. and Johnson B. D., Rate of growth of isolated bubbles in sediments with a distributed diagenetic source of methane. *Limnol. Oceanogr.* **46**, 616–622 (2001).
9. Anderson A. L. and Hampton L. D., Acoustics of gasbearing sediments I. Background. *J. Acoust. Soc. Am.* **67**, 1865–1889 (1980).
10. Anderson A. L. and Hampton L. D., Acoustics of gasbearing sediments II. Measurements and Models. *J. Acoust. Soc. Am.* **67**, 1890–1903 (1980).
11. Minnaert M., On musical air bubbles and the sounds of running water. *Philos. Mag.* **10**(235) (1933).
12. Karl S. G., Williams K. L. and Lim R., Double monopole resonance of a gasfilled, spherical cavity in a sediment. *J. Acoust. Soc. Am.* **103**, (1998).
13. Geological Map of the Baltic Sea Bottom, Gulf of Gdańsk sheet, Polish Geological Institute, Warsaw (1992).
14. Clay C. S. and Medwin H., *Acoustical Oceanography*, Wiley Interscience Publication (1977).
15. Boyle F. A. and Chotiros N. P., Nonlinear acoustic scattering from a gassy poroelastic seabed. *J. Acoust. Soc. Am.* **103**(3), 1328–1336 (1998).
16. Jakacki J., Application of nonlinear acoustical phenomena in investigations of gas bubbles in sea (in Polish). Ph.D. Thesis, Institute of Oceanology of Polish Academy of Sciences, Sopot (2002).
17. Jakacki J., Klusek Z. and Tęgowski J., The nonlinear method of gas bubbles detection in the bottom sediments, *Revista de Acústica*, **XXXIII** 2002 (CD, ISBN: 8487985068).
18. Tęgowski J., Characteristics of backscattered ultrasonic signals from the floor of the southern Baltic (in Polish). Ph.D. Thesis, Institute of Oceanology of Polish Academy of Sciences, Sopot (1994).
19. Pieczka F., *Geomorfologia i Osady Denne Basenu Gdańskiego Peribalticum Problemy Badawcze Obszaru Bałtyckiego*, Ossolineum, Gdańsk, 79118, (1980) (in Polish).
20. Tęgowski J., Jakacki J., Klusek Z. and Rudowski S., Nonlinear Acoustical Methods in the Detection of Gassy Sediments in the Gulf of Gdansk, *HYDROACOUSTICS* **6**, 151–158 (2003).

ACOUSTIC SCATTERING FROM SUBMERGED AND BURIED OBJECTS

ILKKA KARASALO

*Swedish Defence Research Agency
Division of Systems Technology
SE-172 90 Stockholm, Sweden
E-mail: ilkka.karasalo@foi.se*

PATRIK SKOGQVIST

*Royal Institute of Technology
Aeronautical and Vehicle Engineering
SE-100 44 Stockholm, Sweden
E-mail: psk@kth.se*

Two techniques are described for numerical prediction of transient scattering by 3D objects in the water column or buried in the bottom sediment. In the first method, the scattering problem is formulated as a boundary integral equation (BIE) for a three-dimensional body inside a range-independent layered fluid-solid medium. The Green's function of the layered medium is computed by an accurate transform integral method employing exact finite elements and adaptive high-order numerical integration. A Burton-Miller formulation of the BIE is used, leading to a linear combination of weakly singular and 'hypersingular' BIE free from artificial singularities. The BIE is discretized using B-spline basis functions, global high-order integration and point collocation, and then solved iteratively with a preconditioned generalized minimum residual (GMRES) method. The second method is a fast approximative scattering model based on a combination of acoustic ray tracing and Kirchhoff's approximation of the scattered field. Both methods are formulated in the frequency domain, and Fourier synthesis is used for computing transient fields. Examples of scattered pulses predicted by the two techniques are presented. The predicted fields are compared with data from experiments in which a semi-buried object was probed by a ROV-mounted parametric sonar and the scattered field was registered by bistatically located receivers. A method for identification of parameters of the scattering objects, based on the fast scattering model combined with an algorithm for global nonlinear optimization is described. Both the optimization method and the fast scattering model are highly parallelizable, and are implemented on workstation clusters under MPICH, allowing for convenient handling of also computationally demanding broadband excitations. Some examples of parameter inversion results using experimental data from the EU project SITAR are presented.

1 Introduction

In this paper we study computational methods for modelling of acoustic scattering from submerged objects or objects buried in the seabed, and for identification of parameters of such objects by acoustic inversion. The methods are applied to analysis of experimental results from a sea-trial for identification of buried objects from their acoustic scattering signature. The trial was conducted in the Stockholm archipelago in Sept–Oct 2003 as a part of the European research project SITAR (*Seafloor Imaging and Toxicity: Assessment of Risk caused by buried waste*), [1, 2].

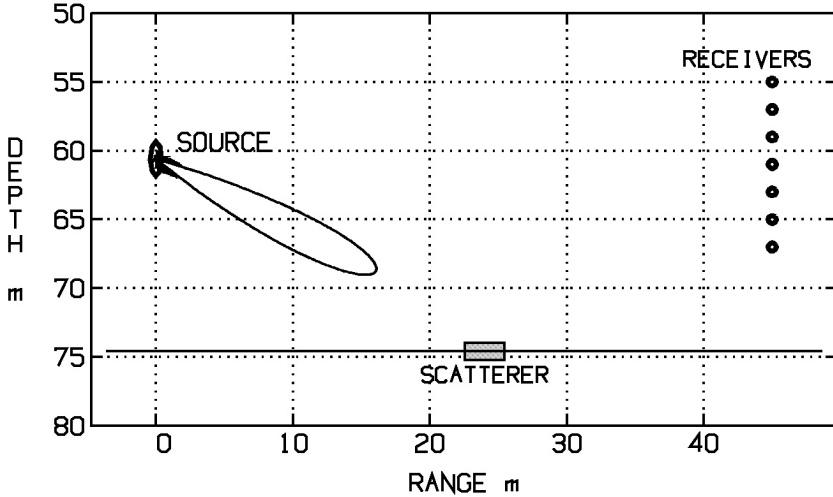


Figure 1. Experimental geometry.

In the experiment, transient pulses from a ROV-mounted TOPAS 120 parametric sonar were emitted within a narrow beam directed towards the object, and the scattered echoes were recorded with a separately located vertical receiver array as shown in Fig. 1. The water depth at the site was ca 75 m, and the source was located ca 11–15 m above the seafloor. In each registration some 80–100 pulses were recorded, with the source fixed in position and orientation. The target was a semi-buried acoustically penetrable box with dimensions ca $130 \times 30 \times 30$ cm, as estimated from a close-range video survey of the target area.

2 Modelling methods

Two modelling methods are considered, a full-field boundary integral equation (BIE) method and a fast approximative Ray–Kirchhoff (RK) method. Both methods use a frequency domain formulation of scattering from a 3D object in a layered, range-independent medium.

The complex acoustic pressure $p(\mathbf{r})$ at a point \mathbf{r} outside a scattering body can be written

$$p(\mathbf{r}) = p_i(\mathbf{r}) + p_s(\mathbf{r}) \quad (1)$$

where $p_i(\mathbf{r})$ and $p_s(\mathbf{r})$ are the acoustic pressure of the incident field, i.e. the field that would be excited without the scatterer present, and the scattered field, respectively. By Green's theorem, at a point \mathbf{r}_0 outside the surface S of the scatterer

$$p_s(\mathbf{r}_0) = \int_S [g(\mathbf{r}, \mathbf{r}_0) \nabla p(\mathbf{r}) - p(\mathbf{r}) \nabla_1 g(\mathbf{r}, \mathbf{r}_0)] \cdot \hat{\mathbf{n}}(\mathbf{r}) dS(\mathbf{r}) \quad (2)$$

where $\hat{\mathbf{n}}$ is the unit outward pointing normal of S at \mathbf{r} and $g(\mathbf{r}, \mathbf{r}_0)$ is the Green's function of the outside medium. ∇ is the gradient operator, and for clarity ∇_j denotes the gradient with respect to the j 'th argument of a function of multiple variables. In a homogeneous fluid medium [3, Sec. 2.3.2]

$$g(\mathbf{r}, \mathbf{r}_0) = -\frac{e^{ik_p|\mathbf{r}-\mathbf{r}_0|}}{4\pi|\mathbf{r}-\mathbf{r}_0|} \quad (3)$$

where $k_p = 2/\lambda$ denotes the wavenumber. In a layered range-independent medium, with vertical z -axis such that $\mathbf{r}_0 = (0, 0, z_0)$, $\mathbf{r} = (x, y, z)$ $g(\mathbf{r}, \mathbf{r}_0)$ is computed by numerical evaluation of the inverse Hankel transform

$$g(r, z, z_0) = \frac{1}{2} \int_{-\infty}^{\infty} G(k, z, z_0) H_0^{(1)}(kr) k dk \quad (4)$$

where k is horizontal wavenumber, $\mathbf{r} = (x^2 + y^2)^{1/2}$, and $G(k, z, z_0)$ the Green's function of the depth-separated wave equation [3, Sec. 4.5].

2.1 Boundary integral equation

Letting $\mathbf{r}_0 \rightarrow S$ in eqn (2) leads to a boundary integral equation (BIE) for the unknown functions $p(\mathbf{r})$ and $\frac{\partial p}{\partial n}(\mathbf{r})$ on the surface $r \in S$

$$\frac{1}{2}p(\mathbf{r}_s) + \int_S \left(\frac{\partial g_1(\mathbf{r}, \mathbf{r}_s)}{\partial n} p(\mathbf{r}) - g(\mathbf{r}, \mathbf{r}_s) \frac{\partial p}{\partial n}(\mathbf{r}) \right) dS(\mathbf{r}) = p_i(\mathbf{r}_s) \quad (5)$$

For a rigid scatterer $\frac{\partial p}{\partial n}(\mathbf{r}) = 0$ and then $p(\mathbf{r})$ is well determined on S by eqn. (5), outside a discrete set of eigenfrequencies of an associated interior problem. For acoustically penetrable scatterers, both $p(\mathbf{r})$ and $\frac{\partial p}{\partial n}(\mathbf{r})$ are unknown, and eqn (5) must be complemented by an additional equation derived from the interior dynamics of the scatterer. For a homogeneous fluid body the interior dynamics is described by a BIE of the form (5) with zero right hand side, and a Green's function of the form (3) with k_p the wavenumber in the interior fluid [4, Sec. 2].

2.2 The BIE method

In the BIE code XFEM-S used in this study the Green's function of the outside layered medium is computed by adaptive high-order evaluation of the transform integral (4) with $g(k, z, z_0)$ computed by exact finite elements [5].

2.2.1 Model of scatterer

The box-shaped scatterer is described by a smooth map of the spherical coordinates θ, ϕ onto the surface of an super-ellipsoid with half-axes 65, 15 and 15 cm as shown in figure 2. The interior of the ellipsoid is a homogeneous fluid with acoustic parameters representative of a TNT explosive, density 1630 kg/m³, velocity 2680 m/s, absorption 0.7 dB/wavelength.

2.2.2 B-spline basis, collocation

A rectangular equidistant grid of knotpoints (θ_j, ϕ_i) is introduced, together with associated bases of B-splines [6] $G_j(\theta)$ and $F_i(\phi)$ with degrees k_G and k_F , and support in $\theta_j \leq \theta \leq \theta_{j+k_G+1}$

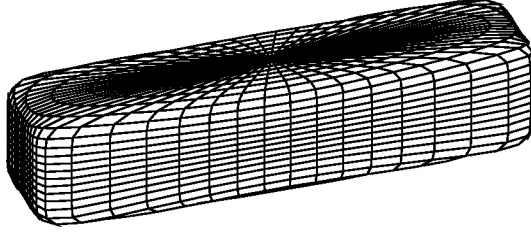


Figure 2. Computational model of the box: A homogeneous fluid body shaped as a super-ellipsoid with half-axes 65, 15 and 15 cm, exponent 10.

and $\phi_i \leq \phi \leq \phi_{i+k_F+1}$, respectively. Approximations of the pressure $p(\theta, \phi)$ and the normal displacement $w(\theta, \phi)$ are sought of the form

$$f(\theta, \phi) = \sum_{i=1-k_F}^N \sum_{j=1-k_G}^{M-1} \gamma_{ij} G_j(\theta) F_i(\phi). \quad (6)$$

The coefficients in these expansions are determined from a system of linear equations composed of *i*) conditions for periodicity of f as function of ϕ , *ii*) conditions for spline-like continuity of f at the ‘poles’ $\theta = 0$ and $\theta = \pi$, *iii*) collocation of the exterior and the interior equations (5) at the knotpoints, cf. [7, Sec. 3].

2.2.3 Numerical integration

The singularity of the kernel in (5) at the collocation point \mathbf{r}_s is handled by choosing as variables of integration ‘tilted’ spherical coordinates (θ', ϕ') such that $\theta' = 0$ at the collocation point. Then, the integrands are smooth functions of (θ', ϕ') , periodic in ϕ' with period 2π . A high-order numerical scheme is then obtained by combining the trapezoidal rule in ϕ' (the periodicity ensuring super-polynomial order of convergence, [8, Sec. 7.4.4]), with any high-order scheme in θ' . In the numerical examples below piece-wise 4-point Gauss-Legendre quadrature [8, Sec. 7.4.6] was used.

2.2.4 Hypersingular BIEs

Since the BIE (5) for both the exterior and interior problems is of the first kind in the normal derivative $\partial p / \partial n$ their straightforward use for numerical solution will lead to loss of accuracy or even failure due to poor conditioning. As is well known [9], equivalent, well conditioned, forms of the BIE are obtained by linearly combining (5) with the BIE derived from the gradient of (2) in a similar way as (5). The kernel of BIEs of the latter kind has, however, a $|\mathbf{r} - \mathbf{r}_s|^{-3}$ singularity, and the choice of a numerical discretization method for such ‘hypersingular’ BIEs therefore requires more care than for (5) alone, [10]–[12].

With the techniques for discretization and quadrature outlined above, hypersingular forms of the BIEs are handled by splitting the second derivative of the Green’s function into terms that are singular and nonsingular, respectively, at $\theta' = 0$. The contributions from the singular terms are then known analytically, and the regular terms are computed by the high-order quadrature schemes used for (5).

2.2.5 Solution of the discretized system

For scatterers with rotationally symmetric shape about the z axis, the discretized BIE system is transformed into block diagonal form by discrete Fourier transform over the azimuthal B-spline

index. The resulting diagonal blocks are of moderate size ($K \times K$ where $K = M + k_G - 1$) and may be solved efficiently by conventional LU decomposition. For other scatterers, such as the box studied here, an iterative method for linear general systems [13], enhanced by preconditioning with a solver for a nearby rotationally symmetric case is used.

2.3 Kirchhoff's approximation

Kirchhoff's approximation of the scattered field $p_s(\mathbf{r})$ is obtained by assuming a reflection coefficient $R(\mathbf{r})$ to be known, such that on the surface S , $p_s(\mathbf{r})$ is given by

$$p_s(\mathbf{r}) = R(\mathbf{r})p_i(\mathbf{r}) \quad \frac{\partial p_s(\mathbf{r})}{\partial n} = -R(\mathbf{r})\frac{\partial p_i(\mathbf{r})}{\partial n} \quad r \in S \quad (7)$$

By inserting eqns (1) and (7) in (2)

$$p_s(\mathbf{r}_0) = \int_S \{ (1 - R(\mathbf{r}))g(\mathbf{r}, \mathbf{r}_0)\nabla p_i(\mathbf{r}) - (1 + R(\mathbf{r}))p_i(\mathbf{r})\nabla_1 g(\mathbf{r}, \mathbf{r}_0) \} \cdot \hat{\mathbf{n}}(\mathbf{r})dS(\mathbf{r}) \quad (8)$$

$$= - \int_S R(\mathbf{r})g(\mathbf{r}, \mathbf{r}_0)\nabla p_i(\mathbf{r}) + p_i(\mathbf{r})\nabla_1 g(\mathbf{r}, \mathbf{r}_0) \cdot \hat{\mathbf{n}}(\mathbf{r})dS(\mathbf{r}) \quad (9)$$

where (9) follows from (8) and Green's theorem applied on $p_i(\mathbf{r})$. The reflection coefficient R is a function of the incidence angle $\theta_{inc} = \theta_{inc}(\mathbf{r})$ and possibly of frequency f , and is defined as the reflection coefficient of a transversally homogeneous layered medium with structure equal to that of the scatterer locally at \mathbf{r} . The direction of incidence is defined as the direction of the intensity vector of the incident field \mathbf{I}_i , and the reflection coefficient $R(\mathbf{r})$ is zero at non-insonified points \mathbf{r} on the surface S , defined as points where $\mathbf{I}_i \cdot \hat{\mathbf{n}}(\mathbf{r}) < 0$.

Fig. 3 shows $|R(\theta_{inc})|$ for the fluid box immersed in seawater, with the interior acoustic parameters given above. $R(\theta_{inc})$ is obtained as the plane-wave reflection coefficient at the interface between two homogeneous fluid halfspaces, and is thus independent of frequency. $|R(\theta_{inc})|$ increases from 0.5 to near 1 in $0 < \theta_{inc} < \theta_{crit}$ and is nearly constant for $\theta_{inc} > \theta_{crit}$ where $\theta_{crit} \approx 32.5^\circ$ is the critical incidence angle.

2.4 The Ray-Kirchhoff (RK) method

Kirchhoff's approximation (9) is computed by numerical evaluation of a surface integral, with an integrand defined by the incident field, the Green's function and the reflection coefficient at the scatterer. Although this is computationally much less demanding than the BIE method, the work required for numerical evaluation of the transform integral for the incident field and the Green's function (4) in a layered medium may still make it impractical as a forward model for iterative parameter identification. A method without this drawback is obtained by replacing the incident field $p_i(\mathbf{r})$ and the Green's function $g(\mathbf{r}, \mathbf{r}_0)$ appearing in (9) by their ray-theory approximations [14].

In the special case when \mathbf{r}_1 and \mathbf{r}_2 are located in adjacent homogeneous halfspaces, the ray approximation is obtained in two steps. First, Fermat's principle [3, Sec. 3.5.4] is used to derive a 4'th degree polynomial equation for the position of the corner point of the two-segment eigenray from \mathbf{r}_1 to \mathbf{r}_2 . The corner point is then found by solving the 4'th degree equation with a fast iteration-free algorithm. The ray-theory approximation of $g(\mathbf{r}_2, \mathbf{r}_1)$ is then

$$g(\mathbf{r}_2, \mathbf{r}_1) = -\frac{T(k)}{4\pi(r_1 r_2)^{1/2}} e^{i(k_1 R_1 + k_2 R_2)}, \quad (10)$$

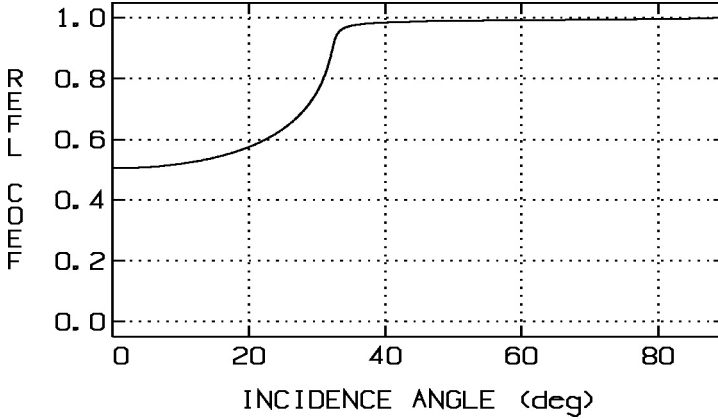


Figure 3. Modulus of the reflection coefficient as function of incidence angle for the model scatterer immersed in water.

where k_1 , k_2 are the wavenumbers in the two halfspaces and k is the horizontal wavenumber at propagation along the eigenray. R_1 , R_2 are the lengths of the two eigenray segments, and $T(k)$ is the transmission coefficient at the halfspace interface

$$T(k) = \frac{2\rho_2\gamma_1}{\rho_2\gamma_1 + \rho_1\gamma_2} \quad (11)$$

where ρ_j and $\gamma_j = (k_j^2 - k^2)^{1/2}$ are, respectively, the density and the vertical wavenumber in halfspace j . The factor $1/(r_1 r_2)^{1/2}$ accounts for the change of sound pressure amplitude induced by the change of the ray tube cross-sectional area [3, Sec. 3.2.2]. Denoting the incidence angles of the ray segments with θ_1 and θ_2 , then $r_1 = R_1 + R_2 c_2 / c_1$ and $r_2 = R_2 c_2 \cos \theta_1 / (c_1 \cos \theta_2) + R_1 \cos \theta_2 / \cos \theta_1$.

The gradient of $g(\mathbf{r}_2, \mathbf{r}_1)$ with respect to \mathbf{r}_2 is required in (9) and is computed by differentiating (10) and the ray endpoint \mathbf{r}_2 with respect to the launch angles and the arclength, and then using the chain rule to convert to derivatives with respect the components of \mathbf{r}_2 . The integral (9) is formulated in ‘tilted’ spherical coordinates θ' , ϕ' with north pole at the point of the insonified region where $\mathbf{I}_i \cdot \hat{\mathbf{n}}(\mathbf{r})$ is minimal. The boundary $\theta'_b(\phi'_b)$ of the insonified region $0 < \theta' < \theta'_b(\phi)$ $0 < \phi' < 2\pi$ is approximated by an interpolating spline, and the integral (9) is computed by high-order adaptive quadrature in θ' and the trapezoidal rule in ϕ' .

2.5 Transient scattering

Computation of transient scattering is handled by Fourier synthesis of mono-frequency fields. The methods are easily parallelizable, at Fourier synthesis as well as at lower levels applicable to single frequency cases, and the algorithms are implemented for parallel execution on PC-clusters, enabling the handling of broad-band scattering within manageable time.

3 BIE vs RK in two model cases

In this section we present results from predictions of transient scattering with the BIE, the Kirchhoff and the Ray-Kirchhoff methods. Two model cases, with the source and a vertical receiver array configured as in Fig. 1, are considered.

The scatterer is modelled as the box-shaped fluid body in Fig. 2, with center in the plane through the source and receivers, and with the long and one short axis horizontal. The long axis of the box is rotated by 19° out of the source-receiver plane.

The source is modelled as a 9 m long vertical array of 65 uniformly spaced point sources weighted and steered to emit a Ricker-like pulse with center frequency 5 kHz within a side-lobe free beam directed towards the scatterer, Fig. 4. The 7 hydrophones of the vertical receiver array are omnidirectional and uniformly spaced, with sensor separation 2 m.

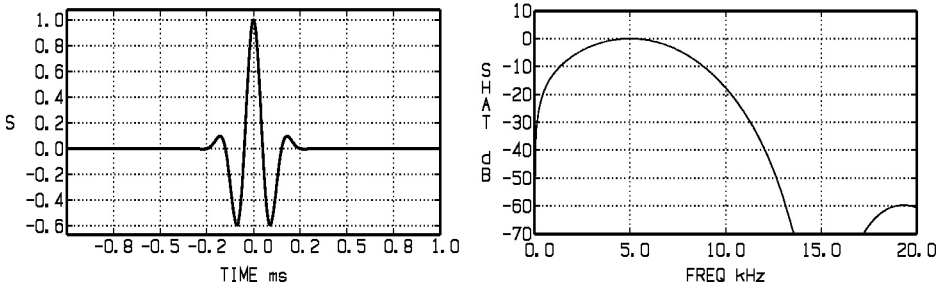


Figure 4. Left: Emitted Ricker-like pulse. Right: Fourier spectrum.

In the first case, the medium is a homogenous water space, with soundspeed $c = 1438$ m/s. The horizontal distances from the source to the center of the scatterer and the receiver array are 26 m and 45 m, respectively. The depths of the center of the source array, the center of the scatterer, and the deepest receiver are 62.3 m, 74 m and 69 m. In the second case, the medium is a homogeneous water halfspace, bounded at depth 74 m by a homogeneous fluid seabed halfspace with parameters $c = 1400$ m/s, $\rho = 1110$ kg/m³ and absorption $\beta = 0.01$ dB/wavelength. The positions of the source and the receivers are as in case 1, but the scatterer is located 20 cm deeper so that it is buried 5 cm below the seafloor.

Fig. 5 shows the transient signals received by the vertical array in case 1, predicted by the BIE (solid) and the Kirchhoff (dotted) methods. Note that the Ray-Kirchhoff and the Kirchhoff methods are identical in this case, since the medium is a homogeneous fluid space. The dashed cross-trace curve shows the arrival times of the specularly reflected scattering component, as predicted by ray theory.

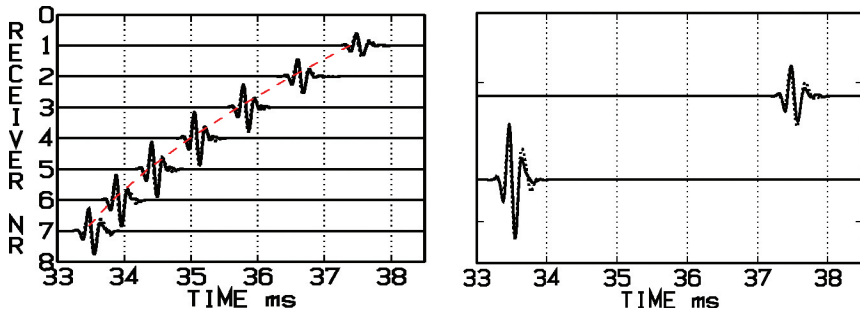


Figure 5. Model-predicted field scattered from a box-shaped fluid body in homogeneous water, BIE (solid), Kirchhoff (dotted). Left: All 7 receivers. Right: Closeup of receivers 1 and 7.

The accuracy of the Kirchhoff predictions of the arrival time and the length of the received pulses is seen to be fairly good at all receivers. The accuracy of the detailed shape of the initial half of the pulses is quite good, and the locations and amplitudes of the first (negative) and the second (positive) peaks are well reproduced. Also, the overall pulse shapes – the number of visible peaks, their signs and arrival times – are predicted correctly. The amplitudes of the peaks in the trailing half of the pulse predicted by Kirchhoff's method are, however, 30-45% too large. It is interesting to note that the shape of the received signals crudely resembles the derivative of the source pulse. The shape would arise when the received signal is dominated by two copies of the emitted pulse with opposite signs, closely spaced in time, such as reflections from the top and the bottom of the box. The large impedance contrast at the surface of the box, however, in this case precludes this simple interpretation of the pulse shapes; they are in fact obtained also when the box is modelled as acoustically impenetrable.

The top frames of Fig. 6 show the predictions in case 2, scattering from the buried box, obtained with the RK (dotted) and the BIE methods (solid). The bottom frames show the RK (dotted) and the transform-integral Kirchhoff predictions in the same case. The RK method is also in this case seen to predict the arrival times and the duration of the pulses, as well as the detailed shape of their leading half, with satisfactory accuracy. The predictions of the trailing half again overestimate the amplitude, here by between 1% (at receiver 7) and 55% (at receiver 2).

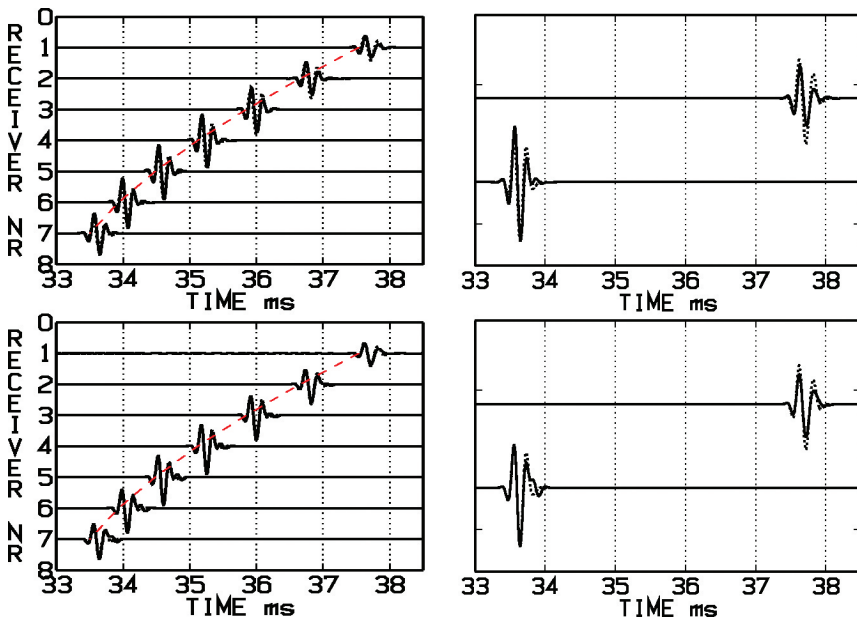


Figure 6. Model-predicted field scattered from a buried box-shaped fluid body. Above: BIE (solid), Ray-Kirchhoff (dotted). Below: Kirchhoff (solid), Ray-Kirchhoff (dotted). Left: All 7 receivers. Right: Closeup of receivers 1 and 7.

As seen in the bottom frames of 6 the difference between the RK and the transform integral Kirchhoff results are significantly smaller than those between the RK and the BIE results. This indicates that the accuracy of the RK method is roughly the same as that of the transform-integral Kirchhoff method. The RK method is, however, much faster and therefore better suited as a forward model for parameter identification. A further conclusion from the results in Figures 5 and 6 is that the fitness function of the inversion should preferably use only leading portions of the received signals.

4 Experimental data

The waveform $\bar{s}(t)$ and its Fourier spectrum $|\hat{\bar{s}}(f)|$ emitted by the TOPAS 120 sonar is shown by the dashed curves in Fig. 7. $\bar{s}(t)$ was obtained from calibration measurements by averaging over ca 130 pings to reduce effects from random perturbations. The solid curves show a smoothed and band-limited approximation $s(t)$ of $\bar{s}(t)$, used as the model source pulse in the simulations. $s(t)$ was obtained by weighted least-squares fitting a smooth spline to $\bar{s}(t)$ such that the conditions $|s(t)| \leq 10^{-4} \max(|\bar{s}(t)|)$ for $|t| > 1.5$ ms and $|\hat{s}(f)| \leq 10^{-4} \max(|\hat{\bar{s}}(f)|)$ for $f \leq 12$ kHz are met.

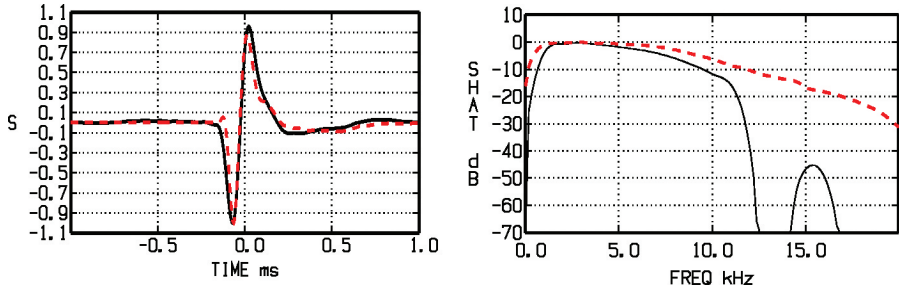


Figure 7. Left: Emitted pulse by calibration measurements (dashed) and smooth band-limited approximation (solid). Right: Fourier spectra.

Fig. 8 shows traces recorded by the vertical array of the pulse reflected from the semi-buried box and the seabed, see Fig. 1. The traces are averages of 84 pings with the transmitter fixed in position and orientation. Only traces from the five middle receivers are shown, since no useful signals were recovered by sensors 1 (top) and 7 (bottom) due to equipment failure. The dashed cross-trace curves indicate ray-theory predictions of the arrival times of the direct arrivals (through sidelobes of the sonar) and the specular reflection from the scatterer. Some computer-aided adjustments of the nominal positions of the individual receivers as well as the scatterer from those of the model cases in Figures 5-6 have been made, to achieve the good agreement shown in Fig. 8 between the predicted and the observed arrival times.

In all receivers, the experimentally recorded echoes are composed of (i) a direct arrival occurring at ca 31.4 ms, (ii) the specular reflection from the scatterer (iii) a relatively quiescent period with length ca 1 ms, and (iv) a ca 5 ms long unstructured tail with larger amplitude than the specular reflection. The quiescent part (iii) of the echoes indicates a very soft and homogenous top sediment layer. The long tails (iv) are likely to be caused by scattering from subbottom layers of more inhomogeneous materials with higher acoustic contrast. It is interesting to note that the detailed and apparently random structures of the long tails are in fact unchanged in all 84 pings, indicating a good stability of the position control system of the ROV.

The left frame of Fig. 9 is a blow-up of the time-interval from 35 ms to 39 ms in Fig. 8 containing the specularly scattered arrivals. The right frame shows simulated echoes, computed with the RK method (solid) together with the specular echo intervals of the observed traces (dashed). In the simulations the medium was assumed to be a homogeneous water space, i.e. no bottom interactions were included in the model. In view of the small acoustic contrast of the top sediment layer, the simulations should still be fairly representative for the specular echo from a semi-buried box.

The arrival times of the model-predicted echoes are seen to agree well with the experimentally observed. However, their amplitudes as function of receiver depth are nearly uniform, with a weakly pronounced maximum at receiver 4, the depth for which the specular reflection occurs at the flat upper surface of the box. In contrast, the experimentally observed echo amplitude is maximal at the deepest receiver, and decreases with depth. Possible reasons for this mismatch are error in the orientation of the model box (causing erroneous predictions of the direction of specular echoes), and

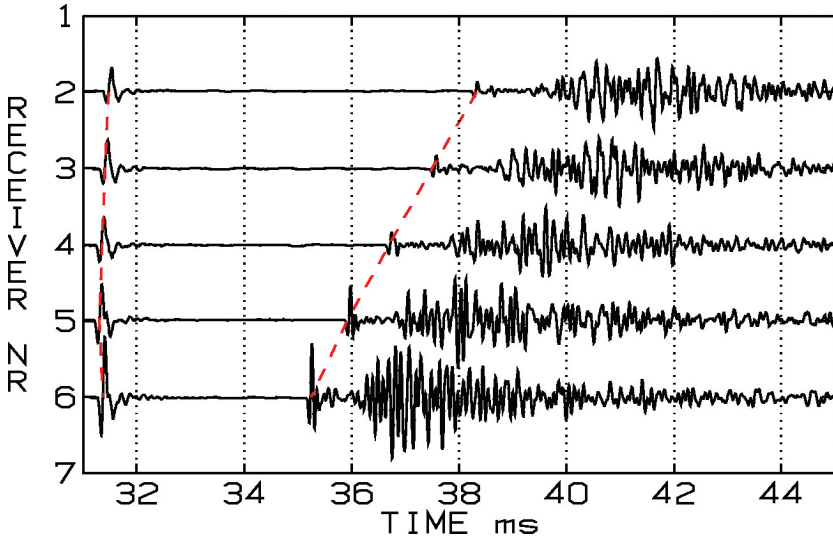


Figure 8. Average over 84 pings of signals recorded by the middle five hydrophones of the vertical array.

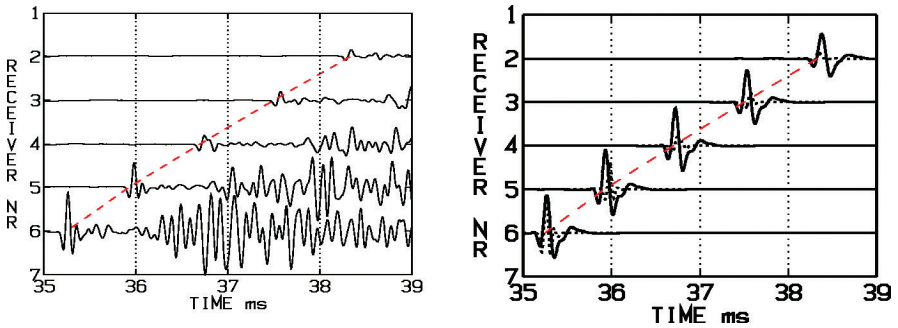


Figure 9. Signals in the middle five hydrophones of the vertical array. Left: Experimental data. Right: Predicted by the RK method (solid) and experimental data (dashed).

an overly smooth shape of the model box (reducing the spatial directivity of the scattered field).

The dotted curves in Fig. 10 are the experimentally observed specular echoes extracted from the left frame of Fig. 9, and rescaled to equal amplitude. The solid curves are similarly re-scaled model predictions with the RK (left) and the BIE (right) methods. For the BIE method, the agreement between the predicted and the experimentally observed echo shapes is seen to be quite good. For the RK method, the overall agreement is reasonably good, however the amplitude of the trailing negative peak is overestimated at all receivers in the same way as in Fig. 5.

5 Identification of buried objects

We consider the problem to estimate a set of parameters of a scattering object, such as size, shape, orientation, sound speed and density, from measurements of the scattered field. We denote by \mathbf{u} a vector of such parameters in a model of the scattering scenario, and by $p(\mathbf{u}) = p(\mathbf{x}, t, \mathbf{u})$ the corre-

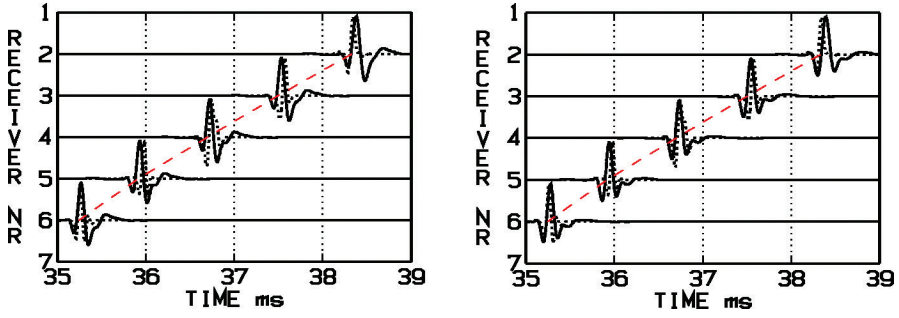


Figure 10. Model-predicted (solid) and experimentally observed (dotted) signals in the vertical array. Signals are re-scaled to equal amplitude. Left: RK. Right: BIE.

sponding model-predicted scattered field, computable by the methods described above. Denoting the experimentally observed field by $\hat{p} = \hat{p}(\mathbf{x}, t)$, the identification problem is then to find \mathbf{u} such that a fitness function $\Phi(\mathbf{u})$ measuring the distance between $p(\mathbf{u})$ and \hat{p} is minimized. In the examples below $\Phi(\mathbf{u})$ was defined as

$$\Phi(\mathbf{u}) = \sum_{i=1}^{N_{rec}} |T_i(\mathbf{u}) - \tau_i|^2 + |A_i(\mathbf{u}) - \alpha_i|^2, \quad (12)$$

where $T_i(\mathbf{u})$ and $A_i(\mathbf{u})$ is the computed arrival time and the normalized amplitude at receiver i , τ_i and α_i are the measured arrival time and the normalized measured amplitude at receiver i . The fitness function (12) is insensitive to details of the pulse shape, and is therefore suitable for use with the RK method, for which the amplitudes of the trailing side-lobes are overestimated as shown in figures 5 and 10. Two examples of the fitness function (12) as function of two parameters of the box-shaped scatterer in Fig. 2 are shown in Figures 11 (the roll and the yaw angles) and 12 (the x - and z -coordinates of the center point). The function is scaled to have maximum value 1, with the greyscale running from 0 (white) to 1 (black).

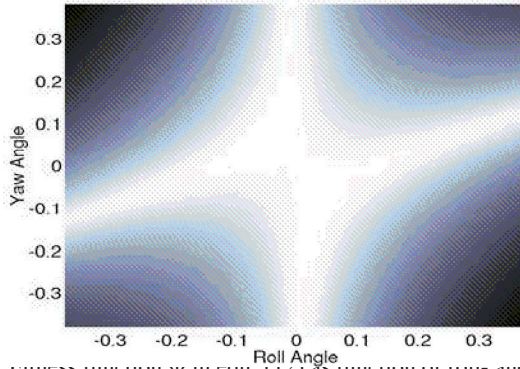


Figure 11. Fitness function Φ in eqn. (12) as function of roll- and yaw angle.

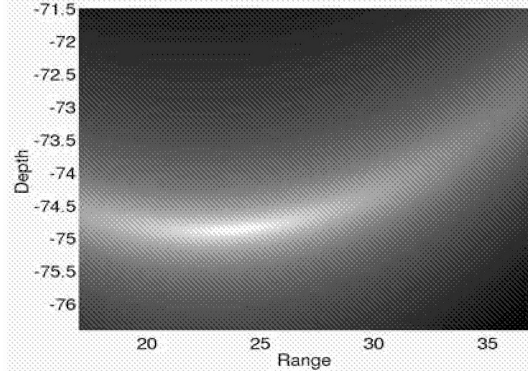


Figure 12. Fitness function Φ in eqn.(12) as function of range and depth of the center of the scatterer.

5.1 Parallel Hybrid Minimization

$\Phi(\mathbf{u})$ is a complicated nonlinear function, in general with multiple local minima, and the solution must be sought by methods for global minimization. The algorithms described below, a differential evolution algorithm (DE) and a hierarchical genetic algorithm (GA), were implemented to run on PC clusters with the RK method as forward model for computing the scattered field $p(\mathbf{u}) = p(\mathbf{x}, t, \mathbf{u})$. In both algorithms, the results of the global search are used as starting points for local minimizations by the downhill simplex method [16].

5.1.1 Differential Evolution (DE) Algorithm

The DE algorithm [17] maintains a population of a fixed number N of points in the space R^D of parameter vectors \mathbf{u} . After g iterations (generations) of the DE algorithm the population is

$$P_g = \{\mathbf{u}_1^g, \dots, \mathbf{u}_N^g\}$$

where the individuals \mathbf{u}_i^g are

$$\mathbf{u}_i^g = (u_{1,i}^g, \dots, u_{D,i}^g) \quad i = 1, \dots, N$$

The first step in computing the population P_{g+1} of the next generation is to compute a set of trial vectors,

$$P'_{g+1} = \{\mathbf{v}_1^{g+1}, \dots, \mathbf{v}_N^{g+1}\}.$$

The i 'th trial vector \mathbf{v}_i^{g+1} is obtained by selecting three random individual numbers $p, q, r \in 1, \dots, N$ other than i such that $p \neq q \neq r \neq p$, and a random component number $k_i \in 1, \dots, D$ and then setting, for $j = 1, \dots, D$,

$$v_{j,i}^{g+1} = \begin{cases} u_{j,p}^g + F \cdot (u_{j,q}^g - u_{j,r}^g) & \text{if } R_j \leq C_R \vee j = k_i \\ u_{j,i}^g & \text{otherwise.} \end{cases} \quad (13)$$

In (13), R_j is a $U(0, 1)$ distributed random number, and F and C_R are constant parameters of the DE algorithm with values in $(0, 1)$.

In the second step, the new population is selected from the current and the trial populations according to

$$\mathbf{u}_i^{g+1} = \begin{cases} \mathbf{v}_i^{g+1} & \text{if } \Phi(\mathbf{v}_i^{g+1}) < \Phi(\mathbf{u}_i^g) \\ \mathbf{u}_i^g & \text{otherwise.} \end{cases} \quad (14)$$

The DE algorithm is run until a prescribed number G_{max} of generations has been reached, or a prescribed number of G_{con} generations have evolved without generating new individuals. The individuals of the final population are then used as starting points for the local minimizer. In the cases studied below, the population size was set to $N = 20$, with the termination constants chosen to $G_{max} = 100$ and $G_{con} = 10$, respectively.

5.1.2 Hierarchical Genetic Algorithm (GA)

A genetic algorithm (GA) operates on a population of individuals (parameter vectors), applying the principle of survival of the fittest to find a sequence of individuals with successively improved fitness values. In the course of a GA search, favorable traits have a tendency to spread faster in a small population than in a large. On the other hand, in a small population the final fitness value will in general be worse than in a large one [15]. In the hierarchical GA method this feature is exploited by dividing the total (large) population into a number of subpopulations called demes (also villages or islands). A so-called coarse-grain parallel GA operates on the demes in parallel, with interchange of genetic data between the demes occurring at intervals. The global minimization step in the present algorithm is a coarse-grain parallel GA with the searches within each of the demes parallelized using a simple master-slave scheme. The GA search in a subpopulation is terminated when

$$\sum_{i=1}^D s_i^2 \leq D \cdot E_g, \quad (15)$$

where s_i^2 is the variance of parameter vector component i in the subpopulation and E_g is a pre-selected tolerance.

5.1.3 Local minimization

The last step in the hybrid methods is a standard implementation of the downhill simplex algorithm [16] in a parallel master-slave scheme. The local minimization is run until

$$|\Phi_{max} - \Phi_{min}| \leq E_l \cdot (|\Phi_{max} + \Phi_{min}|), \quad (16)$$

where Φ_{max} and Φ_{min} are the maximum and the minimum value of the fitness function at the corners of the simplex, and E_l is a tolerance.

6 Parameter identification results

In this section we show results from applying the methods described in sections 2 and 5 for estimating parameters of the box-like scatterer from the experimental data. We seek estimates of seven parameters: (i) the angles of rotation (roll, pitch, yaw) of the box, (ii) the range and depth coordinates of the center of the box, and (iii) the density and sound velocity inside the box.

Initially, a few attempts were made to search for all or several of these parameters simultaneously. However, the convergence of the inversion algorithms in such composite runs turned out to be too slow to provide useful results. Therefore, instead a cruder, step-wise approach was followed, in which only a few parameters were sought in each step, and their values then used in subsequent steps.

In the first step, the roll and yaw angles of rotation of the scatterer, keeping other parameters fixed. Table 1 shows the result of the minimization, the number of iterations, and the number of function evaluations needed to locate a local minimum. The population size was 20 and the method constants were, for GA mutation probability $p_m = 0.013$ and crossover probability $p_c = 0.9$, in the DE method $C_R = 0.9$ and $F = 0.5$.

Table 1. Results of global search for roll and yaw angles.

	Roll	Yaw	Iterations	Function evaluations
GA	-0.86°	11.8°	40	800
DE	-0.74°	10.1°	25	450

The GA method actually finds the minimum after only 7 iterations in this run, but the standard deviation in the population is in that stage still too high to terminate the search. The DE method needs 17 iterations to find the minimum and is terminated after 27 iterations by the condition that the population has not changed in 10 iterations. Fig. 13 shows the fitness function $\Phi(\mathbf{u})$, with the best individual in each generation marked by dots. $\Phi(\mathbf{u})$ has two local minima in the region shown. The individuals of the GA method (left frame) are seen to cluster around the local minima. For the DE method (right frame) less than 25 values are shown, reflecting that the updating procedure of the DE method leaves an individual unchanged unless the trial individual has better fitness. Again, the fitness function in the figures has been scaled to have maximum value 1, and the greyscale runs from 0 (white) to 1 (black).

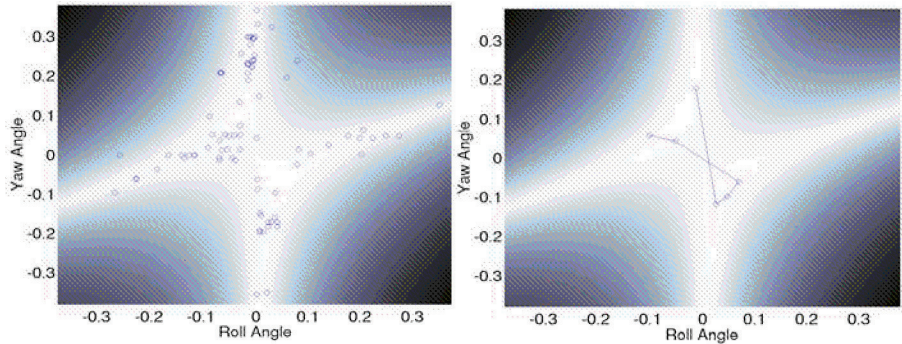


Figure 13. Convergence history. Left: GA method, Right: DE method.

It must be noted that this is a simple example where not all benefits of the global search methods will come into play; a sound local minimizer will probably converge faster to the global minimum.

In the second step, five searches for the interior density and/or sound velocity of the box were estimated and carried out, with results as shown in Table 2. The underlined values are those resulting from the parameter search, other entries show values kept fixed at the search.

Similarly, in a third and a fourth step, the depth and range of the center of the box and the pitch angle of the box, respectively, were inverted for, keeping other parameters fixed at their values from previous inversions. The resulting parameters after all inversion runs are collected in Table 3.

Table 2. Inversion for interior density and sound speed. Inversion results are underlined.

	Run 1	Run 2	Run 3	Run 4	Run 5
Density	<u>1740</u>	<u>1420</u>	1490	1630	<u>1490</u>
velocity	2680	2570	<u>2530</u>	<u>2380</u>	<u>2570</u>

In Fig. 14 the model predicted echoes obtained with the scatterer parameters in the right column of Table 3 are shown together with the experimentally observed specular echoes. Here, unlike in Fig. 10 no re-scaling to equal amplitudes of the traces has been done.

By comparison of Fig. 14 with the right frame of Fig. 9 the parameter inversion is seen to improve the match between the modelled and the experimental data significantly. Most notably, the

Table 3. Parameters of the box-like scatterer before and after inversion.

	Initial	Inverted
Range (m)	24	23.95
Depth (m)	74.85	74.85
Roll (deg)	0	0.9
Pitch (deg)	0	4.8
Yaw (deg)	19	11.7
Density (kg/m^3)	1630	1490
Velocity (m/s)	2680	2570

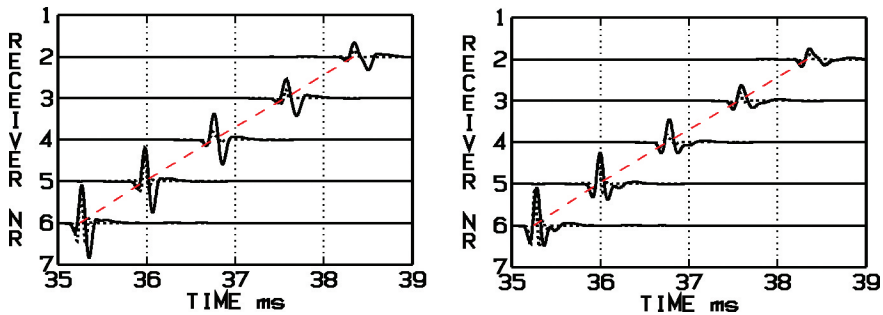


Figure 14. Received signals. Dotted: Experimental data. Solid: Modelled, with parameters by acoustic inversion shown in the right column of Table 3. Left: RK. Right: BIE.

echo amplitude as function of receiver depth in the experimental data is quite well reproduced by the models after inversion. This improvement reflects the sensitivity of the vertical distribution of the scattered echoes to the angles of rotation which were not accurately known at the outset.

7 Summary of results

Two methods for numerical modelling of bistatic transient scattering from submerged or buried objects were described. The methods are based on a full-field boundary integral equation (BIE) technique, and ray theory and the Kirchhoff scattering (RK) approximation, respectively. The accuracy of the RK method was assessed by simulation of experimental scenarios in which pulses scattered by a box-shaped scatterer were recorded by a remote vertical receiver array. The RK method was found to reproduce the dominating features of the received pulses sufficiently well to be useful as a fast forward model in algorithms for identification of parameters of the scatterer by acoustic inversion. The methods were applied to the analysis of data from a sea trial, in which a semi-buried box was insonified by transient pulses from a ROV-mounted parametric sonar. The recorded waveforms - both from auxiliary calibration measurements and from the bistatic trials showed a satisfactory ping-to-ping consistency, reflecting a good stability of the experimental conditions and enabling detailed comparisons with model predictions. Estimates of seven physical parameters of the scatterer, range, depth, roll, yaw, pitch, soundspeed, density, were computed by acoustic inversion. The RK method was used as forward model, with a fitness function measuring the mismatch of arrival times and amplitudes of the first scattered arrivals. The resulting parameter values were found to improve the agreement between data and model predictions significantly compared with those based on prior information only.

8 Conclusions

The main conclusions of this work are

- The experimental configuration, with a transmitter mounted on a ROV equipped with a position control system, enables long recording sequences under stationary conditions, reducing the effects of random perturbations in the data. Dominating features of recorded waveforms agree well with numerical predictions.
- Acoustic inversion of bistatic transient scattering data, with the RK method as a fast forward model in a global search algorithm, has excellent potential as a tool for remote identification of submerged and buried objects.
- Parameter estimates by the simple stepwise inversion technique described in Sec. 6 provided a significant improvement between data and the model predictions. The estimates are, however, in general not a minimum of the fitness as function of all the parameters simultaneously, and thus a more carefully designed minimization procedure should preferably be used in future analyses.

References

1. Jonsson P., Karasalo I., Nilsson A., Balk L. and Caiti A., Underwater acoustic imaging for the assessment of seafloor waste: The SITAR project. In *Proceedings of the Tenth International Congress on Sound and Vibrations*, Stockholm (2003).
2. Staaf Ö., SITAR - Seafloor Imaging and Toxicity: Assessment of Risks caused by buried waste. Systems Technology Annual Report 2003, FOI-R-1245-SE, June 2004, pp. 20-21.
3. Jensen F. B., Kuperman W. A., Porter M. B. and Schmidt H., Computational Ocean Acoustics, American Institute of Physics, New York (1994).
4. Karasalo I., Transient scattering from an object buried in the seabed - Numerical predictions and experimental results. In *Proc. 3'rd UK Conference on Boundary Integral Methods*, Brighton, UK, 109-118 (2001).
5. Karasalo I., Exact finite elements for wave-propagation in range-independent fluid-solid media. *J. Sound Vib.* **172**, 671-688 (1994).
6. Powell M. J. D., Approximation theory and methods. Cambridge University Press (1981).
7. Karasalo I. and Mattsson J., Numerical modelling of acoustic scattering by smooth inclusions in a layered fluid-solid medium. In *High Frequency Acoustics in Shallow Water, SACLANT-CEN Conference Proceedings Series CP-45*, 283-290 (1997).
8. Dahlquist G. and Björck Å., Numerical methods, Englewood Cliffs, Prentice-Hall, Sec. 7.4, 297-301 (1974).
9. Burton A. J. and Miller G.F., The application of integral equation methods to the numerical solution of some exterior boundary-value problems. In *Proc. R. Soc. London, Ser. A*, **323**, 201-210 (1971).
10. Liu Y. and Rizzo F. J., A weakly singular form of the hypersingular boundary integral equation applied to 3-D acoustic problems. *Computer Methods in Applied Mechanics and Engineering* **96**, 271-287 (1992).
11. Guiggiani M. et. al., A general algorithm for the numerical solution of hypersingular boundary integral equations. *Journal of Applied Mechanics* **59**, 604-614 (1992).
12. Krishnasamy G., et. al., Hypersingular boundary integral equations: Some applications in acoustic and elastic wave scattering. *Journal of Applied Mechanics* **57**, 404-414 (1990).
13. Saad Y. and Schultz M. H., A Generalized Minimal Residual Algorithm for Solving Nonsymmetric Linear Systems. *SIAM J. Sci. Stat. Comput.* **7**, 856-869 (1986).
14. Skogqvist P. and Karasalo I., A Fast Acoustic Scattering Method for Buried Objects. In *Proceedings of the Tenth International Congress on Sound and Vibrations*, Stockholm (2003).

15. Cantú-Paz E., A Survey of Parallel Genetic Algorithms, *Calculateurs parallles. Reseaux et System Repartis* **10**(2), 141–171 (1998).
16. Nelder J. A. and Mead R., A simplex method for function minimization. *Computer Journal* **7**, 308–313 (1965).
17. Storn P., Price K., Differential Evolution - A Simple and Efficient Adaptive Scheme for Global Optimization over Continuous Spaces. ICSI, TR-95-012 (1995).

HIGH-FREQUENCY BISTATIC SCATTERING EXPERIMENTS USING PROUD AND BURIED TARGETS

PHILIPPE BLONDEL¹, PETER F DOBBINS^{1,2}

NIC JAYASUNDERE¹ AND MARIO COSCI^{1,3}

¹*Department of Physics, University of Bath, Bath BA2 7AY, UK*

²*Systems Engineering and Assessment Ltd, Bristol BS16 1SU, UK*

³*Visiting student from University of Pisa, Pisa, Italy*

Emergent technologies such as Autonomous Underwater Vehicles and bistatic sonars offer immense leverage to the modern applications of underwater acoustics. However, high-frequency scattering processes need to be better understood, especially in multiple-target environments (e.g., dumpsites or highly cluttered seabeds). Using our facilities at the University of Bath, we have conducted scaled experiments in a large water tank containing several sediment trays representative of continental margin seabeds. This work is part of the SITAR project, funded by the European Commission and investigating the risks caused by buried toxic waste. We therefore used scaled targets comparable to the toxic waste containers found in many dumpsites at sea (fluid-filled cylinders, empty cylinders, spheres, boxes, etc.). Multiple targets (up to 4) were imaged with a narrow acoustic beam at different incidence angles. The receiving hydrophones were positioned to correspond to a vertical linear array some distance away from the targets. This set-up is a scaled-down version of the SITAR sea trials performed in September/October 2003 in the Stockholm Archipelago, except that it offers a totally controlled laboratory environment. Systematic and thorough bistatic measurements were carried out as a function of both scattering angle and bistatic angle. The targets were arranged in different ways, and the differences and similarities between the results associated to these configurations are presented. Advanced deconvolution methods and search routines have been used to reconstruct acoustic scattering inside and outside the different objects. After discussing the influence of the interior of the targets, their distribution, and the influence of the enclosing seabed, we present the possible implications for multiple-aspect surveys. This is followed with presentations of the early results from the processing of the tank and sea trials data, and a discussion of their significance.

1 Rationale

The last decades have shown acoustic instruments were paramount in mapping the seabed and detecting structures at its surface or in its immediate sub-surface. The spatial resolutions now available range from a hundred metres down to a few centimetres, spanning four orders of magnitude and a whole range of physical, geological and anthropological processes [1, 2]. Small or man-made objects located on or below the seafloor are however still rather difficult to find. Important and on-going

research efforts are devoted to their acoustic detection and recognition [3]. Multiple-target environments (e.g., dumpsites, or cluttered zones) are particularly difficult to investigate, and often only the location and extent of the largest targets can be determined. Further details, such as their physical state (integrity/corrosion) or the numbers/positions of smaller targets, are still generally inaccessible.

Simulations and practical use of high-frequency acoustic scattering show the potential offered by bistatic geometries to detect small targets on/in the seabed, and sometimes to identify some of their smaller details or characteristics [4, 5, 6]. The emergence of new technologies, such as Autonomous Underwater Vehicles, adds to the growing interest for bistatic sonars. Using our facilities at the University of Bath, we have therefore decided to investigate experimentally the bistatic scattering from proud and buried objects, and how it could be used to reconstruct their characteristics.

In the following Section, we will introduce the experimental set-up, and justify the different choices made. This Section will present scattering results for bare seabeds, followed with scattering from different types of scaled targets, proud or buried at varying levels, and with varying orientations. It will end with a presentation of results for multiple-target configurations, showing the relative influences of the incidence, scattering and bistatic angles.

The next Section will show how the acoustic waveforms collected at different ensonifying geometries can be used to, first, detect the presence of target(s), second to locate it and even reconstruct its acoustic characteristics. The first task is based on an adaptive implementation of the non-recursive Wiener filters traditionally used in seismic processing, while the localisation of the target(s) uses multidimensional search routines based on a downhill simplex algorithm. Typical processing results from the tank experiments are presented, showing the good agreement between the actual and inferred locations of the targets (as well as their characteristics).

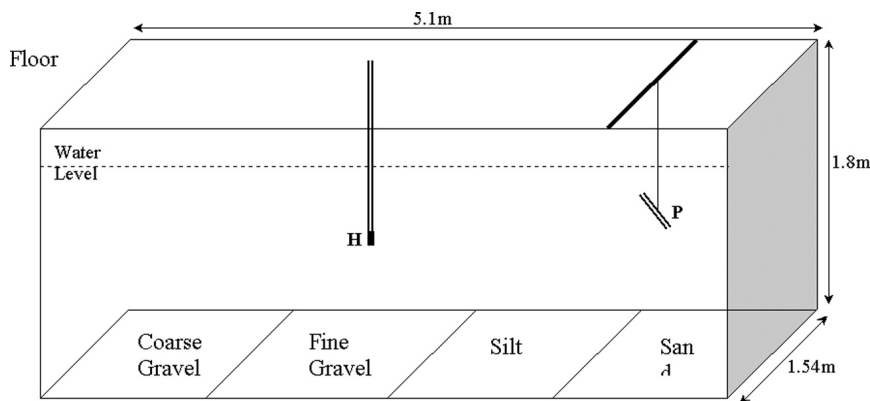
The concluding Section summarises these techniques and their application to experimental tank data. This leads to the SITAR sea trials, performed in September/October 2003 in the Stockholm Archipelago. Their preliminary results will be presented in relation to the tank experiments, including a discussion of similarities (and differences) between both modes of operation, and what can be learnt in both cases.

2 Bistatic Scattering Experiments

2.1 Scaled Tank Experiments

The incentive for this work was the investigation of risks caused by buried toxic waste, as part of the SITAR project (funded by the European Commission) and the preparation of sea trials in the Stockholm Archipelago in 2003. Acoustic studies of the seafloor make an ever-increasing use of high frequencies (10 kHz and beyond). To make sense and quantitatively assess the acoustic measurements thus obtained, several models of bistatic scattering have been developed over the years. They include refinements to the Kirchhoff approximation [7, 8, 9], exact integral solutions [10, 11, 12], Small-Slope Approximation [13, 14, 15], waveguide propagation models [16, 17], composite-roughness models [18, 19] and hybrid models [20, 21, 22]. But the comparison of these models with actual data is hampered by the lack of actual measurements, especially at higher frequencies (above 100 kHz). It is therefore necessary to perform experiments, to understand the optimal imaging geometries and to refine the sonar signal processing techniques.

Very few sea experiments have been performed so far, most of which have taken place in selected shallow-water sites on the continental shelf [5, 23, 24]. These experiments are fraught with difficulties, not all of which could be expected. One can for example list unexpected variations in the seabed, unexpected variations in the water column, or unexpected effects (e.g., ship hull reflections, target burial during the time of the experiment). Because of their complexity, the results of most experiments are still being fully analysed. They have however revealed the complex interactions between targets and their environments.



P – Projector, H – Hydrophone.

Figure 1. The University of Bath underground tank facilities. The walls are made of concrete, and the top of the tank is at floor level. The sediments in the trays are 14 cm deep in average. The water level can be varied and was fixed at 1.475 m in this case. Both the acoustic projector and the hydrophone(s) can be positioned anywhere in the tank. The targets are oriented relative to the X axis (lengthwise), the Y axis (along the 1.54-m width of the tank), or the Z axis (vertically). They were also placed diagonally (XY orientation).

Conversely, laboratory experiments are easier to perform, at least in theory: the environmental variations can be controlled; the target emplacement is known with very high accuracy; the target-background interactions can be directly measured and the experimental uncertainties (e.g., transducer positions) are tightly controlled. Using our facilities at the University of Bath, we have conducted scaled experiments in a large water tank containing several sediment trays representative of continental margin seabeds (Figure 1). We used scaled targets comparable to the toxic waste containers found in many dumpsites at sea. Multiple targets (up to 4) were imaged with a narrow acoustic beam at different incidence angles. The receiving hydrophones were positioned to correspond to a vertical linear array some distance away from the targets. This set-up is a scaled-down version of the SITAR sea trials performed in September/October 2003 in the Stockholm Archipelago, in a totally stable and controlled setting. The influence of the environmental and experimental uncertainties had already been modelled (and measured) by Blondel *et al.* ([4, 24]).

A scaling factor of approximately 10:1 was used in the design of the experiments. The targets were designed to match the numerical models used during the SITAR project [25] and the types of targets likely to be encountered at the trials site. They are listed in Table 1. Target T_1 , for example, is an approximation of a scaled oil drum, whose standard dimensions are 58 cm in diameter, and 88.5 cm in height. Target T_5 is used for comparison with the numerical simulations of [25]. The SITAR sea trials also showed the presence of a large, metal box. A scaled-down version (target T_6) was therefore manufactured, and used in the last series of tank experiments. All 6 targets were used, placed proud, half-buried or flush buried, at different orientations relative to the ensonifying direction, alone or in groups.

The four sediment trays at the bottom of the tank are 30 cm deep, and uniformly filled with sediments typical from the European continental margins. The depth of sediment varies slightly from tray to tray. Those used in this study are filled with silt ($50\mu\text{m}$ mean grain size) and gravel (5 mm mean grain size). The former are a scaled-down version of the soft muddy sediments, with a minute content of gas, expected at the sea trials site (as confirmed later). Karasalo and Skogqvist [26]

Table 1. Dimensions of the scaled targets used in the tank experiments: diameters (D), lengths (L) and other characteristics influencing their acoustic scattering properties.

T_1	Sealed Aluminium tin, fluid-filled, 6.7cm(D) \times 10cm(L)
T_2	Air-filled stainless steel cylinder, 5.8cm(D) \times 10.4cm(L), sidewall thickness 3mm, end cap thickness 2mm
T_3	Solid aluminium cylinder, 5.1cm(D) \times 8.1cm(L)
T_4	Solid steel cylinder, 7cm(D) \times 8cm(L)
T_5	Solid brass ring, 10.5cm(D) \times 7.5cm(L), wall thickness 7.5mm
T_6	Air-filled stainless steel box, 10cm \times 5cm \times 5cm, Wall thickness 2-3mm

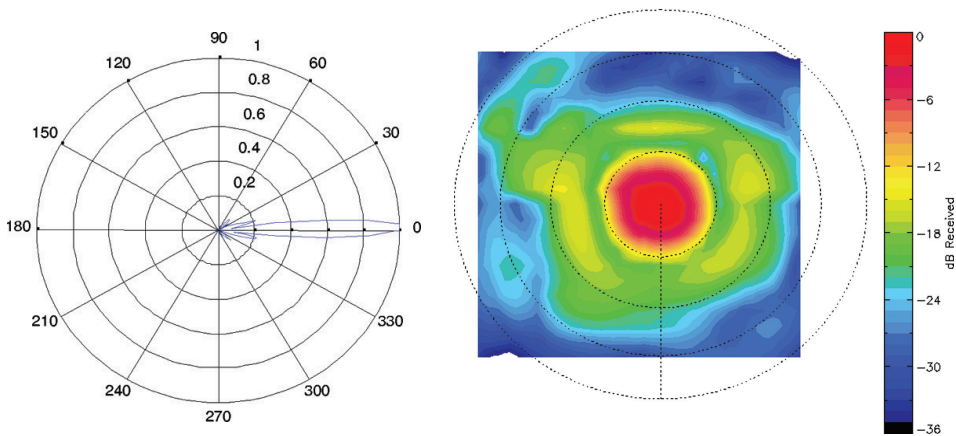


Figure 2. Calibration of the acoustic projector was performed in 2-D (left, in the XY plane) and in 3-D (right, in the XZ plane, with scaling circles every 10°). Note the narrow beamwidth (10°), the small sidelobes, and the asymmetry for the angles further away from the axis of the transducer.

used results from previous inversions at nearby sites to obtain tentative values of 1.047 for the sound speed ratio and 1.1 for the density of the sediments, quite close to the values for the silt tray (1.024 and 1.204 respectively). Only the results for the silt tray are presented in this article. The sediment depth inside the silt tray is ca. 14 cm (giving a theoretical attenuation of 184 dB/m at 238 kHz).

The experiment was arranged in the water tank (5 m \times 1.54 m \times 1.8 m) according to the setup shown in Figure 1. The height of the water column was 1.475m. The acoustic projector is a damped piezoelectric transducer resonant at 238 kHz, excited with a single sinusoid at 238 kHz with 20 V peak-to-peak amplitude (although other signals, e.g. chirps, were also used later). It has a narrow beamwidth (about 10), measured in 2-D and in 3-D [24, 27]. The 3-D calibration shows non-symmetrical variations for the angles further away from the axis of the transducer (Figure 2); this needs to be remembered when analysing scattering from the larger angles. Measurements of the direct signal showed 2 small secondary impulses (respectively 4 and 10 times lower in amplitude), which should also be borne in mind when interpreting the scattered fields. The acoustic projector is mounted on a gantry supported across the tank (Figure 3), allowing its tilt to be set to any desired angle. The transducer was positioned 0.5 m away from the target(s).

The receiver is an omnidirectional hydrophone Brüel & Kjaer (B&K) 8103, fixed to the end of a 9-mm diameter stainless steel tube. The tube is mounted on a translation/rotation stage, positioned in line with the projector and the target (Figure 3, top). Two types of experiments were performed: line scans and rotation scans. In line scans, the hydrophone was positioned 0.5 m above the seabed,

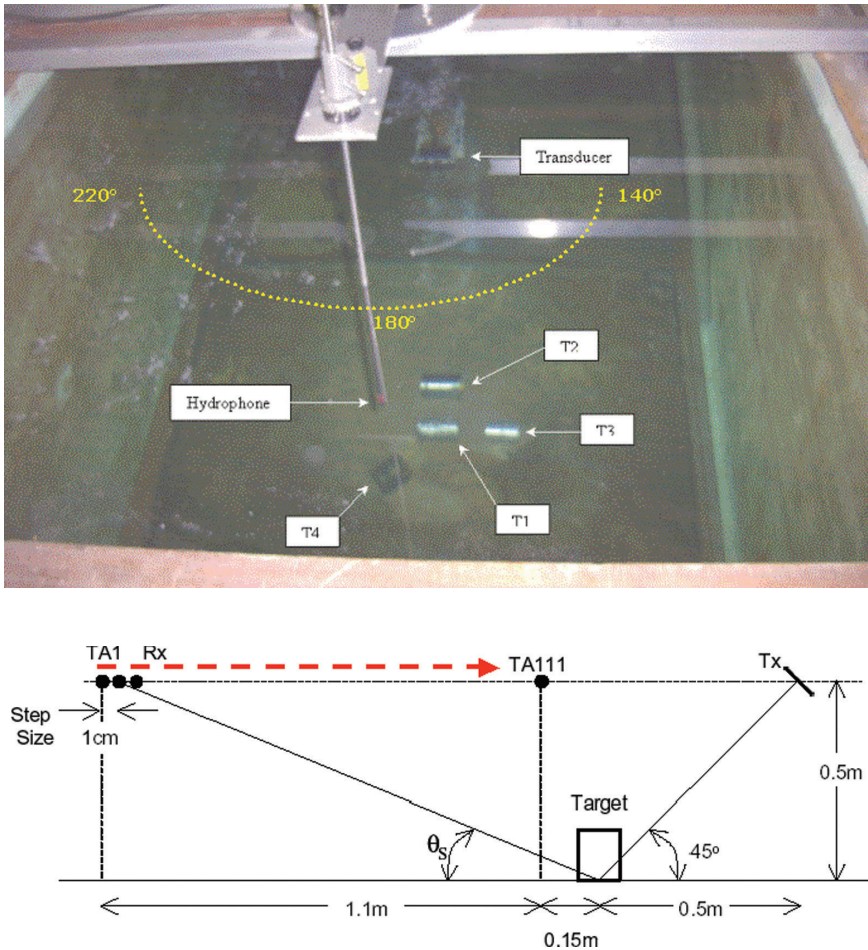


Figure 3. Top: details of a typical rotation scan, for bistatic angles from 140° to 220° . The hydrophone is mounted at the bottom of the stainless steel tube, and measurements at different scattering angles are obtained by vertically moving the tube. Note the positions of targets T_1 – T_4 at the surface of the silt tray. Bottom: diagram of a typical line scan. The hydrophone (RX) starts at position TA1 and scans with 1-cm steps to position TA111, giving a range of scattering angles θ_s . The transmitter (TX) is tilted at 45° in this case.

and remotely translated via a PC with a step size of 1 cm, usually starting 1.1 m away from the target, and finishing 15 cm from the target (Figure 3, bottom). In rotation scans, the tube containing the hydrophone was at a fixed distance of 0.5 m from the main target (Figure 3, top), and remotely rotated via a PC, sampling the scattered acoustic field as a function of bistatic angles between 140° and 220° (180° corresponding to in-plane scattering), with a 2.5° step size. The field was sampled as a function of the scattering angle by manually adjusting the height of the hydrophone over the seabed from 1.375 m to 0.15 m with a step size of 2.5 cm.

These two types of scans correspond to the typical investigation strategies when using ROVs at sea, either “flying lines” over a region or circling objects of interest. They also offer a broader sample of possible bistatic and scattering angles, despite the limitations brought by the finite size of the tank. The total range of configurations sampled is presented in Table 2. The acoustic field was also measured for the bare seabed, before placing the targets and after removing them (to assess any disturbance).

Table 2. Range of bistatic scattering configurations sampled during this study (silt tray only). The orientation of the main axis of the target is by reference to the horizontal plane (X - Y) and the vertical direction (Z). XY orientations correspond to a target placed diagonally to the main direction of the ensonifying beam.

Line scans: incidence angle 45° – scattering angles 15°–75° ° (variable according to configuration)			
<i>Target</i>	<i>Configuration</i>	<i>Bistatic angles</i>	<i>Axis orientation</i>
Bare seabed	N/A	$160^\circ, 170^\circ, 180^\circ, 190^\circ, 200^\circ$	
T_1	Proud	$160^\circ, 170^\circ, 180^\circ, 190^\circ, 200^\circ$	X, XY, Y and Z
	Half-buried	$160^\circ, 170^\circ, 180^\circ, 190^\circ, 200^\circ$	X and Z
	Flush-buried	$160^\circ, 170^\circ, 180^\circ, 190^\circ, 200^\circ$	Z
T_2	Proud	$160^\circ, 170^\circ, 180^\circ, 190^\circ, 200^\circ$	X, XY, Y and Z
	Half-buried	$160^\circ, 170^\circ, 180^\circ, 190^\circ, 200^\circ$	X and Z
	Flush-buried	$160^\circ, 170^\circ, 180^\circ, 190^\circ, 200^\circ$	X and Z
T_3	Proud	$160^\circ, 170^\circ, 180^\circ, 190^\circ, 200^\circ$	X, XY, Y and Z
	Half-buried	$160^\circ, 170^\circ, 180^\circ, 190^\circ, 200^\circ$	Z
	Flush-buried	$160^\circ, 170^\circ, 180^\circ, 190^\circ, 200^\circ$	Z
T_4	Proud	$160^\circ, 170^\circ, 180^\circ, 190^\circ, 200^\circ$	X, XY, Y and Z
T_5	Proud	$160^\circ, 170^\circ, 180^\circ, 190^\circ, 200^\circ$	Z
	Half-buried	$160^\circ, 170^\circ, 180^\circ, 190^\circ, 200^\circ$	Z
	Flush-buried	$160^\circ, 170^\circ, 180^\circ, 190^\circ, 200^\circ$	Z
Line Scans: incidence angle 30° – scattering angles 15°–75° (variable according to configuration)			
<i>Target</i>	<i>Configuration</i>	<i>Bistatic angle</i>	<i>Axis orientation</i>
Bare seabed	N/A	180°	
T_1	Proud	180°	X and Z
T_2	Proud	180°	X and Z
T_3	Proud	180°	Z
Rotation Scans: incidence angle 45° – scattering angles 14°–70°			
<i>Target</i>	<i>Configuration</i>	<i>Bistatic angles</i>	<i>Axis orientation</i>
T_1	Proud	140° – 220° (2.5°)	X and Y
T_2	Proud	140° – 220° (2.5°)	X
	Flush-buried	140° – 220° (2.5°)	X
T_1+T_2	Proud	140° – 220° (2.5°)	Y , 11cm apart
$T_1+T_2+T_3$	Proud	140° – 220° (2.5°)	Y , 5 cm from T_2 in Y direction
$T_1+T_2+T_3+T_4$	Proud	140° – 220° (2.5°)	Y , 11 cm apart except T_3 , which is 5 cm from T_2 in Y direction

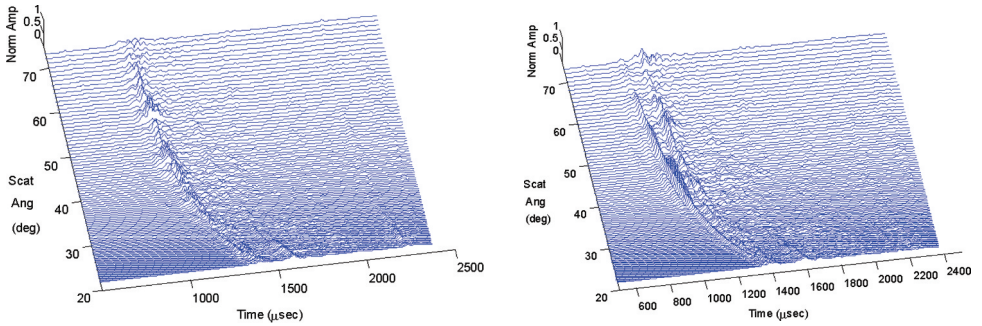


Figure 4. Scattered waveforms for bare silt (left) and with target T_1 proud in the Z direction, i.e., placed vertically on the seabed (right). In this case, the incidence angle is 45° and the bistatic angle is 180° (in-plane scattering). The normalised amplitudes of the scattered waveforms are plotted as a function of time and the scattering angle at which they were measured.

The output signal from the hydrophone is input to a Brookdeal 9452 precision A.C. amplifier with its gain set to 70 dB, and with the low-pass filter cut-off set to 1 MHz. The amplified output is in turn input to a Krohn-Hite 3202 filter, set to high-pass with a cut-off at 200 kHz. The output of the filter is finally connected to a LeCroy LT-264 digital oscilloscope. The received signals are averaged over 1650 waveforms and further band-pass filtered to reduce the noise level. Post-processing included the deconvolution of each acquired waveform with a replica of the incident signal. The complex envelope was computed with a Hilbert transform. The direct signal was then zero-banded before analysis, removing the redundant information of the direct signal from the projector to the hydrophone. For the analysis as a function of scattering angle, the waveforms were time-shifted, so that the scattered signals arrive with the same time delay at the hydrophones, and weighted, to account for the amplitude fall with distance.

2.2 Seabed and Target(s) Scattering

To visualise the experimental measurements, it is easiest to represent the scattered waveforms in the time domain, and look at their relative variations with the scattering angles. The complex amplitude envelope of each waveform is normalised with respect to the maximum amplitude of the data array. “Raw” waveforms already reveal some information, and in particular pronounced differences between the bare seabed and the presence of one or several targets. But they are affected by the original incident signal, usually consisting of several cycles. By deconvolving the scattered waveforms with the projector’s signal, the complex envelope improves the overall image resolution. Figure 3 shows the scattering off the bare seabed (left) and the bare seabed with only one target (right). The acoustic scattering from the target (T_1 , in this case), placed vertical and proud, is significant, at scattering angles between 24° and 65° . It comes immediately before the return from the seabed, which should be expected as it stands higher. There are also some contributions from the reflections of signals from the surface of the water and the tank walls, later in time. As explained in Section 2.1, the acoustic field scattered by the bare seabed was sampled before placing the targets, and after removing them, to assess any disturbance. Visual comparison (and/or subtraction) of the normalised amplitude fields before and after would show any significant differences, likely to cause problems for the next target studies (fortunately, this did not happen during this series of experiments using the silt tray).

Representing the scattered waveforms as contour maps makes it easier to spot differences. Figure 5(left) shows the scattered field, measured as a function of the scattering angle only for one target, in this case T_1 (fluid-filled cylinder). The bistatic angle still is 180° (in-plane scattering) and the

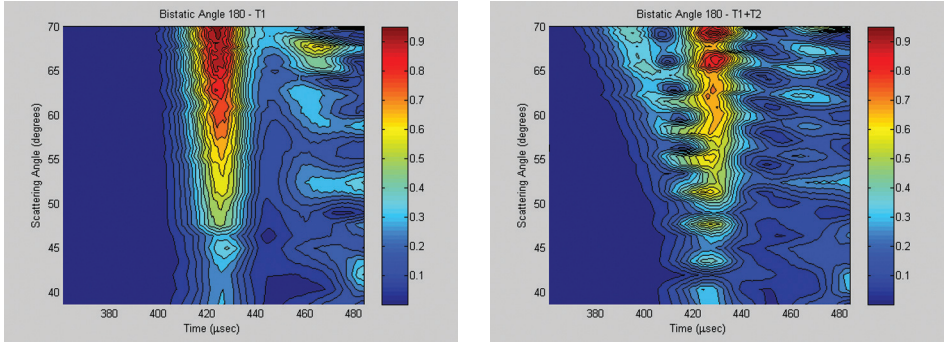


Figure 5. Contour maps of the normalised amplitude as a function of the scattering angle for a bistatic angle of 180° , for target T_1 alone (left) and targets $T_1 + T_2$ (right).

incidence angle is 45° again. The target was placed horizontally along the X axis of the tank (Figure 1). The normalised amplitudes are plotted as a contour map, with 20 contours equidistant between 0 (no return) and 1. The image for T_1 is characterized by a single region of high scattering amplitude, increasing in magnitude with the scattering angle. A small region of somewhat higher normalised amplitudes is visible at later times (ca. $470\mu s$); it is apparently associated to reflections from perturbed parts of the seabed. This contour map can be readily compared to the case of two targets, T_1 and T_2 (air-filled cylinder). The field scattered from T_2 arrives earlier than that of T_1 (Figure 5, right). The image is characterized by interference patterns of the direct arrivals from T_1 and T_2 and an interacting region between them. These can be linked to the different waves propagating at the surface of the targets, some of which will be reemitted [28, 29]. Adding a third target (in this case T_3 , the solid aluminium cylinder) does not alter significantly the overall scattering pattern.

To investigate the contribution of a third target, like T_3 , the bistatic angle needs to change. Figure 6(left) shows the combined scattering of targets T_1 and T_2 , for the same incidence angle of 45° but at a bistatic angle of 160° (i.e. 20° away from in-plane scattering). The images in Figure 6(left) and Figure 5(right) are relatively similar. The relative amplitudes of the peaks corresponding to scattering by T_1 and T_2 are more distinct. This is logical, as with a bistatic angle of 160° , a larger portion of target T_2 is ensonified (cf. Figure 3, top). The same interference patterns between the direct arrivals from T_1 and T_2 are also visible. The high amplitude regions starting at approximately $460\mu s$ are also due to scattering from irregularities on the seabed. Figure 6(right) now shows the combined scattering of targets T_1 , T_2 and T_3 , with the same incidence angle of 45° and bistatic angle of 160° . The contribution of target T_2 has greatly reduced, with interference between the scattered signals from T_1 and T_3 dominating the image. This was also expected, as, when moving away from in-plane scattering in this direction, the geometry of the direct path between the acoustic projector and the hydrophone covers more of target T_3 . The effects of the irregularities at the surface of the sediment tray are now more pronounced when observed with a different bistatic angle. This effect confirms simulations and earlier experiments in the same tank [4].

The addition of a fourth target (in this case T_4 , the solid steel cylinder) does not induce any significant alterations to the overall scattering pattern of the combination of targets $\{T_1 + T_2 + T_3\}$, at least not when plotting contour maps for scattering angles, and a fixed bistatic angle. Instead, to view the contribution from target T_4 , one needs to generate contour maps of the scattering patterns as functions of the bistatic angle (and time), for fixed scattering angles. Figure 7(left) shows the normalised scattered field amplitude for a fixed scattering angle of 67.4° for T_1 , T_2 and T_3 . Figure 7(right) shows the same for all four targets: T_1 , T_2 , T_3 and T_4 . Their comparison shows that T_4 appears at a bistatic angle of 205° around $1040\mu s$, later than any of the other targets (T_4 is placed

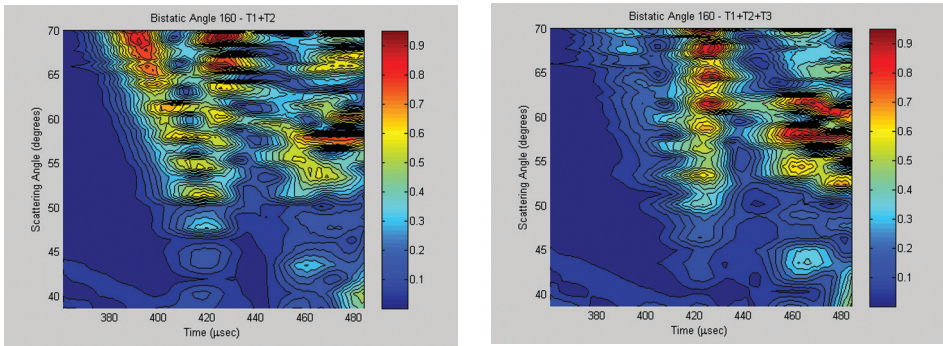


Figure 6. Contour maps of the normalised amplitude as a function of the scattering angle, for a bistatic angle of 160° , for targets T_1+T_2 (left) and targets $T_1+T_2+T_3$ (right).

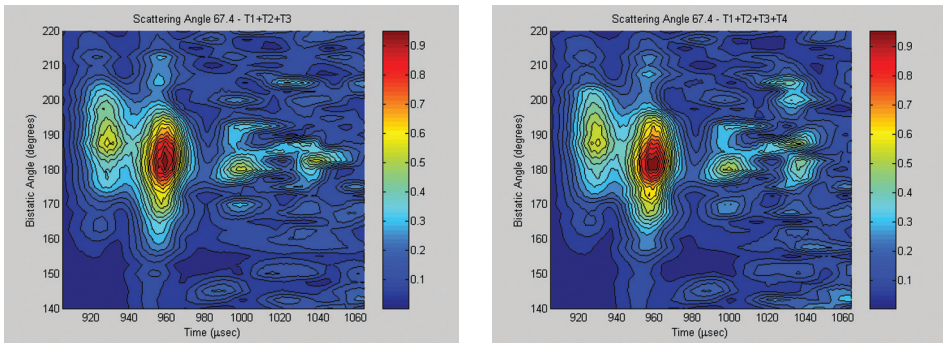


Figure 7. Contour maps of the normalised amplitude, now represented as a function of the bistatic angle, for a scattering angle of 67.4° , for targets $T_1+T_2+T_3$ (left), and targets $T_1+T_2+T_3+T_4$ (right).

further away: cf. Figure 3, top). The high amplitude region near $930\mu\text{sec}$ is due to T_2 , and the one at $960\mu\text{sec}$ is due to the combination of T_1 and T_3 .

3 Target Detection, Localisation and Acoustic Reconstruction

3.1 Target Detection

The previous Section showed that multiple targets could be visually identified by looking at the waveforms in the time-domain, for different scattering angles, and that careful use of different bistatic angles was often desirable. The examples shown here (Figures 4–7) correspond to a simple input signal, but both the tank experiments and, later, the sea trials, used a variety of transmitted signals (Ricker pulses, chirps, etc.). Techniques such as cross-correlation with a replica of the transmitted signal work well for chirp signals. For example, a chirp length of 5 ms would yield an effective range resolution of 7.5 m. The main peak of the cross-correlator output would then have a width in the order of $30\mu\text{s}$, reducing the spatial resolution to just 4.5 cm. But simple matched filtering is not an effective pulse compression technique for Ricker pulses. Ideally, a deconvolution process is required that will generate a narrow impulse at the effective time-of-arrival for any of the signal types likely to be encountered in a high-frequency active sonar system.

The traditional answer, at least in seismic data processing [30, 31], is to use non-recursive implementations of the Wiener filter:

$$r_t = \sum_{i=0}^{N-1} w_i S_{t-i}, \quad (1)$$

where r_t is the output sample at time t and s_t is the input at time t . The output is a weighted running average over N samples, with weights w_i chosen to give a pre-determined impulse at the output when the desired input waveform is present. Generally, a least-squares procedure is used to estimate the set of weights. This filter is effective with clean signals, but where there is noise, when pulses overlap, or if the pulse has been distorted during propagation, the filter fails to generate an impulse of the correct amplitude and at the correct location for every received pulse. The problem is intrinsic because: (1) the autocorrelation function of the input and the cross-correlation between the input and the desired output must be known to compute the correct filter coefficients; (2) when the filter operates in an unknown environment, and the received signal is no longer an exact copy of the transmitted pulse, the information required in (1) may not be available, so the correct filter coefficients cannot be computed.

An estimate of the relative robustness of the process, P , is given by

$$P = \sum_{i=0}^{N-1} w_i \rho_i, \quad (2)$$

where ρ is the cross-correlation between the desired output pulse and the input signal. Clearly, the greater the similarity between input and output, the more stable the process becomes, but at the price of less effective deconvolution.

To overcome these difficulties, one needs an adaptive implementation, adjusting the coefficients in response to variations in the signals. Bozic [32] proposed an algorithm based on a variation of Equation (1):

$$\left. \begin{aligned} \hat{r}_t &= \sum_{i=0}^{N-1} w_{i,t} S_{t-i} \\ e_t &= \hat{r}_t - r_t \\ w_{i,t+1} &= w_{i,t} + \mu e_t S_{t-i} \end{aligned} \right\} \quad (3)$$

Here \hat{r}_t is the desired output impulse and r_t is the filter output at time t . At each discrete time step, the updated values of the filter coefficients, $w_{i,t+1}$ are computed by applying a correction to the previous values $w_{i,t}$, derived from an earlier value of the input S_{t-i} and the difference e_t between the desired and actual filter outputs, weighted by a factor μ . The process must be initialised with a set of weights derived from an ideal replica of the transmitted signal, as in Equation (1), but it may then be ‘trained’ on received signals that are known to be single isolated pulses reflected from the bottom or a target of interest, with μ set to a value (usually close to unity) that gives reliable convergence to the desired output form. Where such reliable inputs are not present, the adaptation can be ‘frozen’ by setting μ to zero. The decision can be automated by monitoring the cross-correlation between the received signals and the ideal transmission replica. If the peak value falls below a predetermined value the input is not suitable for adaptation, so the process can be frozen.

Figure 8 shows the immediate interest of such a scheme. A fair amount of noise has been added to a typical signal (Figure 8a). Traditional processing, with a non-recursive Wiener filter (Figure 8b), detects some of the high variations (the first positive peak and the largest negative peak only), but keeps the high noise levels. Conversely, the adaptive processing of Equation (3) gives a much cleaner signal (Figure 8c). All significant peaks, positive and negative, are detected, and the noise is considerably reduced.

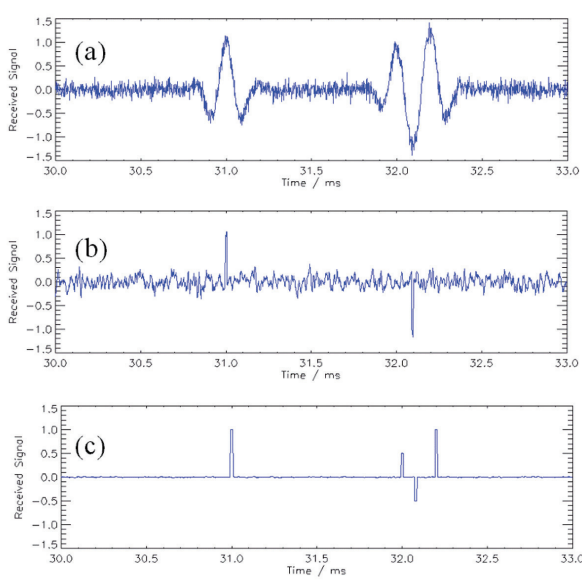


Figure 8. (a) an arbitrary input signal, with high noise, shows the difference between non-recursive Wiener filters (b) and the adaptive implementation optimising the relative weights (c). Note how the noise is considerably reduced in (c), and how the main peaks are correctly detected.

3.2 Localisation – Acoustic Reconstruction

Now that a suitable algorithm can detect the peaks related to high scatterers, it can be used to process each waveform (as visible in Figure 4, for example). Each of these waveforms was acquired for a unique set of incidence angle, bistatic angle, and scattering angle. Let us note the respective positions of the transmitter, scatterer and receiver as (x_T, y_T, z_T) , (x_S, y_S, z_S) and (x_R, y_R, z_R) . In a water column with a constant sound speed c (a reasonable assumption in the case of the SITAR sea trials, where the distances involved were relatively small, and the absolute truth in the case of the tank experiments), all propagation paths from the transmitter to the scatterer and then on to the receiver (the hydrophone) are straight lines. The total travel time T is given by

$$T = \frac{1}{c} \left[\frac{\sqrt{(x_S - x_T)^2 + (y_S - y_T)^2 + (z_S - z_T)^2} \dots}{+\sqrt{(x_R - x_S)^2 + (y_R - y_S)^2 + (z_R - z_S)^2}} \right]. \quad (4)$$

We know this travel time t from the deconvolution process (Section 3.1). We know the positions of the source and the receiver. It is therefore possible to solve Equation (3) for the position of the scatterer. This corresponds to the surface of a 3-D ellipsoid. More than one travel path must therefore be considered, to resolve this ambiguity. However, this leads to errors, as the signals received at different hydrophones will have travelled via different scattering points. A method based on a downhill simplex multidimensional search routine has been developed to minimise this effect. The actual location of the scatterer remains ambiguous, though. This can be remedied by taking the 4 receivers immediately left, right, above and below the receiver considered, and weighing their contributions appropriately [33]. The contours of the error values now lead to a local minimum, close to the actual location. By using the 4 surrounding receivers, the errors tend to cancel, and the ambiguity has been removed.

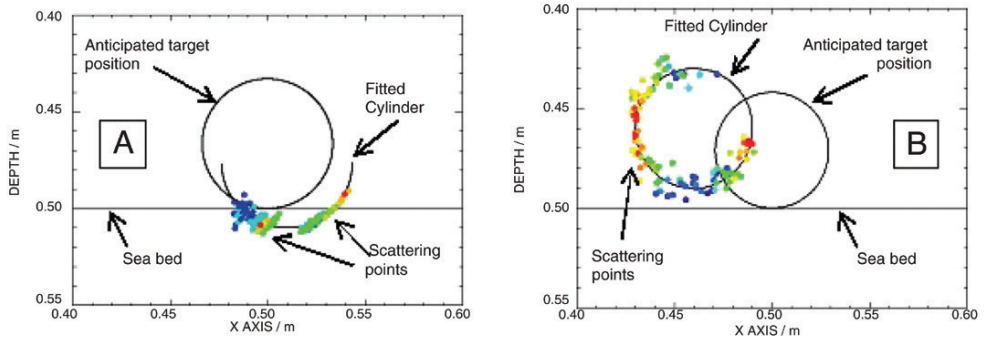


Figure 9. The scattering points, detected and localised using the algorithms presented in the text, are colour-coded according to their respective strengths (from blue, low, to red, high). They are presented next to the anticipated target positions for target T_1 (A) and for target T_2 (B). The offsets from the expected positions are very small, and can be explained by the uncertainty in positioning the targets by hand from the top of the water-filled tank.

Typical results are shown in Figure 9, using data from the tank experiments. The scattering points are localised in 3-D and shown as small circles, shaded to represent their relative scattering strengths (from black, low, to white, high). Figure 9a shows the reconstruction of target T_1 (fluid-filled aluminium tin, 6.7 cm in diameter). This target was placed horizontally on the sediment surface (and aligned along the Y axis, here). The scattering points, as detected and located by the algorithm, seem concentrated on the interface between the target and the seabed. The points do not precisely coincide with the expected target position. However, they can be fitted approximately to the lower portion of a cylinder of the same diameter as the target, 1 cm to the right and 1 cm below. The target was positioned manually from the top of the water-filled tank, so an error of around 1 cm in its anticipated position is not surprising, and is small relative to the overall scale of the experiment. It was also found that the target (weighing slightly more than 0.3 kg in air) would not sit totally proud of the seabed, but depressed the surface slightly. Figure 9b shows a similar analysis, for target T_2 (air-filled stainless steel cylinder, 5.8 cm in diameter). There is clearly a more uniform distribution of scattering all around the surface, as might be expected with the greater impedance mismatch in this case. Again, the fitted cylinder is slightly offset from the expected position (ca. 1 cm in the vertical direction, 4 cm in the horizontal direction), but this result is again satisfactory, especially when remembering the 10:1 scaling factor of these experiments. One can also remark that there are echoes within the same scattered signals, which may provide further information about the target structure (keeping in mind the characteristics of the transducer used, cf. Section 2.1).

Similar results have been obtained with different targets and different target orientations. Overall, they have confirmed the viability of the deconvolution and localisation processes, and they have demonstrated that the scatterer(s) can be located with a precision comparable with the sizes of the targets used in the experiments. Finally, combining the results from runs with hydrophone positions off the X axis will give us the ability to construct 3-D images of the different targets [34], using the algorithms presented in this Section.

4 Tank Experiments and Sea Trials

Using the tank facilities at the University of Bath, we have performed a wealth of bistatic scattering measurements, for multiple targets (up to 4 at the same time), on different types of seabeds (only silt was presented here, but similar experiments have been performed on fine gravel too). Single targets are easily identified, by inspection of the different scattering angles at a fixed bistatic angle;

they are characterised by a single region of high scattering. An additional target, in line with the source, induces interference, but the two targets are still visible. When adding a third target, one must view the measurements at different bistatic angles. In this case, the interference patterns give a clue to the presence of multiple targets. The effect of adding a fourth target is not very apparent in the images as a function of scattering angle. This may be due to the fourth target being just outside the acoustic beam, and its orientation relative to the other targets. However, its presence is revealed by generating images as a function of bistatic angle at a fixed scattering angle. First analyses of the individual scattering patterns show effects similar to those observed for bare seabeds [4, 24], or for targets at lower frequencies or suspended in water [28, 29]. Mainly, our experiments show that, by careful selection of ROV tracks and hydrophone chain positions, it is possible to identify individual targets in a multiple-target environment.

The second part of the work presented here was concerned with the localisation of individual scatterers, using multiple-aspect scattering measurements, and the acoustic reconstruction of their shapes. This work showed it was possible to detect these scatterers even in high-noise signals, using an adaptive implementation of the Wiener filters used in seismic data processing. Once processed, these signals can be used for the localisation of the target(s), using multidimensional search routines based on a downhill simplex algorithm. Typical results from the tank experiments are presented, showing the very good agreement between the actual and inferred locations of the targets (as well as their characteristics, in particular for targets of distinct impedances).

These results are important *per se*. Using realistic, scaled targets, proud, half-buried or flush buried, and real seabed types, Section 2 showed it was possible to visually distinguish between close targets, and to some degree detect their different acoustic characteristics (impedance differences, physical structure of the targets, and possibly different reemitted waves). Using the algorithms presented in Section 3, it proved possible to accurately and automatically detect these targets, and quantify the local variations in scattering strengths. It seems quite reasonable that we can now reconstruct the 3-D structure of multiple-target environments. These results pave the way for multistatic surveys at sea, in environments with multiple targets.

The first example was the SITAR sea trials, which took place in the Stockholm Archipelago in September/October 2003. They concentrated on an old ammunition dumpsite, thoroughly documented and ground-truthed [26, 35]. One half of the sea trials consisted in testing a parametric synthetic sidescan sonar [35, 36]. The other half, aboard HMS Fårösund from the Royal Swedish Navy, consisted in using a Remotely-Operated Vehicle (ROV) with a narrow-beam sonar to image potential targets of interest (Figure 10).

Drawing on the lessons learned during the tank experiments, the quality of the raw and processed data were systematically and thoroughly controlled on-board during acquisition. The time synchronisation of the transmitter and receivers proved in particular important. Early analyses showed it was possible to visualise close targets (using the techniques outlined here), despite the occasional failures of some hydrophones. The ROV flew along lines of interest (line scans), and rotated around particular targets (rotation scans). Attitude control proved paramount in getting good localisation of the individual scatterers, as unexpected deviations from the nominal three-dimensional positions had direct repercussions in the localisation process. The processing of the sea trials data is now going on at the different institutions involved and the first results are encouraging. Using the signal processing routines outlined in this article, individual targets can be detected, and it appears that it is possible to accurately reconstruct their exact scattering characteristics, even in multiple-target settings.

Acknowledgements

C. Dyer (University of Bath) is gratefully acknowledged for helping setting up the initial experiments. O. Gómez Sichi provided helpful comments during the internal review of the manuscript. This work is funded by the European Commission (Framework-V programme SITAR EVK3-2001-00012, coordinated by Prof. A. Caiti, ISME, Italy).

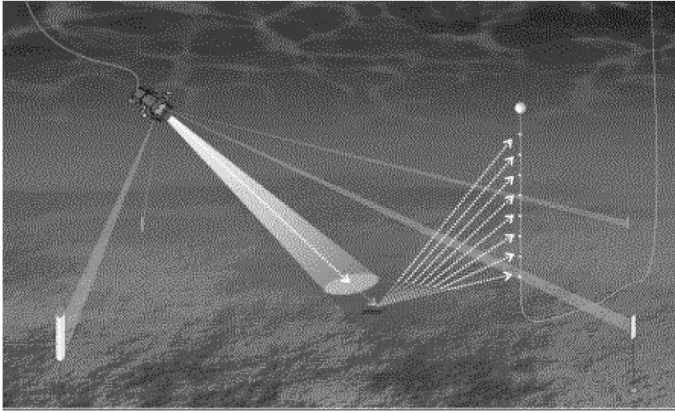


Figure 10. During the SITAR sea trials (late 2003), the ROV was flown above targets of interest, doing both line scans and rotation scans. It was accurately positioned through a transponder net (white, upright cylinders in this diagram). The targets were imaged with a narrow-beam parametric sonar, and the scattered signals were received on a hydrophone chain. Preliminary results are consistent with the conclusions from the tank experiments. Image ©FOI, Sweden.

References

1. Blondel Ph. and Murton B. J., *Handbook of Seafloor Sonar Imagery*, Praxis-Wiley & Sons: Chichester (UK), 314 pp., 1997.
2. Lurton X., *An introduction to underwater acoustics*, PRAXIS-Springer Verlag: Chichester (UK), 380 pp., 2002.
3. Pace N. G., Pouliquen E., Bergem O. and Lyons A. P., *High-Frequency Acoustics in Shallow Water*, NATO Saclant Undersea Research Centre, 612 pp, (1997).
4. Blondel Ph., McCloghrie P., Pace N. G., Heald G. J. and Brothers R., High-frequency bistatic bottom scattering: Modelling and experimental studies. In *Proceedings of the Sixth European Conference on Underwater Acoustics*, Gdansk, Poland, 21–29 (2002).
5. Canepa G., Pace N. G. and Pouliquen E., Field measurements of bistatic scattering strength of a sandy seabed at 118 kHz. In *Proceedings of the Sixth European Conference on Underwater Acoustics*, Gdansk (Poland), 183–188 (2002).
6. Burnett D. S. and Zampolli M., A unified continuum mechanics approach for structural acoustic finite-element modeling of target scattering. In *Proceedings of the Seventh European Conference on Underwater Acoustics*, Delft (Netherlands), 423–430, 2004.
7. Thorsos E. I., Exact numerical methods versus the Kirchhoff approximation from rough surface scattering. In *Computational Acoustics, vol. II: Algorithms and Applications*, edited by D. Lee, R. L. Sternberg, M. H. Schultz (Amsterdam, North-Holland, 1988) pp. 209–226.
8. Wirgin A., Scattering from hard and soft corrugated surfaces: Iterative corrections to the Kirchhoff approximation through the Extinction Theorem. *J. Acoust. Soc. Am.* **85**, 670–679 (1989).
9. Ivanova K. and Broschat S. L., The method of the local parabolic approximation for rough surface scattering. *J. Acoust. Soc. Am.* **94**(4), 2326–2333 (1993).
10. Schenk H. A., Helmholtz integral formulation of the sonar equations. *J. Acoust. Soc. Am.* **79**(5), 1423–1433 (1986).

11. Thorsos E. I., The validity of the Kirchhoff approximation for rough surface scattering using a Gaussian roughness spectrum. *J. Acoust. Soc. Am.* **83**, 78–92 (1988).
12. Kirkup S. M., “The boundary element method in acoustics”, Integrated Sound Software Publications (1998).
13. Voronovich A. G., Small-slope approximation in wave scattering by rough surfaces. *Sov. Phys. JETP* **62**, 65–70 (1985).
14. Thorsos E. I. and Broschat S. L., An investigation of the small slope approximation for scattering from rough surfaces. Part I. Theory. *J. Acoust. Soc. Am.* **97**(4), 2082–2093 (1995).
15. Broschat S. L. and Thorsos E. I., An investigation of the small slope approximation for scattering from rough surfaces. Part II. Numerical studies. *J. Acoust. Soc. Am.* **101**(5), 2615–2625 (1997).
16. Schmidt H. and Glatte J., A fast field model for three-dimensional wave propagation in stratified environment based on the global matrix method. *J. Acoust. Soc. Am.* **78**, 2105–2114 (1985).
17. Schmidt H. and Kuperman W. A., Spectral representation of rough interface reverberation in stratified ocean waveguides. *J. Acoust. Soc. Am.* **97**, 2199–2209 (1995).
18. Kur’yanov B. F., The scattering of sound at a rough surface with two types of irregularity. *Soviet Physics – Acoustics* **8**(3), 252–257 (1963).
19. McDaniel S. T. and Gorman A. D., An examination of the composite-roughness model. *J. Acoust. Soc. Am.* **73**(5), 1476–1486 (1983).
20. Jackson D. R., A model for bistatic bottom scattering in the frequency range 10–100 kHz. *APL-UW Technical Report TR-9305*, University of Washington (1993).
21. Williams K. L. and Jackson D. R., A model for bistatic scattering into ocean sediments for frequencies from 10–100 kHz. *APL-UW Technical Report TR-9505*, University of Washington (1996).
22. Pouliquen E., Bergem O. and Pace N. G., Time-evolution modeling of seafloor scatter. I. Concept. *J. Acoust. Soc. Am.* **105**(6), 3136–3141 (1999).
23. Williams K. L. and Jackson D. R., Bistatic bottom scattering: Model, experiments and model/data comparison. *J. Acoust. Soc. Am.* **103**(1), 169–181 (1998).
24. Blondel Ph., Pace N. G., Heald G. J. and Brothers R., High-frequency bistatic scattering: comparison of tank and sea experiments. In *Acoustical Oceanography*, T.G. Leighton, G. J. Heald, H. D. Griffiths, G. Griffiths (eds), Proceedings of the Institute of Acoustics, vol. 23(2) 2001, pp. 276–282.
25. Skogqvist P. and Karasalo I., A fast acoustic scattering method for buried objects. In *10th International Congress on Sound and Vibration*, Stockholm, A. Nilsson and H. Bodn (eds.), vol. 5, (2003) pp. 2457–2465.
26. Karasalo I. and Skogqvist P., Transient scattering from submerged and buried objects (6 pages). In *Proc. European Conference on Underwater Acoustics* (Delft, Netherlands, July 2004), pp. 451–456.
27. Jayasundere N. and Blondel Ph., Multistatic Imaging of Multiple Targets - Scaled Tank Experiments with a Silt Seabed (6 pages, CD-ROM). In *Proc. European Conference on Underwater Acoustics* (Delft, Netherlands, July 2004).
28. Blonigen F. J. and Marston P. L., Leaky Helical Flexural Wave Backscattering Contributions from Tilted Cylindrical Shells in Water: Observations and Modeling. *J. Acoust. Soc. Am.* **112**(2), 528–536 (2002).
29. Tesei A., Maguer A., Fox W. L. J., Lim R. and Schmidt H., Measurements and Modeling of Acoustic Scattering from Partially and Completely Buried Spherical Shells. *J. Acoust. Soc. Am.* **112**(5), 1817–1830 (2002).
30. Arya V. K. and Aggarwal J. K., *Deconvolution of Seismic Data*, Benchmark Papers in Electrical Engineering and Computer Science, ed. J. B. Thomas. (1982) Vol. 24. Hutchinson-Ross.

31. Telford W. M., Geldart L. P. and Sheriff R. E., "Applied Geophysics – Second Edition", Cambridge University Press, (1990).
32. Bozic S. M., *Digital and Kalman Filtering*, 2nd ed., Edward Arnold (1994).
33. Dobbins P. F., Blondel Ph., Pace N. G. and Karasalo I., SITAR – Localisation and imaging of seafloor targets with multiple-aspect scattering. In *10th International Congress on Sound and Vibration*, Stockholm, A. Nilsson and H. Bodn (eds.), vol. 5 (2003), pp. 2467-2474.
34. Caiti A., Murino V., Palmese M. and Trucco A., Object Reconstruction and Feature Extraction from 3-D Underwater Acoustic Scattering Measurements. In *10th International Congress on Sound and Vibration*, Stockholm, A. Nilsson and H. Bodn (eds.), vol. 5 (2003), pp. 2449–2456.
35. Caiti A. and the SITAR Team, The SITAR Project – Seafloor Imaging and Toxicity: Assessment of Risk caused by buried waste. In *Proc. European Conference on Underwater Acoustics* (Delft, Netherlands, July 2004), pp. 757–762.
36. Zakharia M., Chevriaux Y., Doignon G., Dybedal J., Legallo R. and Pollet C., SITAR prototype, a parametric synthetic sidescan sonar. In *Proc. European Conference on Underwater Acoustics* (Delft, Netherlands, July 2004), pp. 1121–1126.

A SEDIMENT PROBE FOR THE RAPID ASSESSMENT OF SEABED CHARACTERISTICS

JOHN OSLER

*Defence R&D Canada Atlantic,
PO Box 1012, Dartmouth, N.S., Canada, B2Y 3Z7
E-mail: john.osler@drdcrrdc.gc.ca*

ARNOLD FURLONG

*Brooke Ocean Technology,
50 Thornhill Drive, Unit 11, Dartmouth, N. S., Canada, B3B 1S1
Email: afurlong@brookeocean.com*

HAROLD CHRISTIAN

*Christian Situ Geoscience Inc.,
50 Thornhill Drive, Unit 11, Dartmouth, N. S., Canada, B3B 1S1
Email: christian.situ@attglobal.net*

A sediment probe has been developed for use as a tool for the rapid assessment of the seabed parameters that are required to predict the performance of naval sonars and mine burial. The probe, called the Free Fall Cone Penetrometer test (FFCpT), measures acceleration and pore pressure as a function of depth of penetration into the seafloor. It also records hydrostatic pressure and optical backscatter for detection of the water sediment interface. This combination of sensors permits the direct application of geotechnical analysis methods and parametric-based correlations already long established in engineering practice. The probe provides two independent means of calculating the undrained shear strength as well as engineering variables that are used to identify the sediment grain size characteristics. A resistivity module has been developed as a means to determine porosity, from which other parameters, such as sound speed and bulk density, may be estimated using empirical relationships. During its descent to the seabed, the instrument also measures the sound speed in the water column. A comparison of FFCpT results with independent measurements of sediment grain size and porosity indicates that the FFCpT is accurately identifying the characteristics of a diverse range of marine sediments.

1 Introduction

Performance prediction modelling for active sonar requires the geoacoustic properties of the surficial seabed sediments in order to account for the transmission loss and reverberation due to seabed interaction. Calculating the transmission loss and scattering of acoustic energy typically requires the

geoacoustic properties to be parameterized in terms of their density, compressional and shear sound speeds, and their associated attenuations. These parameters are often measured on physical samples, such as cores, or obtained from inversions of purpose designed acoustic experiments. The former are costly to collect and prone to artifacts due to disturbance during collection, handling and storage. In addition, the measurements must be corrected to the *in situ* conditions, notably temperature and pressure, and possibly for dispersion effects as the sound speed on cores is typically measured at much higher frequencies (hundreds of kHz) than those of interest for naval sonar applications. Numerous acoustic techniques have been developed to obtain geoacoustic parameters and can yield excellent results. However, these techniques typically require specialized equipment and detailed analysis that preclude their widespread use. This challenge provides the motivation to develop instruments and techniques that reduce the number of independent parameters that must be measured to effectively parameterize the seabed. This is particularly true in a rapid environmental assessment scenario in which the number and type of measurements must be limited and the analysis streamlined. This paper describes a sediment probe that was developed in a government/industry partnership research program to measure seabed properties quickly and accurately. Although this research is being conducted in the context of naval applications (sonar performance modeling, mine burial prediction, and sediment classification), the probe can be applied in several other applications, such as: marine engineering, cable route surveys, habitat and geological mapping.

2 Instrument Design and Capabilities

The sediment probe, referred to as the Free Fall Cone Penetrometer test (FFCPT) from this point onward, makes direct measurements of geotechnical (large strain) properties of the seabed. It provides two independent means of calculating the undrained shear strength. These geotechnical measurements are also used to determine the dominant sediment behaviour type, or grain size characteristics, of the seabed (e.g., clay, silt, sand, or gravel). When fit with the optional electrical resistivity module, the FFCPT can also obtain geoacoustic (small strain) properties of the seabed. This is done by relating measurements of porosity to other quantities, such as compressional wave sound speed, through the application of empirical relationships. The FFCPT has the same scaling factors as a conventional pushed cone penetrometer, but with a larger diameter to house the instrumentation. It is designed to freefall into the seabed and to survive impacts with rock, if and when that happens. To survey large areas efficiently, the ultimate goal is to be able to deploy the FFCPT from a moving vessel. That goal has been incorporated into all aspects of the FFCPT's design and development.

The FFCPT consists of a nose cone instrumented with geotechnical sensors, power supply, electronics, and tail pressure sensor (Fig. 1). It measures acceleration and dynamic sediment pore pressure as a function of depth of penetration into the seafloor (Fig. 2). The FFCPT also records hydrostatic pressure and optical backscatter (Fig. 2). The former allows the descent velocity of the FFCPT to be monitored during its freefall to the seabed. The latter aids in the detection of the water-sediment interface, especially on high porosity fluidmud seabeds (Fig. 3). Most recently, a sound speed probe has been mounted in the tail in order to obtain the water sound speed profile during the FFCPT's freefall descent (Fig. 1).

The FFCPT has three accelerometers to ensure that at least one will be able to provide a high fidelity measurement (Fig. 2). This is necessary because the FFCPT encounters a wide range of peak accelerations depending on the sediment type that it impacts (Table 1). In Fig. 2, for example, the 2 g accelerometer signal is clipped shortly after the FFCPT impacts the seabed. The FFCPT is presently configured with accelerometer input ranges of 5, 40, and 100 g, selected on the basis of seatrial impacts on many different types of sediment. For a given FFCPT drop, one of the time series of acceleration is integrated to calculate the depth of penetration into the seabed, its velocity during penetration of the seabed, and its freefall velocity upon impacting the seabed. The latter is reconciled with the freefall impact velocity calculated from the hydrostatic pressure sensor. For water depths

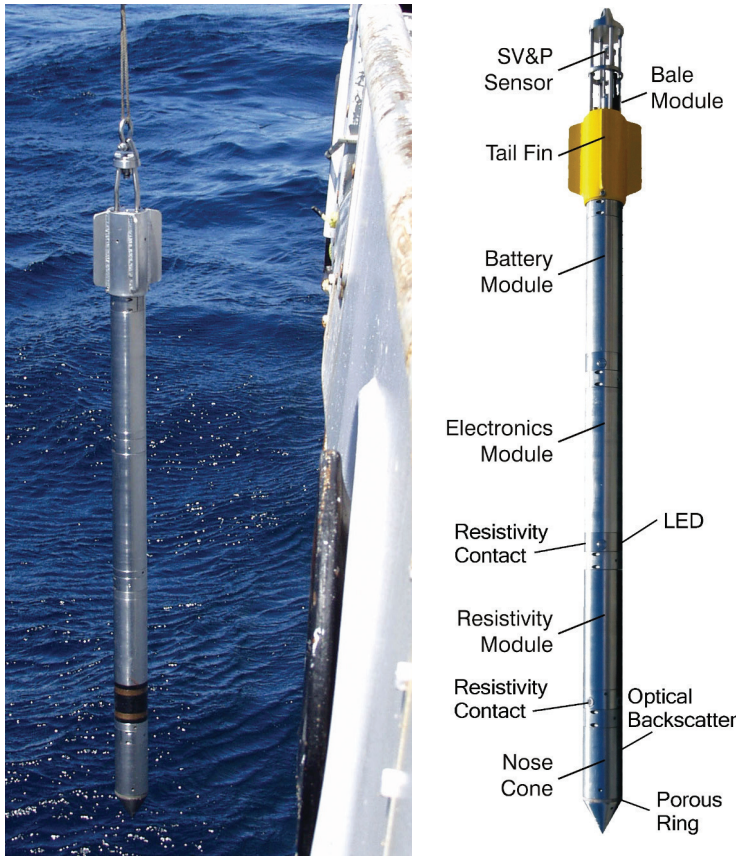


Figure 1. Left: Photograph of the FFCPt during deployments in St. Margaret's Bay in 2002. Right: Diagram indicating the contents of the different modules and sensor locations in the present configuration of the FFCPt. Note the change from the brass rings to point electrodes and the addition of the sound velocity and pressure sensor in the tail.

less than 60 m, the impact velocity of the FFCPt is typically in the range of 8 to 10 m/s. It reaches its terminal velocity within the first 6 to 8 m of its descent. To date, FFCPt deployments have been conducted with it tethered to a 1/4" diameter rope, AMSTEEL Spectron 12, that is flaked on the deck of the research vessel. A plastic tarpaulin is placed on the rough surface of the deck to minimize its influence on the rope. For water depths in excess of approximately 60 m, the drag of the tether rope begins to decrease the impact velocity of the FFCPt. Impact velocities in the range of 5.5 to 7 m/s have been observed in water depths from 130 to 100 m.

Robertson [1] provides a review of how conventional pushed cone penetrometer test (CPT) measurements are related to geotechnical properties. FFCPt measurements at CPT stations were used to establish that these relationships are applicable at the much higher rates of penetration experienced by the FFCPt. Two independent measurements of the undrained shear strength are calculated using the FFCPt. For mine burial prediction, it may be combined with the dimensions of an object to calculate the bearing strength of the seabed, and the probability of burial upon impact or in subsequent

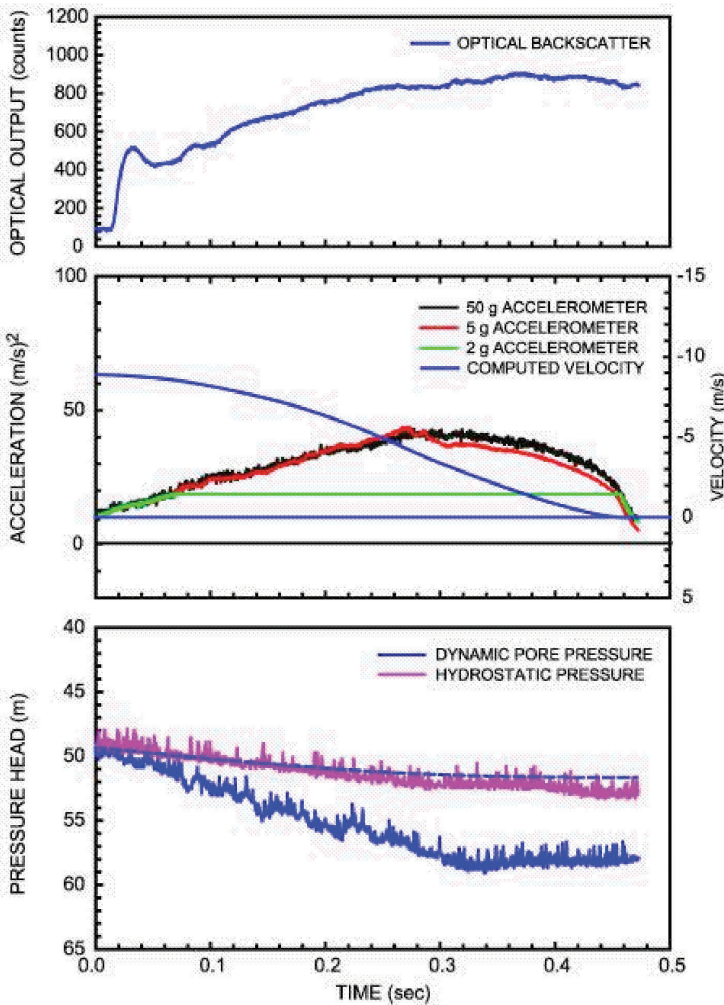


Figure 2. Time series of FFCPt sensors for a deployment at location 7 (Table 1) in St. Margaret’s Bay, Nova Scotia. Top: Uncalibrated optical backscatter that is used to detect the watersediment interface. In raw data, the signal is delayed because the sensor is located 16.8 cm from the tip of the nose cone. Middle: Measured acceleration and computed velocity. Bottom: Dynamic pore pressure measured in the nose cone and hydrostatic pressure measured on the tail of the FFCPt.

scouring. The first technique to calculate undrained shear strength uses the acceleration to calculate the dynamic penetration resistance. The second technique uses the dynamic pore pressure measured by a pressure sensor in the nose cone of the FFCPt. The pressure signal passes through a porous hydrophilic ring to the pressure sensor inside a cavity in the nose cone that is filled with mineral oil. Before conducting experiments, steps are taken to ensure that the cavity does not contain any air and that the pressure transducer has reached thermal equilibrium. The undrained shear strength measurements compare favourably (Fig. 4) and follow a normal consolidation curve (dashed line) in this particular example.

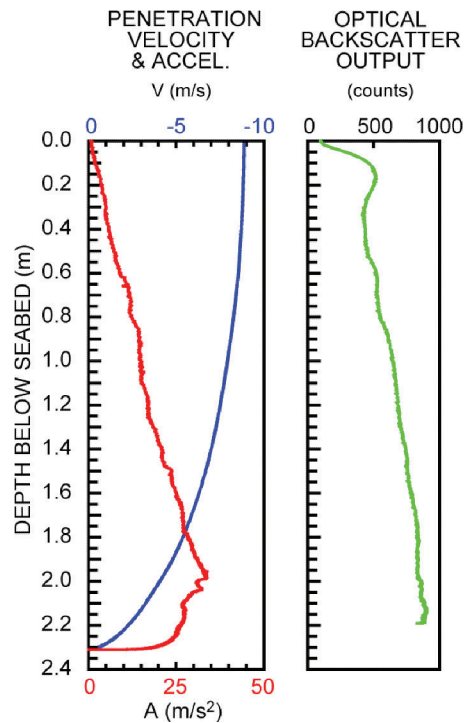


Figure 3. An acceleration sensor time series is integrated in order to create profiles of the FFCPt measurements as a function of depth.

Table 1. Summary of June 2002 FFCPt Deployments in St. Margaret’s Bay, Nova Scotia

FFCpt Station	Latitude (Deg)	Longitude (Deg)	Water Depth (m)	Seabed Penetration (m)	Peak Accel. (m/s ²)	Resistivity (Ω)
71	44°36.441 N	063°59.343 W	50.1	2.5	40	8
72	44°36.534 N	063°59.308 W	49.4	1.85	68	11
73	44°36.629 N	063°59.263 W	40.6	0.54	492	13
61	44°36.252 N	064°00.576 W	44.5	1.63	230	10
62	44°36.410 N	064°00.542 W	43.4	1.61	95	11
31	44°36.591 N	064°00.588 W	40.3	0.93	165	13
32	44°36.668 N	064°00.562 W	38.2	0.88	476	13

Normalized values of the dynamic penetration resistance and dynamic pore pressure (right panels in Fig. 4) are used in a qualitative determination of the sediment behaviour type. The combination of dynamic penetration resistance and dynamic pore pressure sensors permits the direct application of geotechnical analysis methods and parametricbased correlations already long established in engineering practice [1]. When plotted against each other (next section), these parameters yield an

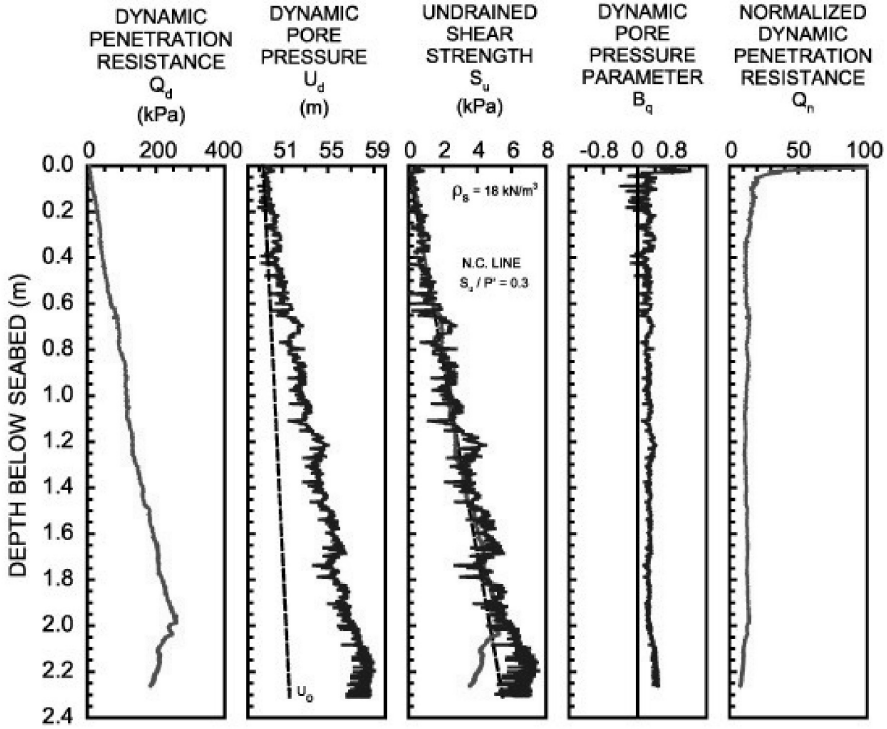


Figure 4. Acceleration is used to determine the dynamic penetration resistance from which the undrained shear strength is calculated. The nose cone pore pressure is used to determine the dynamic sediment pore pressure and a second independent measurement of undrained shear strength. Normalized values of these parameters are used for the empirical sediment classification.

empirical measure of sediment type, based on the zone in which the data lie (Table 2). Discrete measurements at different depths are plotted as dots, colour coded as a function of depth from the seabed to the depth of penetration of the FFCPt into the seabed. In the next section, the performance of the FFCPt is evaluated by comparing its results with independent information collected by sediment cores.

The modular design of the FFCPt permits additional ballast or experimental sensor suites to be integrated into the probe. The first module developed measures resistivity as a means to determine porosity [2]. The measured bulk resistivity is a function of the resistivity of both the pore fluid and the sediment grains as well as the shape of the pore spaces. Assuming that the resistivity of the pore fluid is low, as with seawater, and there is not an abundance of clay minerals, then Archie's [3] Law may be applied. It is

$$\rho_b / \rho_f = a n^{-m}, \quad (1)$$

where ρ_b is the bulk resistivity, ρ_f is the fluid resistivity, a is a constant (usually 1 for unconsolidated sediments), n is the porosity, and m is a function of grain shape (~ 1.5 for sands). Empirical studies suggest that the porosity of the surficial sediments is a physical property of the seabed to which the more traditional properties (density, attenuation, and sound speeds) may be related [4, 5]. For example, using data from over two hundred cores collected in littoral waters with divers or box cores to minimize artifacts, Richardson and Briggs [4] have established a regression relationship between

Table 2. Description of FFCPt Sediment Classification Zones and Corresponding Grain Size Fractions on Sediment Core Samples.

FFCpt Sediment Classification Zone	Sediment Behaviour Type	Comparative Core Grain Size Fraction	Zone Grayscale on plots
1	Sensitive, fine-grained	N/A	
2	Organic sediments: wood waste, peats	N/A	
3	Clays: clay to silty clay	Clay	5%
4	Silt mixtures: clayey silt to silty clay	Silt	15%
5	Sand mixtures: silty sand to sandy silt	Sand	25%
6	Sands: clean sands to silty sands	Sand	35%
7	Gravelly sand to sand	Gravel	45%

porosity, n , in percent, and compressional sound speed, V_p , given by

$$V_p/V_w = 1.574 - 0.015n + 0.0001n^2. \quad (2)$$

The original resistivity module (used for the measurements in this paper) was developed by Brooke Ocean Technology (Dartmouth, Nova Scotia) and ConeTec (Vancouver, British Columbia) using the design principles of a static resistivity CPT system as described by Campanella and Weemee [2]. Conformal with the O.D. of the probe, there are two cylindrical brass electrodes, 1.5 cm wide, separated by 6.7 cm and isolated by sections of an insulating material—Delrin (Fig. 5). Once the probe has penetrated the seabed and come to rest, a bulk resistivity measurement is made by generating a currentswitched AC sinusoidal wave, at a frequency of about 1 kHz. The fluid resistivity required in Eq. 1 was measured in the seawater immediately above the seabed on the same day in a separate deployment. The performance of the original resistivity module is presented in the next section.

Experiments have also been conducted with alternate electrode configurations (Figs. 1 and 5). Point electrodes were potted into small cylinders and situated at different positions along the sidewall of the FFCPt. In one case, the resistivity was measured between two electrodes within the same cylinder. In another case, the resistivity was measured between individual electrodes in separate cylinders. These alternate configurations were motivated by two factors. First and foremost, to be able to make porosity measurements at different depths within the seabed as there can be strong

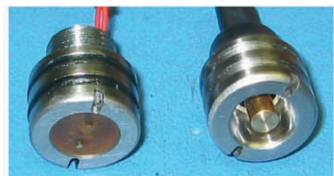


Figure 5. Left: Photograph of the electrical resistivity module used during the June 2002 sea trial. Right: Photograph of two other electrode configurations that have been tested in subsequent experimentation.

gradients in surficial marine sediments. Second, there were concerns that the design of the original resistivity module introduced a mechanically weak zone that might not withstand the rigours of repeated drops. The experiments with the alternate electrode designs have not met with the same success as the original design. It is speculated that this may be due to one or both of the following factors: a) variability in sediment properties immediately adjacent to the probe that is overcome by spatial averaging in the original design; b) the smaller electrodes are more susceptible to the effects of oxidation or poor contact with the sediment.

3 Comparison with Independent Sediment Property Information

The FFCPt, with the original resistivity module fitted (Fig. 5, photo on left), was deployed at a number of locations in St. Margaret's Bay, Nova Scotia, on 6 June 2002. Two measurement locations were colocated with high quality sediment cores and a third is located a short distance from a core (Fig. 6). The experimental area in St. Margaret's Bay has a diverse range of sediments and a comprehensive data set [6] to study tools and techniques for classifying marine sediments. The data set collected by DRDC Atlantic and the NATO Undersea Research Centre includes results from: three swath bathymetry systems (Atlas Hydrosweep MD50, EM3000, and Reson 8125); sidescan sonar (Klein 5500); sediment cores with grain size analysis and multisensor core logging of physical properties (porosity and compressional wave sound speed); stereo photographs; high resolution seismic profiles (EdgeTech XStar chirp system and GeoAcoustics Boomer impulsive system); a commercial seabed classification system Roxann; grab samples; and sediment probe drops (FFCpt, STING, and XBP).

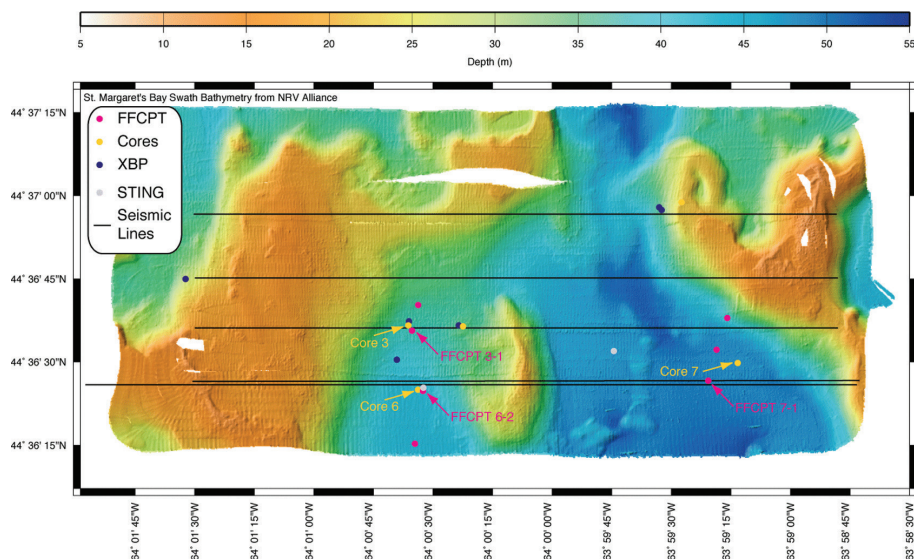


Figure 6. FFCPt and sediment core locations in St. Margaret's Bay, Nova Scotia, superimposed on the Atlas Hydrosweep MD50 swath bathymetry map [6].

The deeper parts of St. Margaret's Bay are covered by a very fine grained, nearly acoustically transparent, clay and silt material. This material was sampled by Core 7 and two FFCPt measurements (71 and 72 in Table 1) were made nearby. The sediment behaviour type measured by the FFCPt (Fig. 7) is contained within zones 3 and 4 and is entirely consistent with the grain size measurements on the core. (Note that the FFCPt result includes sample points from its full depth of penetration, 2.5 m, and that is much deeper than the core's penetration of 1.1 m). The shallower

parts of St. Margaret's Bay are covered by coarser grained sediment. This material was sampled by Core 3 and an FFCPt measurement (31 in Table 1). The sediment behaviour type measured by the FFCPt (Fig. 8) is contained within zone 6 and is consistent with the core sample that indicates that the seabed at this site is in excess of 50% sand.

The last comparison (Fig. 9) is at a location where the seabed has a sand dominated layer for the top 30 cm that overlies finer grained, clay and silt, below that depth. The FFCPt indicates zone 6 material (sand) material at the seabed with a fairly rapid transition through zone 5 to material in zones 4 and 3.

Figure 10 is a comparison of the porosity profiles measured on sediment Cores 3, 6, and 7 with results from the FFCPt. The FFCPt measurements were made using the original resistivity module (Fig. 5, photo on left), the resistivity values in Table 1, and calculated using Eq. 1. The porosity is measured at a single location behind the nose cone (Fig. 1). For clarity, it is represented by a vertical dashed line from the seabed to the FFCPt's depth of penetration. The agreement is excellent for Cores 3 and 6 (left and right panels in Fig. 10). The largest discrepancy is for Core 7 (centre panel in Fig. 10). Three explanations are offered: a) the porosity profile reveals a gradient that when extrapolated may agree quite well with the FFCPt measurement (at a depth approximately 1 m beyond the length of the core); b) the abundance of clay material at this location may be violating assumptions regarding Archie's Law [3]; or c) the physical properties may be different due to the physical separation between the core and FFCPt locations (Fig. 6).

4 Summary

This paper describes a new sediment probe, the Free Fall Cone Penetrometer test (FFCPt), that has been developed to measure geotechnical and geoacoustic properties of the seabed. It is being developed as a tool to enable a rapid assessment of seabed characteristics, some quantitative and some qualitative. A comparison of FFCPt measurements with independent information from sediment cores reveals that the FFCPt is making accurate determinations of sediment type and porosity for a wide range of marine sediments. The FFCPt will enable surveys of seabed characteristics to be made in a fraction of the time and at a fraction of the cost that is associated with conventional methods, such as the collection of sediment cores or hydraulically powered push cone penetrometer measurements.

5 Future Work

The future technical development of the FFCPt will focus on two areas. The first is the integration and testing of the FFCPt with a moving vessel profiler (MVP). The MVP is a "free wheel capable" slip ring winch that will greatly increase the number of times that the FFCPt can be deployed. Initial tests will be conducted with the vessel at rest and then progress to evaluating the viability of making measurements with the FFCPt while the vessel is underway. The second technical development being pursued is the measurement of electrical resistivity during penetration of the FFCPt into the seabed. The static measurements presented in this paper reveal the potential of these measurements but a profile of porosity, rather than a point measurement, is ultimately desired. The high rate of initial penetration poses several technical challenges, such as an excitation rate of several hundred kHz, that are presently being studied.

In addition to these technical developments of the FFCPt, a comparison of sediment properties obtained by the FFCPt and another sediment probe [7] is being undertaken.

Several measurements were made at colocated stations on the Malta Plateau during the collaborative CAN-US-NATO sea-trial Boundary2004. In St. Margaret's Bay, the authors plan to continue investigating the relationship between measurements made by the FFCPt and other survey data (swath bathymetry, sidescan sonar, and high resolution seismic profiles).

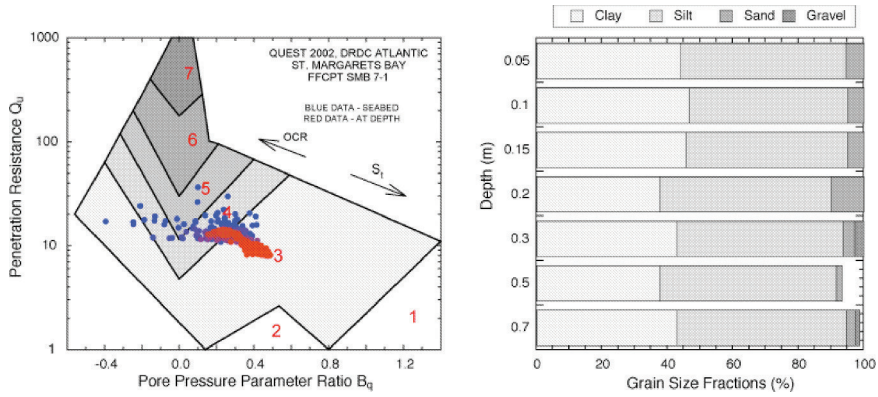


Figure 7. Left: Sediment behaviour type of FFCpt drop 71 at a clay/silt site in St. Margaret's Bay, Nova Scotia. Right: Grain size analysis of Core 7, collected by the NRV Alliance.

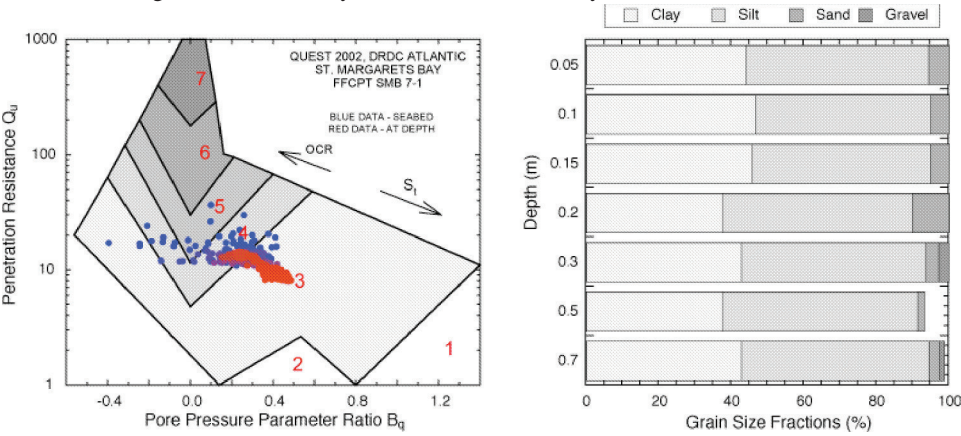


Figure 8. Left: Sediment behaviour type of FFCpt drop 31 at a sandy site in St. Margaret's Bay, Nova Scotia. Right: Grain size analysis of Core 3, collected by the NRV Alliance.

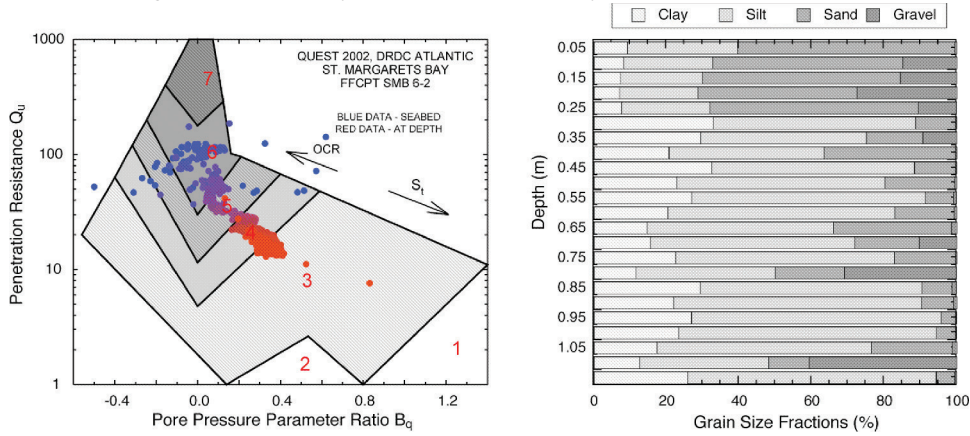


Figure 9. Left: Sediment behaviour type of FFCpt drop 62 at a site in St. Margaret's Bay, Nova Scotia. Right: Grain size analysis of Core 6, collected by the NRV Alliance. The seabed has a surficial layer of sand underlain by finer grained material.

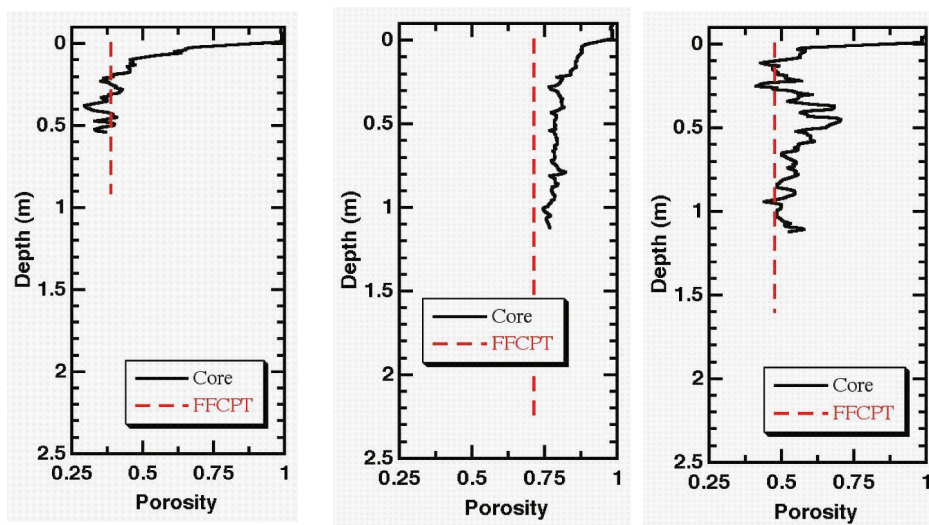


Figure 10. FFCPt and sediment core porosities at locations 3, 7, and 6 (from left to right).

Acknowledgements

The authors wish to thank the officers and crew of *CFAV Quest* for their assistance during sea-trials. Dr. Eric Pouliquen of the NATO Undersea Research Centre and the officers and crew of the *NRV Alliance* collected the sediment cores in St. Margaret's Bay, Nova Scotia and provided the data for the analysis in this paper. Mark Smith and Steve Smyth of Brooke Ocean Technology were involved in the development and testing of the FFCPt. Mark O'Connor of DRDC Atlantic operated the FFCPt during the sea-trials. Ken Wilkie developed the software interface to allow near realtime analysis of FFCPt data. The original prototype of the FFCPt was built by David Heffler and Harold Christian when they were employed by the Geological Survey of Canada – Atlantic. Mark Trevorow of DRDC Atlantic provided expert advice regarding the design of the FFCPt.

References

1. Robertson P. K., Soil classification by the cone penetration test. *Can. Geotech. J.* **27**, 151–158 (1990).
2. Campanella R. G. and Weemees I., Development and use of an electrical resistivity cone for groundwater contamination studies. *Can Geotech. J.* **27**, 557–567 (1990).
3. Archie G. E., The electrical resistivity log as an aid in determining some reservoir characteristics. *Trans. Amer. Inst. of Mineral Metallurgy Eng.* **146**, 5462 (1942).
4. Hamilton E. L. and Bachman R. T., Sound velocity and related properties of marine sediments. *J. Acoust. Soc. Am.* **72**, 1891–1904 (1982).
5. Richardson M. D. and Briggs K., On the use of acoustic impedance to determine sediment properties, *Proc. Inst. Acoustics* **15**, 1523 (1993).
6. Pouliquen E., Trevorow M., Blondel P., Canepa G., Cernich F. and Hollett, R., Multisensor analysis of the seabed in shallow water areas: overview of the MAPLE'2001 experiment. In *Proc. of the 6th European Conf. on Underwater Acoust.*, Gdansk, Poland, 2427 June, 167175 (2002).
7. Turgut, A., Gauss R. and Osler, J., Measurements of velocity dispersion in marine sediments during the Boundary04 Malta Plateau experiment. In *Proc. Oceans 2005, IEEE/MTS*, (in press).

CONTINUOUS ACOUSTIC MONITORING OF PHYSIOLOGICAL AND ENVIRONMENTAL PROCESSES IN SEAGRASS PRAIRIES WITH FOCUS ON PHOTOSYNTHESIS

JEAN-PIERRE HERMAND

*Environmental hydroacoustics laboratory, Université libre de Bruxelles
av. Franklin D. Roosevelt 50 - CP194/05, B-1050 Bruxelles, Belgium
E-mail: jhermand@ulb.ac.be*

The development of methods for the reliable and efficient assessment of the health status of submerged aquatic vegetation is of considerable interest nowadays. The present paper explores the use of acoustics for the remote sensing of physiological processes of aquatic plants in relation to the environment, dealing specifically with the leaf photosynthesis of seagrasses at the scale of a prairie. An exploratory study started in spring 1995 on the basis of long-range transmission measurements carried out over a prairie of *Posidonia oceanica*, an endemic phanerogam of the Mediterranean Sea. Results of a shorter-range experiment carried out at the end of the summer 1999 in the Ustica Island marine reserve (Sicily) are hereby presented. Acoustic signal propagation and ambient noise due to biological processes were measured during four days under controlled experimental conditions. Chirp signals were emitted repeatedly from a broadband sound source and received on a two-hydrophone vertical array; the range was 53 m and the frequency band was 0.216 kHz, broader than during the first experiment. Ground truth data of dissolved oxygen and temperature in the acoustic section were obtained contemporaneously. Detailed statistical analyses of the medium impulse responses, and in particular of their energy time distribution, allowed detecting cyclic variations of the sound propagation characteristics. Some of the latter are strongly correlated with the release of photosynthetic oxygen measured above the foliage by a dissolved oxygen sensor. Photosynthesis is shown to produce excess attenuation of certain acoustic paths and a faster decay of reverberation. The main diurnal variations are ascribed to non dissolved gases that are present in the air channels running inside and along the length of the leaf blades, and to the production of oxygen microbubbles sticking to the blade surface. Other variations can be attributed to gas movements in the rhizome and root systems. The *Posidonia* prairies form a thick layer where gas void fraction varies with the phase of photosynthesis cycle. During the active phases sound speeds lower than in bubble-free seawater, together with absorption and scattering effects, modify the multiple reflections from the rocky substratum. In our experimental setup, modeling results explain why the multipaths with intermediate grazing angles are the most sensitive to photosynthesis. The results confirm the ones obtained in the first experiment of 1995, even if conducted under quite different environmental conditions and with a different measuring arrangement. They indicate that *in situ* measurements of photosynthesis by acoustic methods can provide new insights into the physiology of seagrasses and in particular their response to environmental forcing, at the scale of a prairie. The study is not intended to be species-specific, being now extended to other temperate seagrass species like *Cymodocea* sp. and *Zostera* sp.

1 Introduction

Seagrass prairies are perhaps the most important sublittoral biotic communities in the Mediterranean Sea. They are highly productive ecosystems on which a large number of other ecosystems, and individual species, depend. One of the most characteristic and important ecosystem is formed by *Posidonia oceanica* (L.) Delile, endemic in the Mediterranean and commonly known as 'Neptune grasses' [1]. *Posidonia* prairies are called the 'green lung of the Mediterranean' as they produce a huge quantity of oxygen and inorganic matter, i.e., food. The biomass productivity is similar to a tropical forest. The physiological cycles of these phanerogame is typical as of any land tree, exhibiting flowers and fruits in spring/summer and leaf decay especially in winter.

Although being common and widespread, seagrasses are very sensitive to pollution and habitat modification. They can suffer a number of biotic and abiotic stresses such as storms, excessive grazing by herbivores, disease, invasion of exotic species, point and non-point sources of pollution, increasing water turbidity, excessive nutrients in runoff, and sedimentation; anthropogenic threats like boat anchorage, propeller scarring and bottom trawling nets can be divesting. The situation is particularly critical for prairies in enclosed or semi-enclosed coastal areas that receive a variety of effluents or are subject to certain activities, e.g., dredging for port/harbor construction or maintenance, non-stop pollutant dumping, illegal trawling, aquaculture operations, etc. In many parts of the Mediterranean, seagrass prairies have regressed or eroded away, leaving in their place much-impooverished thanatocenoses, i.e., communities based on dead or dying organisms.

The development of new methods to efficiently assess the health state of marine prairies is of considerable interest nowadays. Traditional direct methods, as diving for inspection and sampling [2]-[4], and indirect methods, as mechanical and high-frequency echographic soundings [5]-[7], require considerable time and/or costly equipment, offering a poor efficiency/reliability to cost ratio. In recent years several methods and systems have been developed to exploit, to different degrees, the complex nature of sound propagation to identify physical parameters of the water column, its boundaries, and the subbottom structures [8]-[16]. Among these, sophisticated acoustic inversion techniques—based on matched-field and matched-waveform processing—proved to be effective and reliable in determining physical properties of the water column and upper sediments. But very little has been done so far in regards to acoustically-derived biological parameters (markers) properly describing submerged aquatic vegetation (SAV).

The use of acoustics to sense *in situ* but remotely the biological processes of seagrasses—including photosynthesis—was explored for the first time in a particularly dense and extensive prairie of *Posidonia oceanica* of the Tuscan Archipelago (SCOGLIO AFRICA'95 experiment) [17, 18]. The aim has been to find the possible ways of monitoring *in situ*, and on the scale of a prairie, the relationships between seagrass physiology and the environmental conditions. We succeeded in investigating, under controlled experimental conditions, the effects of the photosynthesis cycles on short- to long-range propagation of relatively low frequency sound waves. From the water surface to the sea bed the vertical section is considered to be formed by horizontal layers with different physiochemical characteristics, behaving like acoustic waveguides that include sea bed, plants, oxygen and bubble enriched water layers, thermo/pycnoclines, and water surface. The first experiment showed daily changes of frequency-dependent propagation features, including attenuation and dispersion (pulse spreading). The phenomenon of an acoustic wave-guiding in a bottom bubble layer was demonstrated, which is exploitable for inferring the oxygen void fraction in that layer. The exploratory phase of the SCOGLIO AFRICA research was successful as it opened interesting possibilities not only for ecological monitoring and surveillance of the global state of health of seagrass beds, but even for the *in-situ*, non-intrusive study of the metabolism of certain submerged ecosystems in response to environmental factors and stresses.

In the present paper we discuss the results of a second experiment, carried out under quite different acoustic and environmental conditions [19]. The measurements were extended to higher frequencies and the transmission range was much shorter. The site was a small *Posidonia* bed in the

marine reserve of Ustica Island, off the northern coast of Sicily (USTICA'99). Similarly to the first experiment, four days of time series of calibrated measurements of acoustic transmission were obtained. We used low-frequency, broadband, chirp signals emitted repeatedly from a sound source and received on a distant array of two hydrophones, spaced vertically; both source and receiver were fixed near the sea bottom. The ground truth consisted of contemporaneous depth profiles and time series of dissolved oxygen and temperature in the water column, obtained with a multiparameter oceanographic sensor.

Section 2 focuses on seagrass characteristics that are relevant to sound transmission and in particular the photosynthetic apparatus of *Posidonia* species. In Section 3, the process of microbubble formation on the leaves that supports our interpretation of the acoustic results is explained, based on a general account on gaseous movement in seagrasses. Section 4 briefly describes USTICA'99 experiment, the acoustic and environmental measurements, and data processing. Section 5 analyses the effects of photosynthesis on the acoustic impulse response of the medium, providing an interpretation of the observed acoustic variations in terms of the gas transport in the seagrass leaf and 'matte' layers. Section 6 concludes the paper.

Within the confines of this paper we find necessary to focus on the most important results, omitting some other interesting features of the acoustic measurements. The interested reader is referred to Ref. [19] for a more detailed description of the experimental part and interpretation of other results, especially with regard to ambient noise due to biologics.

2 Seagrass prairies

Seagrasses are a type of submerged aquatic vegetation that have evolved from terrestrial plants and have become specialized to live in the marine environment. Like terrestrial plants, seagrasses have leaves, roots, conducting tissues, flowers and seeds, and make up their own food via photosynthesis. Unlike terrestrial plants, however, seagrasses do not have the strong, supportive stems and trunks required to overcome the force of gravity on land. Seagrass blades instead are supported by their natural buoyancy in seawater, and they remain flexible when exposed to waves and currents.

Prairies of *Posidonia oceanica* (L.) Delile are one of the most characteristic communities of the Mediterranean shoals. These marine plants settle most commonly on loose sediments but can also develop on hard and rocky substrata. Under favorable conditions, e.g., on unexposed coastal segments, they colonize vast areas of the sea bottom forming prairies, which can extend from the littoral zone to a depth of approximately 35 to 50 m, depending on light availability at the sea bed. This superior plant (it is not an algae) forms wads of 57 tape-like leaves almost one meter in length. The growth is so dense and widespread that it literally carpets the seabed, forming prairies like any land seed plant being cultivated as a single crop.

The prairies are important because they produce large quantities of inorganic matter (food) and oxygen; for example, and in general terms, 1 m² of leaves of *Posidonia oceanica* (L.) Delile provides 10 l of oxygen per day. *Posidonia* plants considerably enriches other ecosystems and it is an important habitat for numerous marine animals, and other plants and algae, providing food and shelter for a whole range of fish and invertebrates feeding on its leaves or finding sufficient protection for mating and breeding. In particular the plant supports other organisms, both algae and animals—particularly bryozoa and hydras—that settle on the leaves, making up the so called “epiphytic felt”.

The prairies represent also a type of “energy filters”, decreasing the sediment bed-flow reducing coastal erosion and even inducing sedimentation. The roots growth can follow quickly this ‘burial effect’ saving the plants from suffocation. Furthermore the trapped sediments favour the development of bivalve molluscs and a number of worm species.

Other important and similar phanerogamae ecosystems are formed by *Cymodocea* sp. and *Zostera* sp. prairies.

2.1 Seagrass Morphology

Structurally, seagrasses are closely related to terrestrial plants and, like terrestrial plants, have specialized tissues that perform specific tasks within each plant. Nevertheless—due to their morphology and growth habit—seagrasses are sometimes confused with marine macroalgae; however closer examination reveals significant differences. Conversely, algae are relatively simple and unspecialized in structure. While algae possess only a tough holdfast that assists in anchoring the body to a hard substratum, seagrasses possess true roots that not only hold the plant in place, but also are specialized for extracting minerals and other nutrients from the sediment. All algal cells show indeed photosynthetic structures capable of utilizing sunlight to produce chemical energy, but in seagrass instead chloroplasts occur only in leaves where photosynthesis is thus confined. Further, algae are able to take up minerals and other nutrients directly from the water column via diffusion, but seagrasses however, transport minerals and nutrients in xylem and phloem. Finally, while most algae lack specialized reproductive structures, most seagrasses have separate sexes and produce flowers and seeds, with embryos developing inside ovaries.

2.2 *Posidonia oceanica* (L.) Delile Characteristics

The species is an endemic phanerogam of the Mediterranean Sea. It has long ribbon- shaped leaves, grouped in shoots, which develop on various substrates in 1 to 50 m water depths (Fig. 1).

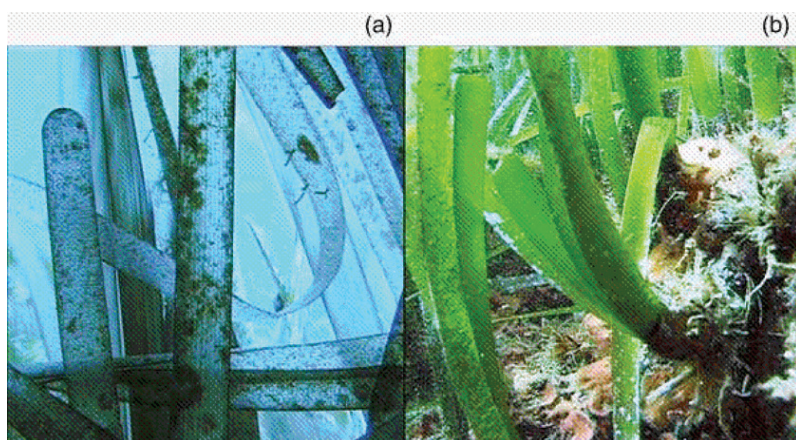


Figure 1. *Posidonia oceanica* leaves. (a) Adult and intermediate leaves covered by epiphytes and encrustation. (b) Juvenile leaves and rhizome. (Photographs taken during USTICA'99 experiments at the end of the summer).

Leaf morphology allows for maximum release of photosynthetic oxygen to the ambient medium [20]. The leaf blade consists of a monolayered epidermis and a three- to four- layered mesophyll (Fig. 2). The blade width and thickness are respectively ≈ 1 cm and ≈ 180 μm .

The major site of photosynthesis is the epidermis where chloroplasts are densely arranged in small, radially elongated cells. The outer wall of epidermal cells is formed by an outer continuous layer (cuticle) and an underlying much thicker (≈ 20 μm) porous region with irregularly shaped cavities. The lacunar system is constituted by connected air channels within the mesophyll. The particularly small dimensions of the lacunar system are a distinctive feature of *P. oceanica*.

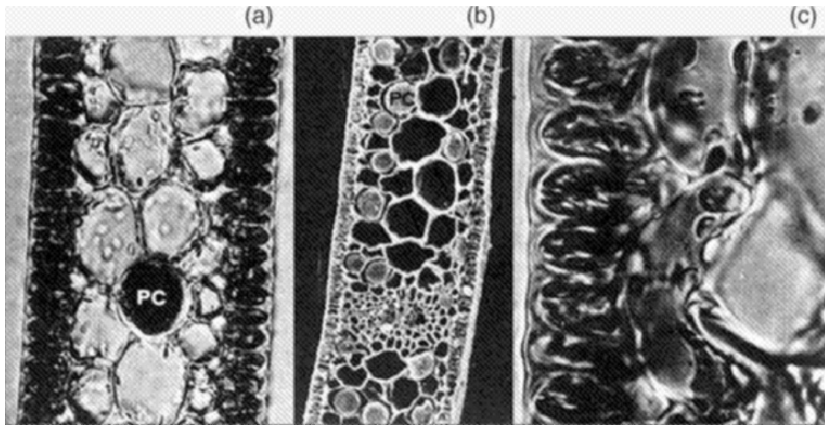


Figure 2. Photosynthesis apparatus of *P. oceanica*. Leaf blade cross sections. (a,b) Monolayered epidermis and mesophyll with large cells and small intercellular spaces (x320 and x200). PC: phenolic cell. (c) Detail of the porous region under the cuticle (x1100). (From P. Colombo, N. Rascio, and F. Cinelli, *Posidonia oceanica* (L.) Delile: a structural study of the photosynthetic apparatus, *Mar. Ecol.*, 4(2), 133-145 (1983). With permission.)

2.3 Photosynthetic Oxygen Production

Photosynthesis is the major driving force for the exchange of gases between seawater, the epidermal cells and the lacunar system. Respiratory activity is nearly an order of magnitude lower and largely involves the lacunar system. Unlike other aquatic plants gaseous exchanges with seawater are effected by molecular diffusion as there are no stomata. The processes of oxygen uptake for respiration and release of photosynthetic oxygen are constrained by the diffusion boundary (unstirred) layer, and to a lesser extent, by the cuticle and cell wall.

Photosynthesis by seagrasses substantially increases the quantity of oxygen in the water column, both in dissolved and bubble state. On sunny days in dense grass beds, when photosynthesis is at its peak, oxygen bubbles from the plants and rises to the surface. Figure 3 shows a 24-h time series of oxygen concentration measured at different water depths during a survey of a *Posidonia* prairie of the Tuscan Archipelago [21]. Here the time variation of oxygen content in the water column over the bed is mainly due to the daily cycle of oxygen productivity, with a night-day difference of 1.5 mg O₂/kg water. Depth and seasonal dependence—including supersaturation conditions below sea surface in spring and summer seasons—were detected by other measurements [17]. Values of produced oxygen of up to 14 l m⁻² day⁻¹ have been reported for prairies of the same area [22]. A productivity of 5 to 10 g of fixed carbon m⁻² day⁻¹ was also reported [23] for *Posidonia*.

3 Photosynthesis bubbles and sound

3.1 Bubbles in Coastal Waters

In coastal waters, the gas content in dissolved and bubble forms is determined by air-sea flux and specific environmental and biomass conditions, including photosynthesis of marine plants, life processes of animals, and decomposition of organic materials.

It is well established that gas bubbles in seawater have a deep influence on sound propagation. The bubble population is sensitive to physical, chemical and biological processes which are very specific to each environment such as the photosynthesis cycle considered in this paper. The density and distribution of bubble radius vary with depth, time of day, season, wind, sea state, turbidity, etc.

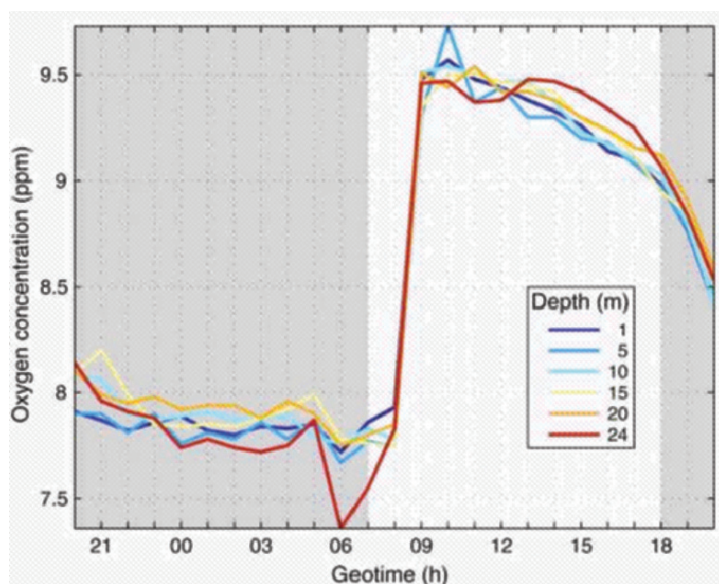


Figure 3. Oxygen concentration vs. geotime at different water depths. The concentration is given in $\text{mg O}_2 / \text{kg water}$ (ppm). The profiles were measured over a *Posidonia* prairie of the Tuscan Archipelago on February 24 and 25, 1997. Sunrise and sunset were at 0706 and 1800 hours, local time.

The presence of bubbles of many different sizes ($10500 \mu\text{m}$)—each with specific sound scattering and absorption cross sections—cause scatter, attenuation and dispersion in a way that depends on the resonance frequency of the bubbles [10]. Over the range of resonance frequencies the medium is highly attenuative and dispersive. At frequencies below resonance, the mixture of bubbles increases the compressibility of the water medium thereby reducing the sound speed below that obtained from pressure, temperature and salinity measurements alone, and causing sound refraction.

It is emphasized that although photosynthesis can considerably increase the water oxygen content, its effects on sound speed are completely negligible if the oxygen is dissolved in water, even if the latter is totally saturated with gas but without bubbles. One of the key points of our research is to show that photosynthesis can be well observed acoustically because of the production of non-dissolved gas (void fraction).

3.2 Microbubble Formation on Leaves

The rate of photosynthesis of submerged aquatic vegetation is strictly dependent on light irradiance, as for terrestrial plants. For marine phanerogams, such as *P. oceanica*, the possible formation of microbubbles on the leaves is related to the availability of a definite amount of light. The mechanisms described were adapted for our purpose from a general account on gaseous movement in seagrasses which does not deal specifically with *P. oceanica* species [24].

As photosynthetic tissue is concentrated in the epidermis, the epidermal cells are the ones experiencing a build-up of oxygen at dark-to-light transition. The resulting diffusion gradient causes oxygen to diffuse towards the ambient medium and the lacunar system. Initially, at low irradiance, oxygen accumulates in the porous wall beneath the cuticle and in the small air spaces of the mesophyll (Fig. 3). Such effect causes an increase of oxygen concentration within the leaf blade. The initial pressurization causes a transient mass flow of lacunar gas to the rhizomes and roots.

Then, with increasing irradiance, the differential pressure (between the plant interior and the ambient medium) increases—pushing oxygen to diffuse into seawater and, whenever the pressure gradient is strong enough—possibly forming bubbles, which at first adhere to the leaf blade. Any submerged gas bubble supported by any surface tends to solute its gas into the surrounding water for a final collapse. On the contrary, the ones attached to the leaves are fed by the continuous oxygen supply coming from the mesophyll. They increase their size up to the point the surface tension detaches the bubble which starts to float and surface. In the meanwhile new bubbles appear upon the leaves and this vital process continues maintaining a large void fraction (the oxygen bubbles) near the sea bottom in addition to oxygen in the porous wall and gas in the lacunar system.

An equilibrium is established between oxygen production rate during the steady- state of photosynthesis, and the processes of bubble formation and dissolution in seawater mostly depend on the degree of stirring, and the photosynthetic oxygen progressively enriches the water column (Figs. 3 and 6).

It should be noted that bubble formation on leaves submerged in water is not always caused by photosynthesis. If the water is cold, bubbles form on leaves as the water warms and gases become less soluble.

4 USTICA'99 experiment

4.1 Site

The experiment was conducted over a *Posidonia* bed off the island of Ustica in September 1999 (Fig. 4). The island lies in the southern Tyrrhenian Sea, off the northern coast of Sicily, at a distance of 65 km from Palermo ($13^{\circ}10' \text{ E}$, $38^{\circ}42' \text{ N}$). In the experimental area, the plants grow directly on a basaltic substratum. They form a real prairie, relatively dense and in good state of health.

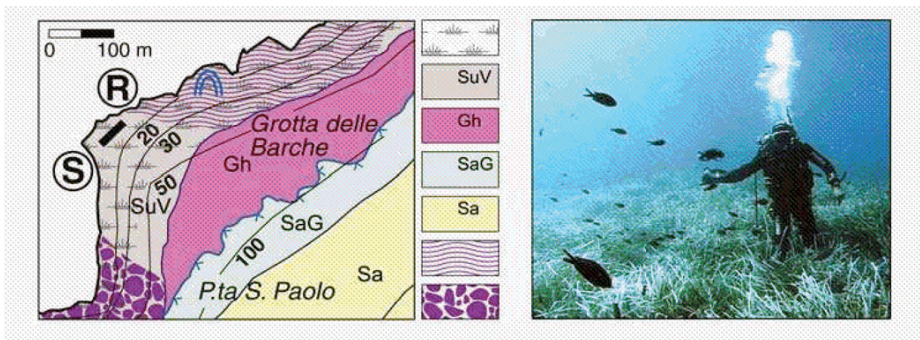


Figure 4. USTICA'99 test site. (a) Sediments, biocenosis, and stratigraphy at the test location. The thick black line shows the position of the acoustic section. S: source. R: receivers. Legend from top to bottom: *Posidonia* prairies; SuV: volcanic substratum; Gh: gravel; SaG: gravelly sand; Sa: sand; corded pahoeohoe; pillow lava. (b) View of the bed of *Posidonia oceanica* (L.) Delile and fish school. Ustica island, off Sicily. September 1999.

4.2 Sound Transmission Measurements

Low-frequency, broad-band signals were transmitted repeatedly between a piezoelectric sound source and a two hydrophone vertical array (Fig. 5). These were rigorously fixed being mounted on stable structures deployed on the sea floor. The relevant distance was 53 m and the water depth in

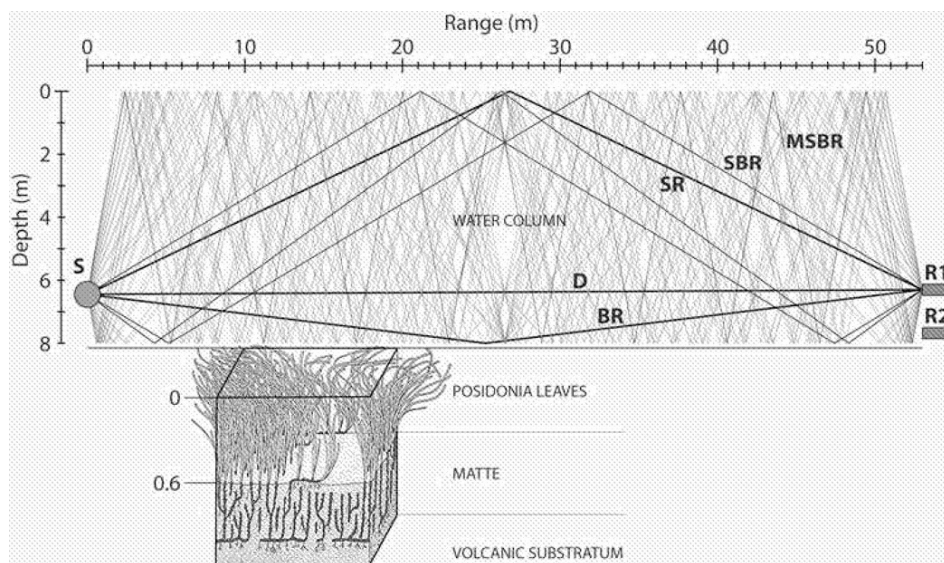


Figure 5. Experimental configuration for the acoustic remote sensing of non-dissolved oxygen produced by *Posidonia* photosynthesis. The positions of the underwater sound source (S) and hydrophones (R1, R2) are indicated. Eigenray diagram: The lines are the acoustic rays joining S and R1. Ray groups 1 through 10 are displayed. The black lines are the early arrivals of groups 1 and 2. The thin black line is one of the four paths belonging to group 10: nine reflections at each of the boundaries. S: surface; B: bottom; R: reflected; M: multiple.

the vertical section varied between 8 m and 8.8 m. The source and two receivers were at respective heights of 1.55 m, 0.3 m and 1.7 m above the sea floor.

The signal transmitted to measure the band-limited impulse response of the acoustic channel consisted of a low power, long duration (15.8 s), linearly frequency modulated (LFM) waveform. The frequency range was 200 Hz–16 kHz. The pulse repetition rate was fixed at 1 per minute to obtain sufficient statistics in sampling the physical and biological processes over the time scales of interest. About 3000 probe signals were transmitted over a 4-day period.

Pulse compression was achieved using a correlation receiver whose impulse response was the signal waveform measured in front the source, equalized for flat spectrum and reversed in time. In spite of limited source peak-power and high-level background noise, the achieved processing gain allowed estimation of the coherent part of the medium response as if the source transmitted an ideal high energy pulse.

4.3 CTD and Dissolved Oxygen Content Data

Physical and chemical conditions of seawater were monitored during the acoustic transmissions with a multiparametric probe. Depth profiles and time series were alternated to obtain vertical and temporal sampling of the water column. Figure 6 shows the time series of oxygen concentration measured just above the *Posidonia* leaves.

Depth profiles obtained at different times of day showed that conductivity (salinity) and temperature were nearly homogeneous over the whole water column. The salinity ranged from 37.8 to 38 ppt. Small, diurnal temperature variations involved the entire water column. For example, on September 24 their amplitudes at the sea surface and seafloor were, respectively, 0.6 and 0.2°C

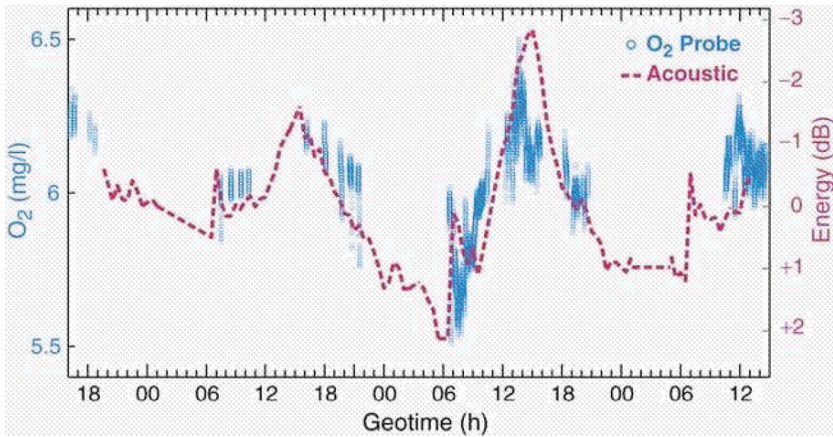


Figure 6. Time series of water oxygen content. The small blue circles are the raw data of oxygen concentration obtained from an oceanographic probe with the oxygen sensor located just above the foliage (left scale). The dashed red line is the variation of received energy for the set of acoustic paths with 7 surface-bottom reflections (right scale). See also Fig. 9.

(Fig. 5.8 in Ref. [19]). During the 0200 to 0900 hours period, the column was perfectly isothermal. Then, a thin mixed layer and small thermocline developed during the day.

4.4 Comparison with SCGLIO AFRICA'95 Experiment

When compared to the first experiment in the Tuscan Archipelago [17, 18] the major differences were the much shorter length of the acoustic path (53 m vs. 1541 m), broader frequency band of transmission (200 Hz–16 kHz vs. 100 Hz–1.6 kHz), lower oxygen productivity of the plants (6.5 mg/l vs. 9.5 mg/l), smaller day-night difference (1 mg/l vs. 2.5 mg/l), lower plant density, lesser homogeneity of the prairie, and acoustically “harder” substratum (basalt vs. sand).

5 Results and interpretation

The acoustic transmission data were analyzed as a function of geotime to assess their sensitivity to the variations of all environmental parameters that are relevant to acoustic frequencies below 16 kHz. Changes in the physical and biological properties of the very shallow water environment were related to geotime-varying characteristics of the acoustic-impulse response, including its energy time distribution.

Figure 7 compares two snapshots of the medium impulse responses (smoothed log envelope) taken early morning before the main respiratory phase and midafternoon during the active photosynthesis phase. Differences in the multipath-reverberation character are noticeable, especially the disappearance in the afternoon of marked blobs of energy.

Figure 8 shows the overall geotime variability of the acoustic-impulse response. Each overlaid curve is the difference between a 0.5-hour and the 3-night average responses (log envelope).

The clustering of the responses clearly shows a night and a day regimes. Along the time axis, three regions can be identified with distinct geotime variability. The regions correspond to different ranges of number of SBR and grazing angle. The leading part of the response—that corresponds to 23 SBR—shows lower variability. The remaining part displays much greater signal-to-signal variability and sensitivity to time-varying environmental conditions. The tail, which is dominated by reverbera-

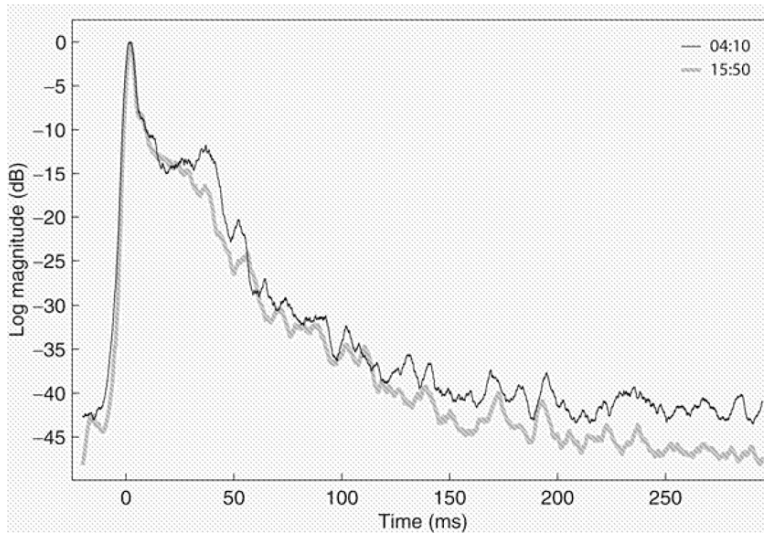


Figure 7. Comparison of a night and a day medium impulse responses. Black: 0410 hours; gray: 1550 hours. September 24, 1999.

tion and contaminated by background noise, shows a marked day-night difference. The middle part of the response that corresponds to 412 SBR at intermediate grazing angles 40° – 70° includes predominantly reflected and scattered energy in the specular direction. The greater sensitivity of these paths to photosynthesis was explained by the combined effects of (a) angle-dependent reflection loss for a basalt half space and (b) void-fraction dependent refraction index in the overlying grass layer [19].

Figure 9 shows the geotime variation of received energy for the set of acoustic paths having 7 SBR at a mean angle of 61° . The energy curve, reversed in the vertical, is replicated in the plot of Fig. 6 for direct comparison. The similarity of shape between the acoustic and dissolved oxygen time series is remarkable. The well-defined energy minima that occurred at 1500 hours correspond to the maximum concentration of oxygen near the foliage (white arrows). Also the maximum of energy coincides with the minimum of bottom oxygen concentration at 0600 hours. The energy difference between 0600 and 1500 hours of 5 dB represents an excess attenuation of ≈ 0.7 dB per bottom bounce. A local energy minimum was consistently observed at 0700 hours for the three days (gray arrows) in correspondence to the oxygen minimum at the end of the respiratory phase. The excess attenuation was attributed to the concomitant flows of gas to the rhizomes and roots described in Section 2.

Careful data analysis showed that the main variations of broad-band acoustic energy—observed on a day scale—were mostly independent on the tidal cycle and changes in wind and subsurface temperature conditions [19]. The latter deserved special attention since sun is the source of both sea-surface heating and seafloor light irradiance on which photosynthesis depends. Solar heating modifies the sound speed profile (SSP) of the water column and solar radiation controls the oxygen production of the seagrass. Since the two phenomena (physical and biological) occur contemporaneously, their respective acoustical effects are not separable on the basis of time delay or timescale differences. It was verified that the small changes of water SSP did not contribute significantly to the main, diurnal acoustic variations. The latter were explained by the change of gas void fraction within the seagrass-leaf layer as discussed below.

The relative importance of temperature gradient and oxygen content was assessed by comparing acoustic data at specific points of the temperature and dissolved-oxygen geotime series. For example, on September 24 a negative temperature (sound speed) gradient increased from zero to 0.7°C (1.5

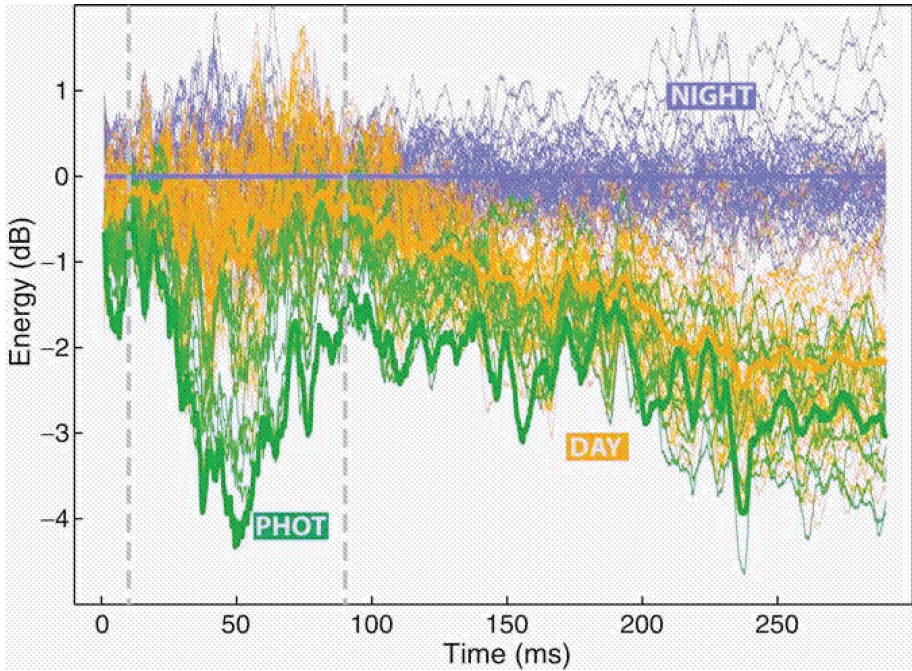


Figure 8. Geotime variability of the medium acoustic-impulse response (log envelope) in the time-delay range 1 to 290 ms. Each thin line is the difference between a 0.5-hour and the 3-night median averages. Blue lines: nighttime 0700-1930 hours, 4 days. Orange lines: day hours, 4 days. Green lines: most active photosynthesis 1300-1600 hours, 1 day. The vertical lines indicate the time window that corresponds to grazing angles in the range 40° - 70° . Top hydrophone data. September 22-25, 1999.

m/s) in the period 1100 to 1830 hours. During the same period, the oxygen concentration at the bottom increased by 0.4 mg/l and then returned to the same value of 6 mg/l (Fig. 6). The medium impulse responses observed at the beginning and end of the period had similar energy time distribution [19]. Hence, points in time with different temperature but similar oxygen conditions had nearly identical acoustic responses. Furthermore, substantial acoustic variations were observed during the isothermal periods at night, which indicated the influence of other environmental variables, including the gas void fraction in the seagrass-matte layer [19].

Our acoustic observations appear to be consistent with the sequence of gas movements described in Section 2 establishing a causal relationship between the photosynthesis daily cycle and the main acoustic variations observed, i.e., the primary peaks and valleys in Fig. 9. Transient mass flows of gas, to the rhizomes and roots at dark-to-light transition and the reverse at light-to-dark, change the void fraction in the matte layer. The latter explains the secondary valleys in Fig. 9.

6 Conclusion and future direction

USTICA'99 experimental results give evidence that photosynthesis product of *Posidonia oceanica* (L.) Delile seagrasses has a marked effect on the transmission of audio frequencies (i.e., underwater sound) over a prairie of this species.

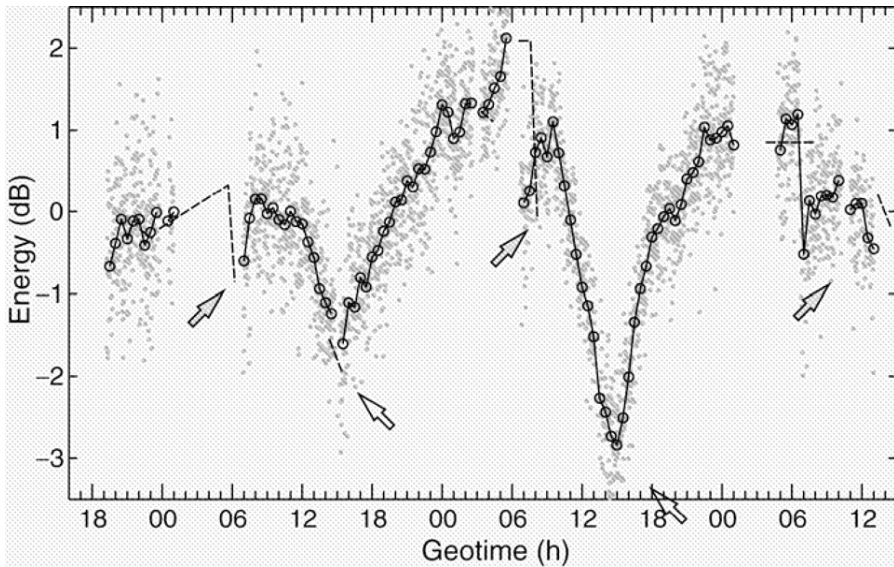


Figure 9. Fractional energy of the medium acoustic-impulse response vs. geotime. The integration time window is 35 to 45 ms, corresponding to 7 surface-bottom reflections. Gray dots: raw data. Circles and lines: half-hour median-averages. Dashed lines: interpreted missing data. The gray and white arrows correspond to the maxima of the respiratory and photosynthesis phases. See also the dashed red line in Fig. 6.

Short-range propagation characteristics of the acoustic channel, including multipath excess attenuation, were analyzed as a function of time of day. As for the first, longer range experiment (SCOGLIO AFRICA'95) the main diurnal variations were ascribed in part to gas microbubbles present on the leaf blades and at the roots during phases of photosynthesis cycle; the variations were strongly correlated with the release of oxygen in the water column measured by a dissolved oxygen sensor above the foliage. Other interpretative analyses of the medium impulse response and ambient noise owing to biologics vs. time of day are given in [19].

In summary the *Posidonia* plants and 'matte' form layers where the respective gas void fraction varies with the time of day. These photosynthesis-driven bubble layers have time-varying and frequency-dependent absorptive, scattering and dispersive properties. At low frequencies, phase speeds lower than in the respective bubble-free media, modify the interaction process of waterborne acoustic energy with the rock substratum. Modeling results in [19] explain why, for the present measurement geometry, refracted multipaths with intermediate grazing angles were the most sensitive to photosynthesis.

The proposed method opens interesting possibilities for ecological monitoring and surveillance, e.g., the non-intrusive, in-situ study of the metabolism of certain submerged aquatic vegetation in response to environmental factors and stresses, and the assessment (real measurement in our case) of the global state of health of seagrass beds.

For the two experiments carried out under totally different conditions the acoustic signal transmission was found to be highly sensitive to the photosynthesis cycle, and there was overall agreement between the results. This suggests that the inverse problem of determining the void fractions of oxygen and gas is solvable in principle. Seagrass parameters such as leaf surface density, physiological status, photosynthetic efficiency can be deduced from the inverted void fractions and supporting environmental data including temperature and irradiance. This will require precise calibration of the

acoustic measurements with in-situ hydrographic data and comprehensive modeling of the seagrass scattering and absorption mechanisms in the frequency band of interest.

Furthermore, our research confirmed that the behavior and the movements both of fish and benthic organisms can be contemporaneously monitored, improving greatly the possibility of an indirect, non invasive study with the possibility of collecting data inaccessible so far as further discussed in [19].

The proposed method is not specific to *Posidonia* seagrass; other temperate seagrass species including *Cymodocea* sp. and *Zostera* sp. are currently being studied. Extension and application of the method for a much longer observation period would allow studying not only the species-specific response to any environmental forcing but also the relationships between leaf photosynthesis and seasonal plant growth and productivity as well as the differences in the seasonal pattern among species, at the scale of a prairie.

Acknowledgements

We thank prof. Antonio Stefanon for his critical review of previous version of the manuscript.

References

1. Cinelli F., Fresi E., Lorenzi C. and Mucedola A. (ed.), *La Posidonia oceanica*. Rivista Marittima, Rome (1995).
2. Colantoni P., Mapping of the *Posidonia oceanica* meadows. In *La Posidonia oceanica*, ed. by F. Cinelli, E. Fresi, C. Lorenzi and A. Mucedola (Rivista Marittima, Rome, 1995) pp. 116-122.
3. Chessa L., Fresi E. and Lorenzi C., The state of health of a *Posidonia oceanica* prairie: study method. In *La Posidonia oceanica*, ed. by F. Cinelli, E. Fresi, C. Lorenzi and A. Mucedola (Rivista Marittima, Rome, 1995) pp. 78-83.
4. Peirano A., Stoppelli N. and Bianchi C., Monitoring and study techniques of sea grasses in Liguria. In *La Posidonia oceanica*, ed. by F. Cinelli, E. Fresi, C. Lorenzi and A. Mucedola (Rivista Marittima, Rome, 1995) pp. 88-91.
5. Newton R. and Stefanon A., Application of side scan sonar in marine biology. *Mar. Biol.* **31**, 287-291 (1975).
6. McCarthy E., Acoustic characterization of submerged aquatic vegetation. In *High Frequency Acoustics in Shallow Water*, ed. by N. Pace, E. Pouliquen, O. Bergem, and A. Lyon (SACLANTCEN Conference Proceedings, 1997) pp. 363-369.
7. Siccardi A. and Bozzano R., A test at sea for measuring acoustic backscatter from marine vegetation. In *Experimental Acoustic Inversion Methods for Exploration of the Shallow Water Environment*, ed. by A. Caiti, J.-P. Hermand, S. Jesus and M.B. Porter (Kluwer Academic, 2000) pp. 145-159.
8. Diachok O., Caiti A., Gerstoft P. and Schmidt H. (ed.), *Full Field Inversion Methods in Ocean and Seismo-Acoustics*, Vol. 12 of Modern Approaches in Geophysics, SACLANT Undersea Research Centre, Kluwer Academic, Dordrecht (1995).
9. Wilson J. H., Rajan S. D. and Null J. M. (ed.), Special issue on inverse techniques and the variability of sound propagation in shallow water. *IEEE J. Oceanic Eng.* **21**(4), (1996).
10. Medwin H. and Clay C. S., *Fundamentals of Acoustical Oceanography*. Academic Press, New York (1998).
11. Hermand J.-P., Broad-band geoacoustic inversion in shallow water from waveguide impulse response measurements on a single hydrophone: theory and experimental results. *IEEE J. Oceanic Eng.* **24**, 41-66 (1999).

12. Caiti A., Hermand J.-P., Jesus S. and Porter M.B. (ed.), *Experimental Acoustic Inversion Methods for Exploration of the Shallow Water Environment*, Kluwer Academic, Dordrecht (2000).
13. Taroudakis M. I. and Markaki M. G. (ed.), *Inverse Problems in Underwater Acoustics*. Springer (2001).
14. Chapman R., Chin-Bin S., King D. and Evans R. (ed.), Special issue (Pt.1) on geoacoustic inversion in range-dependent shallow water environments. *IEEE J. Oceanic Eng.* **28**(3), (2003).
15. Chapman R., Chin-Bin S., King D. and Evans R. (ed.), Special issue (Pt.2) on geoacoustic inversion in range-dependent shallow water environments. *IEEE J. Oceanic Eng.* **29**(1), (2004).
16. Medwin H., *Sounds in the Sea. From Ocean Acoustics to Acoustical Oceanography*. Cambridge University Press, New York (2005).
17. Hermand J.-P., Nascetti P. and Cinelli F., Inversion of acoustic waveguide propagation features to measure oxygen synthesis by *Posidonia oceanica*. In *Proceedings of the Oceans '98 IEEE/OES Conference*, ed. by C.O. Committee, Vol. II, IEEE Oceanic Engineering Society, IEEE, Piscataway, NJ, Sept. 919-926 (1998).
18. Hermand J.-P., Nascetti P. and Cinelli F., Inverse acoustical determination of photosynthetic oxygen productivity of *Posidonia* seagrass. In *Experimental Acoustic Inversion Methods for Exploration of the Shallow Water Environment*, ed. by A. Caiti, J.-P. Hermand, S. Jesus and M.B. Porter (Kluwer Academic, Dordrecht, 2000), pp. 125-144.
19. Hermand J.-P., Acoustic remote sensing of photosynthetic activity in seagrass beds. In *Scaling Methods in Aquatic Ecology: Measurement, Analysis, Simulation*, ed. by L. Seuront and P.G. Strutton (CRC Press LLC, Boca Raton, Florida, 2004) chapter 5, 65-96.
20. Mariani Colombo P., Rascio N. and Cinelli F., *Posidonia oceanica* (L.) Delile: a structural study of the photosynthetic apparatus. *Mar. Ecol.* **4**(2), 133-145 (1983).
21. Nascetti P., Rilievi stagionali e circadiani della produzione di ossigeno di praterie di *Posidonia oceanica* in supporto ad uno studio di inversione acustica. Tesi di laurea in scienze biologiche, Facoltà di Scienze Fisiche, Matematiche e Naturali, Genova (1998).
22. Cinelli F., Mappatura delle praterie di *Posidonia oceanica* (L.) Delile intorno alle isole minore dell'Arcipelago Toscano. Tech. rep., Ministero della Marina Mercantile, Ispettorato Centrale per la Difesa del Mare (1992).
23. Libes M., Productivity-irradiance relationship of *Posidonia oceanica* and its epiphytes. *Aquat. Bot.* **26**, 285-306 (1986).
24. Larkum A., McComb A. and Shepherd S., *Biology of Seagrasses*. Elsevier, New York (1989).

SHALLOW WATER TOMOGRAPHY IN A HIGHLY VARIABLE SCENARIO

CRISTIANO SOARES AND SÉRGIO M. JESUS

*SiPLAB-FCT, Universidade do Algarve
Campus de Gambelas, PT-8005-139 Faro, Portugal
E-mail: {csoares,sjesus}@ualg.pt*

EMANUEL COELHO

*NATO Undersea Research Centre
Viale San Bartolomeo 400, IT-19138 La Spezia, Italy
E-mail: coelho@saclantc.nato.int*

In October 2000, SiPLAB and the Instituto Hidrográfico (IH - PN) conducted the INTIFANTE'00 sea trial in a shallow area off the Peninsula of Tróia, approximately 50 km south from Lisbon, in Portugal. The experiment itself and results obtained in most of the data set have been reported at various occasions in the last two years. This paper focuses on the data acquired during Event 2, where the acoustic propagation path was approximately range independent and the source ship was held on station at a constant range of 5.8 km from the vertical line array. Although these conditions were, in general, relatively benign for matched-field tomography, retrieval of water column and bottom parameters over a 14-hour-long recording revealed to be extremely difficult. This paper analysis in detail the characteristics of this data set and determines the causes for the observed inversion difficulties. It is shown that the causes for the poor performance of the conventional methods are mainly the tide induced spatially correlated noise and the relative source-receiver motion during time averaging. An eigenvalue-based criterion is proposed for detecting optimal averaging time. It is shown that this data selection procedure together with hydrophone normalization and an appropriate objective function provide a better model fit and consistent inversion results and thus a better understanding of the environmental variability.

1 Introduction

Ocean Acoustic Tomography (OAT) was initially proposed for deep water regions where the ray approximation was valid and sound speed could be analytically linked to acoustic ray travel-time [1]. Travel-time based tomography turned out to be highly dependent on the ability to separate closely spaced arrivals and on the precise knowledge on the source-receiver relative position at all times. Instead, matched-field tomography (MFT) is based on some sort of correlation of the full pressure field to the signal received at an array of sensors and only requires relative travel times to which an

approximate knowledge of the source-receiver position is sufficient [2]. In most operational shallow water scenarios, only MFT is applicable due to the close arrivals from bottom and surface reflections and to a perpetual source/sensor motion. In October 2000, SiPLAB and the Instituto Hidrografico (IH - PN) conducted the INTIFANTE'00 sea trial in a shallow water area off the Peninsula of Troia, approximately 50 km south from Lisbon, in Portugal. The experiment itself and results obtained in part of the data set have been reported during these last two years in various occasions [3], [4], [5], [6]. This paper focuses on the data acquired during Event 2, where the acoustic propagation path was approximately range independent and the source ship was held on station at constant range of 5.8 km from the vertical line array (VLA). Although these conditions seem ideal for MFT, retrieval of water column and bottom parameters over an 14 hours long recording using a focalization-like procedure turned out to be extremely difficult and resulted in several mismatched parameter estimates.

This paper analyses in detail the characteristics of that data set and the reasons for inversion failure. Separated eigenvalue analysis of the signal plus noise and noise only data sections revealed that signal and noise subspaces are not well separated since the noise showed to have a strong spatial correlation and the signal energy spread over a wide range of eigenvalues. The causes are attributed to both source-receiver motion and tidal current forcing on the VLA. After identifying the causes, several methods to counter these effects are proposed. In particular, a cross-frequency based objective function in conjunction with a proper selection of the data window length, according to the variable source range, and a data normalization for correct initial phase correlation at each frequency contributed for a decrease of the water column and bottom parameter errors. It is shown that this data selection procedure provides a better understanding of the influence of the environment and thus final inversion results that are consistent with independent measurements.

2 The INTIFANTE'00 sea trial

The INTIFANTE'00 sea trial was carried out on a shallow water area in the vicinity of Setúbal, situated approximately 50 km south of Lisbon, during October 2000. This is known to be an area of intense activity in terms of internal tides, internal waves, and river plumes. This sea trial served several purposes: one, among others, was to study the effect of environmental variability in acoustic tomography through long observation times of continuous acoustic transmissions. Event 2 was designed for this purpose, and this study will therefore focus on that data set.

The experimental area was a rectangular box situated in the border of the continental platform with depths varying from 60 to 140 m. Figure 1 shows a bathymetric map of the northern half of the rectangular box. The black thick line represents the track of the research vessel NRP D. Carlos I, towing the sound source, during Event 2 and extending towards the NW of the 16-hydrophone-4 m spacing VLA. The bathymetry over this NW leg is considered range-independent with an approximate average depth of 118.7 m.

The research vessel NRP D. Carlos I departed from the VLA location at time 13:30 of Julian day 289 and moved at a constant speed of 1.2 knot along NW leg during 2 hours, as depicted in Figure 1. After an interruption for battery changing, signal transmissions resumed at time 21:00, with the NRP D. Carlos I holding a station at approximately 5.8 km from the VLA while continuously transmitting acoustic signals until time 11:30 a.m. of Julian day 290. The acoustic aperture of the VLA was between 30 and 90 m. The wave form emitted during Event 2 was a 2 s duration linear frequency modulated (LFM) sweep in the band 170 to 600 Hz with a repetition rate of 10 s.

During the INTIMATE'00 sea trial a water column temperature survey using a thermistor chain and XBTs was conducted. The X signs in figure 1 denote the locations where the XBTs were released every 3 hours during approximately 2 days. These data were used in this study for the computation of the channel characteristic empirical orthogonal functions.

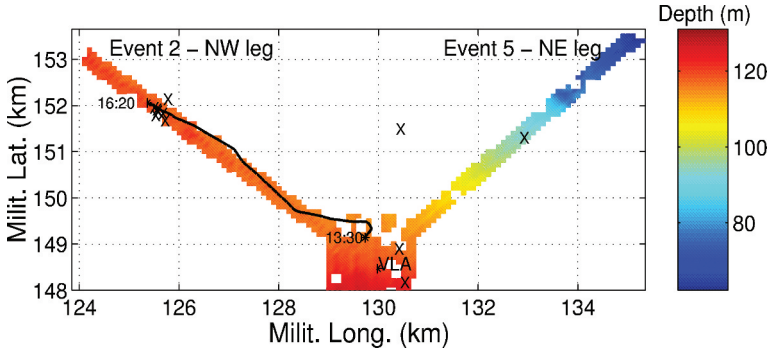


Figure 1. INTIFANTE'00 sea trial site bathymetry with XBT locations and track for Event 2.

3 Acoustic tomography via matched-field

3.1 The environmental model

For any inversion problem in underwater acoustics, the choice of an environmental model able to represent the properties of the propagation channel is an important step. That model, usually called baseline model, includes the available *a priori* information for the problem at hand. Since there were no *in situ* measurements of the seafloor properties during the experiment, a generic baseline model was chosen. It consists of a typical three-layer model with an ocean water column overlying a sediment layer and a bottom half-space, all assumed range independent, as shown in figure 2. For forward model computations the parameters were divided into subsets of water column, geometric, and geoacoustic parameters.

The water column is described by a linear combination of Empirical Orthogonal Functions (EOFs) that are constructed from representative data sampling the depth dependence of the ocean sound speed. The EOFs are obtained using singular value decomposition (SVD) of a matrix \mathbf{C} with columns

$$\underline{C}_i = \underline{t}_i - \bar{\underline{t}}, \quad (1)$$

where \underline{t}_i are the real profiles available, and $\bar{\underline{t}}$ is the average profile. The SVD is known to be

$$\mathbf{C} = \mathbf{U}\mathbf{D}\mathbf{V}, \quad (2)$$

where \mathbf{D} is a diagonal matrix containing the singular values, and \mathbf{U} is a matrix with orthogonal columns, which are used as the EOFs. The temperature profile is obtained by

$$\underline{T}_{\text{EOF}} = \bar{\underline{t}} + \sum_{n=1}^N \alpha_n \underline{U}_n, \quad (3)$$

where $\bar{\underline{t}}$ is the average temperature profile, \underline{U}_n is the n^{th} EOF, and N is the number of EOFs to be combined, judged to accurately represent the temperature profile for the problem at hand. Generally, a criteria based on the total energy contained in the first N EOFs is used. The temperature profiles obtained from the XBT measurements (see \mathbf{X} signs in figure 1 and profiles in figure 3(a)) served as database for the computation of the EOFs. The criteria used to select the number of relevant EOFs was

$$\hat{N} = \min_N \left\{ \frac{\sum_{n=1}^N \lambda_n^2}{\sum_{m=1}^M \lambda_m^2} > 0.8 \right\}, \quad (4)$$

where the λ_n are the singular values obtained by the SVD, M is the total number of singular values, provided that $\lambda_1 \geq \lambda_2 \geq \dots \geq \lambda_M$. For this data set the criteria (4) yielded $N = 2$, i.e., the first

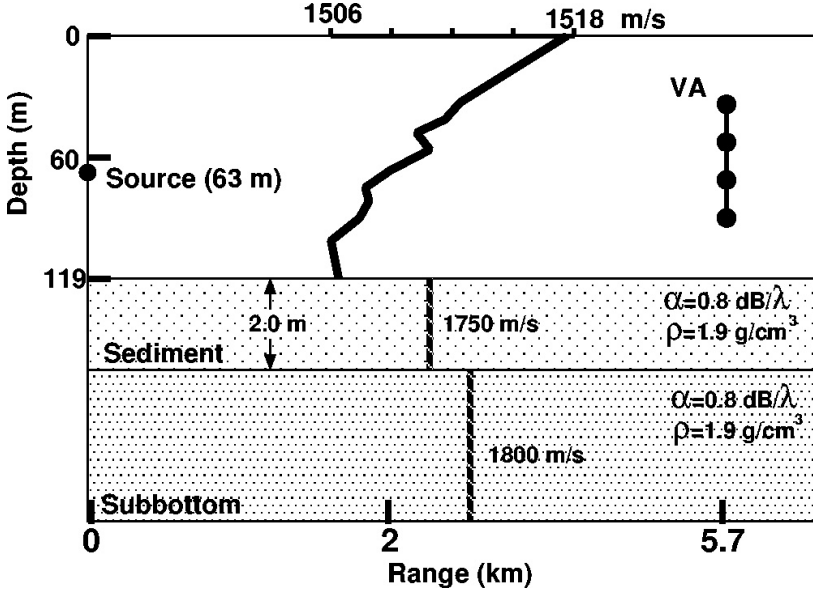


Figure 2. Baseline model for Event 2. All parameters are assumed to be range independent.

two EOFs are sufficient to model the sound speed with the requested accuracy. The coefficients α_n , which are the coefficients of the linear combination of EOFs, are now part of the search space, i.e., they are searched as free parameters. The mean temperature profile and the EOFs obtained from the XBT temperature measurements are shown in figures 3(a) and 3(b).

A direct measurement of the EOF coefficients α_n can be obtained for the times at which temperature profiles were taken. This can be done by projecting those temperature profiles into the EOF subspace as

$$\hat{\alpha}_n(t_k) = \underline{U}_n^T \underline{T}(t_k), \quad (5)$$

where $\underline{T}(t_k)$ is the temperature profile measured at time t_k . Computing estimates of α_n is useful to obtain *a priori* information of their respective intervals of variation, and to compare with the *a posteriori* acoustic estimates.

The geometric subset consists of source range and depth, receiver depth, and array tilt which mainly determine the experiment geometry. The geoacoustic subset consists of the sediment sound-speed, sediment thickness and subbottom sound-speed. During the search the subbottom sound-speed c_b was coupled to the sediment sound-speed c_s , as $c_b = c_s + \delta c_b$, to ensure that non-physical solutions are excluded from the search procedure. In order to test acoustic tomography with sparse populated receiver arrays, only data of every fourth hydrophone was considered in this study, resulting in a reduced acoustic aperture of 48 m and a receiver spacing of 16 m.

3.2 Data model and objective function

Acoustic tomography can be posed as an optimization problem, that is, to find an estimate of the parameter vector $\underline{\theta} = [\theta_\alpha^T \theta_s^T \theta_g^T]^T$ of the deterministic propagation model that best fits, according to a given objective function, the observed data. In Ref. [7] a broadband data model for the acoustic data received at an L -hydrophone array with the form

$$\underline{Y}(\theta_0) = [\underline{Y}^T(\theta_0, \omega_1), \underline{Y}^T(\theta_0, \omega_2), \dots, \underline{Y}^T(\theta_0, \omega_K)]^T$$

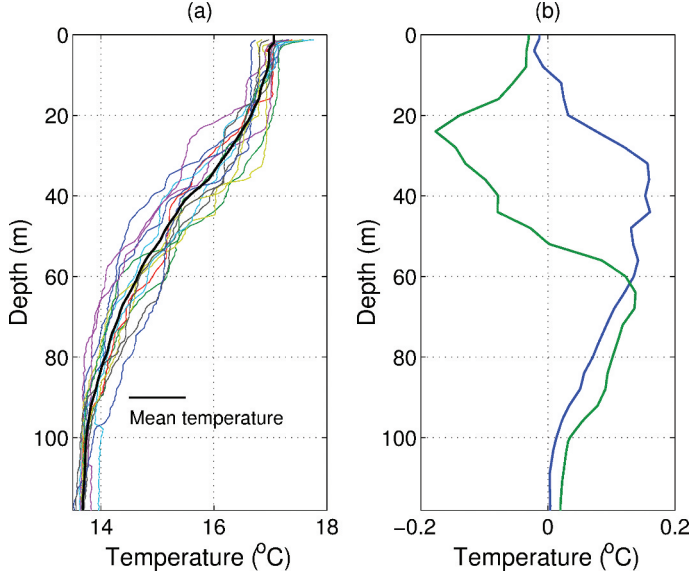


Figure 3. Temperature profiles measured during the INTIMATE'00 sea trial using XBTs, and empirical orthogonal functions obtained from the XBT temperature profiles (b).

$$= \mathbf{H}(\theta_0)\underline{S} + \underline{N}, \quad (6)$$

was proposed in order to introduce, as much as possible, a common frame for the narrow and broad-band cases. The matrix $\mathbf{H}(\theta_0)$ is

$$\mathbf{H}(\theta_0) = \begin{bmatrix} \underline{H}(\omega_1, \theta_0) & 0 & \dots & 0 \\ 0 & \underline{H}(\omega_2, \theta_0) & \dots & 0 \\ \vdots & \vdots & \ddots & \vdots \\ 0 & 0 & \dots & \underline{H}(\omega_K, \theta_0) \end{bmatrix}, \quad (7)$$

where K is the number of frequencies considered and $\underline{H}(\omega_k, \theta_0)$ is the channel response for frequency ω_k , and the number of rows of $\mathbf{H}(\theta_0)$ is KL . θ_0 is the parameter vector representing the relevant parameters to be estimated. The vector \underline{S} has entries $S(\omega_k)\alpha(\omega_k)$. $S(\omega_k)$ is the spectrum of the emitted waveform and $\alpha(\omega_k)$ is a generic random perturbation factor that has been discussed in detail in Ref. [7], and was presented with the purpose of modeling small scale environmental perturbations. This follows from the observation that repeated emissions of a deterministic signal result in successive receptions suffering rapid changes, even at high SNR. The vector \underline{N} represents the noise assumed independent across space and frequency, and has obviously the same notation as \underline{Y} in (6).

It follows that (6) can be used directly to obtain the correlation matrix as

$$\begin{aligned} \mathbf{C}_{YY}(\theta_0) &= \mathbb{E}[\underline{Y}(\theta_0)\underline{Y}^H(\theta_0)] \\ &= \mathbf{H}(\theta_0)\mathbf{C}_{SS}\mathbf{H}^H(\theta_0) + \mathbf{C}_{NN}, \end{aligned} \quad (8)$$

where $\mathbf{C}_{SS} = \mathbb{E}[\underline{S}\underline{S}^H]$ is a signal matrix that measures the frequency cross-correlation of the received signals and has entries

$$[\mathbf{C}_{SS}]_{ij} = \mathbb{E}[S(\omega_i)\alpha(\omega_i)S^*(\omega_j)\alpha^*(\omega_j)]. \quad (9)$$

Matrix \mathbf{C}_{SS} is diagonal if the frequency bins $S(\omega_k)\alpha(\omega_k)$ are uncorrelated across frequency. The matrix \mathbf{C}_{NN} is the noise correlation matrix and is diagonal with $L \times L$ dimensional blocks $\sigma_N^2(\omega_k)\mathbf{I}$ if the noise is uncorrelated over space and frequency. Here it is assumed that σ_N^2 is independent of the frequency. Equation (8) has the classical form found in horizontal array beamforming where the signal matrix stands for the correlation of multiple emitters, while in the present case it stands for the correlation of multiple frequencies.

The objective function used here is the cross-frequency incoherent broadband processor obtained as

$$P(\underline{\theta}) = \frac{\text{tr}\{\mathbf{P}_H(\underline{\theta})\mathbf{C}_{YY}\mathbf{P}_H(\underline{\theta})\mathbf{C}_{YY}\}}{\text{tr}\{\mathbf{P}_H(\underline{\theta})\mathbf{C}_{YY}\}}, \quad (10)$$

using the data model proposed in equation (6) and where $\text{tr}\{\cdot\}$ is the matrix trace operator. Matrix $\mathbf{P}_H(\underline{\theta}) = \mathbf{H}(\underline{\theta})[\mathbf{H}^H(\underline{\theta})\mathbf{H}(\underline{\theta})]^{-1}\mathbf{H}^H(\underline{\theta})$ is a projection matrix, well known from topics such as subspace based, least mean squares, or maximum likelihood methods. Note that equation (10) also generates auto-frequency terms. If the signal is assumed to be uncorrelated across frequencies, and flat spectrum, i.e., \mathbf{C}_{SS} is assumed identity, then a processor equivalent to the conventional incoherent Bartlett processor for K frequencies is obtained:

$$P(\underline{\theta}) = \frac{\sum_{k=1}^K \underline{H}(\omega_k, \theta)^H \mathbf{C}_{YY}(\omega_k) \underline{H}(\omega_k, \theta)}{\sum_{k=1}^K \|\underline{H}(\omega_k, \theta)\|^2}. \quad (11)$$

In practice, \mathbf{C}_{YY} , given by equation (8), is replaced by a sample correlation matrix considering N snapshots, given as

$$\hat{\mathbf{C}}_{YY} = \frac{1}{N} \sum_{n=1}^N \underline{Y}_n(\underline{\theta}_0) \underline{Y}_n^H(\underline{\theta}_0), \quad (12)$$

with $\underline{Y}_n(\underline{\theta}_0)$ containing the K data vectors $\underline{Y}_n(\underline{\theta}_0, \omega_k)$.

Michalopoulou [8] suggested the normalization of the received acoustic field by dividing the received signals by the signals corresponding to the hydrophone with highest SNR, in order to overcome the requirement of knowing the emitted waveform when a coherent processor is used. Observing the phases of the complex field received across the array, it can be found that a sensor coherent and frequency dependent continuous drift occurs over time. Consequently, the coherence of cross-frequency terms computed over the observation time is destroyed, causing diagonalization of the signal matrix \mathbf{C}_{SS} . Normalization using a reference hydrophone can also be useful to increase the coherence of the signals received along time, and reduce the diagonalization of the signal matrix \mathbf{C}_{SS} , and therefore the spreading of energy into different eigenvectors. This data normalization is applied during this study. However, no details on the choice of the reference hydrophone will be given here.

3.3 Parameter focalization applied to OAT

The present estimation problem represents a case where multiple parameters are assumed to be either unknown or known only to a certain degree. Several parameters are therefore to be optimized simultaneously in order to fit the model to the data via environmental focalization [9]. The water column temperature, parameterized by the EOF coefficients, is time variant as well as source position (both range and depth), array tilt and receiver depth. In order to reduce ambiguities, water depth is not included as search parameter but tidal variation is accounted for using a tide prediction model and a reference mean water depth of 118.7 m. Then, adopting the spirit of the focalization procedure, it was decided to account for uncertainty in the seafloor properties, in order to improve the model fit. Table 1 shows the parameters searched, with respective search bounds and quantization steps. The search bounds reflect the use of the available *a priori* knowledge. For example, it was found that by projecting the XBT temperature profiles into the EOF subspace, the measured α_n are confined

Table 1. GA forward model parameters with respective search interval. The compressional speed in the bottom is coupled to the compressional speed in the sediment.

Model parameter	min.	max.	Quantization steps
Temperature			
α_1 (°C)	-5	5	32
α_2 (°C)	-5	5	32
Geometric			
source range (km)	5.4	6.1	32
source depth (m)	70	85	32
receiver depth (m)	85	95	32
tilt (rad)	-0.045	0.045	32
Sediment			
comp. speed (m/s)	1520	1680	32
thickness (m)	1	7	16
Bottom			
comp. speed (m/s)	1	200	32

to the interval -3 and 3. However, during the data inversions a larger variation is allowed in order to avoid obtaining estimates on the boundaries of the search intervals. *A priori* knowledge from the experiment was used to restrict the search limits for the geometrical parameters source range and source depth.

The correlation matrices were computed considering only the time series received at 4 hydrophones, 4, 8, 12 and 16, taking 20 frequencies from 288 to 592 Hz with a step of 16 Hz obtained from 18 Fourier-transformed LFM sweeps, giving an acoustic observation time of ca. 3 minutes. This procedure was repeated with intervals not shorter than 15 minutes.

Although a great deal of *a priori* information is used to keep the size of the search space restricted, it is still of the order 10^{13} . Such a huge search space can be covered using a genetic algorithm (GA), which enables a significant reduction of the number of forward models to be computed. The forward computation model used was the normal mode code C-SNAP [10] and the GA is an implementation proposed by Fassbender [11]. The population size was set to 160 and the number of iterations to 50. Three independent populations were run for each time point. The crossover probability was set to 0.7, initial mutation probability was 0.0096 and the final mutation probability was 0.0026, where its value was linear with the iteration number. In order to allow a more efficient search the solution at a given time point is used in the initialization of the solving procedure of the next time point. For more details see [4].

The inversion results shown in figure 4 were obtained using the conventional Bartlett processor (11). The left column contains the estimates of the α_i (black curves) together with an interpolation of the projections based on the measurements obtained with (5) - colored curves. It can be seen that the α_i are reasonably well estimated at the beginning of the run, taking one or two outliers apart, but then progressively the estimates diverge from the measurements, reaching the largest error at time 290.25. Then the α_i estimates progressively start to converge again to the measured values, where in particular α_2 has some estimates coinciding with the measurements between time 290.35 at the end of the run. In the center column of figure 4, source range estimates (black curve) are of reasonable quality, with few severe errors and most estimation errors within the GPS accuracy and uncertainty caused by cable scopes in the moorings of the receiving system [12], while for the other geometric parameters some difficulties are present, specially at the beginning of the run, and around time 290.3. The geoacoustic parameters (right column) show a chaotic behavior, indicating that the seafloor properties cannot be properly retrieved from this data set.

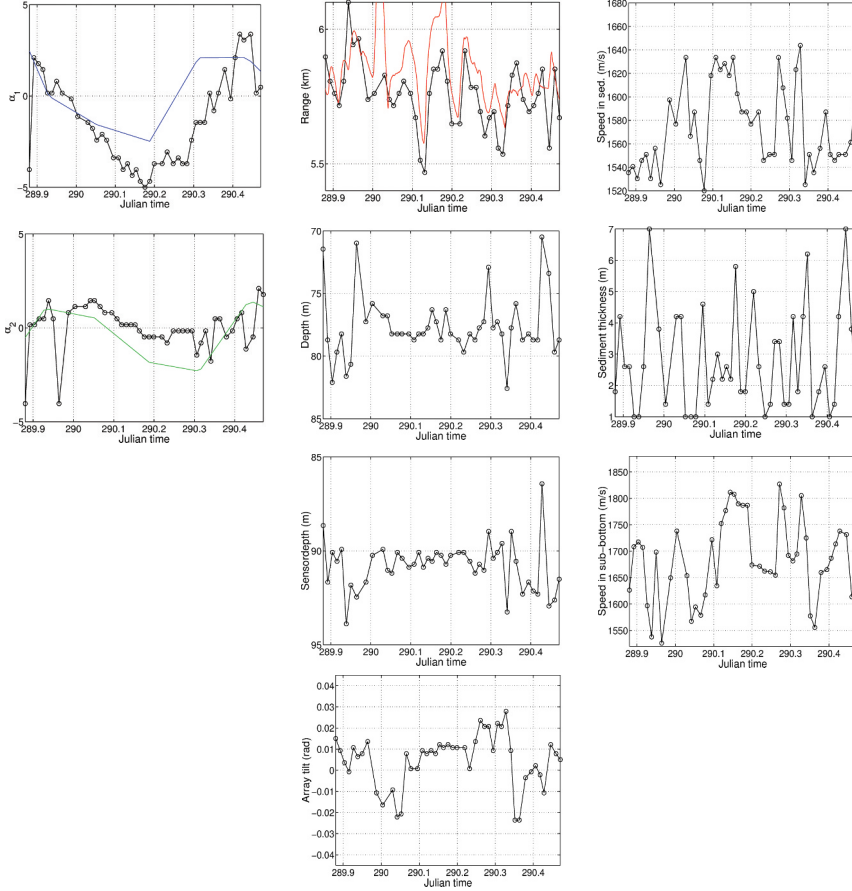


Figure 4. Focalization results obtained for Event 2.

The most important fact is that initially the inversion procedure reasonably yields the expected values for the estimative of the α_i , until a progressive departure between the estimates and the measured values takes place. The main question at this point is to find one or more explanations for that occurrence. From the propagation channel point of view the question is: what has changed to cause such degradation in the quality of the estimation results? The next section attempts to find the causes for the fluctuation of the estimation performance observed above.

4 Datamodels and eigenvalues

Severe parameter estimation difficulties were found in part of the data analysed in the previous section. Such difficulties are potentially generated by two types of model mismatch - physical and statistical. The physical model mismatch can be originated by missing *a priori* environmental information about the channel and geometry, causing an erroneous or too simplistic choice of the physical model. On this side of the problem there is not much to be done since the amount of information is fixed to that available *a priori*. The statistical model mismatch results from wrong assumptions on the statistical properties of signals received on the vertical array, and thus erroneous choice of signal

or noise models. The problem at hand is to recall the statistical model in detail and to investigate whether any of the assumptions has been violated such that the estimation process failed to yield proper model parameter estimates.

The signal model described in (6) assumes that the field measured at the array corresponds to the channel Green's function as the solution of the wave equation at the sensor locations depending on source position and environmental parameters incorporated into a channel response vector $\mathbf{H}(\omega, \theta_0)$. Noise perturbations are conveniently expressed in terms of covariance matrices \mathbf{C}_{UU} , which describe the ocean noise spatial and frequential structure. For the derivation of the matched-field processor in equation (10), it was assumed that the signals were random frequency cross-correlated and that the noise is uncorrelated across space and frequency, falling in the category of sensor noise with a diagonal structured covariance matrix.

The eigendecomposition of the covariance matrix in equation (8) can be of central importance, since the eigenvalues are a mirror of its structure and its positivity allows for the factorization in eigenvalues and eigenvectors

$$\mathbf{C}_{YY}(\theta_0) = \mathbf{V}\mathbf{E}\mathbf{V}^H, \quad (13)$$

with \mathbf{V} unitary and $\mathbf{E} = \text{diag}\{e_1, e_2, \dots, e_{KL}\}$ a diagonal matrix of real eigenvalues ordered such that $e_1 \geq e_2 \geq \dots \geq e_{KL} > 0$. In the case of uncorrelated noise, it can be observed that if the signal matrix \mathbf{C}_{SS} has full rank then there will be $L(K-1)$ eigenvalues equal to σ_U^2 . If, on the other hand, \mathbf{C}_{SS} has rank equal 1, then the signal component is deterministic and $LK-1$ eigenvalues are equal σ_U^2 . In terms of matched-field processing this is the most convenient case, since it corresponds to matching the replica to the eigenvector associated with the largest eigenvalue of matrix \mathbf{C}_{YY} .

The ratio between the first and second eigenvalues ($\frac{e_1}{e_2}$) is often an indicator of the adequateness of the statistical model relative to the data being processed.

In terms of eigenvalue analysis it is suitable to observe the eigenspectrum of the sample correlation matrix, in particular the behavior of the ratio between e_1 and e_2 . This gives a measure of the degree of dominance of the first eigenvalue over time in order to detect changes in the structure of the data, and evaluate its disagreement relative the assumed model. The advantage of the eigenvalue analysis is that it is data-consistent, since it only depends on the received signals.

Figure 5(a) shows the eigenspectra of the sample correlation matrix versus time, with a data gap due to an interruption for changing the batteries of the VLA. Before and shortly after the data gap, the ship is moving away from the VLA location where it can be seen that the eigenspectra energy is spread out reaching significant values up to order 10/12. This is clearly due to a violation of the channel stationarity assumption for cross-covariance matrix estimation where several different channel acoustic responses were averaged together within the data window. After time 289.9 the source ship is free drifting so movements are limited to those necessary to keep the station. Surprisingly a significant energy spreading can also be noticed in the time interval 290 to 290.35 (approximately 9 hours), after which it abruptly falls off. Along the whole interval some spikes are also visible, which can be attributed to ship movements to maintain the station. In order to obtain a quantitative measure of the energy spreadout figure 5(b) shows the evolution of the $\frac{e_1}{e_2}$ ratio (top) and its inverse $\frac{e_2}{e_1}$ (bottom). It is clearly visible that the movement of the source ship in the first part of the run strongly reduces the $\frac{e_1}{e_2}$ ratio, that immediately increases when the ship stalls. As expected from the eigenspectra data an abrupt reduction of the $\frac{e_1}{e_2}$ ratio can also be noticed in the time interval 290 to 290.35. While it is easily understandable that the $\frac{e_1}{e_2}$ ratio remains low while the ship is moving fast, it is not so clear why this ratio remains low in the interval 290 to 290.35 during which the ship was on station and the acoustic channel responses should be relatively stable or do not suffer significant changes during the 3 min averaging window for each covariance matrix estimation. Clearly, the cause for the abrupt decrease of the $\frac{e_1}{e_2}$ ratio in that time interval is not the same as it is before the gap, neither the is the effect the same.

Thus there might be several effects causing these high variations in the spreading of the eigenspectrum. To some extent such spreading might be caused by a disagreement between the received

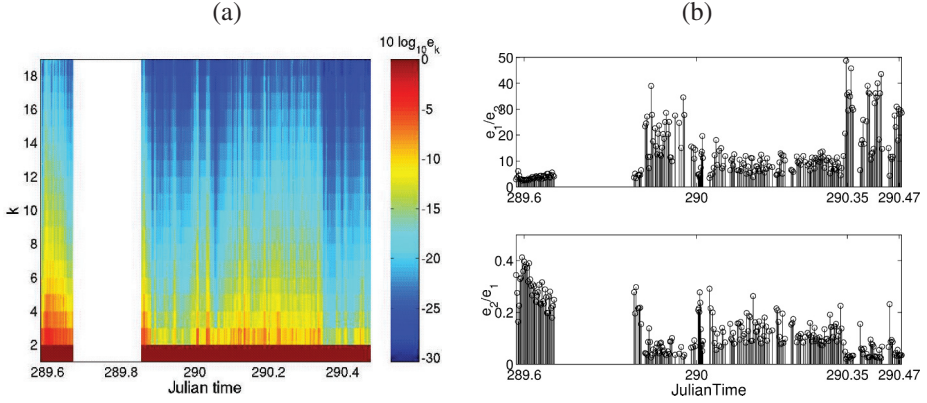


Figure 5. Eigenspectra computed from the cross-frequency correlation matrix (a); ratio between the two greatest eigenvalues $\frac{e_1}{e_2}$ (b - top) and $\frac{e_2}{e_1}$ (b-bottom).

data and the statistical model assumed for the present problem. The rate of change in the degree of spreading at some time points configures this data set as being acquired in a highly variable scenario. The next step is to search for possible causes that can explain this model - data disagreement.

4.1 Acoustic source motion

The parameters concerning the source position are leading parameters in terms of acoustic field sensitivity. Thus one must account for variations in the source position during the signal emissions. In the present case the repetition rate of the emitted signal is 10 s. The number of snapshots used to compute the sample correlation matrix is a compromise between its variance and the time coherence of the propagation channel. A number of snapshots equal to 18 represents about 3 minutes of observation time. This means that the hypothesis of a time-invariant propagation channel can possibly be violated for a given acoustic source motion. From the statistic point of view and in terms of eigenvalues, the variability of the acoustic response will induce a loss of dominance of the largest eigenvalue, due to energy partitioning in different eigenvectors. The gray line of the range vs. time plot of figure 4 reveals that the source ship was moving quite often struggling to keep the station, while being pushed towards the VLA by wind and currents. Ship motion not only implies a change on source range, but also in source depth, since, for a fixed cable scope, the source depth is a function of ship speed according to its characteristics. Thus, during accelerations, changes in the source depth occur. Figure 6(a) shows the ship speed at discrete times when acoustic data was received, and figure 6(b) shows the correlations of ship speed and ship acceleration with the $\frac{e_2}{e_1}$ ratio vs. time (figure 5(b-bottom)). The time axis of the correlation plot is actually in time bins (for a total number of 232) since there is a gap in the data the time bins are not uniformly spaced. It can be seen that the level of $\frac{e_2}{e_1}$ is strongly correlated with the ship speed yielding a correlation above 0.9 and with the peak perfectly placed in the center of the plot, i.e., for a time lag equal to zero. The influence caused by the ship acceleration is more difficult to detect since the change in speed occurs for very short periods of time and involves a second order derivative of the position record, prone to instabilities. However, the maximum correlation still appears at the center of the function. In the present case, the source motion problem can be seen as a short time scale phenomenon. In figure 5(b) it can be clearly seen that some spikes in the $\frac{e_2}{e_1}$ ratio are standing out at several times, and those can be attributed to source motion. However, the overall energy spreading can not be accounted for by acoustic source motion only, which lead us to search for other environmental related causes.

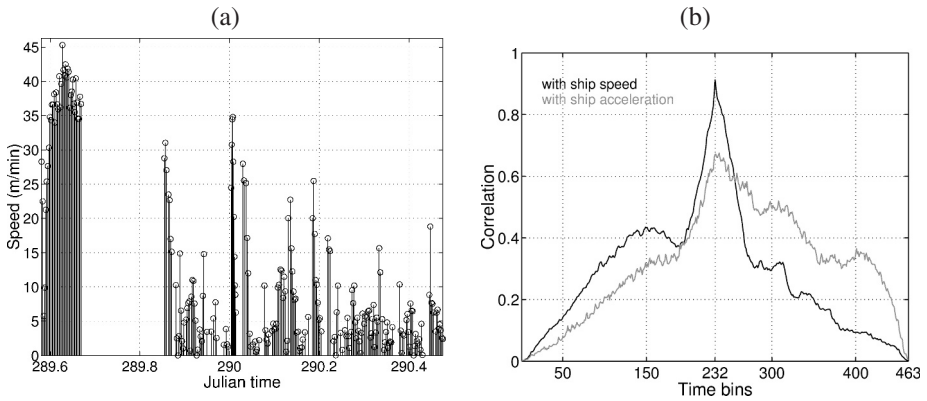


Figure 6. Correlation of ship speed and acceleration functions with the $\frac{e_2}{e_1}$ function shown in figure 5(b).

4.2 Noise level and tidal forcing

Recalling the discussion on eigenvalue analysis in the first half of section 4, it appears that the overall energy spread of the eigenspectrum in the interval 290 to 290.35 could be due to a structured noise background superimposed by short time scale variations due to source ship motion as described in the previous section.

Figure 7(a) shows a noise power estimate for hydrophone #1 as a function of time and frequency. Here the abrupt change in noise level in the time interval 290 to 290.35 is quite clear with several strong lines across the whole frequency band, however, with some predominance below 350 Hz. Observing the colorbar it is also found that the fluctuation of the noise level is up to 30 dB. Finally, in figure 7(b), that shows the noise eigenspectra along time, it can be seen that the noise power abrupt changes are accompanied by statistical changes denoting a correlated signal-like structure in the target interval 290 - 290.35. The noise covariance matrices show strong spatial noise correlation in that period of time, which by itself is a potential reason for the breakdown of the inversion process.

It remains to find out what originated such high noise amplitude and correlation. There are several possible noise origins in the ocean. The most common is ambient noise caused by waves or wind at the ocean surface that translate in a correlated noise field at the vertical array. Other common source of correlated noise is that due to distant shipping but generally manifest itself as a variable spectrum strongly attenuated at frequencies above, say, 200 Hz - which obviously is not the case here. Flow noise and mechanical vibration are also common sources of noise when addressing horizontal towed arrays or vertical arrays in strong currents. Although there are no recordings of the current field during the experiment, historical records show that tidal driven currents up to 2.5 m/s were measured in the area. Figure 7(c) shows a plot of the estimated noise level and the absolute value of the tidal forcing superimposed. The tide was predicted using a tide prediction model. It is not quite obvious that the noise level increases with the tidal forcing, but a correlation between these two quantities reveals that they are in fact strongly correlated, reaching a maximum correlation over 0.8 for zero time lag (figure 7(d)). If the current is sufficiently strong it can cause the VLA line to vibrate between the mooring and the surface buoy. In that case the vibrations can origin mechanical noise propagating along the VLA sensed by the hydrophones and resulting in spatially structured noise over a large frequency band.

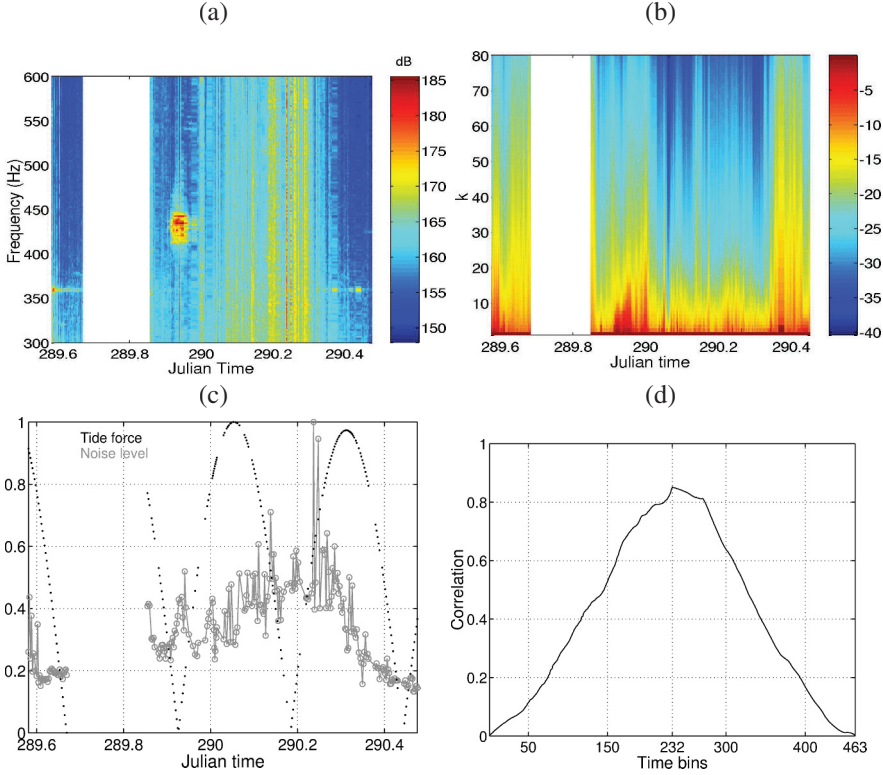


Figure 7. Estimated noise level as a function of time and frequency (a); eigenspectrum of a full rank noise covariance matrix as a function of time (b); average noise level estimated using all hydrophone with absolute tide force value over time (c); correlation of estimate noise level with absolute tide force (d).

5 Data quality improvement for inversion

In the sections above it was shown that various factors have a significant impact on the data structure and therefore on the inversion process. It could be seen, e.g., that if during the observation time the environment or the geometry suffers strong changes, it is likely that the energy received along time at the array tends to be spread into different eigenvectors. This is equivalent to observing a decorrelation of consecutively received signals. The duration of the observation window establishes a trade-off between the coherence of the propagation channel and the variance of the covariance matrix estimate. To handle fast varying environments one can implement an eigen-based processing technique simply based on the maximization of the $\frac{e_1}{e_2}$ ratio with the goal of adaptively determining the observation time. Ideally, this would measure the relative decorrelation rate between signals and noise.

On the other hand, high level and spatially correlated noise have shown to be an important difficulty during part of the experiment. An additional factor of difficulty is the change of the noise structure along time, where the estimated degree of cross-correlations has shown a significant variation, leading to the failure of the assumption of spatially uncorrelated noise. In that case the straight step is to gain knowledge on the noise structure and use it in the derivation of a matched-field processor assuming structured noise. Cross-frequency processors can explore the advantage of the stochastic independence of frequency bins in the frequency domain, as the result of a discrete Fourier transform

Table 2. Summary of the four processing cases. **Cross** stands for cross-frequency processing; **Eig.** **SS** stands for maximization of the $\frac{e_1}{e_2}$ ratio as a function of the number of snapshots; **Eig. Norm** stands for maximization of the $\frac{e_1}{e_2}$ ratio as a function of normalizing the data by the best hydrophone.

	Cross	Eig. SS	Eig. Norm
Case 1	No	No	No
Case 2	Yes	No	No
Case 3	Yes	Yes	No
Case 4	Yes	Yes	Yes

property (see [7] for a complete description of the noise handling assumptions of the cross-frequency processor).

The remaining part of this section describes an attempt to improve the quality of the estimates by mitigating the difficulties discussed above. Three additional inversion results are being reported, where processing features are successively added. Four cases are summarized in table 2:

- Case 1 corresponds to the inversion reported in section 3.3 where the conventional processor is used;
- Case 2 corresponds to the application the cost function presented in equation (10), with a constant number of snapshots equal 18 and performing normalization to the best hydrophone. The idea is to take advantage of the reduced noise correlation across frequencies, since it has been observed that in part of the run extremely strong spatial noise correlation is present;
- Case 3 where the number of snapshots used for each covariance matrix is variable according to the maximization of the $\frac{e_1}{e_2}$ ratio, in order to inspect whether the variability *seen* during the observation window is a source of loss in parameter estimation performance, and finally
- Case 4 where the eigenvalue ratio is tested against the decision of normalization or not. The problem being addressed in this case is that of coping with drifts of the phases of the acoustic field, that prevent the field being summed coherently during the computation of the cross-correlation matrix.

As an example of Case 3, figure 8(a) shows the result of the maximization with respect to the number of snapshots N vs time. The effect of source motion at the beginning of the run is perfectly visible, both before and after the data gap. Then as the ship stalls a raise in the estimates of N is observed. During the rest of the run some variability in \hat{N} can be seen. Figure 8(b) shows that the estimates of N are strongly correlated with ship speed and acceleration. One interesting remark is that the correlation functions in figure 8(b) have a very similar shape of those of figure 6(b), possibly indicating that there is a close relation between the estimates of N and the $\frac{e_1}{e_2}$ ratio.

The inversion results obtained along the four cases are summarized in table 3 in terms of root mean square error (RMSE) for the parameters that can be measured and are subjected to change with time, and in terms of standard deviation for the seafloor parameters that are unknown but assumed to be invariant along the whole run. Although not perfectly monotonic, it can be observed that from case 1 to case 4, an improvement can be observed for each new feature introduced in the processing. Although the improvement seems to be small, there is clearly a tendency to ameliorate the estimation quality, especially in cases 3 and 4. The cross-frequency processor appears to perform better in conjunction with the eigen-based processing introduced in cases 3 and 4. The introduction of the cross-frequencies in case 2 by itself has shown little or no improvement to the estimation, since the length of observation time is not addressed and the noise appears to have some frequency cross-correlation. The estimation results obtained in case 4 are not shown graphically, since, visually, it would be difficult to take striking conclusions.

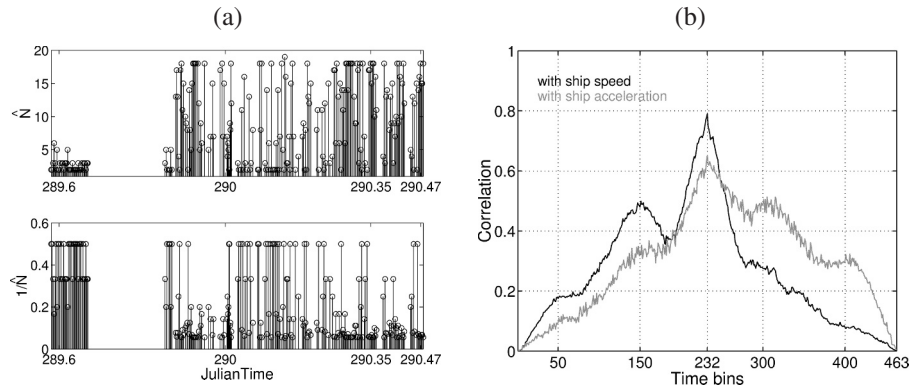


Figure 8. Estimated number of snapshot over time and its inverse (a); Correlation function of the inverse of the estimated N with ship speed and acceleration (b).

Table 3. Inversion performance measured via: ¹ RMSE using GPS source-receiver range and and XBT projected EOF coefficients; ² standard deviation of seafloor parameters (compressional velocity in sediment and subbottom, sediment thickness).

Proc.	RMSE ¹			Std. dev ²		
	R_s (km)	α_1 (°C)	α_2 (°C)	c_s (m/s)	h (m)	c_b (m/s)
case 1	0.125	2.289	1.458	36	1.65	78
case 2	0.126	2.283	1.253	38	1.48	80
case 3	0.121	2.130	1.161	35	1.45	69
case 4	0.117	2.055	1.204	28	1.40	62

6 Conclusion

In scenarios where a great deal of information is available, matched-field methods are highly reliable. Thus, they are suitable to be applied to OAT, where the number of unknown parameters is potentially high.

The INTIFANTE sea trial, conducted in the vicinity of Setúbal in October 2000, served among others, the purpose of acquiring data for testing OAT at ranges up to 6 km in a range-independent shallow water environment. When compared to other more complex scenarios this appeared to be a relatively easy task for MFT inversion of water column properties. Indeed during part of the run the inversion of the water temperature profile provided consistent results. However, in a relatively benign portion where the source ship was maintaining a station at 5.8 km distance from the VLA, the estimations significantly departed from the expected results. The search for the causes of this intriguing performance was the motivation of this paper that took us through various subjects such as the influence of rapid source motion within the limits of the stationarity assumption and the role of highly correlated noise possibly due to tidal flow at the array site. During the study the problem was identified but its origin was not completely understood.

Several processing schemes were implemented in an attempt to compensate these influences. First it was supposed that the overall quality of the data entering the inversion could be ameliorated by using cross-frequency covariance matrices. This resulted in little improvement, since the strong spatial noise correlation extended to the cross-frequency data as well. Then, in two additional attempts an eigenvalue approach was tested in order to improve the data quality. It was shown that energy partitioning into different eigenvectors was caused by source motion during the observation

time defined *a priori*. This was mitigated by optimizing the $\frac{e_1}{e_2}$ ratio for observation time and data normalization. It could be shown that the estimator for the best number of snapshots was highly correlated with the ship speed and acceleration. The inversion results could be progressively improved remaining, however, strongly limited by the high noise level. Further work is necessary to treat this problem should be treated in terms of spatial filtering by making use of *a priori* estimated noise structure.

References

1. Munk W., Worcester P. and Wunsch C. *Ocean acoustic tomography*. Monographs on mechanics. University Press, Cambridge, (1995).
2. Tolstoy A. and Diachok O., Acoustic tomography via matched field processing. *J. Acoust. Soc. Am.* **89**(3), 1119–1127 (1991).
3. Jesus S. M., Coelho E., Onofre J., Picco P., Soares C. and Lopes C., The intifante'00 sea trial: preliminary source localization and ocean tomography data analysis. In *Proc. of the MTS/IEEE Oceans 2001*, Hawaii, USA, November (2001).
4. Jesus S. M., Soares C., Onofre J. and Picco P., Blind ocean acoustic tomography: experimental results on the intifante'00 data set. In *Proc. of the European Conference of Underwater Acoustics*, Gdansk, Poland, June (2002).
5. Jesus S. M., Soares C., Onofre J., Coelho E. and Picco P., Experimental testing of the blind ocean acoustic tomography concept. In *Impact of Littoral Environmental Variability on Acoustic Predictions and Sonar Performance*, Lerici, Italy, September (2002).
6. Jesus S. M. and Soares C., Blind ocean acoustic tomography with source spectrum estimation. In *Proceedings International Conference on Theoretical and Computational Acoustics*, Hawaii, USA, August (2003).
7. Soares C. and Jesus S. M., Broadband matched field processing: Coherent and incoherent approaches. *J. Acoust. Soc. Am.* **113**(5), 2587–2598 May (2003).
8. Michalopoulou Z.-H., Source tracking in the Hudson Canyon experiment. *J. Comput. Acoust.* **4**, 371–383 (1996).
9. Collins M. D. and Kuperman W. A., Focalization: Environmental focusing and source localization. *J. Acoust. Soc. America* **90**, 1410–1422 (1991).
10. Ferla C. M., Porter M. B. and Jensen F. B., C-SNAP: Coupled SACLANTCEN normal mode propagation loss model. Memorandum SM-274, SACLANTCEN Undersea Research Center, La Spezia, Italy (1993).
11. Fassbender T., Erweiterte genetische algorithmen zur globalen optimierung multimodaler funktionen. Diplomarbeit, Ruhr-Universität, Bochum, (1995).
12. Felisberto P., Lopes C. and Jesus S. M., An autonomous system for ocean acoustic tomography. *Sea Technology*, **45**(4), 17–23 (2004).

INVERSIONS OF REFLECTION LOSS MEASUREMENTS OF A SMOOTH WATER/SAND INTERFACE

MARCIA J. ISAKSON, TRACIANNE NEILSEN AND ANDREW WORLEY

Applied Research Laboratories, University of Texas at Austin

Reflection measurements taken from a smooth water/sand interface from 70-160 kHz are inverted for model parameters using several candidate models. The models include the fluid model, the visco-elastic solid model, and the Biot/Stoll model. Inversions were performed using a simulated annealing optimization algorithm with OASES as the forward model. Each model was considered for its ability to fit the experimental data and the plausibility of its parameter values. The fluid and visco-elastic models predict an unphysically low value of the density of the water-saturated sand. The Biot/Stoll model was adequate to invert the data within known parameters. This work demonstrates that reflection data is viable data set on which to invert for sediment parameters.

1 Introduction

An accurate model of sediment acoustics is critical to understanding shallow water sound propagation and to detecting and classifying buried objects such as mines. Indeed, as SONAR becomes more important in shallow water operations, an accurate high frequency acoustic model of the ocean sediment becomes crucial to its application. This study is directed toward sandy sediments and seeks to determine which of the current models best fits measured data. A set of measurements is required that can unambiguously discriminate between the models. The plane-wave reflection loss, as a function of angle and frequency, is chosen because it contains many discriminatory features. The transition between the super- and sub-critical angle regimes is clear and provides an accurate indicator of the dominant acoustic wave speed. The reflection loss at steep angles is largely dependent on wave speed and density. The reflection loss at shallow angles has subtle features associated with a number of wave phenomena, including acoustic attenuation, shear wave speed and in the case of the Biot/Stoll model, the slow wave. It is also a non-invasive measurement that is relatively simple to make. For these reasons, the reflection loss function is likely to be a useful model discriminator.

The previously accepted fluid/fluid approximation of the water/sediment interface fails to account for a large loss in reflection at shallow angles observed in several studies [1,2]. An elastic model can explain the reflection loss by coupling the incident wave into a shear wave or a lossy compressional wave. Coupling to the shear wave is thought to be inefficient due to the large sound speed mismatch. In previous inversions using the elastic model, the shear wave speed was speculated to be as high as 700 m/s in order to increase coupling with the incident wave [1]. This is much higher than the measured value of 60 - 90 m/s taken at 312 Hz [3]. However, there are no measurements of shear wave velocity above 10 kHz because the shear wave is highly attenuated at higher frequencies. When

a poroelastic model is employed, some of the reflectivity loss is coupled into the slow wave, but the previously inverted shear wave speed of 500 m/s is still much higher than the low-frequency shear wave speed [2]. Such large shear wave speeds indicate that current models or inversion techniques are not fully capable of explaining the loss mechanism.

The current study seeks to determine if reflection coefficients measured over a range of frequencies and angles are suitable data for model comparison and acoustic parameter determination. Reflection loss is measured from a flat sediment/water interface as described in Sec. 2. Because of the flat interface, no loss is expected due to Bragg scattering or similar scattering effects. The data are inverted using three different models. Sec. 3 contains descriptions of the candidate models considered: fluid model, the visco-elastic model, and the Biot/Stoll poro-elastic model [4]. Inversions are performed using a simulated annealing optimization algorithm based on rotated coordinates with OASR as the forward model. The inversion technique is explained in Sec. 4, and the inversion results are presented in Sec. 5. Each candidate model is considered for its ability to produce realistic parameters and its fit to the experimental data.

2 Experiment

2.1 Reflection Measurements

Reflection measurements were carried out in a laboratory tank that was 18.29 m long, 4.57 m wide and 4 m deep. (See Fig. 1). The tank contained a 1 m layer of unwashed river sand under a 3 m water column. A more detailed description of the experimental apparatus can be found in [5]. The sediment was well-characterized for such parameters as shear wave speed, porosity, grain type and size [3,6,7].

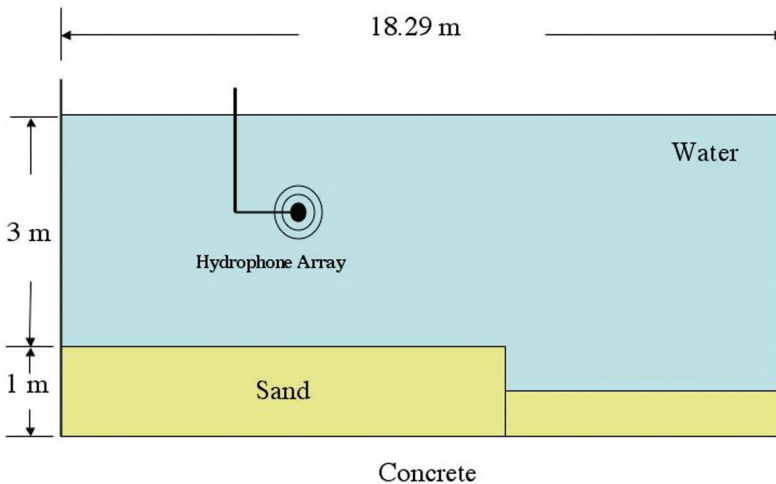


Figure 1. Schematic of Tank Used in Experiment.

Reflection data were taken using an array of two transducers separated by 1.28 m on an aluminum frame. The sending transducer had an oval reflector placed at a 45 degree angle above it to reduce signals scattered from the surface of the water. The sending transducer was driven by a linear chirp from 30 kHz to 160 kHz. The hydrophone registered signals from a number of different sources, a direct path source, a specular reflection from the bottom and scattering sources from elsewhere in the tank (See Fig. 2). These paths were distinguished by arrival times. The received voltage was amplified and filtered to remove signals with frequencies of less than 1 kHz or greater than 1 MHz.

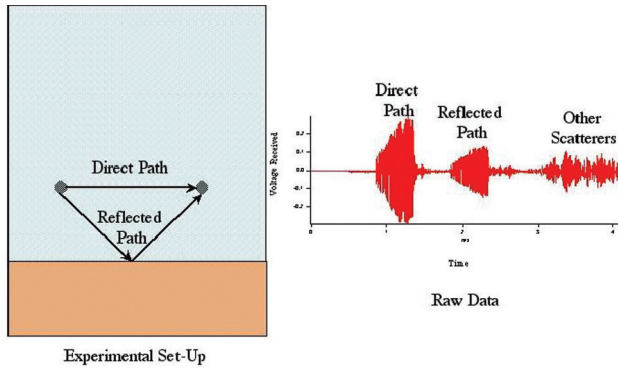


Figure 2. Experimental array geometry and raw data time series.

The frame was attached to a motorized platform and column so that the array could be moved both horizontally and vertically. The height of the array was controlled via a LabView program and the array was placed at 100 different heights above the sand from a few centimeters to a few meters. In this way, the reflected signal from a number of different grazing angles was measured. Twenty sets of data were taken in this manner at different positions along the length of the tank. Data were recorded digitally at 2 MHz.

Before taking acoustic data, the surface of the sand was smoothed and attenuated using a 10 cm diameter, 3 m long PVC pipe (See Fig. 3). The pipe was pulled across the bottom of the sand using the motorized platform and an adjustable column. The bottom was inspected for residual roughness using a laser light sheet method. The laser light sheet has height measurement accuracy of less than 1 mm over a spatial frequency range of 0.1 to 0.7 cycles/cm [8]. No roughness was determined from the laser light sheet method.

In addition to data taken at the sediment/water interface, the entire array was inverted and reflection measurements were taken from the air/water interface for calibration purposes. Since the air/water interface is a perfect reflector, this measurement allowed us to normalize our data for radial spreading, projector and receiver sensitivities and beam patterns.

2.2 Data Analysis Technique

Data were analyzed using the following algorithm. The direct path signal was identified from a measurement in which the signal from the direct path and the reflected path were separated temporally i.e. at a large grazing angle. A shading function was used to extract the direct path. The direct path signal modulated by a bandpass filter was used in a Wiener cross correlation filter using a noise floor of 0.01 times the peak signal power spectrum.

Using this Wiener filter, each signal was easily identified temporally (See Fig. 4). The first signal to arrive was the direct path signal. The next signal to arrive was generally the signal from the bottom reflection and finally signals that were scattered from other sources in the tank arrived. The incident angle was determined by the delay between the direct path signal and the reflected path signal. In Fig. 4, data from a grazing angle at 45 degrees is shown. As the path length for the reflected signal increases, the delay between the direct path signal and the reflected path also increases.

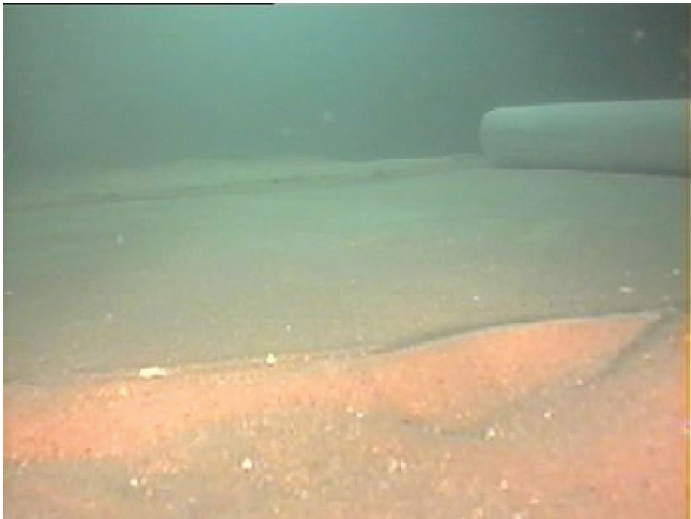


Figure 3. Bottom of tank after smoothing.

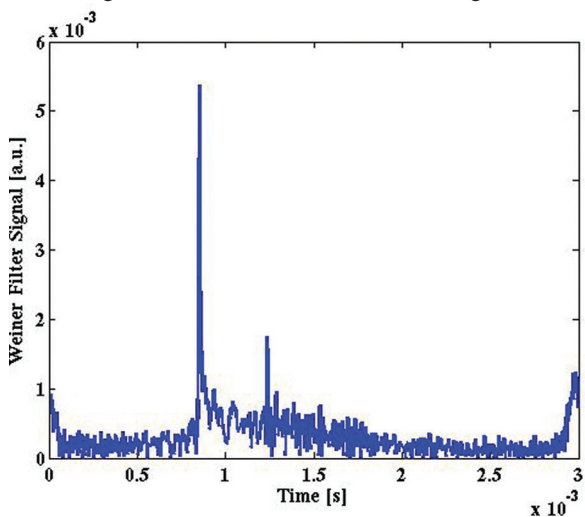


Figure 4. The Weiner filtered signal at 45 degrees grazing.

After the incident angle was computed, the data were bandpass over twelve bands filtered to obtain frequency dependent data. The peak value of the reflected path signal from the Weiner and bandpass filtered time series was recorded for each angle and central frequency. These values were divided by the peak value from the direct path signal for normalization. One hundred data sets from different areas of the sand bed were averaged to remove the effects of local variability in the sand structure and obtain a meaningful statistics.

Finally, these measurements were corrected by the corresponding values of measurements taken from the air/water interface. This process removed any errors due to beam pattern of the transducers.

The signal levels from the air/water interface are shown in Figure 5. Note that the air/water interface curve exhibits the expected amount of radial spreading. The final corrected sand/water reflection loss curve, is shown in Figure 6.

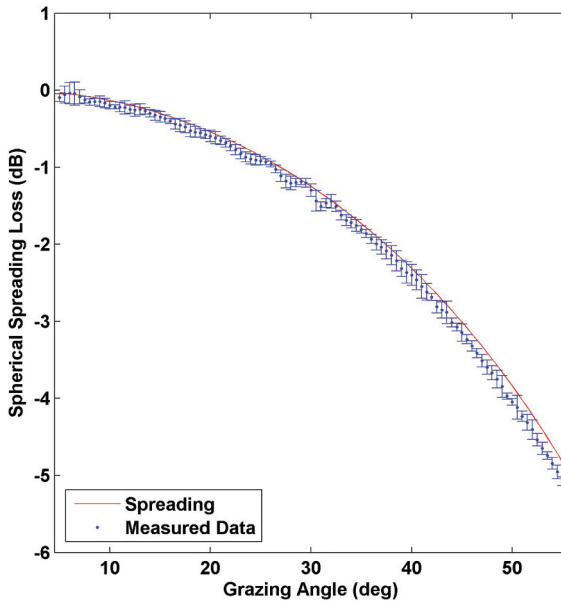


Figure 5. Normalizing measurement from the air/water interface. The error bars indicate one standard deviation.

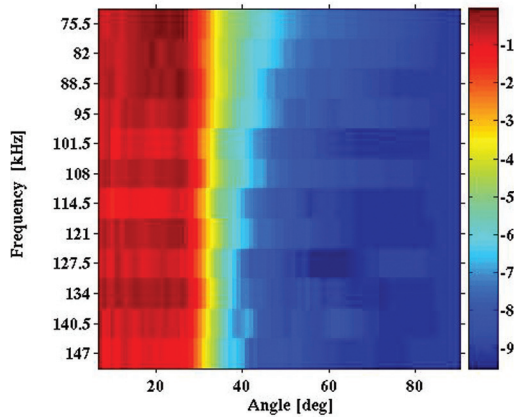


Figure 6. Normalized reflection loss in dB from a sand/water interface as a function of frequency and angle.

There are three important features that should be noted from the data. 1) The reflection coefficient at sub-critical angles is not unity. In fact, it is on the order of -1 dB. 2) The sub-critical reflection coefficient is not monotonically decreasing. 3) There is dispersion evident in the data even over the limited frequency range as can be seen from the change in the critical angle. The critical angle is about 33 degrees at 75 kHz as compared with 31 degrees at 147 kHz.

We use the normalized smooth sand/water interface reflection loss measurements shown in Figure 6 as a basis on which to compare current models of acoustic propagation in sediments.

3 Models

Three models are considered for inversion: the fluid model, the visco-elastic model, and the Biot/Stoll poro-elastic model [3]. Below is a discussion of each model followed by a review of its parameterization.

The fluid model reflection coefficient is determined by the impedance mismatch

$$R = \frac{Z_2 - Z_1}{Z_2 + Z_1} \quad (1)$$

where

$$Z_1 = \frac{\rho_1 c_1}{\cos(\theta_1)} \quad (2)$$

$$Z_2 = \frac{\rho_2 \omega}{(k_2^2 - k_1^2 \sin^2(\theta_1))^{1/2}} \quad (3)$$

$$k_i = \frac{\omega}{c_i} + i a_i \quad (4)$$

Z_1 and Z_2 are the impedances for the first and second media, respectively. Attenuation is introduced into the model by including a complex component into the wave number. The fluid model is, therefore, completely parameterized by the sound speeds in the first and second media, the attenuations of the first and second media, and the densities.

The visco-elastic model considers the bottom as an elastic solid that can support one dilational wave and a shear wave. Thus, the impedance from the second media includes a contribution from the shear wave

$$R = \frac{Z_{tot} - Z_1}{Z_{tot} + Z_1} \quad (5)$$

where

$$Z_{tot} = Z_2 \cos^2 2\theta_2 + Z_s \sin^2 2\theta_s \quad (6)$$

$$Z_1 = \frac{\rho_1 c_1}{\cos(\theta_1)} \quad (7)$$

$$Z_2 = \frac{\rho_2 \omega}{(k_2^2 - k_1^2 \sin^2(\theta_1))^{1/2}} \quad (8)$$

$$Z_s = \frac{\rho_2 \omega}{(k_s^2 - k_1^2 \sin^2(\theta_1))^{1/2}} \quad (9)$$

$$k_i = \frac{\omega}{c_i} + i a_i \quad (10)$$

Z_p and Z_s are the impedances for the compressional and shear waves respectively. As in the fluid model, attenuation is introduced by including a complex component into the wave number.

The visco-elastic model is parameterized by seven parameters: the sound speed of the first medium, the compressional sound speed and attenuation, the shear wave speed and attenuation and the densities.

The Biot-Stoll formulation has been presented extensively in the literature and is only summarized here [4]. In Biot-Stoll theory, the equations of motion are governed by two coupled wave equations:

$$\Delta(He - C\zeta) = \frac{\partial^2}{\partial t^2}(\rho e - \rho_f \zeta) \quad (11)$$

$$\Delta(Ce - M\zeta) = \frac{\partial^2}{\partial t^2}(\rho_f e - \rho \zeta) - \frac{\eta}{K_p} F(\kappa) \frac{\partial \zeta}{\partial t} \quad (12)$$

The fluid and the frame move independently with displacements U and u , respectively. The volumetric strain is defined by $e = \text{div}(u)$, and the local fluid content increase is $\zeta = \text{div}(u - U)$. The first equation above describes the fluid and solid conservation, and the second equation describes the fluid motion relative to the solid with two important first order correction terms. The first term, $m\zeta$, describes the inertial coupling because the fluid flow in the pores is not linearly related to the pressure gradient applied, according to Darcy's law. In the Biot/Stoll formulation m is given by $c\rho_f/\beta$, where c is the tortuosity of the pores, ρ_f is the fluid density, and β is the porosity. The second correction term, $\frac{\eta}{K_p} F(\kappa) \frac{\partial \zeta}{\partial t}$, describes a coupling with viscosity because the fluid flow in the pores does not follow the Poiseuille law: η is the viscosity, and $F(\kappa)$ is included to model the frequency dependence of viscous flow. The variable κ is given by $\alpha(\omega\rho_f/\eta)^{1/2}$, and α is the pore size parameter. The function $F(\kappa)$ approaches unity for low frequencies where the capillary flow can be modeled as parabolic. The moduli H , C and M are derived by Stoll as [4]:

$$H = \frac{(K_r - K_b)^2}{D - K_b} + Kb + \frac{4}{3}\mu \quad (13)$$

$$C = \frac{K_r(K_r - K_b)}{D - K_b} \quad (14)$$

$$M = \frac{K_r^2}{D - K_b} \quad (15)$$

$$D = K_r(1 - \beta(\frac{K_r}{K_{f-1}})) \quad (16)$$

There are thirteen independent parameters in the Biot/Stoll theory. The Biot parameters are generally grouped into three categories. The first category is the bulk parameters and includes the porosity β , fluid density ρ_f , fluid bulk modulus K_f , grain density ρ_g , and grain bulk modulus K_r . These parameters are generally well known and measurable. The next category is the fluid motion parameters: the viscosity η , the permeability κ , the pore size parameter α , and the tortuosity c . These values are less well known and more difficult to measure.

The last category is the frame response parameters which includes the frame shear modulus μ , the shear log decrement α_s , the frame bulk modulus K_b , and the bulk log decrement α_c . These properties are not known and are practically impossible to measure directly.

4 The Inversion Process

The inversion process consists of five major steps: (1) parameterizing the inversion, (2) calculating the forward model, (3) comparing the results of the forward model to the data, (4) determining the next step of the inversion, and (5) analyzing the results of the inversion to determine accuracy. Each step is considered in turn.

4.1 Parameterization

The parameterization differs depending on the model chosen. For each model, the water sound speed and density are considered known. The fluid model has only three parameters that are estimated by the inversion: the sediment sound speed c_p and attenuation α_p and the sediment density, ρ . For the visco-elastic model, there are two additional parameters that describe the shear wave, the wave speed, c_s , and attenuation, α_s . The limits for each parameter are shown in Table 1. A detailed description of the motivation behind the limits of each parameter may be found in reference [9].

The expected value for the compressional sound speed was measured as part of this study using a cross hole method. The value for the compressional attenuation was taken from the Sediment Acoustics eXperiment 1999 (SAX99) measurements [10]. The values for the shear wave speed was

measured by Barbara Luke using the Spectral-AnalySis-of-Waves (SASW) method in 1995 [3]. The value for shear attenuation was extrapolated from shear attenuation study in sandy sediments by Brunson [11]. The density was determined using the porosity measured in the tank and the known values for the density of the sand grains and the water.

For the purposes of this inversion, the density has been allowed to vary lower than the strict theoretical limit set by the porosity, the fluid density and the grain density. This was done to insure that the inversion maximized the cost function at a value other than that of a limit.

For the Biot-Stoll model, there are thirteen independent parameters. Again the water sound speed and density are considered known. For the inversion, the entire parameter space is explored, even though many of the parameters are considered well known. The limits for each of the parameters are shown in Table 2.

Table 1. Parameter Values for the Fluid and Visco-Elastic Models.

Parameter	Limits	Expected Value
Compressional wave speed, c_p	1700–1800 m/s	1740 m/s
Shear wave speed, c_s	20–1000 m/s	Unknown
Compressional attenuation, α_p	0.1–6 dB/Λ	0.1–6 dB/Λ
Shear attenuation, α_s	1.3×10^{-3} –0.33 dB/Λ	Unknown
Density, ρ	1.7–2.3 g/cm ³	1.99 g/cm ³

Table 2. Parameter Values for the Fluid and Visco-Elastic Models.

Parameter	Limits	Expected Value
Porosity, β	0.26–0.47	0.4
Permeability, κ	1×10^{-13} – 1×10^{-9} m ²	6×10^{-12} – 2×10^{-10} m ²
Fluid bulk Modulus, K_f	2.0–2.3 GPa	2.2 GPa
Fluid Density, ρ	0.99–1.01 g/cm ³	1.0 g/cm ³
Grain Bulk Modulus, K_r	32–49 GPa	36 GPa
Grain Density, ρ	2.6–2.7 g/cm ³	2.65 g/cm ³
Viscosity, η	0.0009–0.0011 kg/(m·s)	0.001 kg/(m·s)
Pore Size, α	2 – 6×10^{-5} m	4.4×10^{-5} m
Tortuosity, c	1–3	1.75
Frame Shear Modulus, μ	$(1 \times 10^7$ – $2 \times 10^9)$ Pa - $i(5 \times 10^5$ – $7 \times 10^7)$ Pa	Unknown "
Frame Bulk Modulus, K_b	$(1 \times 10^7$ – $2 \times 10^9)$ Pa - $i(5 \times 10^5$ – $7 \times 10^7)$ Pa	" "

5 Forward Model

The OASES Reflection Coefficient Module (OASR) from the OASES package version 2.1, is used as the forward model in the inversions. OASES is a collection of programs used to model acoustic propagation in layered fluids and sediments [12]. OASR is the sub-module of the OASES analysis package that calculates reflection loss coefficients over a given range of sampling frequencies and grazing angles. In addition, OASR can accommodate both elastic and poro-elastic models of the sea oor and its strata. Therefore, it is an ideal platform for comparing different models. A theoretical description of the reflection model is found in [13]. and generally follows the derivation found in Appendix B of Ref. [4].

The OASR module computes the plane wave reflection coefficient. Since the transducers were spherical, the entire experiment was modeled in OASP, a module of OASES which calculates the depth dependent Green's function and determines the transfer function for a given geometry and beam pattern. The spherical effects above 70 kHz for this geometry were negligible. Therefore, although the data was collected from 30 - 160 kHz, only higher frequencies from 70 - 160 kHz were inverted to insure that the plane wave model was an accurate description.

5.1 Comparing the model to the data

The overall purpose of the inversion algorithm is to obtain estimates of the unknown parameters required to produce modeled values that best match the experimental data. A cost function is defined to quantify the mismatch between model and measurements. When a perfect match is obtained, the value of the cost function is one. The inversion attempts to maximize the cost function by adjusting the model parameters. Therefore, the ideal cost function should have a varied landscape with significant gradients to optimize the chance of finding the global maximum.

The cost function considered for this work is a standard least squares cost function defined by:

$$C(x) = 1 - \frac{1}{N_f N_\theta} \sum_{f, \theta} [R_d(f, \theta) - R_m(f, \theta, \mathbf{x})]^2 \quad (17)$$

where $R_d(f, \theta)$ is the reflection coefficients measured at N_f frequencies, f , and N_θ grazing angles. $R_m(f, \theta, \mathbf{x})$ are the corresponding modeled values obtained for the set of parameters values \mathbf{x} .

5.2 Determining the next step of the inversion

Inversion not only requires a quantitative comparison of experimental and modeled data but also a strategy for sampling the N-dimensional parameter search space. To accomplish this task, a simulated annealing (SA) algorithm is used to optimize the cost function [14]. SA searches for the global maxima of the cost function using random perturbations and sequential variation of parameters with probabilistic criteria to accept and reject possible solutions. In this present work, OASR constructs a forward model based on the parameter variations from SA. The SA algorithm terminates when an acceptable cost function maximum is achieved. However, in the case of the Biot model, the search space was very at so the inversion terminated after a set number of iterations.

5.3 Results

Inversions are performed using the three sediment models to see which can reproduce the measured reflection coefficients with realistic values for the parameters. Inversions were performed over a 12 band frequency range with central frequencies from 75.5 to 147 kHz and over a 80 angle range from 10-90 degrees. Data was measured between 10-60 degrees and at normal incidence and interpolated between 60 and 90 degrees. The comparison of inversion results is accomplished in three ways. (1) The specific parameter estimates obtained by the inversion are compared to the known values to determine which estimates are physically reasonable. (2) The reliability and relative uncertainty of the inversion results are investigated by considering scatter plots of the parameters versus the associated cost functions, as described below. (3) The inversion results are placed in the forward model, and the resulting computed reflection coefficients are compared to the experimental values. These three techniques are used in conjunction to determine if the data, the cost function and the inversion technique are suitable for investigating sediment models and to provide an initial evaluation of the ability of the sediment models to reproduce the measured reflection coefficients.

One way to see which parameters are well determined by the optimization is to plot the value of the parameter versus the value of the cost function in a scatter plot format. Specifically, scatter

plots of all the values sampled in the inversion for each parameter versus the cost function value are considered. Although this is a somewhat simplistic method of determining uncertainties, it provides a qualitative comparison of the reliability of the parameters estimates obtained by the inversion. More rigorous approaches to the problem of estimating uncertainty have been suggested [15, 16, 17]. These methods have not yet been applied to this inversion. In order to reduce clutter on the scatter plots an envelope is drawn to encompass all the highest values of the cost function. Although these envelope lines have been smoothed, a high number of iterations were performed to insure the envelopes have meaning. The cooling schedules were not particularly slow, and the envelopes here are not the same as those obtained using a freeze-bath method [15]. The envelopes do, however, still give a qualitative idea of the relative uncertainties between parameters and confirm the information obtained by the rotated coordinates.

Additionally, a dash-dot line is plotted to indicate the value that corresponds to the maximum cost function. A tight envelope about the final inverted value indicates a well-determined parameter. A at or wide envelope indicates an poorly determined parameter. In some cases, the envelope reveals an upper or lower bound for a parameter. The documented or expected value is shown as a dashed line.

Fluid Model: The first sediment model to be considered is the fluid model. The scatterplots for the fluid model are presented in Fig. 7 and indicate that (a) the sound speed is well-determined at a value slightly lower than the expected value, (b) the attenuation estimate is larger than expected, and (c) the density is fairly well determined at a value significantly lower than the measured value. This value for density corresponds to a porosity of 0.51 which is indicative of a fine sandy clay. However, the porosity was measured in the tank at 0.403 and the mean grain size was measured as 0.25 mm, a fine-medium sand. Therefore, this value for density is considered unphysical for the sediment in the tank [6,7]. In Fig. 8, the reflection coefficient data averaged over the frequency range are compared with the reflection coefficient modeled with the fluid model results. The parameter estimates obtained by the optimization are listed in Table 3.

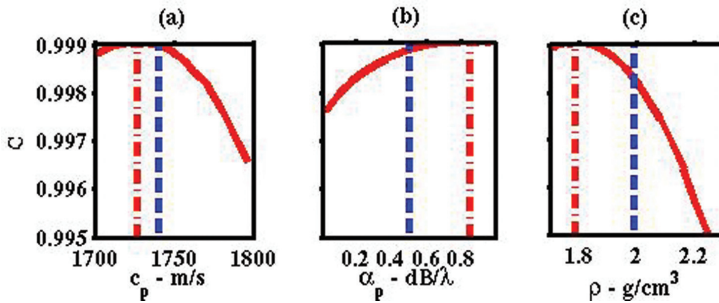


Figure 7. Results from inversion based on the fluid model for (a) sound speed, (b) attenuation, and (c) density. Dotted lines are the inversion results and dashed lines are the documented values.

From Fig. 9, it is clear that the inversion results fit the data fairly well at critical and supercritical angles with an unphysical value for the density.

To explore the sensitivitiy of the inversion, Fig. 9 illustrates how the modeled reflection coefficient is highly dependent on all three of the parameters. In each plot, the solid line represents the data, and the dashed line is the reflection modeled with the expected parameter values listed in Table 4. In Fig. 9(a), the dotted line and the dash-dot line are the reflection when the only sound speed is changed to values of 1500 m/s and 2000 m/s. In (b), the attenuation is varied from 0.001 dB/ λ (dotted line) to 0.8 dB/ λ (dash-dot line). In (c) the density is varied from 1.2 g/cm³ (dotted line) to 2.5 g/cm³ (dash-dot line). Widely different parameter values are considered to illustrate how each of the three parameters describes a different feature of the data although the three parameters are

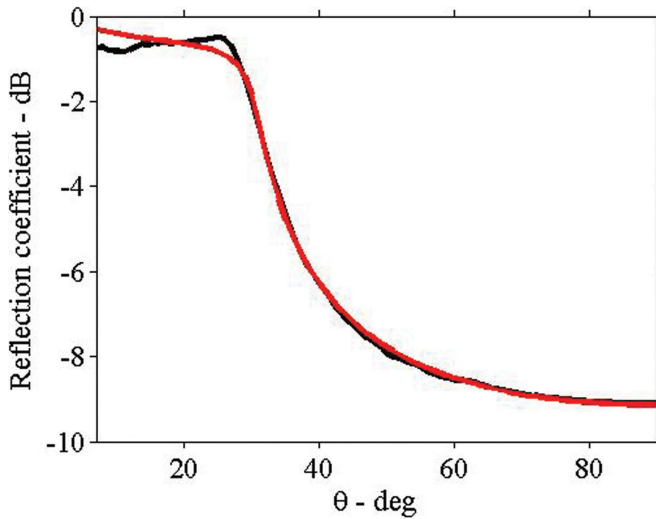


Figure 8. Comparison of measured reflection coefficient in black to values modeled with the inversion estimates based on the fluid model.

interrelated. The sound speed determines the location of the critical angle, the attenuation describes the sub-critical behavior and the density affects the value for the normal reflection coefficient. Comparison of the solid and dashed lines near normal incidence confirm that correct geophysical density does not match the data for the fluid model.

From Fig. 9, it is also clear that the inversion results do not fit the data well at sub-critical angles. Even changing the attenuation within wide bounds cannot account for the behavior of the data sub-critically. In fact, there is no mechanism within the fluid model to account for the behavior of the reflection coefficient sub-critically.

Lastly, since the fluid model is independent of frequency, it cannot accommodate the dispersion observed. Therefore, the fluid model is not considered as a good physical description of the sediment for this experiment.

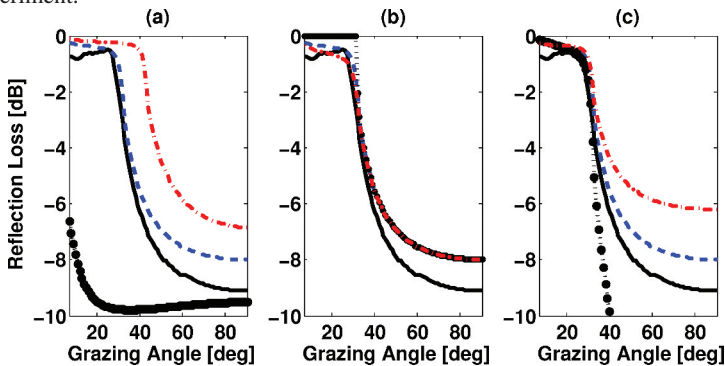


Figure 9. Changes in reflection when (a) sound speed, (b) attenuation, and (c) density are varied individually. The solid line is the measured data. The dashed line is modeled with the expected parameter values. The dotted and dash-dot lines are the resulting reflection when significantly lower and higher values of each parameter are used in the modeling.

Visco-elastic model: The parameter estimates obtained by inversion based on the visco-elastic model are shown in Table 3. From the plots of the parameter values versus cost function shown in Fig. 10, it is evident that the compressional sound speed and density are well defined. The compressional attenuation is also well determined, however, over larger bounds. The shear sound speed has an upper limit of about 400 m/s, too low for efficient mode coupling. In this slow shear wave case, the reflection coefficient is largely unaffected by the presence of the shear wave, and neither of the shear wave parameters can be obtained by the inversion of the reflection coefficient data. Figure 11 contains a comparison of the measured reflection data and the reflection obtained when these inversion results are used in the modeling. It is clear that much like the fluid model, the inversion fits the data well at critical and super-critical angles but does not fit the data at subcritical angles. There are no mechanisms in the visco-elastic model to account for either the behavior at sub-critical angles or the dispersion in the data.

Although the density is well determined in the inversion, its value is much lower than that of the geophysical density. As in the fluid case, this low value is required to match the measured reflection coefficient at normal incidence implying that the visco-elastic model is not describing the physics of the interaction. Additionally, the visco-elastic model is frequency independent and cannot accomodate the dispersion measured.

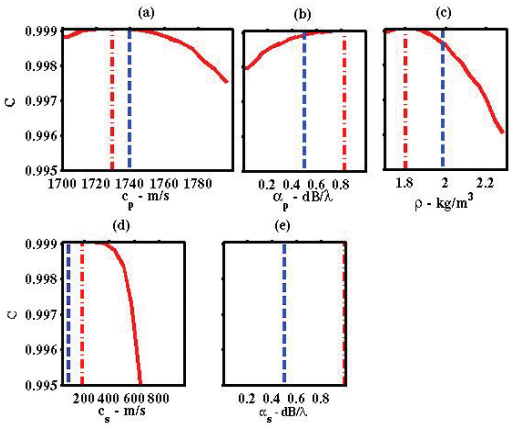


Figure 10. Results from inversion based on the elastic model for (a) sound speed, (b) attenuation, (c) density, (d) shear sound speed, and (e) shear attenuation. Dotted lines are the inversion results and dashed lines are the documented values.

A low density such as that determined by the inversion for the visco-elastic model, could imply that the density being probe by the sound wave is not the static geophysical density. A lowered value for density is also predicted by the Effective Density Fluid Model (EDFM), a simplified poro-elastic model [18]. The visco-elastic model has no provision for an effective density.

Biot-Stoll Model: The final sediment model considered is the Biot-Stoll model. The results of the inversions based on the Biot Stoll model are summarized in Figs. 12 - 15. Table 4 contains the parameter estimates obtained by the inversion, and the calculated values for the wavespeeds and attenuations are in Table 3. The scatterplots for the bulk parameters are shown in Fig. 12, for the fluid parameters in Fig. 13, and for the frame parameters in Fig. 14. Figure 15 is the comparison

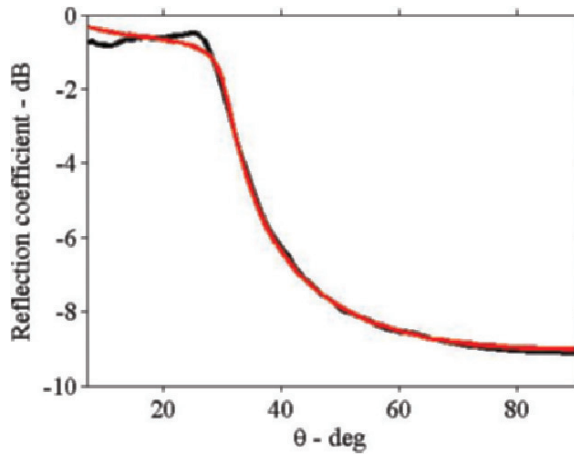


Figure 11. Comparison of measured reflection coefficient in black to values modeled with the inversion estimates based on the elastic model.

of the average data with the average modeled reflection coefficient based on the Biot-Stoll inversion results.

Scatter plots of the inversion results for the bulk parameters are shown in Fig. 12. Since the bulk parameters are generally well known, these parameters had small bounds in the inversion as specified in Table 2. Of the bulk parameters, only changes in porosity between the limits of its theoretical value caused the cost function to vary significantly (See Fig. 12(a)). The inversion indicated a clear upper and lower bound for porosity of 0.31 and 0.43 respectively. The inversion results for the densities and bulk moduli of the fluid and grains, in Fig. 12(b) - (e) do not show well defined maxima over these small bounds.

Results for the fluid motion parameters are shown in Fig. 13. The match between the model and data are sensitive to permeability, Fig. 13(b). The permeability showed a lower bound around $1 \times 10^{-13} \text{ m}^2$ and an upper bound around $1 \times 10^{-11} \text{ m}^2$. Tortuosity, Fig. 13(d), shows a tendency towards lower values. The other two fluid motion parameters, the viscosity in (a) and the pore size in (c) are not sensitive parameters in the inversion.

The inversion also shows that reflection coefficient data is largely insensitive to the frame parameters (See Fig. 14). The exception is that there is an upper bound for the frame shear modulus. This upper bound corresponds to a shear speed of approximately 500 m/s. This is the sound speed at which there would be a measurable coupling between the incident wave and the shear wave. Therefore, the inversion suggests that there is no coupling into the shear mode.

The Biot/Stoll model is frequency dependent. However, the inversion result did not display the dispersion measured in the data. As seen in Fig. 17, the Biot/Stoll results are frequency independent.

The inversion shows that reflection coefficient is sensitive to porosity and permeability within the parameter space searched. The inversion estimate for each parameter is within physical bounds. However, for many of the parameters that are not well known, the inversion maximized the cost function at a limit. Therefore, it is difficult to determine whether these inverted parameters are realistic. An upper bound on the shear frame modulus is also indicated suggesting that there is not a measurable coupling between the compressional mode in the water and the shear mode in the sediment.

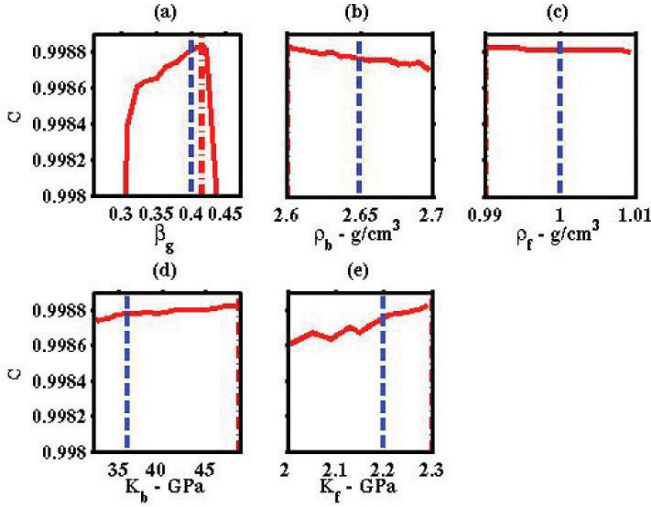


Figure 12. Results from inversion based on the Biot-Stoll model for (a) porosity, (b) grain density, (c) fluid density, (d) grain bulk modulus, and (e) uid bulk modulus. Dash-dot lines indicate the values determined by the inversion. Dashed lines indicate the expected values.

A comparison of the inverted for sound speeds, attenuation and densities for all the models is found in Table 3. The sound speed and attenuation values for the Biot model are calculated using OASES and the Biot parameter set from the inversion. The Biot density was calculated using the inverted values for the grain and fluid density and the porosity. It should be noted that the Biot model is the only model which determined a density within the physical bounds.

Because the Biot values in this table are calculated using a set of parameters that were of determined to various degrees, it is difficult to establish the degree to which the sound speeds and attenuation are determined. Also, the maximum of the cost function is lower for the Biot model than the other model. This is due to the much greater number in the parameters in the Biot model. In fact, the inversion for the Biot model was limited by the number of perturbations since the search space was very at. Lastly, when considering the values for the cost function, it should be noted that the cost function computed the absolute error of two percentages. A greater variation might be measured if the cost function computed relative error.

6 Conclusions

Reflectivity measurements were taken on a smooth water/sediment interface to minimize the contribution from scattering phenomena and to expose the fundamental physical acoustics of the granular medium. The critical angle effect was clearly measurable. The reflection loss at angles steeper than the critical angle was higher than predicted by fluid or visco-elastic wave theory. The values at angles shallower than the critical angle showed a small but measurable loss of around 0.8 dB, which may have far reaching consequences in the application of SONAR and shallow water acoustic propagation.

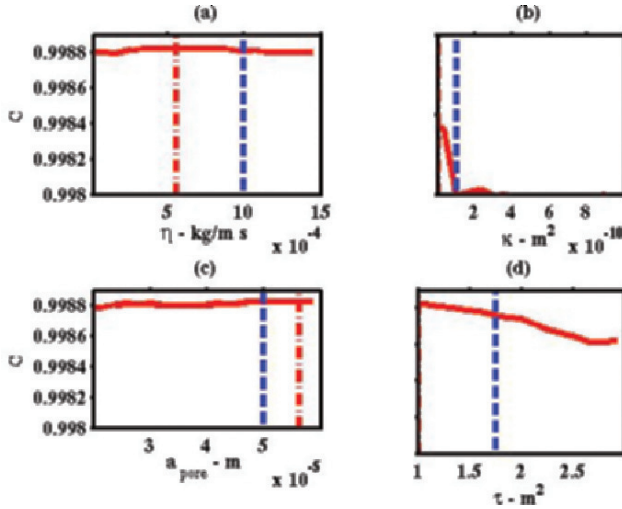


Figure 13. Results from inversion based on the Biot-Stoll model for (a) viscosity, (b) permeability, (c) pore size, and (d) tortuosity. Dash-dot lines indicate the values determined by the inversion. Dashed lines indicate the expected values.

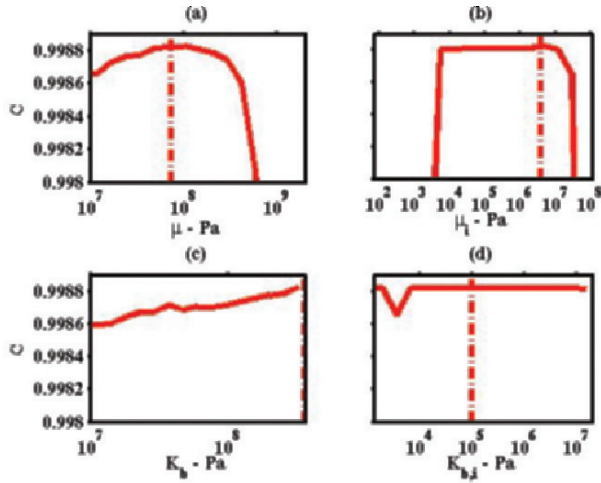


Figure 14. Results from inversion based on the Biot-Stoll model for (a) real and (b) imaginary part of the shear bulk modulus, and (c) real and (d) imaginary parts of the frame bulk modulus. Dash-dot lines indicate the values determined by the inversion. Dashed lines indicate the expected values.

A simulated annealing inversion based on a least-squares match between the data and modeled reflectivity has been applied to examine the ability of the fluid, elastic and Biot-Stoll models to reproduce the data with realistic parameter values. From the inversion results, it is clear that reflection coefficient measurements provide a data set that can be used to determine the parameters for the fluid and visco-elastic models. The compressional sound speed, compressional attenuation and density are all well determined in the inversion. The shear speed is bounded at 500 m/s indicating that there

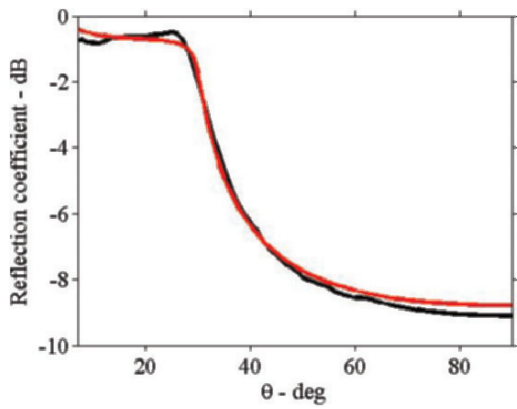


Figure 15. Comparison of measured reflection coefficient in black to values modeled with the inversion estimates based on the Biot-Stoll model.

Table 3. Parameter Values for the Fluid and Visco-Elastic Models. (*) Varies with frequency, value shown is at 100 kHz.

Parameter	Accepted Value	Fluid	Visco-Elastic	Biot-Stoll
c_{fast} , (m/s)	1740	1726	1730	1786*
α_{fast} , (dB/ Λ)	0.3	0.86	0.83	0.1*
c_{shear} , (m/s)	60–90	N/A	180	128*
α_{shear} , (dB/ Λ)	0.5	N/A	0.99	1.76*
c_{slow} , (m/s)	Unknown	N/A	N/A	148*
α_{slow} , (dB/ Λ)	Unknown	N/A	N/A	2.05*
ρ , (g/cm ³)	1.99	1.79	1.81	1.94
Final Cost Function Value		0.999	0.999	0.9988

c_{fast}	-	Fast wave speed,	α_{fast}	-	Fast wave attenuation,
c_{shear}	-	Shear wave speed,	α_{shear}	-	Shear wave attenuation,
c_{slow}	-	Slow wave speed,	α_{slow}	-	Slow wave attenuation,
ρ	-	density.			

is not a measurable coupling into the shear motion evident in the data. The shear attenuation is undetermined due to the lack of coupling into the shear mode. A primary result of this work is to show that fluid and visco-elastic models cannot accurately model the shape and absolute values of the reflectivity curve as a function of grazing angle without an unphysically low value for the sediment density.

Reflection coefficient measurements can also be used for estimates of the parameters for the Biot-Stoll poro-elastic model. Within the parameter search space, an upper and lower bound for porosity

Table 4. Inverted Biot/Stoll parameters.

Parameter	Accepted Values	Inverted Value
β , Porosity	0.4	0.41
ρ_b , Grain density (g/cm ³)	2.65	2.60
ρ_f , Fluid density (g/cm ³)	1.0	0.99
K_r , Grain bulk modulus (GPa)	36 ([19])	49
K_f , Fluid bulk modulus (GPa)	2.2	2.3
η , Viscosity (kg/m·s)	0.001	0.006
κ , Permeability (m ²)	$0.06-2\times10^{-10}$	1.5×10^{-12}
α_p , Pore size (m)	5×10^{-5}	5.6×10^{-5}
τ , Tortuosity (m ²)	1.75	1.0
μ , Frame shear modulus (Pa)	Unknown	$(7.9\times10^7 + i\ 1.2\times10^7)$
K_b , Frame bulk modulus (Pa)	Unknown	$(1.7\times10^7 + i\ 3.9\times10^3)$

and permeability are found. An upper bound for the frame shear modulus is also determined, indicating that the shear wave speed was no greater than 200 m/s. Like the fluid and visco-elastic models, this implies that there is no coupling of the incident wave into the shear mode.

As shown in Fig. 16, the inversion estimates are unable to fit the data at sub-critical angles using any model. There may be an additional physical mechanism responsible for this behavior not accounted for in these models.

Thus, reflection coefficient measurements provide an adequate data set for the inversion of geo-physical parameters. The inversion results for the fluid and visco-elastic models indicate that these models do not adequately describe the physics of the interaction. The Biot-Stoll model inversion fit the data within the physical bounds of the parameters.

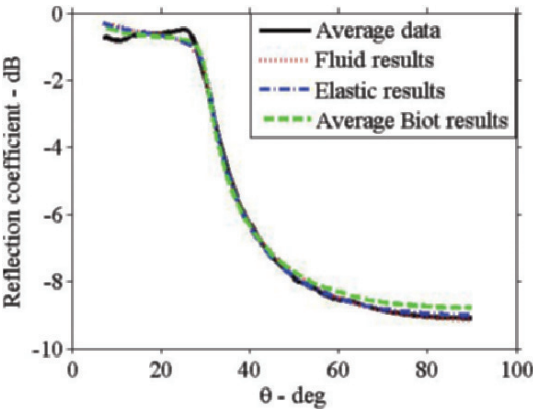


Figure 16. Comparison of measured reflection coefficient (solid) to values modeled with the inversion estimates based on the fluid model (dotted), the elastic model (dash-dot), and the Biot/Stoll model (dashed).

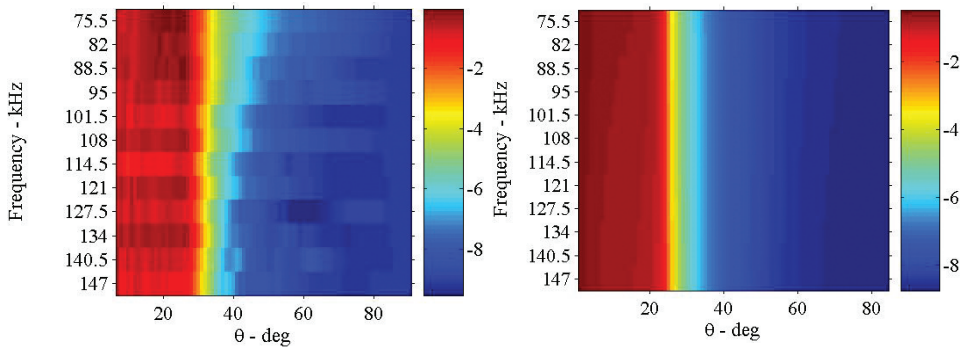


Figure 17. Comparison of measured reflection coefficient as a function of frequency and angle to the Biot/Stoll model inversion results.

References

1. Jensen F. B., Excess attenuation in low-frequency shallow-water acoustics: a shear wave effect? In *Shear Waves in Marine Sediments*, ed. by Hovem J. M., Richardson M. D. and Stoll, R. D. (Kluwer Academic Publishers, Dordrecht, 1991), pages 421–430.
2. Drevet C., Brussieux M. and Sessarego J. P., High frequency acoustics wave reflection on the surf zone seafloor. *Acustica* **85**, (1999).
3. Luke B., In situ measurement of stiffness profiles in the seafloor using the spectral-analysis-of-waves (SASW) method. Technical Report under ARL: UT Independent Research and Development Program, Austin, TX (1995).
4. Stoll R. D., *Sediment Acoustics*, Lecture Notes in Earth Science. Springer Verlag (1983).
5. Boyle F. A. and Chotiros N. P., Experimental detection of a slow acoustic wave in sediment at shallow grazing angles. *Journal of the Acoustical Society of America* **91**, 2615–2619 (1992).
6. Muir T. G., Horton, C. W. Sr. and Thompson L. A., The penetration of highly directional acoustic beams into sediments. *Journal of Sound and Vibration* **64**, 539–551 (1979).
7. Piper J. N., Sediment analysis, Interoffice memo. Applied Research Laboratories (1992).
8. Varghese S. M. and Isakson M. J., The calibration of a laser light sheet method for determining local interface roughness of the ocean floor. *IEEE Journal of Oceanic Engineering*, in press (2005).
9. Isakson M. J. and Neilsen T., The relative sensitivity of reflection loss of the Biot parameters. *Journal of the Acoustical Society of America* (In preparation).
10. Thorsos E. I., Williams K. L., Chotiros N. P., Christoff J. T., Commander K. W., Greenlaw C. F., Holliday D. V., Jackson D. R., Lopes J. L., McGehee D. E., Piper J. E., Richardson M. D. and Tang D. J., An overview of SAX99: Acoustic measurements. *IEEE Journal of Ocean Engineering* **26**, 4–25 (2001).
11. Brunson B., Shear wave attenuation in unconsolidated laboratory sediments. In *Shear Waves in Marine Sediments*, ed. by J. M. Hovem, M.D. Richardson and R.D. Stoll, (Kluwer Academic Publishers., Dordrecht, 1991) pages 141–148.
12. Schmidt H., OASES Version 2.1 User Guide and Reference Manual. Department of Ocean Engineering, Massachusetts Institute of Technology, Cambridge (1997).

13. Stern M., Bedford A. and Millwater H. R., Wave reflection from a sediment layer with depth-dependent properties. *Journal of the Acoustical Society of America* **77**(1), 781–788 (1985).
14. Goffe W., Ferrier G. and Rogers, J., Global optimization of statistical functions with simulated annealing. *Journal of Econometrics* **60**, 65–99 (1994).
15. Jaschke S. E. and Chapman N.R. Matched field inversion of broadband data using the freeze bath method. *Journal of the Acoustical Society of America* **106**, 1838–1851 (1999).
16. Dosso S. E. and Neilsen P. L., Quantifying uncertainty in geoacoustic inversion: II. application to broadband, shallow-water data. *Journal of the Acoustical Society of America* **111**, 143–159 (2002).
17. Dosso S. E., Quantifying uncertainty in geoacoustic inversion: I. A fast gibbs sampler approach. *Journal of the Acoustical Society of America* **111**, 129–142 (2002).
18. Williams K. L., An effective density fluid model for acoustic propagation in sediments derived from Biot theory. *Journal of the Acoustical Society of America* **110**, 2276–2281 (2001).
19. Briggs K., Richardson M., Williams K. L. and Thorsos E. I., Measurement of grain bulk modulus using sound speed measurements through liquid/grain suspensions. *Journal of the Acoustical Society of America* **104**, (1998).

ESTIMATION OF TRANSMISSION LOSS AND ITS UNCERTAINTY

PETER GERSTOFT, CHEN-FEN HUANG AND WILLIAM HODGKISS

*Marine Physical Laboratory
Scripps Institution of Oceanography
University of California San Diego
La Jolla, CA 92093-0701, USA*

A weakness in sonar performance prediction has been the lack of a means for quantifying the impact of uncertainty in estimates of the ocean environment. This paper describes the estimation of transmission loss and its statistical properties based on observations of ocean acoustic data. This problem is solved by first finding an ensemble of relevant environmental model parameters and then using all of these models to map into the transmission loss domain. In this mapping each environmental model is weighted according to its likelihood function. This algorithm is illustrated on vertical array data acquired during the ASIAEX 2001 East China Sea experiment. The environmental parameters are first estimated. Based on the likelihood that each of these environmental models fits the ocean acoustic data, each model is mapped into transmission loss. This enables us to compute a full probability distribution for the transmission loss in both range and depth.

1 Introduction

A weakness in sonar performance prediction has been the lack of a means for quantifying the impact of uncertainty in estimates of the ocean environment. Figure 1 offers an overview of posterior estimation of transmission loss from ocean acoustic data. Ocean acoustic data \mathbf{d} is observed on a vertical or horizontal array. The inverse problem is first solved using Bayes rule to compute the posterior distribution $p(\mathbf{m}|\mathbf{d})$ of environmental parameters \mathbf{m} . We are not interested in the environment itself but rather in better estimates of the transmission field, the usage domain $\mathbf{u}(\mathbf{m})$. Based on the posterior distribution $p(\mathbf{m}|\mathbf{d})$, the distribution of $p(\mathbf{u}(\mathbf{m}))$ is obtained via Monte Carlo simulation. From this transmission-loss distribution, all relevant statistics of the transmission loss can be obtained.

The principle of the inversion is indicated in Fig. 1. Based on the ocean acoustic data \mathbf{d} we statistically characterize transmission loss (the usage domain \mathbf{u}). The vector \mathbf{d} represents the acoustic data observed at N hydrophones and the vector \mathbf{u} represents transmission loss at range and depth. As shown in Fig. 1, this is mapped via a set of M environmental parameters \mathbf{m} . The approach involves a number of steps as outlined below:

1. Determine a model for the ocean acoustic environment and select an appropriate propagation model. These two form the mapping $\mathbf{d}(\mathbf{m})$ from the parameter space \mathbf{m} to data space \mathbf{d} .

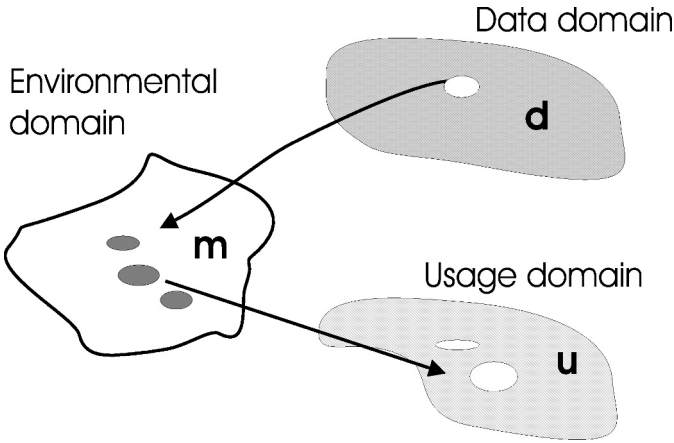


Figure 1. An observation \mathbf{d} is mapped into a distribution of environmental parameters \mathbf{m} that potentially could have generated it. The environmental parameters are then mapped into the usage \mathbf{u} .

2. Determine the mapping $\mathbf{u}(\mathbf{m})$ from the parameter space to usage space. Except for a change in geometry (source depth), here this is similar to $\mathbf{d}(\mathbf{m})$, but could be any other model (e.g., some other metric of sonar performance).
3. Find acceptable models \mathbf{m} from the data. As indicated in Fig. 1, a region around the data can map into several acceptable solutions in the model domain.
4. Map the acceptable models into the usage domain. Several models can map into the same usage region.

As indicated in Fig. 1, the mapping from data to usage domain is non-unique. There are many environmental models that give about the same goodness-of-fit. The maximum likelihood (ML) estimate of the environmental model gives the best fit. Instead of using just one estimated environment, it is proposed to describe the environmental solution probabilistically. This probability is then mapped into the usage domain. Knowing the posterior probability distribution in the usage domain is preferable to having a single point estimate such as the usage domain result corresponding to the ML-solution.

2 Inverse problem framework

In the Bayesian paradigm, the solution to determining parameters of interest \mathbf{m} given an observation \mathbf{d} is characterized by the posterior probability $p(\mathbf{m} | \mathbf{d})$. First, the prior information of the model parameter vector is the probability density $p(\mathbf{m})$. Then, this information is combined with the likelihood function $p(\mathbf{d} | \mathbf{m})$ provided by the combination of data and the physical model to give the posterior probability density $p(\mathbf{m} | \mathbf{d})$ of the model parameters. A clear discussion of inverse theory from a probabilistic point of view is given by Tarantola [1]. Additional details of Monte Carlo sampling of posterior probabilities can be found in Ref [2,3,4,5]. The solution to the inverse problem is then

$$p(\mathbf{m} | \mathbf{d}) = \frac{p(\mathbf{d} | \mathbf{m})p(\mathbf{m})}{p(\mathbf{d})}, \quad (1)$$

where the probability of the data $p(\mathbf{d})$ is independent of the environmental model and here can be neglected (set to unity). The posterior distribution $p(\mathbf{m} | \mathbf{d})$ contains all relevant information and from this distribution all of the relevant features of the environment can be found such as the maximum *a posteriori* (MAP) estimator.

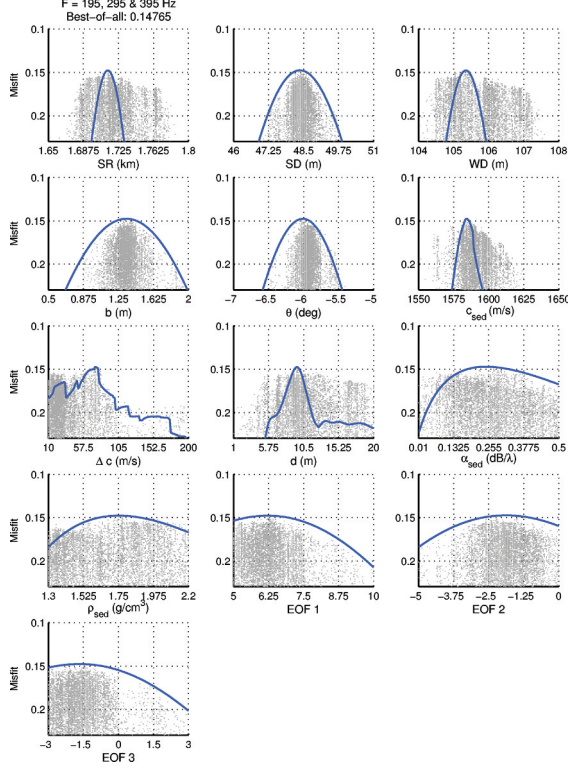


Figure 2. Marginal scatter diagrams of the SAGA search for the model parameters. The vertical axis represents the attained misfit on a linear scale. The thick line is the sensitivity curve of the multi-frequency misfit function using the best-fit model as a baseline.

We are not interested in the environment itself but rather better estimates in the information usage domain $\mathbf{u}(\mathbf{m})$. Based on the posterior distribution $p(\mathbf{m}|\mathbf{d})$, the distribution of $p(\mathbf{u}(\mathbf{m}))$ is obtained and from this distribution all relevant statistics of the usage space can be obtained. In the present application the usage domain is transmission loss.

The posterior distribution of $p(\mathbf{m})$ is first obtained and from this the probability distribution of \mathbf{u} is obtained

$$p(\mathbf{u}) = \int_{\mathcal{M}} \delta[\mathbf{u}(\mathbf{m}) - \mathbf{u}] p(\mathbf{m}) d\mathbf{m} \quad (2)$$

where \mathcal{M} represents the model space. This integral is implemented numerically by using samples from the model space \mathbf{m} based on the posterior distribution $p(\mathbf{m}|\mathbf{d})$ and then binning $\mathbf{u}(\mathbf{m})$. From the distribution $p(\mathbf{u})$ all relevant statistical features of the usage domain, e.g., transmission loss, can be obtained, as for example the mean and variance of \mathbf{u} .

Assuming a simple linear data model as detailed in [2], we obtain the Bartlett objective function $\phi(\mathbf{m})$ and likelihood function $\mathcal{L}(\mathbf{m})$,

$$\phi(\mathbf{m}) = \text{tr} \mathbf{C} - \frac{\mathbf{d}^\dagger(\mathbf{m}) \mathbf{C} \mathbf{d}(\mathbf{m})}{\|\mathbf{d}(\mathbf{m})\|^2}, \quad (3)$$

$$\mathcal{L}(\mathbf{m}) = \left[\frac{N}{\pi \phi(\mathbf{m}^{\text{ML}})} \right]^N \exp \left[-N \frac{\phi(\mathbf{m})}{\phi(\mathbf{m}^{\text{ML}})} \right]. \quad (4)$$

where \mathbf{C} is the data covariance matrix, N number of sensors, and ML refers to the maximum likelihood estimate.

3 ASIAEX inversion

Data from the 2001 East China sea experiment (see [6]) are used to illustrate the method. A 16-element vertical array was deployed in 105-m deep water. For the inversion (Fig. 2), a source towed at 48.5-m depth is used. Matched-field geoacoustic inversion using the selected frequencies 195, 295, and 395 Hz was carried out at $T = 29$ min over a parameter space of 13 parameters including geometrical, geoacoustic, and ocean sound speed EOF coefficients. Based upon the GPS position of R/V Melville, the source was approximately 1.7-km away from the VLA.

Figure 2 shows the marginal dot diagrams for the model parameters. The vertical axis is the Bartlett objective function (Eq. (3) normalized with $\text{tr}(\mathbf{C})$) with respect to the parameters sampled during the SAGA inversion [5] with the normal mode code SNAP as a forward model. The thick line superimposed on each scatter plot was obtained by using the best-fit model corresponding to the optimal value of the objective function as a baseline and computing the sensitivity for the optimized parameter. We see that the sampled values for the array bow and tilt parameters (b and θ) are spread mainly inside the sensitivity curve and align mostly with the best-fit values. A similar behavior is observed for the ocean sound speed EOF coefficients but with a wider span. The sensitivity curves are smooth except for Δc and d . The non-smoothness of the curves are due to the number of propagating modes changing when varying the geoacoustic parameters. The consistency between the local (line) and global (dots) searches shows that this set of parameters is weakly correlated with the other parameters. For the geoacoustic parameters, most sampled values wander outside the curve. This reveals the more complicated structure of the multi-dimensional search space. Note that the sampled values for the source range (SR) and the water depth (WD) are spread uniformly throughout the range of the parameter interval. This is due to the strong coupling between these two parameters.

A second inversion is now carried out to determine the uncertainty for two of the most important model parameters. For simplicity, we assume that only water depth and sediment sound speed have any associated uncertainty. All other parameters are fixed at the optimal values found in the inversion detailed above. Varying only the above two parameters gives posterior probability indicated in Fig. 3. It is based on the likelihood formulation, Eq. (4) and using the same data as in the inversion.

3.1 ASIAEX TL Prediction

The posterior probability (Fig. 3) is used to compute the posterior probability of $\mathbf{u}(\mathbf{m})$ using a frequency of 500 Hz and a source depth of 20 m. Except for water depth (bounds 100 to 120 m) and bottom sound speed (bounds 1550 to 1750 m/s), we keep the environment fixed at the values found in the inversion. In the present application, we evaluate $p(\mathbf{u}(\mathbf{m}))$ using grid integration (summing the values at discrete grid points). First the probability for TL at midwater depth (50 m) is evaluated, Fig. 4. The prior probability assumes even weighting of all the explored environmental models with the same bounds as above. The prior distribution (top) is spread out over a wide range but the posterior distribution (bottom) is more narrow. For the first 200 m, the propagation is only little influenced by the waveguide parameters and thus there is little difference between posterior and prior distributions. We then examine the probability at one point (50-m depth and 830-m range). This is done by taking a cut through the contour plots in Fig. 4 at 830-m range (indicated by a white line, corresponding to a peak in TL curve), as shown in Fig. 5. The posterior (solid) is much more concentrated than the prior (dashed).

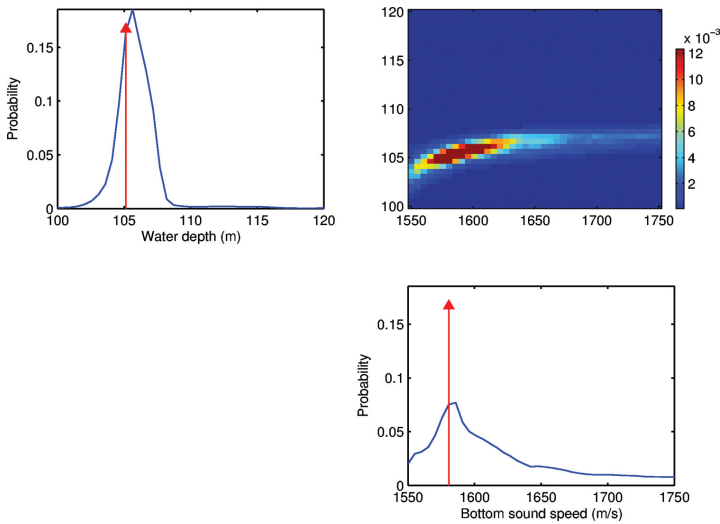


Figure 3. Marginal probabilities for water depth and bottom sound speed. The contour plot shows the 2D distribution. The gray vertical arrow indicates the ML solution (saga best fit). Note, that the maximum in the marginal distribution might not correspond to the ML maximum.

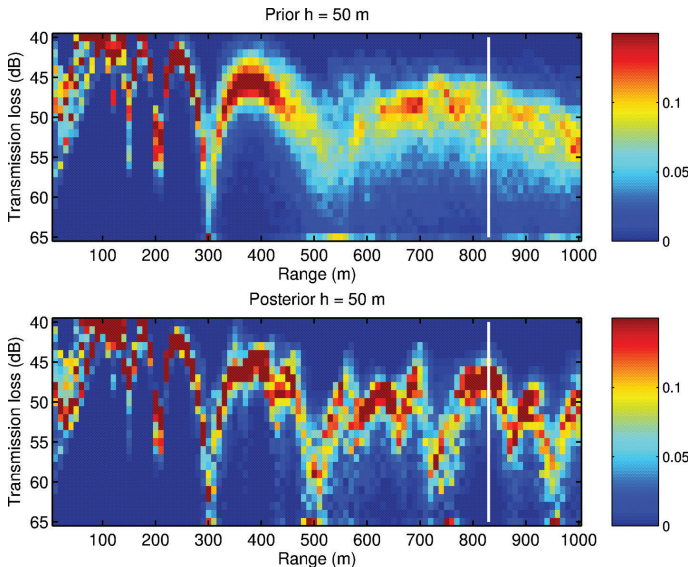


Figure 4. Prior (top) and posterior (bottom) probability distributions for transmission loss versus range at 50-m depth.

Contours of the median TL then are computed for the prior and posterior fields, Fig. 6. A good way to understand the uncertainty is to plot the 5th to 95th percentile ranges (gray area) of the prior and posterior fields, Fig. 7. Close to the source, there is little uncertainty for both prior and posterior fields as the sound field is not influenced by the waveguide parameters. Further away from the source, the prior uncertainty increases earlier in range than the posterior does, as the waveguide

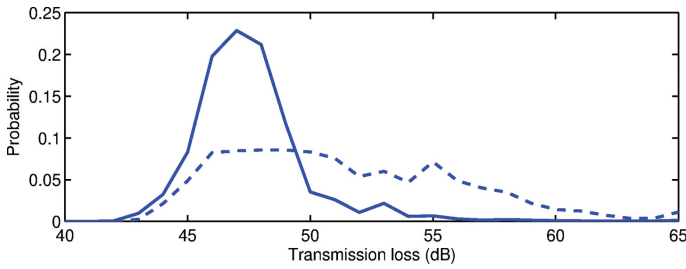


Figure 5. Posterior (solid) and prior (dashed) probabilities at 830-m range and 50-m depth. These correspond to a cut (white lines) though the contours in Fig. 4.

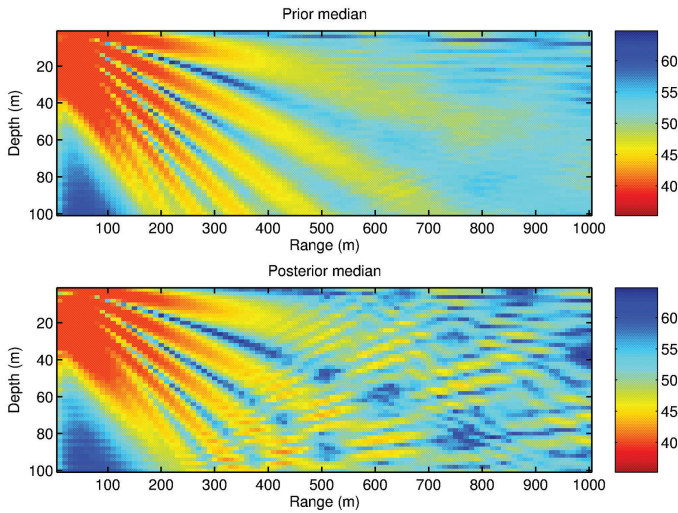


Figure 6. Median transmission loss (dB) based on prior (top) and posterior (bottom) distributions of environmental parameters (water depth and sediment sound speed).

parameters are less well determined. It also is seen that around the nulls of the median fields, Fig. 6, the variations in the fields are the largest, Fig. 7.

The uncertainty is easily conveyed by plotting the median TL (gray) combined with the 5th and 95th percentiles (represented by the gray area), see Fig. 8. Clearly, the posterior spread has decreased significantly.

4 Conclusions

An algorithm for estimating the statistical properties of transmission loss based on the output from a geoacoustic inversion has been described using a likelihood formulation. The likelihood function is developed assuming the error in the observed data is Gaussian. The examples presented here used data on vertical arrays, but any data could be used. The approach taken here then maps the environmental parameters via their probability distributions into a probability distribution of transmission loss.

In the transmission loss domain, we can compute the full posterior distribution at all frequencies, ranges and depths. In the examples, we demonstrated how to use the full transmission loss probability distribution and extracted characteristic features such as median and lower/upper percentiles from this distribution.

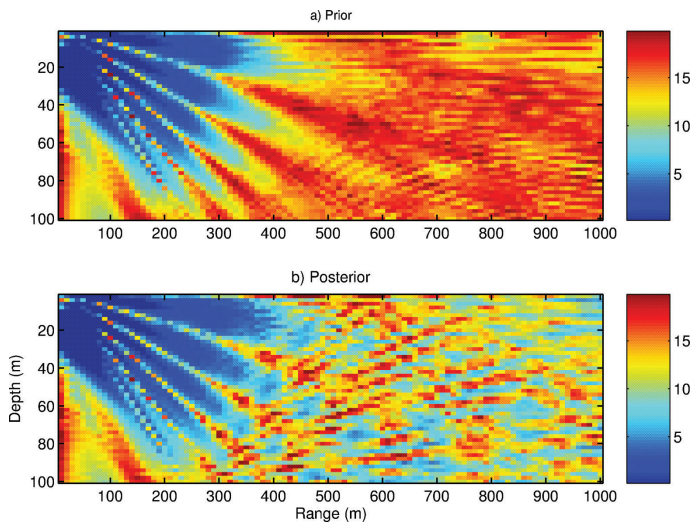


Figure 7. Range (dB) between 5th and 95th percentiles of the transmission loss for prior (top) and posterior (bottom) probabilities.

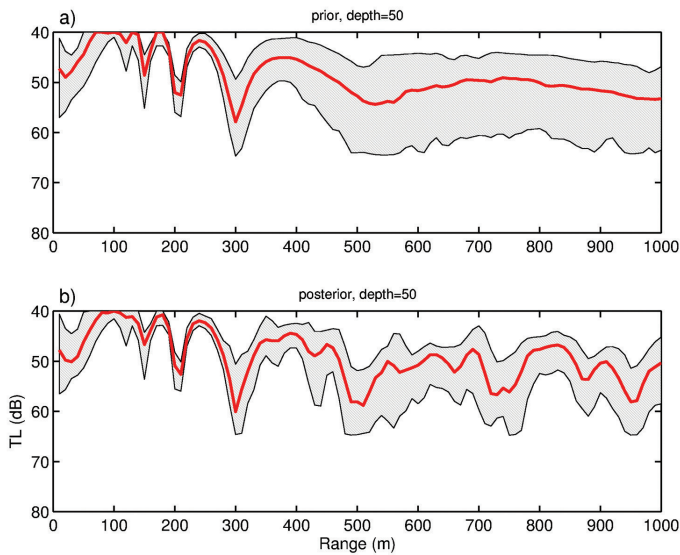


Figure 8. The median TL (gray) at 50-m depth (dashed) based on all (a) prior samples and (b) posterior samples. The gray area indicates the range between the 5th and 95th percentiles.

Acknowledgements

This work was supported by the Office of Naval Research.

References

1. Tarantola A., *Inverse Problem Theory: Methods for Data Fitting and Parameter Estimation*. Elsevier, New York, (1987).
2. Gerstoft P. and Mecklenbräuker C. F., Ocean acoustic inversion with estimation of *a posteriori* probability distributions. *J. Acoust. Soc. Am.* , **104**, pp. 808–817 (1998).
3. Dosso S. E., Quantifying uncertainties in geoacoustic inversion. I: a fast Gibbs sampler approach. *J. Acoust. Soc. Am.* , **111**, pp. 129–142 (2002).
4. Mosegaard K. and Tarantola A., Probabilistic approach to inverse problems, Chapter in *International Handbook of Earthquake and Engineering Seismology*, (<http://web.ccr.jussieu.fr/tarantola/>) (2002).
5. Gerstoft P., Inversion of seismoacoustic data using genetic algorithms and *a posteriori* probability distributions. *J. Acoust. Soc. Am.*, **95**, pp. 770–782 (1994).
6. Huang C.-F. and Hodgkiss W. S., Matched Field Geoacoustic Inversion of Low Frequency Source Tow Data From the ASIAEX East China Sea Experiment. *IEEE Oceanic Eng.*, to appear 2004.

A FORWARD MODEL FOR GEOACOUSTIC INVERSION BASED ON RAY TRACING AND PLANE-WAVE REFLECTION COEFFICIENTS

JENS M. HOVEM

*Norwegian University of Science and Technology,
Acoustic Research Center,
N-7491 Trondheim, Norway, and
Forsvarets Forskningsinstitutt, Horten, Norway*

HEFENG DONG

*Norwegian University of Science and Technology,
Acoustic Research Center,
N-7491 Trondheim, Norway*

XIUKUN LI

*Faculty of Underwater Acoustic Engineering,
Harbin Engineering University,
150001 Harbin P.R. China*

For geoacoustic inversion a fast and accurate forward model is essential, and in recent years a number of such models have been developed. In this paper, as a possible alternative, we describe a newly developed acoustic propagation model based on ray tracing named PlaneRay. A special and essential feature of this model is a unique sorting and interpolation routine for efficient determination of a large number of eigenrays, also for range dependent environments. The bottom is modeled with plane wave reflection coefficient and in principle any number of acoustic or elastic layers can be included. However, in the current version only a simple model with a fluid sediment layer over a solid half space is implemented.

1 Introduction

Geoacoustic inversion for determining sea floor properties requires an accurate forward model for the calculation of the acoustic field as function of space, frequency and time. Computation speed is essential since the forward model will have to run a large number of times with different bottom parameters in order to find the set of parameters set that gives an acceptable fit with a measured acoustic field. The most common models are models based on normal modes [1], the parabolic equation [2, 3] and propagation models based on the wave number integration technique [4, 5]; all these models have been extended to deal with range dependent problems. In general these models

are found to be quite accurate for both range independent and range dependent scenarios, but speed can in some cases be a problem. As a possible alternative, we have developed a forward acoustic propagation model, named PlaneRay [6] based on ray tracing. An essential feature of this model is a unique sorting and interpolation routine, and the model has proved to be quite efficient in determining eigenrays also for range dependent environments. The bottom is modeled with plane wave reflection coefficient, which from a programming point of view can treat any number of elastic or acoustic layers. Figure 1 shows the general shallow water propagation problem that is addressed in the model. The receivers are located on a horizontal line in the water. The bottom can be a fluid sedimentary layer over an elastic half space and both can be range dependent. The sound speed profile can only be a function of depth and not with range. The effect of a layered bottom is included with plane wave reflection coefficients and rays are only traced to the water-sediment interface and not into the bottom.

The use of ray tracing for propagation modeling is not new or original and many such models have been developed and presented in the literature earlier. In particular, we point to the model of Westwood and Vidmar [7] and to the paper of Westwood and Tindle [8] where this model is applied for time-series simulation shallow water propagation with a homogenous fluid bottom. The main difference is that the PlaneRay can handle range-dependent bottom topography and structure, but no rays are traced into the bottom as is done with the model of [7, 8]. In this paper we first describe the PlaneRay model and then present some results from testing and comparison with other models for both range independent and range dependent scenarios.

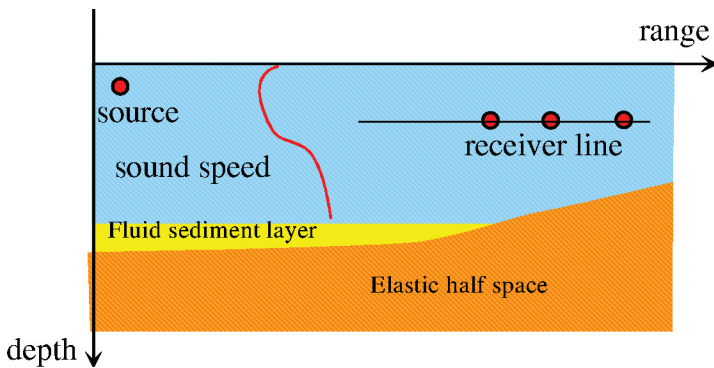


Figure 1. The PlaneRay model computes the received field from a source at receivers located on a horizontal line. The sound speed profile is only function of depth. The bottom can be a fluid sedimentary layer over an elastic half space and both can be range dependent.

2 Model description

The algorithm can be considered as having three stages:

1. The initial ray tracing using a large number of rays to map out the entire sound field.
2. Sorting and interpolation to determine the trajectories and the ray history of the eigenrays connecting the source to the receivers.
3. Synthesis of the acoustic field in frequency domain by coherently adding the contributions of the eigenrays, and calculation of the full-waveform time responses by Fourier transformation.

2.1 Initial ray tracing

The input information is the range dependent bathymetry, a sound speed profile and the source location and the receiver depth. The initial ray tracing is done by launching a relative large number of rays, (typically 1000 rays) with angles selected to cover the entire space between a fixed source location and out to receiver on a horizontal line at the specified receiver depth. For each ray, the model computes the ranges and the travel times to the locations where the ray intersects the receiver depth, and records the locations and the angles for reflection from the bottom and the surface. All this information is stored and used in the following stages. Notice that the rays are not traced into the bottom and that both the sound speed profile and the bathymetry are fixed; therefore the ray tracing is only executed once for each site.

The theory of acoustic waves [9, 10] is well known and shall not be developed here. The implementation used in the PlaneRay model is to divide the water column into a large number of layers with the same thickness Δz . Within each layer, the sound speed is approximated with a straight line so that, in the layer $z_i < z < z_{i+1}$, the sound speed is taken to be

$$c(z) = c_i + g_i(z - z_i), \quad (1)$$

where c_i is the sound speed at depth z_i , and the sound speed gradient in the segment is g_i . Since the sound speed in each of these layers has a constant gradient, the ray in each layer follows a circular arc; the arc's radius of curvature $R_i(z)$ is given by the local sound speed gradient $g_i(z)$ and the ray parameter ξ ,

$$R_i(z) = -\frac{1}{\xi g_i(z)}. \quad (2)$$

The ray parameter is defined as:

$$\xi = \frac{\cos \theta_s}{c(z_s)} \quad (3)$$

where θ_s is the initial angle of the ray's trajectory at the source depth z_s and the sound speed is $c(z_s)$. After travelling through the layer from z_i to z_{i+1} the ray's range increment is

$$r_{i+1} - r_i = -R_i(\sin \theta_{i+1} - \sin \theta_i), \quad (4)$$

which also can be written in the form

$$r_{i+1} - r_i = \frac{1}{\xi g_i(z)} \left[\sqrt{1 - \xi^2 c^2(z_{i+1})} - \sqrt{1 - \xi^2 c^2(z_i)} \right]. \quad (5)$$

The local sound speed gradient is approximated by

$$g_i = \frac{c(z_{i+1}) - c(z_i)}{z_{i+1} - z_i}. \quad (6)$$

The travel time increment is

$$\tau_{i+1} - \tau_i = \frac{1}{|g_i|} \ln \left(\frac{c(z_{i+1})}{c(z_i)} \frac{1 + \sqrt{1 - \xi^2 c^2(z_i)}}{1 + \sqrt{1 - \xi^2 c^2(z_{i+1})}} \right). \quad (7)$$

The algorithm makes repeated use of Equations (6) and (7), stepping with depth increments Δz in such a way that the new depth z_{i+1} is given by the old depth z_i as

$$z_{i+1} = z_i \pm \Delta z. \quad (8)$$

The plus sign indicates a ray going downwards and the minus sign, a ray going upwards. Evidently the sign has to change when the ray strikes the bottom and the surface, and when the ray goes through

a turning point. The acoustic intensity is calculated by using the principle that the power within a space limited by a pair of rays with initial angular separation of $d\theta_0$ centered on the initial angle θ_0 will remain between the two rays, regardless of the rays' paths. The acoustic intensity as function of horizontal range, $I(r)$ is according to this principle given by

$$I(r) = I_0 \frac{r_0^2}{r} \frac{\cos \theta_0}{\sin \theta} \left| \frac{d\theta_0}{dr} \right| = I_0 \left(\frac{r_0^2}{r} \right) \left(\frac{c_0}{c} \right) \frac{\cos \theta_0}{\sin \theta} \left| \frac{d\theta_0}{dr} \right|. \quad (9)$$

When the water depth varies with distance the ray parameter is no longer constant, but changes with the bottom inclination angle. An incoming ray with angle is reflected to the angle θ_{in} is reflected to the angle θ_{ref} when the bottom angle is α :

$$\theta_{ref} = \theta_{in} + \alpha. \quad (10)$$

Consequently, the ray parameter has to change to

$$\begin{aligned} \xi_{ref} &= \frac{\cos(\theta_{ref})}{c} = \frac{\cos(\theta_{in} + \alpha)}{c} = \\ &= \xi_{in} \cos(2\alpha) - \frac{\sqrt{1 - \xi_{in}^2 c^2}}{c} \sin(2\alpha). \end{aligned} \quad (11)$$

Beam displacement is also implemented in the model as an option. When the incident grazing angle is lower than the critical angle the ray appears to be displaced a certain distance Δl along the interface. The beam displacement is

$$\Delta l = \frac{\partial \delta}{\partial k} = 2k \frac{\rho_0 \rho (\gamma_0^2 + \gamma_1^2)}{\gamma_0 \gamma_1 (\rho_1^2 \gamma_0^2 + \rho_0^2 \gamma_1^2)}. \quad (12)$$

Where δ is the phase angle of the reflection coefficient for the interface between the water (0) and the bottom (1) for angles lower than the critical angle [11]:

$$\delta = 2 \tan \left(-i \frac{\rho_0 \gamma_1}{\rho_1 \gamma_0} \right). \quad (13)$$

In Equations (12) and (13), k is the horizontal wave number, γ_0 and γ_1 are the vertical wave numbers and ρ_0 and ρ_1 are the densities of the water and the bottom medium respectively. The beam displacement of Equation (13) is a function of frequency and valid only for the half-space model. In the PlaneRay model the beam displacement is introduced in the initial ray tracing for one frequency specified by the user and can therefore only be used for narrow band signals.

A typical plot of range to receiver depth as function of initial launch angle will look as shown in Figure 2. The grouping of angle, range pairs in rather smooth curves are noticeable and this behavior is utilized in the sorting and interpolation scheme.

The first step in the modeling is to apply the algorithm described above to a relative large number of rays spanning the whole range of initial angles that are relevant for the actual studies. For each ray the trajectory, travel time and the transmission loss are calculated and stored in the computer disk together with the ray history in terms of number, angle and locations of bottom and surface reflections and turning points. Since the sound speed profile and the bathymetry are supposed to be fixed and not changed this ray tracing calculation is only done once for each site.

2.2 Sorting and interpolation

The next step is to determine the eigenrays and their trajectories and the approach used in PlaneRay is based on interpolation on the results of the initial ray tracing. However, the interpolation has to be done on rays that have same type of ray history. This consideration is illustrated in Figure 3 which

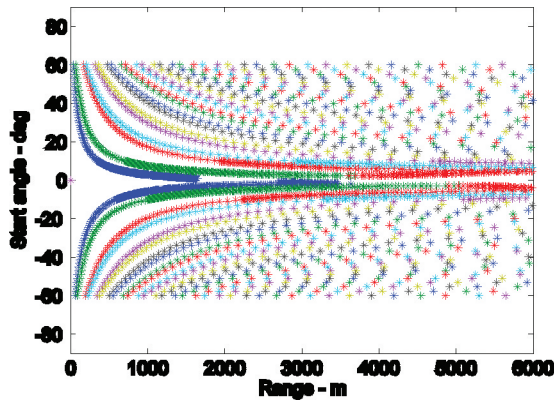


Figure 2. Recording of the ranges to the given receiver depth intersection as function of the rays initial angle resulting from the initial ray tracing.

shows a simple example of ray tracing with constant water depth and sound speed. The figure shows three ray paths from the source to reach three receivers at the same depth but different ranges. All the three rays have one reflection from the surface and two reflections from the bottom. The two rays intersecting the receiver depth at ranges r_1 and r_2 are the two rays from the initial ray tracing and the desired ray is the one with start angle θ_0 reaching the target at range r_0 .

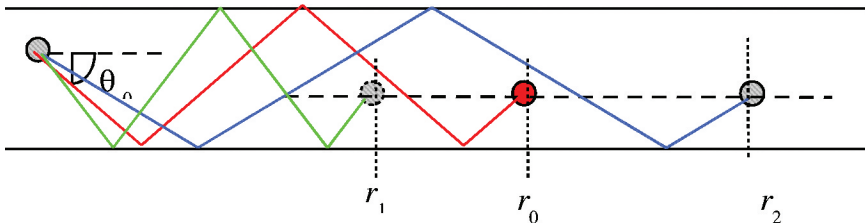


Figure 3. The eigenray to the receiver at range r_0 is found by interpolating between the two rays arriving at the same receiver depth at ranges r_1 and r_2 .

Notice that all the rays have the same number of reflections from the surface (one) and the bottom (two). Therefore the relation between initial angle θ_0 and receiver range can be expected to follow a reasonable smooth curve amenable to interpolation. In the case of a constant sound speed $c(z) = \text{constant}$ there will be 5 classes of arrivals and these are shown in Table 1.

With a depth dependent $c(z)$ there will be additional classes in order to include upper and lower turning points. The user is required to supply a selection table of classes to be included in the synthesis of the complete time and frequency response.

2.3 Synthesis of the sound field

The received sound field is synthesized by coherently adding the contributions of the eigenrays and the bottom reflections. No rays are traced into the bottom and a layered bottom is described entirely

Table 1. Classes of arrivals.

Class	Bottom hits	Surface hits	
Class 0	0	0	Direct ray
Class 1	$n - 1$	n	Positive and negative start angle
Class 2	n	n	Positive start angle
Class 3	n	n	Negative start angle
Class 4	n	$n - 1$	Positive and negative start angle

by plane ray reflection coefficients. In the current implementation the bottom is modeled with a fluid sedimentary layer over a homogenous solid half space. The thickness of the layer and the parameters of the layer and the half space can vary with range in any manner specified by the user.

The bottom reflection coefficient of this bottom is calculated as

$$R_b = \frac{r_{01} + r_{12} \exp(-2i\gamma_{p1}D)}{1 + r_{01}r_{12} \exp(-2i\gamma_{p1}D)} \quad (14)$$

where γ_{p1} is the vertical wave number for sediment layer and D is the thickness of the sediment layer. The reflection coefficient between the water and the sediment layer, r_{01} , is given as

$$r_{01} = \frac{Z_{p1} - Z_{p0}}{Z_{p1} + Z_{p0}}, \quad (15)$$

and r_{12} is the reflection coefficient between the sediment layer and the solid half space,

$$r_{12} = \frac{Z_{p1} \cos^2 2\theta_{s2} + Z_{s2} \sin^2 2\theta_{s2} - Z_{p2}}{Z_{p1} \cos^2 2\theta_{s2} + Z_{s2} \sin^2 2\theta_{s2} + Z_{p2}} \quad (16)$$

In Equations (15) and (16) Z_{ki} is the acoustic impedance for the compressional ($k = p$) and shear ($k = s$) waves in water column ($i = 0$), sediment layer ($i = 1$) and solid half-space ($i = 2$), respectively. θ_{s2} is the transmitted grazing angle for the shear wave in the solid half-space.

Figure 4 shows an example of the bottom loss as function of angle and frequency for a sediment layer with the thickness $D = 5$ m, density 1500 kg/m^3 and sound speed 1700 m/s over a homogenous half space with density 2500 kg/m^3 and compressional sound speed 4700 m/s and shear speed 2200 m/s . Notice that the anomalous high reflection loss at the angles is less than 20 degrees, this will be discussed later.

3 Case studies

3.1 Range independent cases

In this part we will present some results calculated by PlaneRay model for range independent cases and compare the results of the OASES, wave number integration model [4, 5]. The first case is the so called Pekeris' case [12] with water depth 100 m, layer thickness $D = 0$. The sound speed in water is constant $c_0 = 1500 \text{ m/s}$, density $\rho_0 = 1000 \text{ kg/m}^3$ and absorption coefficient $\alpha_1 = 0 \text{ dB}/\lambda$. The sediment parameters are sound speed $c_2 = 1700 \text{ m/s}$, density $\rho_2 = 1500 \text{ kg/m}^3$ and absorption coefficient $\alpha_2 = 1.0 \text{ dB}/\lambda$. The source is at a depth of 25 m and the receivers are located on a horizontal line at 75 m depth, extending to a maximum range of 10 km.

Figure 5 shows the frequency and time responses at a large number of receivers from 0 to 10000 m. Figure 5a shows the frequency response in terms of transmission loss and Figure 5b the waveforms. The transmitted wave from the source is a Ricker wavelet with approximate band width of 200 Hz, the sampling frequency is 2000 Hz and the responses are calculated by coherent addition of

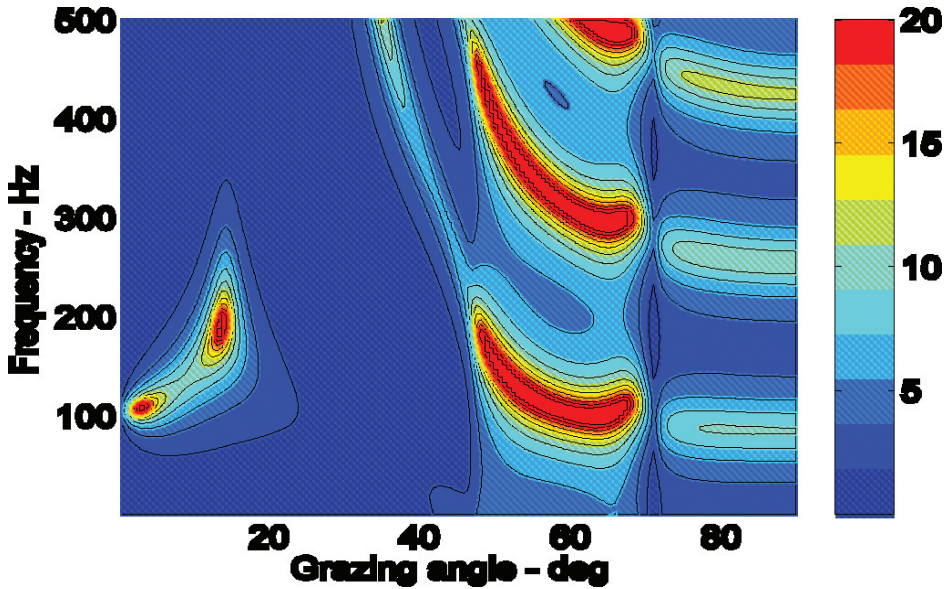


Figure 4. Bottom reflection loss for a sediment layer with thickness $D = 5$ m and with density 1500 kg/m^3 and sound speed 1700 m/s over a homogenous half space with density 2500 kg/m^3 and compressional sound speed 4700 m/s and shear speed 2200 m/s .

a number of rays for each receiver position. That number of rays is given by the maximum number of bottom or surface interactions; that is the maximum value of n in Table 1. In the current example the maximum number of interactions was chosen to be 8, consequently the number of contributing rays for each receiver position is equal to 33. The time responses are plotted versus reduced time, that is, the main time delay has been subtracted. The critical angle effect is clearly seen in Figure 5b, as the rapid reduction of the amplitude of the reflected arrivals when the angle at the bottom exceeds the critical angle.

Figure 6 shows the comparison of the transmission loss as function of range for the selected frequencies of 50, 75, 100 and 125 Hz. The agreement is quite good and the two results show about the same variation in transmission loss with range, due to mode interference. Notice, however, that there is shift in the interference patterns, most noticeably at low frequencies and long ranges.

The next case is with a homogenous mud bottom with a sound speed of 1450 m/s and density of 1200 kg/m^3 . These parameters give an angle of intromission of 23.5 degrees and very high bottom reflection loss for steeper angles. The results, shown in Figure 7, show good agreement with the OASES model for the higher frequencies, but there is seems to be a systematic bias for the lowest frequency of 50 Hz. Furthermore, there are a number of erroneous peaks in the transmission loss; these are caused by discontinuities at the end points of the interpolation for calculation of the transmission loss from Equation 9 and can be removed, or reduced, by using more rays in the initial ray tracing.

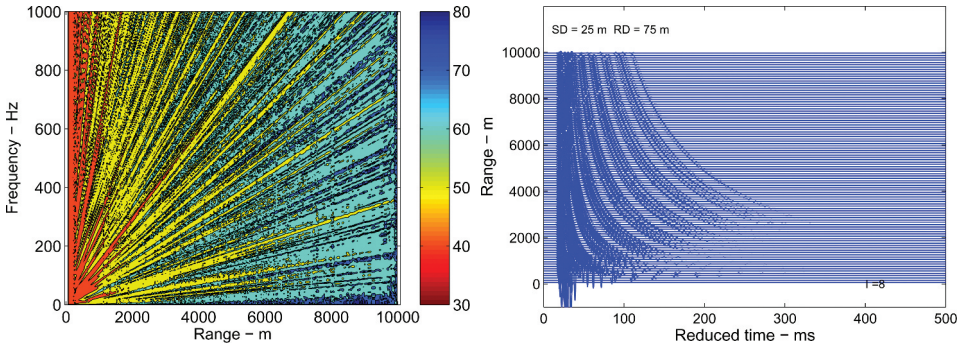


Figure 5. Frequency and time response of a Pekeris' wave guide. Left: Transmission loss as function of range and frequency. Right: Time response for a number of receivers with distances from 100 meter to 10 km from the source. The source signal is a short transient (Ricker wavelet).

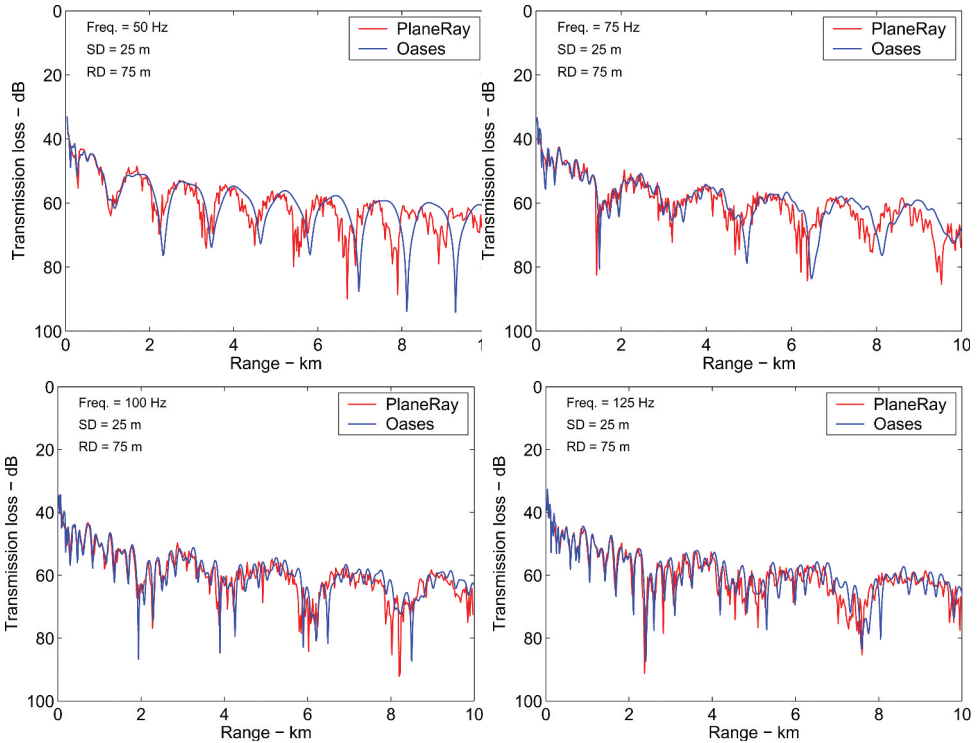


Figure 6. Comparison of the transmission loss as function of range for different frequencies by PlaneRay (gray line) and OASES (black line) for Pekeris' waveguide with homogeneous bottom in range independent environment.

3.2 Sediment layer over a solid half space

As stated before the model does not trace rays down in the bottom and the effect of a deeper interface is entirely modeled through the bottom reflection coefficient. It is therefore interesting to compare the PlaneRay results with a model that treats a layered bottom correctly. We consider the case shown in Figure 8 and we will present several cases with different bottom properties, but in all cases the water depth is $H = 100$ m and the layer thickness is $D = 5$ m. The bottom parameters for the three 3 different cases are given in Table 2.

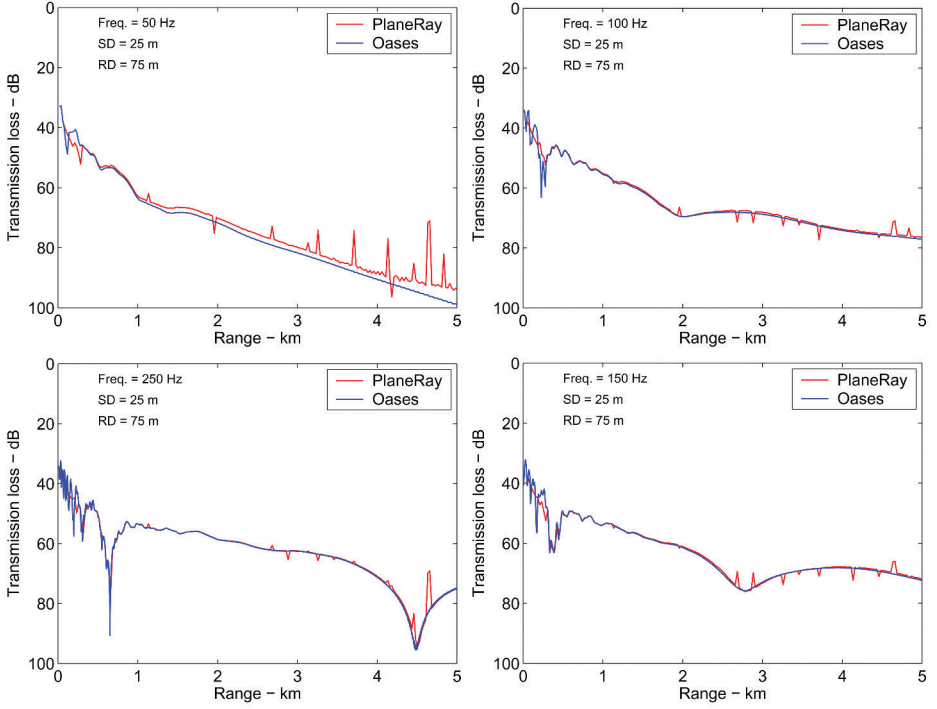


Figure 7. Transmission loss as function of range for the frequencies of 50, 100, 150 and 200 Hz for CASE = 1 in Table 2. The gray curves are from the ray trace model, the black curves are the OASES results.

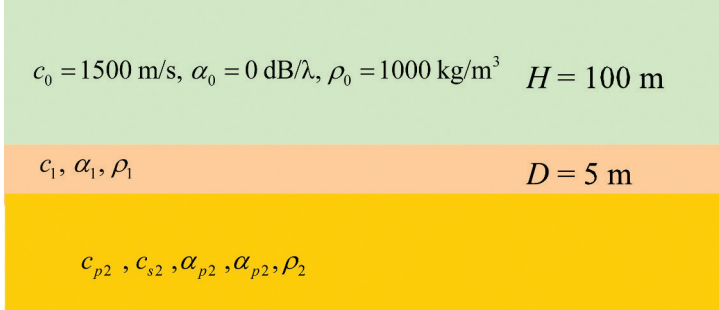


Figure 8. The bottom structure for the CASE 1, 2 and 3. The parameter values given in the figure are the same for all cases, the other parameters are given in Table 2.

Figure 9 shows the result of CASE 1 in Table 2 with a mud layer of 5 m over a sedimentary half space. The agreement with the OASES results is quite good with the exception of isolated values due to interpolation discontinuities as mentioned and observed earlier.

Table 2. Layered bottom cases.

CASE	Description	Sediment Sound speed c_1 Density ρ_1 Attenuation α_1	Solid half-space Sound speed c_{p2} Density ρ_2 Attenuation α_{p2}	Solid half-space Shear speed c_{s2} Shear attenuation α_{s2}
1	Mud layer over sediment	1450 m/s 1200 kg/m ³ 1.0 dB/λ	1800 m/s 2000 kg/m ³ 1.0 dB/λ	0 0
2	Sediment layer over bedrock, high shear speed	1700 m/s 1800 kg/m ³ 0.5 dB/λ	4700 m/s 2500 kg/m ³ 0.5 dB/λ	2200 m/s 0.5 dB/λ
3	Sediment layer over bedrock, low shear speed	1700 m/s 1800 kg/m ³ 0.5 dB/λ	4700 m/s 2500 kg/m ³ 0.5dB/λ	2000 m/s 0.5 dB/λ

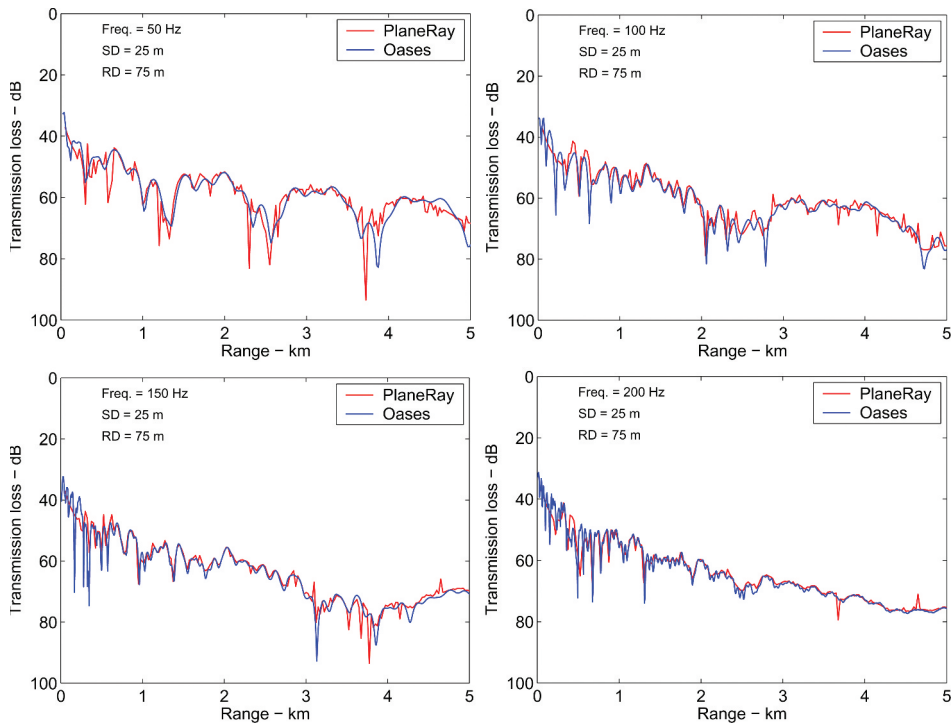


Figure 9. Transmission loss as function of range for the frequencies of 50, 100, 150 and 200 Hz for CASE = 1 in Table 2. The gray curves are from the ray trace model, the black curves are the OASES results.

3.3 Sediment layer over hard bedrock

The case with a sediment layer over hard bedrock is particularly interesting because this can result in abnormal high transmission loss for certain parameter combination and for certain frequency bands as discussed by Hovem and Kristensen [13] and by Ainslie [14].

Figure 10 shows the result of comparison using the values of CASE 2 in Table 2, the case with the high shear speed of 2200 m/s. The two results agree in the general dB level, but there are differences in the details. Agreement with the OASES results is quite good.

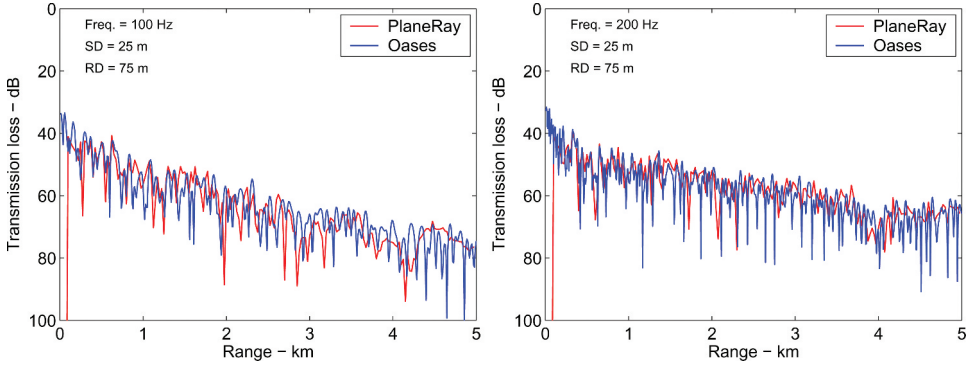


Figure 10. Transmission loss as function of range for the frequencies of 100 and 200 Hz. The gray curves are from the ray trace model, the black curves are the OASES results.

Notice that both models predict significantly higher transmission loss for 100 Hz than for 200 Hz. This difference in transmission loss is investigated further by using the PlaneRay model for the two cases (CASE 2 and CASE 3 of Table 2), with sediment shear speed of respectively 2200 m/s and 2000 m/s with the results shown in Figure 11. For the frequency of 100 Hz the transmission loss for the high shear speed case, 2200 m/s, is considerably higher than for the lower shear speed of 2000 m/s, but for 200 Hz the two cases show very little difference in transmission loss. The reason for this is that certain combinations of bottom parameters can result in anomalous high bottom reflection loss for low grazing angles and for certain frequencies. Figure 4 shows an example of bottom reflection loss as function of frequency and grazing angle calculated with the shear speed of 2200 m/s, the other parameters being the same.

The high reflection loss can be attributed to the excitation of an interface wave at the boundary between the sediment layer and the solid half space [14, 14]. With the slightly lower shear speed of 2000 m/s, the condition for this excitation is not fulfilled, resulting in a more normal reflection loss.

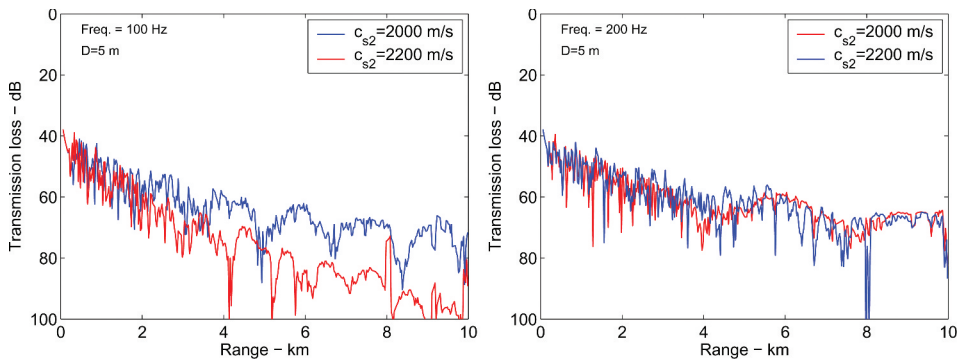


Figure 11. Transmission loss as function of range for the frequencies of 100 and 200 Hz. The gray curves are for the high shear speed of 2200 m/s and the black curves are for the lower shear speed of 2000 m/s. All results are from the ray trace model.

3.4 Range dependent case

In this section we consider the range dependent case of the Inversion Workshop 2001 Test Case 1 [15]. In Figure 12 the left panel shows the sound speed profile and the right panel shows the bottom topography and some of the rays that contribute to the sound field at a receiver located at range of 2000 m and depth of 25 m.

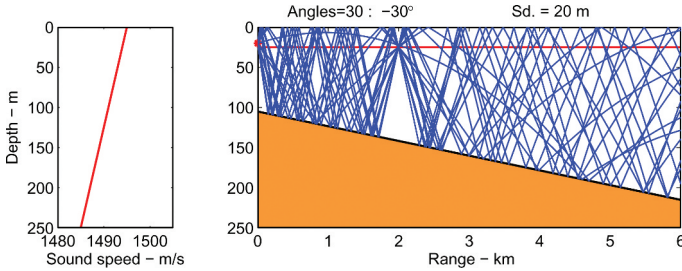


Figure 12. Sound speed profile (left), and (right) bottom topography and the rays that contribute to the sound field at a receiver located at range of 2000 m and depth of 25 m.

Figure 13 shows the simulated time responses for the case indicated in Figure 12. Notice that the strong first arrivals, for all ranges up to more that 2 km, are carried by the rays that have not been reflected at the bottom or the sea surface.

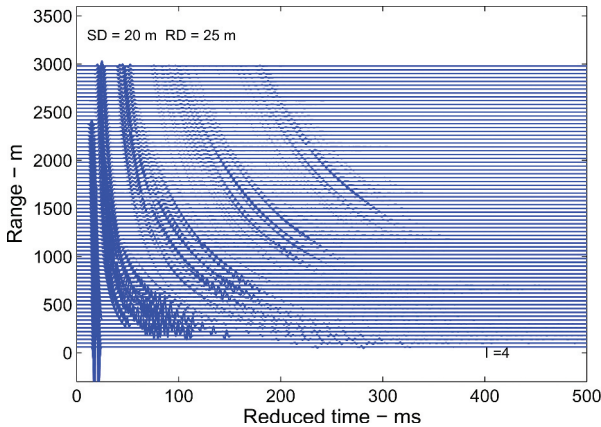


Figure 13. Simulated time responses as function of range for the sloping bottom case of Figure 12. The source signal is a short transient (Ricker wavelet).

Figure 14 shows the transmission loss as function of range for the frequencies of 50, 100, 200 and 400 Hz and the results of the PlaneRay model is compared with the propagation model RAM [3]. The main features agree fairly well, in particular for the higher frequencies, but there are differences in the details. There is a large discontinuity error at 0.6 km, which is the range where the first arrival is a ray that has passed through a turning point.

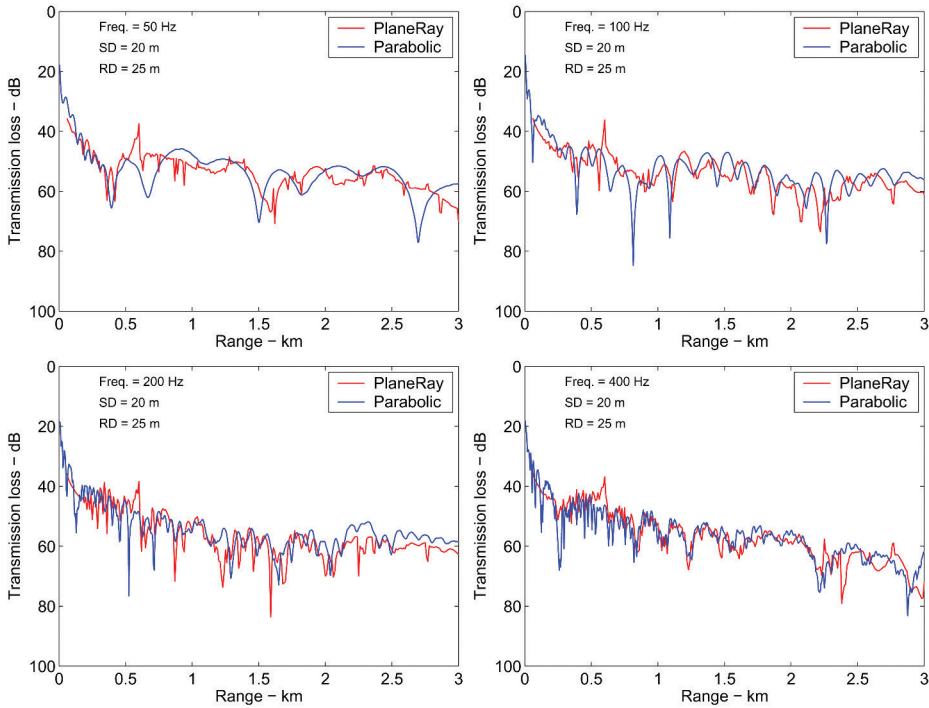


Figure 14. Transmission loss in dB as function of range for the selected frequencies 50, 100, 200 and 400 Hz. The gray curves are calculated by PlaneRay, the black by the propagation model RAM using the parabolic approximation.

3.5 Comparison with experimental data

In 2001 ARL conducted a series of acoustic transmission runs off the coast of Florida using a hydrophone cable on the seafloor and broadband acoustic pulses of imploding light bulbs. The total length of the array is about 500 meter with 52 hydrophones with symmetric logarithmic spacing i.e., with high density of phones in the middle and increasing spacing towards the end. In this paper we are only considering one shallow water site at 45 m water depth with nearly flat bottom. In this run the hydrophone array was deployed in a straight line at the bottom and the light bulbs were fired at 30 m depth at various distances in the both end-fire positions of the array. Figure 15 shows an example of comparison between the measured data and the modeled results using PlaneRay¹. In this case, the receiving hydrophone array spans the range of 650 to 1200 meter 5450 to 6000 m from or the source. The general agreement in multi path structure and the critical angle effect can clearly be observed in both the synthesized and the measured time response. The synthesized results shown in the left side panel of figure 15 is calculated by using a sound speed value for the bottom equal to 1900 m/s, as this gives a best comparison with the multipath structure of the observed signals. A lower value for the sound speed results in a lower critical angle and less multipath structure.

4 Conclusion and future work

PlaneRay is a new propagation model based on ray tracing and coherent addition of contributions of a large number of eigenrays. A special feature of the model is a unique sorting and interpolation scheme for efficient determination of the eigenrays. The model is applicable to certain range-

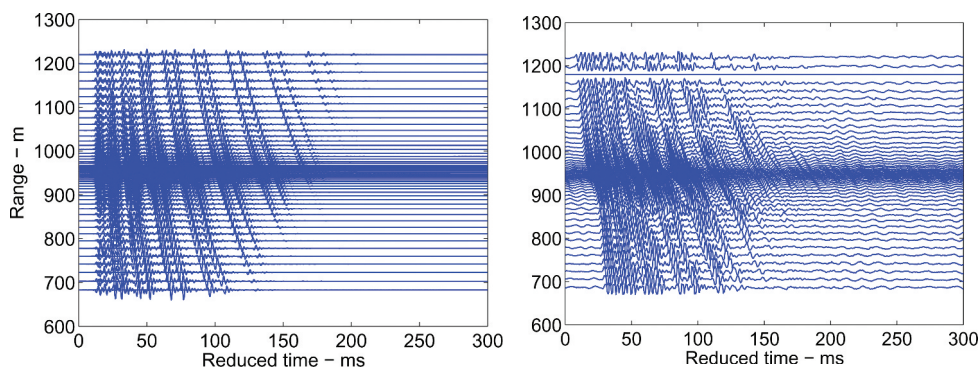


Figure 15. Comparison between the modeled results from PlaneRay (left panel) and the measured results from ARL East Coast Data for 52 receivers spanning the range from 650 m to 1200 m (right panel).

dependent propagation conditions where the bottom topography and the bottom structure and composition may change with horizontal distance, but the sound speed profile must be range-independent. The model have been tested and compared with other propagation models with some good results, but work is continuing on improving the accuracy. The model now is being converted and implemented as forward model in Saga package [16].

Notes

1. The experimental data was made available by David P. Knobles, Applied Research Laboratories, The University of Texas at Austin, Texas.

References

1. Jensen F. B. and M. C. Ferla, SNAP: The SACLANTEN normal-mode acoustic propagation model. SM-121, SACLANT Undersea Research Centre, La Spezia, Italy (1979).
2. Collins M. D., A split-step Pade solution for parabolic equation method. *J. Acoust. Soc. Am.* **93**, 1726–1742 (1993).
3. Collins M. D., User guide for RAM version 1.0 and 1.0p, <ftp://ram.nrl.navy.mil/pub/RAM/> (2001).
4. Schmidt H., SAFARI: Seismo-acoustic fast field algorithm for range independent environments (User's guide). SR-113, SACLANT Undersea Research Centre, La Spezia, Italy (1987).
5. Schmidt H., OASES 1.6: Application and upgrade notes. Massachusetts Institute of Technology, Cambridge, MA (1993).
6. Hovem J. M., Marine Acoustics, (To be published by Applied Research Laboratories, The University of Texas at Austin, Texas).
7. Westwood E. K. and Vidmar P. J., Eigenray bnding and time series simulation in a layered-bottom ocean, *J. Acoust. Soc. Am.* **81**, 912–924 (1987).
8. Westwood E. K. and Tindle C. T., Shallow water time simulation using ray theory. *J. Acoust. Soc. Am.* **81**, 1752–1761 (1987).
9. Jensen F. B., Kuperman W. A., Porter M. B. and Schmidt H., Computational Acoustics, AIP, Press, New York Jersey (1993).
10. Clay C. S. and Medwin H., Acoustical Oceanography: Principles and Applications, Wiley-Interscience, USA, (1977).

11. Tindle C. T. and Bold G. E. J., Improved ray calculations in shallow water. *J. Acoust. Soc. Am.* **70**(3), 813–819 (1981).
12. Pekeris A. L., The theory of propagation of explosive sound in shallow water. *Geol. Soc. Am. Mem.* 27 (1948).
13. Hovem J. M. and Kristensen Å., Reflection loss at a bottom with a fluid sediment layer over a hard solid half-space. *J. Acoust. Soc. Am.* **92**(1), 335–340 (1992).
14. Ainslie A. M., Conditions for the excitation of interface waves in a thin unconsolidated sediment layer. *J. Sound and Vibration* **268**, 249–267 (2003).
15. Chapman N. R., ChinBing S., King D. and Evans R. B., Benchmarking geoacoustic inversion methods for range-dependent waveguides. *IEEE J. Oceanic Eng.* **28**, 320–330 (2003).
16. Gerstoft P., SAGA User Manual 4.1: An inversion software package. SM-333, SACLANT Undersea Research Centre, La Spezia, Italy (1997).

INVERSION OF THE PROPELLER HARMONICS FROM A LIGHT AIRCRAFT FOR THE GEOACOUSTIC PROPERTIES OF MARINE SEDIMENTS

MICHAEL J. BUCKINGHAM,
ERIC M. GIDDENS AND FERNARDO SIMONET

*Marine Physical Laboratory
Scripps Institution of Oceanography
University of California, San Diego
9500 Gilman Drive, La Jolla, CA 92093-0238, USA*

In a recent series of experiments, the sound from a light aircraft flying over a shallow ocean channel was detected on acoustic sensors in the atmosphere, throughout the water column and buried in the sediment. The predominant feature of the sound signature is a series of propeller harmonics extending over the frequency range from about 100 to 800 Hz. As the aircraft flies over the sensor station, a significant Doppler-downshift in the frequency of a given harmonic occurs. The difference in the Doppler-shifted frequencies on approach and departure provides the basis of a full-wave inversion technique for estimating the speed of sound in the sea bed. Once the sound speed is known, the remaining geoacoustic parameters of the sediment may be determined from the correlations that are known to exist between them.

1 Introduction

It has been known for many years, from the observations of [1, 2] and [3], that the sound from large, fixed-wing, multi-engine propeller aircraft (e.g., Lockheed Orion P-3C, de Havilland Twin Otter) is detectable beneath the ocean surface. Recently at Scripps Institution of Oceanography experiments have been performed with a single-engine, propeller-driven light aircraft to establish whether the sound from such an airborne source could form the basis of shallow-water inversion techniques for recovering the geoacoustic properties of the seabed. The first trial flights, using a Socata Tobago TB 10 (2-blade propeller, 180-shp) flying at a speed of 106 knots (53 m/s) and altitude of 66 m, were made during mid-2002 over the Pacific Ocean, about 1 km off the shoreline between Del Mar and La Jolla, southern California. These were followed by a second set of experiments at the same location in September and October 2003 using two aircraft, a Diamond Star DA40 (3-blade propeller, 180-shp) flying at 120 knots (60 m/s), altitude 66 m, and a Cessna 172 (2-blade propeller, 180-shp) at 106 knots, altitude 100m.

In all cases, the sound from the propeller was detected by a microphone mounted just above the sea surface, hydrophones distributed vertically throughout the 15 m deep water column, and hydrophones buried about 1 m deep in the sediment. The bandwidth of the received signals extends from about 100 to 800 Hz. The signals themselves take the form of a series of narrow harmonics, each

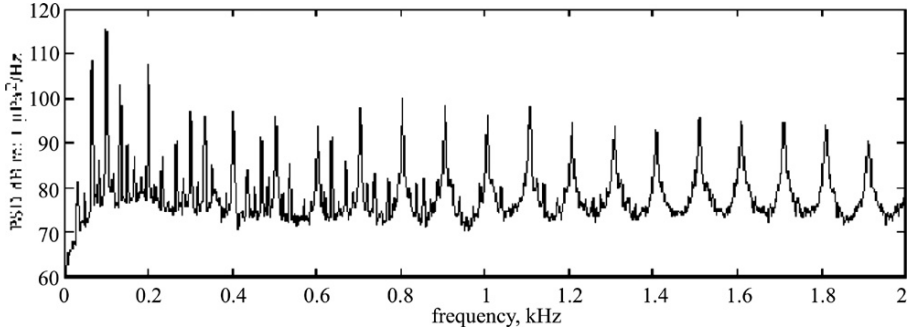


Figure 1. Spectrum of static DA40.

showing a pronounced Doppler down-shift in frequency as the aircraft overflies the sensor station. The harmonics received on the sensors in the water column and buried in the seabed can be inverted to obtain the sound speed and attenuation in the sediment. There is also potential for obtaining the near-normal incidence reflection coefficient of the seabed from the water column sensors, which, if successful, would return directly the density and hence the porosity of the sediment.

2 Propeller sound

The sound from a light aircraft, generated mainly by the propeller, is periodic but not sinusoidal. It follows from elementary Fourier analysis that the acoustic signal consists of a fundamental tone with a sequence of harmonics at multiples of the fundamental. The frequency of the fundamental, or first harmonic, is equal to the speed of the engine, usually expressed in revolutions per minute (rpm), times the number of propeller blades, N . Thus, when expressed in cycles per second, the frequency of the fundamental is

$$f_1 = \frac{(rpm) \times N}{60} \text{ Hz}, \quad (1)$$

where it is assumed that the propeller is driven directly off the engine, as is usually the case with light aircraft. For an engine turning over at 2000 rpm and driving a three-blade propeller, the fundamental frequency is 100 Hz, with harmonics at 200, 300,, Hz. An example of the power spectrum of the sound from a light aircraft, a Diamond Star DA40 with a three-blade propeller, is shown in Fig. 1. In this case, the aircraft was stationary on the ground, with the engine running at 2000 rpm. The microphone was a few centimeters above the ground on the port side, in the plane of the propeller, at a horizontal distance of 10 m from the spinner. The propeller harmonics are clearly visible up to a frequency of 2 kHz. Below 1 kHz, additional spectral lines are present, associated with the firing rate of the engine.

Under similar experimental conditions, the horizontal directionality of the sound from the aircraft was measured through a quadrant extending from the plane of the propeller on the port side of the aircraft to the axis of the spinner. In Fig. 2, showing the aspect dependence of the first propeller harmonic and the first engine harmonic, it can be seen that the intensity of both harmonic lines varies only weakly throughout the angular range.

3 Doppler shifts

In the experiments conducted a couple of kilometers north of Scripps pier, the sensor station was about 1 km offshore, where the water depth is nominally 15 m. A microphone was located approximately 1 m above the sea surface, a vertical array of 11 non-uniformly spaced hydrophones spanned

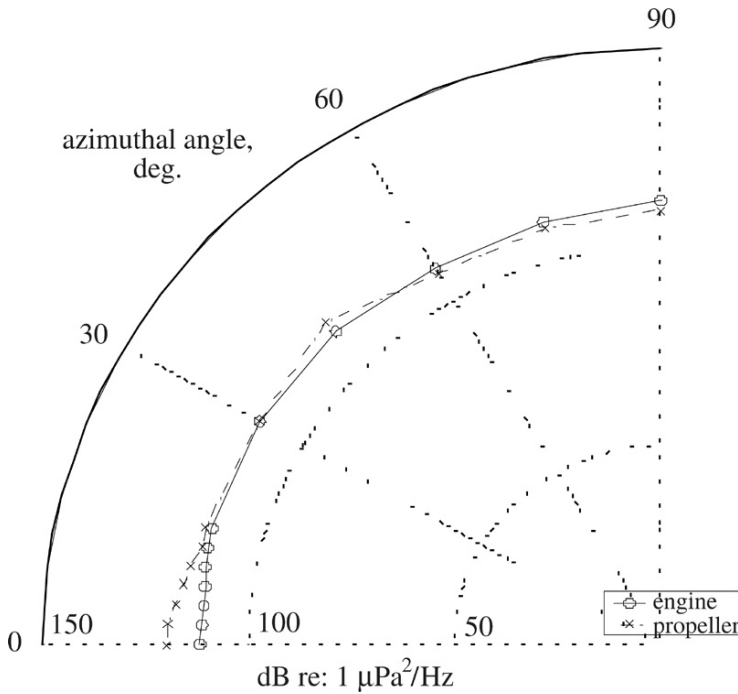


Figure 2. Aspect dependence of first propeller and engine harmonics.

the water column, and three hydrophones were buried in the sediment at various depths down to 1 m. The aircraft passed directly over the sensor station in straight, level flight at a nominal altitude of 66 m, and was detected on the sensors in all three layers, that is, the atmosphere, the water column and the sediment.

On the approach to the sensor station, the frequency of any given harmonic is Doppler-upshifted and on departure it is downshifted. This behavior is illustrated in the spectrograms of Fig. 3, which show the acoustic signature of a Diamond Star DA40 aircraft, as recorded on the microphone in the air, a hydrophone near the bottom of the water column, and a hydrophone buried to a depth of approximately 0.5 m in the sediment. In this case, the aircraft was flying at 120 knots (60 m/s) and the engine was turning over at 2400 rpm. The propeller harmonics are detectable in the water column and the sediment for about ten seconds on either side of the zenith, which translates into a horizontal detection range of about 600 m.

Around the closest point of approach (CPA), the harmonics from the Diamond Star exhibit a Doppler down-sweep, much like the harmonics from the turboprop aircraft flying at 250 knots (125 m/s) that were recorded by [4] in the atmosphere and in deep water at a depth of 20 m beneath the surface. The Doppler-shifted harmonics may be characterized in terms of a difference frequency, that is, the difference between the maximum upshifted frequency on approach and the minimum downshifted frequency on departure. From inspection of the Doppler-shifted harmonics in Fig. 3, it is evident that the difference frequency, Δf , is significantly greater in air than in seawater or sediment. In fact, from geometrical (ray) acoustics and Snell's law, the difference frequency may be shown to scale inversely with the local speed of sound and thus in going from air to seawater Δf is reduced by a factor of 0.23, which is the ratio of the sound speed in the two media.

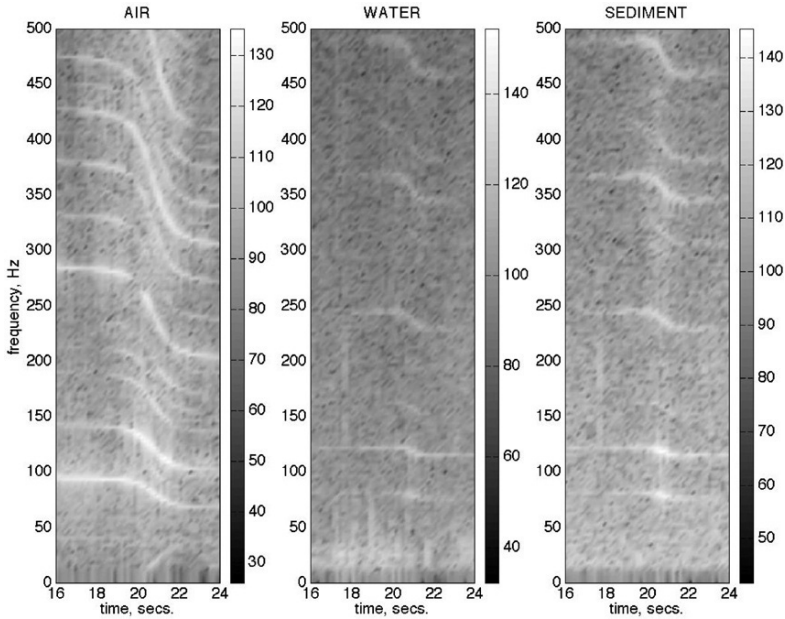


Figure 3. Propeller harmonics from the DA40 in air, water and sediment.

The difference frequency is the basis of a technique for measuring the speed of sound in all three layers, the atmosphere, the water column and the sediment. However, rather than use an inversion based on the simple Snell's law result, it is preferable to take account of the modal structure in the water column. This is achieved with a full wave-theoretic model of acoustic propagation in the three-layered medium. The model may also be used to illustrate the pronounced asymmetries in the field that occur as a result of the Doppler up- and down-shifts that occur, respectively, on approach to and departure from the sensor station.

4 Fore-aft asymmetries in the field

Fore and aft of the source, the sound field in all three layers shows significant asymmetries, due largely to the Doppler upshifts and downshifts, respectively, in the frequencies of the harmonics. In the water column, for example, a given harmonic may excite more modes ahead of the source than behind. To investigate such effects, a wavenumber-integral solution of the wave equation has been developed, which yields the sound field in the atmosphere, the water column and the sediment, taking account explicitly of the horizontal motion of the airborne source. In essence, the model consists of three wavenumber integrals, one for each of the layers, which are evaluated numerically to yield the respective acoustic pressure fields. In the current implementation of the model, it is assumed that the sound speed in each layer is uniform but this condition may easily be relaxed, allowing future versions of the model to handle sound speed profiles in the layers.

Fig. 4 is an example of a transmission loss plot for a moving, airborne source, computed from the wavenumber-integral model. It shows the envelope of the pressure field excited by a single harmonic in the three-layer medium ahead of and behind the source. The aircraft, at an altitude of 50 m and

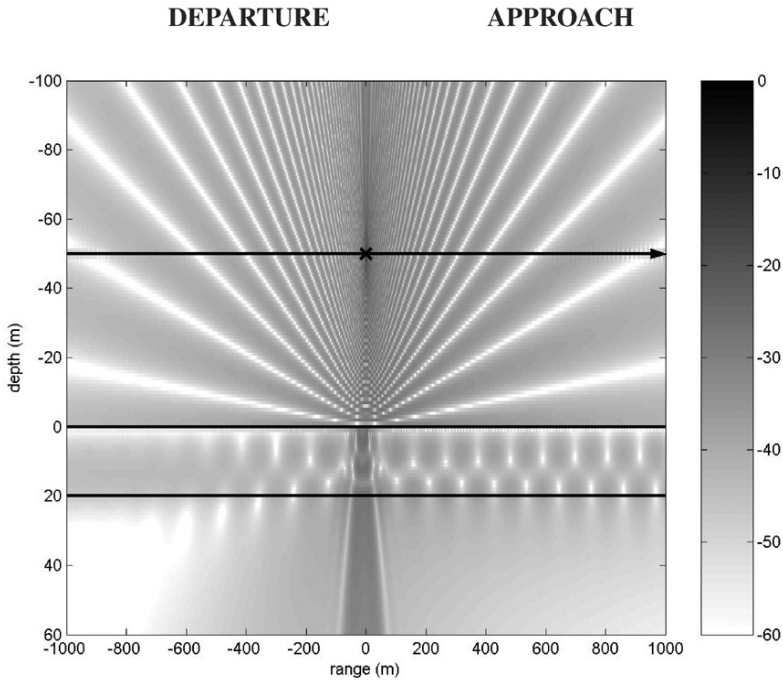


Figure 4. Transmission loss from a moving source in a three-layer medium. (The grey scale is in arbitrary dB.)

traveling at a speed of 75 m/s, is overflying a 20 m deep channel; and the sound speeds in the layers are 350 (air), 1500 (seawater) and 1800 m/s (sediment). The unshifted frequency of the harmonic is 100 Hz, corresponding to the fundamental of a three-blade propeller turning at 2000 rpm. All three layers exhibit prominent sound-field asymmetries, the most pronounced being in the water column, where it can be seen that there are two modes ahead of the source, giving rise to inter-modal interference, but only one mode behind. In this particular case, the Doppler up- and down-shifts in frequency are such that the second mode is supported when the aircraft is on approach but is cut-off on departure. Also visible in Fig.4 are the evanescent tails of the modes in the sediment immediately beneath the seafloor, as well as asymmetrical Lloyd's mirror fringes in the atmosphere, which arise from constructive and destructive interference between the direct and sea-surface reflected rays.

5 Inversions for sediment parameters

The wavenumber-integral propagation model could provide the basis for a full-wave, matched-field inversion for the geoaoustic properties of the sediment beneath a shallow-water channel. Aircraft acoustic data from either a sensor buried in the sediment or a hydrophone in the water column may be used in the inversion procedure. In a typical matched-field algorithm, a cost function is formed, providing a measure of the difference between the data and a suitable theoretical model, and the set of geoaoustic parameters that yields a global minimum is considered to represent the actual properties of the sediment. The fact that several of the geoaoustic parameters are strongly correlated [5, 6, 7], and hence are not independent, sometimes seriously constrains matched-field inversions [8, 9]. Such correlations between geoaoustic parameters are usually not exploited in techniques used for finding

the global minimum, although in some cases the correlations are employed to reduce the number of parameters sought in the search routine. An alternative to the matched-field approach, and one that is less computationally intensive, actually relies on the fact that the geoacoustic parameters of a sediment are correlated: one property of the sediment, say the compressional wave speed, is determined directly from the data and the remaining properties are computed using the correlations that exist between them. A set of algebraic expressions, derived by [10], for the inter-relationships between the wave and mechanical properties of marine sediments provides the link between the measured wave property and the remaining geo-acoustic parameters. The speed of the compressional wave in the sediment may be determined from a Doppler-shifted aircraft harmonic, as detected by a sensor in the water column. The full time-series, extending from several seconds before the closest point of approach (CPA) to several seconds after, is Fourier transformed to obtain a high-resolution spectrum of the Doppler-shifted signal. Several pairs of sharp peaks appear in the spectrum, each pair corresponding to a normal mode. The higher (lower)-frequency peak in any modal pair corresponds to the up (down)-shifted frequency of the mode on approach (departure). Once the frequencies of a pair of modal peaks have been determined, a straightforward algebraic routine yields the unshifted frequency of the harmonic and also the speed of sound in the sediment. The expressions for the relationships [11] between the wave and mechanical properties of the sediment are then used to evaluate the compressional attenuation, the shear speed, the shear attenuation, the porosity, the density and the grain size. The compressional and shear attenuations that are returned from the correlations are the intrinsic attenuations, representing energy that is converted irreversibly into heat as the waves propagate through the porous sediment. Direct measurements, on the other hand, return the effective attenuation, which in addition to the intrinsic attenuation includes any extra sources of loss, for instance, due to scattering from inhomogeneities such as shell fragments in the medium. The effective attenuation is highly variable, since it is governed by the random distribution of inclusions in the sediment. The theoretical correlations [11] and hence the inversions, should yield the lower limit to the distribution of measured compressional and shear effective attenuations, which in fact appears to be the case [12].

6 Concluding remarks

Some half dozen experiments have now been performed with a single-engine light aircraft overflying a sensor station in the ocean. A sequence of harmonics produced by the aircraft's propeller has been detected by a microphone mounted immediately above the sea surface, by a vertical array of eleven hydrophones distributed non-uniformly throughout the water column, and by hydrophones buried to a depth of about 1 m in the sediment. The frequency range of the observed harmonics extends from approximately 100 to 800 Hz. Most of the flying experiments have been conducted north of Scripps pier, off La Jolla, California, where the water depth is approximately 15 m; but the most recent trial, in October 2004, was at the site of the ONR-sponsored Sediment Acoustics Experiment (SAX99 and SAX04) about 2 km south of Fort Walton Beach in the northern Gulf of Mexico [12]. The nominal depth at the SAX site is 17 m. As part of all the flying experiments, a SeaBird temperature profiler is deployed, allowing the sound speed profile in the water column to be estimated. Based on an analytical, full-wave model of acoustic propagation in the multi-layered air-water-sediment waveguide, preliminary estimates of the compressional wave speed in the sediment north of Scripps pier indicate a value of 1700 m/s. This result was derived from the measurements in the water column of the Doppler-shifted frequencies of the first engine harmonic on approach and departure, 82.1883 and 76.2087 Hz, respectively. From the correlations between the compressional speed and the remaining geoacoustic parameters, the estimated values of the latter are: compressional (intrinsic) attenuation, 0.19 dB/m/kHz; shear speed, 147 m/s; shear (intrinsic) attenuation, 22.3 dB/m/kHz; porosity, 0.379; density, 2077 kg/m³; critical grazing angle, 26.9; sound speed ratio, 1.1215. The sediment in the region north of Scripps pier is known to be a fine-to-medium sand. Previous measurements by

Buckingham [13, 14] in similar materials but at higher frequencies yield sound speed ratios spanning the range 1.1 to 1.15. Thus, the result from the aircraft inversion is consistent with the idea that frequency dispersion in sediments is weak, of the order of 1% per decade according to Buckingham's theory [10] of wave propagation in marine sediments.

Acknowledgments

This work was supported by Dr. Ellen Livingston, Ocean Acoustics Code, the Office of Naval Research, under grant number N00014-04-1-0063.

References

1. Buckingham R. J., Noise signature of an aircraft in level flight over a hydrophone in the sea. *J. Acoust. Soc. Am.* **52**, 993–999 (1972).
2. Buckingham H., Helbig R. A. and Hagy J. D. Jr., Spectral characteristics of sound transmission through the rough sea surface. *J. Acoust. Soc. Am.* **54**, 99–109 (1973).
3. Richardson W. J., Greene C. R. Jr., Malme C. I. and Thomson D. H., *Marine Mammals and Noise*, Academic Press, New York (1995).
4. Ferguson B. G., Doppler effect for sound emitted by a moving airborne source and received by acoustic sensors located above and below the sea surface. *J. Acoust. Soc. Am.* **94**, 3244–3247 (1993).
5. Richardson M. D. and Briggs K. B., On the use of acoustic impedance values to determine sediment properties. In *Acoustic Classification and Mapping of the Seabed*, eds. N. G. Pace and D. N. Langhorne (University of Bath, Bath, 1993), Vol. 15, pp. 15–24.
6. Richardson M. D. and Briggs K. B., Empirical predictions of seafloor properties based on remotely measured sediment impedance. In *High-Frequency Ocean Acoustics*, eds. M. B. Porter, M. Siderius, and W. A. Kuperman, (La Jolla, 2004), in press.
7. Buckingham E. L. and Bachman R. T., Sound velocity and related properties of marine sediments. *J. Acoust. Soc. Am.* **72**, 1891–1904 (1982).
8. Buckingham M. D. and Fishman L., Efficient navigation of parameter landscapes. *J. Acoust. Soc. Am.* **98**, 1637–1644 (1995).
9. Buckingham L. and Chapman N. R., Matched field inversion of broadband data using the freeze bath method. *J. Acoust. Soc. Am.* **106**, 1838–1851 (1999).
10. Buckingham M. J., Wave propagation, stress relaxation, and grain-to-grain shearing in saturated, unconsolidated marine sediments. *J. Acoust. Soc. Am.* **108**, 2796–2815 (2000).
11. Buckingham M. J., Compressional and shear wave properties of marine sediments: Comparisons between theory and data. *J. Acoust. Soc. Am.* in press (2004).
12. Richardson M. D., Briggs K. B., Bibee D. L. *et al.*, Overview of SAX99: environmental considerations. *IEEE J. Oceanic Eng.* **26**, 26–53 (2001).
13. Buckingham E. L., Sound velocity and related properties of marine sediments, North Pacific. *J. Geophys. Res.* **75**, 4423–4446 (1970).
14. Buckingham E. L., Compressional-wave attenuation in marine sediments. *Geophys.* **37**, 620–646 (1972).

INVERSION OF SHALLOW WATER AMBIENT NOISE DATA BY MEANS OF DIFFERENTIAL EVOLUTION AS A GLOBAL SEARCH METHOD

DICK G. SIMONS, CAMIEL VAN MOLL

TNO Physics and Electronics Laboratory, Oude Waalsdorperweg 63, 2509 JG The Hague, The Netherlands and Department of Earth Observation and Space systems (DEOS), Delft University of Technology, Kluyverweg 1, 2629 HS, Delft, The Netherlands

CHRIS H. HARRISON

*NATO Undersea Research Centre,
Viale S. Bartolomeo 400, 19138 La Spezia, Italy*

As the vertical directivity of the ambient noise is dependent on the reflective properties of the seabed, geo-acoustic parameters can be inferred by inversion of the noise. This is clearly demonstrated in a paper by Harrison and Simons [1]. In this work the seabed reflection loss is directly found by comparing the upward- and downward-propagating noise. These are determined by beamforming the ambient noise field received on a vertical array of hydrophones. Geo-acoustic parameters were derived with a handsearching technique that relies on inspection of the experimental (angle- and frequency dependent) reflection loss for critical angle, fringe spacing and modulation depth. By applying a global optimisation technique as an automatic search method improved estimates for the geo-acoustic parameters were obtained. For the global search method a relatively new technique, called “differential evolution”, is applied [2]. Compared to a genetic algorithm a ten times higher efficiency is obtained, since differential evolution finds the optimal parameter setting with only one tenth of the number of forward model evaluations. For these inversions two different models for the seabed reflection loss were employed. First we assumed the seabed to consist of a single homogeneous fluid sediment layer on top of a homogeneous fluid subbottom. As the fringe pattern of some of the measured reflection loss data suggests the existence of at least two layers, the data were also inverted using a seabed model comprising two fluid sediment layers on top of a homogeneous fluid subbottom.

1 Introduction

As the coherence and vertical directivity of the ambient noise depends on the reflective properties of the seabed, geo-acoustic parameters can be inferred by inversion of the noise. This is clearly demonstrated by, among others, [1] and [3].

Carbone measures the broadband noise coherence with a vertically separated pair of hydrophones, which was compared with noise model calculations searching over geo-acoustic parameter space.

In [1] an approximation of the plane wave reflection coefficient of the seabed (as a function of grazing angle and frequency) is directly found by comparing the upward- and downward-propagating noise. These are determined by beamforming the ambient noise field received on a vertical array of hydrophones. Geo-acoustic parameters were derived with a hand-searching technique that relies on inspection of the experimental (angle- and frequency dependent) reflection loss for critical angle, modulation depth and fringe spacing. From these phenomena sound speed, impedance mismatch and layer thickness can already be determined fairly well. The potential of this method was demonstrated with experimental data from several sites in the Mediterranean. Pros and cons of the method are extensively discussed. Important strengths of the method are that no noise model is required and that it tolerates an unknown noise source distribution and noise from distant shipping. The paper [1] does not go further than hand searches for the geo-acoustic parameters, since the main point was to demonstrate merely that a solution is possible. It was concluded that by applying a global optimisation technique as an automatic search method, improved estimates for the geo-acoustic parameters should be obtained. It should however be emphasised that results from this inversion are not necessarily unique.

In this paper we compare the measured reflection coefficient with calculations using models for the plane wave reflection coefficient, searching over geo-acoustic parameter space. For these inversions we first assume the seabed to consist of a single homogeneous fluid sediment layer on top of a homogeneous fluid subbottom. As the fringe pattern of some of the measured reflection loss data suggests the existence of at least two layers, the data are also inverted using a seabed model comprising two fluid sediment layers on top of a homogeneous fluid subbottom. These models are described in section 2. Also, the smearing effect of the beamforming is discussed in that section.

For the global search method a relatively new technique, called “differential evolution” [2], is applied. A brief description of differential evolution, and a comparison with a genetic algorithm, is given in section 3. The ambient noise experiments and the data selected for this study are described in section 4. The inversion results are given and discussed in section 5. Section 6 presents a summary and some conclusions.

2 Ambient noise inversion – applied theory

An approximation of the bottom reflection coefficient is obtained by calculating the ratio of the downward and upward array response. Theoretically, this is given by (see [4]):

$$\hat{R}(\theta_s, f) = \frac{A_-}{A_+} = \frac{A(-\theta_s)}{A(\theta_s)} = \frac{\int_{-\pi/2}^{\pi/2} \frac{R(\theta, f)}{1 - R(\theta, f)} B(\theta, \theta_s, f) \sin 2\theta d\theta}{\int_{-\pi/2}^{\pi/2} \frac{1}{1 - R(\theta, f)} B(\theta, \theta_s, f) \sin 2\theta d\theta} \quad (1)$$

with:

A_+	upward array response
A_-	downward array response
θ	grazing angle of incidence at the seabed
θ_s	steering angle of the beamformer
f	frequency
R	true bottom reflection coefficient
B	beam pattern of the vertical array

The real bottom loss BL is given by $BL = -20^{10} 10 \log |R|$, whereas the approximated bottom loss is given by $\widehat{BL} = -20^{10} 10 \log |\hat{R}|$. The effect of beamforming is smearing out of features in BL , especially at the lower frequencies.

We search with an optimisation method for the geo-acoustic parameters by matching measured and modelled bottom loss \widehat{BL} using the following energy function:

$$E(\mathbf{m}) = \frac{1}{C} \sum_{\theta, f} \left(\widehat{BL}_{\text{cal}}(\theta, f, \mathbf{m}) - \widehat{BL}_{\text{exp}}(\theta, f) \right)^2 \quad (2)$$

with:

\mathbf{m}	the vector containing the unknown geo-acoustic parameters;
C	a normalisation constant
$\widehat{BL}_{\text{cal}}$	calculated or modelled bottom loss in dB (including smearing effect)
$\widehat{BL}_{\text{exp}}$	the measured bottom loss in dB.

Two models for the seabed have been employed: a seabed consisting of a single fluid sediment layer on top of a homogeneous fluid subbottom (see figure 1a) and a seabed consisting of two fluid homogeneous sediment layers on top of a fluid subbottom (see figure 1b).

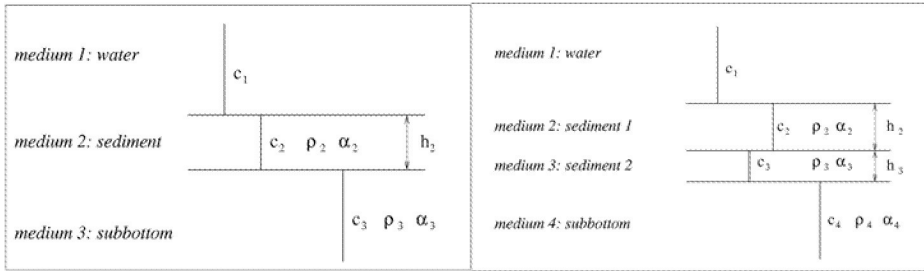


Figure 1. a (left): The single-sediment geo-acoustic bottom model. b (right): The two-sediment geo-acoustic bottom model.

Each sediment and subbottom is assumed to have a constant sound speed, density and attenuation.

To limit the size of the parameter search space, we do not invert for the densities ρ_2 , ρ_3 and ρ_4 . Density is coupled to sound speed according to one of the empirical relations given by [5]. Further, we assume $\alpha_4 = \alpha_3 = \alpha_2 = \alpha$, because the reflection coefficient is less sensitive to attenuation in the deeper layers.

For these layered structures analytical solutions for the reflection coefficient are given by [6]. For the two-sediment layered structure the reflection coefficient R is given by:

$$R = \frac{R_{12} + R_{24} \exp(2i\phi_2)}{1 + R_{12}R_{24} \exp(2i\phi_2)} \quad (3)$$

with:

$$R_{24} = \frac{R_{23} + R_{34} \exp(2i\phi_3)}{1 + R_{23}R_{34} \exp(2i\phi_3)} \quad (4)$$

where R_{jk} is the (Rayleigh) reflection coefficient for the interface between medium j and k (medium 1 = water, medium 2 = sediment no.1, etc., see figure 1):

$$R_{jk} = \frac{\frac{\rho_k c_k}{\sin \theta_k} - \frac{\rho_j c_j}{\sin \theta_j}}{\frac{\rho_k c_k}{\sin \theta_k} + \frac{\rho_j c_j}{\sin \theta_j}} \quad \text{for } (k = j + 1, j = 1, 2, 3) \quad (5)$$

Here $\theta_1 = \theta$ and the vertical phase delays are given by:

$$\phi_2 = k_2 h_2 \sin \theta_2 \quad \text{and} \quad \phi_3 = k_3 h_3 \sin \theta_3 \quad (6)$$

Further, Snell's law applies:

$$k_4 \cos \theta_4 = k_3 \cos \theta_3 = k_2 \cos \theta_2 = k_1 \cos \theta_1 \quad (7)$$

where the wavenumber in medium j is given by $k_j = 2\pi f / c_j$. For the single-sediment situation the reflection coefficient is given by

$$R = \frac{R_{12} + R_{23} \exp(2i\phi_2)}{1 + R_{12} R_{23} \exp(2i\phi_2)} \quad (8)$$

In these equations the sound speed c_j is complex when the attenuation $\alpha_j \neq 0$. The imaginary part of c_j is then given by:

$$\frac{c_j \alpha_j}{40\pi^{10} \log e} = \frac{c_j \alpha_j}{54.575} \quad (9)$$

3 Description of differential evolution

In underwater acoustics genetic algorithms (GA) were introduced in [7]. Its principle of operation is summarised as follows. To optimise an energy function E , GA improves populations of q parameter combinations during successive generations. A GA optimisation run starts by creating at random an initial population of size q . Each member represents a certain parameter value combination \mathbf{m} and its energy E is calculated. Because a population member with a lower E has a higher fitness, it attains a higher probability to be selected in one (or more) of the pairs of parents to be formed. This results in $q/2$ pairs of parents with a larger proportion of fit members. From each pair of parents two children are created by a random exchange of parental values, steered by the crossover probability p_c , followed by random changes of the N_p parameter values, with mutation probability p_m . A set of q children vectors results. The next generation is established by taking at random $f_r q$ members of these children and selecting the $(1 - f_r)q$ most fit members of the current population. This process is repeated over several hundreds of generations.

A GA has the following setting parameters: population size q , crossover probability p_c , mutation probability p_m , reproduction size f_r and the number of generations N_G . These have to be selected carefully and can be problem-specific, i.e., they depend on the optimisation problem at hand (see e.g. [8]).

Differential evolution (DE), just like GA, starts with an initial population of q randomly chosen parameter value combinations \mathbf{m} . These \mathbf{m} 's are improved during successive generations of constant size q , in the sense that a descendant replaces an \mathbf{m} , becoming its successor, if it has a lower energy. The distinctive feature of DE is the way in which these descendants are created. In [3] various ways to generate new \mathbf{m} 's are described. Here only the following procedure is considered. At the start of generation k the parameter vectors $\mathbf{m}_{k,1} \dots \mathbf{m}_{k,q}$, are given and for each of them a descendant is created, being a potential successor. To create this descendant $\mathbf{d}_{k,i}$ of $\mathbf{m}_{k,i}$ first a partner $\mathbf{p}_{k,i}$ is constructed according to

$$\mathbf{p}_{k,i} = \mathbf{m}_{k,i_1} + F(\mathbf{m}_{k,i_2} - \mathbf{m}_{k,i_3}) \quad (10)$$

with three different vectors \mathbf{m}_{k,i_1} , \mathbf{m}_{k,i_2} and \mathbf{m}_{k,i_3} chosen at random from the population and F a scalar multiplication factor between 0 and 1. The descendant $\mathbf{d}_{k,i}$ of $\mathbf{m}_{k,i}$ results from applying crossover to $\mathbf{m}_{k,i}$ and $\mathbf{p}_{k,i}$ with crossover probability p_c . A higher value of p_c leads (on the average) to more dimensions of $\mathbf{p}_{k,i}$ to be copied into $\mathbf{d}_{k,i}$, while the values for the remaining dimensions are taken from $\mathbf{m}_{k,i}$; $\mathbf{d}_{k,i}$ only replaces $\mathbf{m}_{k,i}$ becoming its successor, if its energy is lower.

The setting parameters of DE are population size q , multiplication factor F , crossover probability p_c and the number of generations N_G .

Comparing GA and DE, both show improvement of a fixed sized population of parameter combinations. However, in each generation of GA a fixed fraction of the population is replaced by children, whether they are better or not. In DE each member of the population will be replaced by its descendant only if this descendant has lower energy. On the other hand, the fitness of a member increases the probability of that member to play a role in the creation of children in GA, where in DE this fitness does not influence the probability of a member to be selected. Another difference is the way a partner $\mathbf{p}_{k,i}$ is found for $\mathbf{m}_{k,i}$. While in GA the partner is an element of the given generation, in DE it is constructed from the population and thus not an element of this generation. The partner creation process in DE is steered by the multiplication factor F and replaces the mutation mechanism of GA.

In [8] it was demonstrated that, compared to a GA, a ten times higher efficiency is obtained with DE, as DE finds the global optimum with only one tenth of the number of forward model evaluations.

4 The selected ambient noise data

For this study we selected the North Elba case (silt bottom, water depth 121 m) from the five sites in the Mediterranean where ambient noise measurements were carried out. The motivation for selecting the North Elba data is the irregularity of the interfering fringes in the observed bottom loss, which might be evidence for the presence of two sediment layers. This is considered to be a challenging situation for inversion.

The experiments were described in great detail by [1]. They were carried out with a moored 64 element vertical array with an acoustic aperture of 62 m roughly centered in the water column. Only the middle 32 regularly spaced hydrophones (aperture 16 m, element spacing 0.5 m) were used for the processing, which consisted of beamforming of manually selected portions of noise data. Each portion comprises a few seconds of ambient noise data. The resulting array responses versus angle and frequency were averaged over many portions of data. The up-to-down ratio of the array response is thus based on a few minutes of data in total.

5 Inversion results

5.1 Single sediment layer inversions – the North Elba data

We discuss the inversion results of the bottom loss data obtained from the North Elba ambient noise data (see figure 5a) assuming a single sediment model for the seabed (see figure 1a). As explained in section 2 we do not invert for density, hence the number of parameters sought amounts to 4. The search bounds of the parameters to be inverted are given in Table 1. A constraint in the inversion algorithm is $c_3 > c_2$ ($c_1 = 1514$ m/s).

Table 1. Parameters to be inverted for: single-sediment inversions of the North Elba data.

Parameter	Search range	Inversion result
c_2 [m/s]	1400 – 1700	1520.4 ± 0.6
ρ_2 [g/cm ³]	N.A.	1.562 ± 0.002
h_2 [m]	0.1 – 5	3.40 ± 0.03
α [dB/]	0 – 2	0.00031 ± 0.00004
c_3 [m/s]	1500 – 1900	1538.4 ± 1.5
ρ_3 [g/cm ³]	N.A.	1.620 ± 0.004

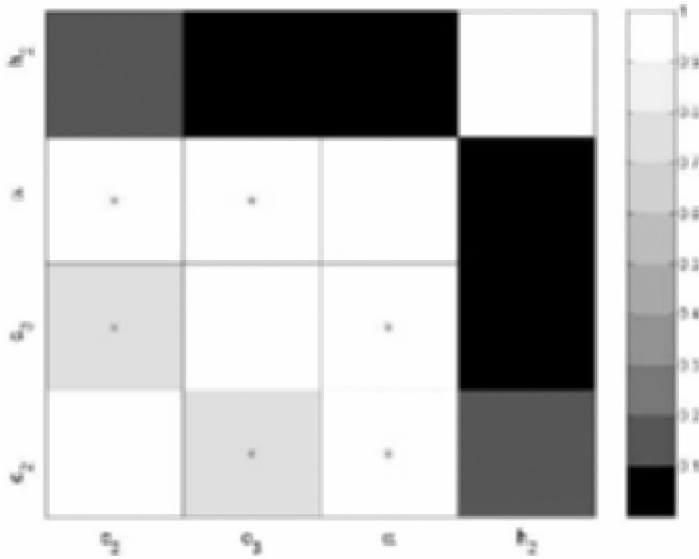


Figure 2. Single-sediment inversions of the North Elba data: magnitude of the correlation coefficient for all parameter combinations. A star is plotted if the correlation is statistically significant.

DE was run 57 times. In the following we perform a statistical analysis of the final parameter estimates of 52 successful runs. Parameter correlation is illustrated in figure 2 showing the magnitude of the linear correlation coefficient calculated for all combinations of the parameter estimates. The statistical significance of each of the correlation coefficients was also determined: the stars in the figure indicate for which parameter combination the confidence of the observed correlation coefficient exceeds 95%.

In figure 3 parameter estimates are plotted against each other for combinations with strong coupling. There is no correlation between the sediment geo-acoustic parameters (c_2 , c_3 and α) and the sediment thickness h_2 .

Histograms of the parameter estimates are given in figure 4. The corresponding mean and standard deviations for each parameter are given in table 1. It can be concluded that all parameters are accurately determined. The parameter values obtained are further assessed in section 5.2.2 where we discuss inversions of the same data with a two-sediment layer model. Using equation 1 we have calculated the beam-smeared bottom loss \widehat{BL} for the mean values of the inversion results as given in table 1, the result of which is given in figure 5d. The deviation from the measured (beam-smeared) bottom loss, as presented in figure 5a, is given in figure 5e. The same is done for the parameters reported in [1], obtained using the hand-searching technique (see figure 5b and c). A considerable improvement is obtained with the automated search technique.

5.2 Inversions with two sediments

5.2.1 Synthetic case

First, the performance of the inversion with two sediments is assessed using a synthetic reflection coefficient created for the parameter values given in table 2. Again, we do not invert for density (see section 2), hence the number of parameters sought amounts to 6. Constraints in the inversion

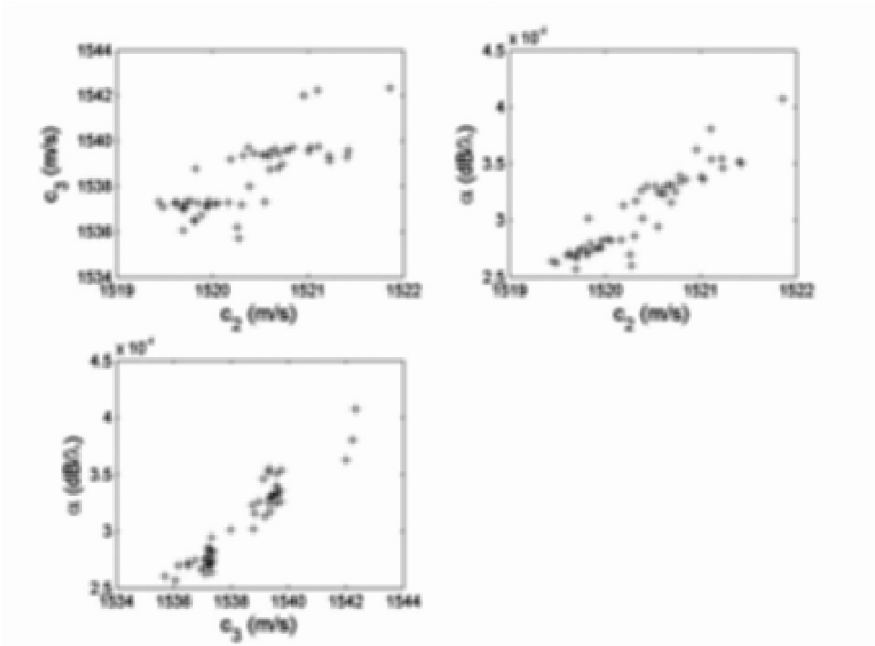


Figure 3. Single-sediment inversions of the North Elba data: The 52 parameter estimates plotted against each other for those combinations with strong coupling.

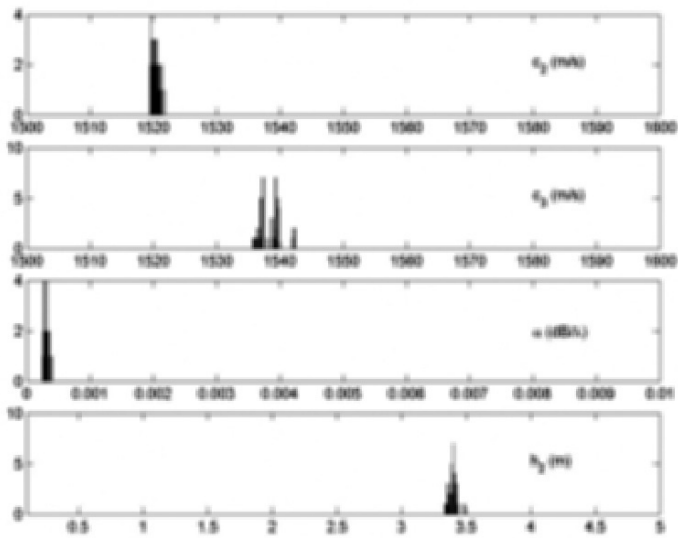


Figure 4. Single-sediment inversions of the North Elba data: histograms of the 52 estimates for each parameter.

algorithm are: $c_4 > \max(c_2, c_3)$ and $h_2 + h_3 < 5\text{m}$ ($c_1 = 1514\text{m/s}$). The inversion was run 171 times. On the basis of the energy function values obtained for these runs, two solutions to the

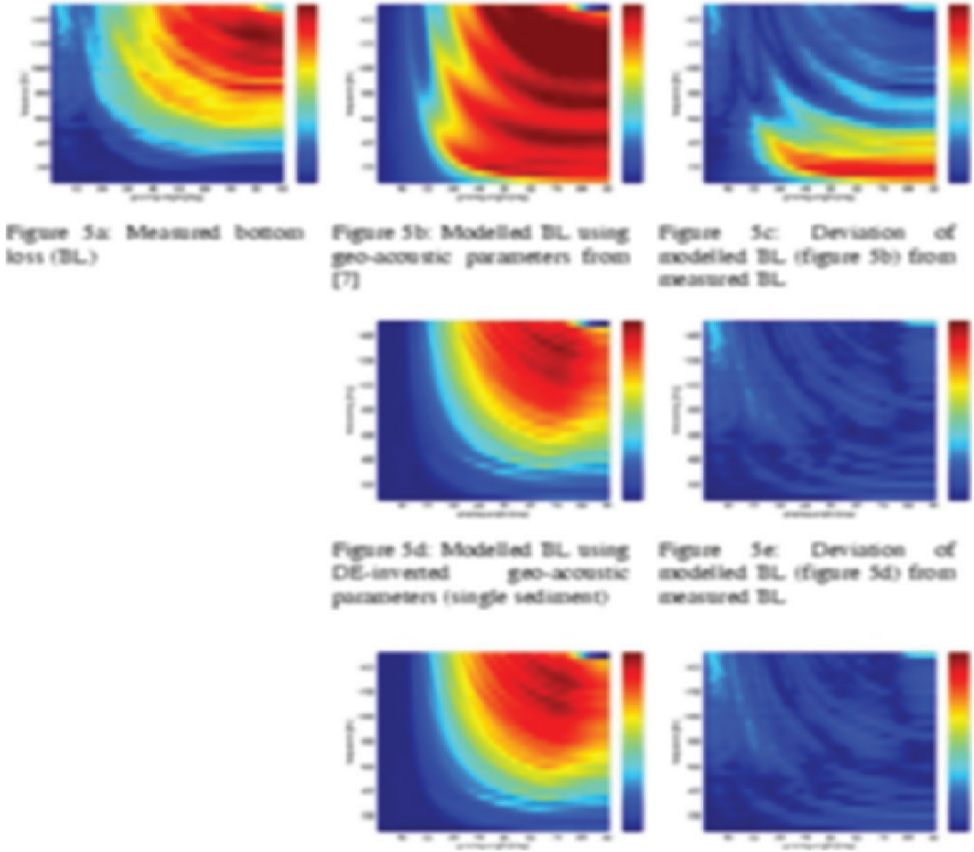


Figure 5. (a) Measured bottom loss (BL); (b) Modelled BL using geo-acoustic parameters from [1]; (c) Deviation of modelled BL (b) from measured BL ; (d) Modelled BL using DE-inverted geo-acoustic parameters (single sediment); (e) Deviation of modelled BL (d) from measured BL ; (f) Modelled BL using DE-inverted geo-acoustic parameters (two sediments); (g) Deviation of modelled BL (f) from measured BL .

inversion problem can be distinguished, see figure 6. First, we select the best solutions for which $E < 0.01$ (111 out of 171). For these solutions parameter correlation is illustrated in figure 7, which shows the magnitude of the linear correlation coefficient calculated for all combinations of parameter estimates. Again, we indicate for which parameter combination the confidence of the observed correlation coefficient exceeds 95%. As in the case of the single sediment inversions of measured data (see previous paragraph), the geo-acoustic parameters of the two sediments (c_2 , c_3 , c_4 and α) are strongly coupled. Also, the thicknesses of the sediments, h_2 and h_3 , are strongly coupled, but there is virtually no correlation between the geo-acoustic parameters and the thicknesses. Histograms of these parameter estimates are given in figure 8. The corresponding mean and standard deviations for each parameter are given in table 2. It can be concluded that all parameters are accurately determined and that their mean values are in excellent agreement with the true values.

Next, we select the somewhat worse solutions where E is around 0.07 (see the second peak in the histogram for E , figure 6). Histograms of these parameter estimates are given in figure 9. The corresponding mean and standard deviations for each parameter are given in table 2. It is observed

that a single layer solution is found now, i.e., a sediment layer with a sound speed nearly equal to that of the first layer with a thickness equal to the sum of the two sediments (being 3 m). Further, c_3 becomes equal to c_4 and, consequently, h_3 becomes undetermined. Still, this somewhat worse solution is physically plausible. The somewhat higher sound speed found in the lower 1 m of the 3 m sediment (1540 m/s in stead of the true 1530 m/s) and also below the sediment (1575 m/s in stead of the true 1570 m/s) is compensated by a somewhat higher attenuation (0.055 dB/ λ in stead of the true 0.05 dB/ λ).

The good performance of this synthetic inversion problem is promising for inversion of measured data using a two-sediment geo-acoustic model. However, the two solutions discussed also illustrate the non-uniqueness of the solution of geo-acoustic inverse problems. For this synthetic case the two solutions can clearly be distinguished by their energy. For the inversion of experimental data it is expected that it can be less obvious which solution to choose.

Table 2. Parameters to be inverted for: two-sediment inversions of the synthetic data.

Parameter	Search range	True value	Inversion result	
			Best solution $E < 0.01$	Solutions with $E \approx 0.07$
c_2 [m/s]	1400 – 1700	1540	1540.1 \pm 0.3	1539.1 \pm 0.2
ρ_2 [g/cm ³]	N.A.	1.624	1.625 \pm 0.001	1.622 \pm 0.001
h_2 [m]	0.1 – 5	2.0	2.000 \pm 0.007	3.006 \pm 0.002
c_3 [m/s]	1400 – 1700	1530	1530.1 \pm 0.3	1575.1 \pm 0.3
ρ_3 [g/cm ³]	N.A.	1.594	1.595 \pm 0.001	1.714 \pm 0.001
h_3 [m]	0.1 – 5	1.0	1.001 \pm 0.007	1.3 \pm 0.4
c_4 [m/s]	1500 – 1900	1570	1570.1 \pm 0.4	1575.1 \pm 0.2
ρ_4 [g/cm ³]	N.A.	1.702	1.702 \pm 0.001	1.714 \pm 0.001
α [dB/ λ]	0 – 2	0.05	0.051 \pm 0.001	0.055 \pm 0.001

5.2.2 The North Elba data

We now discuss the inversion results of the bottom loss data obtained from the North Elba ambient noise data (see figure 5a) assuming a two-sediment model for the seabed (see figure 1b). The inversion algorithm is the same as that for the synthetic inversions described in the previous paragraph. The inversion was run 200 times, of which 114 successful runs were selected. Histograms of the corresponding parameter estimates are given in figure 10. It seems that sediment thicknesses are not well resolved. However, for the total sediment thickness, $h_2 + h_3$, we do obtain a peaked distribution. Also, as in the synthetic case, h_2 and h_3 are correlated. Figure 11 presents a plot of the estimates for h_2 plotted against those for h_3 . It seems obvious to make a selection based on total sediment thickness. We chose $3.3 \text{ m} < h_2 + h_3 < 3.5 \text{ m}$. Histograms of the selected solutions are given in figure 12. (Of course, the distribution for $h_2 + h_3$ is very peaked now, but h_2 and h_3 separately remain unresolved). The corresponding mean and standard deviations for each parameter are given in table 3. The inversion result reported in [1] is also included for comparison. For completeness, parameter coupling of the selected solutions is shown in figure 13, a similar behaviour as that of the synthetic inversion problem (figure 7). Basically, a single sediment solution is obtained, because the inversion result for c_2 equals that of c_3 and a peaked distribution is only obtained for $h_2 + h_3$ and not for h_2 or h_3 separately. Further, the solution agrees well with the single-sediment solution given in table 1. However, it does not agree well with the solution of [1], albeit that both solutions are representative of a silt bottom.

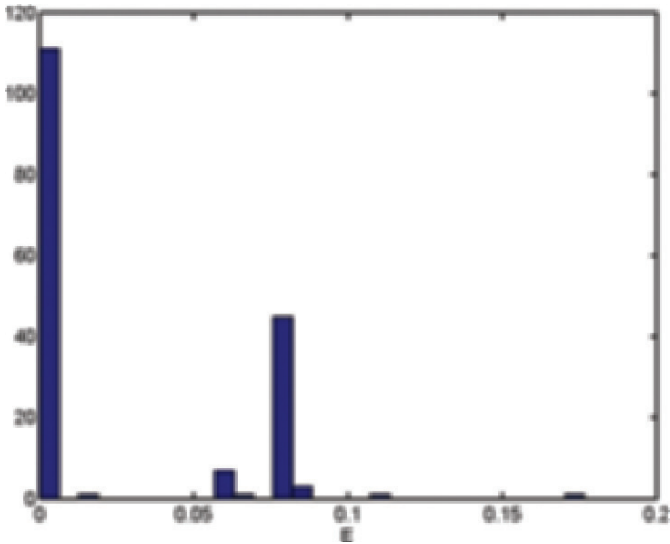


Figure 6. Two-sediment inversions of the synthetic data: histogram of the final energy function values obtained for the 171 successful inversions.

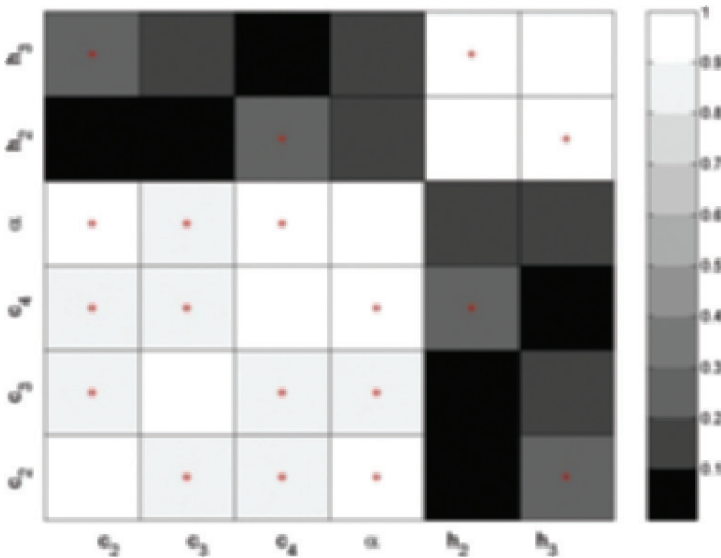


Figure 7. Two-sediment inversions of the synthetic data: magnitude of the correlation coefficient for all parameter combinations. A star is plotted if the correlation is statistically significant.

Finally, we have calculated the beam-smearred bottom loss BL for the mean values of the inversion results as given in table 3, the result of which is given in figure 5f. The deviation from the measured (beam-smearred) bottom loss, as presented in figure 5a, is given in figure 5g. No further

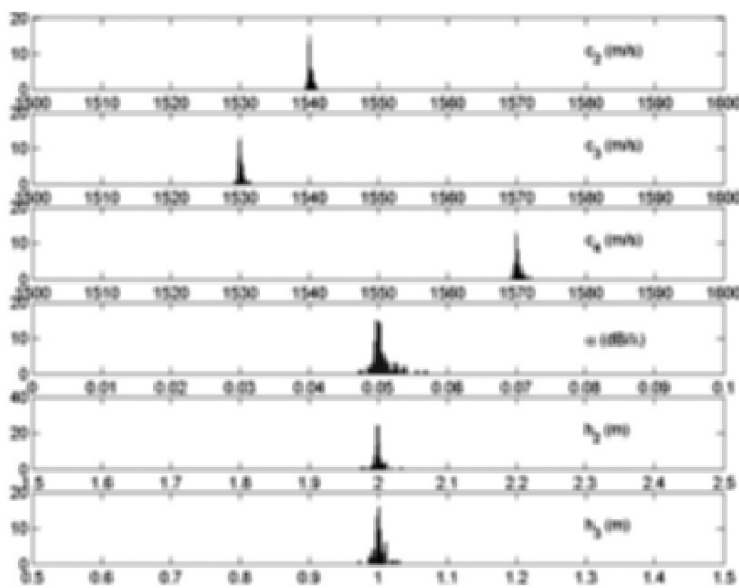


Figure 8. Two-sediment inversions of the synthetic data: histograms of the best estimates for each parameter ($E < 0.01$).

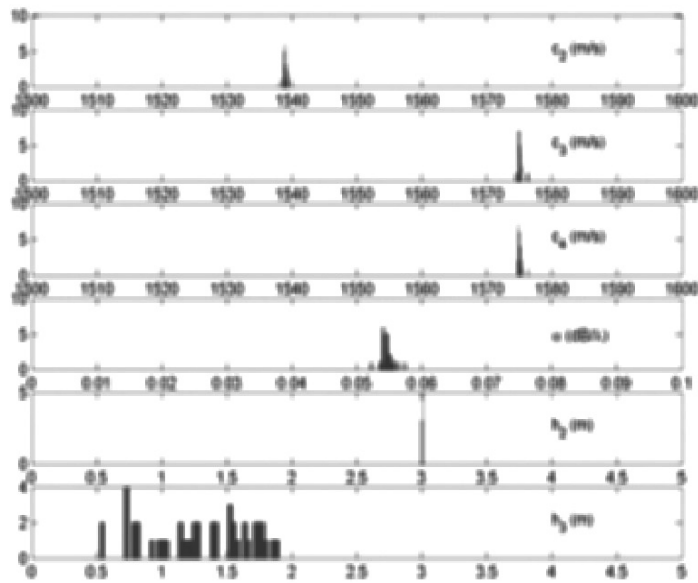


Figure 9. Two-sediment inversions of the synthetic data: histograms of the somewhat worse estimates ($E \approx 0.07$).

improvement compared to the single-sediment solution (figure 5d and 5e) is obtained, which is not surprising, as the single-sediment and two-sediment inversion results are basically the same.

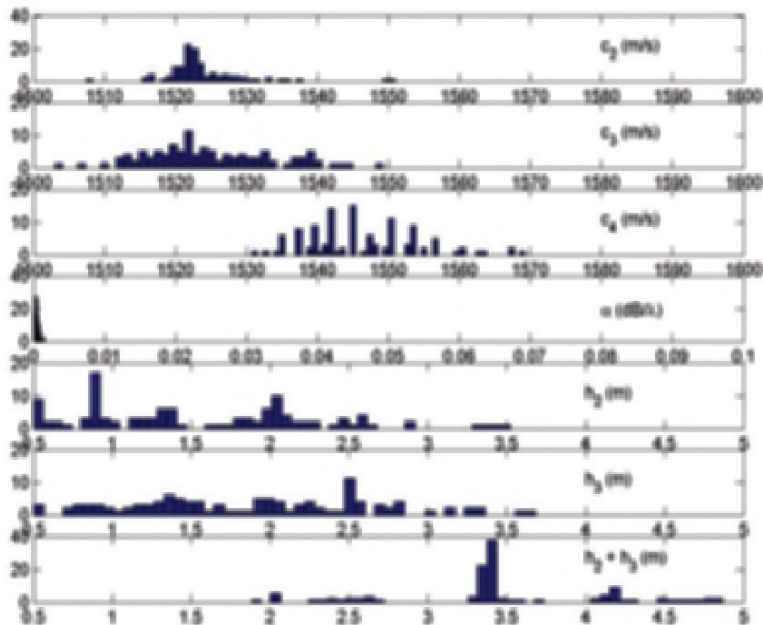


Figure 10. Two-sediment inversions of the North Elba data: histograms of the 114 estimates for each parameter. Note that we included the histogram for total sediment thickness.

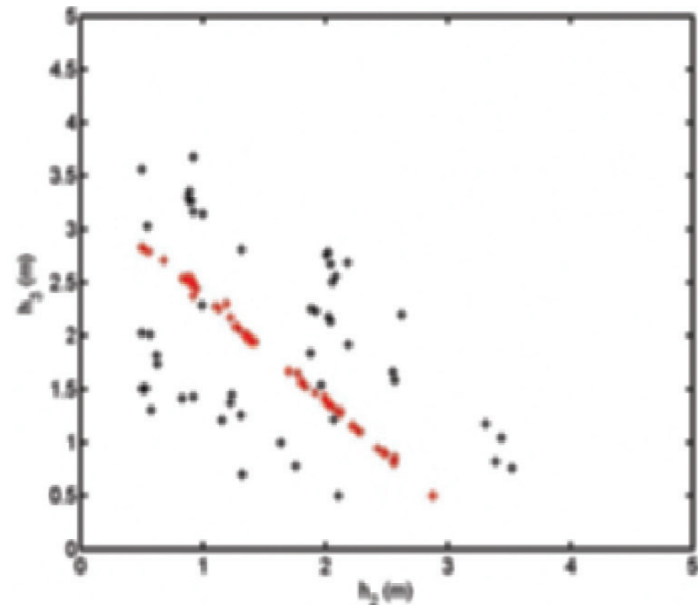


Figure 11. Two-sediment inversions of the North Elba data: The 114 estimates for h_2 plotted against those for h_3 . The selected solutions are indicated by the gray symbols.

6 Summary and conclusions

An approximation of the plane wave reflection coefficient of the seabed (as a function of grazing angle and frequency) can be found by comparing the upward- and downward-going noise. In [1]

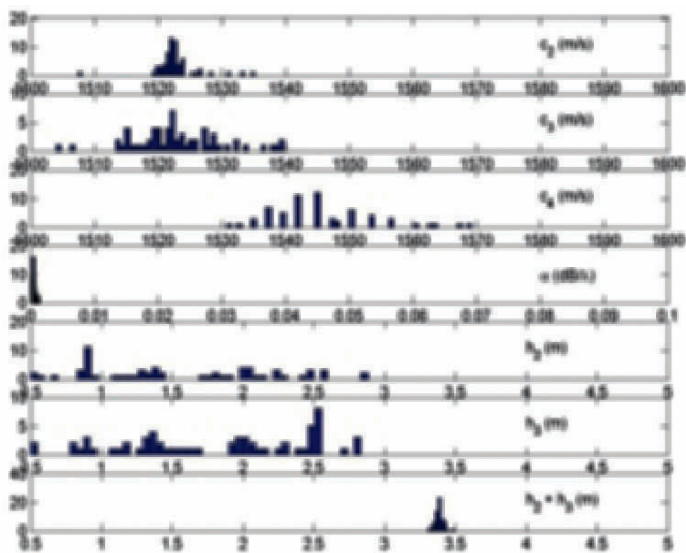


Figure 12. Two-sediment inversions of the North Elba data: histograms of the parameter estimates, which were selected on total sediment thickness.

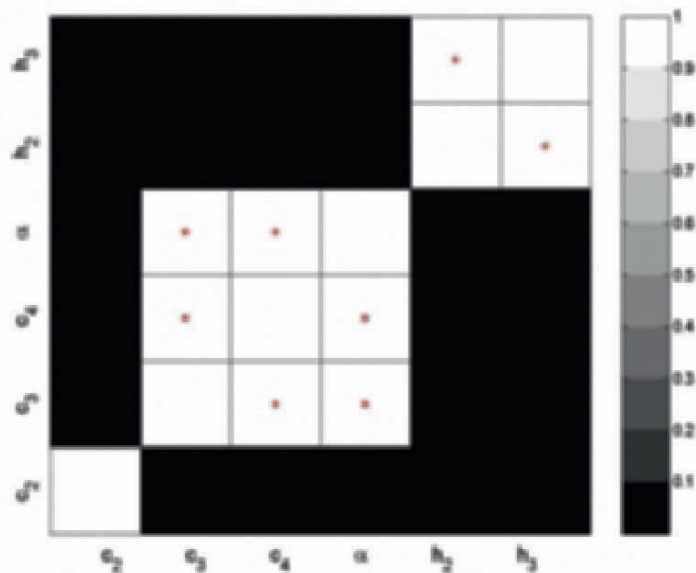


Figure 13. Two-sediment inversions of the North Elba data: magnitude of the correlation coefficient for the selected solutions. A star is plotted if the correlation is statistically significant.

these were determined by beamforming the ambient noise field received on a vertical array of hydrophones. Geo-acoustic parameters were derived with a hand-searching technique that relies on inspection of the experimental reflection loss for critical angle, modulation depth and fringe spacing.

Table 3. Parameters to be inverted for: two-sediment inversions of the North Elba data.

Parameter	Search range	Inversion results	
		Harrison & Simons [1]	This work
c_2 [m/s]	1400 – 1700	1600	1523 ± 4
ρ_2 [g/cm ³]	N.A.	1.8	1.57 ± 0.01
h_2 [m]	0.1 – 5	0.7	1.57 ± 0.65
c_3 [m/s]	1400 – 1700	1530	1523 ± 7
ρ_3 [g/cm ³]	N.A.	1.75	1.57 ± 0.03
h_3 [m]	0.1 – 5	2.1	1.82 ± 0.65
c_4 [m/s]	1500 – 1900	1600	1546 ± 8
ρ_4 [g/cm ³]	N.A.	1.8	1.64 ± 0.02
α [dB/λ]	0 – 2	0.14 ¹	0.0005 ± 0.0003
$h_2 + h_3$ [m]	N.A.	N.A.	3.38 ± 0.03

In this article we inferred geo-acoustic parameters by inversion of the measured reflection coefficient with a global optimisation technique as an automatic search method. For this study we selected the North Elba data (silt bottom), one of the sites in the Mediterranean where ambient noise measurements were carried out (see [1]). The measured reflection coefficient was compared with calculations using models for the plane wave reflection coefficient, searching over geo-acoustic parameter space. For these inversions we assumed the seabed to consist of a single homogeneous fluid sediment layer on top of a homogeneous fluid subbottom. The data were also inverted using a seabed model comprising of two fluid sediment layers on top of a homogeneous fluid subbottom. For the global search method a relatively new (but fast) technique, called “differential evolution” [3], was applied.

It was found that all parameters could be accurately determined. With the two-layer geo-acoustic model basically a single-sediment solution is obtained, which is in excellent agreement with the solution obtained with the single-sediment model. However, they do not agree well with the solution reported in [1], albeit that all solutions are representative of a silt bottom.

A comparison of the beam-smeared bottom loss, calculated for the geo-acoustic parameters inverted, with the measured bottom loss shows that a considerable improvement can be obtained with an automated search technique.

Notes

1. Attenuation of first sediment layer.

References

1. Harrison C. H. and Simons D. G., Geoacoustic inversion of ambient noise: A simple method. *J. Acoust. Soc. Am.* **112**(4), 1377–1389 (2002).
2. Rainer Storn and Kenneth Price, Differential evolution – A simple and efficient adaptive scheme for global optimization over continuous spaces. ICSI Technical Report TR-95-012, (1995).
3. Carbone N. M., Deane G. B. and Buckingham M. J., Estimating the compressional and shear speeds of a shallow-water seabed from the vertical coherence of ambient noise in the water column. *J. Acoust. Soc. Am.* **103**, 801–813 (1998).
4. Harrison C. H. and Simons D. G., Geoacoustic inversion of ambient noise: A simple method. Conference on Acoustical Oceanography, Southampton UK, 9-12, edited by T.G. Leighton, Proc. Inst. of Acoust. 23, pp 91-98 (2001).

5. Hamilton E. L. and Bachman R. T., Sound velocity and related properties of marine sediments. *J. Acoust. Soc. Am.* **72**(6), 1891–1904 (1982).
6. Jensen Finn B., Kuperman William A., Porter Michael B., Schmidt Henrik, Computational Ocean Acoustics. American Institute of Physics, New York, (1994).
7. Gerstoft Peter, Inversion of seismoacoustic data using genetic algorithms and a posteriori probability distributions. *J. Acoust. Soc. Am.* **95**(2), 770–782 (1994).
8. van Moll Camiel and Simons Dick G., Improved Performance of Global Optimisation Methods for Inversion Problems in Underwater Acoustics. Proc. of the 7th European Conference on Underwater Acoustics, Delft 5-8 July, (2004).

REFLECTION LOSS AND SUB-BOTTOM PROFILING WITH AMBIENT NOISE

CHRIS HARRISON

*NATO Undersea Research Centre,
Viale San Bartolomeo 400, 19138 La Spezia, Italy*

Measurements of ambient noise directionality on a vertical array (VLA) can already be converted into bottom reflection loss as a function of angle and frequency using a recently developed technique (GAIN = GeoAcoustic Inversion of Noise). The performance of this technique has now been assessed under various weather conditions at 13 moored sites and 6 drift tracks with arrays operating at design frequencies of respectively 1.5, 4.17, 8.3 KHz. Theoretical arguments and experiments with drifting arrays in 2002 and 2003 have shown that the reflection measurement is local and that one can indeed detect spatial changes in reflection loss. The technique is extended by converting the reflection loss at each location into an impulse response as a function of travel time and angle. A minimum phase representation of the complex reflection coefficient is reconstructed by spectral factorization prior to Fourier transformation. The method is applicable to any bottom loss measurement and requires the reflection coefficient to be known over a range of frequencies and the grazing angle in question to be above critical. The evolution of the impulse response as the VLA drifts horizontally can then be plotted as a sub-bottom profile referenced to the seabed/water interface (SUPRA-GAIN = SUB-bottom PROfiling using Ambient noise). First it is shown how this is possible by simulation, and limitations of the technique for above and below critical angle cases are discussed. Then experimental examples are given for two moored VLA sites and one VLA drift track in the Mediterranean Sea. Convincing angular variation of the impulse response is shown for the moored sites, and this is consistent with earlier published inferred layering for the sites. The sub-bottom profile along the drift track compares extremely well with a boomer profile taken on another occasion along the same track. Thus the technique offers the possibility of sub-bottom profiling from a single platform with no sound source.

1 Introduction

In sonar applications of underwater acoustics bottom reflection loss is usually treated as a frequency domain quantity. That is to say, at each frequency and grazing angle it has an amplitude and a phase. In this sense the reflection loss is the frequency response or transfer function of the seabed, and with realistic seabeds this function can be complicated because of multiple arrivals and internal reflections from sediment layers, not to mention various types of wave (compression, shear, visco-elastic, and so on) [1]. Looking at the same phenomena in the time domain we see explicit arrivals from the layers

and again later arrivals from inter-layer reflections. In this alternative sense the time domain picture is an impulse response of the seabed. This arrival structure manifests itself as the ‘layering’ seen in most geophysical surveying and sub-bottom profiling techniques. Clearly the two view points are equivalent. In fact the complex plane wave reflection coefficient (the transfer function) at a particular grazing angle is the Fourier transform (FT) of the impulse response for that angle. In this paper we set these thoughts in the context of a recently established ‘noise inversion’ technique where the modulus square of the reflection coefficient is deduced from beam-steered ambient noise measurements on a vertical array (VLA) [2, 3, 4, 5]. Harrison shows that the up-to-down-ratio at each angle is, in fact, the modulus square of the plane wave reflection coefficient. This technique has already been shown theoretically and experimentally [6] to function as a survey technique with a drifting VLA measuring ‘local’ properties with a footprint of order the water depth. The possibility of converting this result directly to a sub-bottom profile is an intriguing prospect which was investigated in Ref. [7]. This paper summarises the findings.

2 Sub-bottom profile from simulated reflection loss

Before moving on to experimental examples we simulate the calculation of the impulse response first starting with a known complex reflection coefficient and then starting only with its modulus. The hypothetical environment consists of four layers including the water and a bottom half-space. Sound speeds are respectively 1500, 1600, 1700, 1800 m/s; densities are 1, 1.4, 1.6, 1.8; and attenuations are 0, 0.14, 0.15, 0.15 dB/λ. The sediment layers are 1.5 and 2.0m thick. Using a simple layer model, as suggested by Jensen ([1], Section 1.6.4), we calculate the complex plane wave reflection coefficient, as shown in Fig. 1, and we inverse Fourier transform it at each angle, as shown in Fig. 2(a). A perfect reflection with $R = +1$ would result in the Fourier transform of the windowing function (a hamming ‘pulse’) being centred on time zero. For this reason a small time offset has been included in the illustrations. There are several interesting points, namely: the visible phase change in the arrival below the critical angle; the branches at each of the three critical angles; the multiple reflections close to the critical angle; and most importantly the clear arrivals at the correct time for each boundary at high angles.

A possible way of handling the modulus of the reflection coefficient is to inverse Fourier transform its square. The result is then the autocorrelation function of the impulse response (Fig. 2(b)). Clearly this shows layer separations rather than layer depths, and the ordering may be incorrect. Alternatively if we want to start with only the modulus of the reflection coefficient and we want to retrieve the layer ordering we must, somehow, reconstruct the phase in order to do the Fourier transform. An appropriate technique is spectral factorization. This is an operation that finds a unique ‘minimum phase’ time series that has the given spectrum (see e.g. [8]). The Kolmogoroff spectral factorization method makes use of the Hilbert transform by moving it to the exponent [9]. Given a real spectrum h_R we shift it to the exponent by writing it as $h_R = \exp(\ln(h_R)) \equiv \exp(g_R)$. Applying the Hilbert transform to g_R we obtain an imaginary part g_I and we construct the complex function $g = g_R + ig_I$. Now the complex h becomes $h = \exp(g_R)\exp(ig_I)$. Thus the original real spectral quantity h_R now has (an unchanged) amplitude $\exp(g_R)(= h_R)$ and a new phase g_I . Having retrieved the phase we can now Fourier transform complex h to obtain the desired impulse response.

In short, the operation to retrieve a time series $r(t)$ from the modulus of the reflection coefficient $|R|$ is

$$r(t) = \mathcal{F}^{-1}\{\exp(\mathcal{H}(\ln(|R(\omega)|)))\}, \quad (1)$$

where \mathcal{F} is the Fourier transform, and \mathcal{H} is the operation of adding the Hilbert transform generated imaginary part to the original real part. Applying the Kolmogoroff method to the modulus of reflection coefficient shown as reflection loss in Fig. 1 we obtain the impulse responses shown in Fig. 2(c). Comparing this with the true time series (Fig. 2(a)) we see that at large angles the layer boundaries

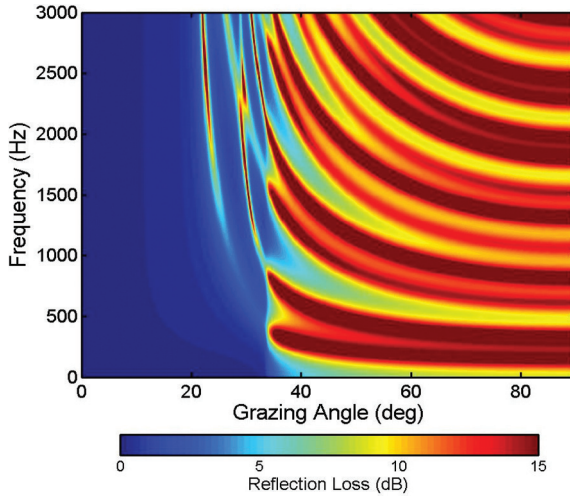


Figure 1. Modelled reflection loss for two sediment layers (thicknesses 1.5 and 2m) in between two half spaces.

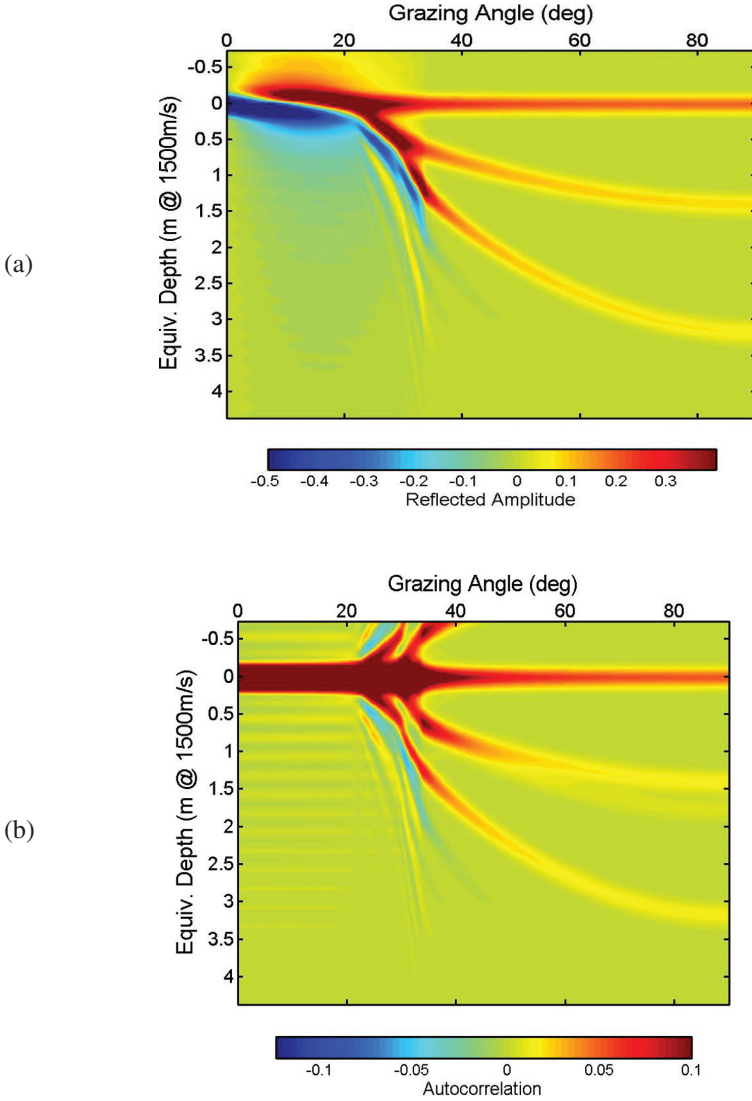
are well distinguished. Their order and their number are (in this example) clear, and their intensities are close. This is already a benefit from the inversion point of view. One can also see a multiple reflection at around $30^\circ - 40^\circ$. At angles lower than the biggest critical angle there are differences between Figs. 2(a) and (c) caused by the minimum phase condition; the variation of the pulse shape with angle seen in Fig. 2(a) is absent in Fig. 2(c). This is hardly surprising since at these angles there is hardly any frequency variation for the Hilbert transform to work on. Thus the result has a uniform zero phase for all angles. Also the branching is unclear, and the spectral factorization method seems to settle down only when the reflection coefficient is real (i.e., when clear of all critical angles). Performance is discussed in more detail in Ref. [7]. The conclusion is that the method appears to extract valuable information, in particular the number of effective layers, from the modulus of the reflection coefficient which would otherwise require considerable effort in a parameter search technique.

3 Sub-bottom profile using reflection loss inferred from ambient noise measurements

We now apply the spectral factorization process to some experimental data obtained with a moored or drifting vertical array (VLA). In each case 32 equally spaced elements of the VLA (separation 0.5m) were sampled at 6KHz, beam-formed and analysed as described in [7] to obtain a reflection loss as a function of angle and frequency.

3.1 Moored experiments

Experiments were carried out at the three moored sites during MAPEXbis2000. In all cases the noise data needs to be preprocessed because the measurement frequency band is so narrow compared with the spectral detail (see [7]). An example from E. Elba (mud) is shown in Fig. 3. In the vicinity of this site other authors have found a thin layer ($<0.5\text{m}$) of high speed sediment over a thicker layer of lower speed. The inferred reflection loss is shown in Fig. 7 of [2], and from a hand search two



sediment layers were found with thicknesses 0.8 and 3.5m and speeds 1530 and 1471m/s. In Fig. 3 the angle variation is very smooth and clean from 90° down to 20° . The two obvious features are the negative arrival (dark gray) which reaches 0.693m at 90° and the weaker positive arrival at 3.85m. These agree well with the equivalent depths of 0.78m and 3.57m from [2].

3.2 Drifting array experiment

In the drift experiment we have the same type of information at our disposal for all positions along the drift track. So there is the potential to construct a bottom profile with a beam looking at any angle (not withstanding the low angle limitations and the insensitivity to azimuth). Note that in the case of a vertical beam the reservations about performance of the spectral factorization technique are irrelevant.

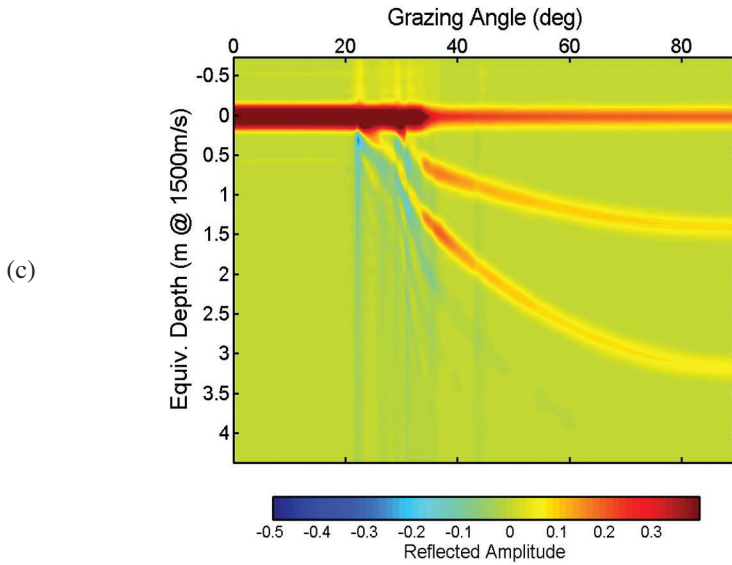


Figure 2. (a) The inverse Fourier transform of the complex reflection coefficient (i.e., the impulse response) from Fig. 1. Two-way travel time is converted to an equivalent depth at 1500 m/s. (b) The inverse Fourier transform of the modulus-square of reflection coefficient, which is the autocorrelation of the impulse response. (c) The result of spectral factorization applied to the modulus of the reflection coefficient.

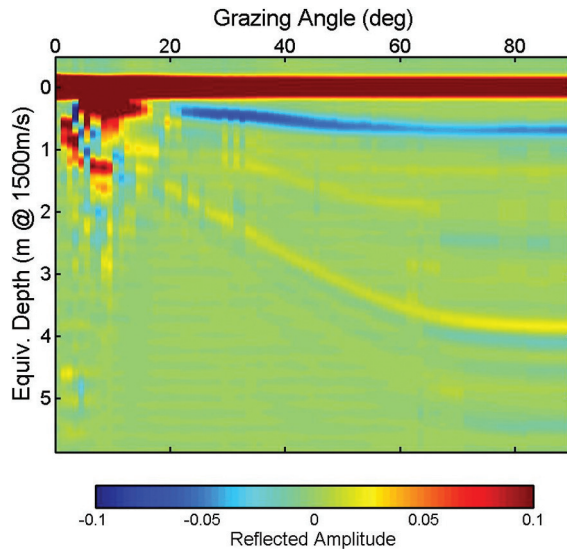


Figure 3. Experimental impulse response derived by spectral factorization from ambient noise measured on a moored VLA at a mud site east of Elba.

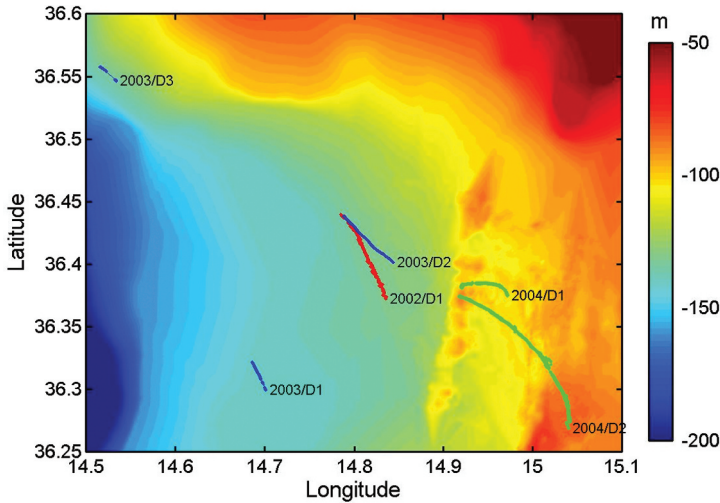


Figure 4. Drift tracks in the vicinity of the Malta Plateau and the Ragusa Ridge during BOUNDARY 2002, 2003, 2004.

A total of six drift experiments have now been carried out during BOUNDARY 2002, 2003, and 2004. In 2002 the array had a design frequency of 1500Hz whereas all the other drifts used a 32 element array with design frequency 4167Hz. Tracks are shown in Fig. 4.

In experiments during BOUNDARY2002 the VLA was allowed to drift for about 12 hours covering about 5 miles near the Ragusa Ridge south of Sicily. A selection of reflection loss plots is shown in Fig. 5. The profile constructed from arrivals between 80° and 90° is shown in the upper part of Fig. 6. The horizontal scale is geo-time (measured in hours after midnight on 22 April 2002) which translates into position. One can see clear layers between about 1 and 5 m depth that undulate independently of each other. On a later occasion (after these calculations were done) the track was revisited with a seismic profiling boomer to supply a 'ground-truth'. The lower part of Fig. 6 shows the boomer record, zero-referenced by taking out the travel time to the seabed. Note that the boomer does not have a perfect impulse response; it has a very sharp initial pulse followed by ringing. Considering that this comparison constitutes a blind test of the spectral factorization algorithm, agreement is quite remarkable.

4 Conclusions

By applying spectral factorization to the modulus of the reflection coefficient and then Fourier transforming the result an angle-dependent impulse response was calculated. Using a simulated example the spectral factorized solution was compared with the true Fourier transform of the complex reflection coefficient. In this case the algorithm was able to determine layer structure including layer ordering, and results were indistinguishable at high angles from the true impulse response. However at angles below the highest critical angle the minimum phase response understandably fails to reproduce the detailed changes in pulse shape of the true response and yields instead a simple positive pulse at all angles. Although the technique can be applied generally to incoherent layer reflections the main interest in this paper is application to reflection loss inferred from directional ambient noise measurements made using a VLA. Examples taken from a moored site and a drift track in the Mediterranean Sea were investigated. The moored site produced convincing results that

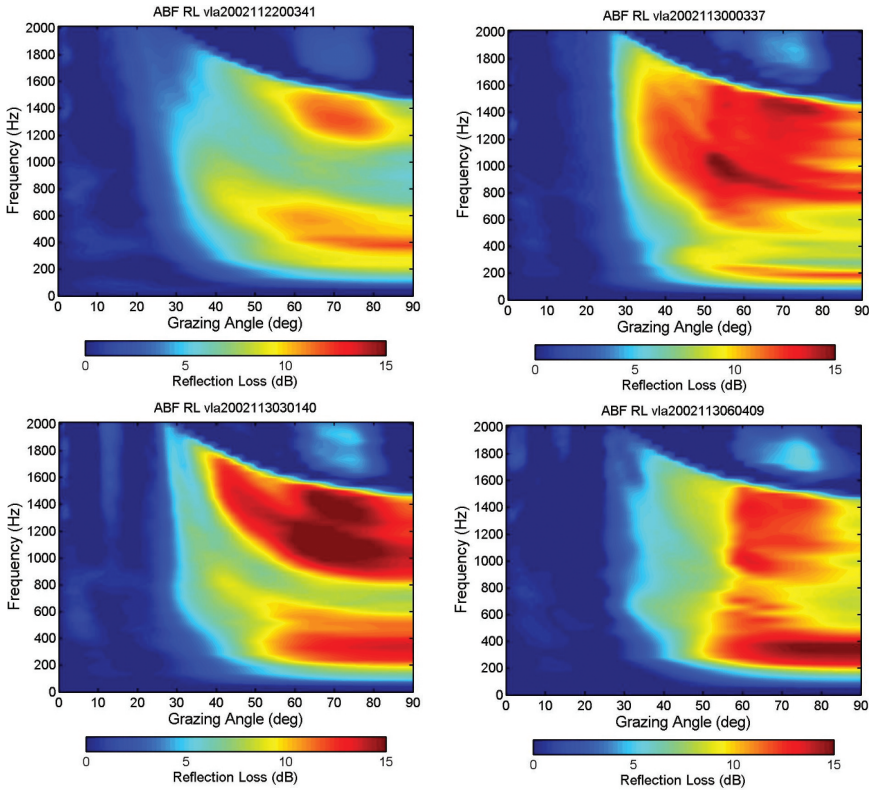


Figure 5. A selection of reflection loss plots during the drift experiment. Times are: 20:03, 00:33, 03:01, 06:04, corresponding approximately to -4, 0, 3, 6 (hr) in Fig. 6.

were in close agreement with earlier publications on this data and other measurement techniques. In particular spectral factorization appears to give a good idea of the ordering and number of layers. The time-varying reflection loss from the VLA drift experiment can be translated into depth profiles for beams at almost any angle since the data is the equivalent of a geophysical move-out experiment carried out about once per water depth in range. The general behaviour of the layers, especially when compared with nearby boomer records, gives confidence that the result is close to a true sub-bottom profile. In particular, the boomer record along almost the same track is strikingly similar. One could argue that the approach does not bring one any closer to geoacoustic parameters than the more conventional frequency domain inversion techniques. However it does offer the possibility of at least determining the number of layers, if not determining their order. In addition there are many other time domain inversion techniques that are available such as: forward and backwards linear prediction, the Levinson-Durbin algorithm, and the Schur algorithm for predicting reflection coefficients from a given autocorrelation sequence [8]. Finally the method offers the possible benefit of sub-bottom profiling with a single platform and without the necessity to make any additional sound, the frequency range and depth of penetration being determined by the array length and hydrophone density.

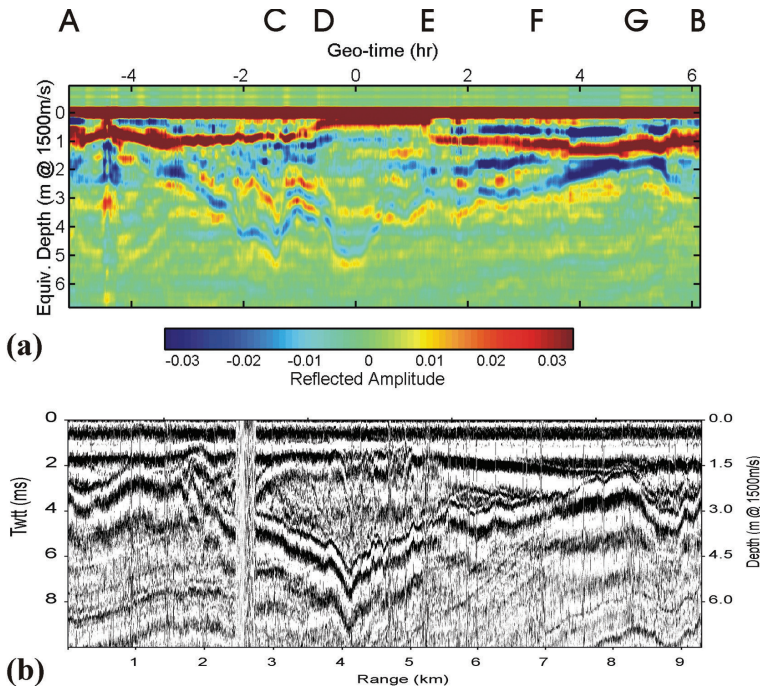


Figure 6. (a) Sub-bottom profile derived, via reflection loss, from ambient noise received by a drifting VLA. (b) Zero-referenced and aligned boomer sub-bottom profile for comparison.

References

1. Jensen F. B., Kuperman W. A., Porter M. B. and Schmidt H., Computational Ocean Acoustics, American Institute of Physics, New York (1994).
2. Harrison C. H. and Simons D. G., Geoacoustic inversion of ambient noise: a simple method, *J. Acoust. Soc. Am.* **112**, 1377–1389 (2002).
3. Tang D. J., Inversion of sediment property using ambient noise. *J. Acoust. Soc. Am.* **113**, (2003).
4. Desharnais F., Thomson D. J. and Gillard C. A., Source depth and array tilt effects on seabed inversion of ambient noise. *J. Acoust. Soc. Am.* **113**, (2003).
5. Donnelly M. K. and Matt G. A., Geoacoustic inversion of ambient noise: a modelling study. Proceedings of Underwater Defence Technology (UDT), Stockholm, June (2003).
6. Harrison C. H. and Baldacci A., Bottom reflection properties deduced from ambient noise: Simulation of a Processing Technique. SACLANT Undersea Research Centre, Report SM-392 (2002).
7. Harrison C. H., Sub-bottom profiling using ocean ambient noise. *J. Acoust. Soc. Am.* **115**, March (2004).
8. Proakis J. G. and Manolakis D. G., Digital Signal Processing Principles, Algorithms, and Applications, Prentice Hall, NJ (1996).
9. Claerbout J., Fundamentals of geophysical data processing, Blackwell Scientific Pubs., Palo Alto; now available as free download on Stanford Exploration Project web site (1985).

INVERSION OF GEOACOUSTIC MODEL PARAMETERS USING SHIP RADIATED NOISE

N. ROSS CHAPMAN¹, REZA M. DIZAJI² AND R. LYNN KIRLIN²

*University of Victoria,
School of Earth and Ocean Sciences¹
Department of Electrical Engineering²
Victoria, British Columbia, Canada V8W 3P6
E-mail: chapman@uvic.ca*

Estimation of geoacoustic model parameters is an underlying research issue in understanding acoustic propagation in shallow water environments, where the propagation is generally bottom limited. Inversion methods based on matched field processing have become widely used in applications with experimental data. Traditionally, the experiments have been carried out with controlled source geometries and either vertical or horizontal arrays. This paper presents an experimental approach that makes use of the random noise radiated by passing ships as the sound source for the inversion. The inversion uses a recently developed cross-relation matched field processor that is insensitive to the waveform of the random noise signal radiated by the ship. Ship noise data were measured on a 16element vertical line array in shallow water off the west coast of Vancouver Island. The data were filtered into low (73–113 Hz) and high (190–270 Hz) frequency bands, and processed in an inversion algorithm based on back propagation of the spectral components of the noise signal. The geoacoustic model that generated the most accurate focus at the source location was taken as the best estimate. The band limited data allowed estimation separately of geoacoustic model parameters of the sea floor with the high frequencies, and then for the deeper layers using the low frequencies. The estimated model parameters compared well with ground truth data from a seismic survey and from sediment samples at the site.

1 Introduction

Matched field inversion has proved to be an effective technique for estimating geoacoustic parameters of the ocean bottom, and there is an extensive literature describing various different approaches for inverting acoustic field data in shallow water. The inversion experiments have been carried out using either broad band [1]–[3] or narrow band [4, 5] controlled sound sources, and receiving systems based on either vertical [1]–[5] or horizontal hydrophone [6] arrays. Geoacoustic inversion is generally cast as an optimization process in which a cost function based on a matched field processor is used to assess candidate geoacoustic models that are randomly selected from a multi-dimensional model parameter space. The objective of the search is to determine the model that provides the

best correlation between the measured and calculated acoustic fields. Since the dimension of the space is generally very large, efficient search methods such as simulated annealing [7]-[8], genetic algorithms [4] or hybrid methods [9] have been applied.

In this paper we describe an adaptive matched field inversion for estimating geoacoustic properties in a shallow water environment [10]. The method makes use of ambient noise radiated by passing ships as the sound source, and a vertical line array receiver. The ship noise is a broad band random signal with a complicated spectrum that consists typically of continuous and tonal components. We introduce a cross-relation matched field processor for processing the ship noise data that is insensitive to the characteristics of the source signal [11]. The inversion is designed in a multi-stage process (e.g. [12]) in which successively lower frequency bands are used to estimate the depth dependence of the geoacoustic model parameters. The model parameter space is explored using a coarse grid search in which a simple criterion based on the focus of the back-propagated signal field at the source position is applied to select the best geoacoustic model. Although not as efficient as simulated annealing or genetic algorithms for exploring the model parameter spaces, the limited grid search reduces the computational load significantly and is effective for demonstrating the MF inversion of broadband data. The method is applied to invert ship noise data measured during an experiment carried out on the continental shelf off the west coast of Canada. Inversion of ship noise data using a conventional matched field processing approach is described by Battle *et al.* [13].

2 Cross-relation Matched Field Processor

In this section we describe the pairwise or cross-relation MF processor for random noise signals. The ocean environment is modeled as a parallel set of N linear transfer functions as shown in Figure 1. The transfer function h_i corresponds to the acoustic paths from the source that generate the field at the i th array sensor. The noise w_i is assumed to be additive, spatially white and temporally uncorrelated with the input signal, S . The cross-relation (CR) in Eq. (1) between the transfer function and the received signal y_i at pairs of sensors follows from the definitions for the received signal at each sensor:

$$\begin{aligned} y_p(n) &= h_p(n; \alpha) * S(n) \quad \text{and} \\ y_q(n) &= h_q(n; \alpha) * S(n) \\ h_p(n; \alpha) * y_q(n) &= h_q(n; \alpha) * y_p(n); \quad p, q = 1, 2, \dots, N; \quad n = 1, 2, \dots, L. \end{aligned} \quad (1)$$

Here α , is the set of geoacoustic and geometric model parameters, and n is a time index for L time samples. The cross relation shows that the outputs of each channel pair are related by the channel responses. For random sources we can construct two different cross-relation MF processors, according to the specific channel that is used to form the estimator [10, 11]. To obtain the cross-CR processor, we multiply in Eq. (1) by the conjugate of the received signal at a third sensor y_k , and then apply the expectation operator, E , to the product:

$$h_p(n; \alpha) * E(y_q(n) y_k^*(n_l)) = h_q(n; \alpha) * E(y_p(n) * y_k^*(n_l)) \quad (2)$$

where $p, q = 1, \dots, N$; $p \neq q$; $k = 1, \dots, N$; $k \neq p, q$; and n_l is a time index, independent of n . For wide sense stationary sources, Eq. (2) becomes

$$h_p(n; \alpha) * R_{y_q, y_k}(n - n_1) = h_q(n; \alpha) * R_{y_p, y_k}(n - n_1)$$

and after transforming to the frequency domain,

$$\begin{aligned} H_p(mF; \alpha) S_{y_q, y_k}(mF; \alpha) &= H_q(mF; \alpha) S_{y_p, y_k}(mF) \\ p, q &= 1, 2, \dots, N; \quad k = 1, \dots, N, \quad k \neq p, q \end{aligned} \quad (3)$$

Here, H is the Fourier transform of h , and $S_{y_p, y_q}(f)$ is the cross-power spectral density of y_p and y_q . The above equations can be written in the following matrix form to solve for all channel responses simultaneously [10, 11]:

$$S_{y, cross_CR} H = 0 \quad (4)$$

where

$$H = [H_1, H_2, \dots, H_N]^T, \quad H_p = [H_p(0), H_p(F), \dots, H_p((L-1)F)]^T, \quad p = 1, 2, \dots, N$$

$$S_{y, cross_CR} = \left[\underbrace{S_{1,2,3,\dots}^T, S_{p,q,k;k \neq p,q,\dots}^T, S_{N,N-1,N-2}^T}_{\frac{N(N-1)(N-2)}{3} \text{ blocks}} \right]^T$$

$$S_{p,q,k;k \neq p,q}^{1 \times NL} = \begin{bmatrix} \underbrace{0}_{1 \times (p-1)L} & \underbrace{S_{y_q, y_k}}_{1 \times L} & \underbrace{0}_{1 \times (q-p-1)L} & \underbrace{-S_{y_q, y_k}}_{1 \times L} & \underbrace{0}_{1 \times L} \end{bmatrix}$$

$$S_{y_q, y_p} = [S_{y_q, y_p}(0) \dots S_{y_q, y_p}((L-1)F)]^T.$$

In order to construct a MF processor with high resolution properties, we introduce the following least square form for the cross-CR processor:

$$P_{S, \alpha}^{cross_CR} = \|S_{x, cross_CR} H\|^{-1}. \quad (5)$$

The unknown model parameters, α , are estimated by maximizing the equations (5). The received signal, Y , has been replaced by the system output, X , in these equations. In explicit form, the high resolution crossCR processor is given by:

$$P_{\alpha}^{cross_CR} = \frac{1}{\sum_{f_l} \sum_{p=1}^N \sum_{q=1, q \neq p}^N \sum_{k=1, k \neq p,q}^N |S_{x_p, x_k}(f_l) H_{q; \alpha}(f_l) - S_{x_q, x_k}(f_l) H_{p; \alpha}(f_l)|^2}. \quad (6)$$

We note that the information over frequency is summed non-coherently. The application for source localization has been described in [10, 14] where the processor was shown to be robust to environmental mismatch, similar to the Bartlett MF processor, and to have high resolution properties, similar to the minimum variance processor. In the remainder of this paper, we describe the application for geoaoustic inversion to experimental data.

3 Geoacoustic Inversion Experiment

The data were obtained in an experiment called PACIFIC SHELF carried out in shallow water off the west coast of Vancouver Island (Figure 2). A 16-element vertical line array (VLA) was deployed in 400 m water and monitored by one ship, CFAV ENDEAVOUR, while another ship, CSS W.E. RICKER, towed a continuous wave sound source along a series of tracks centred at the array.

The VLA consisted of 16 hydrophones equi-spaced at 15 m, with an aperture of 225 m that spanned the water column from 80 to 315 m. The array was suspended from a surface float using a two-stage suspension system to provide mechanical isolation from the sea surface motion. The hydrophone data were filtered, amplified, and digitized at 1500 samples/s with a 12-bit A/D at an underwater electronics unit located at the top of the VLA. The digital data were transmitted over an RF link from the surface float to the monitoring ship, and subsequently recorded on exabyte tape. Power for the system was supplied by wet and dry cell batteries which were contained in a sealed

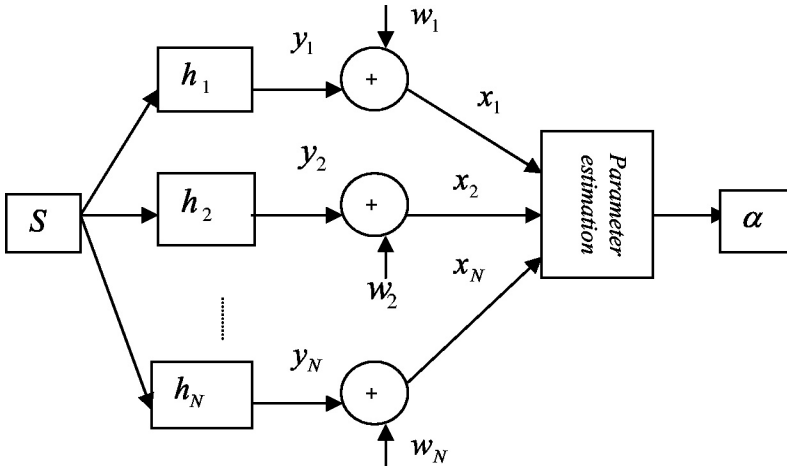


Figure 1. The multichannel model of the acoustic experiment. The system output, x_i , is expressed as the sum of the received signal and the noise.

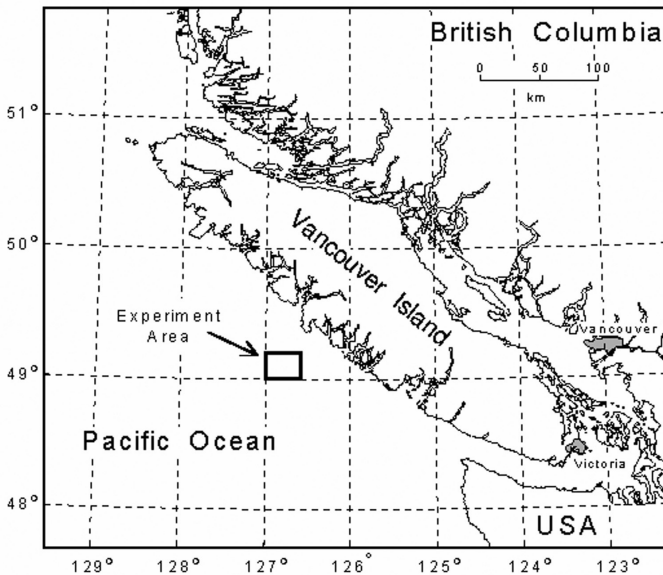


Figure 2. The experimental site on the continental shelf off the west coast of Vancouver Island.

box at the base of the surface float. The system could operate for a period of 5 days before recharging was necessary.

In the experiment described here, ship noise data from the CSS W.E. RICKER were recorded as the ship followed the track shown in Figure 4. The noise data in 5s time windows were processed to obtain spectral components averaged over 25 s (Figure 4).

Two frequency bands were used in the inversion, a low frequency band from 73–113 Hz, and a higher band from 190–270 Hz. Lower frequencies below 70 Hz were not used because of contami-

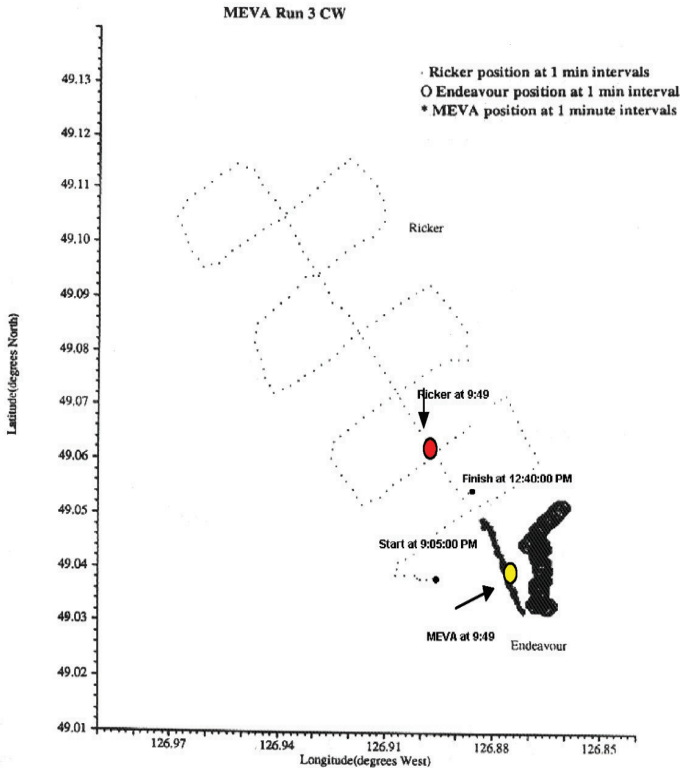


Figure 3. The position of ship (black circle) and array (white circle) on the experimental track. The range at this position was 3.3 km.

nation from other merchant ships in the nearby shipping channel. Twenty spectral components were averaged incoherently in the broadband inversions, so that the resolution in the lower band was 2 Hz, and 4 Hz in the higher band. The source and receiver positions were obtained from GPS (global positioning system) data that were recorded every two minutes at the source ship and at the array. The source-to-receiver ranges were determined from these data, with a maximum error of 100 m. We consider a section of the track where the bathymetry between the source ship and the VLA was range independent, and the source motion was tangential to the array. At this point, the recorded range between the array and the ship was 3.33 km. The VLA was freely drifting in the tidal currents during the experiment, and tilt meters on the array indicated that the array tilt was less than $1-2^\circ$. The drift was at most 25 m for the data analyzed here, based on the recorded GPS position.

The sound speed profile was measured using expendable sound velocity probes that were deployed during the experiment. Bathymetry was recorded on both ships, and these data were supplemented by archival data to determine the bottom profile along the track.

4 Inversion Method

The MF inversion algorithm consists of four components, the geoacoustic model, the high-resolution cross-correlation MF processor, a criterion to evaluate the geoacoustic models, and a search method to explore the model parameter space. For this application, we assume that the environment is range

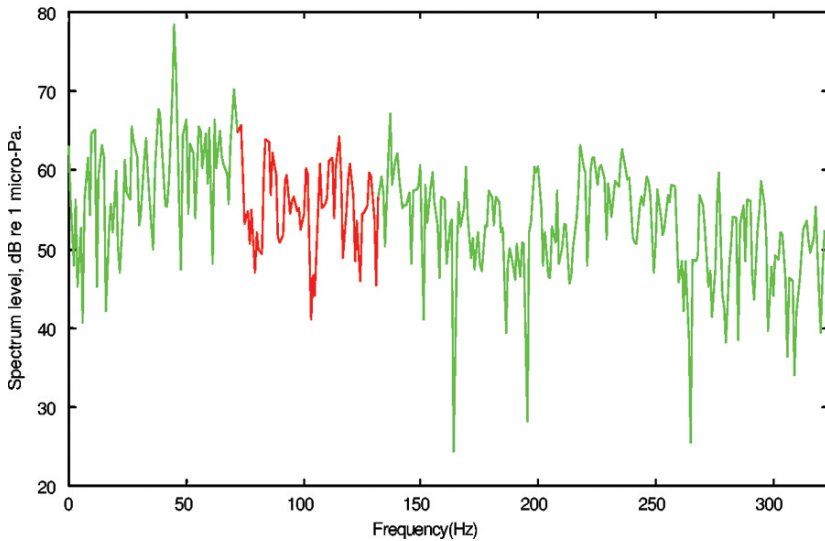


Figure 4. A sample of ship noise data from the experimental track. The low frequency band, 73–113 Hz, is highlighted in gray.

independent, and use the normal mode method ORCA [15] to calculate replica acoustic fields. Our approach for assessing the candidate geoacoustic models is based on backpropagation of the replica field at the array [16]. We calculate an ambiguity surface using the broad band crossrelation processor, by back propagating the measured field in environments defined by the candidate model parameters. The criterion for assessing the models is based on a focal function [16] (see Appendix). It is defined as the spatial variance of the backpropagated field with respect to the known source location in a neighbourhood around the source position. If the geoacoustic parameters are accurately modeled, the distribution of back-propagated energy about the source position is minimized. The estimated values for the geoacoustic model parameters are assumed to be those that minimize the focal function. Our experience has shown that this measure has greater resolution than a measure based on only the peak value of the ambiguity surface at the true source position. The dynamic range of the focal function is considerably greater than that for the ambiguity surface peak value, especially for parameters with very low sensitivity.

The search process in this inversion with broadband data is a simple grid search. We use a twostage inversion process that operates at each stage with a specific frequency band of the ship noise data. This simple approach is based on the depth dependence of acoustic wave penetration in the ocean bottom with respect to frequency. The sea floor parameters are estimated first using the high frequency band. For this band, we assume that the model parameters of the deeper layers are insensitive, and can be fixed at the nominal values during the inversion. The parameters of the first layer are then estimated using the lower frequency band, making use of the estimated values for the sea floor parameters from the first stage. The twostage frequency approach allows significant reduction of the search space at each stage, so that limited grid search methods with fewer parameters are effective. In principle, it would be possible to use very low frequencies below 70 Hz to estimate parameters for the deeper layers, but this was not attempted here because of contamination from shipping noise in this band.

5 Inversion of ship noise data

The geoacoustic model for the experimental site is shown in Figure 5. The layered structure of the model is based on results from an analysis of head wave data from another portion of the experiment that provided estimates of the sound speeds for the deeper layers [17]. However, since no sea floor head waves were observed in the experiment, there was no information about the geoacoustic properties of the sea floor or the first sediment layer. In this MF inversion, we estimate the water depth at the array and the sediment sound speed at the sea floor, and then the thickness of the first layer. The first two parameters are estimated in the initial stage of the inversion, using high frequency data in the band 190–270 Hz. For these frequencies, the bottom interaction is primarily with the sea floor. The thickness of the first layer is then estimated in the next stage using lower frequency data in the band 73–113 Hz for which there is more effective penetration to deeper depths. In calculating the replica fields, parameter values for the attenuations, densities and shear wave speeds were taken from the literature [18] or from ground truth data, and the water column sound speed profile was measured during the experiment. The nominal values of the model parameters are listed in Table 1.

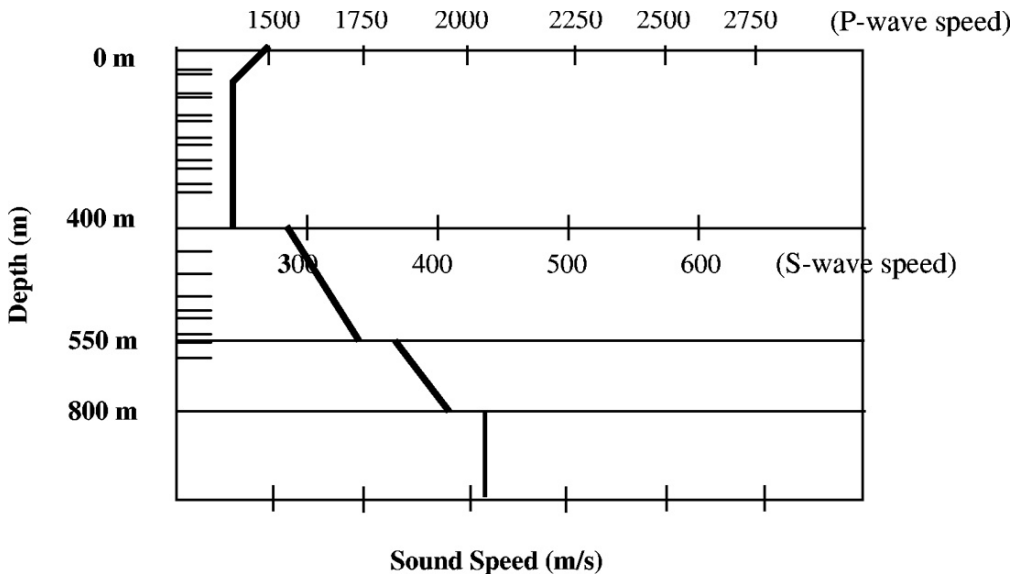


Figure 5. Multi-layer geoacoustic model of the bottom at the experimental site, indicating nominal values for the parameters.

Table 1. Nominal values of the geoacoustic model parameters.

Layer	Depth (m)	c_p (m/s)	c_s (m/s)	α_p (dB/ λ)	α_s (dB/ λ)	ρ (g/cm ³)
Sand-silt	0–150	1550–1700	100–350	0.2	0.5	1.6
Layer 2	150–300	1800–1950	350–500	0.2	0.5	1.8
Basement	(350+)	2100	550	0.2–10	0.5–10	2.1

In the first stage, the water depth and sea floor sound speed were searched over a grid of 30 values, six water depths and five sea floor sound speeds. The two-dimensional search ranges were 370–420 m with a resolution of 10 m for the water depth, and 1510–1590 m/s with a resolution of 20 m/s for the sound speed. The focal function was calculated for an ambiguity surface window from

3–4 km in range and 1–60 m in depth around the source location. The ambiguity surface windows indicate the degree of focus of the back-propagated fields and are displayed in Figure 6 for each pair of parameter values. Each row displays the focus for five values of the sea floor sound speed from 1510–1590 m/s. Water depth increases in each column from 370–420 m. The figure demonstrates how the model parameters interact in obtaining the focus. As expected, the backpropagated field is focused near the sea surface. Across each row as the sea floor sound speed changes, the focus is sharpened but the range does not change. In each column, the increasing water depth from 370 to 420 m causes the focal range to increase by about 200 m. This coupling between source range and water depth is consistent with the so-called mirage effect observed in MFP [19]. The strongest focus as a function of the two parameters is obtained in window 18, for values of 400 m for the water depth and 1550 m/s for the sea floor sound speed. The focal function that was computed from the data in Figure 6 is plotted versus search index in Figure 7. For reference, the first search index corresponds to the pair of values [370m, 1510 m/s], and the minimum value is obtained for index 18, [400 m, 1550 m/s].

Using these values in the second stage of the inversion, the thickness of the first layer was searched over a one-dimensional grid of 21 values from 50250 m, in steps of 10 m, using the high frequency data. The window size for the focal function calculations was the same as in the first stage. As indicated by the very limited dynamic range in the focal function for this grid search (Figure 8), the variation of the thickness of the first layer has little effect on the pressure field in the high frequency band. The first layer thickness was instead estimated using the ship noise in the lower frequency band. The ambiguity surface windows are displayed in Figure 9, and the focal function for the grid search using the same search parameters is shown in Figure 10. Each row in Figure 9 displays the focus for seven values of the layer thickness from 50250 m/s. The focus of the back-propagated field is again near the sea surface, but the depth resolution for the lower frequency band is significantly lower. The effect of the changing layer thickness is to sharpen the focus, with the best focus for a thickness of 100 m corresponding to search index 6.

The estimated values from the two stage inversion are consistent with the measured bathymetry of 400 m for the water depth at the array, and with the estimated depth of around 130 m for the sediment layer thickness based on the analysis of head wave data from shots from another segment of the experiment [17]. The inversion results for the sediment sound speed are in good agreement with the value obtained from waveform inversion of the shot data [20]. The sediment type inferred from grab samples in the vicinity is generally medium-grain silty sand. The estimated sound speed of 1550 m/s is consistent with the value expected for this type of sediment material.

The approach applied in this inversion makes the fundamental assumption that the model parameters are not strongly correlated, so that subsets of the parameters can be inverted in one frequency band while the values of other parameters are fixed. Although this assumption is flawed, the impact has been minimized to some degree by the frequency subspace method. For the high frequency band, only the sea floor parameters are sensitive, so that nominal values can be used for the parameters of the deeper layers. In using the lower frequency band for inverting the sediment layer thickness, we use the estimated sediment sound speed as an average value for the layer. This assumption is supported by the consistency of the estimated thickness with the estimate from the head wave data.

The validity of the geoacoustic model is demonstrated by using it for localization of a 45Hz CW signal that was transmitted from a projector that was towed during the source track shown in Figure 10. The source depth was about 30 m for the data sample. This scenario was selected in order to test the robustness of the geoacoustic model in predicting acoustic fields for frequencies outside the band that was used in the inversion. The ambiguity surface calculated using the cross-CR processor for the 45-Hz tonal is shown in Figure 11. The peak location is in excellent agreement with the location expected from the GPS data.

We note that the method assumes that the position of the ship is known. However, since the ship location can be estimated accurately using the high frequency band [10, 14], the method can be

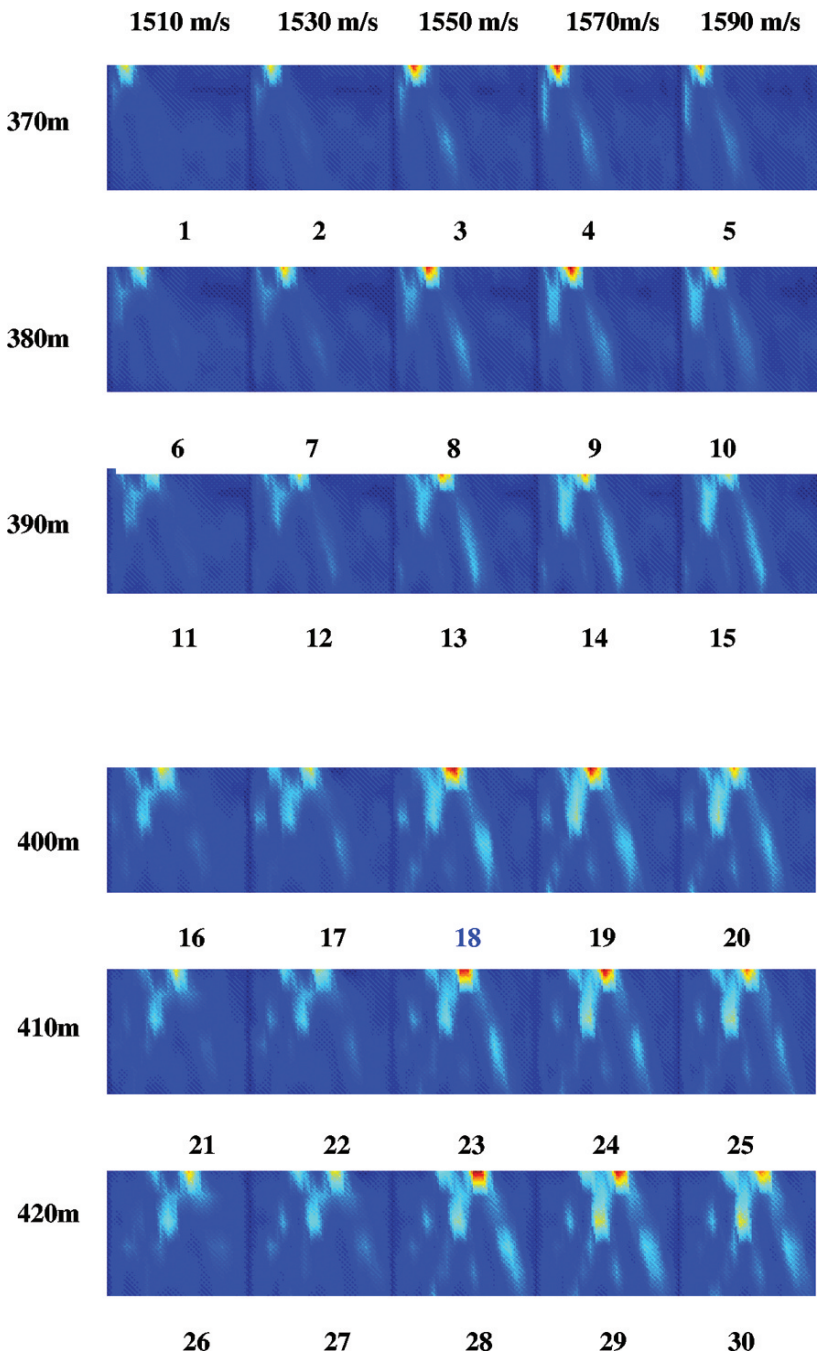


Figure 6. Ambiguity surface windows showing the focus of back-propagated signal near the source location for the high frequency band.

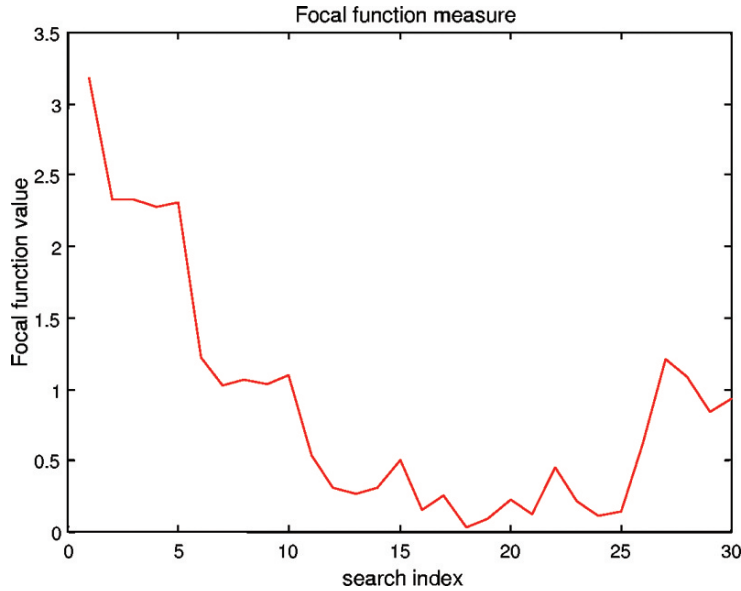


Figure 7. Focal function for the first stage of the inversion to estimate water depth and sediment sound speed. The estimated values corresponding to the minimum at search index 18 are 400 m and 1550 m/s for the water depth and sound speed, respectively.

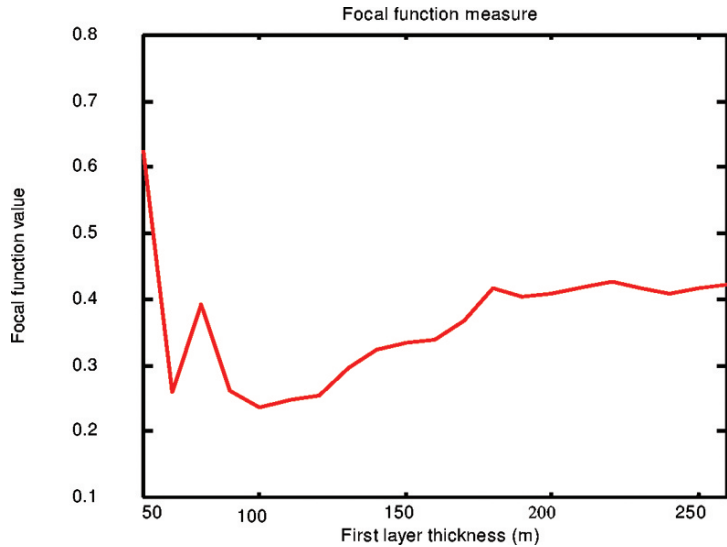


Figure 8. Focal function for the second stage of the inversion to estimate the thickness of the first sediment layer using the high frequency band. The dynamic range is small, and the minimum value is ambiguous between about 80 and 130 m.

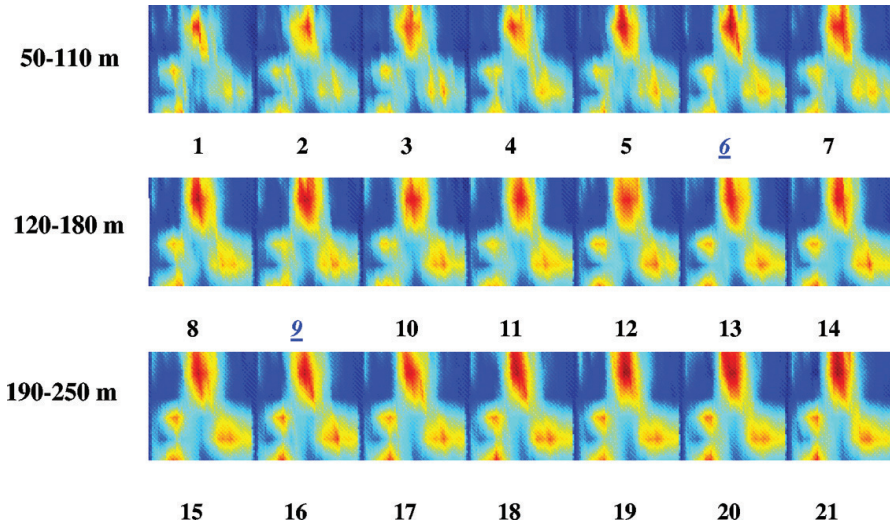


Figure 9. Ambiguity surface windows showing the focus of back-propagated signal near the source location for the second stage of the inversion using the low frequency band.

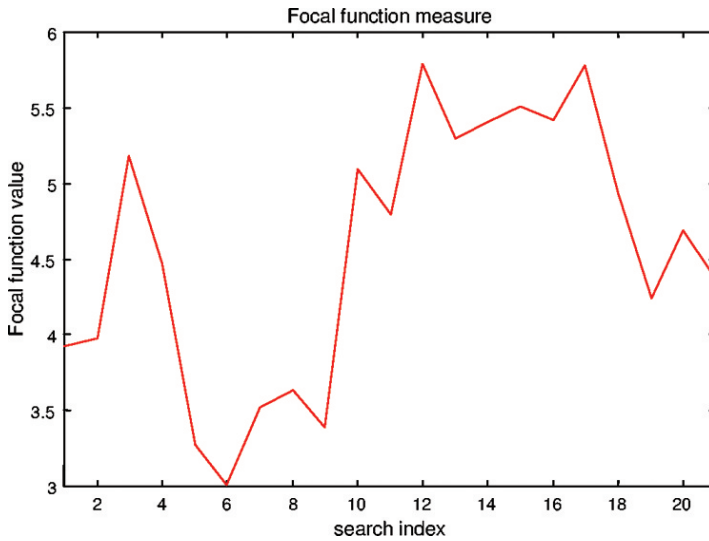


Figure 10. Focal function for the second stage of the inversion to estimate the sediment layer thickness using the ship noise in the low frequency band. The estimated value corresponding to search index 6 is 100 m.

adapted by inverting the experimental geometry simultaneously with the sea floor properties in the first stage of the inversion.

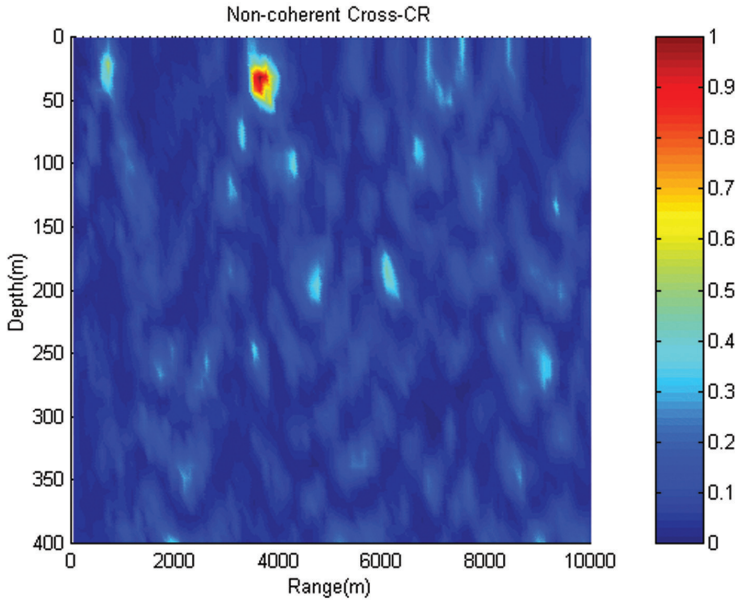


Figure 11. The ambiguity surface for a 45-Hz tonal, calculated using the estimated geoacoustic profile. The maximum value occurs at 3.6 km range and 30 m depth.

6 Discussion

This paper introduced a matched field processor based on the cross relation between measured and modeled signals at different sensors in an array. The processor was applied to invert broadband ship noise data in order to estimate geoacoustic model parameters at an experimental site. The inversion was carried out using a two stage process and a simple grid search to investigate candidate model parameters. First the parameters of the geoacoustic model at the sea floor were estimated using high frequency data for which depth penetration in the sediment is limited to within a few wavelengths of the water bottom, and subsequently a lower frequency band was used to estimate parameters of the first sediment layer. The performance of the method may be improved by using more efficient grid search algorithms, and lower frequencies to investigate deeper sediment layers.

Acknowledgements

This research was supported by a partnership program among the Natural Sciences and Engineering Research Council of Canada (NSERC), MacDonald-Detwiller (MDA), and the Department of National Defence of Canada (DND).

References

1. Jaschke L. and Chapman N. R., Matched field inversion of broad band data using the freeze bath method. *J. Acoust. Soc. Amer.* **106**, 1838–1851 (1999).
2. Chapman N. R. and C. E. Lindsay, Matched field inversion for geoacoustic model parameters in shallow water. *IEEE J. Oceanic Eng* **21**, 347–354 (1996).
3. Tolstoy A., Using matched field processing to estimate shallow water bottom properties from shot data in the Mediterranean Sea. *IEEE J. Oceanic Eng* **21**, 471–479 (1996).

4. Gerstoft P., Inversion of seismoacoustic data using genetic algorithms and a posteriori probability distributions. *J. Acoust. Soc. Amer.* **95**, 770–782 (1994).
5. Hermand J.-P. and Gerstoft P., Inversion of broad band multitone acoustic data from the Yellow Shark summer experiments. *IEEE J. Oceanic Eng* **21**, 324–346 (1996).
6. Caiti A., Jesus S. and Kristensen A., Geoacoustic seafloor exploration with a towed array in a shallow water area of the Strait of Sicily. *IEEE J. Oceanic Eng* **21**, 355–365 (1996).
7. Collins M. D., Kuperman W. A. and Schmidt H., Nonlinear inversion for ocean-bottom properties. *J. Acoust. Soc. Amer.* **92**, 2770–2783 (1992).
8. Lindsay C. E. and Chapman N. R., Matched field inversion for geoacoustic model parameters using adaptive simulated annealing. *IEEE J. Oceanic Eng* **18**, 224–231 (1993).
9. Fallat M. and Dosso S. E., Geoacoustic inversion via local, global, and hybrid algorithms. *J. Acoust. Soc. Amer.* **105**, 3219–3230 (1999).
10. Dizaji R. M., Matched field processing with broadband random sources, Ph.D. thesis, University of Victoria (2000).
11. Chapman N. R., Dizaji R. M. and Kirlin R. L., Matched field processing a blind system identification technique. In *Advanced Signal Processing Handbook*, edited by S. Stergiopoulos, (CRC Press, Boca Raton, 2001) pp. 4-1–4-31.
12. Knobles D. P., Koch R. A., Udagawa T. and Westwood E. K., The inversion of ocean waveguide properties using a nonlinear least squares approach. *J. Comput. Acoustics* **6**, 1–15 (1998).
13. Battle D. J., Gerstoft P., Kuperman W. A., Hodgkiss W. S. and Siderius M., Geoacoustic inversion of tow-ship noise via near field matched field processing. *IEEE J. Oceanic Eng* **28**, 454–467 (2003).
14. Dizaji R. M., Chapman N. R. and Kirlin R. L., A cross-relation based matched field processing technique for source localization with random noise sources. In *Proceedings IEEE Oceans99* (IEEE, Seattle, WA, USA, 1999), Vol. II, pp. 732–737.
15. E. K. Westwood, Tindle C. T. and Chapman N. R., A normal mode model for acousto-elastic ocean environments. *J. Acoust. Soc. Amer.* **100**, 3631–3645 (1996).
16. Dizaji R. M., Chapman N. R. and Kirlin R. L., A phase regulated back wave propagation technique for geoacoustic inversion. *J. Acoust. Soc. Amer.* **111**, 800–808 (2002).
17. Godin O. I., Chapman N. R., Laidlaw M. A. and Hannay D. E., Head wave data inversion for geoacoustic parameters of the ocean bottom off Vancouver Island. *J. Acoust. Soc. Amer.* **106**, 2540–2551 (1999).
18. Hamilton E. L., Geoacoustic modeling of the sea floor. *J. Acoust. Soc. Amer.* **68**, 1313–1340 (1980).
19. D'Spain G. L., Murray J. J., Hodgkiss W. S., Booth N. O. and Shey P. W., Mirages in shallow water matched field processing. *J. Acoust. Soc. Amer.* **105**, 3245–3265 (1998).
20. Chapman N. R. and Hannay D. E., Broadband matched field inversion for estimation of geoacoustic properties. In *Shallow Water Acoustics*, edited by R. Zhang and J. Zhou (China Press, Beijing, 1997), pp. 145–150.

Appendix: The focal function

The essence of the back wave propagation technique is the convergence of back propagated waves at the true source location. We assume that this occurs if the environmental model parameters are exactly matched to the true environment. However, for the condition of mismatch in the model parameters, there is generally a spatial distribution of the field around the source. This fact leads us to consider the energy distribution of the back-propagated field near the source as a criterion to determine the best match in the environmental model parameters. A measure of the field distribution is obtained by calculating the field spatial variance with respect to the true source location in a

window around the source. Its value is minimized when most of the signal energy concentrates at the source point, i.e., where a best match occurs.

Let us define $f(r, z)$, $|r - r_0| < \frac{N}{2}$, $|z - z_0| < \frac{M}{2}$ as the energy in a $M \times N$ spatial window around the true source location $S(r_0, z_0)$ where $\|f\| = 1$ (see Fig. A.1), and $\|\cdot\|_F$ denotes the Frobenius norm. The criterion is to minimize the spatial variance of the back-propagated field energy with respect to the true source location. If we denote $f(r, z) = \frac{|P_b^\alpha(r, z, \gamma)|^\beta}{\|P_b^\alpha(r, z, \gamma)\|_F^\beta}$ as the distance probability density function, the focal function criterion can be interpreted as the mean square distance from the true source location:

$$BWP_{criterion} = \frac{1}{MN} \sum_{m=-M/2}^{M/2} \sum_{n=-N/2}^{N/2} d^2(r, z) f(r, z),$$

where

$$d(r, z) = \sqrt{(r - r_0)^2 + (z - z_0)^2},$$

and $P_b(r, z)$ is the measured field.

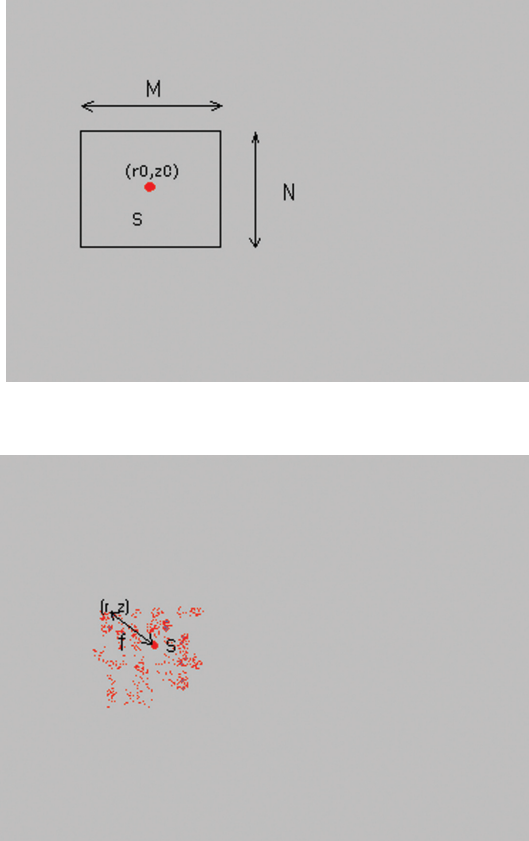


Figure A.1. (a) The convergence of back propagated wave energy for true environmental parameters (low spatial variance) and (b) in the case of mismatch (high spatial variance).

MATCHED-FIELD PROCESSING OF HUMPBACK WHALE SONG OFF EASTERN AUSTRALIA

AARON THODE, PETER GERSTOFT, MELANIA GUERRA, DALE STOKES

*Marine Physical Laboratory,
Scripps Institution of Oceanography, San Diego, USA*

MICHAEL NOAD

*School of Veterinary Science,
University of Queensland, St. Lucia, Queensland*

DOUGLAS C. CATO

Defence Science and Technology Organization, Sydney, NSW

Matched-field processing (MFP) is a technique for tracking an acoustic source in range and depth by comparing the output of an ocean acoustic propagation model with measured acoustic data collected across multiple hydrophones. In October 2003 a MFP experiment was conducted using humpback whale sounds recorded during the spring migration off the Sunshine Coast in Queensland, in conjunction with a larger experiment conducted by the Humpback Acoustic Research Collaboration (HARC). Humpback whale sounds with frequency content between 50 Hz to 1 kHz were recorded on a five-hydrophone vertical array deployed in 24 m deep water near Noosa, Queensland. The vertical array consisted of a set of flash-memory autonomous recorders attached to rope with an anchor at one end, and a subsurface float at the other. Acoustic data were simultaneously collected and monitored on five sonobuoys deployed over approximately 2 km range. The azimuth and range of the whale could be estimated via relative time-of-arrival measurements on the buoys. Using the range estimates as bounds on the matched-field processing, an inversion using the calls was performed on the vertical array data using a genetic algorithm. Inversion parameters included animal range, depth, and array geometry. Preliminary results of the inversion and resultant 3-D position fixes are presented. [Work supported by the US Office of Naval Research, Ocean Acoustic and Marine Mammal Programs]

1 Introduction

The annual spring migration of humpback whales off eastern Australia has been monitored visually and acoustically off the Sunshine Coast in Queensland for several years [1, 2, 3]. The 2003 field season was the first year of an expanded two-year research program called the Humpback Acoustic Research Collaboration (HARC). The organization and goals of HARC are presented elsewhere in

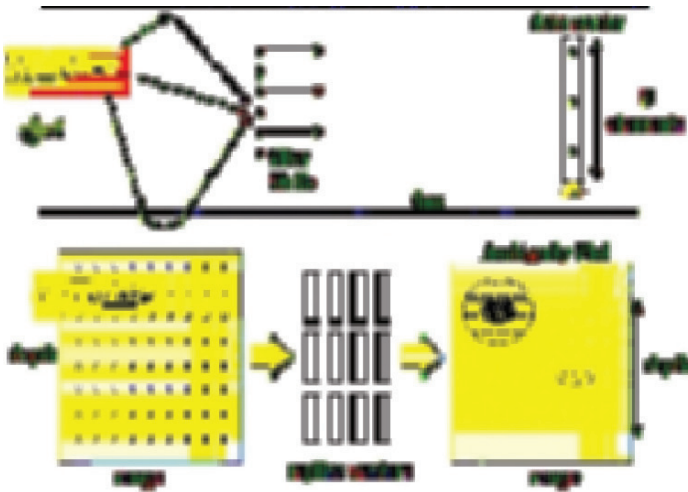


Figure 1. Concept of MFP.

this conference. Songs from singing whales are acoustically tracked by cross-correlating sounds from an animal across 3-5 hydrophones distributed over a 3 km aperture. The derived differences in a sound's arrival times are then used to generate a set of hyperbolas whose intersection yields an animal's range and azimuth from the array center.

In 2003 a six-hydrophone vertical array was deployed to determine whether matched-field processing (MFP) tracking methods could be applied to humpback whale song in shallow water, thus providing information about the depth of the singing animal. The term MFP is a general description of any tracking technique that involves a comparison between a measured acoustic field and a set of modeled fields computed with a propagation model [4, 5]. While MFP can take place with any array geometry, a vertical array provides a convenient and compact deployment for performing the technique [6]. Figure 1 illustrates how sound from an acoustic source is received on several hydrophones of a vertical array. Due to the effect of multipath from the ocean surface and bottom, the relative amplitude and phase of a given frequency component will vary between each hydrophone. To determine the range and depth of the source, a numerical model is run that simulates the acoustic field produced by a hypothetical source over a grid of ranges and depths. For each location the relative amplitude and phase of the chosen frequency component across the array is computed. The modeled fields are then correlated with the measured data, and the location that yields the highest correlation is selected as the true source range and depth. Thus this procedure, when combined with the azimuthal information provided by the distributed sonobuoy array, should provide a 3-D fix of the whale position.

In practice the ocean environment, including the sound speed profile and sediment properties, is not sufficiently characterised to enable an accurate numerical simulation. Thus a "focalization" technique can be used that treats the ocean bottom properties, array geometry, and water column sound speed profile as additional parameters to solve [7, 8]. As searching over this wide parameter space yields many local suboptimal matches, a global inversion technique such as a genetic algorithm [9] or simulated annealing [10] is typically used.

The MFP technique was successfully tested on blue whales in 1996 off the California coast, over frequency ranges between 17 and 112 Hz [11]. It was not clear, however, whether the technique would work at the higher frequencies characteristic of humpback whale song, an example of which is shown in Figure 2.

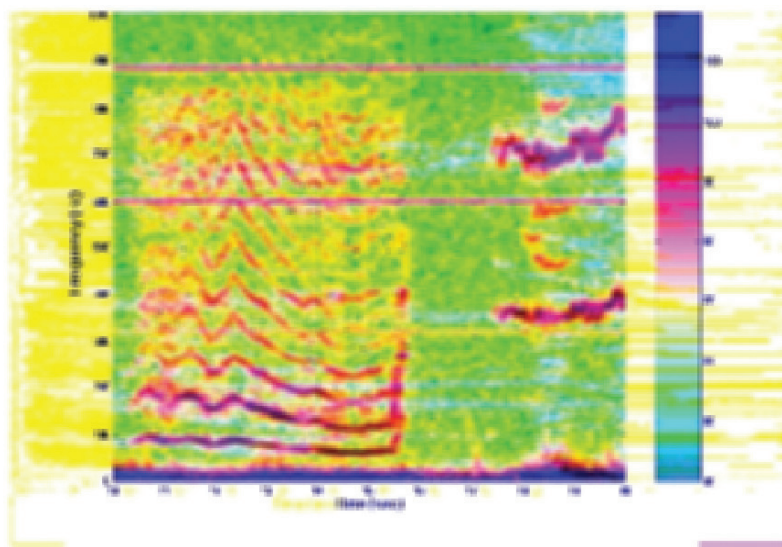


Figure 2. Spectrogram of humpback whale call used in MFP inversion. Note broadband energy content between 50-800 Hz.



Figure 3. Autonomous recorder used in vertical array deployment.

2 Experimental Setup

The vertical array was deployed over a period of two weeks in late October 2003 in 23 to 25 m deep water near Noosa, Queensland, about half a kilometer beyond the deepest hydrophone of the distributed array. The array consisted of six autonomous recorders taped to a rope. The system was anchored to the bottom with a plow anchor, and two subsurface floats kept the assembly straight. The entire system was light enough to be deployed and retrieved by hand from a small vessel.

The acoustic recorders are derived from a marine mammal tag designed by Bill Burgess of Greeneridge Sciences, Inc [12]. Each recorder uses 4 AAA batteries to sample sound at 16 bit resolution, and pressure, temperature, and two-way tilt at 1 Hz. The data are stored on a 1 Gb flash-memory chip, and the data are downloaded via IR port after the instruments are recovered. At a 2 kHz sampling rate the instruments can be deployed for around three days before they need to be recovered. An example of what the instrument looks like is shown in Figure 3.

During the observation period in question up to 40 pods a day passed by both array systems, of which at least five animals were singing close enough to the distributed array so that the range and azimuth of the singer could be estimated. On October 23, 2003 one animal was estimated to pass within 300 m of the vertical array, so this track was selected as a promising data set to apply the MFP technique, even though only four recorders were working at the time. The inversion software package SAGA [13] was used to perform the processing, using a normal-mode propagation code,

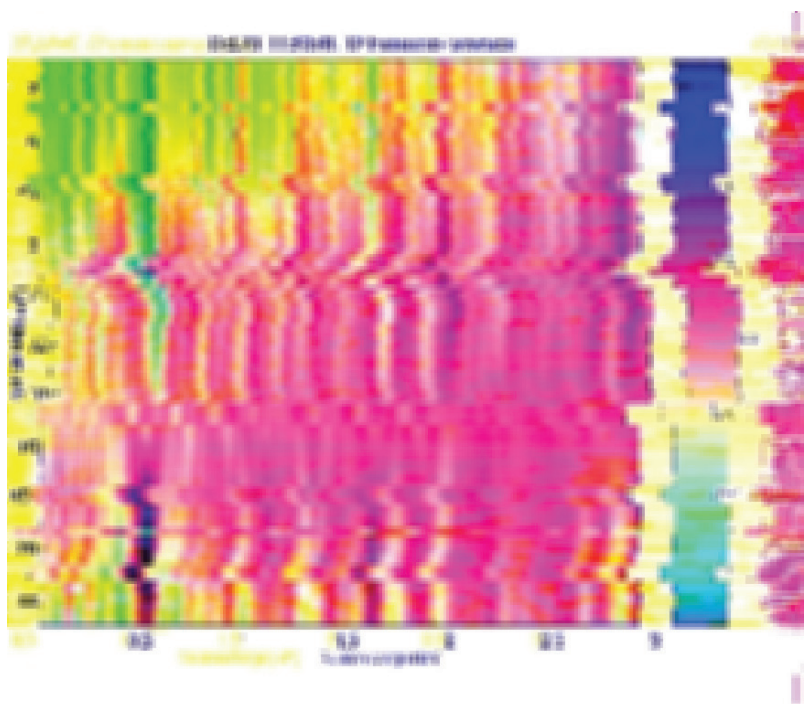


Figure 4. Plot of correlation between measured data and modeled acoustic field, as a function of range and depth, using 12 frequencies spaced between 100 and 1000 Hz.

a Bartlett MFP processor, and a genetic algorithm for a global optimization procedure. A typical global inversion takes about 15 minutes. The results were checked with simulations to ensure that the global inversion procedure was not prone to converging to false local minima.

3 Results

Figure 4 shows an ambiguity surface conducted on one call at 11:53, using 12 frequency components incoherently averaged using a Bartlett processor, which is simply the normalized correlation between the measured and modeled fields. A value of 0 indicates no matched between data and model, while a value of 1 indicates a perfect match. The animal seems to be located at 20 m depth at 633 m range. Contemporary hyperbolic fixing placed the animal at 510 m range. The animal seems to be only a few meters above the ocean bottom when making this call. Note that caution must be exercised when using relatively few hydrophones because one can obtain false locations with relatively high correlations, as seen in the figure.

4 Conclusions

Matched-field processing of humpback whale song has been demonstrated using a set of autonomous acoustic recorders attached to fishing gear. Future work will example other close approaches during times when more hydrophones were working, and in 2004 an eight-hydrophone array is planned to be deployed as part of the second year of HARC.

References

1. Noad M. J. and Cato D. H., Acoustic surveys of humpback whales: Calibration experiments off the east coast of Australia, *J. Acoust. Soc. Amer.* **112**, 2398 (2002).
2. Noad M. J. and Cato D. H., Comparison of acoustic and visual surveying of humpback whales off east Australia, *J. Acoust. Soc. Amer.* **108**, 2540 (2000).
3. Noad M. J., Cato D. H., Bryden M. M., Jenner M.-N. and Jenner C. S., Cultural revolution in whale songs, *Nature* **400**, 537 (2000).
4. Bucker H. P., Use of calculated sound fields and matched field detection to locate sound sources in shallow water, *J. Acoust. Soc. Amer.* **59**, 368–373 (1976).
5. Baggeroer A. B., Kuperman W. A. and Mikhalevsky P. N., An overview of matched field methods in ocean acoustics, *IEEE Journal of Oceanic Engineering* **18**, 401–424 (1993).
6. Booth N. O., Baxley P. A., Rice J. A., Schey P. W., Hodgkiss W. S., D'Spain G. L. and Murray J. J., Source localization with broad-band matched-field processing in shallow water, *IEEE Journal of Oceanic Engineering* **21**, 402–412 (1996).
7. Collins M. D., Fialkowski L. T., Makris N. C. and Perkins J. S., In 15th Int. Conference on Acoustics, (1995), pp. 223–226.
8. Collins M. D. and Kuperman W. A., Focalization: Environmental focusing and source localization, *J. Acoust. Soc. Amer.* **90**, 1410–1422 (1991).
9. Gerstoft P., Inversion of acoustic data using a combination of genetic algorithms and the Gauss-Newton approach, *J. Acoust. Soc. Amer.* **97**, 2181–2190 (1995).
10. Dosso S. E., Wilmut M. J. and Lapinski A. L. S., An adaptive-hybrid algorithm for geoacoustic inversion, *IEEE Journal of Oceanic Engineering* **26**, 324–336 (2001).
11. Thode A. M., D'Spain G. L. and Kuperman W. A., Matched-field processing and geoacoustic inversion of blue whale vocalizations, *J. Acoust. Soc. Amer.* **107**, 1286–1300 (2000).
12. Burgess W. C., The bioacoustic probe: A general-purpose acoustic recording tag, *J. Acoust. Soc. Amer.* **108**, 2583 (2000).
13. Gerstoft P., Saga users guide 2.0, an inversion software package, SACLANT Undersea Research Centre Research Report No. SM-333, 1997.

INVERSIONS OF HORIZONTAL AND VERTICAL LINE ARRAY DATA FOR THE ESTIMATION OF GEOACOUSTIC MODEL PARAMETERS

DAG TOLLEFSEN

*Norwegian Defence Research Establishment
Maritime Systems Division, Horten, Norway
E-mail: dag.tollefsen@ffi.no*

MICHAEL J. WILMUT AND ROSS CHAPMAN

*University of Victoria, School of Earth and Ocean Sciences
Victoria, British Columbia, Canada
E-mail: {mjwilmut,chapman}@uvic.ca*

This paper describes results from geoacoustic inversion of low-frequency acoustic data recorded at a receiving array divided into two sections, a sparse bottom laid horizontal array (HLA) and a vertical array (VLA) deployed in shallow water. The data are from an experiment conducted by the Norwegian Defence Research Establishment (FFI) in the Barents Sea. A two-layer range-independent geoacoustic model, consistent with seismic profiles from the area, described the environment. Inversion for geoacoustic model parameters was carried out using a fast implementation of the hybrid adaptive simplex simulated annealing (ASSA) inversion algorithm, with replica fields computed by the ORCA normal mode code. Low-frequency data from six shot sources at ranges 3-9 km from the array were considered. Estimates of sediment and substrate p-wave velocities and sediment thickness were found to be consistent between independent inversions of data from the two sections of the array.

1 Introduction

Inversion of acoustic field data for the estimation of seabed geoacoustic parameters has been a topic of considerable recent attention in underwater acoustics [1, 2]. The objective is to estimate environmental parameters relevant for use in acoustic propagation models for e.g., sonar performance predictions or matched-field localization. Several applications of matched-field inversion methods have been demonstrated using vertical array (VLA) data [3, 4]. The VLA has often been the preferred tool of research due to its ability to sample the spatial variability of the acoustic field with respect to depth in the water, which in general carries a high sensitivity to seabed parameters. The use of a horizontal line array (HLA) deployed on the sea floor [5] can be preferable in many practical respects, such as covertness, relative ease of deployment and stability of the array. A relevant question is whether similar sensitivity to seabed parameters can be obtained from HLA data.

FFI conducted an experiment in shallow water in the Barents Sea in 1999. The experiment made use of explosive sound (shot) sources and a 31-element acoustic array divided into two sections: a 21-element VLA spanning the lower two-thirds of the water column (water depth 320 m) and a 10-element HLA (length 820 m) at the seabed. This paper presents results from geoacoustic inversion of low-frequency acoustic data from both these arrays. Data from six sources at ranges 3-9 km from the arrays were considered. Inversion for geoacoustic model parameters was carried out using a fast implementation of the hybrid adaptive simplex simulated annealing (ASSA) inversion algorithm [6]. The experimental configuration provides a unique opportunity to compare the inversion performance of co-located vertical and bottom-moored horizontal line arrays.

The remainder of this chapter is organized as follows: the acoustic experiment and supporting geophysical measurements is described in section 2. The matched-field inversion method is described in section 3. Inversion of experimental data is described in section 4. Section 5 summarizes results.

2 The Experiment

The acoustic experiment was conducted using a vertical and horizontal array deployed in a relatively flat area of the Barents Sea. The geometry of the experiment and a bathymetry profile is shown in Fig. 1. The area of experiment was surveyed by geophysical equipment carried by the FFI research vessel R/V H U SVERDRUP II, including an echosounder, an airgun seismic system and SIMRAD TOPAS PS018 bottom penetrating sonar. The seismic profiles indicated a Quaternary sediment layer of thickness 20-35 m overlying consolidated sediment (siltstone) of several hundred meters thickness. An interpreted seismic section for the area is shown in Fig. 2. A seismic refraction velocity measurement indicated a compressional (p-wave) velocity of 2400 m/s for the siltstone layer. No in-situ measurements of Quaternary sediment properties were conducted at the site. Average p-wave velocity and density values were thus assigned based on measurements of deep cores of Quaternary sediment collected in the general region [7]. For p-wave attenuation, reference values from Hamilton [8] were assigned.

The baseline geoacoustic model developed for the site is shown in Table 1. The model consisted of a homogeneous fluid sediment layer over a fluid halfspace. A sound speed profile measured at the array site prior to the collection of acoustic data (Fig. 3) was used for the water layer. Shallow Signal Underwater Sound (SUS) explosive sources of types Mk-61 and Mk-64 were detonated at ranges from 3 km to 9 km from the VLA, in two directions endfire to the HLA. Data from six sources were selected for analysis; these are indicated in Fig. 1. Nominal source depths were 18 m, actual source depths were estimated by an analysis of measured bubble pulse periods. Nominal source ranges were determined by Global Positioning System (GPS) ranging.

Table 1. Baseline geoacoustic model.

<i>Layer</i>	<i>Thickness</i> [m]	<i>P-wave velocity</i> [m/s]	<i>P-wave attenuation</i> [dB/λ]	<i>Density</i> [g/cm ³]
Water	320	Profile	–	1.00
Sediment	20-35	1770	0.40	2.00
Substrate		2400	0.10	2.20

The vertical section of the array consisted of 21 hydrophones uniformly spaced 10 m apart. This 200 m long section was bottom moored, with the deepest element 4 m above the seabed. The horizontal section consisted of 10 hydrophones of geometric element spacing from 20 m to 240 m, total length 820 m, bottom-laid and oriented westward from the vertical array. The VLA position and HLA orientation was estimated from measured travel times from twelve explosive sources detonated in a circle of 2 km radius around the arrays. For estimation of array tilt, three current meters were attached near the top, middle and bottom of the vertical section.

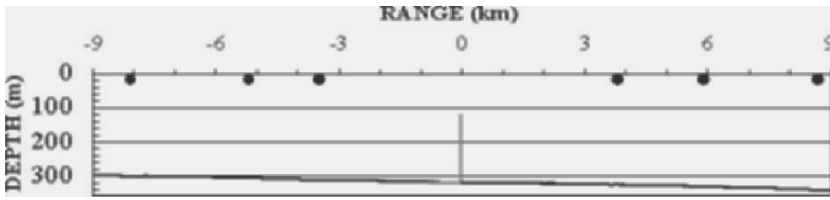


Figure 1. Bathymetry profile (solid black line), analyzed shots (black circles) and array (thick gray line at center of plot).

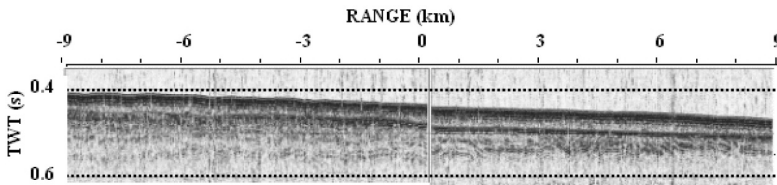


Figure 2. Seismic section from the site of experiment. The horizontal scale is from 9 km west (left edge of section) to 9 km east (right edge of section). The position of the VLA is at the center of the section. The vertical scale is two-way travel time in seconds, with the two dashed lines of the figure indicating 0.4 s (upper line) and 0.6 s (lower line) respectively. The dark gray line indicates the water-sediment boundary. The light gray line indicates a seismic reflector.

Data at two sets of frequencies were selected as such:

- *mf1*: five frequencies of 40.4, 58.5, 81.4, 97.1, and 127.5 Hz, selected at peaks of the frequency spectra,
- *mf2*: six frequencies from each of two 6-Hz wide bands centred at spectral peaks near 40.4 Hz and 70.8 Hz.

3 Inversion method

A matched-field geoacoustic inversion method was applied to synthetic and experimental VLA and HLA data from the present data set in [9]. This section contains a brief outline of the method.

3.1 Matched-field

Matched-field inversion is in essence a correlation process where the acoustic field measured at an array is matched with replica fields generated by an acoustic propagation model for a given model environment. A search over candidate models is performed, and the optimal model is taken to be the one yielding the best correlation or match with measured data. Match is here measured by an objective function based on the incoherent average over spatially coherent Bartlett processors at specific frequencies

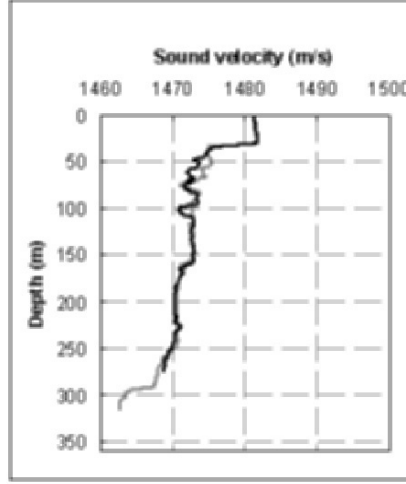


Figure 3. Sound velocity profiles in water, measured at array site before (gray line) and after (black line) collection of acoustic data.

$$E(m) = 1 - \frac{1}{M} \sum_{k=1}^M \left[\frac{\left| \sum_{j=1}^N p_j^+(f_k) q_j(m, f_k) \right|^2}{\sum_{j=1}^N |p_j(f_k)|^2 \sum_{j=1}^N |q_j(m, f_k)|^2} \right] \quad (1)$$

where j is a summation index over N hydrophones (summation in depth for a VLA and in range for a HLA), k is a summation index over M frequencies, p the measured complex pressure field, q the replica pressure field for model m at frequency f_k and $+$ is the complex conjugate. The objective function takes values between 0 and 1, with 0 indicating a perfect match.

3.2 Search algorithm

The search for an optimal seabed model is facilitated using the adaptive simplex simulated annealing (ASSA) algorithm [6]. The method combines a global random search method (simulated annealing) with a local directed search method (downhill simplex), using an adaptive adjustment of the search space for maximum efficiency. There are a few control parameters; the most crucial are the initial temperature (T_0), temperature reduction factor (β), and maximum number of temperature steps in simulated annealing. The method has been validated using synthetic data from geoacoustic inversion workshops for range-independent [10] and range-dependent [11] environments.

3.3 Seabed representation

The baseline geoacoustic model for the environment at the experimental site was described by two range independent fluid layers. For the inversions in this paper, the model included the following features: (i) a constant-gradient p-wave velocity profile in sediment, the gradient restricted to positive values, (ii) an equivalent flat bathymetry approximation to a sloping bottom and (iii) no variation of

sediment thickness with range. In addition, a single measured sound speed profile was used in water. This permitted use of a range-independent propagation model in replica field computations.

3.4 Forward model

The normal mode acoustic propagation model ORCA [14] for range-independent media was used to compute replica pressure fields. The model correctly accounts for attenuation and shear wave effects as well as near-field effects due to leaky (continuous) modes. The model can also be executed in a fast real-axis mode using a perturbation approach to approximate modal attenuations and ignoring the two other effects. The most recent version of this code was included in the implementation of the ASSA inversion algorithm developed for the present work.

3.5 Model parameters

The seven geoaoustic model parameters included in the inversions and their search bounds are listed in Table 2. P-wave attenuation in the substrate was held fixed at the baseline value.

Table 2. Model geoaoustic parameters and search bounds.

<i>Parameter</i>	<i>Symbol</i>	<i>Unit</i>	<i>Lower Limit</i>	<i>Upper Limit</i>
Sediment thickness	h	m	1.0	50
Sediment p-velocity top	c_{1T}	m/s	1480	1900
Sediment p-velocity bot	c_{1B}	m/s	1480	1900
Substrate p-velocity	c_2	m/s	1900	3800
Sediment density	ρ_1	g/cm ³	1.50	2.20
Substrate density	ρ_2	g/cm ³	1.50	2.40
Sediment p-wave attenuation	α_1	dB/ λ	0.10	0.80

The geometric parameters included in the inversions are listed in Table 3. To account for a small slope in bathymetry, the following approach was adopted. The effective water depth for an equivalent flat bathymetry [12] was computed for each source range:

$$D \equiv \left(\frac{1}{r_s} \int_0^{r_s} \frac{dr}{d^2(r)} \right)^{-1/2}. \quad (2)$$

In this equation, r_s is the source range and $d(r)$ is the measured bathymetry. A small search interval around the water depth computed from Equation (2) (for each source) was included to represent the possibility of a constant offset in measured bathymetry. For the resulting model water depth D , source depths and VLA element depths were then scaled [13] with the water depth ratios by:

$$z_{se} = z_s D / H_s ; z_{re} = z_r D / H_r \quad (3)$$

with z_s the nominal source depth and H_s the measured water depth at the source position, z_r the nominal element depth, and H_r the measured water depth at the array site. Finally, a straight-line tilt was included as a search parameter for the VLA. For the HLA, all elements were set to the model water depth.

Table 3. Model geometric parameters and search bounds.

<i>Parameter</i>	<i>Symbol</i>	<i>Unit</i>	<i>Lower Limit</i>	<i>Upper Limit</i>
Water depth ^a	<i>D</i>	m	-6.5	+6.0
VLA tilt	<i>T</i>	deg	-3.0	+3.0
Source range ^a	<i>r</i>	m	-80	+85

^aRelative to a nominal value.

4 Inversion of experimental data

4.1 Inversion details

Separate inversions were run using data from six sources (one source at a time) for the two sets of frequencies. Inversions were run using the ASSA with initial temperature $T_0 = 0.30$, reduction factor $\beta = 0.975$, five perturbations at each of maximum 500 temperature steps and a maximum of 300 additional local downhill steps after quenching (the temperature set to zero). The ASSA inversions converged after about 250 temperature steps and an additional 300 local downhill steps, with a total number of 6000-7000 calls to the forward model (accepted and rejected models). Using our fast implementation of the ASSA code, the inversions (for data set *mf1*) took less than two minutes on a Pentium III 1.0 GHz laptop computer. The HLA inversion converged after about the same number of iterations but in this case took ten to fifteen minutes; for the HLA inversions, the ORCA model was run in the more time consuming complex mode to correctly model media attenuations and near-field effects for the present situations.

4.2 Parameter sensitivity

One-dimensional plots of the value of the objective function (Equation (1)), hereafter denoted model energy, versus geoacoustic model parameter value are provided for three shots from inversions of data set *mf1* in Figs. 4 and 5 for the VLA and HLA respectively. Each individual frame displays energy versus parameter value for all accepted models. From left to right are the seven geoacoustic parameters of each problem (Table 2); from top to bottom are sources E8, E5 and W3¹. A total of about 1500 accepted models are included in each frame.

The relative widths of the distributions near the minimum energy give an indication of model parameter sensitivity. In this case, the most sensitive parameters are the sediment p-wave velocity (top and bottom) and sediment thickness. Sensitivity to substrate p-wave velocity is less, while densities are not sensitive parameters. For HLA data, parameter estimates and sensitivity to individual model parameters is similar to that observed for VLA (except for source W3). An observation of interest is that sensitivity of sediment attenuation increases slightly with source range; this is indicated in inversions both of VLA and HLA data. Sensitivities for inversions using data set *mf2* data were qualitatively similar; these will not be shown here.

4.3 Parameter estimates

Parameter estimates are tabulated in Tables 4 to 7. The listed values are those of the lowest energy model from each inversion. Substrate density and geometric parameters are not included in the tables.

Estimates of p-wave velocity in sediment are in all cases considerably lower than the baseline model value of 1770 m/s (Table 1). Using data set *mf1*, gradients in p-wave velocity are estimated differently by VLA and HLA data. A strong gradient of p-wave velocity in sediment is estimated by use of VLA data, this is weaker or absent when using HLA data. This discrepancy is not seen when

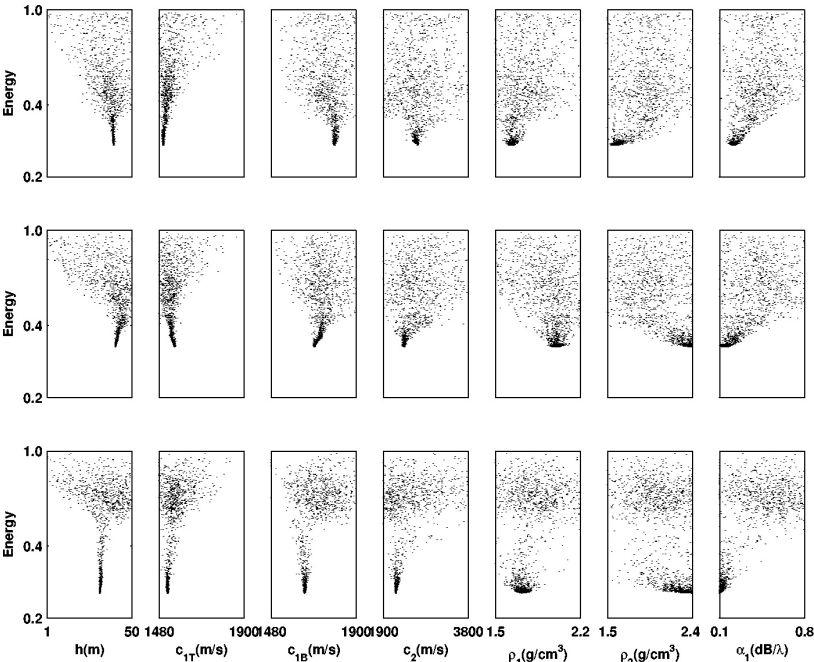


Figure 4. Model parameter sensitivity for experimental data received at a 21–element VLA. Results are from inversions of multi-frequency data (set *mf1*) at source range 8.7 km (upper frames), 5.9 km (middle frames) and 2.9 km (lower frames). Each dot represents a model accepted by ASSA.

using data set *mf2*. Estimates of substrate p-velocity uctuate between values below and above the baseline value of 2400 m/s.

The energy of the best model obtained by inversions of data set *mf1* from the shots E3 and W5 on the HLA (Table 5) is above 0.50 which is considered high. High energies in inversions can be related to (i) the quality of data, (ii) inaccuracies in model geometry (inexact knowledge of array element positions), (iii) simplifications in the geoacoustic model, and (iv) the ability of the sparse HLA to sample the acoustic fields for varying source-array ranges. These were the two Mk-61 sources detonated closest in range to the HLA, thus data were slightly saturated on a number of hydrophones in these cases.

Table 4. Geoacoustic parameter estimates by inversion of VLA data set *mf1*.

Shot	h	c_{1T}	c_{1B}	c_2	ρ_1	α_1	E
W8	45.2	1515	1864	2385	2.00	0.28	0.27
W5	40.3	1503	1789	3535	1.77	0.34	0.31
W3	31.5	1523	1645	2182	1.72	0.10	0.25
E3	42.4	1596	1596	2987	2.11	0.42	0.41
E5	40.6	1558	1694	2378	2.00	0.14	0.32
E8	39.6	1501	1794	2671	1.63	0.22	0.27

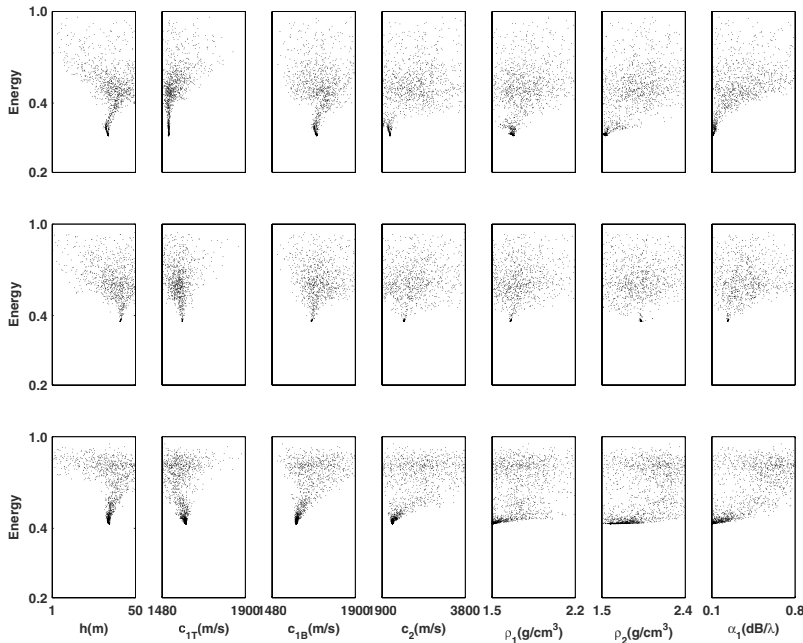


Figure 5. Model parameter sensitivity for experimental data received at a 10–element HLA. Results are from inversions of multi-frequency data (set *mf1*) at source range 8.7 km (upper frames), 5.9 km (middle frames) and 2.9 km (lower frames). Each dot represents a model accepted by ASSA.

Table 5. Geoacoustic parameter estimates by inversion of HLA data set *mf1*.

<i>Shot</i>	<i>h</i>	<i>c</i> _{1<i>T</i>}	<i>c</i> _{1<i>B</i>}	<i>c</i> ₂	ρ_1	α_1	E
W8	42.5	1615	1703	2203	1.54	0.11	0.26
W5	47.6	1524	1843	3421	2.10	0.10	0.50
W3	34.6	1601	1601	2140	1.51	0.10	0.42
E3	47.1	1681	1682	2165	2.13	0.25	0.54
E5	41.0	1582	1678	2393	1.65	0.23	0.38
E8	34.0	1512	1705	2080	1.68	0.11	0.29

4.4 VLA and HLA comparison

The parameter estimates from the best energy models from each VLA and HLA inversion are plotted in Figures 6 and 7 for selected geometric and geoacoustic model parameters, for data sets *mf1* and *mf2* respectively. In the Figures, reference values for water depth, sediment thickness and p-wave velocities (from Table 1) are included. The reference water depth is the effective depth computed from Equation (2) using a measured bathymetry profile. There is good agreement between these reference values and the model water depths obtained from inversions. This suggests the validity of the equivalent flat bathymetry approximation for this environment. The reference values for sediment thickness are based on measured two-way seismic travel times and a p-velocity in sediment of 1600 m/s. For sediment thickness, estimates vary between 32–42 m, in good agreement with these reference values. Estimates of p-wave velocity in sediment are the mean (depth-averaged) values.

Table 6. Geoacoustic parameter estimates by inversion of VLA data set *mf2*.

<i>Shot</i>	<i>h</i>	c_{1T}	c_{1B}	c_2	ρ_1	α_1	E
W8	43.1	1503	1801	2192	2.20	0.21	0.20
W5	37.0	1486	1755	2223	1.89	0.13	0.21
W3	36.4	1501	1720	2309	1.83	0.10	0.17
E3	32.1	1513	1648	2145	1.91	0.11	0.27
E5	45.7	1502	1809	2512	2.20	0.21	0.34
E8	42.7	1483	1836	2236	2.14	0.17	0.27

Table 7. Geoacoustic parameter estimates by inversion of HLA data set *mf2*.

<i>Shot</i>	<i>h</i>	c_{1T}	c_{1B}	c_2	ρ_1	α_1	E
W8	39.7	1495	1795	2023	2.02	0.27	0.29
W5	35.5	1582	1641	2210	2.20	0.10	0.31
W3	37.8	1481	1757	2331	1.95	0.34	0.39
E3	33.3	1481	1718	2235	2.02	0.10	0.47
E5	48.8	1509	1851	2132	2.13	0.10	0.34
E8	36.3	1526	1747	3194	1.65	0.27	0.31

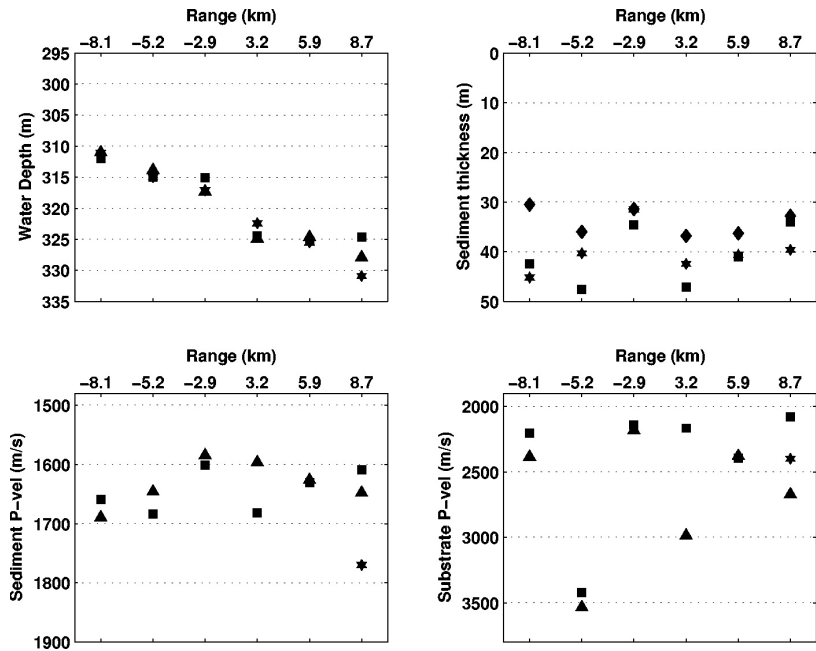


Figure 6. Estimates of geometric and geoacoustic model parameters by matched-field inversion of shot data (set *mf1*) recorded at a 21-element VLA (triangles) and endfire to a 10-element HLA at the seabed (squares). Six sources, range to the VLA (positive eastward) indicated. Reference values (stars) are from the baseline geoacoustic model.

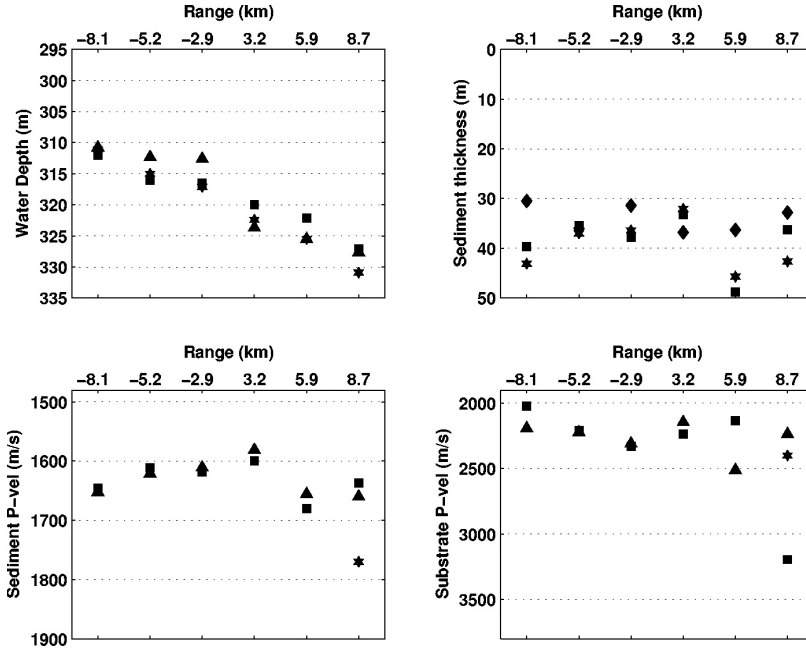


Figure 7. Estimates of geometric and geoacoustic model parameters by matched-field inversion of shot data (set *mf2*) recorded at a 21-element VLA (triangles) and endfire to a 10-element HLA at the seabed (squares). Six sources, range to the VLA (positive eastward) indicated. Reference values (stars) are from the baseline geoacoustic model.

A good agreement of mean values of 1580–1660 m/s is obtained in all inversions. Estimates of p-wave velocity in substrate are within 2100–2390 m/s in most cases. For both p-wave velocity parameters, the estimates obtained by inversion of acoustic data are lower than the baseline model values.

The results indicate comparable inversion performance for the VLA and HLA. In order to understand this, we can develop a simple means for comparison between the two array configurations. For a VLA, the inversion performance depends on how well the array samples the higher order bottom interacting modes. In this case, the array spans the lower two-thirds of the water column and effectively samples the entire modal spectrum across the frequency band. For comparison, we can define an effective vertical aperture for the HLA as

$$L_{eff} = L \tan \phi \quad (4)$$

where L is the horizontal array length and ϕ is the propagation angle of the mode [15]. Using a value of $\phi = 20^\circ$ for the highest order mode, we get an effective vertical aperture of 300 m, equivalent to the water depth. We can thus assume that the length of the HLA is sufficient to provide similar sampling of the bottom interacting modes.

A second factor that needs to be taken into consideration [16] is the ability of the array to represent the number of modes contributing to the acoustic field at the array. For the 21-element VLA, the number of elements exceeds the number of modes for all frequencies used in the inversions, and good performance can be expected. For the ten-element HLA, the requirement is not fulfilled at the higher frequencies of data set *mf1*. This may cause degraded performance and in part explain the relatively poor results observed for inversion of short-range *mf1* data on the HLA.

5 Summary

Low-frequency acoustic data from shot sources endfire to a sparse ten-element HLA at the seabed and a 21-element VLA have been inverted for geoaoustic model parameters. Data at frequencies within 40-128 Hz from six sources deployed at ranges from 3 km to 9 km in two directions from the array were used. A range-independent seabed model consisting of a fluid sediment layer over a fluid halfspace was used for the area, consistent with prior geophysical information. A fast implementation of the hybrid adaptive simplex simulated annealing (ASSA) inversion algorithm was used, with replica fields computed by the ORCA normal mode propagation model.

Results from independent inversions of VLA and HLA data were consistent between the six shots. An average p-wave velocity in sediment of 1580-1660 m/s was estimated, with a fairly strong positive gradient. Substrate p-wave velocity was estimated to 2100-2390 m/s. These estimated values are lower than the baseline geoaoustic model values of 1770 m/s and 2400 m/s respectively. For sediment thickness, estimates were in reasonable agreement with values of the baseline geoaoustic model.

The consistency of geoaoustic model parameter estimates obtained from separate inversions of HLA and VLA data is the main result achieved in this paper. This suggests that in situations where data from a vertical array is not available, data from sources endfire to a horizontal array at the seabed can alternatively be used for geoaoustic inversion. An array of some minimum length and number of elements in relation to processing frequencies is required.

Notes

1. For the following, the sources will be labelled from W8 (for the shot at 8 km to the west of the array) to E8 (for the shot at 8 km east of the array).

References

1. Chapman R. and Taroudakis M. (eds.), Geoaoustic inversion in shallow water. *J. Computat. Acoustics* **8**(2), (2000).
2. Gerstoft P., Inversion of seismoacoustic data using genetic algorithms and a posteriori probability distributions. *J. Acoust. Soc. Am.* **95**, 770-781 (1994).
3. Dosso S. E., Jeremy M. L., Ozard J. M. and Chapman N. R., Estimation of ocean bottom properties by matched-field inversion of acoustic field data. *IEEE J. Oceanic Eng.* **18**, 232-239 (1993).
4. Lindsay C. E. and Chapman N. R., Matched field inversion for geoaoustic model parameters using adaptive simulated annealing. *IEEE J. Oceanic Eng.* **18**, 224-231 (1993).
5. Knobles D. P., Koch R. A., Thompson L. A., Focke K. C. and Eisman P. E., Broadband sound propagation in shallow water and geoaoustic inversion. *J. Acoust. Soc. Amer.* **113**, 205-222 (2003).
6. Dosso S. E., Wilmut M. J. and Lapinski A.-L. S., An adaptive-hybrid algorithm for geoaoustic inversion. *IEEE J. Oceanic Eng.* **26**, 324-336 (2001).
7. J. Settem, Acoustic properties of Quaternary sediments in the Barents Sea. IKU Petroleumsforskning, Trondheim, Norway, Rep. 23.2579.00/01/96 (1996).
8. Hamilton E. L., Geoaoustic modeling of the sea floor. *J. Acoust. Soc. Amer.* **68**, 1313-1340 (1980).
9. Tollefsen D., Wilmut M. J. and Chapman N. R., Estimates of geoaoustic model parameters from inversions of horizontal and vertical line array data. *IEEE J. Oceanic Eng.*, submitted (2004).
10. Tolstoy A., Chapman N. R. and Brooke G. H., Benchmarking geoaoustic inversion methods. *J. Computat. Acoustics* **6**(1/2) 1-28 (1998).

11. Chapman N. R., Chin-Bing S., King D. and Evans R. B., Benchmarking geoacoustic inversion methods for range dependent waveguides. *IEEE J. Oceanic Eng.* **28**, 320–330 (2003).
12. Zakarauskas P., Dosso S. E. and Fawcett J. A., Matched-field inversion for source location and optimal equivalent bathymetry. *J. Acoust. Soc. Amer.* **100**, 1493–1500 (1996).
13. Harrison C. H. and Siderius M., Effective parameters for matched field geoacoustic inversion in range-dependent environments. *IEEE J. Oceanic Eng.* **28**, 432–445 (2003).
14. Westwood E. K., Tindle C. T. and Chapman N. R., A normal mode model for acousto-elastic ocean environments. *J. Acoust. Soc. Amer.* **100**, 3631–3645 (1996).
15. Bogart C. W. and Yang T. C., Source localization with horizontal arrays in shallow water: Spatial sampling and effective aperture. *J. Acoust. Soc. Amer.* **96**, 1677–1686 (1994).
16. Tantum S. L. and Nolte L. W., On array design for matched-field processing. *J. Acoust. Soc. Amer.* **107**, 2101–2111 (2000).

ISSUES OF ENVIRONMENTAL VARIABILITY IN INVERSE PROBLEMS IN OCEAN ACOUSTICS

DAVID P. KNOBLES, MASON GRAY, ROBERT A. KOCH AND ADAM COOK

*Applied Research Laboratories
The University of Texas at Austin
P. O. Box 8029
Austin, TX 78758*

Discussed are examples of range-dependent sound propagation in littoral seas that yield insight on the ability to design an inverse problem to estimate properties of the seabed. Broadband acoustic data at two locations collected along propagation paths whose water depth is not constant are modeled using information from geo-acoustic inversion analyses along approximately constant water depth propagation paths. An example of the effects of surface roughness on an infinite 3-D wedge are presented that raises the issue of the coupling between the effects of scattering and seabed attenuation in 3-D environments.

1 Introduction

In littoral seas, environmental variability in range, azimuth, and time are factors that can affect the ability to use experimental acoustic data as part of an inversion and propagation analysis to estimate properties of the seabed. The Geo-acoustic Inversion Workshop on inversion in range-dependent environments [1] was an important step for the ocean acoustics community in investigating the feasibility of conducting geo-acoustic inversion in range-dependent environments. However, the knowledge base for defining an inverse problem in realistic littoral ocean environments is still far from mature. It is thus helpful to examine both real and simulated data that aid in revealing some of the difficulties that a general inversion approach must address.

This paper examines three cases involving range-dependent acoustic propagation. Two cases involve measured acoustic data while a third case involves simulated data. The first data set considers range-dependent propagation upslope to a bottom-mounted horizontal line array (HLA) oriented perpendicular to the slope of the seabed. Employing a measured sound speed profile (SSP) at two locations along the propagation path and a geo-acoustic profile obtained from the analysis of acoustic data along a bathymetry contour, the predictability of both broadband acoustic data generated from an impulsive source and multi-tonal data are examined. In a second data set, the ability to predict broadband acoustic data generated from impulsive sources for both upslope and downslope propagation paths is considered. Here, issues of a range-dependent geo-acoustic profile are considered. Finally, for a wedge shaped waveguide the effects of surface roughness are demonstrated for a propagation direction where there exist both a forward and a refracted path for each acoustic mode. No inversion results for these three cases using a methodology such as simulated annealing are presented. Rather

the point of this paper is to demonstrate by example classes of problems that need to be addressed in order to define a meaningful inverse problem in typical littoral seas.

2 Examples of effects on propagation from range and azimuth variability

2.1 Propagation Along Sloped Soft Seabed

Figure 1 shows the waveguide geometry and the location of sources and receivers for the range-dependent component of an acoustic experiment that occurred in the Gulf of Mexico in 1998 about 100 km south of Port Aransas, TX. The acoustic data were collected on a bottom mounted HLA in about 110 m of water, and the sources included light bulb implosions and a towed continuous wave (CW) projector with frequency tonals at 53, 103, 153, and 503 Hz. The depth of both the CW and light bulb source was 30 m. Previous studies were made for the range-independent component of the experiment where received time series data generated by light bulb implosions [2] and the received broadband noise of a moving surface ship [3] were analyzed for the information they contained on the geo-acoustic structure of the seabed. The geo-acoustic properties of the seabed include a sound speed ratio at the water sediment interface of about 0.97 and a thick sediment that has a sound speed gradient of between 1.5 and 1.75 s⁻¹. With a small sediment attenuation (on the order of 0.01-0.02 dB/m-kHz) low loss refracted energy is returned to the seabed resulting in very low transmission loss (TL) below 500 Hz. The validation of the geo-acoustic profile includes a large measure of geophysical ground truth, source localization by matched field processing, the ability to predict CW data not used in the inversion, and previous inversion and propagation analyses of experiments in the same region. This is one littoral area where the average geo-acoustic properties are well known.

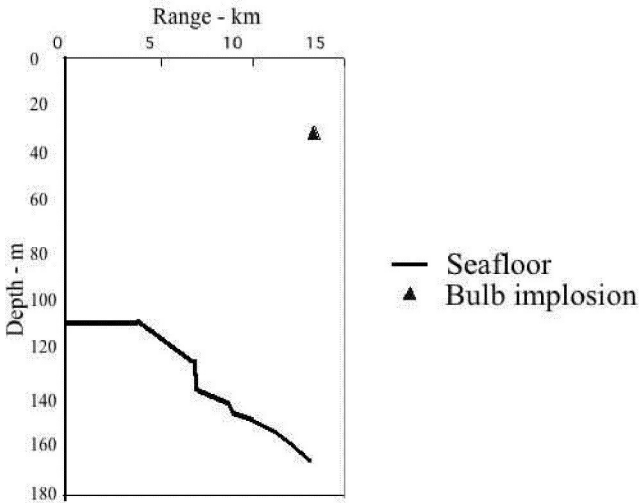


Figure 1. Waveguide geometry and location of sources and receivers.

An obvious question is how well does an acoustic propagation model using a geo-acoustic profile obtained from acoustic data collected along a constant water depth propagation path [2, 3] predict the propagation for paths across the sloped bathymetry in Fig. 1? The range-dependent acoustic data are received time series, generated from a light bulb implosion in about 160 m of water, and TL versus range derived from the received time series from a multi-tonal source.

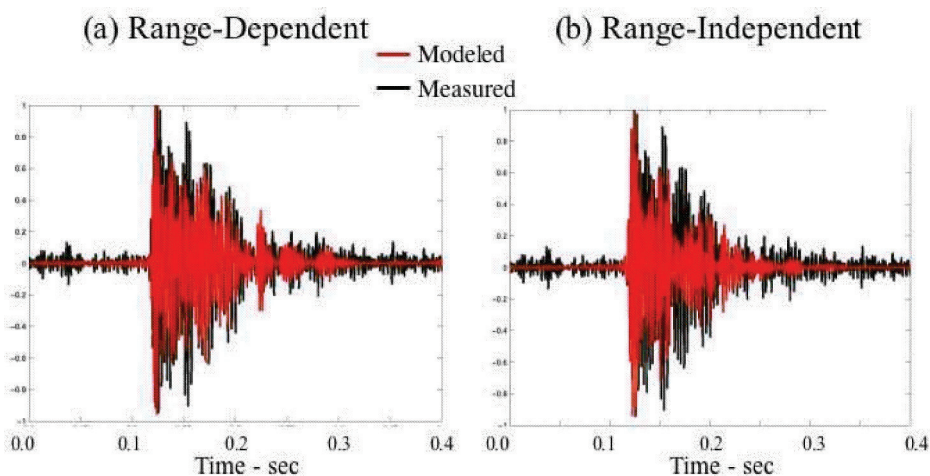


Figure 2. Comparison of measured and modeled time series in 50-500 Hz band.

Figure 2 shows a comparison between measured and modeled time series received on one of the hydrophones of the HLA for the propagation geometry in Fig. 1. The frequency band is 50-500 Hz. The simulated time series was produced using the RAM parabolic equation algorithm [4] by inverse Fourier transforming the product of the frequency response and a measured source spectrum for a light bulb. The modeled time series in Fig. 2(a) includes the sloping bathymetry in Figure 1, whereas Fig. 2(b) is the result when the water depth is fixed at the receiver depth. In Fig. 2(a) there is overall good agreement between the measured and the simulated time series whereas Fig. 2(b) demonstrates that neglecting the variable bathymetry causes the modeled time series to be truncated. A tentative conclusion is that if (1) the geo-acoustic profile is well known and is approximately homogenous on spatial scales on the order of source-receiver ranges and (2) the bathymetry and SSP are properly taken into account, then the received acoustic field can be well predicted along range-dependent propagation paths. This conclusion, using real data, is consistent with the results in ref. [1] that considered only simulated data.

Figure 3 shows the comparison between the simulated and measured TL at 53, 103, 153, and 503 Hz. The propagation is upslope along the same propagation track as the light bulb event. While the overall agreement is fair, one observes a mismatch in phase that increases as the range and frequency increases. The small phase mismatch evident in Fig. 3 is not apparent in the time series in Fig. 2, at least not on the temporal scale examined.

It is not possible to tell whether the TL mismatch is a result of a small error in the geo-acoustic profile, such as could occur if the properties of the seabed were not constant over the propagation path, or if the measured SSP's did not properly represent the true range-dependence of the SSP in the water column at the time of the acoustic measurements. Most likely we may ascribe this mismatch to a slightly range-dependent SSP mismatch. The change in sediment thickness, known to increase as one proceeds to deeper water, is not thought to be an important factor since the sediment thickness is already on the order of 70 m at the receiver location. To use the range-dependent TL data to estimate geo-acoustic properties of the seabed, one would in principle need additional variables in an inversion representing perturbations of a nominal representation of the range-dependent waveguide based on measurements and previous information, such as the inversions performed along constant water depth propagation paths. Clearly, this makes the inverse problem significantly more difficult as compared to range-independent inversions.

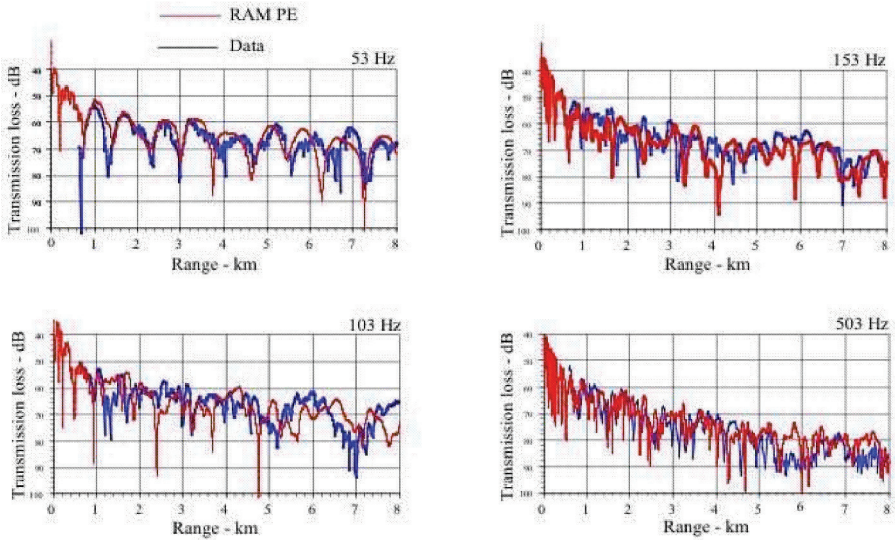


Figure 3. Comparison of measured and modeled TL.

2.2 Propagation in Waveguide With Both Range and Azimuth Dependence

A second example of propagation along a slope is from an experiment conducted off the coast of the United States about 70 miles east of Jacksonville, FL. As in the case of the Gulf of Mexico experiment, light bulb implosions were used for sources. Figure 4 illustrates the geometry of the waveguide, a proposed sediment structure, and the position of the sources and receiver for the range-dependent component of the experiment. An HLA on the bottom was oriented with its line of bearing along the 50 m water depth isobath.

Hovem and Knobles [5] reported an analysis of acoustic data from sources deployed on the 50 m isobath. Stotts et al. made another analysis of the same experiment, for the HLA deployed in deeper water [6]. Since the array was about 530 m in length (about 11 water depths), and the seabed had a sound speed ratio greater than unity, a critical angle effect was observed across the length of the array for the time series generated by light bulb implosions for the range-independent analysis in ref. [5]. Specifically, for short-range events new arrivals appeared with increasing source-receiver range on the array, and the corresponding inferred critical angle gives a surface sediment speed of about 1800 m/s.

It was found that employing the geo-acoustic profile derived in [5] the acoustic model reproduced well the measured data at short ranges; however, as the source-receiver range increased, the predicted time series was too long for both upslope and downslope events. A remedy was to allow the sediment to become softer as the range increased as depicted in Fig. 4. Figures 5 and 6 show the comparison of the measured and simulated time series in the 50-500 Hz band for both upslope and downslope events. The time spread evolution is governed by acoustic interaction with a soft and absorptive seabed away from the receiver, which rests on a highly reflective low loss bottom. A possible scenario that explains the inferred sediment structure is the following. Near the 50 m isobath the Gulf Stream intruded for a period of time and stripped off a portion of a softer sediment area. The HLA deployed just happened to be placed on the spot where the softer sediment had been removed by Gulf Stream currents. While this may not be the only possibility, it does demonstrate the more important point that geo-acoustic inversion in littoral areas will in general need to account for the possibility that the geo-acoustic structure is both range- and azimuth- dependent.

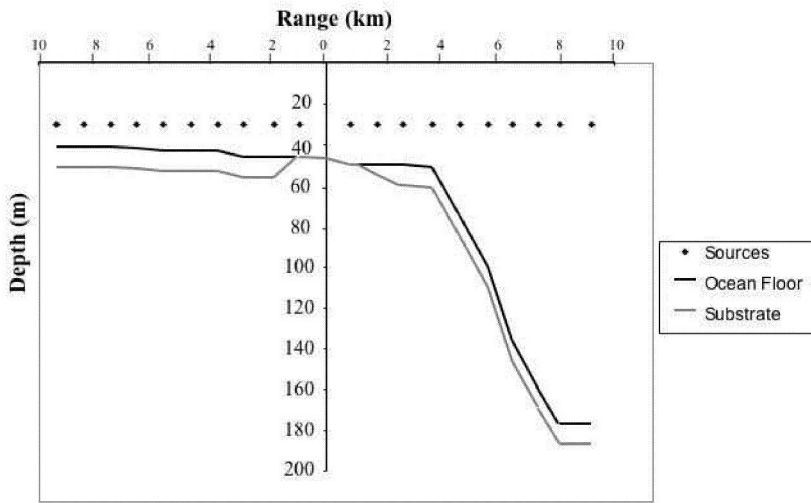


Figure 4. Waveguide geometry and location of sources and receivers.

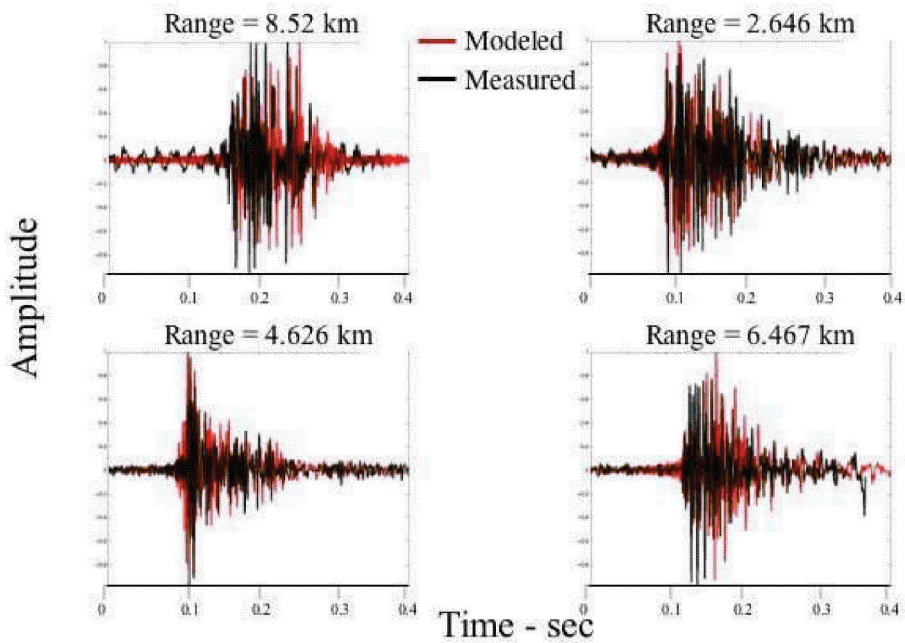


Figure 5. Comparison of measured and modeled time series for upslope propagation.

2.3 Effects of Scattering in a Wedge Shaped Waveguide

While the perfect 3 – *D* wedge is at best an idealization of propagation in a continental shelf environment, it is useful to demonstrate the issue of coupling of the physical mechanisms of scattering from, and absorption within, the seabed. A numerical implementation of a reverberation model was

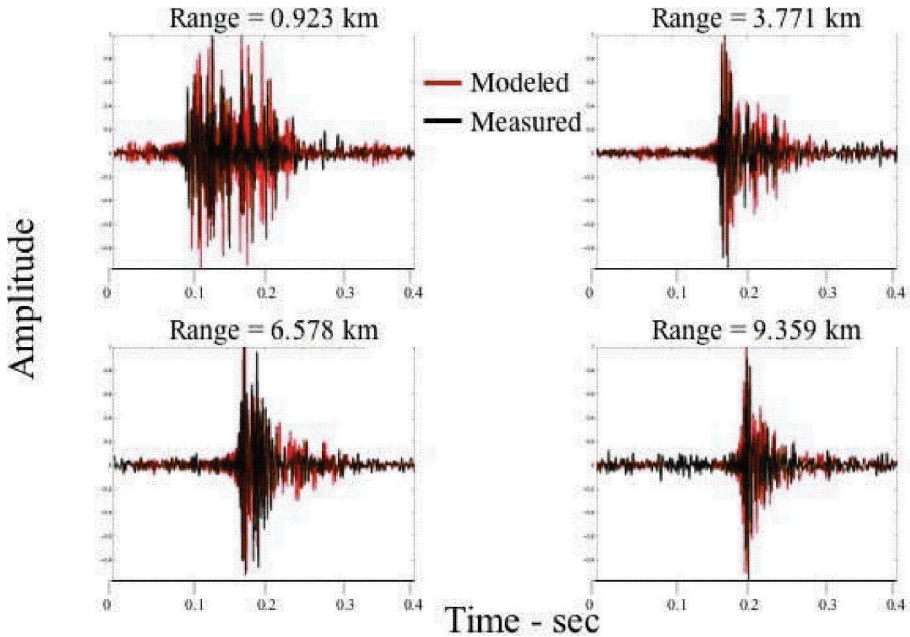


Figure 6. Comparison of measured and modeled time series for downslope propagation.

developed by extending a 2-D two-way coupled mode approach to a 3 - D two-way coupled mode approach for a selected class of problems. The approach to an exact 3 - D reverberation model in a Cartesian coordinate system solves the 2 - D coupled mode integral equations [7, 9] for modal amplitudes $R(x, z)$, where represents the y component of the acoustic wavenumber. The modal amplitudes in the full 3 - D space, $R(x, y, z)$, are recovered as a Fourier integral of $R(x, z)$ over [10].

Figure 7 compares the transmission loss at 10 Hz along the y -axis at a depth of 200 m for a 3 - D wedge for an analytic solution [11] and the 3 - D coupled mode result. The slope of the wedge is 5.72 degrees and the source depth is 30 m. This computation was made as one of several methods to validate the numerical approach. The interference pattern results from the well known effect that each mode interferes with itself because it has both a forward and a refractive component. Figure 8 shows the prediction of the 3 - D coupled mode result when a roughness is superimposed on the surface of the wedge. The rough surface was defined as a sinusoidal water depth variation in the x -direction with a wavelength of half the acoustic wavelength and an amplitude of 5 m. The roughness causes scattering; thus, the refractive component of each mode is reduced causing an overall loss of flux in the forward y direction. This result raises the issue of how one separates in a unique manner the effects of a loss of flux due to rough surface and volume scattering and loss due to absorption within the volume of the seabed. Both mechanisms create a loss of flux in the forward direction. In the present example the loss of intensity of the refracted arrival due to scattering causes an increase in the transmission loss along the y -axis. Clearly, this effect could also have been simulated by sediment absorption. It remains an open question as to how future experiments can distinguish these two effects.

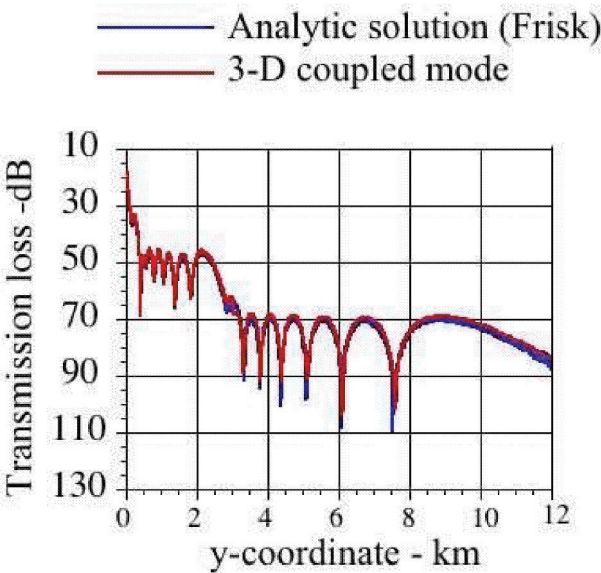


Figure 7. Comparison of analytic solution at 10 Hz and 3-D coupled-mode solution for infinite wedge.

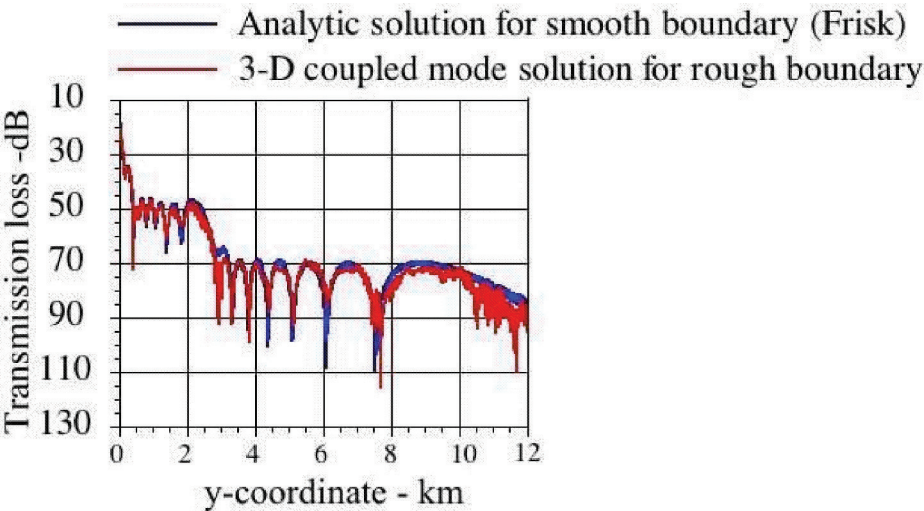


Figure 8. Demonstration of the effects of surface roughness added to the infinite wedge problem.

3 Summary

Several examples were presented that involved the propagation of sound in range- and azimuth-dependent littoral waveguides. The examples demonstrate how range and azimuth inhomogeneities in the SSP, the geo-acoustic profile, and scattering from the seabed complicates the definition of a geo-acoustic inverse problem. It should not be concluded that meaningful geo-acoustic inversions in such waveguides are not feasible: instead, the examples give a more realistic picture of issues that inverse problems in littoral areas need to address.

Acknowledgements

This work was supported by the U.S. Office of Naval Research.

References

1. See papers in special Issue on Geo-acoustic Inversion in Range-Dependent Ocean Waveguides, IEEE J. Oceanic Eng. 28, (2003).
2. Knobles D. P., Koch R. A., Thompson L. A. and Focke K. C., Sound propagation in shallow water and geo-acoustic inversion. *J. Acoust. Soc. Am.* **113**, 205–222 (2003).
3. Koch R. A. and Knobles D. P., Geo-acoustic inversion with ships as sources. *J. Acoust. Soc. Am.* **117**, 626–637 (2005).
4. Collins M. D., A split step Pade solution for the parabolic equation method. *J. Acoust. Soc. Am.* **93**, 1736 (1993).
5. Hovem J. and Knobles D. P., A range-dependent propagation model based on a combination of ray theory and plane-wave reflection coefficients. *J. Acoust. Soc. Am.* **112**, 2393 (2002).
6. Stotts S. A., Knobles D. P., Koch R. A., Grant D. E., Focke K. C. and Cook A. J., Geo-acoustic inversion in range-dependent ocean environments using a plane wave reflection coefficient approach. *J. Acoust. Soc. Am.* **115**, 1078–1102 (2004).
7. Knobles D. P., Solutions of coupled-mode equations with a large dimension in underwater acoustics. *J. Acoust. Soc. Am.* **96**, 1741–1747 (1994).
8. Knobles D. P., Stotts S. A., Koch R. A. and Udagawa T., Integral equation coupled mode approach applied to internal wave problems. *J. Acoust. Soc. Am.* **9**, 149–167 (2001).
9. Knobles D. P., Stotts S. A., and Koch R. A., Low frequency coupled mode sound propagation over a continental shelf. *J. Acoust. Soc. Am.* **113**, 113, 781–787 (2003).
10. Knobles D. P., Scattering in a 3-D wedge with a rough bottom boundary. *J. Acoust. Soc. Am.* **114**, 2429 (2003).
11. Frisk G. V., Ocean and Seabed Acoustics: A Theory of Wave Propagation (Prentice-Hall, Englewood Cliffs, NJ, 1994).

Author Index

B

Becker K. M.	99
Blondel Ph.	155
Boni P.	109
Buckingham M. J.	257

C

Cato Douglas C.	303
Chapman N. R.	289, 309
Christian H.	171
Coelho E.	197
Coffin M.	47
Cook A.	321
Cosci M.	155

D

Dizaji R. M.	289
Dobbins P. F.	155
Dong H.	241
Dosso S. E.	17, 87

F

Fallat M.	73, 87
Furlong A.	171

G

Garlan T.	1
Gerig A. L.	109
Gerstoft P.	233, 303
Giddens E. M.	257
Gray M.	321
Guerra M.	303

H

Harrison C.	73, 265, 281
Hermant J.-P.	29, 183
Hines P. C.	47
Hodgkiss W.	233
Holland C. W.	17, 87, 109
Hovem J. M.	241
Huang C.-F.	233

I

Isakson M. J.	213
---------------	-----

J

Jakacki J.	125
Jayasundere N.	155
Jesus S. M.	197

K

Karasalo I.	137
Kirlin L.	289
Klusek Z.	125
Knobles. D. P.	321
Koch R. A.	321

L

Le Gac J.-C.	1
Li X.	241

M

Meyer M.	29
Miller J.	57
Moll C.	265

N

Neilsen T.	213
Nielsen P. L.	73, 87
Noad M.	303

O

Osler J.	171
----------	-----

P

Potty G.	57
----------	----

S

Siderius M.	87
Simonet F.	257
Simons D. G.	265
Skogqvist P.	137
Soares C.	197
Stéphan Y.	1
Stokes D.	303

T

Tęgowski J.	125
Thode A.	303
Tollefsen D.	309

W

Weber N.	1
Wilmot M. J.	309
Worley A.	213

Subject Index

A

Active phase conjugation, 34
adaptive simplex, 19, 87, 90, 96, 309, 312, 319
Adjoint modelling, 30
airborne source, 260
aircraft noise, 257
ambient noise, 269
Archie's Law, 176
array
 horizontal, 74, 202, 309, 321
 tilt, 236
 vertical, 31, 197, 198, 265, 269, 303, 309
ASIAEX experiment, 62, 63, 233, 236
ASSA, 19, 23, 78, 309, 310, 312

B

Backpropagation, 29
backscattered signal, 129
backscattering, 3, 129
Barents Sea experiment, 310
Bartlett processor, 89, 202, 236, 311
Bayesian inversion, 17–20, 22, 24, 25, 90, 96, 234
beamforming, 202, 265
Biot/Stoll model, 213, 214, 218, 219, 225, 229
BOUNDARY experiment, 74–76, 85, 123, 285, 286
boundary integral equation, 137
buried
 hydrophone, 257
 object, 138, 156
 organic material, 125
 target, 156
 toxic waste, 155, 156

C

clutter, 109
coherent reflection, 2
covariance, 19, 205

D

differential evolution, 265
downhill simplex method, 19, 90, 148, 167, 312

E

echo sounder, 2, 66
EOFs, 199, 236

F

factorization
 in eigenvalues, 205
 spectral, 281, 284–287
FAF'96 experiment, 34
Focalisation, 30
focalization, 198
Free Fall Cone Penetrometer, 171

G

GAIN, 281
GAMARAY, 78, 87
genetic algorithms, 268, 290
geoacoustic inversion, 2, 3, 5, 18, 19, 73, 74, 76, 88, 236, 238, 241, 310, 312, 319, 321
GMRES method, 137
GPS, 236, 310
Gulf of Mexico experiment, 322

H

HARC, 303

I

internal tide, 198
internal waves, 198
INTIFANTE'00 sea trial, 197, 198

J

Jacksonville experiment, 324

K

Kirchhoff approximation, 137, 156

L

leaky modes, 313

M

MAPEX experiment, 87, 88
Margaret's Bay deployments, 173
Matched equivalent-space signal, 30
matched-field
 inversion, 19, 236, 289, 309–311
 localization, 309

processing, 47, 73, 205
 processor, 205
 tomography, 197
 maximum likelihood, 19, 202, 234
 MFP, 303

mismatch

amplitude, 145
 data, 89
 estimate, 198
 model, 204
 sound speed, 213

modal inversion, 100

mode dispersion, 57

Model-based matched filter, 35

N

New Jersey shelf experiment, 99

non-linear inversion, 57

North Elba experiment, 269

O

OASES, 213, 220, 221, 226, 246, 247

ORCA, 294, 309, 313

P

PACIFIC SHELF experiment, 291

parabolic equation, 241

Pekeris waveguide, 57, 106, 246

perturbation approach, 57, 313

Phase regulated back wave propagation, 33

PlaneRay, 242, 244, 246

Posidonia oceanica, 184

PRIMER experiment, 62, 63

Processor

incoherent cross-frequency, 31
 matched-phase, 31
 minimum variance, 31
 minimum variance distortionless
 response, 31

propeller harmonics, 257, 258, 260

R

Ragusa Ridge, 110

RAM, 252

ray tracing, 137, 241

ray travel time, 197

Ray–Kirchhoff method, 138

Retrogradation, 30

reverberation, 17, 74

Ricker wavelet, 246

S

SAGA, 235, 236, 254, 305

SCARAB experiment, 21

scattering, 2, 74, 122, 129, 137, 155

SCOGLIO AFRICA'95 Experiment, 184

seabed characterization, 1, 2, 4–7, 11–13

sediment layer inversion, 269

sediment probe, 171

sediment tomography, 57

simulated annealing, 19, 78, 87, 90, 96, 213,
 214, 221, 227, 290, 309, 310, 312,
 319

SiPLAB, 197

SITAR project, 138, 155–157, 165, 167,
 168, 170

SNAP, 236

sonar, 5, 213, 226, 310

Split-step Fourier algorithm, 32

submarine volcanoes, 109

SUPRA-GAIN, 281

SUS source, 310

SWELLEX-3 experiment, 36

T

tank experiment, 131, 214

Time reversal, 30

transmission loss, 73, 171, 233, 244, 260

U

USTICA'99, 185

W

wavelet based approach, 58

WEST SARDINIA'89 experiment, 31

whale song, 303

Y

YELLOW SHARK'94 Experiment, 30

